

transactions of the ASME

Published Quarterly by
The American Society of
Mechanical Engineers
Volume 97 • Series C • Number 1
FEBRUARY 1975

journal of heat transfer

EDITORIAL STAFF

Editor, **J. J. JAKLITSCH, JR.**
Production Editor,
MARINA EVDCHENKO

HEAT TRANSFER DIVISION

Chairman, **L. H. BACK**
Secretary, **F. W. SCHMIDT**
Senior Technical Editor, **E. M. SPARROW**
Technical Editor, **L. H. BACK**
Technical Editor, **A. E. BERGLES**
Technical Editor, **R. B. KINNEY**
Technical Editor, **J. L. NOVOTNY**
Technical Editor, **R. SIEGEL**
Technical Editor, **R. L. WEBB**

POLICY BOARD, COMMUNICATIONS

Chairman and Vice-President
S. P. KEZIOS

Members-at-Large

R. E. ABBOTT
I. BERMAN
J. W. HOLL
D. F. WILCOCK

Policy Board Representatives

Basic Engineering, **A. R. CATHERON**
General Engineering, **S. P. ROGACKI**
Industry, **J. E. ORTLOFF**
Power, **G. P. COOPER**
Research, **A. P. FRAAS**
Codes and Stds., **P. M. BRISTER**
Nom. Com. Rep.,
J. W. HOLL
Business Staff
345 E. 47th St.
New York, N. Y. 10017
212/752-6800

Mng. Dir., Com., **C. O. SANDERSON**

OFFICERS OF THE ASME

President, **R. B. ROBERTSON**
Exec. Dir. & Sec'y, **ROGERS B. FINCH**
Treasurer, **DONALD E. MARLOWE**

EDITED and PUBLISHED quarterly at the
offices of The American Society of
Mechanical Engineers, United Engineering
Center, 345 E. 47th St., New York, N.Y.
10017. Cable address, "Mechanear,"
New York. Second-class postage paid
at New York, N. Y., and at additional
mailing offices.

CHANGES OF ADDRESS must be received at
Society headquarters seven weeks before
they are to be effective. Please send
old label and new address.

PRICES: To members, \$15.00, annually; to
nonmembers, \$30.00. Single copies, \$10.00 each.
Add \$1.50 for postage to countries outside the
United States and Canada.

STATEMENT from By-Laws. The Society shall not
be responsible for statements or opinions
advanced in papers or . . . printed in its
publications (B13, Par. 4).

COPYRIGHT 1975 by the American Society of
Mechanical Engineers. Reprints from this
publication may be made on condition that full
credit be given the TRANSACTIONS OF THE
ASME, SERIES C—JOURNAL OF HEAT
TRANSFER, and the author and date of
publication stated.

INDEXED by the Engineering Index, Inc.

- 1 Jerome L. Novotny, 1934-1974
- 1 Journal of Heat Transfer Referees, 1974
- 4 1975 Winter Annual Meeting—Call for Papers
- 5 Mean Temperature Difference for Heat Exchanger Design—A General Approximate Explicit Equation (75-HT-S)
W. Roetzel and F. J. L. Nicole
- 9 Heat Transfer and Friction Loss Performance of Perforated Heat Exchanger Surfaces (75-HT-J)
C. Y. Liang and Wen-Jei Yang
- 16 Modified Single-Blow Technique for Performance Evaluation on Heat Transfer Surfaces (75-HT-V)
C. Y. Liang and Wen-Jei Yang
- 22 Heat Transfer and Temperature Field Experiments in a Cavity With Rotation, Recirculation, and Coolant Throughflow (75-HT-P)
E. M. Sparrow, T. C. Buszkiewicz, and E. R. G. Eckert
- 29 An Analytical Solution for a Planar Nongray Medium in Radiative Equilibrium (75-HT-Z)
C. C. Lin and S. H. Chan
- 35 Radiation Induced Thermal Stratification in Surface Layers of Stagnant Water (75-HT-CC)
D. M. Snider and R. Viscanta
- 41 The Influence of Radiation on Arc Constriction in the Anode Region (75-HT-N)
E. Pfender and J. Schafer
- 47 Natural Convection in a Horizontal Layer of Water Cooled From Above to Near Freezing (75-HT-H)
R. E. Forbes and J. W. Cooper
- 54 Pseudosteady-State Natural Convection Inside Sphere (75-HT-Y)
M. Y. Chow and R. G. Akins
- 60 Transport Phenomena in Thermally Stratified Boundary Layers (75-HT-BB)
D. W. Pepper and S. C. Lee
- 66 Laminar Flow in a Porous Tube With Suction (73-WA/HT-1)
J. P. Quaile and E. K. Levy
- 72 A Theoretical Study of Dropwise Condensation (75-HT-U)
H. Tanaka
- 79 Film Condensation on Inclined Plane Surfaces (75-HT-DD)
N. V. Suryanarayana and G. L. Malchow
- 83 Measurement of the Condensation Coefficient of Mercury by a Molecular Beam Method (75-HT-Q)
U. Narusawa and G. S. Springer
- 88 Laser Interferometric Investigation of the Microlayer Evaporation Phenomenon (75-HT-T)
C. M. Voustinos and R. L. Judd
- 93 Nucleation Site Actiation in Saturated Boiling (75-HT-X)
M. Shoukri and R. L. Judd
- 99 New Method to Determine Latent Heat of Liquids by Means of Dielectric Data (75-HT-R)
W. Leidenfrost
- 104 Convective Heat Transfer From a Desert Surface (75-HT-AA)
R. T. Bailey, J. W. Mitchell, and W. A. Beckman
- 110 Erosion of Metals by High Pressure Combustion Gases: Inert and Reactive Erosion (75-HT-M)
E. G. Plett, A. C. Alkidas, R. E. Shrader, and M. Summerfield
- 116 Toward a General Theory of Cutting: A Relationship Between the Incident Power Density and the Cut Speed (75-HT-W)
K. A. Bunting and G. Cornfield
- 123 Microwave Induced Temperature Rises in Rabbit Eyes in Cataract Research (75-HT-O)
A. F. Emery, P. Kramar, A. W. Guy, and J. C. Lin

(Contents continued on page 28)

CONTENTS (CONTINUED)

Technical Briefs

- 129 Free Convection From a Horizontal Cylinder With Isothermal and Constant Heat Flux Surface Conditions
C. B. Kim, T. J. Pontikes, and D. E. Wollersheim
- 130 Lower Bounds to the Critical Rayleigh Number for Completely Confined Fluids Inside Arbitrary Configurations
D. Pnueli
- 133 The Effect on Laminar Free Convection Heat Transfer of the Temperature Dependence of the Coefficient of Volumetric Expansion
A. Brown
- 135 Combined Free and Forced Convection Laminar Heat Transfer in a Vertical Annulus
D. Maitra and K. Subba Raju
- 137 On the Determination of Temperature Distribution in Laminar Pipe Flow With a Step Change in Wall Heat Flux
C. E. Smith, M. Faghri, and J. R. Welty
- 139 Laminar Film Condensation on a Vertical Plate—Effect of Magnetic Field
K. N. Murty, C. K. Sarma, and P. K. Sarma
- 141 Laminar Film Condensation With Heat Generation
M. Epstein and D. H. Cho
- 142 Nonstationary Homogeneous Nucleation
K. G. Harstad
- 144 Application of the Reynolds Flux Model of Critical Heat Flux for Direct Heat Flux Scaling in Nonuniform Rod Bundles
J. C. Purcupile, F. E. Motley, and F. F. Cadek
- 145 Thermal Stresses in a Sphere Due to Local Heating Followed by Complete Cooling
T. S. Chen, K. Thirumalai, and J. B. Cheung
- 148 Heating Time and Heating Temperature Dependence of Thermal Conductivity of As-Received Aluminum Alloy 2024-T351
S. Al-Araji and J. V. Beck
- 149 Discontinuities in Radiative Transfer Analysis Using Quadrature Formulas
K. C. Weston and D. W. Drago
- 151 Effects of Radiative Cooling on the Temperature Distribution in MHD Channel Flows
D. R. Wilson and A. Haji-Shiekh
- 153 Flame Spread Over Thin Solid Fuels
P. J. Pagni
- 155 Numerical Prediction of High Altitude Zero-Pressure Balloon Vertical Motion
J. F. Kreider and F. Kreith

Discussions

- 158 Discussion on a previously published paper by R. E. Chupp and R. Viskanta
- 158 Discussion on a previously published paper by J. C. Muehlbauer, J. D. Hatcher, D. W. Lyons, and J. E. Sunderland
- 159 Discussion on a previously published paper by J. H. Lienhard and V. K. Dhir

Errata

- 78 An errata on G. Ahmadi, "Heat Conduction in Solids With Random Initial Conditions," published in the Nov. 1974 issue of the *Journal of Heat Transfer*, pp. 474-477
- 3 Prior Publication Notice

Jerome L. Novotny, 1934–1974

The editors of the JOURNAL OF HEAT TRANSFER note with sadness the passing of our colleague, Professor Jerome L. Novotny of the University of Notre Dame. As was his way in everything that he undertook, Professor Novotny served the Journal as a dedicated, responsible, and energetic editor. He was also highly productive in scholarly and professional activities, having authored or co-authored 36 technical papers and directed nine doctoral dissertations. His ASME involvements included four technical committees in the Heat Transfer Division as well as his services as a Technical Editor. The heat transfer community has lost a valued member with the passing of Professor Novotny.

W. Roetzel¹

Senior Chief Research Officer.

F. J. L. Nicole²

Senior Research Officer.

Chemical Engineering Research Group,
Council for Scientific and Industrial Research,
Pretoria, South Africa

Mean Temperature Difference for Heat Exchanger Design—A General Approximate Explicit Equation

An approximate equation together with empirical coefficients is presented for the fast calculation of the mean temperature difference of nine countercurrent cross-flow arrangements, as applied in air-cooled heat exchangers. The same equation can be used for other flow systems, as demonstrated for one shell-and-tube arrangement.

1 Introduction

In heat exchanger design a mean temperature difference is usually applied, and considerable attention has been given to its estimation [1–14].³ For many flow arrangements various approaches, mainly using diagrams, are available which are very useful for manual design calculations. For computerized cost-optimized design [15] using fast calculation methods [16] diagrams cannot be used directly and equations are preferable for the determination of the mean temperature difference. For countercurrent cross-flow arrangements, as applied in air-cooled heat exchangers, equations were developed [12, 17] using a model which was also shown experimentally [18] to be applicable for fin-tube bundles. However, these equations are implicit in terms of the desired mean temperature difference and they have to be solved by trial and error which is very time consuming even on a digital computer.

Furthermore, for those flow arrangements for which analytical equations exist, these are frequently implicit or very complicated. Thus for computerized design explicit simple approximate equations are desirable for the fast calculation of mean temperature difference with sufficient accuracy.

2 General Equation

The idea is to use a generally valid type of empirical equation with a different set of coefficients for each flow arrangement. With

¹ Present address: Bayer AG, Verfahrenstechnik R150, 415 Krefeld 11, Germany.

² Present address: South African Coal, Oil & Gas Corporation, Sasolburg, 9570, South Africa.

³ Numbers in brackets designate References at end of paper.

Contributed by the Heat Transfer Division for publication in the JOURNAL OF HEAT TRANSFER. Manuscript received by the Heat Transfer Division July 23, 1974. Paper No. 75-HT-S.

respect to the limiting case of pure countercurrent flow the concept of correcting the logarithmic mean temperature difference

$$\Delta T_{1,m} = \frac{(T_1 - t_2) - (T_2 - t_1)}{\ln \frac{(T_1 - t_2)}{(T_2 - t_1)}} \quad (1)$$

according to

$$\Delta T_m = F_T \cdot \Delta T_{1,m} \quad (2)$$

appears very useful for an empirical approach. In equation (2) the actual mean temperature differences on both sides can also be replaced by the dimensionless mean temperature differences

$$r = \frac{\Delta T_m}{T_1 - t_1} \quad (3)$$

and

$$r_{1,m} = \frac{\Delta T_{1,m}}{T_1 - t_1} \quad (4)$$

yielding:

$$r = F_T \cdot r_{1,m} \quad (5)$$

The dimensionless logarithmic mean temperature difference can be calculated from equations (1) and (4) or it can be determined from the effectiveness of both streams

$$p = \frac{T_1 - T_2}{T_1 - t_1} \quad (6)$$

and

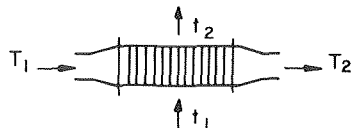
$$q = \frac{t_2 - t_1}{T_1 - t_1} \quad (7)$$

using

$$r_{1,m} = \frac{p - q}{\ln \frac{1 - q}{1 - p}} \quad (8)$$

The correction factor F_T in equations (2) or (5) is now expressed

Table 1

Table 1 Values of $a_{i,k}$ for 1 row, 1 pass					
	$i = 1$	2	3	4	
$k = 1$	-4.62×10^{-1}	-3.13×10^{-2}	-1.74×10^{-1}	-4.20×10^{-2}	
2	5.08×10^0	5.29×10^{-1}	1.32×10^0	3.47×10^{-1}	
3	-1.57×10^1	-2.37×10^0	-2.93×10^0	-8.53×10^{-1}	
4	1.72×10^1	3.18×10^0	1.99×10^0	6.49×10^{-1}	

as a function of this dimensionless logarithmic mean temperature difference for countercurrent flow and the ratio

$$R = \frac{p}{q} = \frac{T_1 - T_2}{t_2 - t_1} \quad (9)$$

Because $r_{1,m}$ is introduced as a variable one should preferably (but not necessarily) use equations (5) and (3) for the calculation of the mean temperature difference.

After considering the general form of mean temperature difference diagrams and the boundary conditions the following function was found to be suitable for the correction factor

$$F_T = 1 - \sum_{i=1}^m \sum_{k=1}^n a_{i,k} \cdot (1 - r_{1,m})^k \cdot \sin(2 \cdot i \cdot \arctan R) \quad (10)$$

Independent of the (finite) values of the coefficients $a_{i,k}$, the function yields the following correct limiting values. For $R = 0$ or $R = \infty$ equation (10) gives $F_T = 1$; if one stream is isothermal, the mean temperature difference is equal to the logarithmic mean temperature difference. In the other limiting case where both fluid temperatures change very little $p \rightarrow 0$ and $q \rightarrow 0$, then $r_{1,m} \rightarrow 1$ and equation (10) yields $F_T \rightarrow 1$ and there is no need to distinguish between different flow arrangements.

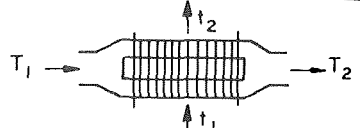
A further big advantage of equation (10) is that one can easily distinguish between symmetric and asymmetric flow arrangements. In the case of a symmetric flow arrangement where one can interchange both streams yielding the same mean temperature difference, (e.g., pure crossflow) all constants $a_{i,k}$ with even values of i are zero.

3 Determination of Coefficients for Cross-Flow Arrangements

3.1 Exact Values. For determination of the exact values for the mean temperature difference attained in an air-cooled heat exchanger fin-tube bundle, the following assumptions have been shown to be applicable [18].

(i) The fluid flowing in turbulent flow inside the tubes is completely mixed within any one tube at a given cross section (heat transfer coefficient, however, is finite) but unmixed from row to row within any one pass, and then completely mixed in box-type headers between passes.

Table 2

Table 2 Values of $a_{i,k}$ for 2 row, 1 pass					
	$i = 1$	2	3	4	
$k = 1$	-3.34×10^{-1}	-1.54×10^{-1}	-8.65×10^{-2}	5.53×10^{-2}	
2	3.30×10^0	1.28×10^0	5.46×10^{-1}	-4.05×10^{-1}	
3	-8.70×10^0	-3.35×10^0	-9.29×10^{-1}	9.53×10^{-1}	
4	8.70×10^0	2.83×10^0	4.71×10^{-1}	-7.17×10^{-1}	

(ii) The presence of transverse fins applied externally to the tubes prevents the air from mixing in the longitudinal direction parallel to the tubes and effectively prevents mixing in this direction even between tube rows provided the tube pitch is not too large compared to the fin-tube dimensions.

(iii) Complete mixing of the air occurs in the direction normal to the air flow and parallel to the fins.

Exact values of the mean temperature difference over the entire range of attainable stream effectivenesses were calculated by the iterative solution of the implicit equations for the following arrangements where the reference indicates the source of the equations:

- (i) 1 to 4 rows in a single pass [12]
- (ii) 2 rows with a single row per pass [4]
- (iii) 3 rows with a single row per pass [11]
- (iv) 4 rows with two rows per pass and with a single row per pass [17]

For the pure cross-flow case the exact values were calculated by summing the terms in the double infinite series developed by Nusselt [1].

3.2 Determination of Coefficients. The coefficients $a_{i,k}$ of the approximating equation (10), were calculated using a standard least squares estimation program [19]. This program was used to minimize the absolute error of the (dimensionless) mean temperature difference. Thus the relative accuracy is increased in the normal operating region where higher mean temperature differences are obtained. The largest relative errors occur when the mean temperature difference tends to zero but this is outside the range used in practical design.

For asymmetric arrangements, the coefficients were calculated by fitting a surface through 80 exact values of the dimensionless mean temperature difference according to equations (10) and (5). Sixteen coefficients with $m = 4$ and $n = 4$ were found to be necessary for a sufficiently accurate fit. The coefficients $a_{i,k}$ are given for each of eight arrangements in Tables 1-8. The absolute standard error in dimensionless mean temperature difference ($0 \leq r \leq 1$) is in all these cases, less than 4×10^{-3} .

The pure cross-flow case, i.e., and arrangement where both

Nomenclature

$a_{i,k}$ = coefficients in equation (10)
 F_T = logarithmic mean temperature difference correction factor
 i, k = summation counters in equation (10)
 m, n = maximum values of i and k , respectively
 p, q = effectivenesses defined by equations (6) and (7)

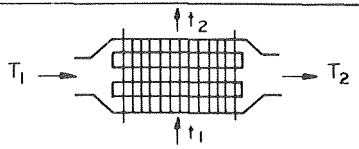
R = ratio of effectivenesses (equation (9))
 r = dimensionless mean temperature difference
 $r_{1,m}$ = dimensionless mean temperature difference in countercurrent flow
 T, t = fluid temperatures as defined in Tables 1-10

$\Delta T_{1,m}$ = logarithmic mean temperature difference for countercurrent flow
 ΔT_m = mean temperature difference for a given flow arrangement

Subscripts

1 = inlet conditions
 2 = outlet conditions

Table 3

Table 3 Values of $a_{i,k}$ for 3 row, 1 pass					
	$i = 1$	2	3	4	
$k = 1$	-8.74×10^{-2}	-3.18×10^{-2}	-1.83×10^{-2}	7.10×10^{-3}	
2	1.05×10^0	2.74×10^{-4}	1.23×10^{-1}	-4.99×10^{-2}	
3	-2.45×10^0	-7.46×10^{-1}	-1.56×10^{-1}	1.09×10^{-1}	
4	3.21×10^0	6.68×10^{-1}	6.17×10^{-2}	-7.46×10^{-2}	

streams are considered to be completely unmixed, is a symmetric case. Only eight coefficients are necessary and 40 exact values were used. The coefficients $a_{i,k}$ are given in Table 9. The absolute standard error is 1×10^{-3} .

4 Extension of Equation to Other Flow Arrangements

In order to show that the same approximating equation (10) is applicable for other flow arrangements the coefficients $a_{i,k}$ were determined for a 1-2 shell-and-tube exchanger, i.e., an exchanger with 1 shell pass and 2 tube passes.

The exact values were calculated using the equation given by Bowman, Mueller, and Nagle [4]. As this is also a symmetrical case, only 40 exact values were used for the determination of the eight coefficients $a_{i,k}$. These are given in Table 10. The standard error is 4×10^{-3} .

5 Conclusions

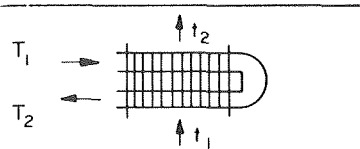
(i) The approximating equation (10) together with the coefficients given in Tables 1-9 is ideal for computerized design of air-cooled heat exchangers, because iterative determination of the mean temperature difference is avoided. As good accuracy was obtained extension of equation (10) to higher values of m and n does not appear worth while.

(ii) Equation (10) should be applicable for any flow arrangements (e.g., shell-and-tube heat exchangers).

References

- 1 Nusse, W., "Eine neue Formel für den Wärmedurchgang im Kreuzstrom," *Techn. Mechan. u. Thermodynamik*, Vol. 1, No. 12, 1930, pp. 417-422.
- 2 Nagle, W. M., "Mean Temperature Differences in Multipass Heat Exchangers," *Ind. & Engng. Chem.*, Vol. 25, No. 6, June 1933, pp. 604-609.
- 3 Smith, D. M., "Mean Temperature Difference in Cross-Flow," *Engineering*, Nov. 1934, pp. 479-81, 606-607.
- 4 Bowman, R. A., Mueller, A. C., and Nagle, W. M. "Mean Temperature Difference in Design," *TRANS. ASME* Vol. 62, May 1940, pp. 283-294.
- 5 Gardner, K. A., "Mean Temperature Difference in Unbalanced-Pass

Table 5

Table 5 Values of $a_{i,k}$ for 2 row, 2 pass					
	$i = 1$	2	3	4	
$k = 1$	-2.35×10^{-1}	-7.73×10^{-2}	-5.98×10^{-2}	5.25×10^{-3}	
2	2.28×10^0	6.32×10^{-1}	3.64×10^{-1}	-1.27×10^{-2}	
3	-6.44×10^0	-1.63×10^0	-6.13×10^{-1}	-1.14×10^{-2}	
4	6.24×10^0	1.35×10^0	2.76×10^{-1}	2.72×10^{-2}	

Exchangers," *Ind. & Engng. Chem.*, Vol. 33, No. 10, Oct. 1941, pp. 1215-1223.

6 Gardner, K. A., "Mean Temperature Difference in Multipass Exchangers," *Ind. & Engng. Chem.*, Vol. 33, No. 12, Dec. 1941, pp. 1495-1500.

7 Takahashi, Y., "Mean Temperature Difference in Multi-Pass Cross-Flow Heat Exchangers," *Transactions. The Japan Society of Mechanical Engineers*, Vol. 8, No. 30/II, 1942, pp. 1-9.

8 Takahashi, Y., "Mean Temperature Difference in Two-pass Cross-Flow Heat Exchangers," *Transactions. The Japan Society of Mechanical Engineers*, Vol. 9, No. 36, 1943, pp. 85-89.

9 Korst, H. H., "Mean Temperature Difference in Multi-Pass Cross-flow Heat Exchangers," *Proceedings of the 1st U. S. National Congress of Applied Mechanics*, ASME, 1952, pp. 949-955.

10 Mason, J. L., "Heat Transfer in Cross-Flow," *Proceedings of the 2nd U. S. National Congress of Applied Mechanics*, ASME, 1955, pp. 801-803.

11 Stevens, R. A., Fernandez, J., and Woolf, J. R., "Mean Temperature Difference in One, Two, and Three-Pass Cross-Flow Heat Exchangers," *TRANS. ASME*, Vol. 79, Feb. 1957, pp. 287-297.

12 Schedwill, H., "Thermische Auslegung von Kreuzstromwärmetauschauschern," *Fortschr.-Ber. VDI-Z.*, Vol. 6, No. 19, 1968.

13 Roetzel, W., "Mittlere Temperaturdifferenz bei Kreuzstrom in einem Rohrbündel-Wärmetauscher," *Brennstof-Wärme-Kraft (BWK)*, Vol. 21, No. 5, 1969, pp. 246-250.

14 *VDI-Wärmeatlas, Berechnungsblätter für den Wärmeübergang*, VDI-Verlag GmbH, Düsseldorf, 1974.

15 Peters, D. L., and Nicole, F. J. L., "Efficient Programming for Cost-Optimised Heat Exchanger Design," *The Chem. Engr.* No. 259, Mar. 1972, pp. 98-111.

16 Roetzel, W., "Heat Exchanger Design With Variable Transfer Coefficients for Cross-Flow and Mixed Flow Arrangements," presented at the Heat Transfer and the Design and Operation of Heat Exchangers Conference, Johannesburg, Apr. 1974. *International Journal of Heat and Mass Transfer*, Vol. 17, 1974, pp. 1037-1049.

17 Nicole, F. J. L., "Mean Temperature Difference in CrossFlow Heat Exchange, Applied to Multipass Air-Cooled Fin-Tube Units With a Finite Number of Rows," MSc (Engng.) thesis, University of Pretoria, CSIR Special Report CHEM 223, Nov. 1972.

18 Nicole, F. J. L., "Mean Temperature Difference for the Design of Air-Cooled Fin-Tube Heat Exchangers," presented at the Heat Transfer and the Design and Operation of Heat Exchangers Conference, Johannesburg, Apr. 1974.

19 Middleton, J. A., "Least-squares Estimation of Non-Linear Parameters—NLIN," Share Program Library Agency, Program Order Number 360D-13.2.003.

Table 4

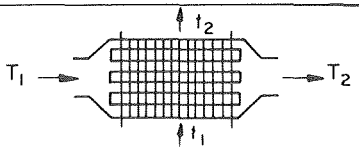
Table 4 Values of $a_{i,k}$ for 4 row, 1 pass					
	$i = 1$	2	3	4	
$k = 1$	-4.14×10^{-2}	-1.39×10^{-2}	-7.23×10^{-3}	6.10×10^{-3}	
2	6.15×10^{-1}	1.23×10^{-1}	5.66×10^{-2}	-4.68×10^{-2}	
3	-1.20×10^0	-3.45×10^{-1}	-4.37×10^{-2}	1.07×10^{-1}	
4	2.06×10^0	3.18×10^{-1}	1.11×10^{-2}	-7.57×10^{-2}	

Table 6

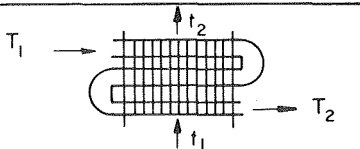
Table 6 Values of $a_{i,k}$ for 3 row, 3 pass					
	$i = 1$	2	3	4	
$k = 1$	-8.43×10^{-1}	3.02×10^{-2}	4.80×10^{-1}	8.12×10^{-2}	
2	5.85×10^0	-9.64×10^{-3}	-3.28×10^0	-8.34×10^{-1}	
3	-1.28×10^1	-2.28×10^{-1}	7.11×10^0	2.19×10^0	
4	9.24×10^0	2.66×10^{-1}	-4.90×10^0	-1.69×10^0	

Table 7

Table 7 Values of $a_{i,k}$ for 4 row, 2 pass					
	$i = 1$	2	3	4	
$k = 1$	-6.05×10^{-1}	2.31×10^{-2}	2.94×10^{-1}	1.98×10^{-2}	
2	4.34×10^0	5.90×10^{-3}	-1.99×10^0	-3.05×10^{-1}	
3	-9.72×10^0	-2.48×10^{-1}	4.32×10^0	8.97×10^{-1}	
4	7.54×10^0	2.87×10^{-1}	-3.00×10^0	-7.31×10^{-1}	

Table 9

Table 9 Values of $a_{i,k}$ for Pure crossflow					
	$i = 1$	2	3	4	
$k = 1$	6.69×10^{-2}	0.0	3.95×10^{-2}	0.0	
2	-2.78×10^{-1}	0.0	-2.20×10^{-1}	0.0	
3	1.11×10^0	0.0	4.54×10^{-1}	0.0	
4	1.36×10^{-1}	0.0	-2.58×10^{-1}	0.0	

Table 8

Table 8 Values of $a_{i,k}$ for 4 row, 4 pass					
	$i = 1$	2	3	4	
$k = 1$	-3.39×10^{-1}	2.77×10^{-2}	1.79×10^{-1}	-1.99×10^{-2}	
2	2.38×10^0	-9.99×10^{-2}	-1.21×10^0	4.00×10^{-2}	
3	-5.26×10^0	9.04×10^{-2}	2.62×10^0	4.94×10^{-2}	
4	3.90×10^0	-8.45×10^{-4}	-1.81×10^0	-9.81×10^{-2}	

Table 10

Table 10 Values of $a_{i,k}$ for 1-2 Shell-8-tube					
	$i = 1$	2	3	4	
$k = 1$	-4.74×10^{-1}	0.0	-2.03×10^{-1}	0.0	
2	5.57×10^0	0.0	1.76×10^0	0.0	
3	-1.86×10^1	0.0	-4.61×10^0	0.0	
4	2.20×10^1	0.0	3.86×10^0	0.0	

APPENDIX

Example

To facilitate application a numerical example is given.

A liquid is to be cooled from 125°C to 45°C using air. The air undergoes a temperature rise of 70°C from 25°C to 95°C. Four tube rows in a single pass are to be used. The mean temperature difference must be determined.

In terms of the stream effectivenesses, with

$$T_1 = 125^\circ\text{C}, T_2 = 45^\circ\text{C},$$

$$t_1 = 25^\circ\text{C}, t_2 = 95^\circ\text{C},$$

$$p = \frac{125 - 45}{125 - 25} = 0.8$$

$$q = \frac{95 - 25}{125 - 25} = 0.7$$

$$R = \frac{125 - 45}{95 - 25} = 1.143$$

Using the coefficients $a_{i,k}$ for 4 rows in a single pass (Table 4) and summing the terms in equation (10) the correction factor, F_T , to be applied to the logarithmic mean temperature difference, $\Delta T_{l,m}$, is

$$F_T = 0.547$$

Using equation (1), or equations (4) and (8) if the stream effectivenesses are preferred for the calculation,

$$\Delta T_{l,m} = 24.7^\circ\text{C}$$

Thus the approximate mean temperature difference for this example using equation (2) is

$$\Delta T_m = 0.547 \times 24.7 = 13.5^\circ\text{C}$$

The true dimensionless mean temperature difference is 0.131 [17] giving a true correction factor from equation (5) of 0.530 and a true $\Delta T_m = 13.1^\circ\text{C}$.

C. Y. Liang¹
Doctoral Graduate.

Wen-Jei Yang
Professor.

Department of Mechanical Engineering,
The University of Michigan,
Ann Arbor, Mich.

Heat Transfer and Friction Loss Performance of Perforated Heat Exchanger Surfaces²

A scale-up modeling technique has been developed to examine the effects of perforation geometry on the heat transfer and friction loss performance of compact heat exchangers having plate-perforated rectangular fin surfaces. The test cores, each consisting of a number of aluminum plates separated by wooden spacers to form parallel flow channels, were tested in a subsonic wind tunnel. The effects of the Reynolds number, plate surface porosity, core frontal porosity, and slot geometry on the heat transfer rate, friction loss, and noise intensity are determined. It is found that under certain circumstances plate perforation will produce significant improvement in heat transfer for the same pressure drop and pumping power. These studies are directed to the design of air-cooled condensers for Rankine cycle automotive engines, marine power propulsion systems, and the dry cooling towers of extra-high capacity electric power plants.

Introduction

With increasing emphasis on economic and energy saving considerations, a great deal of research effort has been devoted to the development of new heat transfer augmentation techniques to produce more efficient heat exchange equipment. The direct goal is to reduce the size of the heat exchanger for a specified heat transfer rate, or to increase the heat transfer capacity of an existing heat exchanger. Different types of heat transfer surfaces have been introduced.

Among the extended surfaces of the plate-fin and the tubular types, the louvered-plate-fin surface has been favored because of its high area-to-volume ratio and its higher heat transfer coefficient resulting from boundary layer interruptions. However, the high heat transfer performance is accompanied by high resistance to flow. The perforated-plate-fin surface has heat transfer and friction loss performance comparable to the louvered-plate fin surface. However, the compactness of the louvered fin type heat exchangers is limited by the geometry of the louvers. If very high compactness is required, such as for the condenser in the Rankine-cycle automotive steam power plant, perhaps only the plain-plate-

fin surface or perforated-plate-fin surface can serve the purpose. The excellence of the latter surface over the former has been demonstrated in reference [1].³

By virtue of its high heat transfer and low friction loss performance, the perforated fin tubular heat exchangers can be made either in small size and light weight as air-cooled condensers in marine [2, 3] and automotive [4, 5] propulsion systems or in large size as air-cooled heat exchangers in dry cooling towers of extra-high capacity electric power plant [6]. Kays [7] has reported that perforation results in a substantial increase in heat transfer performance without introducing a pronounced form drag. This observation was later confirmed by Pucci, et al. [2] and Shah and Osborn [3]. Wong, et al. [4] have tested very compact (22 fins per in.) perforated-fin air-cooled condenser cores for Rankine-cycle automotive propulsion systems. Their test data supported Kay's observation. However, the recent work of Mondt and Siegl [8] has indicated some conflict in the generality of these observations. Over a range of area densities (heat transfer area divided by core volume), no significant improvement in heat transfer was observed for the same pressure drop. Miller and Leeman [9] have also concluded no beneficial effect due to perforations.

This present paper serves two main purposes: (1) to determine the effects of the system parameters on the heat transfer and friction factors of perforated plate surfaces; (2) to rationalize the conflicting performance data previously reported [3, 4, 8, 9]. The system parameters include perforation geometry and arrangement,

¹ Presently Assist. Professor of Engineering, Oakland University, Rochester, Mich.

² This study was supported by the National Science Foundation under Grant number GK 39734.

Contributed by the Heat Transfer Division for publication in the JOURNAL OF HEAT TRANSFER. Manuscript received by the Heat Transfer Division May 16, 1974. Paper No. 75-HT-1.

³ Numbers in brackets designate References at end of paper.

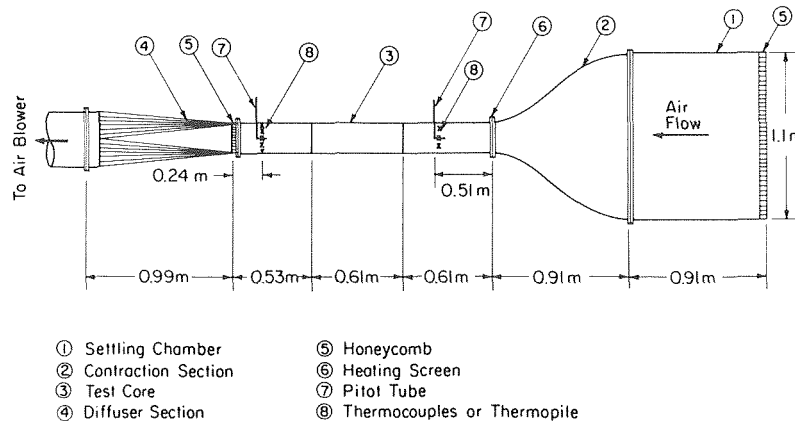


Fig. 1 A schematic diagram of experimental apparatus

channel length-to-hydraulic diameter ratio, plate surface porosity, and frontal core porosity. In order to achieve fine detail, a scale-up modeling technique was chosen, with individual units approximately eight times larger than those fins used in compact condensers.

Experimental Apparatus and Procedure

A schematic diagram of the experimental facility designed for transient testing is presented in Fig. 1. It consisted of a heat exchanger test core situated in a subsonic wind tunnel.

The heat exchanger test core, as shown in Fig. 2, was constructed for scale-up modeling testing of the plate-rectangular fin surface. It consisted of a number of aluminum plates separated by wooden spacers to form parallel flow channels. The aluminum plates were 0.0813 cm thick, 19.1 cm wide and their length varied from 0.152 m to 0.610 m. All plates were identically perforated with slotted holes of a staggered arrangement (see Fig. 3). The number and size of the slotted holes determine the surface porosity (σ_s) while the thickness of the wood slabs was varied to give different values of the frontal porosity (σ_F). The total number of the plates and slabs determines the frontal area of the test core which was 15.2 cm wide (W), 15.2 cm high, and 0.152 m to 0.610 m long (L) in the flow direction. Thus, the W/t ratio for the test core was 188. This may be compared with 79.9, the W/t ratio for a fin of 0.0102 cm thickness and 0.815 cm height, which is that of a prototype heat exchanger used as reference. For both systems, the ratios were large enough to justify neglect of side effects on the flows through the channels.

Aluminum was selected as the material for the test plate because

(i) its high thermal conductivity tends to create a uniform temperature distribution, (ii) it is easy to perforate by drilling or punching, and (iii) two heat exchangers [4, 7] whose performance is compared with the present data were made of this material.

The test section of the wind tunnel, 1.75 m long and having a working section of 15.2 cm², was constructed with 1.91 cm thick plywood. Air was induced to flow through the wind tunnel by the air blower driven by a dynamometer unit. The air flow rate ranged from 90 kg/hr to 2500 kg/hr. Two pitot tubes, one upstream and the other downstream of the test core, were installed in the test section of the wind tunnel. The pitot tubes were connected to a CGS 523-1 (range 690 N/m²) Barocel differential pressure transducer and the following four pressure differences were read from a CGS 1023 electronic manometer: total to static pressure differences at both upstream and downstream, and total to total and static to static pressure differences between upstream and downstream of the test core. The air flow rate and the friction loss in the test core were evaluated from these pressure measurements.

Temperatures were measured by gage 40 copper-constantan thermocouples. The inlet air temperature was measured by three thermocouples fastened onto the stem of the upstream pitot tube. The average exit air temperature was measured by a thermocouple grid which consisted of 20 thermocouples joined in series and was located about 1 in. behind the static holes of the downstream pitot tube. Steady-state temperature measurements were made on an L & N 8662 precision potentiometer while transient temperature measurement was recorded on a Honeywell model 1406 visicorder.

A heating screen was installed at the inlet of the test section. It consisted of a layer of 100 × 100 mesh, 0.00787 cm diameter ni-

Nomenclature

a = slot spacing, cm	h_{STD} = heat transfer power defined by equation (5), W/(m ² ·K)	P_t = transverse pitch, cm
A = heat transfer area, m ²	j = heat transfer factor defined by equation (3)	Re = Reynolds number defined by equation (1)
b = plate spacing, cm	K_c, K_e = entrance and exit pressure loss coefficients in equation (2)	t = plate thickness, cm
c_a = specific heat of air at constant pressure J/(kg·K)	L = length of test core in flow direction, m	W = width of test core, cm
d_s = slot width, cm	\dot{m}_a = mass flow rate of air, kg/s	W_s = width of slot
D_h = hydraulic diameter, m	NTU = number of heat transfer units defined as $(h_a A)/(m_a c_a)$	γ = heat transfer area ratio defined by equation (4)
E_{STD} = flow friction power defined by equation (6), kW/m ²	ΔP = static pressure drop across test core, N/m ²	μ = absolute viscosity, N·s/m ²
f = Fanning friction factor defined by equation (2)	P_l = longitudinal pitch, cm	ρ = density of air, kg/m ³
g_c = conversion factor, 1.0(kg·m)/(N·s ²)	Pr = Prandtl number	σ_F = frontal porosity, $1/(1 + t/b)$
G = mass velocity \dot{m}_a/A_c , kg/(m ² ·s)		σ_s = plate porosity, $\frac{\pi}{4} + \left(\frac{W_s}{d_s} - 1\right) \frac{P_l}{d_s} \left(\frac{a}{d_s} + \frac{W_s}{d_s}\right)$
h = heat transfer coefficient, W/(m ² ·K)		

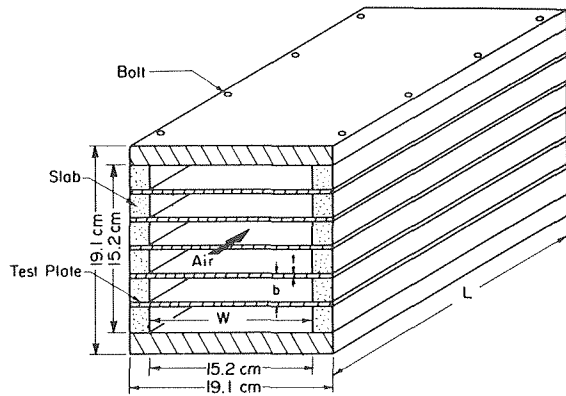


Fig. 2 Test core

chrome wire screen which was firmly sandwiched between two pairs of brass bus bars at the top and bottom. Electric current was supplied through a knife switch by a variable current a-c welder. In order to bypass the excessive power when it was necessary, a 1 m long, 0.635 cm OD thin wall stainless steel tubing was installed in parallel with the heating screen. The tubing was internally cooled by means of municipal water supply. It was estimated that the effect of radiant heat transfer between the screen and the test core was insignificant (less than 0.2 percent) as compared to the convective heat transfer between air flow and the test core.

For testing, the desired air velocity through the test section was set by means of adjusting the speed control for the dynamometer unit. The air temperatures upstream and downstream of the test core and all four pressure measurements were taken. A step power input from the a-c welder, enough to raise the temperature of the incoming air by about 15°K, was suddenly applied to the heating screen by closing the knife switch. The transient temperature of the air leaving the test core was continuously recorded on the visicorder. The air temperature was recorded again after it had attended a final steady value. The same procedure was repeated for other flow rates. The test core was allowed to be cooled down to the ambient temperature before measurements for another run were to be taken. Transient heating and cooling gives essentially the same result on heat transfer coefficients. The former was adopted because the quicker response of the spring loaded knife switch at the "on" position results in a current change behaving more closely to an ideal step response.

Test Results

The heat transfer and friction loss performance of the perforated plates were presented in terms of the heat transfer factor j and the friction factor f , respectively. All f and j data were reduced by treating the test plates as nonperforated ones. For heat transfer calculation, all physical properties of air were evaluated at the mean temperature of the air during the transient.

The flow velocity entering the core is calculated by using the Bernoulli equation. The flow velocity inside the core is calculated based on continuity. The Reynolds number is defined on the basis of the hydraulic diameter D_h of the flow channels in the core as

$$\text{Re} = \frac{D_h G}{\mu} \quad (1)$$

where $D_h = 2wb/(w + b)$ for the present system.

The friction factor f is determined from the static pressure drop across the test core corrected for entrance and exit losses [1].

$$f = \frac{D_h}{4L} \left[\frac{2g_c \rho \Delta P}{G^2} - (K_c + K_e) \right] \quad (2)$$

The heat transfer factor j is defined as

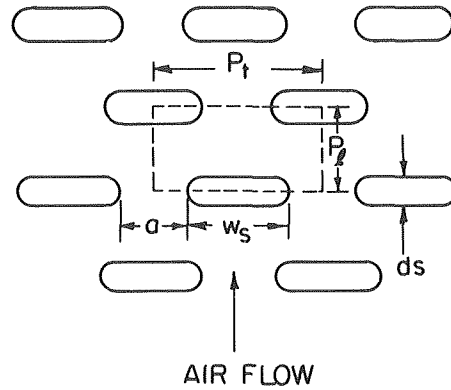


Fig. 3 Plate perforation pattern

$$j = \frac{\gamma h}{G C_a} \text{Pr}^{2/3} \quad (3)$$

where γ , a ratio of the heat transfer area of a perforated plate to that of a nonperforated one with the same physical dimension, can be determined from

$$\gamma = 1 - \sigma_s + \frac{2\pi + \left(\frac{W_s}{d_s} - 1\right)}{\frac{P_t}{d_s} \left(\frac{W_s}{l} + \frac{a}{l}\right)} \quad (4)$$

The heat transfer coefficient h was determined by a modified single-blow transient test technique described in [10, 12]. The total mass of the aluminum plates was used as the mass of the test core while h was determined for the surface area of the test plates exposed to the air flow. A comparison of test data reported in this study with those in the literature is presented in [10].

Twenty test cores were fabricated and tested in an effort to determine the effect of the governing physical parameters d_s/l , W_s/l , a/W_s , σ_s , σ_F , L/D_h , and Re on f and j . Two surface porosities (0.128 and 0.228) and two plate spacings (0.554 cm and 0.871 cm) were employed. For performance comparison, the test results were also presented in terms of the heat transfer power h_{STD} and the flow friction power E_{STD} , where h_{STD} and E_{STD} are defined as

$$h_{STD} = \left(\frac{C_a \mu}{\text{Pr}^{2/3}} \right) \frac{j \text{Re}}{S_{TD} D_h} \quad (5)$$

and

$$E_{STD} = \frac{1}{2g_c} \left(\frac{\mu^3}{\rho_a^2} \right) \frac{f \text{Re}^3}{S_{TD} D_h^3} \quad (6)$$

The subscript STD stands for standard conditions of dry air at 533°K and 1 atm.

The test results were correlated for the f and j factors with the Reynolds number. The effects of the physical parameters were examined individually, and the results are reported in detail in [10]. Only representative test results are given here from Fig. 4 to Fig. 12. The geometric properties of the test cores are listed in Table 1. The effects of the physical parameter on f and j are summarized in the following.

1 Effect of Re. Three distinct flow regimes can be identified in all the experimental results (Figs. 4 to 10). The laminar flow regime is evidenced by a continuous decrease in f and j with an increase in Re . The transition flow regime is marked by an upturn of f and j as Re continues to increase beyond the laminar value. This regime prevails until a value of Re is reached beyond which the values of f and j begin to fall with a further increase in Re , and the fluid flow is now in the turbulent flow regime. It is generally observed in this study that perforations induce earlier transition from laminar to turbulent flow and they produce significant in-

Table 1 Geometric properties of test core

	NP-1	S2-1	S4-1	S4-2	S4-3	S4-4	S4-11	S4-21	S4-31	S4-52
d_s , cm	-	0.0159	0.318	0.318	0.318	0.318	0.318	0.318	0.318	0.318
W_s , cm	-	1.27	5.08	5.08	5.08	5.08	5.08	5.08	1.27	5.08
P_1 , cm	-	0.605	1.22	1.22	0.686	0.686	1.22	1.22	1.17	1.63
P_c , cm	-	2.54	10.2	10.2	10.2	10.2	10.2	10.2	2.54	7.62
a , cm	-	1.27	5.08	5.08	5.08	5.08	5.08	5.08	1.27	2.54
b , cm	0.554	0.554	0.554	0.871	0.554	0.871	0.554	0.554	0.554	0.871
D_h , m	0.0107	0.0107	0.0107	0.0165	0.0107	0.0165	0.0107	0.0107	0.0107	0.0165
L , m	0.610	0.610	0.610	0.610	0.610	0.610	0.152	0.350	0.610	0.610
\mathcal{F}	1.0	0.943	0.906	0.906	0.832	0.832	0.906	0.906	0.951	0.906
d_s/t	-	2	4	4	4	4	4	4	4	4
W_s/t	-	16	64	64	64	64	64	64	16	64
a/W_s	-	1	1	1	1	1	1	1	1	0.5
σ_s	0	0.128	0.128	0.128	0.228	0.228	0.128	0.128	0.128	0.128
σ_F	0.872	0.872	0.872	0.915	0.872	0.915	0.872	0.872	0.872	0.915
L/D_h	56.9	56.9	56.9	36.9	56.9	36.9	14.2	28.4	56.9	36.9
NTU Range	0.6-2.2	1.1-2.5	0.8-2.0	0.4-1.3	1.0-2.0	0.5-1.1	0.3-0.7	0.5-1.3	0.8-2.4	0.5-1.2

$t = 0.0813$ cm, $W = 15.2$ cm, height of test core = 15.2 cm

crease in f and j factors only in the transitional and turbulent flow regimes. This is intimately related to the vortex shedding phenomena from the slots, as will be discussed in detail in the succeeding section.

2 Effect of d_s/t . Fig. 4 compares the performance of cores S2-1 and S4-31 having $d_s/t = 2$ and 4, respectively. It is observed that perforations reduce the critical Re from 6000 for nonperforated core NP-1 to about 4000 for core S2-1 and 3000 for core S4-31. Test cores with larger d_s/t ratio have smaller critical Re, and lower f and j factors at large Re.

3 Effect of W_s/t . Fig. 5 shows that the test core with smaller W_s/t consistently yields slightly higher f and j values in the turbulent flow regime. However, the value of the critical Re is not affected.

4 Effect of Slot a/W_s . It can be observed from Fig. 6 that a/W_s , which is a measure of the slot overlapping, does not play a significant role on either the heat transfer or the friction loss performance.

5 Effect of σ_s . Regardless of perforation size and geometry,

test core with high plate porosity σ_s (Fig. 7) induces earlier transition, and yields high f and j factors in the turbulent flow regimes. This observation is in agreement with results reported in [3] for σ_s up to 32 percent.

6 Effect of σ_F . Fig. 8 compares the performance of cores S4-3 and S4-4 with $\sigma_F = 0.872$ and 0.915, respectively. Transition occurs at lower Re for core S4-3. It is generally observed that σ_F does not affect f and j factors in the laminar regime and in the turbulent regime at large Re.

7 Effect of L/D_h . Test cores S4-11, S4-21, and S4-1 in Fig. 9 have the same perforation geometry and σ_F , but their L/D_h ratios are 14.2, 28.4, and 56.9, respectively. Transition occurs at about the same Re, but cores with smaller L/D_h ratios yield higher f and j factors in the laminar and turbulent flow regimes. The effect of L/D_h should be negligible if the smallest employed L is long enough since the flow would become quasi-steady after sufficient boundary interruption, which will be discussed in the succeeding section.

8 Effect of Plate Arrangements. Three cores were fabri-

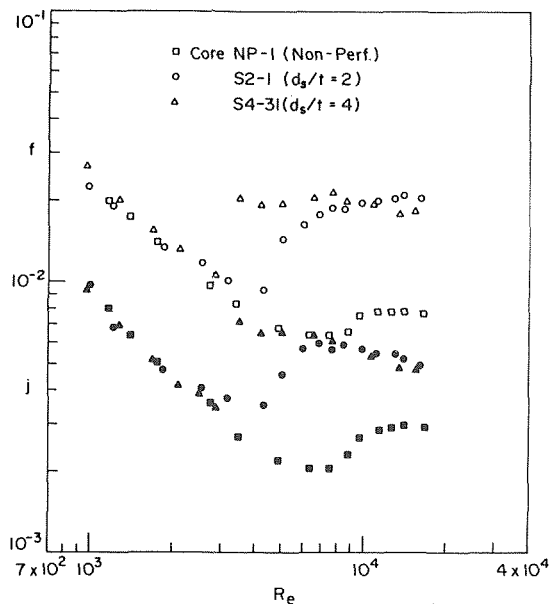


Fig. 4 Effect of d_s/t

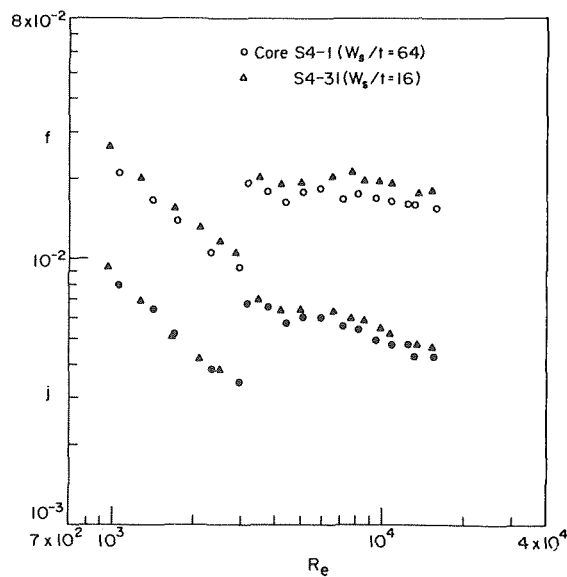


Fig. 5 Effect of W_s/t

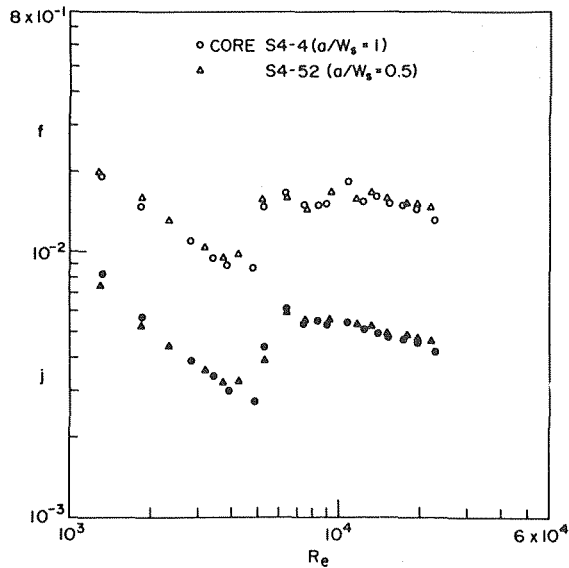


Fig. 6 Effect of a/W_s

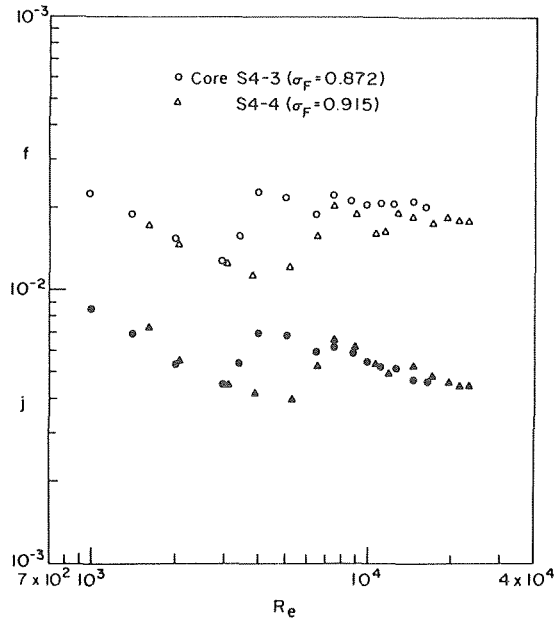


Fig. 8 Effect of σ_F

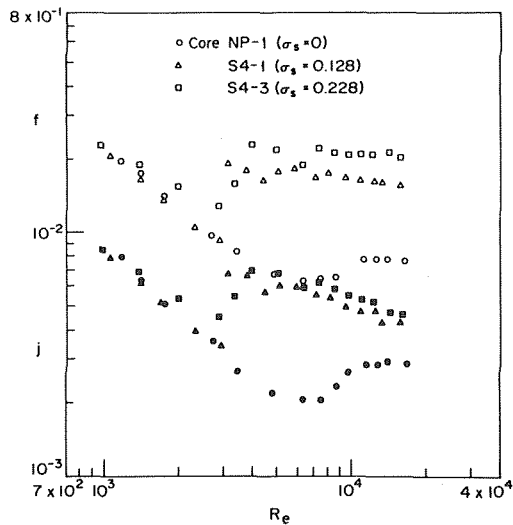


Fig. 7 Effect of σ_s

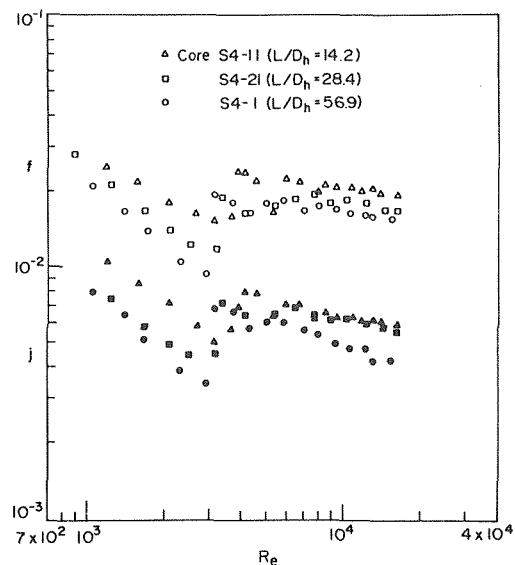


Fig. 9 Effect of L/D_h

cated to test the effect of plate arrangement on their performance. All perforated plates had $0.318 \text{ cm} \times 5.08 \text{ cm}$ oval slots to give $\sigma_s = 0.128$. All three test cores had $\sigma_F = 0.872$ and $L/D_h = 56.9$. Core SP4-1 consisted of both perforated and nonperforated plates stacked together alternately. Core S4-1 was constructed with only perforated plates whose slots were "in-line" with the neighboring plates. This is the plate arrangement used in all perforated test cores unless specified otherwise. In core S4-41, the perforated plates were stacked in such a manner that the slots in the test plates were staggered with respect to those in the adjacent plates. In other words, the slot in one test plate would be stationed midway between the two slots in the adjacent plate. Transition takes place at the same Re for all three cores, but core SP4-1 had markedly lower f and j factors in both the transition and turbulent flow regimes as illustrated in Fig. 10. While core SP4-1 was relatively quiet in both the transition and turbulent flow regimes, cores S4-41 and S4-1 suffered very severe flow-induced noise and vibration problems at high Re , which will be discussed later.

Performance comparison of perforated test cores S4-1 and SP4-1 with respect to the nonperforated test core NP-1 was presented

in the form of h_{STD} versus $(\Delta P_{core})_{STD}$ in Fig. 11 and h_{STD} versus E_{STD} in Fig. 12, respectively. $(\Delta P_{core})_{STD}$ stands for the pressure drop across the test core (excluding the entrance and exit pressure losses due to sudden contraction and expansion) evaluated from the f data under standard condition. It can be observed that the perforated cores yield higher heat transfer coefficient for the same pressure drop and pumping power expenditure in the transitional and turbulent flow regions. Core S4-1 gives the best performance, but suffers from the problem of severe noise and vibration at high Re , which is not shown in the illustrations.

9 Error Analysis of Data. An error analysis was carried out to determine the uncertainties in the test data using the method described in [13]. The factors taken into account included the uncertainties in the physical constants, geometric measurement of test core, temperature and pressure measurement. The uncertainties in f and j were estimated to be about 3 percent and 6 percent, respectively.

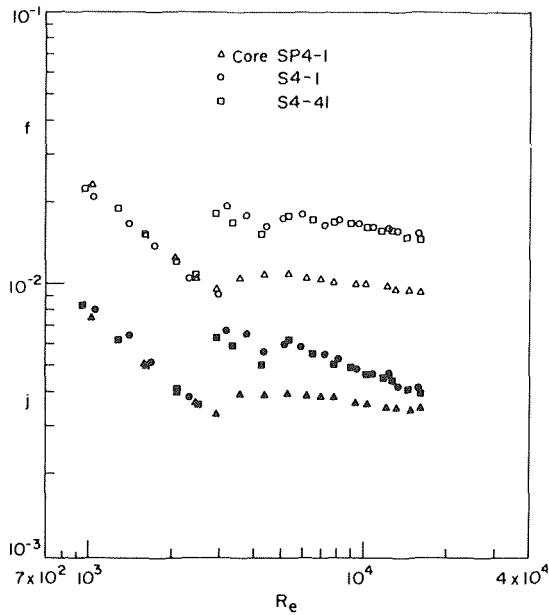


Fig. 10 Effect of plate arrangement

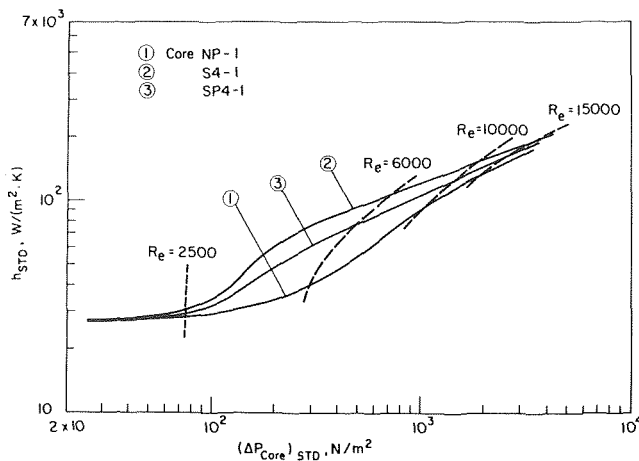


Fig. 11 h_{STD} versus $(\Delta P_{core})_{STD}$ for cores NP-1, S4-1, and SP4-1

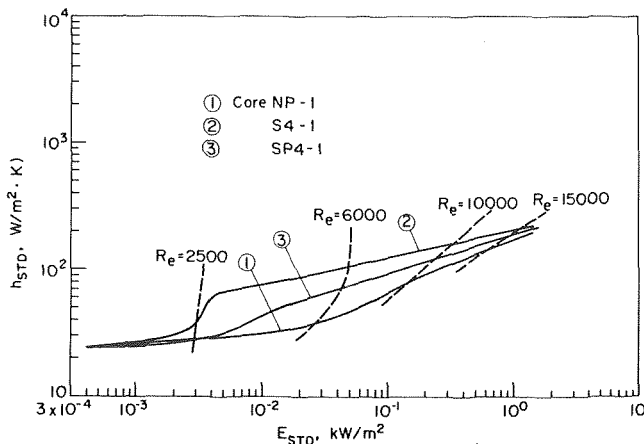


Fig. 12 h_{STD} versus E_{STD} for cores NP-1, S4-1, and SP4-1

Discussion

It is well known that the thermal resistance due to the thermal boundary layer constitutes the major part of the total resistance to convective heat transfer. Interrupting thin prime (in the case of regenerators) or secondary (fins in the case of recuperators, for example) heat transfer surfaces with perforations, thus disrupting the growth of thermal boundary layer formed on these surfaces, is an augmentation technique which has attracted considerable attention in recent years. Perforations enhance convective heat transfer by reducing the "average thickness" of the thermal boundary layer, but they also reduce the available area for heat transfer. In laminar flow regime, the increase in heat transfer coefficient is often offset by the reduction in the heat transfer area so that there is not appreciable change in j defined by equation (3). This observation is in agreement with the work by Mondt, et al. [8] and Miller, et al. [9] who concluded no beneficial effect due to perforation, since their test data lie entirely in the laminar flow regime. Beyond the onset of transition, there is a marked increase in f and j factors for the perforated test cores accompanied by the problem of noise generation and plate vibration [3, 10, 11]. A high pitch noise of a particular frequency (depending on air flow velocity) was emitted from test core, and the test plates vibrated vigorously with the same frequency as the noise. It was shown in [11] that the mechanism responsible for the flow-induced noise and vibration problem is due to vortex shedding from the perforated slots. A flow visualization study is presently being conducted by the authors using the dye-injection and hydrogen bubble technique in a towing tank. The results obtained confirmed that the early transition to turbulent flow is indeed caused by the alternative vortex shedding of vortex from the perforated slots. When traveling downstream of the slot, the vortices "eat" into the thermal boundary layer, and their mixing motion greatly increases the heat transfer. Furthermore, the vortices trigger the early onset of transition and induce the flow to become turbulent, which is a much more efficient heat transport mechanism than laminar flow. Hence, the result is an appreciable increase in total heat transfer despite reduced heat transfer area. This observation is substantiated by the test result reported in [3, 4]. It is well known that vibration of the heat transfer surface affects the heat transfer performance of the surface although no general correlation has been obtained yet [14]. It is estimated, however, that the effect of flow induced noise and vibration on the f and j data was negligible in this study.

Although the transport mechanism of the fluid flow over perforated surfaces is still far from being understood, the results obtained in the present study confirm that perforations can substantially improve the performance of heat transfer surfaces in the transitional and turbulent flow regimes. The penalty is flow-induced noise and vibration.

Conclusion

A scale-up modeling technique is developed to examine the effects of the physical parameters on the heat transfer and friction loss performance of compact heat exchangers of the plate-perforated rectangular fin surfaces. The technique is simple and quick to carry out and it may also be employed to determine the optimum perforation geometry of the compact heat exchanger. It is further concluded from this study that

1 Perforations induce early transition from laminar to turbulent flow. The higher the values of d_s/t and σ_s and the lower the value of σ_F , the earlier transition takes place.

2 Perforations do not produce significant change in heat transfer and friction performance of heat transfer surfaces in the laminar flow regime, but they do yield higher f and j factors in the transition and turbulent flow regimes. For the same pressure drop and pumping power, perforated surfaces yield a substantial increase in heat transfer over the nonperforated ones.

3 Flow induced noise and vibration were observed to occur for flow over perforated test surfaces in the transitional and turbulent

flow region. The result of noise measurement has indicated that the level of noise emitted from the perforated test core increases with σ_s and L/D_h and decreases with σ_F . The test cores with larger d_s/t ratio emit noise of higher frequency.

References

- 1 Kays, W. M., and London, A. L., *Compact Heat Exchangers*, Second ed., McGraw-Hill, New York, 1964.
- 2 Pucci, P. F., Howard, C. P., and Piersall, C. H., Jr., "The Single Blow Transient Test Technique for Compact Heat Exchanger Surfaces," *Journal of Engineering for Power*, Series A, Vol. 89, 1967, p. 29.
- 3 Shah, R. H., and Osborn, H. H., "Final Report—Advanced Heat Exchanger Design of Compact Heat Exchangers When Operating in a Marine Environment," Air Preheater Company, Wellesville, New York, May 1967.
- 4 Wond, S., Duncan, J. D., Graumann, D. W., Gibson, J. C., and Killackey, J. J., "Compact Condenser for Rankine Cycle Engine," Final Report 71-7464 (prepared for Environmental Protection Agency), AiResearch Manufacturing Co., Los Angeles, Calif., June 1971.
- 5 Yang, W. J., Choy, K. H., and Clark, J. A., "Heat Transfer and Friction Loss Performance of Flat Perforated Plates," Final Report (prepared for Environmental Protection Agency), Dept. of Mech. Eng., Univ. of Michigan, Ann Arbor, Mich., Sept. 1972.
- 6 Forgo, L., "Some Extra High Capacity Heat Exchangers of Special Design," Proc. 1972 International Seminar on Recent Developments in Heat Exchangers, International Center for Heat and Mass Transfer, Trogir, Yugoslavia, 1972.
- 7 Kays, W. M., "The Heat Transfer and Flow Friction Characteristics of a Wavy Fin, A Strip Fin, and a Perforated Fin Heat Transfer," TR No. 39, Dept. of Mech. Eng., Stanford Univ., Stanford, Calif., 1958.
- 8 Mondt, J. R., and Siegl, D. C., "Performance of Perforated Heat Exchanger Surfaces," ASME Paper No. 72-WA/HT-52.
- 9 Miller, H. L., and Leeman, C. A., "Heat Transfer and Pressure Drop Characteristics of Several Compact Plate Surfaces," AIChE Preprint 9, 13th National Heat Transfer Conf., Denver, Colo., 1972.
- 10 Liang, C. Y., "Flow Over Perforated Surfaces for Compact Heat Exchanger Applications," PhD thesis in progress, Mech. Eng. Dept., University of Michigan, Ann Arbor, Mich., 1974.
- 11 Yang, W. J., and Liang, C. Y., "Flow Induced Vibration and Noise in Perforated Plate Heat Exchanger," Paper No. TMDI presented at 10th Anniversary Meeting of Soc. Eng. Sci., Raleigh, N. C., Nov. 1973.
- 12 Liang, C. Y., Yang, W. J., and Clark, J. A., "Slotted-Fin Tubular Heat Exchangers for Cooling Towers," AIAA Paper No. 74-661 and ASME Paper No. 74-HT-6 presented at the AIAA-ASME Thermophysics and Heat Transfer Conference held in Boston, Mass., July 1974.
- 13 Kline, S. J., and McClintock, F. A., "Describing Uncertainty in Single Sample Experiments," *Mech. Engrg.*, Vol. 75, 1953, p. 3.
- 14 Bergles, A. E., "Survey and Evaluation of Techniques to Augment Convective Heat and Mass Transfer," *Progress in Heat and Mass Transfer*, Vol. 1, 1969.

C. Y. Liang¹
Doctoral Candidate.

Wen-Jei Yang
Professor.

Department of Mechanical Engineering,
The University of Michigan,
Ann Arbor, Mich.

Modified Single-Blow Technique for Performance Evaluation on Heat Transfer Surfaces

The existing single-blow, maximum-slope transient technique has been commonly applied for determining heat transfer performance of heat exchanger units or surfaces. However, results lack in accuracy and technical difficulties arise when it is applied to heat exchanger surfaces or units with NTU value smaller than 3.5. In the present paper, a modified single-blow technique is developed which can be applied to systems of any NTU values. Both theoretical analysis and experiments are performed. The validity of the present technique is borne out by the good agreement between experimental data and the existing theoretical solutions.

Introduction

A number of experimental techniques have been developed for testing the performance of heat transfer surfaces and heat exchangers, i.e., to determine the heat transfer coefficient between the heat transfer surface or matrix in the heat exchanger and the flowing fluid. They can be classified into the steady state [1-3]² and the transient methods [4-10].

The steady-state method uses a constant heat source to supply heat continuously to the surface by using a hot fluid, condensing vapor on the other side of the surface [1, 2] or by electrical power dissipation within the surface itself [3]. According to Newton's law of cooling, the average heat transfer coefficient h can be determined by dividing the convective heat flux by the difference between the average surface and fluid temperatures. This involves a rather delicate, if not difficult, task in measuring the average surface temperature. In the case when two fluids are employed, h can be reduced from the overall heat transfer coefficient between the two fluids whose terminal temperatures are measured. This method suffers from the definite limitation that serious errors occur when applied to test cores of large L/D_h ratio. It is shown in reference [1] that for $NTU > 3$ or $NTU < 0.2$, errors in temperature measurement result in excessive errors in the computed value of the heat transfer coefficient even with excellent instrumentation.

The transient method employs one fluid to either supply or re-

move heat from the heat transfer surface or matrix. When the inlet fluid temperature varies with time as $f(\theta)$, convective heat transfer becomes time-dependent which results in timewise changes in the enthalpies of both the surface and the fluid. This phenomenon can be described by an analytical model assuming that the average heat transfer coefficient remains constant and that the surface and fluid temperatures vary with time and position along the flow passage. Its solution is then matched with the measured outlet fluid temperature response curve to determine the heat transfer coefficient. A heating screen installed at upstream of the test core is commonly used as heat source.

Two typical time functions of the inlet fluid temperature $f(\theta)$ have been employed, namely, a stepwise change [5-10] and a sinusoidal change in $f(\theta)$ for the single-blow method and the periodic method, respectively. The former is more popular since experiments would be easier to perform. The analytical solution for the single-blow method has been obtained by Schumann [7]. In using the response curve of the outlet fluid temperature to determine h , Locke [8] stressed on the use of the maximum slope which is uniquely related to the NTU of the system while Howard [9] extended Locke's analysis to include the effects of longitudinal conduction by finite difference technique. Mondt and Siegl [10] has proposed to correlate the initial fractional step rise at zero time with the Schumann's solution. They are referred to as the maximum slope method and the initial rise method, respectively. The drawback common to all single-blow methods is that due to the finite heat capacity of the heating screen, the inlet fluid temperature can never, in reality, follow a step change at zero time as assumed in the analysis. This deviation may result in considerable inaccuracy in h . In the case of the maximum slope method, a point of inflection occurs at $NTU = 2$ in the analytically obtained NTU versus maximum slope curve. Furthermore, for heat exchangers of low NTU values, the theoretical analysis predicts that the maxi-

¹ Presently Assistant Professor of Engineering, Oakland University, Rochester, Mich.

² Numbers in brackets designate References at end of paper.

Contributed by the Heat Transfer Division for publication in the JOURNAL OF HEAT TRANSFER. Manuscript received by the Heat Transfer Division May 29, 1974. Paper No. 75-HT-V.

imum slope of the exit fluid temperature response curve occurs near or at zero time, and consequently the accuracy of the measured value of maximum slope depends strongly on how close the actual change in the inlet fluid temperature is to a step-wise change as assumed in the analysis as well as how fast the recording instruments can respond to the initial change. Therefore, an improvement in the existing transient method is definitely needed by using the actual response of the inlet fluid temperature as $f(\theta)$ in the analysis.

Analysis

The formulation of heat transfer between the heat transfer surface and the fluid in a heat exchange is well known (for example, references [11, 12]). The phenomenon can be described by the energy equations

$$\frac{\partial T_s^*}{\partial \theta^*} = T_f^* - T_s^* \quad (1)$$

$$\frac{\partial T_f^*}{\partial \theta^*} + b_1 \frac{\partial T_f^*}{\partial x^*} = b_2 (T_s^* - T_f^*) \quad (2)$$

subject to the appropriate initial and boundary conditions

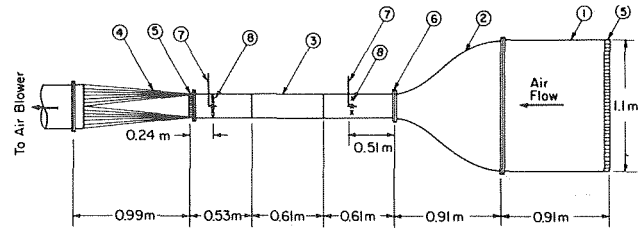
$$T_s^*(0, x^*) = T_f^*(0, x^*) = 0 \quad (3)$$

$$T_f^*(\theta^*, 0) = f(\theta^*) \quad (4)$$

T_s^* and T_f^* are the dimensionless solid and fluid temperatures based on the initial and inlet fluid temperatures. θ^* is defined as the ratio of the physical time θ to the constant τ_{sys} of the solid-fluid system. x^* is a dimensionless position variable, and is equal to the number of heat transfer units when evaluated at the exit of the solid-fluid system. b_2 is the ratio of heat capacities between the solid surface and the fluid. $f(\theta^*)$ is the forcing function which describes the timewise change of the inlet fluid temperature. $f(\tau^*) = 1$ and $\sin \omega^* \theta^*$ correspond to the single-blow and periodic methods, respectively. In the present single-blow method, the experimentally determined $f(\theta^*)$ is employed:

$$T_f^*(\theta^*, 0) = 1 - e^{-\theta^*/\tau^*} \quad (5)$$

τ^* is defined as τ_i/τ_{sys} , in which τ_i is the time constant of the measured inlet fluid temperature to be determined experimentally.



① Settling Chamber
② Contraction Section
③ Test Core
④ Diffuser Section
⑤ Honeycomb
⑥ Heating Screen
⑦ Pilot Tube
⑧ Thermocouples or Thermopile

Fig. 1 Test Apparatus

The time constant τ_i depends on the heat capacities of both the heating screen and inlet-fluid thermocouple probe and the heat conductances between these surfaces and the incoming fluid. Only if τ_i be zero, then $f(\theta^*)$ is unity and the existing single-blow methods yield accurate results for the systems of any NTU. In reality, the measured inlet fluid temperature behaves as an exponential function of time, deviating significantly from a step response for the systems as will be shown later in the text.

Solutions of equations (1) and (2) subjected to the appropriate initial and boundary conditions (3), and (5) can be obtained by means of Laplace transform technique. The transformed differential equations and the transferred boundary condition in time are

$$S \bar{T}_s^* = \bar{T}_f^* - \bar{T}_s^* \quad (6)$$

$$S \bar{T}_f^* + b_1 \frac{d\bar{T}_f^*}{dx^*} = b_2 (\bar{T}_s^* - \bar{T}_f^*) \quad (7)$$

$$\bar{T}_f^*(S, 0) = \frac{1}{\tau^* S (S + \frac{1}{\tau^*})} \quad (8)$$

where S is the Laplace variable and the superscript $-$ denotes the Laplace transform function. The solution for \bar{T}_f^* is

$$\bar{T}_f^* = \frac{e^{-\frac{S}{b_1} (1 + \frac{b_2}{1+S}) x^*}}{\tau_i^* S (S + \frac{1}{\tau^*})} \quad (9)$$

Nomenclature

A = heat transfer area, m^2
 A_c = core minimum free flow area, m^2
 b = plate spacing, cm
 b_1 = constant defined as $(v_f/A_c)b_2$
 b_2 = constant defined as $m_s c_s / m_f c_f$
 c = specific heat at constant pressure, $J/(kg.K)$
 D_h = hydraulic diameter of flow passage, m
 f = Fanning friction factor
 g_c = conversion factor, 1.0 $kg.m/(N.s^2)$
 G = mass velocity, (\dot{m}_f/A_c) , $kg/(m^2.s)$
 h = heat transfer coefficient $W/(m^2.K)$
 j = Colburn heat transfer factor
 K_c, K_e = entrance and exit pressure loss coefficients
 L = free flow length of test core, m
 m = mass, kg
 \dot{m}_f = mass flow rate of fluid, kg/s
 NTU = number of heat transfer units defined as $hA/\dot{m}_f c_f$

Nu = Nusselt number
 P = pressure, N/m^2
 Pr = Prandtl number
 Re = Reynolds number
 S = Laplace transform variable
 t = plate thickness, cm
 T = temperature, K; T_0 = initial temperature; $T_{f,i}$ = inlet fluid temperature
 T^* = dimensionless temperature defined as $(T - T_0)/(T_{f,i} - T_0)$
 t^* = dimensionless time defined as NTU/b_1
 V = velocity, m/s
 v_f = volume of fluid in test core per unit length in flow direction, m^3/m
 x = length coordinate in flow direction, $x = 0$ and $x = L$ corresponding to entrance and exit of test core, respectively

x^* = dimensionless length coordinate defined as $(hAx)/(\dot{m}_f c_f L)$
 η, ξ = dummy variable, dimensionless
 θ = time, s
 θ^* = dimensionless time defined as θ/τ_{sys}
 μ = absolute viscosity, $N.s/m^2$
 ρ = density
 τ_i = time constant of inlet fluid temperature, s
 τ_{sys} = time constant of solid-fluid system defined as $(m_s C_s)/(hA)$, s
 ω^* = dimensionless frequency

Subscripts

e = exit
 f = fluid
 i = inlet
 o = initial
 s = solid
 ∞ = fully developed
 \textcircled{T} = constant wall temperature
 \textcircled{H} = constant wall heat flux

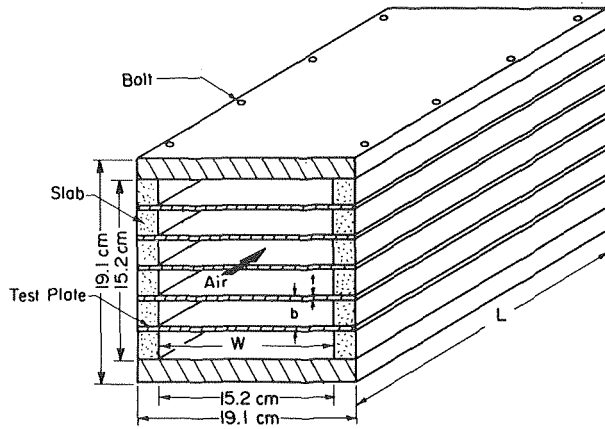


Fig. 2 Test core

Replacing x^* by NTU, the inverse Laplace transform yields the exit fluid temperature as in two time domain as

(i) when $\theta^* < t^*$, or equivalently $\theta < L/V_c$,

$$\bar{T}_f^*(\theta^*, NTU) = 0 \quad (10)$$

(ii) when $\theta^* \geq t^*$, i.e., $\theta \geq L/V_c$,

$$T_f^*(\theta^*, NTU) = \frac{1}{\tau^*} \int_{t^*}^{\theta^*} e^{-(\theta^* - \eta)/\tau^* - b_2 t^*} \times \{e^{-(\eta - t^*)} I_0[2\sqrt{b_2 t^*}(\eta - t^*)] + \psi_2(\eta, NTU)\} d\eta \quad (11)$$

wherein

$$t^* = NTU/b_1$$

$$\psi_2(\eta, NTU) = \int_0^{\eta - t^*} e^{-\xi} I_0[2(b_2 t^* \xi)^{1/2}] d\xi$$

Test Apparatus

Heat transfer and friction loss performance of heat transfer surfaces were conducted in a 15.2 cm square test section (of 1.9 cm thick plywood construction) of an open circuit subsonic wind tunnel shown in Fig. 1. The settling chamber and the contraction section having a contraction ratio of 53:1 serve to reduce the free stream turbulence and ensure a smooth air flow into the test section. Honeycomb straighteners were installed to guide the air flow. Air was induced to flow through the wind tunnel by a centrifugal air blow-

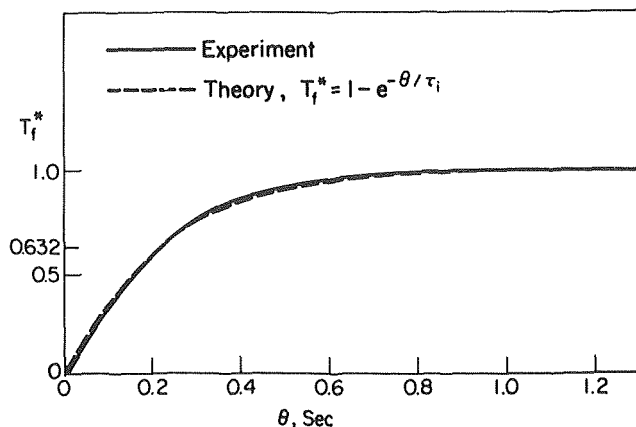


Fig. 3 Temperature response of inlet fluid to a step power input to heating screen for air velocity of 11.9 m/s

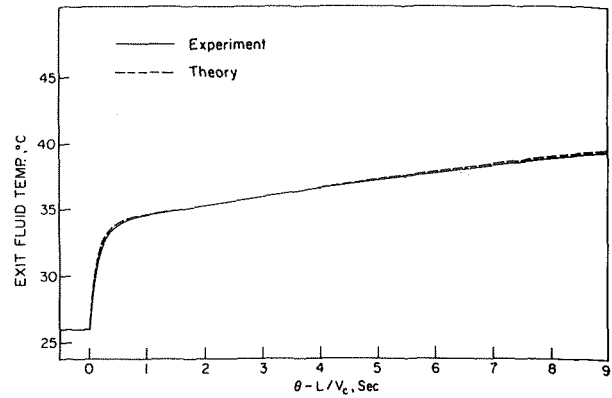


Fig. 4 Response of exit air temperature to a step power input to heating screen at air velocity of 24.2 m/s

er driven by a dynamometer unit. The air flow rate can be varied from 90 kg/h to about 2500 kg/hr. Uniformity of air flow was indicated by horizontal and vertical pitot tube traverse in the middle plane of the test section. It was found that 1.27 cm from the wall, the flow velocity was within 1.0 percent of the flow velocity at the center line of the wind tunnel (at $V = 10$ m/s). With a heating screen installed at the inlet of the test section, the free stream turbulence level was less than 1.5 percent throughout the range of air flow rate used in the present experiment. The test core (Fig. 2) consisted of a number of 0.0813 cm (thickness) \times 19.1 cm (width) \times 0.61 m (length in flow direction) aluminum plates separated by wooden spacers to form parallel flow channels. Only 15.2 cm out of 19.1 cm width of these plates was exposed to the air stream. The plates and the wooden slabs were stacked together by four pairs of 0.476 cm bolts to form a test core. The thickness of the wooden slab can be varied to give different values of the frontal porosity of the test core).

Two 0.322 cm OD pitot tubes were installed in the test section, one upstream and the other downstream of the test core. The pitot tubes were connected to a CGS (CGS Scientific Corporation) type 531-1 differential pressure transducer with a CGS type 1023 electronic manometer as readout unit. With this pressure transducer unit, it is possible to measure a differential pressure of 0.0127 cm of water with an accuracy of ± 2 percent.

Air temperatures were measured by means of gage 40 copper-constantan thermocouples. Three thermocouples were fastened onto the upstream pitot tube and were used to measure the air temperature at upstream of the test core. A thermocouple grid which consisted of twenty thermocouples joined in series was placed 2.54 cm behind the static holes of the downstream pitot tube. It was used to monitor the average air temperature at the exit of the test core. Ice baths were used for the reference junctions of the thermocouples. Steady-state temperature was measured by means of a Leeds and Northrup 8662 precision potentiometer while transient temperature measurement was recorded with a Honeywell model 1406 viscororder. It was estimated that the effect of radiant heat transfer between the screen and the test core was insignificant (less than 0.2 percent as compared to the convective heat transfer between the air flow and the test core).

A heating screen was installed at the inlet of the test section. It consisted of a layer of 100 \times 100 mesh, 0.00787 cm dia nichrome wire screen which was sandwiched between two pairs of 0.635 cm \times 1.91 cm \times 30.5 cm brass buss bars, and was firmly held at top and bottom by screws. Electric current was supplied to the heating screen from a variable current a-c welder. In order to bypass the excessive electric power when it was necessary, a 1 m long, 0.635 cm OD stainless steel tubing was installed in parallel with the heating screen. The tubing was internally cooled by the circulation of water from the municipal water supply.

The response of the heating screen to a step input of electric current at different air flow velocities was first investigated with an empty wind tunnel. All temperature measurements were made by the downstream thermocouple grid. After the initial temperature was noted, an electric current was suddenly applied to the heating screen by closing the spring-loaded knife switch. The temperature response curve of the air behind the heating screen was continuously recorded by the visicorder. The same procedure was repeated at different air flow rates. The solid line in Fig. 3 represents the temperature response curve obtained for the air velocity of 11.9 m/s. The time constant τ_i , defined as the time for the air temperature to reach 0.632 of its final steady-state value, was determined to be 0.224 s. It is obvious that the inlet fluid temperature does not respond stepwisely with time as assumed in the existing single-blow methods. An exponential curve generated by substituting this value of τ_i into equation (5) was superimposed as the dotted line in the figure. The excellent agreement between the two curves in Fig. 5 proves that the response of the air passing through the heating screen subjected to a stepwise input of electric current closely follows an exponential behavior, and thus justified the need to further improve the existing single-blow methods. The relationship between τ_i and V_i for the present experimental setup was accurately described by $\tau_i = 2.38 V_i^{-0.495}$.

Test Procedure and Data Reduction

All friction data reported here were obtained under quasi-isothermal condition. Four pressure measurements were made for each run: (i) total to static pressure difference upstream of test cores, ΔP ; (ii) total to static pressure difference downstream; (iii) static to static pressure difference between upstream and downstream, ΔP_{1-1} , and (iv) total to total pressure difference upstream and downstream.

After the pressure measurements were made, the air temperature upstream and downstream was measured with the potentiometer. An electric current, sufficient to heat up the incoming air by about 15 K was suddenly applied to the heating screen. The temperature of the air downstream was continuously recorded with the visicorder during the heating period. The air temperature was recorded again after it had attended a final steady value.

The same procedure was repeated for other flow rates. Sufficient time, usually from 15 to 20 min, was allowed for the test core to be cooled down to the ambient temperature before measurements were made for the next run. Such condition is reached when the difference between the upstream air temperature and the down-

stream becomes negligibly small.

The air flow velocity entering the test core was calculated by using Bernoulli equation $V_i = [2g_c \Delta P / \rho_f]^{1/2}$. The air flow velocity inside the core was calculated from $V_c = (A_i/A_c)V_i$ where A_i and A_c represent the free flow area before the entrance of and inside the test core, respectively. The Reynolds number was defined based on the hydraulic diameter D_h of the flow channel and the core velocity V_c .

The Fanning friction factor f was computed by using equation

$$f = \frac{D_h}{4L} \left[\frac{2g_c \rho_f \Delta \rho_{1-1}}{G^2} - (K_c + K_e) \right] \quad (12)$$

with the effect of flow acceleration being neglected. The entrance and exit pressure loss coefficients K_c and K_e were determined from Figs. 5-3 of reference [2].

The heat transfer coefficient h was determined by matching the exit air temperature response curve with equation (11). A point is selected at time θ on the air temperature response curve. By substituting the values of θ , V_c and an assumed value of h into equation (11), the exit fluid temperature T_f^* was calculated, and was then compared with the measured value of T_f . If the difference was within an accepted degree of accuracy, say 0.5 percent, then the assumed value of h was considered to be correct. A new point on the response curve at a larger time was then selected and the procedure for determining the value of h was repeated. However, if the theory failed to agree with the response, a new value of h was picked and the procedure was repeated until the correct value of h was found. Five points were selected which were equally spaced on the temperature response curve for the response time between 1-9 s. The arithmetical mean value of the five heat transfer coefficients was taken to be the average heat transfer coefficient for the test core at that particular air flow velocity. The computation routine was performed by means of a digital computer. The bulk mean air temperature was used to evaluate the physical properties of air for the heat transfer calculation. The total mass of the aluminum plates was used as the mass of the test core while the heat transfer area of the test core was taken to be the total area of the test plates exposed to the air flow.

The solid line in Fig. 4 was the exit air temperature response curve for test core NP-1 at $Re = 16600$. It was compared with the dotted line representing the theoretical prediction by equation

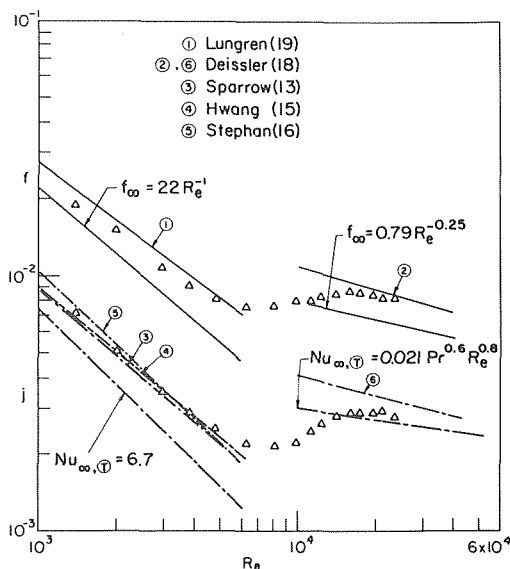


Fig. 5 Heat transfer and friction loss performance of test core NP-2 as compared with theory for uniform surface temperature case

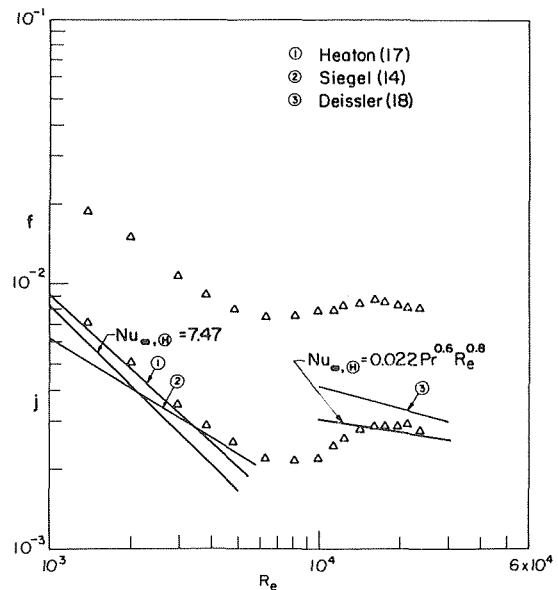


Fig. 6 Heat transfer and friction loss performance of test core NP-2 as compared with theory for uniform surface heat flux case

(11) using the five-point average h . The validity of this iteration method for determining an average h is demonstrated by the excellent agreement between the two curves.

The heat transfer results were presented in terms of the Colburn j -factor defined as $j = Nu/(Re \cdot Pr^{1/3})$.

Error Analysis. An error analysis was carried out to determine the uncertainties in the experimental data by using the method described in [20]. The best estimate of uncertainties were presented under three categories:

1. Uncertainty in physical properties					
Quantity	c_f	μ_f	ρ_f	c_s	ρ_s
Percent error	0.5	1.0	0.5	0.5	1.0
2. Uncertainty in geometric measurement					
Quantity	W	b	L	t	
Probable error, cm	0.08	0.008	0.08	0.006	
3. Uncertainty in instrumentation					
Quantity	T_f (steady)	T_f (transient)	ΔP		
Probable error	0.1 K	0.2 K	—		
Percent error	—	—	—	1.5	

The uncertainties in f and j factor were estimated to be about 3 percent and 6 percent, respectively.

Result and Discussion

Several cores were tested. Heat transfer and friction loss results of two representative cores are presented in Figs. 5–7 for comparison with the existing analytical solution and test data. Physical dimensions of the cores are given in Table 1.

Fig. 5 shows the experimental results for f and j versus Re for core NP-2. Judging from both the heat transfer and flow friction behavior, laminar flow takes place for $Re < 5000$. The flow becomes turbulent when $Re > 15000$. Several lines representing the theoretical results for hydrodynamically and thermally developing flow inside rectangular ducts are presented in the figure for comparison. For laminar flow, the Karman-Pohlhausen method was employed by Sparrow [13] for the case of uniform temperature (denoted by subscript ①) on both surfaces, and by Siegel and Sparrow [14] for the case of uniform wall heat flux (denoted by subscript ②). Hwang and Fan [15] obtained finite difference solution for both boundary conditions. Stephen [16] obtained an approximate series solution for the uniform wall temperature case. Heaton, et al, [17] employed integral technique to obtain series solution for the uniform wall heat flux case. Nu_{∞} denotes the case when both the velocity and temperature profiles in the channels are fully developed. Its value is used in evaluating the j factor. Theoretical solutions for both boundary conditions are presented separately in Figs. 5 and 6 for comparison with the test data of core NP-2. Theoretical results for turbulent flow in the combined thermal and hydrodynamic entrance region were obtained by Deissler [18] for both uniform wall temperature and uniform wall heat flux cases.

It can be observed that in the laminar flow regime, the theoretical results and experimental data agree well for the uniform wall temperature case with both flow and temperature developing which closely describes the flow conditions in the test core. However, in the turbulent flow regime, f and j data are about 6 percent and 15 percent lower than the theoretical prediction. This can be explained by the fact that turbulent boundary layer development inside ducts is strongly affected by the entrance condition as well as the free stream turbulence level. In the test core, a laminar boundary layer develops at the entrance and is followed by transition to turbulent flow. Therefore, lower friction loss and heat transfer would be obtained as compared with the case when a turbulent boundary layer develops from the entrance as is assumed in the analysis.

Fig. 7 presents the experimental results for test core NP-1 with larger length to hydraulic diameter ratio than test core NP-2. The good agreement with the analytical solutions substantiate the ob-

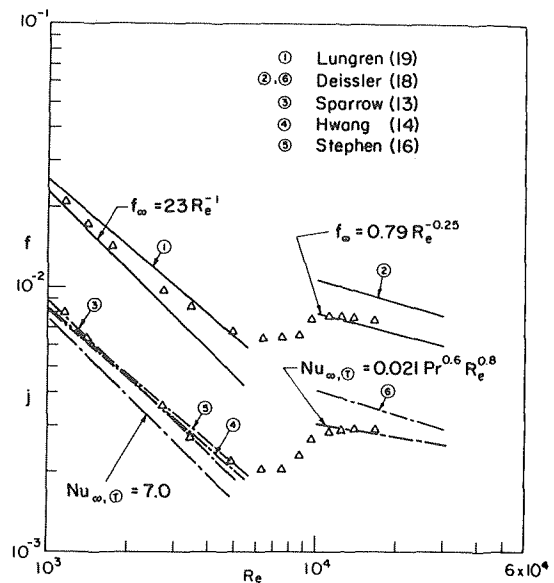


Fig. 7 Heat transfer and friction loss performance of test core NP-1 as compared with theory for uniform surface temperature case

servations made for core NP-2. Both cores represent the heat exchange systems of low NTU values.

Conclusions

A “modified single-blow” transient technique is developed to determine the heat transfer performance of heat exchanging units or surfaces. The technique can be applied to heat exchange systems of any NTU values. The validity of the modified method is borne out by good agreement between the present experimental results and the existing theoretical predications.

Acknowledgment

This study was supported by the National Science Foundation under grant number GK 39734.

References

- 1 Kays, W. M., and London, A. L., “Heat Transfer and Flow Friction of Some Compact Heat Exchanger Surfaces, Part 1—Test System and Procedure; Part 2—Design Data for Thirteen Surfaces,” *TRANS. ASME, Vol. 72*, 1950, pp. 1075–1097.
- 2 Kays, W. M., and London, A. L., “Compact Heat Exchangers,” 2nd ed., McGraw-Hill, New York, 1964.

Table 1 Properties of test cores

Description	NP-1	NP-2
t , cm	0.0813	0.0813
b , cm	0.554	0.884
core width, cm	15.2	15.2
core height, cm	15.2	15.2
L , m	0.61	0.61
front porosity	0.872	0.915
D_h , m	0.0107	0.0166
L/D_h	56.9	36.9
t/b	0.147	0.0930
aspect ratio	27.5	17.4
NTU range	0.6–2.2	0.3–1.3

- 3 Yang, W. J., Choy, K. H., and Clark, J. A., "Heat Transfer and Friction Loss Performance of Flat Perforated Plates," Final Report (prepared by Environmental Protection Agency), Department of Mechanical Engineering, University of Michigan, Ann Arbor, Mich., Sept. 1972.
- 4 Stang, J. H., and Bush, J. E., "The Periodic Method for Testing Compact Heat Exchangers," ASME Paper No. 72-WA/HT-57, presented at the Winter Annual Meeting, Nov. 1972.
- 5 Pucci, P. F., Howard, C. P., and Piersall, C. H., "The Single Blow Transient Testing Technique for Compact Heat Exchanger Surfaces," *Journal of Engineering for Power*, TRANS. ASME, Vol. 89, 1967, pp. 29-40.
- 6 Shah, R. K., and Osborn, H. H., "Advanced Heat Exchanger Designs of Compact Heat Exchangers When Operating in a Marine Environment," Final Report, Air-Preheater Company, Wellesville, N.Y., May 1967.
- 7 Schumann, T. E. W., "Heat Transfer: A Liquid Flowing Through a Porous Prism," *Journal of the Franklin Institute*, Vol. 28, No. 1, July 1929, pp. 405-416.
- 8 Lock, G. L., "Heat Transfer and Friction Characteristics of Porous Solid," Report No. TR-10, Department of Mechanical Engineering, Stanford University, Stanford, Calif., 1950.
- 9 Howard, C. P., "The Single Blow Problem Including the Effect of Longitudinal Conduction," ASME Paper No. 64-GT2-11, presented at Gas Turbine Conference and Product Show, Houston, Texas, Mar. 1964.
- 10 Mondt, J. R., and Siegler, D. C., "Performance of Perforated Heat Exchanger Surfaces," ASME Paper No. 72-WA/HT-52 presented at the Winter Annual Meeting, N. Y., Nov. 1972.
- 11 Yang, W. J., "Dynamic Response and Resonance Phenomena of a Single-Solid, Single-Fluid Heat Exchangers, Part I," *Trans. Japan Soc. Mech. Engrs.*, Vol. 27, No. 180, 1961, pp. 1275-1285.
- 12 Carslaw, H. S., and Jaeger, J. C., *Conduction of Heat in Solids*, Oxford University Press, Oxford, England, Chapter 15, 1959.
- 13 Sparrow, E. M., "Analysis of Laminar Forced Convection Heat Transfer in Entrance Region of Flat Rectangular Ducts," NACA TN 3331, 1955.
- 14 Siegel, R., and Sparrow, E. M., "Simultaneous Development of Velocity and Temperature Distributions in a Flat Duct With Uniform Wall Heating," *AIChE Journal*, Vol. 5, No. 1, 1959, p. 73.
- 15 Hwang, C. L., and Fan, L. T., "Finite Difference Analysis of Forced Convection Heat Transfer in Entrance Region of a Flat Rectangular Duct," *App. Science Res.*, Series A, Vol. 13, 1964, p. 401.
- 16 Stephen, K., *Chem. Ing. Tech.*, Vol. 31, 1959, 773 quoted in reference [13].
- 17 Heaton, H. S., Reynolds, W. C., and Kays, W. M., "Heat Transfer in Annular Passages. Simultaneous Development of Velocity and Temperature Fields in Laminar Flow," *International Journal of Heat and Mass Transfer*, Vol. 7, 1964, pp. 763-781.
- 18 Deissler, R. G., "Analysis of Turbulent Heat Transfer and Flow in Entrance Regions of Smooth Passages," NACA TN 3016, 1954.
- 19 Lungren, T. S., Sparrow, E. M., and Starr, J. B., "Pressure Drop Due to Entrance Regions in Ducts of Arbitrary Cross Section," *Journal of Basic Engineering*, TRANS. ASME, Vol. 86, 1964, p. 620.
- 20 Kline, S. J., and F. A. McClintock, "Describing Uncertainty in Single Sample Experiments," *Mechanical Engineering*, Vol. 75, 1953, p. 3.

E. M. Sparrow
T. C. Buszkiewicz
E. R. G. Eckert

Department of Mechanical Engineering,
University of Minnesota,
Minneapolis, Minn.

Heat Transfer and Temperature Field Experiments in a Cavity With Rotation, Recirculation, and Coolant Throughflow

Local wall heat transfer coefficients and fluid temperature distributions were measured in a cavity consisting of a pair of parallel disks and a cylindrical shroud. One of the disks was rotating, whereas the other disk and the shroud were stationary. Coolant air entered the cavity through a central aperture in the rotating disk and exited through an annular gap at the rim of the rotating disk. The coolant flow rate, the disk rotational speed, and the cavity aspect ratio (disk separation distance to radius) were varied throughout the course of the experiments. The latter parameter took on values as large as two. The heat transfer results and the fluid isotherm maps suggested that the flow pattern within the cavity was markedly different depending upon whether the coolant stream or the pumping action of the rotating disk was predominant. The surface distributions of the heat transfer coefficients reversed the direction of their spatial variation over the range from no rotation to high rotation. However, the maximum values of the Nusselt number curves for no rotation were as high as the maximum values of the curves for corresponding cases with high rotation. The isotherm maps for the no-rotation cases revealed that the major portion of the cavity was filled with nearly isothermal fluid. On the other hand, in the presence of strong rotation, there were substantial fluid temperature variations throughout the cavity.

Introduction

In addition to the well-known heat transfer problems associated with the blades and the disks of high temperature turbines, there are other heat transfer problems encountered in such rotating devices. In particular, adjacent to the rotating shaft, there may be cavities and enclosures of various sizes and shapes that are formed by the structural members of the machine. Some or all of the walls of such cavities are rotating. The walls may be heated by conductive, convective, or radiative transfer from high temperature components. To maintain temperatures within tolerable limits, a coolant (typically bleed air) is passed through the cavity.

The task of determining convective heat transfer coefficients in such cavities, taking account of rotation, coolant throughflow, and recirculation, must be faced in the design of turbines, compressors, and other rotating devices. Present design practice is based on highly simplified models of the convective process. To shed light

on the actual convective heat transfer processes taking place in such cavities and to provide information for updating the computational models, a research program has been undertaken by the Heat Transfer Laboratory of the University of Minnesota. Some experimental results from that research program, encompassing local and average heat transfer coefficients and flow visualization photos and sketches (via injected smoke), have been published [1, 2].¹

The present paper deals with a cavity configuration different from those which were reported on previously. Furthermore, as part of the present research, temperature field measurements were made in the air within the cavity. These measurements are believed to be the first of their kind, and they shed light on whether or not an isothermal zone exists in the core of the cavity, as postulated in some computational models. Wall heat transfer measurements were also made and the corresponding Nusselt numbers are reported here.

A schematic diagram of the cavity configuration that was used in the present experiments is presented in Fig. 1. As seen therein,

¹ Contributed by the Heat Transfer Division for publication in the JOURNAL OF HEAT TRANSFER. Manuscript received by the Heat Transfer Division March 29, 1974. Paper No. 75-HT-P.

¹ Numbers in brackets designate References at end of paper.

the cavity is cylindrical in form. One of the end faces is a disk which is attached to a hollow shaft. The disk and shaft were rotated by a variable speed motor. The coolant air, supplied by a building air system and subsequently cooled in a heat exchanger, was ducted into the cavity via the hollow shaft. The air exited from the cavity through a narrow annular gap situated at the rim of the rotating disk.

The other end face of the cavity was a stationary disk whose axial position could be adjusted to provide different cavity aspect ratios. Both of the disks were unheated. The cylindrical wall (hereafter referred to as the shroud) was a stainless steel sheet heated from behind by electrical resistance ribbon. A layer of polyurethane foam was molded around the shroud to provide insulation and rigidity.

A rake-type thermocouple probe facilitated the determination of the temperature distribution in the air within the cavity. By successively orienting the probe in the two positions indicated in Fig. 1 (solid and dashed lines), temperatures at ten radial stations could be measured. The probe could be traversed axially to permit a complete survey of the temperature field. During the heat transfer data runs, the probe was removed from the cavity.

The experiments covered the following range of parameters: (a) ratio of disk-to-disk separation distance to radius of cylindrical shroud—0.44 to 2; (b) pipe Reynolds number of incoming coolant flow—15,000 to 50,000; (c) rotational speed of rotating disk—0 to 3000 rpm (rotational Reynolds numbers up to about 10^6).

Aside from the aforementioned references [1, 2], our survey of the literature indicated very little published information on heat transfer in shrouded, parallel-disk systems with rotation, recirculation, and coolant throughflow. Very recently, Haynes and Owens [3] studied such a system with a different coolant flow pattern from the present one and for relatively small spacing-to-radius ratios (0.06 to 0.18). Publications dealing with related problems are cited in [1] and will not be repeated here.

Experimental Apparatus

The general features of the experimental apparatus have already been outlined in the Introduction. A somewhat more detailed description will be presented here. Further information is available in the thesis [4] on which this paper is based.

The cylindrical shroud was the thermally active portion of the apparatus. The shroud had a radius of 22.9 cm (9 in.) and an overall length of 53.3 cm (21 in.), with the thickness of the stainless steel sheet being 0.064 cm (0.025 in.). On the convex surface of the sheet, thirty calibrated copper-constantan thermocouples were affixed along an axial line. The electrical resistance heating ribbon wrapped around the convex surface of the shroud was wired to accommodate various separation distances between the disks. For each of several predesignated separation distances, the circuitry provided for a main heater whose axial length was equal to the separation distance and a pair of flanking guard heaters. The polyurethane layer molded around the shroud was about 15 cm (6 in.) thick and was internally instrumented with thermocouples to facilitate heat loss estimates.

The rotating disk was made of Benelex 401, a pressed wood

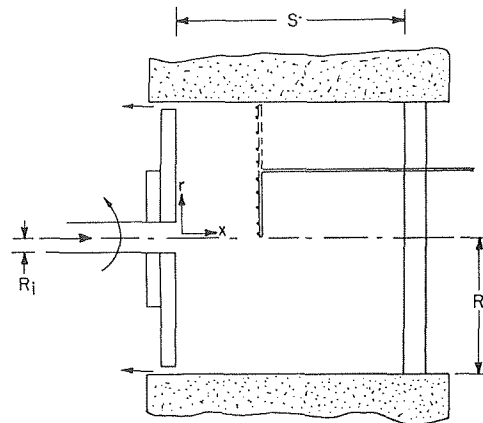


Fig. 1 Schematic diagram of the cavity

product, with a smaller backing disk of the same material as shown in Fig. 1. Both disks were about 2.5 cm (1 in.) thick. The coolant air stream entered the cavity via a 5.08 cm (2 in.) dia aperture situated at the center of the rotating disk. A 1.27 cm (0.5 in.) annular gap between the tip of the rotating disk and the shroud served as the exit aperture for the coolant air.

The temperature of the air leaving the cavity was measured by 18 miniature thermocouples (36 gage wire) situated in the annular gap. These thermocouples were installed in six groups, with three thermocouples in each group. The groups were equally spaced at 60-deg intervals around the circumference. Within each group, the three thermocouples were arranged uniformly across the gap, with an inter-thermocouple spacing of 0.305 cm ($1/8$ in.). All the thermocouple junctions were carefully aligned to lie in a common plane which coincided with the cavity-facing surface of the rotating disk. The lead wires of each thermocouple were led through hypodermic tubing for support.

On the basis of preliminary computations, it was estimated that the heat losses through the rotating disk would be very small compared with the heating power supplied to the shroud. On this basis, it was deemed unnecessary to instrument the rotating disk, thereby avoiding the problems involved with transmitting thermocouple emf's through slip rings.

For the heat transfer runs, a stationary disk which was a composite structure of insulating materials was used. Thermocouples were installed therein to facilitate heat loss estimates. A different stationary disk, designed to support and guide a probe, was employed for the runs in which temperature traverses were made. The probe body consisted of stainless steel tubing through which thermocouples were threaded. As shown in Fig. 1, five thermocouples were brought out through holes in the tubing, with the junctions themselves extending out 0.48 cm ($3/16$ in.) from the surface of the tubing. As previously explained, the temperatures at a total of 10 radial positions could be sensed at each axial station. The radial positions thus obtained were 0.635, 2.54, 5.08, . . . , 20.3, and 22.2 cm.

Nomenclature

c_p = specific heat at constant pressure
 \dot{E} = net power added to air
 h = local heat transfer coefficient, equation (1)
 k = thermal conductivity of air
 \dot{m} = coolant mass flow rate
 Nu = local Nusselt number, hR/k
 q_w = local wall heat flux

R = radius of cylindrical shroud
 R_i = radius of coolant delivery pipe
 Re_i = coolant inlet Reynolds number, equation (4)
 $Re_{\omega, R}$ = disk rotational Reynolds number, equation (4)
 r = radial coordinate
 s = spacing between disks

T_{bi} = inlet bulk temperature
 T_{bo} = outlet bulk temperature
 T_f = fluid reference temperature = T_{bi}
 T_w = local wall temperature
 x = axial coordinate
 μ = viscosity
 ν = kinematic viscosity
 ω = disk rotational speed

Table 1 Relation between ω and $Re_{\omega,R}$

ω (rpm)	$Re_{\omega,R}$
0	0
500	1.8×10^5
1500	5.3×10^5
3000	1.1×10^6

The coolant air was delivered to the cavity through a rotating hollow shaft that was rigidly connected to the rotating disk. The bore diameter of the shaft was 5.08 cm (2 in.) and the length-diameter ratio was 22. Owing to the tube length and to longitudinal slots situated at the upstream end of the shaft, it can be expected that the flow delivered to the cavity contains a significant rotational component. The flow rate of the coolant air was measured by a calibrated orifice situated well upstream of the rotating shaft.

In the operation of the system, the heater power was set so that the temperature differences between the shroud and the entering air were in the range of 33 to 50°C (60 to 90°F). Therefore, fluid property variations were not a significant factor. All measurements were made with high-precision laboratory grade instruments.

Heat Transfer Results

Data Reduction Procedures. The determination of local heat transfer coefficients on the shroud from measurements of heater power and shroud surface temperature will now be discussed. The local coefficients were evaluated from

$$h = q_w / (T_w - T_f) \quad (1)$$

in which q_w and T_w respectively denote the local values of wall heat flux and temperature, and T_f is a fluid reference temperature. The local heat flux was found by prorating the electric power input to the heater and applying corrections for axial conduction in the stainless steel surface plate and for radial conduction out through the polyurethane insulation. In addition, the wall temperature T_w is a directly measured quantity.

The selection of the fluid reference temperature T_f requires careful consideration. The fluid temperature measurements to be presented later confirm that a large zone of isothermal fluid (i.e., a free stream or a core) is not present in the cavity when there is rotation. Therefore, the usual practice of employing a free stream or core temperature as a fluid reference temperature is not an available option in the present problem. Under these circumstances, it appeared to the authors that the inlet bulk temperature of the coolant air would be the most reasonable reference temperature. In particular, it is highly likely that, in practice, the coolant inlet bulk temperature would be known.

The measurement of the coolant temperature at the cavity inlet represents a formidable task. First of all, owing to frictional heating in bearings and seals and the associated heat transfer to the hollow rotating shaft, the cross-sectional temperature distribution in the coolant flow entering the cavity is somewhat nonuniform. Therefore, a direct experimental determination of the entering bulk temperature would necessitate detailed profile measurements for both velocity and temperature.² To perform such detailed measurements with extended probes entering from the downstream end of the enclosure poses problems of unusual difficulty. Furthermore, in the presence of rotation, the probes might well disturb the flow. In view of these considerations, it was decided to employ an indirect means of determining the inlet bulk temperature.

For this purpose, an overall energy balance on the cavity as a whole can be written, so that

$$T_{bi} = T_{b0} - (\dot{E} / \dot{m} c_p) \quad (2)$$

² The temperature measurements for such a bulk temperature determination would have to be much more detailed than those which have been performed within the cavity proper.

where T_{bi} and T_{b0} are, respectively, the inlet and outlet coolant bulk temperatures, \dot{E} the net power added to the flowing fluid, \dot{m} the coolant mass flow rate, and c_p the specific heat. In evaluating the net power, the following contributions were taken into account: (a) the electric power input to the shroud heaters, (b) the heat losses through the shroud insulation and through the stationary disk, and (c) the work done on the fluid by the rotating disk³ (evaluated with the help of the Schultz-Grunow correlation [5]). The heat losses through the rotating disk were estimated and found to be very small compared with the aggregate of the heater power and the work done by the rotating disk. Thus, \dot{E} was readily computed.

Another input that is needed in equation (2) is the outlet bulk temperature T_{b0} . Strictly speaking, the determination of T_{b0} requires measurement of the velocity and temperature profiles at the exit plane followed by integration of the velocity-temperature product across the section. In practice, in view of the small measured temperature variations across the exit cross section (typically 2°F) and the flat velocity profiles typical of turbulent flow, there appears to be ample justification for computing T_{b0} as the arithmetic average of the exit-plane thermocouple readings.

With values of \dot{E} and T_{b0} as described in the foregoing, and with mass flow data from the orifice meter, the inlet bulk was evaluated from equation (2). The computed values of T_{bi} are listed in Appendix D of [4].

In light of the preceding paragraphs, all of the information needed to evaluate local heat transfer coefficients from equation (1) is thus available. A dimensionless form of the results was obtained by employing a local Nusselt number

$$Nu = hR/k \quad (3)$$

in which R is the radius of the cylindrical shroud and k is the thermal conductivity of the air evaluated at the arithmetic mean of the inlet and exit bulk temperatures. Inasmuch as R and k do not vary along the shroud, the variation of Nu with axial position along the shroud is a true representation of the variation of h itself.

The local Nusselt number results on the shroud will be presented as a function of the dimensionless axial coordinate x/R where, as indicated in Fig. 1, positive x is measured along the shroud in the direction from the rotating disk to the stationary disk. The results are parameterized by the cavity aspect ratio s/R (s = spacing between disks), the coolant inlet Reynolds number Re_i , and the disk rotational speed ω (or, alternatively, the disk rotational Reynolds number $Re_{\omega,R}$). These Reynolds numbers are defined as

$$Re_i = 2\dot{m} / \mu \pi R_i, \quad Re_{\omega,R} = R^2 \omega / \nu \quad (4)$$

in which R_i is the radius of the hollow shaft which delivers coolant to the cavity. The air properties in Re_i and $Re_{\omega,R}$ were, respectively, evaluated at the inlet bulk temperature and at the mean bulk temperature.

The heat transfer results reported here are for three cavity aspect ratios, $s/R = 0.44, 0.89, \text{ and } 2.0$. In [4], additional heat transfer results for $s/R = 1.33$ are available. Data were obtained at three coolant inlet Reynolds numbers, $Re_i = 15,000, 25,000, \text{ and } 50,000$ and, for each one of these Reynolds numbers, at four rotational speeds, $\omega = 0, 500, 1500, \text{ and } 3000$ rpm. For the conditions of the experiments the relationship between disk rotational speed and disk rotational Reynolds number is given in Table 1.

The Prandtl number for all cases was approximately 0.7.

Presentation of Results. The local Nusselt numbers are presented in Figs. 2, 3, and 4. Each figure corresponds to a fixed aspect ratio, $s/R = 0.44, 0.89, \text{ and } 2.0$, respectively. Fig. 2 contains four graphs encompassing all the four rotational speeds listed in

³ At the highest rotational speed ($\omega = 3000$ rpm), the disk work was six to ten percent of \dot{E} , whereas at $\omega = 1500$ rpm it ranged from one-half to two percent.

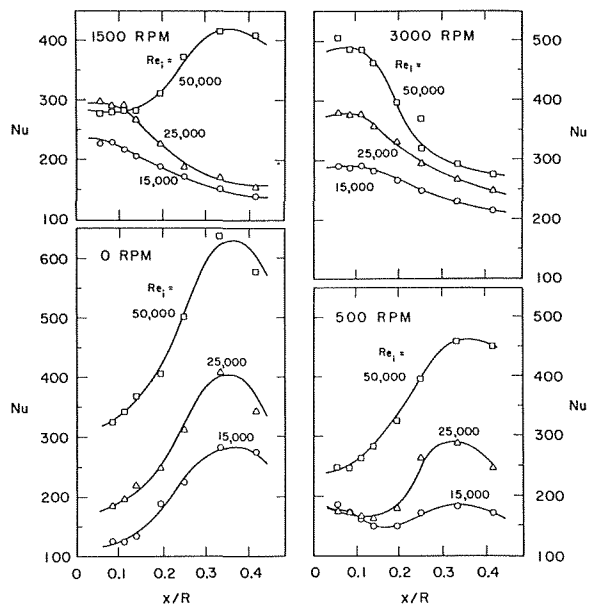


Fig. 2 Local heat transfer results for cavity aspect ratio $s/R = 0.44$

Table 1, whereas Figs. 3 and 4 are subdivided into (a) and (b) parts, with part (a) for $\omega = 0$ and 500 rpm and part (b) for 1500 and 3000 rpm. In each of the graphs appearing in these figures, the local Nusselt number is plotted as a function of x/R , with the curves being parameterized by the coolant inlet Reynolds number Re_i .

An overall inspection of these figures reveals three distinct behaviors in the Nu versus x/R curves: (1) The Nusselt number increases along the shroud as one proceeds from the rotating disk to the stationary disk (i.e., in the positive x -direction); this behavior

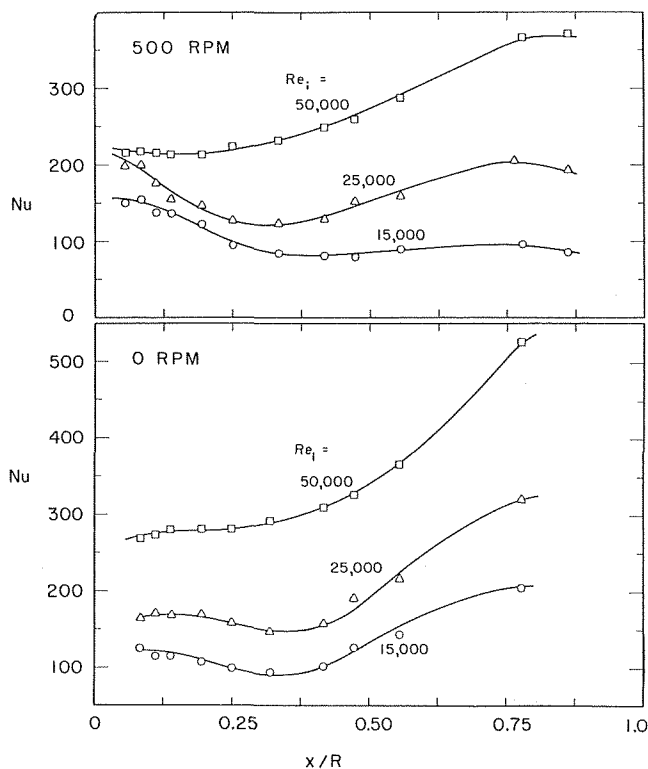


Fig. 3(a) Local heat transfer results for cavity aspect ratio $s/R = 0.89$; $\omega = 0$ and 500 rpm

occurs at low rotational speeds. (2) The Nusselt number decreases in the positive x -direction; this behavior occurs at high rotational speeds. (3) The Nusselt number at first decreases with x , attains a minimum, and then increases with increasing x ; this behavior is observed at intermediate rotational speeds.

A more precise description of these trends requires elaboration of the role of the parameters Re_i and s/R . For example, when s/R is large and at intermediate values of Re_i , behavior of type (2) is already in evidence at intermediate rotational speeds. Other similar observations may be made by inspection of the figures, but they need not be enunciated here. Rather, attention will be now turned to describing a model to explain the observed trends.

Considering the coolant stream entering the cavity, its axial momentum tends to carry it into the cavity in the form of an axial jet. On the other hand, the pumping action of the rotating disk tends to divert fluid from the coolant stream into a radial outflow along the disk. There is, therefore, a competition between the perseverance of an axial jet traversing the cavity and a radial outflow on the disk.

The likelihood that the coolant jet will succeed in traversing the axial length of the cavity is favored by low rotational speeds, high rates of coolant flow, and small values of the aspect ratio s/R . Suppose that the axial jet strongly predominates and impinges on the stationary disk. The impinging fluid spreads radially on the stationary disk and, upon reaching the shroud, turns and flows axially toward the cavity exit situated at the rim of the rotating disk. Such a backflow would be expected to give rise to a boundary layer which thickens in the direction of decreasing x . Correspondingly, the heat transfer coefficient would decrease with decreasing x (or increase with increasing x). This is the behavior previously described as type (1).

The diversion of the coolant into a radial outflow on the rotating disk is favored by high rotational speeds, low rates of coolant flow, and large values of the aspect ratio s/R . When there is a strong radial outflow on the rotating disk, a portion of the flow will impinge on the shroud, turn, and proceed axially along the shroud, thereby setting up a recirculation pattern. As the flow moves along the shroud, the boundary layer thickens and, correspondingly, the transfer coefficient should decrease. This behavior was previously identified as type (2).

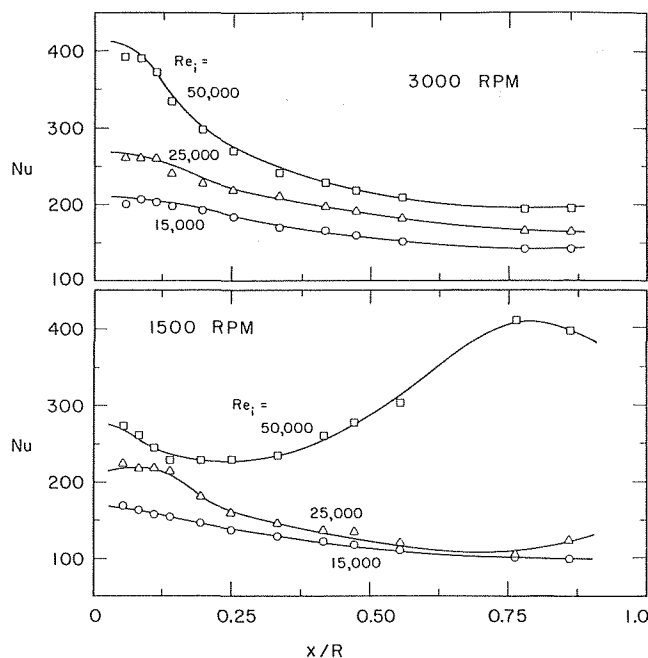


Fig. 3(b) Local heat transfer results for cavity aspect ratio $s/R = 0.89$; $\omega = 1500$ and 3000 rpm

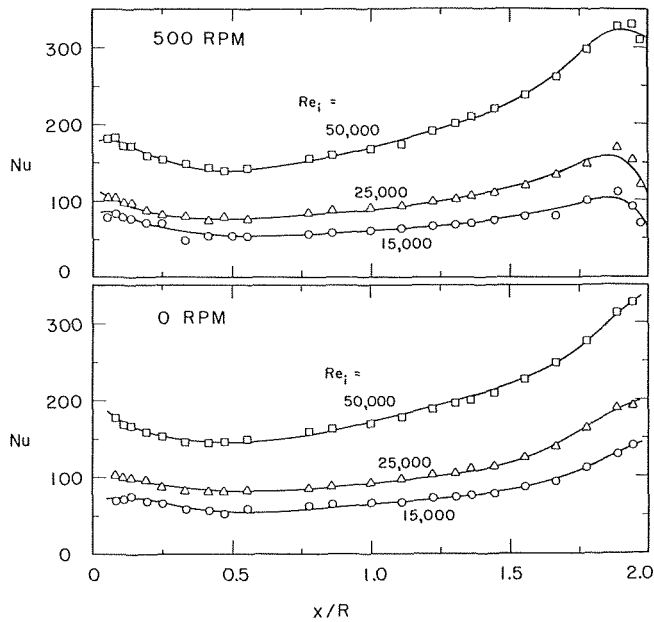


Fig. 4(a) Local heat transfer results for cavity aspect ratio $s/R = 2$; $\omega = 0$ and 500 rpm

The existence of oppositely directed axial flows at the two ends of the shroud can explain the type (3) behavior of the heat transfer results. The two axial flows are those described in the previous paragraphs. Their simultaneous occurrence, with each confined to a different end of the shroud, would be favored by intermediate operating conditions. The axial flow induced by the radial outflow on the rotating disk would account for the decrease in the transfer coefficient as x increases away from the rotating disk, and the axial backflow created by the coolant jet would account for the observed behavior near the stationary disk.

Although most of the major trends evidenced in Figs. 2-4 can be rationalized by the just-discussed model, it is quite likely that the actual flow pattern in the cavity is more complicated than that implied by the model. Furthermore, there are some trends which remain unexplained, for instance, the drop-off of the curves at the larger values of x/R in the lower graphs of Fig. 2. Nevertheless, considering the simultaneous presence of rotation, recirculation, and throughflow, it is remarkable that there is such a high degree

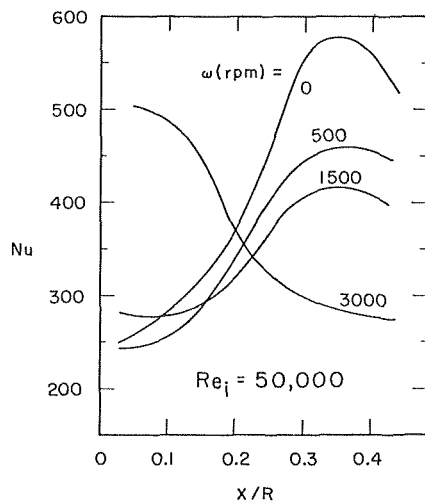


Fig. 5 Effect of rotational speed on local heat transfer results; $s/R = 0.44$ and $Re_i = 50,000$

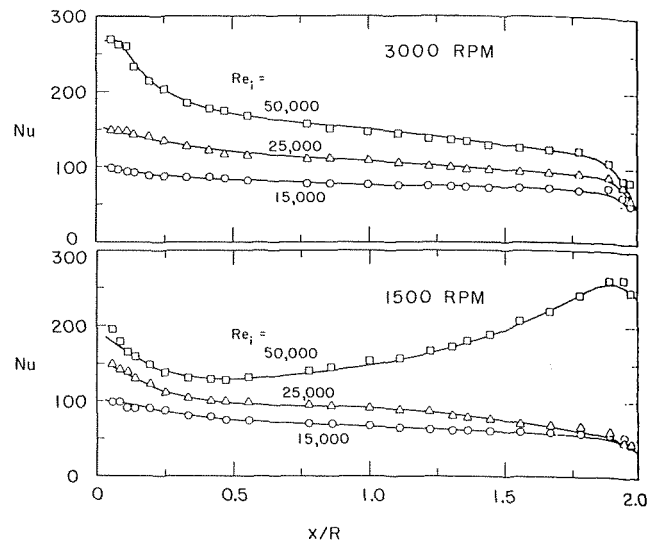


Fig. 4(b) Local heat transfer results for cavity aspect ratio $s/R = 2$; $\omega = 1500$ and 3000 rpm

of regularity in the results.

There are other trends which can be identified in Figs. 2-4. At a fixed rotational speed and cavity configuration, the transfer coefficients are higher at larger coolant flow rates. In addition, at a fixed rotational speed and coolant flow, the transfer coefficients increase as the aspect ratio decreases.

There is one additional finding that will be mentioned, and this must be regarded as quite surprising. That is, the maximum values of the Nusselt number curves for no rotation are as high as (and, frequently higher than) the maximum values of the curves for corresponding cases which include rotation. A finding of similar substance was also encountered in a laminar flow analysis for a somewhat different cavity configuration [6]. In that study, the computed velocity distributions indicated that the effect of rotation was to break up a well-ordered flow recirculation that characterized the no-rotation case, thereby diminishing the transfer coefficients.

Fig. 5 has been prepared in order to highlight the effects of rotational speed at fixed values of coolant flow rate and cavity aspect ratio. The figure is specific to the case $Re_i = 50,000$ and $s/R = 0.44$, but the trends are rather general. In the figure, the shifting of the Nu distribution from one which increases with x (low rpm) to one which decreases with x (high rpm) is clearly portrayed. Furthermore, the high values of Nu for the case of no rotation confirm the observations of the last paragraph.

Average heat transfer coefficients were also evaluated from the following definitions

$$\bar{h} = Q/A(T_w - T_f), \quad \overline{(T_w - T_f)} = \int_0^1 (T_w - T_f) d(x'/s) \quad (5)$$

where Q is the rate of heat transfer from the entire shroud surface to the air. Space limitations preclude the presentation of these results, but they are available in [4]. It is found that \bar{h} increases with increasing Re_i (for fixed ω and s/R) and with decreasing s/R (for fixed ω and Re_i). As expected, the trends with ω are not as easily categorized. It is, however, interesting to note that the \bar{h} results are relatively insensitive to rotational speed at large disk-to-disk separation distances.

Temperature Distributions

The distribution of temperature throughout the cavity was measured for all of the cases for which heat transfer results were presented in the preceding portion of this paper. From these measurements, isotherms were constructed for each case. Journal space limitations permit presentation of only a representative sample of the isotherm maps, but the remainder are available in [4]. Also, [4]

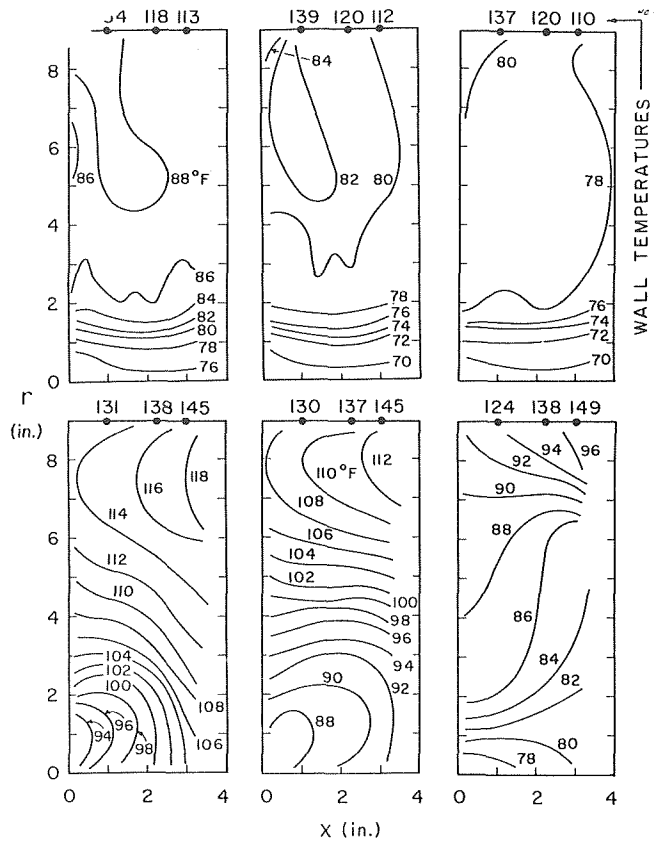


Fig. 6 Isotherm maps for cavity aspect ratio $s/R = 0.44$. Upper row of graphs: $\omega = 0$ rpm. Lower row of graphs: $\omega = 3000$ rpm. Left to right: $Re_i = 15,000, 25,000, 50,000$.

contains information on reproducibility and on the small influences of probe body heat conduction on the measured temperatures.

Representative isotherm maps for a cavity aspect ratio $s/R = 0.44$ are presented in Fig. 6. The upper row of graphs is for the no-rotation case, whereas the lower row of graphs is for $\omega = 3000$ rpm. In each set of graphs, Re_i increases from left to right, from 15,000 to 25,000 to 50,000. The ordinate of each graph is the radial coordinate r , whereas the abscissa is the axial coordinate x . The coolant inlet aperture is situated at $x = 0, 0 \leq r < 1$.

By inspecting the graphs for the no-rotation cases, it is seen that the major portion of the cavity is filled with fluid that is very nearly isothermal. Steeper gradients are encountered along the interface between the coolant jet and the isothermal zone. Adjacent to the shroud, the presence of a thermal boundary layer can be inferred. The temperature decreases along the shroud with increasing x , suggesting an axial flow adjacent to the shroud, the flow being in the negative x -direction. This flow pattern is consistent with the model that was described in connection with the heat transfer results.

The isotherm patterns for the 3000 rpm cases are markedly different from those discussed in the foregoing. The graphs for $Re_i = 15,000$ and 25,000 contain isotherms that turn back on themselves as they enter the cavity and then return to the rotating disk. These suggest a diversion of the entering coolant stream into a radial outflow, the diversion being caused by the pumping action of the rotating disk. The temperature increases along the shroud, indicating the presence of an axial flow in the positive x -direction. According to the model that was discussed earlier in the paper, this axial shroud flow is caused by the radial outflow on the rotating disk. It is especially interesting to observe that an isothermal zone no longer dominates the cavity as was true for the no-rotation

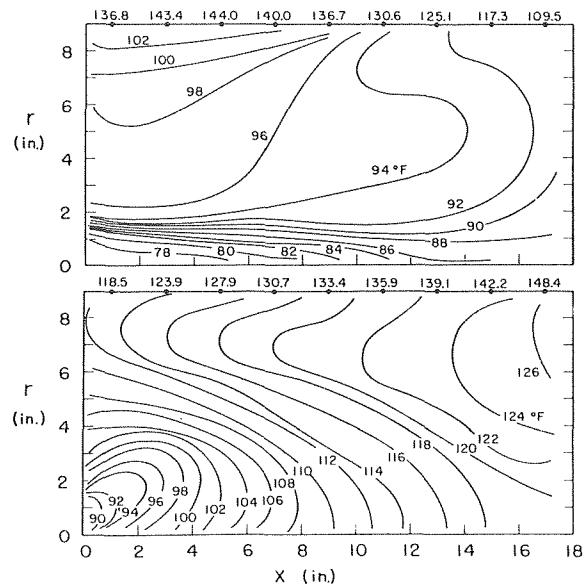


Fig. 7 Isotherm maps for cavity aspect ratio $s/R = 2$ and $Re_i = 25,000$. Upper graph: $\omega = 0$ rpm. Lower graph: $\omega = 3000$ rpm.

cases. The shapes of the other isotherms are difficult to interpret with certainty, but they could well indicate a recirculation zone.

For the case in which $\omega = 3000$ rpm and $Re_i = 50,000$ (graph at lower right of Fig. 6), there are no isotherms which turn back from the entering coolant stream toward the rotating disk. Apparently, the incoming axial momentum of the coolant stream is great enough to propel the jet across the cavity. On the other hand, the fact that the shroud temperatures increase with positive x indicates the presence of an axial flow in that direction, presumably induced by the pumping action of the rotating disk. It would appear that in this case, neither the coolant stream nor the disk pumping fully dominate the flow pattern in the cavity.

Although the results of Fig. 6 are specific to the $s/R = 0.44$ aspect ratio cavity (i.e., the smallest s/R investigated herein) the trends indicated therein are also in evidence for the other cavity aspect ratios. Fig. 7 has been prepared to substantiate this finding. The figure is for $s/R = 2$ and $Re_i = 25,000$, with the upper graph corresponding to $\omega = 0$ rpm and the lower graph corresponding to $\omega = 3000$ rpm. By examining these graphs and comparing them with their counterparts in Fig. 6, it is clear that the flow patterns discussed with respect to the latter figure continue to apply to Fig. 7.

The isotherm maps presented in Figs. 6 and 7, as well as the additional results available in [4], are generally supportive of the flow field model discussed earlier in the paper. However, it is apparent from the isotherm maps that there are additional aspects of the flow field which are too complex to be explainable by a relatively simple qualitative model.

It is worth noting that in those cases where the isotherms turn back from the entering coolant stream toward the rotating disk, the temperature level adjacent to the inlet aperture is higher than for the other cases. On the other hand, the temperature level in the upstream air supply system was not markedly higher. These facts suggest the possibility that relatively warmer air from the cavity was sucked into the inlet aperture owing to the rotation-induced pressure depression near the axis. The warmer air thus ingested near the axis could then mix with the cooler air from the upstream supply, thereby giving rise to a temperature elevation of the air that emerges into the cavity.

An interesting and practically important finding evidenced by the isotherm maps is the nonuniformity of the temperature within the cavity proper when the disk rotation is the predominant factor

in shaping the flow pattern. This suggests that heat transfer estimates based on computational models which presuppose an isothermal core may be seriously in error.

Acknowledgment

The research described in this paper was supported by the Power Branch of the Office of Naval Research.

References

1 Yu, J. P., Sparrow, E. M., and Eckert, E. R. G., "Experiments on a Shrouded, Parallel-Disk System With Rotation and Coolant Throughflow," *International Journal of Heat and Mass Transfer*, Vol. 16, 1973, pp. 311-328.

2 Sparrow, E. M., Shamsundar, N., and Eckert, E. R. G., "Heat Transfer in Rotating Cylindrical Enclosures With Axial Inflow and Outflow of Coolant," *Journal of Engineering for Power*, Vol. 95, 1973, pp. 278-280.

3 Haynes, C. M., and Owen, J. M., "Heat Transfer From a Shrouded Disk System With a Radial Outflow of Coolant," ASME paper No. 74-GT-4.

4 Buszkiewicz, T. C., "Heat Transfer and Temperature Distributions in a Cavity With a Rotating Boundary and Coolant Throughflow," MS thesis, Department of Mechanical Engineering, University of Minnesota, Minneapolis, Minn., 1975.

5 Schultz-Grunow, F., "Der Reibungswiderstand rotierender Scheiben in Gehäusen," *Z. Angew. Math. Mech.*, Vol. 15, 1935, pp. 191-204.

6 Hennecke, D. K., Sparrow, E. M., and Eckert, E. R. G., "Flow and Heat Transfer in a Rotating Enclosure With Axial Throughflow," *Wärme- und Stoffübertragung*, Vol. 4, 1971, pp. 222-235.

C. C. Lin

Graduate Student and Assoc. Professor.

S. H. Chan¹

Professor.

Department of Mechanical Engineering,
Polytechnic Institute of New York,
Brooklyn, N. Y.

An Analytical Solution For a Planar Nongray Medium in Radiative Equilibrium

The problem of energy transfer through a nongray absorbing and emitting medium, bounded by two black surfaces, in radiative equilibrium is investigated. A nearly exact analytical solution for the temperature distribution within the nongray medium is found by an asymptotic matching technique. The nongray characteristics of the medium are accounted for by using the exponential wide-band model. The analytical solution is valid for all optical thickness and has an error of less than 0.5 percent as compared to the existing numerical solution.

Introduction

The problem of energy transfer through absorbing-emitting gases has received considerable attention because of its practical importance. The difficulty in solving the resulting mathematically complicated equation can be reduced considerably by using various approximations, such as the gray gas approximation and the box model approximation, etc. In the infrared gaseous radiation, the absorption coefficient takes the form of many discrete bands, as a result of the vibrational and rotational energy transitions of the molecules. In this case, the gray gas approximation is applied by using some kind of mean absorption coefficients, e.g., the Planck mean in the optically thin limit and the Rosseland mean in the optically thick limit. Cess, et al. [1]² have shown that, even in the optically thin limit, the gray gas approximation gives poor results.

Due to the highly nongray nature of the infrared gaseous radiation, various wide-band absorption models have been proposed. Crosbie and Viskanta [2] have studied the effect of different band shapes on the radiative transfer in a nongray planar medium. In their study, the widely accepted exponential wide-band model is also included. Edwards, et al. [3-6] have made an extensive study of the total band absorptance based on the exponential model and their results have been correlated by a single continuous function [7]. When the line structure is not important, the slab band absorptance [8] can be used for parallel-plate problems to eliminate

the angular integration, in addition to the frequency integration. For other geometries, the geometric band absorptance recently introduced by Chan [9] appears to be applicable. However, even the problems involving the simplest geometry of parallel plates, closed form solutions are rarely found. This is especially true for nongray gases where solutions generally have to resort to numerical methods. Only in the case of radiative equilibrium under the limiting condition of large path length has a nongray analytical solution been obtained [10]. Under such a condition, there is no temperature jump at the boundary and the gas temperature near the surface can be simply taken as the surface temperature in arriving at the solution. However, this is not true even when the optical thickness exceeds 100 [2]. The purpose of this paper is to present an approximate analytical solution valid for all optical conditions. It makes use of the slab band absorptance [8] and an asymptotic matching technique [11-14]. The analytical solution is compared to the elaborate numerical results obtained by [2] and other solutions using less realistic models.

Basic Equations

The physical system under consideration is shown in Fig. 1. It consists of a stationary layer of an absorbing-emitting gas bounded by two infinite black plates at different temperatures. The gas is in radiative and local thermodynamic equilibrium. No heat source is present in the gas. Then, the conservation of energy gives

$$dq_R/dy = 0 \quad (1)$$

where q_R is the radiative heat flux

$$q_R = \int_0^\infty q_{R\omega} d\omega \quad (2)$$

The spectral radiative flux $q_{R\omega}$ is given by

¹ Presently at the Argonne National Laboratory, Reactor Analysis and Safety Division, Argonne, Ill.

² Numbers in brackets designate References at end of paper.

Contributed by the Heat Transfer Division for publication in the JOURNAL OF HEAT TRANSFER. Manuscript received by the Heat Transfer Division August 1, 1974. Paper No. 75-HT-Z.

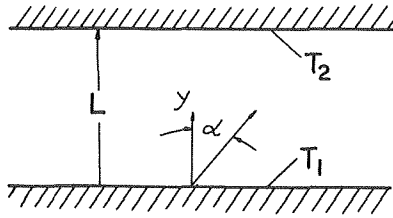


Fig. 1 Physical system

$$q_{R\omega}(y) = e_{\omega}(T_1) - e_{\omega}(T_2) + 2 \int_0^y \kappa_{\omega} [e_{\omega}(y') - e_{\omega}(T_1)] E_2(\kappa_{\omega}(y - y')) dy' - 2 \int_y^L \kappa_{\omega} [e_{\omega}(y') - e_{\omega}(T_2)] E_2(\kappa_{\omega}(y' - y)) dy' \quad (3)$$

where e_{ω} is the spectral Planck function

$$e_{\omega} = 2\pi h c^2 \omega^3 / [\exp(\frac{hc\omega}{kT}) - 1] \quad (4)$$

and E_2 is the exponential integral function defined by

$$E_n(t) = \int_0^1 \mu^{n-2} e^{-t/\mu} d\mu \quad (5)$$

When the pressure is high or path length is large, κ_{ω} can be represented by the exponential-winged band model [9]

$$\kappa_{\omega} = (C_1/C_3) \exp[(\omega - \omega_0)/C_3] \quad \omega < \omega_0 \quad (6)$$

and, consequently, the slab band absorptance takes the form [9]

$$\bar{A} = \frac{1}{C_3} \int_0^1 2\mu \int_{\Delta\omega} (1 - e^{-\kappa_{\omega} y/\mu}) d\omega d\mu = \ln \tau + E_1(\tau) + \gamma + \frac{1}{2} - E_3(\tau) \quad (7)$$

where τ is the optical thickness

$$\tau = C_1 y / C_3 \quad (8)$$

Assuming the absorption coefficient to be independent of the temperature and combining equations (1) through (8), the governing equation becomes

$$\int_0^{\tau} \bar{A}'(\tau - \tau') \frac{d\phi}{d\tau'} d\tau' - \int_{\tau}^{\tau_0} \bar{A}'(\tau' - \tau) \frac{d\phi}{d\tau'} d\tau' = [1 - \phi(0)] \bar{A}'(\tau) + [M - \phi(\tau_0)] \bar{A}'(\tau_0 - \tau) \quad (9)$$

where $\bar{A}' = d\bar{A}/d\tau$, $\tau_0 = C_1 L / C_3$, $\phi(\tau) = e_{\omega 0}(\tau) / e_{\omega 0}(T_1)$, $M = e_{\omega 0}(T_2) / e_{\omega 0}(T_1)$, and $e_{\omega 0}$ is the Planck function evaluated at the band center ω_0 . Because the band width is small, e_{ω} has been assumed to be independent of the wave number within the band region. For simplicity, only one vibrational rotational band is considered here. This is true for diatomic gases like carbon monoxide and nitric oxide.

Asymptotic Solution

It appears that the method of matched asymptotic expansions was first applied to the integral equation of radiative transfer by Emanuel [11] who studied the problem of radiative equilibrium in an optically thick gray gas. Later the method was applied to a non-gray gas under the large path limit by Cess [12]. In the present section, it is extended to a nongray gas with any optical thickness. The gas temperature now can take a jump at the boundary rather than the continuous temperature as in the case of semi-infinite medium [12]. Such a jump is not known a priori and must be found by the asymptotic matching technique.

Equation (9) will be solved in three separate regions: the outer solution for the central region, $0 \ll \tau \ll \tau_0$, and two inner solutions near the lower boundary, $\tau \rightarrow 0$, and the upper boundary, $\tau \rightarrow \tau_0$. An asymptotic matching method [14] will be used to match the solutions in the overlapped regions. The path length, τ_0 , is assumed to be large, i.e., $\tau_0 \gg 1$, in seeking for the outer and inner solutions, but the finally matched solution is expected to be accurate for any values of τ_0 as to be seen later.

(a) **Outer Solution.** In the region away from the boundary, the large path limit as discussed Mighdoll and Cess [11] is employed. In this region, $\bar{A} \approx \ln \tau$ and the influence of the radiation from the boundary is negligible. Equation (9) becomes

$$\int_0^1 \frac{1}{\eta - \eta'} \frac{d\phi}{d\eta'} d\eta' = 0 \quad (10)$$

where $\eta = \tau/\tau_0 = y/L$. This is a singular integral equation with Cauchy's kernel, the solution is given in Mikhlin [15] as

$$d\phi/d\eta = C/\sqrt{\eta(1-\eta)} \quad (11)$$

Nomenclature

a_0, a = coefficient of asymptotic series expansion
 \bar{A} = dimensionless slab band absorptance
 c = speed of light, 2.998×10^8 m/s
 C_1 = integrated intensity [m^{-2}]
 C_3 = band width parameter [m^{-1}]
 e_{ω} = Planck's function [$W/m^2/m^{-1}$]
 $e_{\omega 0}$ = Planck's function evaluated at ω_0
 E_n = exponential integral of n th order
 h = Planck's constant, 6.625×10^{-34} JS
 k = Boltzmann's constant, 1.380×10^{-23} J/K
 L = distance between plates [m]
 M = ratio of emissive power, $e_{\omega 0}(T_2)/e_{\omega 0}(T_1)$
 q_R = total radiation heat flux [W/m^2]
 $q_{R\omega}$ = spectral radiation heat flux [$W/m^2/m^{-1}$]
 Q = dimensionless radiation heat flux

T = temperature [K]
 u = optical coordinate for gray gas model, $\kappa_p y$
 u_0 = optical thickness for gray gas model, $\kappa_p y$
 y = physical coordinate [m]
 α = angle with coordinate y [rad]
 γ = Euler-Mascheroni constant, 0.5772156
 $\Delta\omega$ = effective band width [m^{-1}]
 η = dimensionless coordinate, y/L
 $\bar{\kappa}$ = average absorption coefficient for box model [m^{-1}]
 κ_p = Planck mean coefficient [m^{-1}]
 κ_{ω} = spectral absorption coefficient [m^{-1}]
 μ = direction variable, $\cos \alpha$
 σ = Stefan-Boltzmann constant, 5.668×10^{-8} J/Sm²K⁴
 τ = optical coordinate for exponential band model, $C_1 y / C_3$

τ_0 = optical thickness for exponential band model, $C_1 L / C_3$
 τ^* = optical coordinate, $\tau_0 - \tau$
 τ_0^* = optical thickness, τ_0
 $\bar{\tau}$ = optical coordinate for box model, $\bar{\kappa} y$
 $\bar{\tau}$ = optical thickness for box model, $\bar{\kappa} L$
 ϕ = dimensionless emissive power, $e_{\omega 0}/e_{\omega 0}(T_1)$
 ψ = dimensionless emissive power, $[e_{\omega 0} - e_{\omega 0}(T_1)]/[e_{\omega 0}(T_2) - e_{\omega 0}(T_1)]$
 ω = wave number [m^{-1}]
 ω_0 = band center [m^{-1}]

Subscripts

1 = lower wall quantity
 2 = upper wall quantity
 g = gray gas quantity
 b = box model quantity

Table 1 Values of a_0 and a_1

τ_0	0.1	0.2	0.5	1.0	2.0	5.0	10.0	20.0
$-a_0$	0.2989	0.3438	0.4169	0.4556	0.5025	0.5522	0.5776	0.5947
a_1	0.0152	0.0258	0.0510	0.0836	0.1338	0.2270	0.3055	0.3744

where C is an arbitrary constant, attributed to the nonuniqueness of the solution of the singular integral equation. After integration

$$\phi(\eta) = C \sin^{-1}(1 - 2\eta) + D \quad (12)$$

The above equation is generally good only in region away from the boundaries, and, consequently, no boundary conditions can be specified to determine the unknown constants C and D . In the present study, both constants are to be determined by matching the outer solution with the inner solutions. It is noted, however, when $\tau_0 \rightarrow \infty$, the temperature is continuous at the boundaries, i.e., $\phi(0) = 1$ and $\phi(\tau_0) = M$, and the constants can be uniquely determined to yield

$$\psi(\eta) = 0.5 - [\sin^{-1}(1 - 2\eta)]/\pi \quad (13)$$

where

$$\psi(\eta) \equiv [e_{\omega_0}(\eta) - e_{\omega_0}(T_1)]/[e_{\omega_0}(T_2) - e_{\omega_0}(T_1)] \quad (14)$$

Mighdoll and Cess [11] also arrived at the same result as equation (13) using the exponential kernel approximation.

(b) **Lower Boundary Solution (Inner Solution).** Near the lower boundary, there is a temperature slip at the boundary so that $\psi(0)$ is not identical to zero. For example, even if τ_0 is as large as 100, $\psi(0) = 0.05$ for the band of the exponential type [2]. This is due to the increasingly dominant role of the wing region in controlling the temperature distribution as path length increases. No matter how thick the optical thickness evaluated at the band center is, there is always a wing region not optically thick.

Near the boundary, the complete expression of the slab band absorptance given by equation (7) should be used and the influence of the upper boundary is negligible. Equation (9) reduces to

$$\int_0^\tau \bar{A}'(\tau - \tau') \frac{d\phi}{d\tau'} d\tau' - \int_\tau^{\tau_0} \bar{A}'(\tau' - \tau) \frac{d\phi}{d\tau'} d\tau' = [1 - \phi(0)]\bar{A}'(\tau) \quad (15)$$

Let

$$d\phi/d\tau' = [1 - \phi(0)]\theta(\tau'), \quad (16)$$

equation (15) can be written alternatively as

$$\int_0^\tau \bar{A}'(\tau - \tau') \theta(\tau') d\tau' - \int_\tau^{\tau_0} \bar{A}'(\tau' - \tau) \theta(\tau') d\tau' = \bar{A}'(\tau) \quad (17)$$

For large τ_0 , $\theta(\tau)$ is monotonic, analytic at $\tau = 0$ and behaves as $\tau^{-1/2}$ for large τ . As a first order approximation, the solution is [12]³

$$\theta(\tau) = a_0(a_1 + \tau)^{-1/2} \quad (18)$$

The above solution can also be obtained by assuming an asymptotic series expansion of $\theta(\tau)$ and matching it with the outer solution. The first term of the asymptotic series should be similar to equation (18). This becomes obvious when the solutions are matched at the overlapped region.

In seeking for the asymptotic solution, the two constants a_0 and a_1 in equation (18) are determined by substituting equation (18)

into equation (17) with $\tau_0 \rightarrow \infty$ and forcing them to satisfy the resulting equation at two locations [12]. They can also be found by requiring the asymptotic solution of the temperature distribution to be equal to the exact numerical solution at these two locations. In this paper, we elect the latter, because Crosbie and Viskanta [2] have presented numerical solution for the temperature distribution over a wide range of optical thickness. The values of a_0 and a_1 are thus found to be -0.595 and 0.375 , respectively, as shown in the last column of Table 1. From equations (16) and (18), the approximate solution of $\phi(\tau)$ is obtained as

$$\phi(\tau) = \phi(0) + 2a_0[1 - \phi(0)][\tau + a_1]^{1/2} - \sqrt{a_1} \quad (19)$$

Here the boundary condition, $\phi(\tau) = \phi(0)$ at $\tau = 0$, has been employed. $\phi(0)$ is still an unknown, to be determined by asymptotic matching.

(c) **Upper Boundary Solution (Inner Solution).** The condition near the upper boundary is similar to that of the lower boundary. Taking advantage of this similarity and defining a new variable as

$$\tau^* = \tau_0 - \tau \quad (20)$$

The governing equation becomes

$$\int_0^{\tau^*} \bar{A}'(\tau^* - \tau^{*'}) \frac{d\phi}{d\tau^{*'}} d\tau^{*'} - \int_{\tau^*}^{\tau_0^*} \bar{A}'(\tau^{*'} - \tau^*) \frac{d\phi}{d\tau^{*'}} d\tau^{*'} = [M - \phi(\tau_0)]\bar{A}'(\tau^*) \quad (21)$$

where $\tau_0^* = \tau_0$. Furthermore let

$$d\phi/d\tau^* = [M - \phi(\tau_0)]\theta(\tau^*) \quad (22)$$

equation (21) can be written as

$$\int_0^{\tau^*} \bar{A}'(\tau^* - \tau^{*'}) \theta(\tau^{*'}) d\tau^{*'} - \int_{\tau^*}^{\tau_0^*} \bar{A}'(\tau^{*'} - \tau^*) \theta(\tau^{*'}) d\tau^{*'} = \bar{A}'(\tau^*) \quad (23)$$

which is of the same form as equation (17) and therefore the solution should be the same. The approximate solution of equation (21) is then

$$\phi(\tau^*) = \phi(\tau_0) + 2a_0[M - \phi(\tau_0)][(\tau^* + a_1)^{1/2} - \sqrt{a_1}] \quad (24)$$

where the upper boundary condition, $\phi(\tau^*) = \phi(\tau_0)$ at $\tau^* = 0$, has been employed.

(d) **Asymptotic Matching.** For the matching of the lower boundary solution and the outer solution, the method of asymptotic matching [11, 14] is employed. The outer expansion ($\tau \gg 1$) of the inner solution is matched with the inner expansion ($\eta \ll 1$) of the outer solution. For $\tau \gg 1$, equation (19) can be expanded as

$$\phi(\tau) = \phi(0) - 2a_0\sqrt{a_1}[1 - \phi(0)] + 2a_0[1 - \phi(0)]\tau^{1/2} + \dots \quad (25)$$

On the other hand, the inner expansion of the outer solution, given by equation (12) yields

$$\phi(\tau) = D - (\pi/2)C + (2C/\sqrt{\tau_0})\sqrt{\tau} + \dots \quad (26)$$

Comparing the foregoing two equations gives the following relations

$$D - (\pi/2)C = \phi(0) - 2a_0\sqrt{a_1}[1 - \phi(0)] \quad (27)$$

³In fact, a more general solution should include another term, $a_2 \exp(-a_3\tau)$. However, this additional term is of the secondary importance and therefore the solution of reference [12] is still used.

$$C = a_0\sqrt{\tau_0}[1 - \phi(0)] \quad (28)$$

Similar relations are obtained by the matching of the upper boundary solution, equation (24), and the outer solution, equation (12). They are

$$D + (\pi/2)C = \phi(\tau_0) - 2a_0\sqrt{a_1}[M - \phi(\tau_0)] \quad (29)$$

$$C = -a_0\sqrt{\tau_0}[M - \phi(\tau_0)] \quad (30)$$

Equations (25)–(28) can be used to solve C , D , $\phi(0)$, and $\phi(\tau_0)$ as follows

$$C = (M - 1)a_0\sqrt{\tau_0}/(\pi a_0\sqrt{\tau_0} - 4a_0\sqrt{a_1} - 2) \quad (31)$$

$$D = (M + 1)/2 \quad (32)$$

$$\phi(0) = [\pi a_0\sqrt{\tau_0} - 4a_0\sqrt{a_1} - (m + 1)]/(\pi a_0\sqrt{\tau_0} - 4a_0\sqrt{a_1} - 2) \quad (33)$$

$$\phi(\tau_0) = [M(\pi a_0\sqrt{\tau_0} - 4a_0\sqrt{a_1}) - (M + 1)]/(\pi a_0\sqrt{\tau_0} - 4a_0\sqrt{a_1} - 2) \quad (34)$$

(e) Approximate Solution for Temperature Distribution.

A single expression of $\phi(\tau)$ applicable throughout the whole region can be obtained by adding the solutions of each region and subtracting the overlapped solution [11, 14]. Adding equations (12), (19), and (24) and subtracting equations (25) and the overlapped solution between the outer solution and the upper boundary solution yields

$$\phi(\tau) = \frac{M + 1}{2} - \frac{a_0(M - 1)}{\pi a_0\sqrt{\tau_0} - 4a_0\sqrt{a_1} - 2} \left[\sqrt{\tau_0} \sin^{-1}\left(1 - 2\frac{\tau}{\tau_0}\right) - 2(\sqrt{\tau + a_1} - \sqrt{\tau}) + 2(\sqrt{\tau_0 - \tau + a_1} - \sqrt{\tau_0 - \tau}) \right] \quad (35)$$

or

$$\psi(\tau) = \frac{1}{2} - \frac{a_0}{\pi a_0\sqrt{\tau_0} - 4a_0\sqrt{a_1} - 2} \left[\sqrt{\tau_0} \sin^{-1}\left(1 - 2\frac{\tau}{\tau_0}\right) - 2(\sqrt{\tau + a_1} - \sqrt{\tau}) + 2(\sqrt{\tau_0 - \tau + a_1} - \sqrt{\tau_0 - \tau}) \right] \quad (36)$$

The foregoing equation is antisymmetric about $\tau = \tau_0/2$, as is expected for the problem of radiative equilibrium. The dimensionless emissive power of the gas at the boundary, $\tau = 0$, is

$$\psi(0) = \frac{1}{2} - \frac{a_0}{\pi a_0\sqrt{\tau_0} - 4a_0\sqrt{a_1} - 2} \left[\frac{\pi}{2} \sqrt{\tau_0} - 2\sqrt{a_1} + 2(\sqrt{\tau_0} + a_1 - \sqrt{\tau_0}) \right] \quad (37)$$

which shows the existence of the temperature slip.

From the foregoing equation, it is seen that when $\tau_0 \rightarrow \infty$, $\psi(0) \rightarrow 0$ which approaches the correct value of the optically thick limit. It is also true in the optically thin limit because when $\tau_0 \rightarrow 0$, $\psi(0) \rightarrow 1/2$. Thus, the asymptotic matching method yields the solution correctly in both limits, though the derivation of this solution is based on the assumption of large path length ($\tau_0 \gg 1$).

(f) **Radiative Heat Flux.** Once the temperature distribution (or more correctly the dimensionless emissive power) is known, any other quantities of engineering interest can be easily found. For example, the radiative flux can be obtained by combining equations (2), (3), and (7),

$$q_R = \sigma T_1^4 - \sigma T_2^4 + C_3[e_{\omega_0}(T_2) - e_{\omega_0}(T_1)]Q(\tau) \quad (38)$$

where

$$Q(\tau) = \bar{A}(\tau_0 - \tau) + \int_{\tau}^{\tau_0} \psi(\tau')\bar{A}'(\tau - \tau')d\tau' - \int_0^{\tau} \psi(\tau')\bar{A}'(\tau' - \tau)d\tau' \quad (39)$$

Under the condition of radiative equilibrium, Q is a constant and thus can be evaluated by setting $\tau = 0$,

$$Q = \bar{A}(\tau_0) - \int_0^{\tau_0} \psi(\tau')\bar{A}'(\tau')d\tau'. \quad (40)$$

With both $\bar{A}(\tau)$ and $\psi(\tau)$ being expressed in closed forms, it may be possible to integrate equation (40) analytically. However, because only the straightforward integration is involved, numerical integration is recommended.

Gray Gas and Box Model Solutions

Using less realistic band models, analytic solutions can also be obtained. For completeness, they are presented in the following.

According to the gray gas model, the wave number dependent absorption coefficient can be replaced by an averaged quantity, say, the Planck mean coefficient, κ_p . Then upon the use of the exponential kernel approximation, $E_2(t) \simeq (3/4) \exp(-3t/2)$, the solution can be readily found as [16, 17]

$$\psi_g(u) = (2 + 3u)/(4 + 3u_0) \quad (41)$$

$$Q_g = 3u_0/(4 + 3u_0) \quad (42)$$

where

$$u = \kappa_p y, \quad u_0 = \kappa_p L \quad (43a)$$

$$\psi_g = [T^4(u) - T_1^4]/[T_2^4 - T_1^4] \quad (43b)$$

and

$$Q_g = [q_R + \sigma T_2^4 - \sigma T_1^4]/[\sigma T_2^4 - \sigma T_1^4] \quad (43c)$$

In order to facilitate the comparison between the gray gas and the present asymptotic solutions, the relation between their dimensionless variables should be identified. Taking the CO fundamental band for example, the band center and the band width parameter are [18, 19]

$$\omega_0 = 2143 \text{ cm}^{-1}, \quad C_3 = 38(T/300)^{1/2} \quad (44)$$

respectively. So the optical thickness u is related to τ by

$$u = (2.194e_{\omega_0}\tau)/(\sigma T^{1/2}) \quad (45)$$

When the temperature difference is small, the linearization

$$T^4 - T_1^4 \simeq 4T_1^3(T - T_1)$$

and

$$e_{\omega_0}(T) - e_{\omega_0}(T_1) \simeq (de_{\omega_0}/dT)_{T=T_1}(T - T_1)$$

are applicable. Thus

$$\psi = \psi_g \quad \text{and} \quad Q = 1.823\sigma T_1^{5/2}Q_g/(de_{\omega_0}/dT)_{T=T_1} \quad (46)$$

The box model approximates a band by a rectangular box of an effective band width, $\Delta\omega$, with a suitably determined average absorption coefficient, $\bar{\kappa}$. Similar to the gray gas model, the solution can be found as

$$\psi_b(\bar{\tau}) = (2 + 3\bar{\tau})/(4 + 3\bar{\tau}_0) \quad (47)$$

$$Q_b = 3\bar{\tau}_0/(4 + 3\bar{\tau}_0) \quad (48)$$

where

$$\bar{\tau} = \bar{\kappa}y, \quad \bar{\tau}_0 = \bar{\kappa}L \quad (49a)$$

$$\psi_b(\bar{\tau}) = [e_{\omega_0}(\bar{\tau}) - e_{\omega_0}(T_1)]/[e_{\omega_0}(T_2) - e_{\omega_0}(T_1)] \quad (49b)$$

$$Q_b = (q_R + \sigma T_2^4 - \sigma T_1^4)/\{\Delta\omega[e_{\omega_0}(T_2) - e_{\omega_0}(T_1)]\} \quad (49c)$$

For the CO fundamental band [18],

$$\Delta\omega = 214(\tau/300)^{1/2}$$

and

$$\bar{\kappa} = C_1/\Delta\omega$$

Thus the relation between the dimensionless variables are

$$\bar{\tau} = 0.1308\tau, \quad \psi = \psi_b \quad \text{and} \quad Q = 5.632 Q_b.$$

Results and Discussion

Though in the previous section a_0 and a_1 are uniquely determined from equations (17) and (18) with $\tau_0 \rightarrow \infty$, a close examination of equation (37) reveals that they are generally a function of

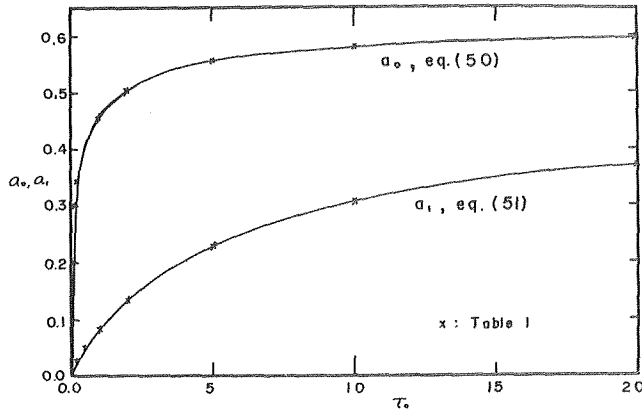


Fig. 2 Values of a_0 and a_1

Table 2 Dimensionless emissive power for $\tau_0 = 0.1$

τ/τ_0	Reference [2]	Equation (36)		
		Table 1 ($a_0 = -0.2989$, $a_1 = 0.0152$)	Equations (50) and (51) ($a_0 = -0.1843$, $a_1 = 0.0126$)	Limiting values ($a_0 = -0.595$, $a_1 = 0.375$)
1.0	0.54121	0.54121	0.52727	0.50941
0.95	0.53596	0.53596	0.52367	0.50909
0.90	0.53147	0.53147	0.52046	0.50844
0.85	0.52723	0.52667	0.51751	0.50762
0.80	0.52315	0.52259	0.51475	0.50669
0.75	0.51917	0.51859	0.51213	0.50568
0.70	0.51526	0.51473	0.50960	0.50461
0.65	0.51140	0.51097	0.50714	0.50349
0.60	0.50758	0.50727	0.50473	0.50233
0.55	0.50379	0.50362	0.50236	0.50116
0.50	0.50000	0.50000	0.50000	0.50000

τ_0 . Table 1 summarizes their values which are obtained by equating equation (36) to the exact numerical values of [2] at $\tau = 0$ and $\tau = 0.05 \tau_0$ for each τ_0 . Their use in equation (36) will undoubtedly improve the accuracy of the equation.

From Table 1 it is observed that a_0 and a_1 approach 0 as $\tau \rightarrow 0$ and approach limiting values as $\tau_0 \rightarrow \infty$. The limiting values of a_0 and a_1 are -0.595 and 0.375 , respectively. For convenience a_0 and a_1 are correlated by the expressions:

$$a_0 = 0.595[1 - \exp(-4.12\tau_0 + 4.32\tau_0^2 - 1.98\tau_0^3 + 0.345\tau_0^4 - 0.0186\tau_0^5)] \quad (50)$$

$$a_1 = 0.375[1 - \exp(-0.358\tau_0 + 0.161\tau_0^2 - 0.0663\tau_0^3 + 0.01116\tau_0^4 - 0.0005956\tau_0^5)] \quad (51)$$

which yield correct values at $\tau_0 = 0, 0.5, 1, 2, 5, 10$, and ∞ . The foregoing equations are also plotted in Fig. 2.

The present asymptotic solution, equation (36), for the distribution of the emissive power is compared to the exact solution obtained numerically [2] in Tables 2, 3, and 4 for $\tau_0 = 0.1, 1$, and 10 , respectively. The asymptotic solution using the respective values of a_0 and a_1 , as presented in third column of the tables, deviated no more than half a percent from the exact solution. The fourth column of Table 2 gives the result by using equations (50) and (51). Even if the limiting values of a_0 and a_1 are used in equation (36) for all τ_0 's, the resulting values as shown in the last column of the tables agree remarkably well with numerical results, with an error less than 6 percent.

The temperature profiles are also plotted in Fig. 3, together with the gray gas and box model solutions. The superiority of the asymptotic solution over the latter methods is clearly illustrated. A similar comparison for the temperature slip at $\tau = 0$ is given in Fig.

Table 3 Dimensionless emissive power for $\tau_0 = 1.0$

τ/τ_0	Reference [2]	Equation (36)	
		Table 1 or equations (50) and (51) ($a_0 = -0.4556$, $a_1 = 0.0836$)	Limiting values ($a_0 = -0.595$, $a_1 = 0.375$)
1.0	0.66855	0.66855	0.67054
0.95	0.64431	0.64431	0.65195
0.90	0.62514	0.62376	0.63378
0.85	0.60763	0.60540	0.61608
0.80	0.59108	0.58848	0.59880
0.75	0.57516	0.57255	0.58185
0.70	0.55968	0.55732	0.56517
0.65	0.54452	0.53259	0.54869
0.60	0.52957	0.52821	0.53237
0.55	0.51475	0.51404	0.51615
0.50	0.50000	0.50000	0.50000

Table 4 Dimensionless emissive power for $\tau_0 = 10$

τ/τ_0	Reference [2]	Equation (36)	
		Table 1 or equations (50) and (51) ($a_0 = -0.5776$, $a_1 = 0.3055$)	Limiting values ($a_0 = -0.595$, $a_1 = 0.375$)
1.0	0.8538	0.8538	0.8559
0.95	0.7913	0.7913	0.7955
0.90	0.7477	0.7457	0.7499
0.85	0.7101	0.7072	0.7111
0.80	0.6759	0.6729	0.6763
0.75	0.6440	0.6411	0.6440
0.70	0.6136	0.6112	0.6135
0.65	0.5844	0.5824	0.5842
0.60	0.5559	0.5545	0.5557
0.55	0.5278	0.5271	0.5277
0.50	0.5000	0.5000	0.5000

4. Again the excellent agreement of the asymptotic solution with the numerical solution over the whole range of the optical thickness is demonstrated while other solutions grossly overpredict the temperature slip for most of the optical range. For moderate value of τ_0 , the band center of the exponential band becomes optically thick, but the gray gas and the box models are not, resulting in a higher radiative jump at the boundary than that of the exponential model. For large values of τ_0 , the box model is more opaque everywhere in the band than the exponential and gray gas models, because there is always a transparent region in the wing of the exponential band and also because the band of the gray gas model is ex-

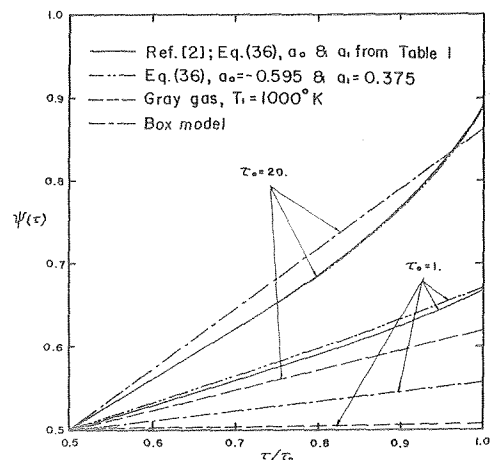


Fig. 3 Dimensionless emissive power

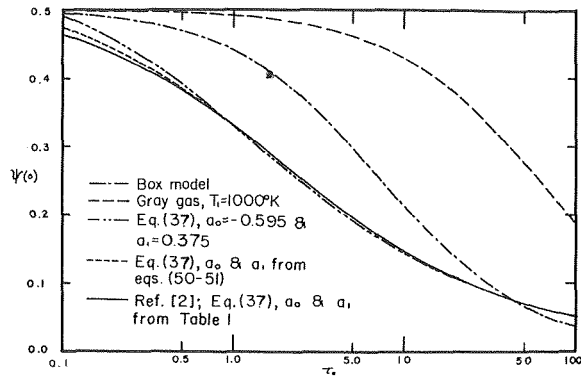


Fig. 4 Dimensionless temperature slip at $\tau = 0$

tended and flattened to the whole spectrum such that its optical thickness is thinner than others. This explains the fact that the box model begins to underpredict the slip at $\tau_0 \approx 40$ and the gray gas result approaches slowly toward the optically thick limit. More distinctive behavior due to the use of the exponential band model and the use of the gray gas or box model have been delineated elsewhere [1].

The dimensionless radiative flux of various solutions are compared in Fig. 5. The asymptotic solution is indistinguishable from that of reference [2], irrespective of whether the limiting values or the correct values of a_0 and a_1 from Table 1 are used. Except for small optical depth, both the box and gray gas models deviate considerably from reference [2].

It should be noted that the outer solution is valid for any expressions of the total band absorptance as long as they vary logarithmically with the optical depth in the optically thick limit. For example, the more general expression which accounts for the line structure as given by reference [3 or 7] does yield logarithmic behavior in the optically thick limit. Because the inner solution contains two undetermined parameters a_0 and a_1 which are governed by the expression of the total band absorptance, the inner solution is also valid when other expressions are used if a_0 and a_1 are adjusted accordingly. The new values of a_0 and a_1 can be obtained by substituting equation (18) and the new expression of the total band absorptance in equation (17) with $\tau_0 = \infty$ and forcing both sides of the resulting equation to be equal at two locations. Therefore, the present analytical solution given by equation (36) is valid for the exponential wide-band model in general; it is applicable not only to the high pressure limit but also other pressure ranges in which the line structure may be important.

Conclusions

1 A two-parameter nongray analytic solution for the temperature distribution (in terms of the dimensionless emissive power) of the radiative equilibrium has been found. It is valid for all optical thickness and its accuracy is within 0.5 percent as compared to the existing numerical solution.

2 The present solution given by equation (36) is equally valid for other forms of the band absorptance that vary logarithmically with τ in the optically thick limit. The corresponding values of a_0 and a_1 can be easily found from equations (17) and (18).

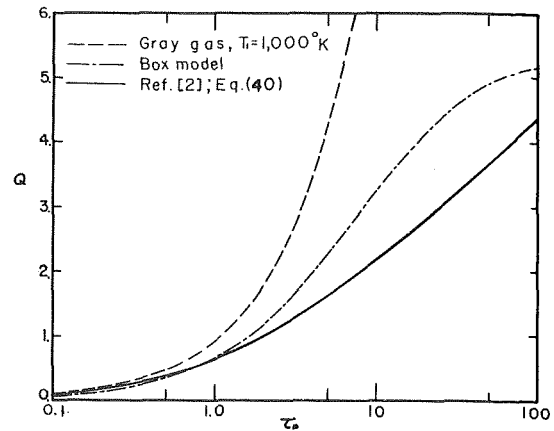


Fig. 5 Dimensionless radiative flux, Q

References

- Cess, R. D., Mighdoll, P., and Tiwari, S. N., "Infrared Radiative Heat Transfer in Nongray Gases," *International Journal of Heat and Mass Transfer*, Vol. 10, 1967, p. 1521.
- Crosbie, A. L., and Viskanta, R., "Effect of Band or Line Shape on the Radiative Transfer in a Nongray Planar Medium," *JQSRT*, Vol. 10, 1970, p. 487.
- Edwards, D. K., and Menard, N. A., "Comparison of Models for Correlation of Total Band Absorptance," *Applied Optics*, Vol. 3, 1964, p. 621.
- Edwards, D. K., and Menard, W. N., "Correlation for Absorption by Methane and Carbon Dioxide Gases," *Applied Optics*, Vol. 3, 1964, p. 847.
- Edwards, D. K., "Absorption of Radiation by Carbon Monoxide Gas According to the Exponential Wide Band Model," *Applied Optics*, Vol. 4, 1965, p. 1352.
- Edwards, D. K., Glassen, L. K., Hauser, W. C., and Tuchscher, J. S., "Radiation Heat Transfer in Nonisothermal Nongray Gases," *JOURNAL OF HEAT TRANSFER, TRANS. ASME, Series C*, Vol. 89, 1967, p. 219.
- Tien, C. L., and Lowder, J. E., "A Correlation for Total Band Absorptance of Radiating Gases," *International Journal of Heat and Mass Transfer*, Vol. 9, 1966, p. 698.
- Edwards, D. K., and Balakrishnan, A., "Slab Band Absorptance for Molecular Gas Radiation," *JQSRT*, Vol. 12, 1972, p. 1379.
- Chan, S. H., "Geometric Band Absorptance of a Nongray Gas With Arbitrary Configurations," *International Journal of Heat and Mass Transfer*, Vol. 17, 1974, p. 381.
- Mighdoll, P., and Cess, R. D., "Infrared Radiative Equilibrium Under Large Path Conditions," *AIAA Journal*, Vol. 6, 1968, p. 1778.
- Emanuel, G., "Radiative Transport in an Optically Thick Planar Medium," *International Journal of Heat and Mass Transfer*, Vol. 11, 1968, p. 1413.
- Cess, R. D., "A Radiative Transfer Model for Planetary Atmosphere," *JQSRT*, Vol. 11, 1971, p. 1969.
- Cole, J. D., *Perturbation Method in Applied Mechanics*, Blaisdell, Waltham, Mass., 1968.
- van Dyke, M., *Perturbation Method in Fluid Mechanics*, Academic Press, New York, 1964.
- Mikhlin, S. G., *Integral Equations*, Pergamon Press, Oxford, 1957, p. 131.
- Viskanta, R., and Grosh, R. J., "Heat Transfer in a Thermal Radiation Absorbing and Scattering Medium," *International Heat Transfer Conference*, Boulder, Colo., 1961, p. 820.
- Sparrow, E. M., and Cess, R. D., *Radiation Heat Transfer*, Wadsworth, Belmont, Calif., 1966, p. 226.
- Penner, S. S., *Quantitative Molecular Spectroscopy and Gas Emissivities*, Addison-Wesley, Reading, Mass., 1959.
- Abu-Romia, M. M., and Tien, C. L., "Measurements and Correlations of Infrared Radiation of Carbon Monoxide at Elevated Temperatures," *JQSRT*, Vol. 6, 1966, p. 143.

D. M. Snider¹

Graduate Assistant.

R. Viskanta

Professor.

School of Mechanical Engineering,
Purdue University,
West Lafayette, Ind.

Radiation Induced Thermal Stratification in Surface Layers of Stagnant Water

Analysis is developed for the time dependent thermal stratification in surface layers of stagnant water by solar radiation. The transient temperature distribution is obtained by solving the one-dimensional energy equation for combined conduction and radiation energy transfer using a finite difference method. Experimentally, solar heating of water is simulated using tungsten filament lamps in parabolic reflectors of known spectral characteristics. The transient temperature distribution resulting from radiant heating of pure water in a glass-walled test cell is measured with a Mach-Zehnder interferometer. Measured and predicted temperature profiles show good agreement, thus verifying the radiation and total energy transfer models in stagnant water. It is found that the boundary condition at the air-water interface and internal radiant heating rate must be correctly specified in order to properly model stratification of water by radiation.

Introduction

Increased energy demand has resulted in large amounts of water being diverted for cooling of electric power generating plants. The heated water when returned to its source increases the temperature of the receiving water and often changes its thermal structure, i.e., temperature and density distributions. Concern with thermal pollution and water quality in lakes, reservoirs, and ponds has generated a need to gain understanding of thermal stratification in stagnant waters and to develop modeling capability. The vertical temperature and density variations in a body of water have important effects on chemical and physical properties, dissolved oxygen content, water quality, aquatic life and ecological balance as well as mixing processes in water. Models for predicting hydraulic and thermal characteristics in waters are needed by electric utilities and regulatory agencies responsible for determining if the thermal pollution standards which have been designed to protect aquatic life from thermal impacts will be met. Also, the models may provide better understanding of complex hydraulic phenomena, and such information is invaluable to those concerned with ecology and water quality.

Direct field measurements of the thermal structure in lakes or reservoirs have been reported in the literature, and a number of

mathematical models for simulating thermal behavior have also been developed. A comprehensive survey of the literature pertinent to the problems of energy transfer in stagnant waters has been presented by Dake and Harleman [1]² and more recently by Ou, et al. [2] and there is no need to review these surveys. Both experimental and analytical studies have been undertaken for the purpose of determining the thermal structure, i.e., temperature distribution in the vertical direction, and the analyses have been primarily based on one-dimensional energy transfer models. Solar radiation is recognized as the principal natural heat load in waters [3]; however, confusion still exists as to how to properly account for it. Some investigators have considered the radiation to be absorbed at the water surface (i.e., opaque) and others treated the water as being semitransparent but ignored the spectral nature of radiation. Since the ultraviolet and infrared parts of the incoming solar radiation are largely absorbed within the first centimeters of the water and the visible part penetrates more deeply and carries significant energy to depths, on the order of tens of metres, the modeling of water as a gray medium is open to question and needs to be examined. Experimental studies modeling thermal stratification in a laboratory where conditions can be reasonably well controlled are practically nonexistent. The notable exception is the work of Dake and Harleman [4] who have studied stratification of water in a tank by radiation. The existing radiant and total energy transfer models in stagnant waters have not been verified experimentally.

¹ Presently at Aerojet Nuclear Co., Idaho Falls, Idaho

Contributed by the Heat Transfer Division for publication in the JOURNAL OF HEAT TRANSFER. Manuscript received by the Heat Transfer Division August 16, 1974. Paper No. 75-HT-CC.

² Numbers in brackets designate References at end of paper.

The purpose of this study is to improve understanding of internal energy transfer processes in stagnant water and to lay ground work for modeling of more complex hydraulic systems. To this end, thermal stratification of water induced by solar radiation is simulated experimentally in a laboratory tank, and the data are then used to evaluate the validity of the radiant and the unsteady total (one-dimensional) energy transfer models in stagnant water.

Analysis

Physical Model and Basic Equations. Consider a lake, reservoir or a pond of such large extent that the energy transfer is essentially one-dimensional, i.e., the temperature varies in the vertical direction only. Any inflows and outflows into the body of water are neglected, and with only slight winds, the water is assumed to be stagnant allowing for neglect of advective energy transfer. The water is assumed to be heated by solar radiation and/or convection. Due to the diurnal and seasonal variations in incident solar radiation, atmospheric and meteorological conditions, the heating depends on the time of the day, month and the season; however, in the present analysis the incident solar flux is taken as constant. The convective heat and mass transfer coefficients at the water surface depend on the surface temperature but are assumed uncoupled from atmospheric and meteorological conditions. The variation of these parameters with time can readily be included for specific situations if data are available. The physical model, although crude in this respect, serves to illustrate the basic physical approach.

Within the range of temperatures encountered, the variation of density, specific heat, thermal conductivity, spectral absorption and scattering coefficient of water is slight and can be justifiably neglected. Under the foregoing assumptions the unsteady energy equation governing the temperature distribution becomes

$$\rho c \frac{\partial T}{\partial t} = - \frac{\partial}{\partial x} \left(-K \frac{\partial T}{\partial x} + F \right) \quad (1)$$

The first term on the right-hand side of this equation represents molecular diffusion and the second radiative transfer. The radiative transfer contribution is evaluated explicitly in the following subsection.

At the air-water interface, energy is transferred by convection, evaporation or condensation and radiation. The instantaneous energy balance at the interface can be expressed as

$$k \frac{\partial T}{\partial x} \Big|_{x=0} = h(T_w - T_\infty) + h_{fg}g(p_w - p_\infty) + \epsilon_w \sigma (T_w^4 - T_e^4) \quad (2)$$

The first term on the right-hand side of equation (2) accounts for convection, the second for evaporation or condensation, and the third for radiation transfer in the thermal (infrared) part of the spectral region where water is effectively opaque to radiation. In writing equation (2) the spectrum of the radiation incident on the water surface, as is customary in problems of geophysical nature, has been divided into two bands: (1) the solar ($0 \leq \lambda < \lambda_s$), and (2) the thermal (infrared) ($\lambda_s \leq \lambda < \infty$) bands. This separation is not only desirable from the computational point of view but is also realistic physically because water is semitransparent in the visible and the near infrared parts of the spectrum. However, in the infrared part of the spectrum ($\lambda > 2 \mu\text{m}$) the water is effectively opaque [5], and radiative transfer can be considered to be a surface rather than a volumetric phenomenon. An energy balance at the bottom results in

$$-k \frac{\partial T}{\partial x} \Big|_{x=L} = q_b + \int_0^{\lambda_s} \alpha_{b\lambda} F_{b\lambda}(L) d\lambda \quad (3)$$

where q_b represents the conductive heat transfer into the soil, and the second term accounts for the absorption of transmitted solar radiation. The emission of radiation by the soil has been neglected. The temperature distribution in the water at a selected initial time is taken as

$$T(x,0) = T_0(x) \quad (4)$$

Radiative Transfer. Analysis of radiative energy transfer within waters has been presented by Viskanta and Toor [5, 6] using concepts of radiative transfer theory, and the details are omitted here. In the model, a specified solar radiation field is incident on a plane layer of water of finite depth L . A fraction of the incident flux is reflected, and the remaining fraction is transmitted across the interface at $x = 0$ into the water. The air-water interface is assumed to be optically smooth, and hence reflection and transmission can be predicted from Fresnel's equations of classical electromagnetic theory. As the radiation propagates into the water it is absorbed and scattered until it reaches the bottom at $x = L$, where it is absorbed and diffusely reflected. The radiation reflected from the bottom then propagates through the water until it reaches the water-air interface where part of the incident radiation is transmitted into the air; the remaining part is specularly reflected down into the water. Volumetric emission of radiation by water is small compared to absorption and can therefore be neglected. For temperature levels which occur in natural waters, emitted radiation is in the infrared part of the spectrum where water is relatively opaque, and thus emission by water is considered to be a surface phenomenon. This has already been accounted for in equation (2).

Separating the incident solar radiant flux into a collimated,

Nomenclature

c = specific heat	k = thermal conductivity	tion entering water from air,
D = diffusion coefficient	L = depth of the layer of water	$\theta_c = \sin^{-1}(1/n_\lambda)$
E_n = exponential integral function defined by equation (7)	n = index of refraction of water	λ = wavelength
F = local radiative flux	p = partial pressure of water vapor in the air	μ = direction cosine, $\mu = \cos \theta$
F_0 = surface absorbed flux defined by equation (11)	R_n = exponential integral reflection function defined by equation (9)	ρ = density of water and directional reflectivity
F_c° = collimated component of the radiative flux incident on the air-water interface at angle θ deg	T = temperature	σ = Stefan-Boltzmann constant
F_d° = diffuse component of the radiative flux incident on the air-water interface	T_n = exponential integral transmission function defined by equation (8)	τ = directional transmissivity of the air-water interface
g = mass transfer coefficient	T_0 = initial temperature	
H = internal volumetric rate of radiant energy absorption defined by equation (10)	t = time	
h = heat transfer coefficient	x = length coordinate measured from the water surface	
h_{fg} = heat of vaporization	α = absorptivity of the water surface and thermal diffusivity	
	ϵ = emissivity of the water surface	
	κ = absorption coefficient of water	
	θ_c = critical angle for a beam of radiation entering water from air,	
	$\theta_e = \sin^{-1}(1/n_\lambda)$	
	λ = wavelength	
	μ = direction cosine, $\mu = \cos \theta$	
	ρ = density of water and directional reflectivity	
	σ = Stefan-Boltzmann constant	
	τ = directional transmissivity of the air-water interface	
		Subscripts
		b = bottom
		e = effective ambient temperature of the surroundings
		inc = incident
		s = solar
		w = water surface
		∞ = free stream
		λ = wavelength

$F_{c\lambda}^\circ$, and diffuse, $F_{d\lambda}^\circ$, components, using the forward approximation for multiple scattering [6], and assuming that the bottom soil is a diffuse reflector, the radiative flux can be expressed as [5]

$$F(x) = \int_0^\infty 2\left\{\frac{1}{2}\mu^\circ\tau_\lambda(\mu^\circ)F_{c\lambda}^\circ e^{-\kappa_\lambda x/\mu} + F_{d\lambda}^\circ T_3(\kappa_\lambda x) + F_{b\lambda}R_3[\kappa_\lambda(L+x)] - F_{b\lambda}E_3[\kappa_\lambda(L-x)]\right\}d\lambda \quad (5)$$

where the spectral radiative flux leaving the bottom is given by

$$F_{b\lambda} = 2\rho_{b\lambda}\left[\frac{1}{2}\mu^\circ\tau_\lambda(\mu^\circ)F_{c\lambda}^\circ e^{-\kappa_\lambda L/\mu} + F_{d\lambda}^\circ T_3(\kappa_\lambda L)\right]/[1 - 2\rho_{b\lambda}R_3(2\kappa_\lambda L)] \quad (6)$$

The exponential, transmission and reflection integral functions $E_n(x)$, $T_n(x)$ and $R_n(x)$, respectively, are defined as

$$E_n(x) = \int_0^1 e^{-x/\mu} \mu^{n-2} d\mu \quad (7)$$

$$T_n(x) = n^2 \int_{\mu_c}^1 \tau(\mu) e^{-x/\mu} \mu^{n-2} d\mu \quad (8)$$

$$R_n(x) = \int_0^1 \rho(\mu) e^{-x/\mu} \mu^{n-2} d\mu \quad (9)$$

The direction cosine μ inside the water is related to the direction cosine μ° outside the water by Snell's law of refraction and the critical angle θ_c is given by $\theta_c = \sin^{-1}(1/n_\lambda)$. The first and second terms on the right-hand side of equation (5) represent attenuation of the transmitted collimated and diffuse components of the incident solar flux, respectively. The third term represents multiple internal reflection, and the fourth term represents the contribution to the flux due to the diffuse reflection from the bottom.

The total volumetric rate of internal absorption of solar radiant energy $H(x)$, i.e., the total divergence of the radiative flux, is obtained by differentiating equation (5) and there results

$$-\frac{\partial F}{\partial x} = H(x) = \int_0^\infty 2\kappa_\lambda\left\{\frac{1}{2}\mu^\circ/\mu F_{c\lambda}^\circ e^{-\kappa_\lambda x/\mu} + F_{d\lambda}^\circ T_2(\kappa_\lambda x) + F_{b\lambda}R_2[\kappa_\lambda(L+x)] + F_{b\lambda}E_2[\kappa_\lambda(L-x)]\right\}d\lambda \quad (10)$$

If the incident flux, spectral absorption coefficient and index of refraction of water and its impurities, water surface and bottom reflectivities and the depth are known, the local radiative flux and internal absorption of radiant energy in water can be predicted. The numerical details and some specific results are given in a section on Method of Solution.

Experiment

A laboratory investigation was undertaken for the dual purpose of providing accurate data for verifying the analytical model and gaining improved understanding of the energy transfer processes in the immediate vicinity of the air-water interface, when the water is heated by solar radiation. Solar heating was simulated in the laboratory using tungsten filament lamps in Research, Inc. parabolic solar reflectors of known spectral characteristics. The transient temperature distribution in the water enclosed in a rectangular glass-walled test cell was measured using a Mach-Zehnder interferometer of typical rectangular design with 25 cm dia optics. A He-Ne laser served as the light source for the interferometer. Since the interferometer senses differences in refractive index of the water it requires no physical contact of a foreign object with the fluid and does not disturb or distort the temperature and radiation fields. It is therefore considered one of the best methods for obtaining quantitative temperature profiles [7].

The inside dimensions of the rectangular test cell were 10 cm along the optical path, 25 cm wide and 40 cm deep. The side walls, 2.5 cm thick plexiglass, acted as spacers between the 2.5 cm thick windows. A sheet metal shield completely covered the interferome-

ter leg in which the test cell rested. A hole in the shield allowed only water to be heated while the shield protected other components from radiant heating and reduced free convection in the interferometer leg. Urethane insulation, 5 cm thick, was placed along the side walls, and 2.5 cm thick sections covered the optical windows. The insulation on the windows could be easily removed to take photographs of the interference fringes. The details of the apparatus are given elsewhere [8].

A reference temperature needed for interpreting interferograms was measured with a thermocouple located 2 cm below the water surface. The interferometer beam did not cover the lower part of the test cell, so thermocouples in the lower region provided the only means of temperature measurement. A multichannel, integrating voltmeter with print-out and visual display recorded the millivolt output of the thermocouples.

The test cell was cleaned, filled with distilled water, covered and left undisturbed for some time to eliminate all convection currents and to attain a uniform room temperature. The heating lamps were then set at the desired voltage while the cell was shielded. The shield was removed, and the water exposed to a step change in the irradiation. At prescribed intervals, the interference patterns were photographed with a 35 mm camera and thermocouple emf readings simultaneously recorded. After each experiment, distances between water surface and thermocouples were measured using a cathetometer which was accurate to 0.05 cm.

The interferograms were interpreted using the accurate relation between index of refraction and temperature of Tilton and Taylor [9] to obtain temperature profiles. To adequately study the region near the interface where large temperature gradients existed, the area was magnified before photographing. Subsequently, the interferograms were analyzed using a measuring microscope. The details of the data reduction procedure and discussion of experimental errors are given by Snider [8].

Method of Solution

Prediction of Solar Heating. Before the temperature distribution during thermal stratification of water by radiation can be predicted, the internal volumetric absorption rate of radiant energy must be determined. A detailed discussion outlining the prediction of H and F has been presented elsewhere [5]. In order to establish the usefulness of the analytical model, radiant heating rate and flux in the water were predicted for several operating conditions of the tungsten filament lamps simulating the solar heating of the water in the test cell. Different internal and surface heating rates were obtained by operating the heater at three different temperatures of 2520 K, 2880 K, and 3250 K. The reflectivities of the air-water and water-test cell bottom (plexiglass) interfaces were estimated from Fresnel's equations. Since it was of interest to accurately predict the total local volumetric absorption rate and the radiative flux these quantities were evaluated over the spectral range of interest, $0.2 \mu\text{m} < \lambda < 7 \mu\text{m}$, using approximately 60 bands.

The extent to which the reflectivity of the bottom affects the radiative transfer in water is illustrated in Fig. 1 where the volumetric absorption rate of radiation is compared for three different reflectivities, i.e., $\rho_b = 0, 0.1$ and 1.0 . Little difference is seen to exist between the results for reflectivities of 0 and 0.1. It is important to note that near the bottom, the volumetric radiant energy absorption rate is small and approximating the bottom as a black body would not appreciably affect the prediction of the rate. For the estimated reflectivity of the plexiglass bottom, $\rho_b \approx 0.005$, the results are essentially the same as for $\rho_b = 0$.

Numerical Solutions. Since the boundary conditions are nonlinear and the internal radiant energy absorption rate is not a simple expression, a closed form analytical solution is not possible. Numerical integration of equation (1) with boundary and initial conditions, equations (2), (3), and (4), was obtained using an explicit finite difference method [10]. A uniform grid size was used throughout the depth of the layer of water. Different grid sizes

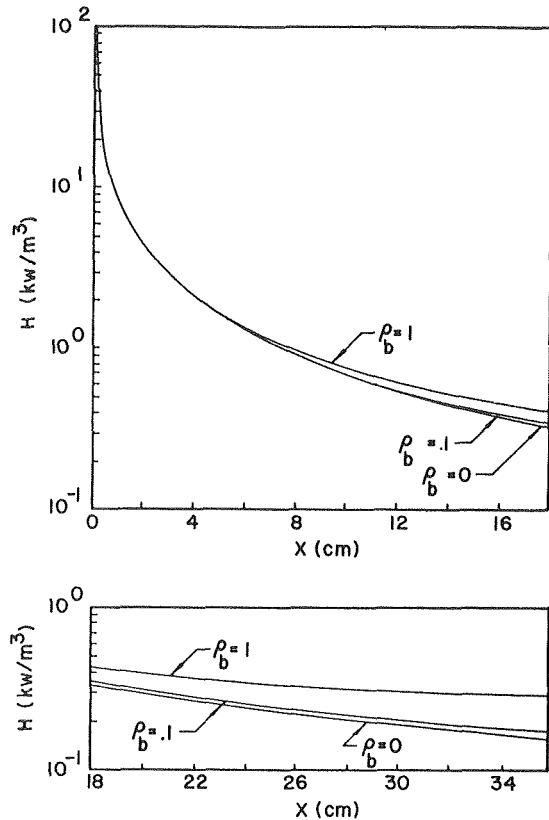


Fig. 1 Effect of the bottom reflectance on the volumetric radiant energy absorption rate, $L = 38.1$ cm; single lamp at 3250 K

were considered and the results obtained were checked for stability and convergence. Comparison of the results obtained using the explicit finite difference method with those based on exact analytical solutions for limiting cases yielded excellent agreement. The results reported in the paper are for a grid size of 0.2 mm. The computational details are given elsewhere [8]. Suffice it to note that in the numerical calculations of the incident radiative flux was separated into bands where water is either effectively opaque or semitransparent to radiation. In the band where water is semitransparent, the rate of volumetric radiant energy absorption was predicted from equation (10). In the opaque bands the solar energy absorbed in the first half of a finite difference node was considered absorbed at the surface ($x = 0$). The radiative flux absorbed at the surface, i.e.,

$$F_0 = \int_{\Delta\lambda_{\text{opaque}}} \alpha_\lambda F_{\text{inc},\lambda} d\lambda \quad (11)$$

could be computed once and included in the boundary condition at the air-water interface by subtracting F_0 from the right-hand side of equation (2).

The heat loss by convection and evaporation from the water surface could not be accurately specified from basic principles for the experimental test arrangement. Presently, no analysis or correlation is available in the literature for predicting the energy transfer from heated water cooled by free convection, evaporation and radiation at the air-water interface [11]. In the absence of more precise knowledge, the turbulent free convection heat transfer coefficient h was estimated using an empirical relation presented in the literature by McAdams [12] for cooling of horizontal heated plates in an unbounded air environment,

$$h = C(T_w - T_\infty)^{1/3} \quad (12)$$

The constant C was adjusted from 0.22 to 0.48 in order to improve agreement between analysis and data for a single experimental condition (i.e., given time t) at a heater lamp temperature of 2880

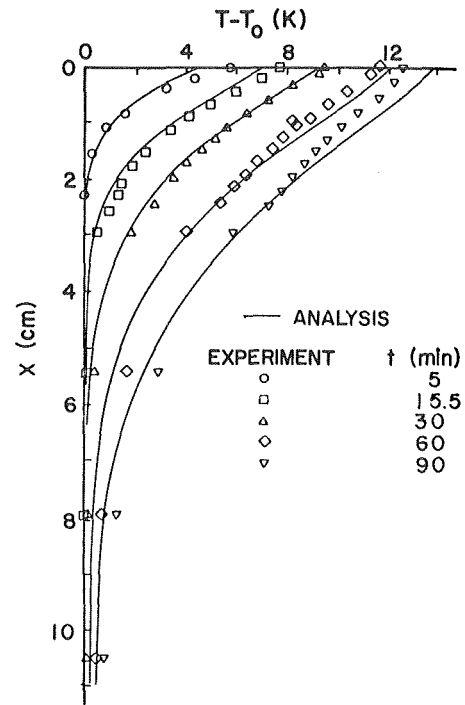


Fig. 2 Comparison of measured and predicted temperature distributions for lamps at 2520 K, $T_0 = T_\infty = 25$ C and $L = 38.1$ cm

K. After the initial adjustment to 0.48 the constant was then used in predicting the convective heat transfer coefficient for all other experimental conditions. The adjustment of the empirical constant was required because the water surface was not an unbounded flat plate but was a free surface surrounded by about 13 cm high walls which produced a "chimney" effect, and the fluid was not pure air but a binary air-water mixture. The mass transfer coefficient g was determined from the analogy between heat and mass transfer [13],

$$g = (h/\rho c_p)(\alpha/D)^{-2/3} \quad (13)$$

It is recognized that this relation is strictly speaking valid for forced and not free convection. Mass transfer tends to reduce density gradients; therefore, the analogy between heat and mass transfer in the present case is not expected to be as simple as for forced flow. The relationship was used, however, because a better correlation appropriate for the physical situation considered in the experiment was not available in the literature. The adjustment of constant C in equation (12) has partly compensated for the departure of equation (13) from reality.

Results and Discussion

A comparison of predicted and measured temperature distributions in water heated by thermal radiation is shown in Figs. 2, 3, and 4. Absorption of radiation produced strong thermal stratification in the surface layers of the water. Examination of the results reveals good agreement between predictions and data, thus verifying the radiation and total energy transfer models. Since for the laboratory simulation the water layer near the surface absorbed the largest fraction of the energy incident from the lamps, the temperature near the surface is greatest and decreases with depth. The results show that there is little radiant heating of the water near the bottom of the test cell. This finding is consistent with the radiant heating rates illustrated in Fig. 1 which show that near the bottom of the cell H has decreased by several orders of magnitude as compared with the value at the surface.

During the heating process, the numerical model predicts a reversal of the temperature gradient near the interface (see Fig. 4 at $t = 90$ min). The interferogram presented in Fig. 5 clearly shows

that the reversal of the temperature gradient near the water surface has indeed occurred. As expected, the phenomena develops for long heating times when the heat loss from the surface by convection, evaporation and radiation is greater than the energy absorbed at the surface.

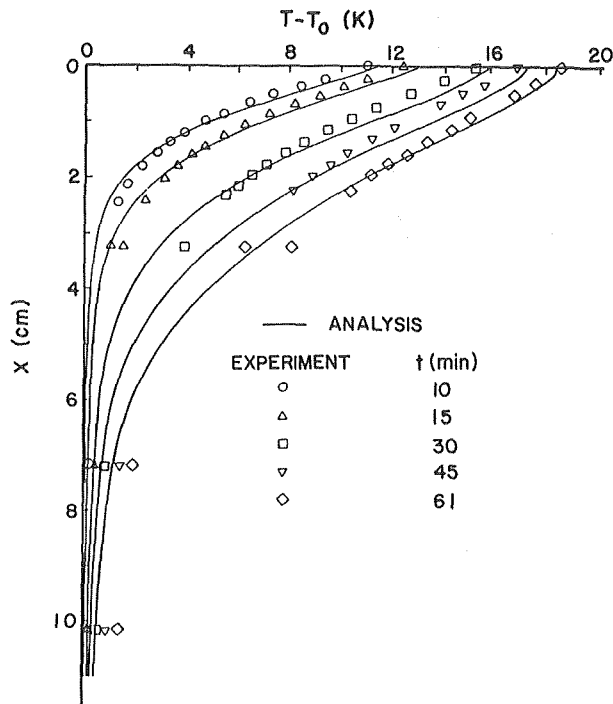


Fig. 3 Comparison of measured and predicted temperature distributions for lamps at 2880 K, $T_0 = T_\infty = 25$ C and $L = 38.1$ cm

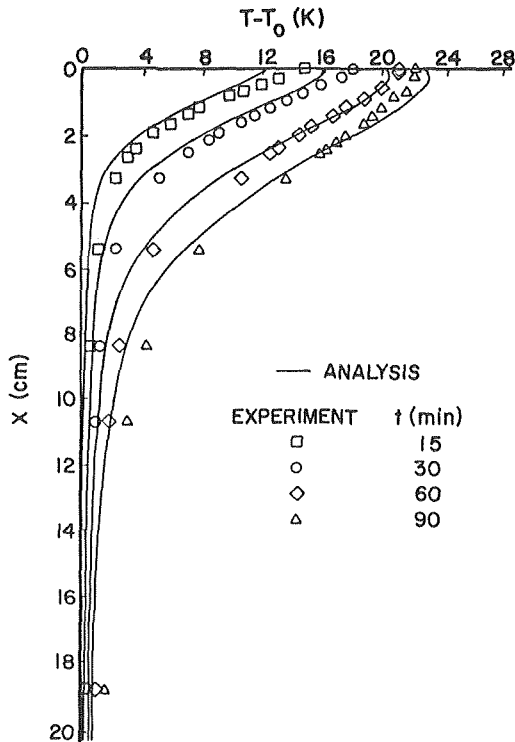


Fig. 4 Comparison of measured and predicted temperature distributions for lamps at 3250 K, $T_0 = T_\infty = 25$ C and $L = 38.1$ cm

The greatest radiant heating occurs at or near the interface. For this reason it is desirable to obtain some insight into the effects of inaccuracies in predicting the surface radiant flux F_0 on the internal temperature distribution. Since in the numerical solution of the energy equation the radiant energy absorbed by the layer of water in one-half the grid spacing below the interface was assumed to be absorbed at the surface, the effects of variation about this value were easily made. Fig. 6 illustrates the effect of variations in the surface absorbed flux on the temperature distribution. As expected, the difference is greatest near the surface and decreases

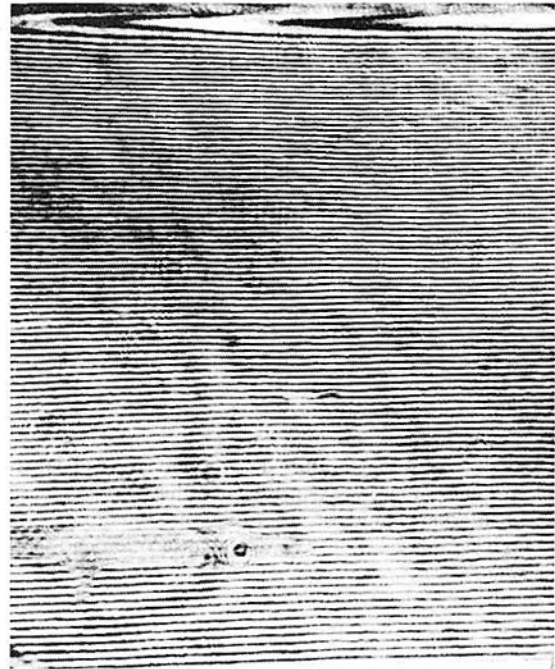


Fig. 5 Interferogram illustrating temperature gradient reversal near the water surface; lamps at 3250 K, $T_0 = T_\infty = 25$ C, $L = 38.1$ cm and $t = 90$ min

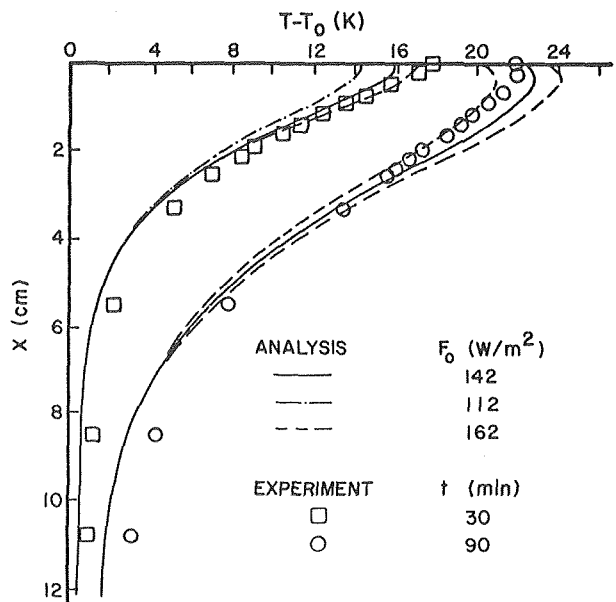


Fig. 6 Effect of variation in radiant energy flux considered absorbed at the surface on predicted temperature distribution for lamps at 3250 K, $T_0 = T_\infty = 25$ C, and $L = 38.1$ cm

with depth, and its influence becomes more pronounced with time. It is interesting to note the small effect the variation in surface heat flux has on the predicted temperature a few centimeters below the surface, indicating the importance of the internal volumetric absorption of radiation.

Figs. 2 to 4 show that the temperature was underpredicted at depths of 5 cm and greater. The discrepancies in predicted temperatures away from the interface indicate underprediction of the volumetric absorption rate of radiant energy. The probable source of the discrepancy is most likely the uncertainty of the spectral absorption coefficient of water or inaccuracies in determining the spectral incident flux. If the incident flux is underestimated, the temperatures predicted at distances away from the interface would be too low, while the temperatures near the surface would be nearly correct. If the spectral absorption and scattering coefficient are in error, particularly in the visible and near infrared parts of the spectrum, the internal heating rate will not be correctly determined. The presently available spectral extinction coefficient data for water from the published literature indicate that discrepancies exist between the data reported by various investigators [15]. The spectral extinction coefficient recommended by Hale and Querry is smaller in some and larger in other parts of the spectrum than those used by Viskanta and Toor [5].

Conclusions

The relatively good agreement between numerical predictions and experimental data indicates that thermal stratification in a stagnant layer of water induced by solar radiation can be predicted with confidence. Based on results obtained in this study, the following conclusions can be drawn:

- 1 The predicted temperature distribution strongly depends on rate of internal volumetric absorption of radiation.

- 2 The internal volumetric absorption rate can be correctly predicted if good knowledge of the spectral absorption and scattering coefficients for water and its impurities are available, and the radiation reflection characteristics at the water surface and bottom are known.

- 3 To accurately predict the temperature distribution in water heated by solar radiation, the boundary condition at the water surface must be correctly specified.

This study has provided improved understanding of energy transfer and has contributed to the confidence in the modeling capability of thermal stratification in stagnant waters heated by solar radiation. Future studies, however, need to be more in accord with the energy transfer processes occurring in nature. The diurnal

heating and cooling cycle, the effects of impurities in the water, inflow and outflow of water, surface waves, and other phenomena occurring in natural bodies of water must be included in future modeling efforts.

Acknowledgment

This research has supported by the U. S. Department of Interior, Office of Water Resources Research through the Water Resources Research Center of Purdue University under Annual Allotment Project No. OWRR-A-029-IND.

References

- 1 Dake, J. M. K., and Harleman, D. R. F., "An Analytical and Experimental Investigation of Thermal Stratification in Lakes and Ponds," Hydrodynamics Laboratory Report No. 99, Massachusetts Institute of Technology, Cambridge, Mass., 1966.
- 2 Ou, J.-W., Tinney, E. R., and Yang, W.-J., "Thermal Stratification in Deep Reservoirs Due to Solar Radiation," in *Flow Studies in Air and Water Pollution*, ASME, New York, 1973, pp. 9-23.
- 3 Ruttner, F., *Fundamentals of Limnology*, University of Toronto Press, Toronto, 1963, pp. 7-55.
- 4 Dake, J. M. K., and Harleman, D. R. F., "Thermal Stratification in Lakes: Analytical and Laboratory Studies," *Water Resources Research*, Vol. 5, No. 2, Apr. 1969, pp. 484-495.
- 5 Viskanta, R., and Toor, J. S., "Radiant Energy Transfer in Waters," *Water Resources Research*, Vol. 8, No. 3, June 1972, pp. 595-608.
- 6 Viskanta, R., and Toor, J. S., "Effect of Multiple Scattering on Radiant Energy Transfer in Waters," *Journal of Geophysical Research*, Vol. 78, No. 18, June 1973, pp. 3538-3551.
- 7 Hauf, W. and Grigull, U., "Optical Methods in Heat Transfer," in *Advances in Heat Transfer* J. P. Hartnett and T. F. Irvine, Jr., eds., Vol. 6, Academic Press, New York, 1970, pp. 219-362.
- 8 Snider, D. M., "An Experimental and Analytical Study of Thermal Structure in Heated and Cooled Stagnant Waters," MSME thesis, Purdue University, West Lafayette, Indiana, 1973.
- 9 Tilton, L. W., and Taylor, J. K., "Refractive Index and Dispersion of Distilled Water for Visible Radiation at Temperatures 0 to 60°C," *United States National Bureau of Standards Journal of Research*, Vol. 20, No. 4, Apr. 1938, pp. 419-480.
- 10 Carnahan, B., Luther, H. A., and Wilkes, O. J., *Applied Numerical Methods*, Wiley, New York, 1969.
- 11 Gebhart, B., "Natural Convection Flows and Stability," in *Advances in Heat Transfer*, J. P. Hartnett and T. F. Irvine, Jr., eds., Vol. 9, Academic Press, New York, 1973 pp. 273-348.
- 12 McAdams, W. H., *Heat Transmission*, Third ed., McGraw-Hill, New York, 1954, pp. 180-182.
- 13 Rohsenow, W. M., and Choi, H. Y., *Heat, Mass and Momentum Transfer*, Prentice Hall, Inc., Englewood Cliffs, N. J., 1961, pp. 412-418.
- 14 Collier, J. G., *Convective Boiling and Condensation*, McGraw-Hill, New York, 1972, pp. 312-313.
- 15 Hale, G. M., and Querry, M. R., "Optical Constants of Water in the 200-nm to 200- μ m Wavelength Region," *Applied Optics*, Vol. 12, No. 3, Mar. 1973, pp. 555-563.

E. Pfender
J. Schafer²

Heat Transfer Division,
Department of Mechanical Engineering,
University of Minnesota,
Minneapolis, Minn.

The Influence of Radiation on Arc¹ Constriction in the Anode Region

An improved analytical model for the description of the anode contraction zone of a high intensity arc takes radiation effects into account. The conservation equations for the anode contraction zone and the adjacent undisturbed arc column are solved numerically with a relaxation method. Results for atmospheric pressure argon arcs at three different currents demonstrate that radiation losses reduce temperature peaks substantially and, at the same time, provide a smooth matching of arc column and contraction zone solutions. Although the model seems to be adequate for a large portion of the anode contraction zone, the results indicate that refinements of the model are necessary for the region close to the anode, in particular, deviations from LTE have to be taken into account.

1 Introduction

Although electric arcs have been known for more than 150 years, the electrode regions in arcs are still poorly understood. This holds in particular for the anode region of high intensity, thermal arcs, which are the subject of this paper.

The anode region of a high intensity arc is defined as that part of the discharge path which contains the anode, the region of the net negative space charge (anode fall region) and the transition region toward the plasma column.

In the past, the anode region attracted relatively little interest. There are three major reasons which are responsible for this lack of interest. First of all, the anode region has little influence on the remaining parts of the discharge in contrast to the cathode region. Second, the complexity of the anode region does not lend itself to a theoretical treatment. This complexity refers to the interaction and relative importance of electrical, thermal, and fluiddynamic effects in the anode region. Although attempts have been made to solve certain problems in the anode region [1-3]³ there is still no comprehensive theory describing the observed phenomena in the anode region of high intensity, thermal arcs. The last reason is associated with the difficulties of obtaining and interpreting experimental data in the anode region. The extreme values of temperature, current density, and field strength prevailing in this region and the steep gradients of these parameters make diagnostics a

formidable task. In addition, these extreme conditions in the anode region may cause deviations from LTE which creates another problem as far as the interpretation of experimental data is concerned. It is even doubtful whether or not the velocity distributions of the various plasma components (electrons, ions, neutrals) are still Maxwellian close to the anode.

In the case of an anode spot, the highly disturbed surface state contributes further to this complexity. It is more or less a matter of taste whether one considers the location of an anode spot as a highly distorted metal lattice or an extremely dense, metal plasma. The anode surface which does not exist as such any more, becomes now a transition zone between solid state and a probably nonideal gaseous plasma. These facts explain why there are only very little and rather scattered experimental data available in the literature about the anode region. Many findings are more or less concerned with phenomenological observations only.

This paper represents an extension of previous studies [4] in which a simple analytical model for the anode region has been introduced. The model takes an initial arc contraction into account due to the low temperature of the anode ("thermal pinch"). The resulting magnetic pinch effect leads to an entrainment of cold gas which determines, via an energy balance, the final shape of the arc in the anode region. The effect of radiation has not been included in the previous model and the investigations were restricted to nitrogen as working fluids.

The model adopted for this study takes radiation into account and since radiation is particularly important for argon, results are presented for argon at atmospheric pressure.

2 The Analytical Model

The model adopted for this analysis is based on a wall-stabilized, rotationally symmetric arc as shown schematically in Fig. 1. The electrodes are normal to the arc axis and both the anode and

¹ Sponsored by the National Science Foundation Grant GK-35230.

² Now with the Research Div., Carrier Corp., Syracuse, N. Y. 13201.

³ Numbers in brackets designate References at end of paper.

Contributed by the Heat Transfer Division for publication in the JOURNAL OF HEAT TRANSFER. Manuscript received by the Heat Transfer Division July 30, 1974.

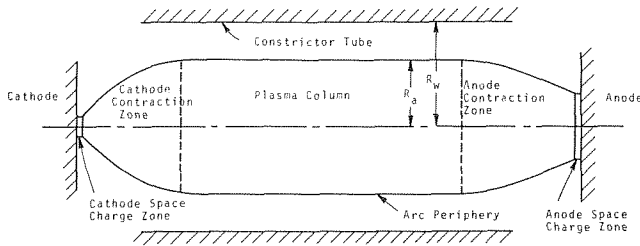


Fig. 1 Schematic of an axisymmetric Arc with Enlarged Electrode Regions

cathode regions are divided into three zones—the contraction, the space charge (sheath), and the electrode surface zone. In this paper, the anode contraction zone with the adjacent arc column will be considered assuming that the plasma is in LTE.

A The Arc Column. In a fully developed arc column the energy equation, neglecting radiation, reduces to the Elenbaas-Heller equation which can be readily integrated [5]. When radiation is included, the energy equation assumes the following form

$$\text{div}(k \text{ grad } T) + \sigma E^2 - U = 0 \quad (1)$$

where the plasma is assumed to be optically thin. In order to obtain temperature and current density distributions in the arc column the energy equation together with the current equation

$$I = 2\pi E \int_0^{R_a} \sigma r dr \quad (2)$$

is solved numerically with appropriate boundary conditions. In this paper the axis temperature of the arc and the wall temperature of the constrictor tube are specified as boundary conditions. The arc radius, R_a , is defined by the isotherm $T = T_{cr}$ for which the electrical conductivity becomes negligibly small. For $T > T_{cr}$ the electrical conductivity increases sharply. In Section 3 solutions for three different arc centerline temperatures will be shown.

B The Anode Contraction Zone. In the anode contraction zone heat is conducted not only in radial, but due to the low temperature of the anode, in axial direction as well. This leads to an initial constriction of the arc ("thermal pinch") because of the necessity to balance the additional heat loss to the anode. As the arc contracts, the current density and the associated self-magnetic field increase inducing the well-known pumping action, i.e., gas is entrained in the negative r -direction and accelerated in axial direction away from the anode (anode jet). The cooling effect caused by this entrained cold gas reduces the arc diameter further which, in turn, causes an even stronger anode jet. This seemingly unstable constriction mechanism is finally balanced by the increasing tem-

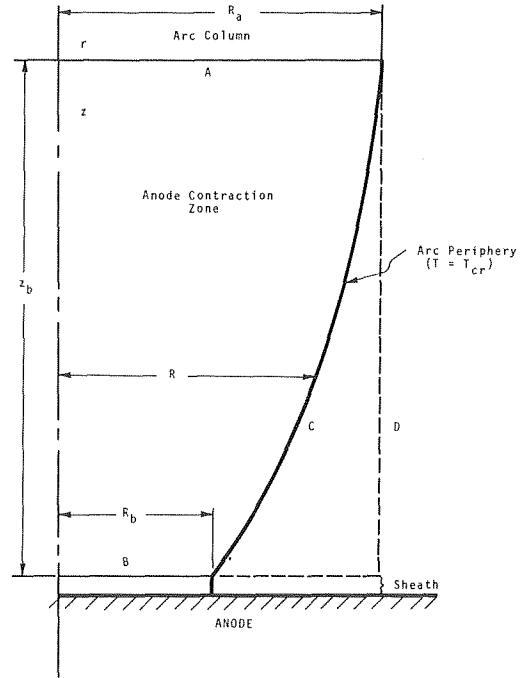


Fig. 2 Schematic diagram of the anode region

perature gradient and the associated heat transfer which tends to enlarge the arc diameter.

C Thermodynamic and Transport Properties. The thermodynamic properties (density and enthalpy of the plasma) required for this analysis are taken from Drellishak, et al. [6] whereas transport properties (electrical and thermal conductivity of the plasma) are taken from Devoto [7]. Measured radiation properties from Evans and Tankin [8] are used in this analysis. It should be emphasized that the uncertainties associated with some of the transport properties will also be reflected in the results of this analysis.

Before establishing the equations which describe the behavior of the arc in the anode contraction zone, the underlying assumptions will be listed and briefly discussed.

1 Basic Assumptions. The assumptions are summarized in the following list with reference to Fig. 2

- (a) Steady-state prevails.
- (b) LTE exists in the arc and in the contraction zone.
- (c) The plasma is assumed to be optically thin.
- (d) Heat generation due to viscosity is negligible.
- (e) The temperature distribution on A is the same as in the

Nomenclature

A, B, C, D = refers to surfaces in Fig. 2
a, b = abbreviations defined in conjunction with equation (12)
c = velocity of light
E = electric field strength
F = Lorentz force per unit volume
H = self-magnetic field
h = enthalpy
I = arc current
j = current density
k = thermal conductivity
r = radial coordinate

R = radius of arc in anode region
R_a = radius of undisturbed arc column
R_w = wall radius
T = temperature
T_{cr} = "critical temperature," temperature of gas where electrical conductivity becomes negligibly small
T₁ = low temperature at intersection of surfaces B and D
U = radiated power per unit volume
u = component of velocity vector

in z -direction
v = component of velocity vector in r -direction
 \bar{v} = velocity vector
z = axial coordinate
 γ = slope factor
 σ = electrical conductivity
 ϕ = electrical potential
 ρ = mass density
 ξ = dummy variable
 $(\rho u)_0$ = axial mass flux on arc axis
 $(\rho v)_d$ = radial mass flux at arc periphery

Table 1 Results for fully-developed arcs in argon
($p = 1 \text{ atm}$)

ARC	AXIS TEMP. [°K]	FIELD STRENGTH [V/cm]		ARC CURRENT [amp]		ARC RADIUS [cm]
		a	b	a	b	
1	11,000	3.05	3.05	59.3	59.3	0.54
2	12,000	3.1	4.0	96.4	99.0	0.58
3	13,000	3.3	4.5	139.6	171.4	0.60

a: Without radiation; b: With radiation.

undisturbed arc column and the potential is uniform over this surface.

(f) The thickness of z_b is in the order of 1 mm.

(g) The axial temperature gradient on surface B is assumed to follow a parabolic function dropping from zero on the axis to negative values. Along the circle of intersection between surfaces B and D , this negative value shall be compatible with the temperature gradient on surface D .

(h) Current density profiles on B and A are similar.

(i) There is no current flow beyond surface C and the radial component of the current density is negligible compared with the axial component.

(j) Temperature distribution along D is assumed in the form of a third degree polynomial which satisfies the condition $T(z_b, R_a) = T_1$.

As the results indicate, assumption (b) loses its validity as the anode is approached. Therefore, deviations from LTE have to be considered in a more sophisticated model. Assumption (c) postulates that radiation is emitted from an optically thin plasma, i.e., the effect of absorption is entirely neglected for line as well as for continuum radiation. In line with assumption (b) LTE radiation properties are introduced. Continuum radiation is influenced little by this assumption because the continuum emission coefficient depends little on deviations from kinetic equilibrium.

Assumption (g) requires some further explanation. Increasing arc constriction for a given current leads, in a fully developed arc column, to an increase of the axis temperature. A similar effect is anticipated in the anode contraction zone, although axial heat con-

duction toward the anode will play a certain role. Since the axial temperature gradient in the contraction zone close to the column end may be positive changing to a strongly negative gradient as the anode is approached, the temperature itself must peak somewhere in the vicinity of the anode. For the sake of simplicity the axial temperature peak is assumed to fall on surface $B(z = z_b)$ although it is probably more realistic to assume that this peak occurs for $z < z_b$. This, however, does not change the solutions in the contraction zone; it merely shifts the surface B to a location $z < z_b$ so that this surface is no longer the interface between sheath and contraction zone. The described situation is similar to that experienced in a boundary layer with ohmic heat dissipation [9]. In this case the temperature profile exhibits a peak which becomes more pronounced as the heat dissipation increases.

Although assumption (j) appears to be rather arbitrary, calculations with different temperature profiles indicate that their influence on arc contraction is of minor importance [10]. The other assumptions are either standard or do not require additional discussion.

2 *The Governing Equations.* With the previously mentioned assumptions the conservation equations may be written in the following form.

Conservation of mass:

$$\text{div}(\rho \vec{v}) = 0 \quad (3)$$

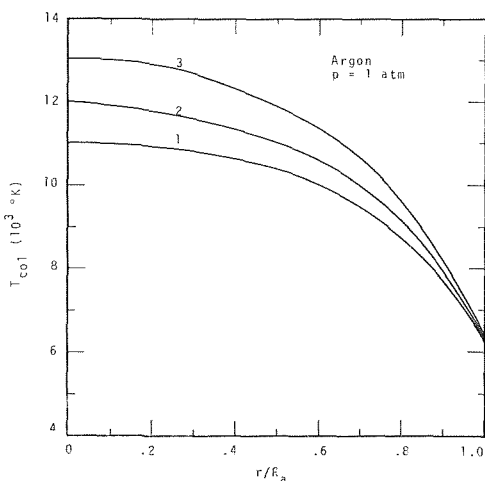


Fig. 3 Temperature distribution in the arc column

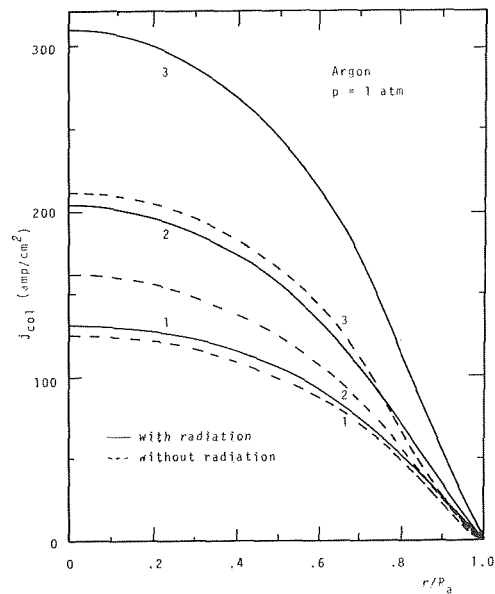


Fig. 4 Current densities in the arc column

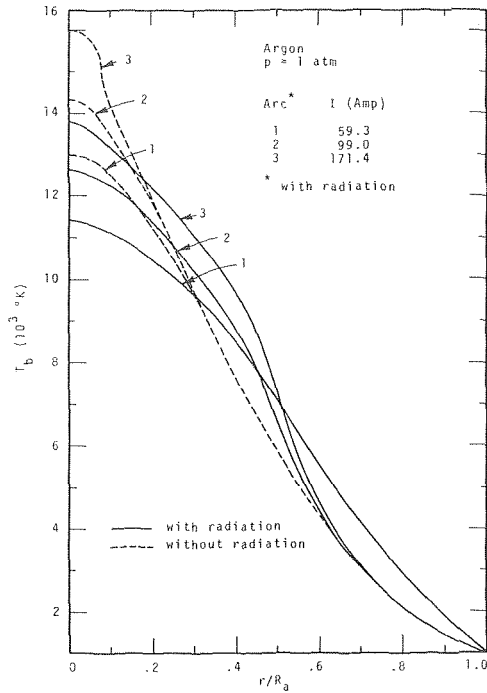


Fig. 5 Temperatures on the anode end of the contraction region

Conservation of momentum:

$$\rho \frac{d\vec{v}}{dt} = -\text{grad}p + \frac{1}{c} \vec{j} \times \vec{H} \quad (4)$$

where $\text{rot} \vec{H} = 4\pi/c \vec{j}$
for rotational symmetry:

$$H(r) = \frac{4\pi}{c} \frac{1}{r} \int_0^r j \xi d\xi$$

Therefore, the momentum equations may be written as:

$$z \text{ direction: } \rho \left(u \frac{\partial u}{\partial z} + v \frac{\partial u}{\partial r} \right) = -\frac{\partial p}{\partial z} \quad (5)$$

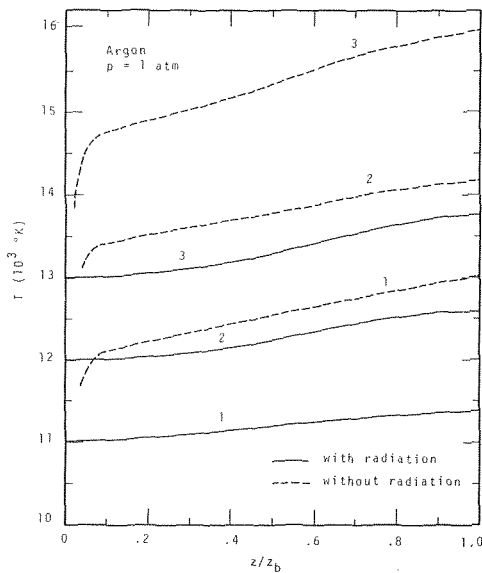


Fig. 6 Temperatures on the center line of the contraction region

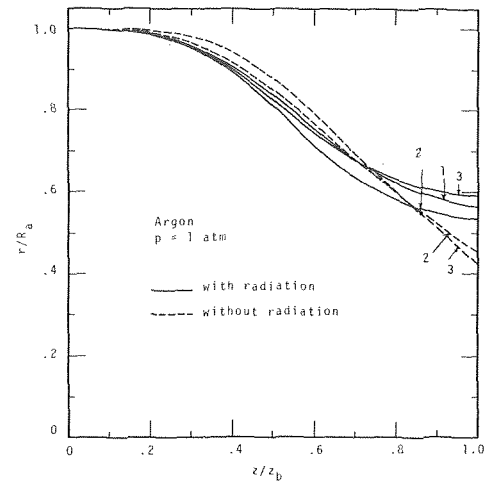


Fig. 7 Arc peripheries in the contraction region

$$r \text{ direction: } \rho \left(u \frac{\partial v}{\partial z} + v \frac{\partial v}{\partial r} \right) = -\frac{\partial p}{\partial r} - \frac{4\pi j}{c^2} \int_0^r j \xi d\xi \quad (6)$$

Conservation of energy:

$$\text{div}(k \text{ grad } T) - \rho \vec{v} \cdot \text{grad}h + \sigma E^2 - U = 0 \quad (7)$$

Conservation of current:

$$\text{div} \vec{j} = 0 \quad (8)$$

Ohm's law:

$$\vec{j} = \sigma \vec{E} \quad (9)$$

$$\text{since } \frac{1}{c} |\vec{v} \times \vec{H}| \ll |\vec{E}|$$

or in integrated form

$$I = 2\pi E \int_0^R \sigma r dr \quad (10)$$

In order to solve this system of coupled differential equations, boundary conditions will be specified with reference to Fig. 2.

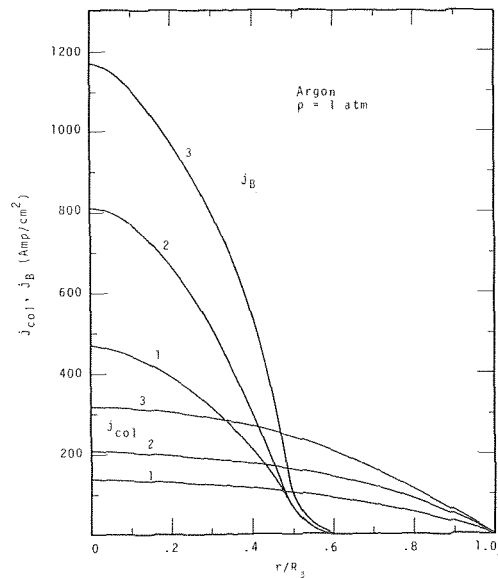


Fig. 8 Current densities on the column and anode ends of the contraction region

3 *Boundary Conditions.* Thermal boundary conditions are required for surfaces *A*, *B*, and *D* and, in addition, electrical boundary conditions are necessary for surfaces *A* and *B*.

Thermal boundary conditions:

$$\text{Surface } B: \frac{\partial T}{\partial z}(z_b, r) = \left(\frac{r}{R_a}\right)^2 \frac{\partial T}{\partial z}(z_b, R_a) \quad (11)$$

$$\text{Surface } D: T(z, R_a) = T_{cr} - a\left(\frac{z}{z_b}\right)^2 + b\left(\frac{z}{z_b}\right)^3 \quad (12)$$

$$\text{where } a = (T_{cr} - T_1)(3 - 2\gamma)$$

$$b = 2(T_{cr} - T_1)(1 - \gamma)$$

γ represents a slope factor ($0 < \gamma < 1$).

The temperature distribution along surface *D* follows from equation (12) with $\gamma = 0.2$. The temperature gradient along surface *B* is given by equation (11) with $\partial T/\partial z(z_b, 0) = 0$ and $\partial T/\partial z(z_b, R_a) = -10^4 \text{ }^\circ\text{K/cm}$.

Electrical boundary conditions:

$$\text{Surface } A: \phi(0, r) = 0$$

$$\text{Surface } B: j\left(z_b, \frac{r}{R_b}\right) = j\left(0, \frac{r}{R_a}\right)\left(\frac{R_a}{R_b}\right)^2$$

$$\text{and } j = 0 \text{ for } r > R$$

3 Results and Discussion

For deriving the previously mentioned boundary conditions on Surface *A*, temperature and current density distributions in the undisturbed arc column have to be calculated. Atmospheric pressure argon arcs with axis temperatures of 11,000, 12,000, and 13,000 °K will be considered, assuming a wall temperature $T_w = 1000 \text{ }^\circ\text{K}$. Solutions of equations (1) and (2) in terms of temperature and current density distributions are shown in Figs. 3 and 4, respectively. Also included in Fig. 4 are results of earlier calculations [10] in which radiation has been neglected. Further relevant data for these arcs are contained in Table 1 including data of reference [10].

Since thermodynamic and transport properties which are involved in this calculation are identical with those applied in Reference [10], comparisons of the results with and without radiation are feasible.

Numerical solutions of the governing equations in the anode contraction zone are obtained by applying the Southwell relaxation method [11]. The contraction zone is divided into 21 (z direction) by 41 (r direction) nodal elements. The results of these calculations are shown in Figs. 5 through 10. The dashed lines refer to results from reference [10].

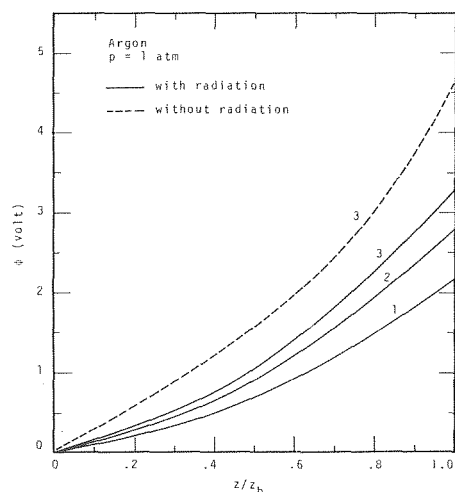


Fig. 9 Potentials on the center line of the contraction region

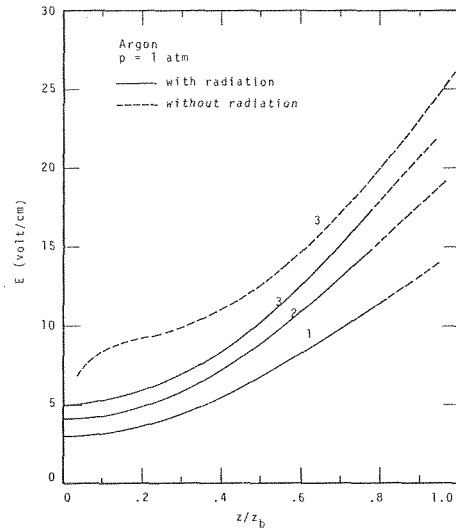


Fig. 10 Field strengths on the center line of the contraction region

Fig. 5 shows the radial temperature distributions close to the anode. All curves merge at 1000 °K at $r = R_a$ which is the assumed low temperature of the gas surrounding the arc. Radiation losses from the arc lead to a substantial reduction of the peak temperatures and to a corresponding lowering of the temperature gradients.

Temperature distributions along the arc center line (Fig. 6) indicate a significant difference between the solutions with and without radiation. The dashed curves clearly show a need for a transition region between the arc column and the contraction zone; otherwise an unrealistically steep temperature gradient would result at the interface. If radiation is taken into account the solutions of the column match smoothly with those of the contraction zone.

Fig. 7 demonstrates that radiation reduces the severe contraction of the arc close to the anode which is consistent with the results of Fig. 6. Lowering of the axis temperature and, therefore, of the electrical conductivity in the arc core requires a larger conducting cross section of the arc to accommodate the same current.

The current densities at the anode end of the contraction zone are shown in Fig. 8 and, for comparison, the corresponding current densities for the undisturbed arc column are also included in this figure. The increase of the current densities by a factor of 3 to 4, combined with an increase of the field strength (Fig. 10) in this zone, gives rise to a strong increase of the heat dissipation which, in turn, explains the temperature increase in the arc contraction zone.

The center-line potential distribution in the contraction zone is shown in Fig. 9 and Fig. 10 shows the corresponding field strengths. The field strengths at the interface between contraction zone and arc column match smoothly. For values of $z/z_b > 0.8$ convergence problems of the computer solutions seem to indicate that the model does not hold close to the anode. The field strengths for $z/z_b > 0.8$ are so large that the assumption of LTE (kinetic equilibrium) breaks down.

The calculation of the flow field in the anode contraction zone is based on the same simplifications as outlined in reference [4]. Results of these calculations are summarized in reference [12]. The strength of the anode jet is reduced if radiation effects are included which is a consequence of the less severe constriction of the arc close to the anode.

4 Conclusions

The results of this study demonstrate that radiation significantly reduces the peak temperatures in the arc contraction zone close to the anode. This temperature reduction results in a smooth

matching of the solutions in the undisturbed arc column with those in the anode contraction zone and eliminates in this way the artificial transition zone. This fact suggests that the model is adequate for this portion of the contraction zone.

Toward the anode end of the contraction zone serious convergence problems of the computer solutions have been experienced. The magnitude of the field strength in this region indicates that kinetic equilibrium between electrons and heavy particles may no longer exist. In addition, the steep temperature gradients and the associated thermal diffusion effects may cause deviations from chemical equilibrium. One or both of these effects may be responsible for substantial deviations from LTE.

It should also be mentioned that reabsorption of radiation in the plasma is neglected, i.e., the arc column as well as the contraction zone are considered to be optically thin.

Finally, the choice of the boundary conditions in particular along surface B may have an important influence on the results of these calculations. Although the boundary conditions appear to be reasonable, they contain a certain degree of arbitrariness. Much experimental work remains to be done in order to establish accurate boundary conditions.

The shortcomings of the present model adjacent to the anode suggest modifications which should include deviations from LTE, reabsorption effects and, finally, anode surface effects (melting, evaporation).

References

- 1 Bez, W., and Höcker, K. H., "Die Bewegung von Ladungsträgern in nicht-nomogenen Feldern," *Zs. Naturf.*, Vol. 9a, 1954, p. 64.
- 2 Bez, W., and Höcker, K. H., "Theorie des Anodenfalls," Part I: *Zs. Naturf.*, Vol. 9a, 1954, p. 72. Part II: *Zs. Naturf.*, Vol. 10a, 1955, p. 706. Part III: *Zs. Naturf.*, Vol. 10a, 1955, p. 714. Part IV: *Zs. Naturf.*, Vol. 11a, 1956, p. 118. Part V: *Zs. Naturf.*, Vol. 11a, 1956, p. 192.
- 3 Ecker, G., "Electrode Components of the Arc Discharge," *Ergeb. der exakten Naturwiss.*, Vol. 33, 1962, p. 1.
- 4 Chou, T. S., and Pfender, E., "Spot Formation at the Anode of High Intensity Arcs," *Wärme- und Stoffübertragung*, Vol. 6, 1973, p. 69.
- 5 Finkelnburg, W., and Maecker, H., *Elektrische Bögen und Thermisches Plasma*, Handbuch der Physik, Bd. XXII (Springer-Verlag, Berlin, 1956, English translation: ARL 62-302 1962).
- 6 Drellishak, K. S., Knopp, C. F., and Cambel, A. B., "Partition Functions and Thermodynamic Properties of Argon Plasma," *Phys. Fluids* Vol. 6, 1963, p. 1280.
- 7 Devoto, R. S., "Transport Coefficients of Partially Ionized Argon," *Phys. Fluids*, Vol. 10, 1967, p. 354.
- 8 Evans, D. L.; Tankin, R. S., "Experimental Measurements of the Emission and Absorption of Radiation by an Argon Plasma," ARL 67-0157, July, 1967.
- 9 Kerrebrock, J. L., "Electrode Boundary Layers in D.C. Plasma Accelerators," *J. Aerospace Sci.*, Vol. 28, 1961, p. 631.
- 10 Chou, Tien S., "Anode Contraction Mechanism of High Intensity Arcs," PhD thesis, University of Minnesota, June, 1971.
- 11 Schneider, P. J., *Conduction Heat Transfer*, Addison-Wesley, Reading, Mass., 1955.
- 12 Schafer, J. P., MS thesis, University of Minnesota, Sept. 1972.

R. E. Forbes
J. W. Cooper¹

Mechanical Engineering Department,
Mississippi State University,
State College, Miss.

Natural Convection in a Horizontal Layer of Water Cooled From Above to Near Freezing

Natural convection in horizontal layers of water cooled from above to near freezing was studied analytically. The water was confined laterally and underneath by rigid insulators, and the upper horizontal surface was subjected to: (1) a constant 0C temperature, rigid conducting boundary, and (2) a free, water to air convection boundary condition, in which the convective heat transfer coefficient was held constant at values of $5.68 \text{ W/m}^2 \cdot \text{K}$ and $284 \text{ W/m}^2 \cdot \text{K}$ (1.0 and $50.0 \text{ Btu/hr ft}^2\text{F}$) and the temperature of the ambient air was maintained at 0C. The ratios of the width to the depth of the rectangular water layers under consideration were $W/D = 1, 3,$ and 6 . Initially the water is assumed to be at a uniform temperature of either 4C or 8C, and then the upper surface boundary condition was suddenly applied.

It was observed in all cases for which the initial water temperature was 4C, that the water remained stagnant and became thermally stratified. Heat transfer application of either of the surface boundary conditions to water initially at 8C produced large convective eddies extending from the bottom to the top of the layer of water. As the liquid layer cooled further, two distinct horizontal regions appeared, the 4C isothermal line separating the two. This produces a region of hydrodynamic instability in the fluid since the maximum density fluid (4C) is physically located above the less dense fluid in the lower portion of the cavity. The large eddies which appeared initially were confined to the hydrodynamically unstable region bounded by the 4C isotherm and the bottom of the cavity. The action of viscous shearing forces upon the stable water above the 4C isotherm produced a second "layer" of eddies.

An alternating direction implicit finite difference method was used to solve the coupled system of partial differential equations. The paper presents transient isotherms and streamlines and a discussion of the effect of maximum density on the flow patterns.

Introduction

The imposition of temperature gradients upon a parcel of fluid leads to the formation of density gradients, since the density is inherently temperature dependent. The fluid may remain stable in this condition until a certain minimum value of the Rayleigh number, which is a function of the properties of the fluid and the temperature gradient, is attained. As this "critical" Rayleigh number is exceeded, the fluid becomes unstable and the action of gravity

on the density gradients produces convective circulation within the fluid mass. Convective motion in water, however, behaves in a rather peculiar manner when the temperature domain encompasses the 4C point, for the density of water is a maximum at this temperature. The primary objective of this investigation is to describe numerically the behavior of convective motion of water in this region of maximum density for several different geometries, boundary conditions, and temperature gradients.

Free convection in relatively thin horizontal layers of fluid heated from below has been extensively studied both experimentally and theoretically. The interested reader is referred to references [1-3].² It must be noted however, that little attention has been devoted to the related problem of convective motion induced in horizontal fluid layers cooled from above. In 1965 Foster [4, 5] published results of an analytical and experimental study of convective motion in a fluid cooled uniformly from above.

¹ Currently at Brown Engineering.

² Numbers in brackets designate References at end of paper.

Contributed by the Heat Transfer Division for publication in the JOURNAL OF HEAT TRANSFER. Manuscript received by the Heat Transfer Division, July 26, 1973. Paper No. 75-HT-H.

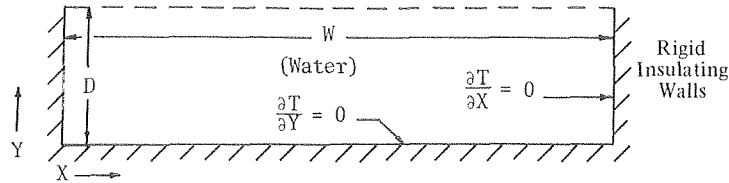


Fig. 1 The rectangular cavity

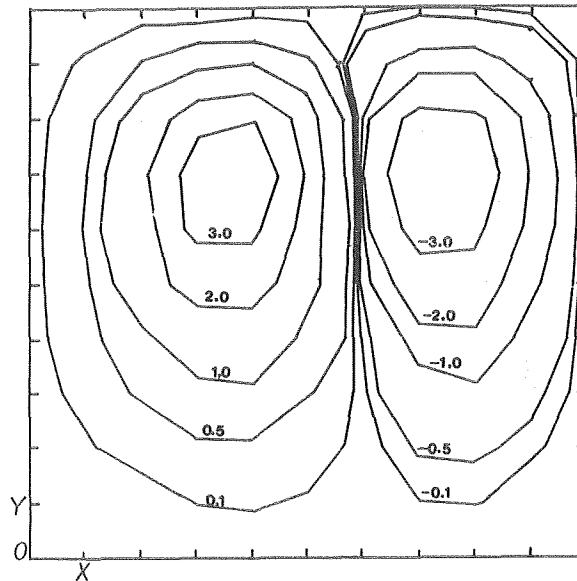


Fig. 2 Transient streamlines: $W/D = 1.0$, $T_0 = 8\text{C}$, time = 0.5 s, constant surface temperature

The behavior of convective circulation of water in the vicinity of maximum density has been recently studied by a number of persons. Heat transfer rates, temperature profiles, and velocity gradients produced by a heated vertical plate in water in the region of 4C were determined experimentally and theoretically by Schecter and Isbin [6] in 1958. Tien [7, 8] has presented the results of studies of the thermal stability of a horizontal layer of water near 4C and also on the effects of density inversion in horizontal layers of liquids cooled from above.

Desai and Forbes [9] have recently published results of a finite difference study of free convection in water in the vicinity of maximum density. Theoretical heat transfer and free convective flow patterns were determined in water in a rectangular enclosure with

insulated horizontal boundaries and vertical boundaries maintained at different temperatures. The flow was bicellular, in contrast to the generally expected one cell flow for this case, and the heat transfer occurred primarily by conduction. No work has been published considering the transient behavior of horizontal water layers cooled from above to near freezing. This problem is of considerable practical interest in the freezing of large bodies of water since the density inversion in water produces conditions which lead to the onset of freezing at the water surface.

The work reported here represents an initial effort directed toward an analytical solution and an understanding of the problem of freezing of large bodies of water cooled from above (lakes, bays, etc.).

Nomenclature

C_p = specific heat	T_{inf} = temperature of ambient air	
D = cavity depth	t = time	
g = acceleration of gravity	W = cavity width	
h = convective heat transfer coefficient	u, v = velocities in x and y directions	$\rho(T)$ or $\rho(\theta)$ = density as a function of temperature
Pr = Prandtl number $\frac{\mu C_p}{k}$	x, y = Cartesian coordinates	τ = dimensionless time
Ra' = Rayleigh number	X, Y = dimensionless coordinates	ψ = stream function
$Pr. \frac{\bar{\rho}(\bar{\rho} - \rho(\theta))gD^3}{\mu^2}$	U, V = dimensionless velocity components	Ψ = dimensionless stream function
T = water temperature ($^{\circ}\text{C}$)	α = thermal diffusivity	ζ = vorticity
T_0 = initial water temperature	μ = dynamic viscosity	Ω = dimensionless vorticity
T_n = water surface temperature	$\bar{\rho}$ = density at $(T_n + T_0)/2$ (gm/cc)	θ = dimensionless temperature
		ν = kinematic viscosity

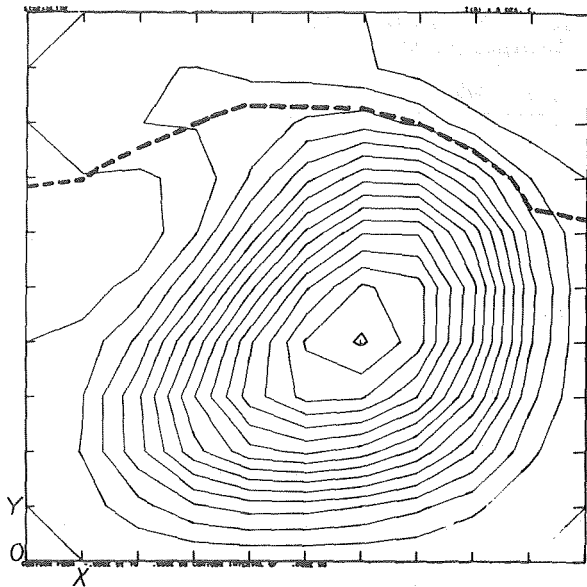


Fig. 3 Transient streamlines: $W/D = 1.0$, $T_0 = 8C$, time = 250 s, constant surface temperature

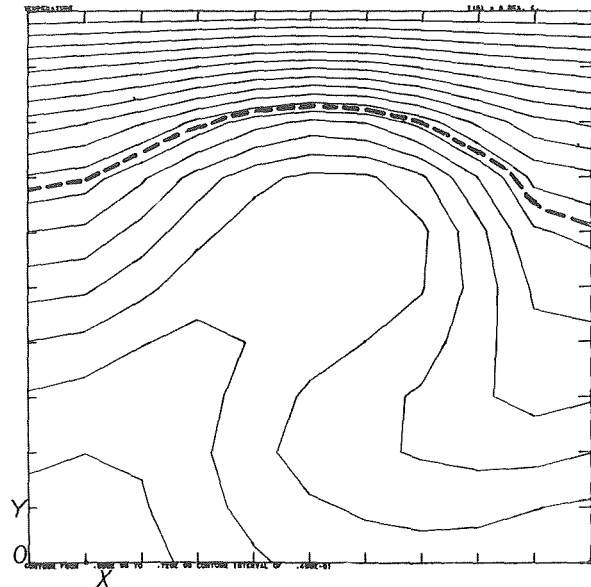


Fig. 4 Transient isotherms: $W/D = 1.0$, $T_0 = 8C$, time = 250 s, constant surface temperature

The Problem

The basic geometric configuration considered is that of a two-dimensional rectangular cavity (Fig. 1) of depth D and width W . The lateral and lower boundaries are rigid insulators. Two different cases are considered for boundary conditions at the upper horizontal boundary. These cases are: (1) a constant $0C$ temperature, rigid conducting boundary, and (2) a free, water to air convection boundary condition, in which the convective heat transfer coefficient is held constant at values of $5.68 \text{ W/m}^2 \cdot K$ and $284 \text{ W/m}^2 \cdot K$ (1.0 and $50.0 \text{ But/hr ft}^2\text{F}$) and the temperature of the ambient air is maintained at $0C$. The ratios of the width to the depth of the rectangular water layers under consideration were $W/D = 1, 3$, and 6 . Initially the water is assumed to be at a uniform temperature of either $4C$ or $8C$, and then the upper surface boundary condition is suddenly applied.

The flow is considered laminar and two-dimensional. These as-

sumptions necessitated that the fluid depth D , be restricted to 1 cm . An increase in D above this magnitude produced numerical instabilities and prevented the obtaining of a meaningful solution. For two dimensional flow where density variations are considered only in the buoyancy term the dimensionless equations governing the problem are:

Vorticity:

$$\frac{\partial \Omega}{\partial \tau} + \frac{U}{Pr} \frac{\partial \Omega}{\partial X} + \frac{V}{Pr} \frac{\partial \Omega}{\partial Y} = \frac{\partial}{\partial X} (Ra') + \nabla^2 \Omega, \quad (1)$$

$$\text{where } Pr = \text{Prandtl number} = \frac{C_p \mu}{k}$$

$$\text{and } Ra' = \text{Rayleigh number} = Pr \cdot \frac{\bar{\rho}(\bar{\rho} - \rho(\theta))gD^3}{\mu^2}$$

Energy:

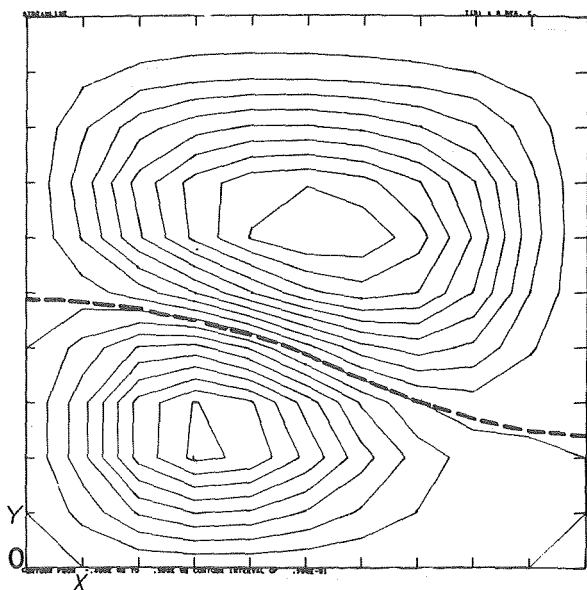


Fig. 5 Transient streamlines: $W/D = 1.0$, $T_0 = 8C$, time = 500 s, constant surface temperature

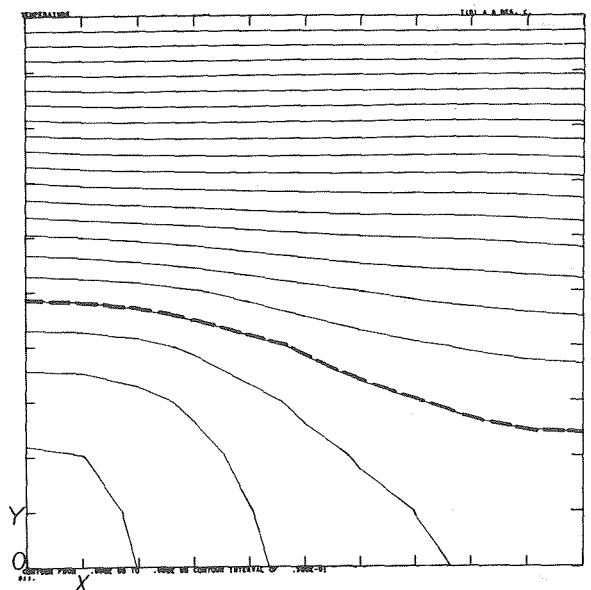


Fig. 6 Transient isotherms: $W/D = 1.0$, $T_0 = 8C$, time = 500 s, constant surface temperature

Table 1 Maximum and minimum values of stream functions

Figure	W/D	Constant Temperature Boundary			
		T ₀	ψ _{max}	ψ _{min}	Δψ
2	1	8	3.0	-3.0	1.0
3	1	8	0.0	-6.0	0.40
5	1	8	0.5	-0.4	0.05
7	1	8	0.00128	0.0	0.00008

$$\text{Pr} \frac{\partial \theta}{\partial \tau} + U \frac{\partial \theta}{\partial X} + V \frac{\partial \theta}{\partial Y} = \nabla^2 \theta \quad (2)$$

Stream Function:

$$\Omega = -\nabla^2 \Psi \quad (3)$$

Velocities:

$$U = \frac{\partial \Psi}{\partial Y} \quad (4)$$

$$V = -\frac{\partial \Psi}{\partial X}$$

In the foregoing formulation the equations have been made dimensionless through use of the following dimensionless variables:

$$\begin{aligned} \tau &= \frac{\nu t}{D^2}; U = \frac{uD}{\alpha}; V = \frac{vD}{\alpha} \\ X &= \frac{x}{D}; Y = \frac{y}{D}; \\ \Psi &= \frac{\psi}{\alpha}; \Omega = \frac{\xi D^2}{\alpha} \end{aligned} \quad (5)$$

The initial and boundary conditions may now be written in the form

$$\Psi(X, Y, 0) = 0$$

$$\theta(X, Y, 0) = 1$$

$$U(X, Y, 0) = V(X, Y, 0) = 0$$

$$U = V = 0 \text{ on all boundaries}$$

$$\frac{\partial \theta}{\partial X}(0, Y, \tau) = \frac{\partial \theta}{\partial X}\left(\frac{w}{D}, Y, \tau\right) = \frac{\partial \theta}{\partial Y}(X, 0, \tau) = 0$$

At the free surface (Y = 1) the boundary condition is either:

$$\theta(X, 1, \tau) = 0 \text{ where } \theta = \frac{T - T_n}{T_0 - T_n} \quad (7)$$

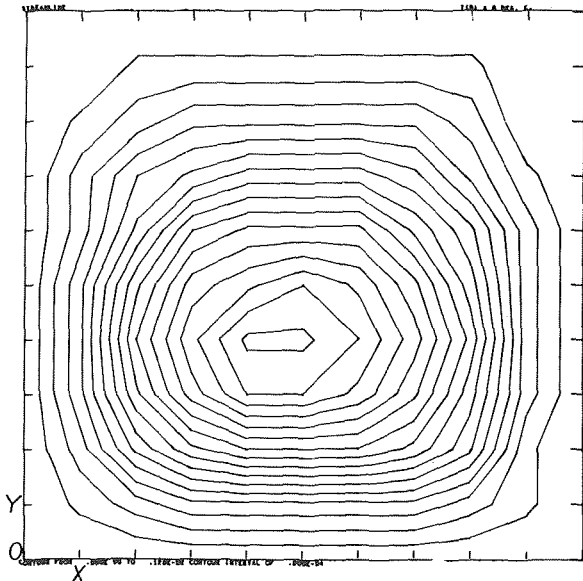


Fig. 7 Transient streamlines: W/D = 1.0, T₀ = 8C, time = 62.5 min, constant surface temperature

Table 2 Maximum and minimum dimensionless temperatures

Figure	W/D	Constant Temperature Boundary			
		T ₀	θ _{max}	θ _{min}	Δθ
4	1	8	0.72	0.0	0.04
6	1	8	0.60	0.0	0.03
8	1	8	0.034	0.0	0.002

for temperature at the surface fixed or:

$$h[T_{y=D} - T_{inf}] = -k \left[\frac{\partial T}{\partial Y} \right]_{y=D} \text{ where } \theta = \frac{T - T_{inf}}{T_0 - T_{inf}} \quad (8)$$

for the case of convection at the surface.

Solution Method

The resulting system of coupled nonlinear partial differential equations was solved using finite difference techniques.

The vorticity and energy equations, (1) and (2), respectively, are parabolic equations because of the presence of the $\partial/\partial \tau$ term. If a solution for the Ω and θ fields has been found at $\tau = n \Delta \tau$ ($n = 0$ corresponds to the initial condition), then the solution at $\tau = (n + 1) \Delta \tau$ may be calculated in several ways. The implicit alternating direction (ADI) method discussed by Wilkes [10] is used herein. This method is used primarily because the energy and vorticity equations are transformed into tridiagonal systems of equations which may be solved directly using a simple iterative method discussed by Wilkes. An additional advantage to using the ADI method is that larger time increments may be used without loss of stability. Having calculated the temperatures and interior vorticity values at the advanced point in time, the values of the stream function at the advanced point in time are calculated using the method of successive over-relaxation. These "new" values of the stream function are then used in the calculation of the velocity components U and V and the boundary values of the vorticity. This sequence, beginning with the ADI solution of the energy equation, is applied repeatedly until the desired results are obtained.

The temperature dependent density in equation (1) was expressed as a function of temperature by the polynomial

$$\rho(T) = 0.99984247 + 0.6460(10^{-4})T - 0.8(10^{-5})T^2. \quad (9)$$

The density as given by equation (9) compares very favorably to

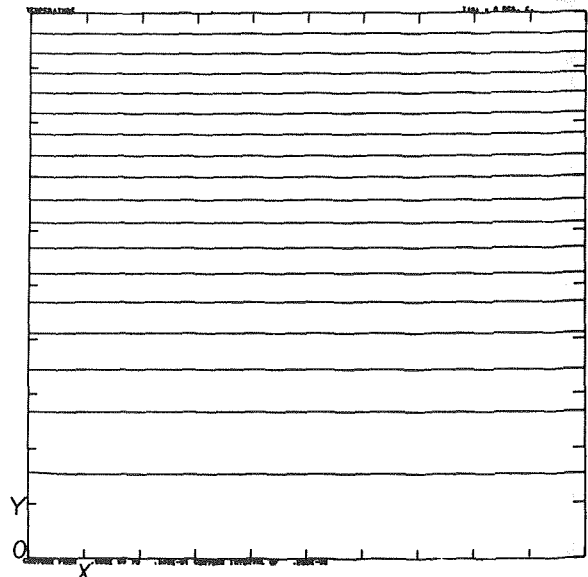


Fig. 8 Transient isotherms: W/D = 1.0, T₀ = 8C, time = 62.5 min, constant surface temperature

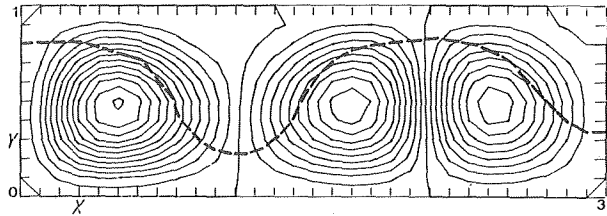


Fig. 9 Transient streamlines: $W/D = 3.0$, $T_0 = 8C$, $h = 284 \text{ W/m}^2 \cdot \text{K}$, time = 3 min

the experimentally measured density in the range 0 to 8C, as given by the *Handbook of Physics and Chemistry*.

Results

The results are most meaningful if presented in the form of transient isotherms and streamlines. The streamlines give a graphic representation of the velocity field while the isotherms indicate areas in which the maximum density occurs. Specifically, the 4C isotherm, when superposed on the streamline pattern, will give an indication of the effect of maximum density on the flow field.

Theoretical Results: Constant Temperature Boundary.

For each geometric configuration studied ($W/D = 1, 3, 6$), two different initial water temperatures are considered. In the first case the water is set initially at a uniform temperature of 8C and at $\tau = 0$ the surface temperature is abruptly lowered to 0C. The initial uniform temperature in the second case is 4C and again the surface temperature is suddenly lowered to 0C. The results obtained are in the form of plots of the streamlines and isotherms (Figs. 2–10).

The maximum and minimum values of the stream function and the contour intervals for each case are given in Table 1. The maximum and minimum temperatures and corresponding contour intervals are given in Table 2. It should be noted that the upper boundary of the cavity corresponds to the $\theta = 0$ isotherm. The 4C isothermal line, when it exists, is shown as a heavy dashed line on the plots of the streamlines as well as on the isothermal line plots.

Consideration of the square cavity with initial water temperatures of 8C and 4C and constant surface temperature of 0C provided rather interesting results. A discussion of the 8C initial uniform water temperature case is given first. Fig. 2 reveals the flow pattern within the square region shortly ($\tau = 0.002$ or 0.5 s real time) after the application of the 0C boundary temperature. This same flow configuration has been observed many times (see, for example, Samuels and Chruchohill [11], in both experimental and theoretical investigations of natural convection in horizontal layers of fluid heated from below. Since at this time, the 4C isotherm lies very near the water surface, the entire cavity region is hydrodynamically unstable; that is, an inverted density gradient exists throughout the entire body of water. The water current ascends in the central region between the two eddies, and descends adjacent to the two lateral sides of the cavity. This flow pattern deteriorates very rapidly as the 4C isotherm begins its descent through the layers of water.

Figs. 3 and 4 represent the streamlines and isothermal lines, respectively, at $\tau = 1.0$ or 250 s real time. At this point in time the

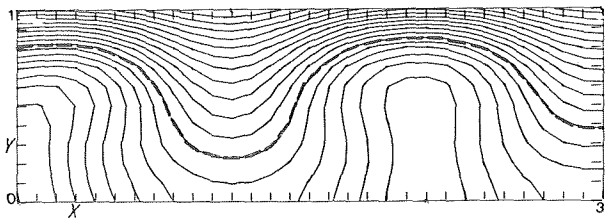


Fig. 10 Transient isotherms: $W/D = 3.0$, $T_0 = 8C$, $h = 284 \text{ W/m}^2 \cdot \text{K}$, time = 3 min

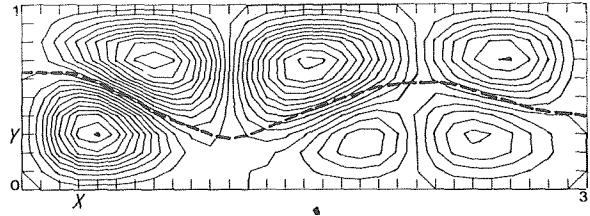


Fig. 11 Transient streamlines: $W/D = 3.0$, $T_0 = 8C$, $h = 284 \text{ W/m}^2 \cdot \text{K}$, time = 4 min

eddy which appeared on the left side of the flow field at $\tau = 0.002$ has at least momentarily disintegrated. The direction of the circulation for the remaining eddy is determined to be clockwise by observing the distortion of the temperature distribution (Fig. 4) caused by the eddy motion. Note the position of the 4C isotherm relative to the eddy. It is obvious that this region of maximum density provides the driving force for the eddy motion. Of course, the water above the 4C isotherm is always hydrodynamically stable. As the region of maximum density descends further, an interesting phenomenon is observed. The position of the 4C isotherm at dimensionless time $\tau = 2.0$ or real time ≈ 500 s is shown in Fig. 6. It is quite obvious that this isothermal line separates the two eddies which appear in Fig. 5 at $\tau = 2.0$ or 500 s. The eddy appearing in the lower portion of Fig. 5 lies entirely beneath the 4C isotherm and, therefore, is the result of unstable density gradients. This circulating flow exerts a viscous shearing stress upon the stable water above the region of maximum density, and it is this shearing stress that provides the energy necessary for eddy formation in the region of hydrodynamic stability. This phenomenon was observed experimentally by Heitz and Westwater [12] early in 1971. The straight parallel isotherms which appear in the upper portion of Figure 6 indicate that heat transfer in the stable region is largely by conduction. It is also seen that the eddy in the unstable region continues to distort the temperature distribution, and, therefore, heat is transferred in this region primarily by convection. Figs. 7 and 8 depict the flow pattern and temperature distribution, respectively, at $\tau = 5.0$ or 62.5 min. The 4C region has now passed out of the domain of the problem and therefore, the fluid body is entirely stable. The large eddy appearing in Fig. 7 is the same eddy which previously appeared above the region of maximum density. The momentum of the eddy motion, at this time, has not yet been dissipated by the opposing viscous forces, but consideration of the magnitudes of the stream function (Table 1) reveals that the fluid velocities are much smaller than those depicted in Fig. 5. Indeed, the fluid motion is so minute that the temperature field appears undisturbed (Fig. 8) and the water seems to have stratified. Heat transfer, therefore, at this time is purely conductive.

The square cavity with initial water temperature of 4C will now be discussed. The imposition of the 0C upper surface boundary temperature cannot lead to eddy formation, as the density gradient in this case is always stable. Limitations in the numerical method produced results to the contrary, however. Finite discontinuities existing in the temperature field near the grid points at each of the upper corners of the cavity produced minute perturbations which apparently were amplified sufficiently by the numeri-

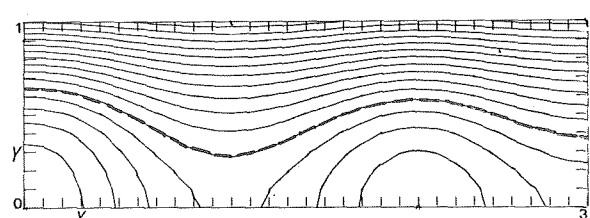


Fig. 12 Transient isotherms: $W/D = 3.0$, $T_0 = 8C$, $h = 284 \text{ W/m}^2 \cdot \text{K}$, time = 4 min

Table 3 Maximum and minimum values of stream functions

Figure	W/D	h	Convection Boundary Condition		
			ψ_{\max}	ψ_{\min}	$\Delta\psi$
9	3	0.006775	1.8	-2.4	0.2
11	3	0.006775	0.2	-0.22	0.02
13	3	0.006775	0.21	-0.10	0.01
15	6	0.006775	0.18	-0.22	0.02

cal process so as to produce, analytically, very slight fluid motion. Indeed, the velocities arising from this process were negligible as compared to those resulting from fluid instability. The fluid motion was not sufficient to cause distortion of the temperature field and the heat transfer was purely conductive.

Results obtained for the $W/D = 3$ and 6 enclosures were essentially identical to those for the square cavity differing only in the number of eddies produced by the motion. Three pairs of coupled eddies were produced in the $W/D = 3$ enclosure as the 4C isotherm descended through the layer and seven pairs were produced in the $W/D = 6$ enclosure. In all cases studied, the motion was "damped out" as the 4C isotherm reached the enclosure bottom with the resulting stable fluid layer in the entire cavity.

Theoretical Results: Convection Boundary Condition. Two different values of the convective heat transfer coefficient are considered for the two initial water temperatures, 8C and 4C, and three different geometric configurations ($W/D = 1, 3, 6$). The first value of the convective heat transfer coefficient to be considered is $h = 5.68 \text{ W/m}^2 \cdot \text{K}$ (or $1 \text{ Btu/hr ft}^2\text{F}$), which corresponds to the condition of natural convection in air, and the second value is $h = 284 \text{ W/m}^2 \cdot \text{K}$ (or $50 \text{ Btu/hr ft}^2\text{F}$), which simulates the condition of rapid forced convection in air. Results for these cases are presented in the form of streamline and isotherm line plots (Figs. 9 to 14). The maximum and minimum values of the stream function and corresponding contour intervals are tabulated in Table 3, and the maximum and minimum values of the dimensionless temperature and contour intervals are shown in Table 4.

It was observed in all cases, for which $h = 5.68$, that eddy formation is quite dilatory. The nature of the phenomenon is best realized by noting that the time required for the surface temperature to decrease from $T_0 = 8\text{C}$ ($\theta = 1$) to $T_{\max} = 6.4\text{C}$ ($\theta_{\max} = 0.792$) is one hour and four minutes ($\tau = 15$). The region of maximum density had not yet appeared within the domain of the problem. This behavior is attributed to the smallness of the imposed temperature gradient.

Attention will now be focused on the cases for which $h = 284$. The dimensionless temperature gradient at the surface may be written in the form

$$\left[\frac{\partial \theta}{\partial Y} \right]_{Y=1} = - \left[\frac{hD}{k} \right] (\theta)_{Y=1}$$

since the initial value of θ at $Y = 1$ is unity for both values of h under consideration, and D and k are constants, a 50-fold increase in h will produce a 50-fold increase in the magnitude of the initial temperature gradient at the water surface. This comparatively large thermal gradient should be expected to generate considerable

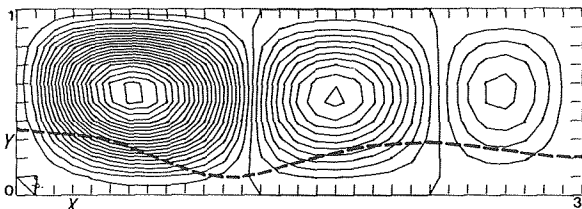


Fig. 13 Transient streamlines: $W/D = 3.0$, $T_0 = 8\text{C}$, $h = 284 \text{ W/m}^2 \cdot \text{K}$, time = 5 min

Table 4 Maximum and minimum dimensionless temperature

Figure	W/D	Convection Boundary Condition		
		θ_{\max}	θ_{\min}	$\Delta\theta$
10	3	0.78	0.18	0.03
12	3	0.63	0.15	0.03
14	3	0.56	0.12	0.02
16	6	0.62	0.14	0.02

hydrodynamic instability throughout the horizontal layers of liquid. The theoretical results invariably verify this postulation.

First considering the case for which $W/D = 3$, initial temperature, $T_0 = 8\text{C}$, and $h = 284 \text{ (50.0 Btu/hr ft}^2\text{F)}$, the reader is referred to Fig. 9 and Fig. 10 which reveal the flow pattern and temperature distribution 3 min after initiation. Since at this time the region of maximum density is very near the upper surface of the cavity, the flow pattern appearing in Fig. 9 is very similar to the flow which occurs in horizontal fluid layers heated from below. The maximum value of the stream function given in Table 3 indicates that the motion is rather rapid. The extreme contortion of the temperature field shown in Fig. 10 also provides some indication as to the velocity of the fluid. Figs. 11 and 12 reveal that, 4 min after initiation, the 4C isotherm descends far enough through the liquid so as to produce two layers of eddies. The lower eddies are the result of an unstable density gradient and the upper eddies are caused by the action of viscous shearing stresses upon the water above the unstable region. It is noted from Table 3 that as the 4C isotherm progresses downward with time, the fluid velocity decreases. Figs. 13 and 14 (5 min after initiation) provide an even clearer picture of the effect of the region of maximum density on free convection in water. The 4C isothermal line is observed to exist near the bottom of the enclosure and it is seen that $\partial\theta/\partial Y$ is almost constant in the hydrodynamically stable portion of the water. Heat transfer is almost invariably by conduction in stable regions and by convection in regions of instability.

Typical streamline and isotherm patterns are shown in Figs. 15 and 16 for the $W/D = 6$ enclosure. The nature of the flow is very similar in nature to the previously discussed case where $W/D = 3$, however the enclosure now contains seven pairs of eddies. Again, the flow was observed to stagnate as the 4C isotherm reached the enclosure bottom.

Isotherm patterns similar to those shown in Figs. 10, 12, 14, and 16 were observed by Tankin and Farhadeih [13] who studied isotherm and flow patterns in freezing water using a Mach-Zehnder interferometer. Fig. 13 of their study indicates that for cooling on the lower cavity boundary the isotherms computed herein are rep-

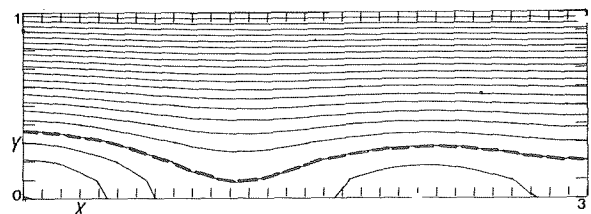


Fig. 14 Transient isotherms: $W/D = 3.0$, $T_0 = 8\text{C}$, $h = 284 \text{ W/m}^2 \cdot \text{K}$, time = 5 min

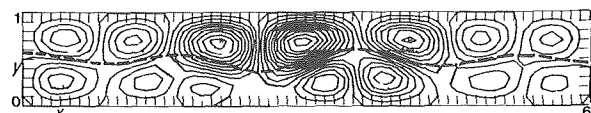


Fig. 15 Transient streamlines: $W/D = 6.0$, $T_0 = 8\text{C}$, $h = 284 \text{ W/m}^2 \cdot \text{K}$, time = 4 min

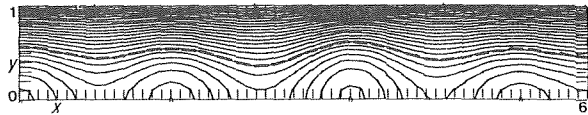


Fig. 16 Transient isotherms: $W/D = 6.0$, $T_0 = 8\text{C}$, $h = 284 \text{ W/m}^2 \cdot \text{K}$, time = 4 min

representative of those measured experimentally using the interferometer.

It may be noted that all isotherms do not strictly obey the adiabatic boundary condition ($dT/dn = 0$) at the lateral and bottom boundary. This is a consequence of the relative coarseness of the grid utilized and the method of obtaining iso-plots from the temperature matrix. The adiabatic boundary condition was used mathematically in all calculations.

Only speculation may be made as to the reason for the asymmetrical nature of the streamline and temperature fields. This is thought to be a consequence of the location of the coordinate origin and the method of numerical calculation.

A plot of average water surface temperature versus time is shown for the $W/D = 6$ enclosure in Fig. 17 for the case of $h = 284 \text{ W/m}^2 \cdot \text{K}$ ($50 \text{ B/hr ft}^2\text{F}$). The surface temperature initially has a value near 8C and decreases as the convective circulation becomes stronger. The surface temperature approaches zero asymptotically due to the insulated lateral and side walls of the container.

Conclusions

The effect of a descending region of maximum density upon free convective motion in horizontal water layers generally appears to be the same for all geometries and boundary conditions considered in this study. In all cases, for which convection is possible, the 4C isothermal line divides the depth of the water into a region of hydrodynamic instability below the isotherm, and a stable region of water above the isotherm. As the 4C isotherm reaches the bottom of the cavity the absence of regions of hydrodynamic instability cause the fluid motion to be damped out by viscous forces. Heat transfer is then by conduction only through the fluid and the isotherms are characteristic of those seen in conduction in a solid media.

References

1 Benard, H., "Les Tourbillons Cellulaires Dans Une Nappe Liquide," *Revue Generale Des Sciences*, Vol. 11, 1900, p. 1261.

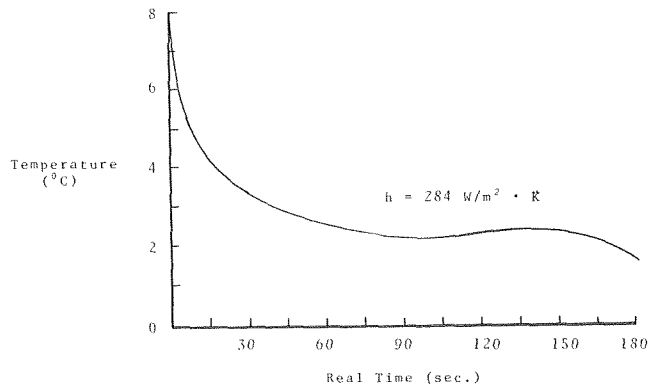


Fig. 17 Variation of average water surface temperature with time: $T_0 = 8\text{C}$, $W/D = 6$

- 2 Jeffreys, H., "The Stability of a Layer of Fluid Heated Below," *The Philosophical Magazine*, Vol. 2, 1926, p. 833.
- 3 Pellow, A., and Southwell, R. V., "On Maintained Convective Motion in a Fluid Heated Below," *Proceedings of the Royal Society of London*, Vol. 176, 1940, p. 312.
- 4 Foster, T. D., "Stability of a Homogeneous Fluid Cooled Uniformly From Above," *The Physics of Fluids*, Vol. 8, No. 7, 1965, p. 1249.
- 5 Foster, T. D., "Onset of Convection in a Layer of Fluid Cooled from Above," *The Physics of Fluids*, Vol. 8, No. 10, 1965, p. 1770.
- 6 Schechter, R. S., and Isbin, H. S., "Natural-Convection Heat Transfer in Regions of Maximum Fluid Density," *AIChE Journal*, Vol. 4, No. 1, 1958, p. 81.
- 7 Tien, C., "Thermal Instability of a Horizontal Layer of Water Near 4C ," *AIChE Journal*, Vol. 14, No. 4, July 1968, p. 652.
- 8 Tien, C., "Free Convective Heat Transfer in a Horizontal Layer of Liquid—The Effect of Density Inversion," *AIChE Preprint* 21, presented at Twelfth National Heat Transfer Conference, Aug. 1971.
- 9 Desai, V. S., and Forbes, R. E., "Free Convection in Water in the Vicinity of Maximum Density," *Environmental and Geophysical Heat Transfer*, TRANS. ASME, Nov. 1971.
- 10 Wilkes, J. D., "The Finite Difference Computations of Natural Convection in an Enclosed Rectangular Cavity," PhD thesis, University of Michigan, 1963.
- 11 Samuels, M. R., and Churchill, S. W., "Stability of a Fluid in a Rectangular Region Heated from Below," *AIChE Journal*, Vol. 13, No. 1, 1967, p. 77.
- 12 Heitz, W. L., and Westwater, J. W., "Critical Rayleigh Numbers for Natural Convection of Water Confined in Square Cells With L/D from 0.5 to 8," *JOURNAL OF HEAT TRANSFER*, TRANS. ASME, Series C, Vol. 93, May 1971, p. 188.
- 13 Tankin, R. S., and Farhadieh, R., "Effects of Thermal Convection Currents on Formation of Ice," *International Journal of Heat and Mass Transfer*, Vol. 14, 1971, pp. 95-961.

M. Y. Chow¹
R. G. Akins

Department of Chemical Engineering,
Kansas State University,
Manhattan, Kan.

Pseudosteady-State Natural Convection Inside Spheres

Natural convection heat transfer to water contained within five different sized spheres was studied. Pseudosteady-state was maintained by keeping the driving force for convection constant, i.e., the temperature outside the sphere was increased steadily so that the temperature difference between the outside and the center remained constant. Flow visualization was used to determine flow patterns within the spheres. Laminar flow was found to exist below Rayleigh numbers of about 10^7 . The flow patterns along with the position of the circulation centers are presented and compared with recent numerical solutions. The overall heat transfer in the laminar region was fitted by least squares and the following correlation obtained:

$$\text{Nu} = 0.80 \text{ Ra}^{0.30}$$

Introduction

It is well known that a sphere has the characteristic of minimum surface-to-volume ratio, therefore many storage tanks are spherical, thereby minimizing materials of construction and heat losses. The study of natural convection inside a sphere is of importance for understanding the heat transfer to fluid contained within spherical tanks, since forced convection is often absent. Our knowledge of heat and/or mass transfer to liquid drops may also benefit from these studies.

Recently, a considerable amount of interest has been shown in the subject of internal convective heat transfer problems. In 1956, Schmidt [1]² investigated the transient natural convection heat transfer inside a sphere when it was subjected to a change in wall temperature. Five spheres with diameters from 100 to 500 mm were used along with water, butyl alcohol, methyl alcohol, and ethyl alcohol in Schmidt's study. From the experimental data the following heat transfer correlation was obtained:

$$\text{Nu} = 0.098 (\text{Ra})^{0.345}$$

Shaidurov [2] constructed a 14.7 mm spherical cavity from two hemispheres cut in plexiglass blocks. The blocks, with the cavity filled with a liquid, were inserted between a heater and a cooler which were tightly pressed against them. He studied the case of heating at the bottom and cooling at the top and the case of heating at one side and cooling at the other side. The flow patterns and velocity profiles on the vertical diameter were presented for the second case. The local heat transfer correlation for γ , the angle in a

counterclockwise direction from the south point, ≤ 90 deg was described by the equation

$$\overline{\text{Nu}} = C(\text{Ra})^{1/4}$$

where the coefficient C was given as 0.25, 0.23, and 0.19 for $\gamma = 0, 45, \text{ and } 90$ deg, respectively. For $\gamma > 90$ deg the "one quarter" law was replaced by a slower-rising relation which became $\text{Nu} \approx 1$ as γ approached the convection-free position ($\gamma = 180$ deg).

Exact solutions for natural convection in spherical cavities are difficult to obtain because of the nonlinear, coupled character of the basic equations and the complexities involved with spherical geometry. Most of the theoretical work appears to have been done by the Russians [3, 4, 5]. Among those, the most complete solution so far was the one given by Pustovoit [4]. He studied the transient natural convection heat transfer inside a sphere when the temperature at the walls was subjected to a step change. The approximate solution was obtained by expanding the temperature, pressure, and velocity in terms of a Grashof number series. Only the first-order approximation was solved and no explicit results were given owing to the unwieldiness of the equations involved. Recently Whitley and Vachon [6] published numerical solutions of transient, laminar, free-convection in spherical containers. They applied implicit central difference schemes to solve for streamlines and isotherms for air in a container, 1 ft in diameter, subjected to a 10° increase in the wall temperature. The solutions were presented at dimensionless times of 0.030 and 0.10.

The present paper presents the results of an experimental investigation of natural convection heat transfer to water enclosed in a sphere. General pseudosteady-state³ laminar flow patterns are dis-

¹ Presently at Sargent and Lundy Engineers, Chicago, Ill.

² Numbers in brackets designate References at end of paper.

Contributed by the Heat Transfer Division for publication in the JOURNAL OF HEAT TRANSFER. Manuscript received by the Heat Transfer Division July 29, 1974. Paper No. 75-HT-Y.

³ This term is used throughout this paper to indicate constant driving force conditions, although the temperatures within the sphere were not constant with time.

cussed and the velocity profiles for laminar flow at the horizontal axis are presented. The overall heat transfer was found to be correlated by:

$$Nu = 0.80 Ra^{0.30}$$

Experimental Apparatus

The design and construction of the equipment and instruments are described in three groups: (1) those associated with the internal fluid, (2) those associated with the external fluid, and (3) the photographic equipment.

1 Internal Fluid, Sphere, and Temperature Measuring Devices. Distilled water with industrial grade microballons dispersed at a concentration of about 0.3 gm/l was used as the internal fluid. Pyrex, round bottom, boiling flasks of 3000, 1000, and 500 ml were used for the larger spheres. However, since they were not satisfactory in sizes below 500 ml because of the relatively large neck to spherical volume, two smaller spheres with volumes of 83 ml and 48 ml were made with small necks. All of the spherical containers had ratios of neck to sphere volumes of less than 0.05 and the area removed by the neck was always less than 0.01 of the total surface area. The time constant of each sphere was determined by recording the response of the center of the sphere to a step forcing in the external fluid temperature; the time required for 63.2 percent of the total change to take place was used as the time constant.

The temperature at the center of the sphere and of the fluid outside the sphere were measured with $\frac{1}{16}$ -in., sheathed, copper-constantan thermocouples. The thermocouples were connected to a two-channel strip chart recorder so that the temperature difference between the center and the external fluid could be recorded along with either of the two temperatures.

2 Circulation and Control of the External Fluid. The main purpose of the equipment in this group was to supply and control heat for the process of natural convection heat transfer. A 50 l rectangular tank made of plate glass was used as the external fluid container. In order to maintain a uniform temperature throughout the external fluid and especially near the sphere, the external water was circulated at a rate of 25 l/min from one corner of the bath, through a centrifugal pump, and back into the bath through four jets located below the sphere. The mixing in the bath was evaluated by recording the temperature at many locations in the bath as it was heated. No temperature variations with position were detected, therefore, the external fluid temperature was measured thereafter using one thermocouple positioned about 2 cm from the sphere. Two 80 l tanks were filled with water and preheated to about 80°C; the external bath was cooled (along with the water inside the sphere) to about 5°C; and then the hot water was pumped into the bath, quickly mixed, and left through an overflow. By adjusting the hot water flow rate, the bath could be maintained at a desired temperature above that of the center of the sphere. Although somewhat crude (due to manual adjustment of the hot water flow), this procedure was adequate to maintain temperature differences within $\pm 0.2^\circ\text{C}$, with the time averaged temperature differences even more accurate.

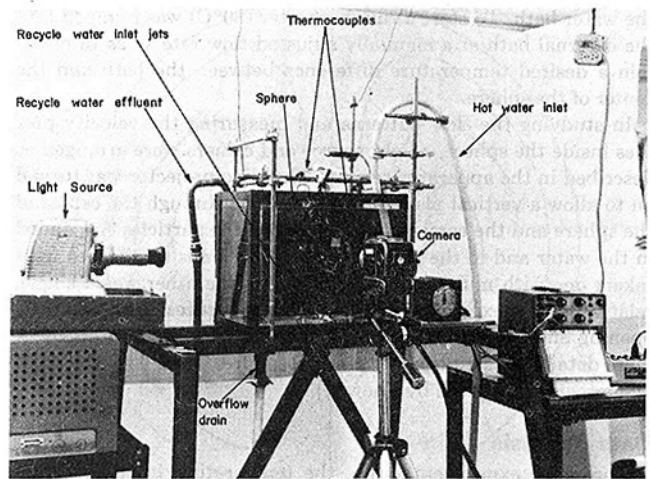


Fig. 1 Assembled apparatus

3 Light Source and Camera Arrangement. The purpose of this group of equipment was to illuminate the particles suspended in the sphere and to take pictures of their movement to show the flow patterns. A 300 W slide projector was used for the light source. The wall of the bath perpendicular to the light source was blocked with a black plate which had a $\frac{1}{8}$ -in. vertical slit down the center, thus allowing only a vertical plane of light to pass through the wall. The position of the sphere was adjusted so that the vertical plane of the light passed through its center. The neck of the sphere was positioned so that it was not in this plane of light and was at a 45 deg angle above the horizontal. A camera was located perpendicular to the plane of light and therefore could photograph a major circle through the sphere. An appropriate combination of lenses and extension rings was used to provide close-up pictures. Fig. 1 shows the assembled apparatus.

Experimental Procedure

Three tenths g of industrial grade glass microballons IG 101, manufactured by Emerson & Cuming, Inc., were poured into 1000 ml of distilled water and the solution was stirred well. These hollow glass spheres, ranging in size from 10 to 300 microns in diameter, had a density of 0.337 g/cc. The water and suspended particles to be used as the working fluid were drawn from the lower section of a container after allowing 20 minutes for the particles larger than about 20 microns to float to the top. An estimate of the floating rate is given in reference [7]. The distilled water (with particles) was then poured into the glass sphere in which natural convection was to be studied. A thermocouple was positioned at the center of the sphere.

The external bath was filled with tap water and ice cubes and the sphere was fixed in the center of the bath. The amount of ice put in the bath was adjusted so that the temperature of the water bath was cooled to about 5°C and time was allowed so that the water inside the glass sphere could reach thermal equilibrium with

Nomenclature

C_p = heat capacity of fluid inside sphere
 D = diameter of sphere
 g = local acceleration of gravity
 Gr = Grashof number, $\frac{\beta g \Delta T \rho^2 R^3}{\mu^2}$
 h = average heat transfer coefficient based on ΔT and inside spherical surface
 k_f = thermal conductivity of fluid inside sphere at temperature T_{av}

Nu = Nusselt number inside the sphere, $\frac{hD}{k_f}$
 Pr = Prandtl number, $\frac{C_p \mu}{k_f}$
 R = radius of sphere
 Ra = Rayleigh number, $Gr Pr$
 T = fluid temperature
 T_c = fluid temperature at center of sphere
 T_s = inside wall temperature

T_{av} = average fluid temperature = $0.75 T_s + 0.25 T_c$
 ΔT = fluid temperature difference between inside wall and center of sphere
 β = volumetric coefficient of expansion of fluid
 μ = dynamic or absolute viscosity of fluid
 ρ = fluid density

the water bath. To start a run, hot water (80°C) was pumped into the external bath at a manually adjusted flow rate so as to maintain a desired temperature difference between the bath and the center of the sphere.

In studying the flow patterns and measuring the velocity profiles inside the sphere, a light source and camera were arranged as described in the apparatus section. The slide projector was turned on to allow a vertical plane of light to shine through the center of the sphere and the camera was focused on the particles suspended in the water and in the plane of light. Two kinds of pictures were taken; one with multiple exposures, while the other was a single, relatively long exposure. The multiple exposures were made by opening and closing the camera lens for specific time intervals. A more detailed description of these procedures along with the actual photographs is given by Chow [7].

Data Analysis

During an experimental run, the temperature in the external bath was continuously increased at a rate such that the temperature difference between the bath and the center of the sphere remained constant. The temperature difference and the temperature rise were recorded. The rate of heat transfer through the spherical wall was determined by the volume of water inside the sphere and the rate of temperature increase at the center. This assumes that the relative temperature distribution within the sphere was constant with time after pseudosteady-state was reached. Also the calculated heat transfer rate was an average over the entire sphere.

The average inside wall temperature of the sphere was calculated through knowledge of the wall thickness, its conductivity, the average heat flux, and the bath temperature. The resistance to heat transfer of the inside film, the wall, and the outside film were estimated to be 70 percent, 25 percent, and 5 percent, respectively. Of course, the actual inside surface temperature varied from the average with position—being higher than the average where the rate of heat transfer was low, e.g., at the vertical poles, and being

lower than average where the heat transfer was high. The effect of this was to slightly moderate the rate of heat transfer over the entire surface. It was the difference between the center temperature and this calculated average inside wall temperature that was used in defining the Nusselt and Grashof numbers.

Discussion of Results

1 Flow Patterns. Before starting a run, the water inside the sphere was at a uniform temperature and at rest. As the heating began, the fluid near the inside walls moved up along the walls and down through a large central core. At the beginning, the thickness of the fluid layer flowing upward along the wall was equal to about twenty percent of the radius and had a maximum velocity of about 35 cm/min. The thickness of this upward-moving layer decreased and the velocity slowed during an initial period equal to about three time constants, after which a constant flow pattern was established. It was after the establishment of the constant flow pattern that pseudosteady-state was assumed and data were collected.

When the Rayleigh number was less than about 10^7 , the general pseudosteady-state flow patterns were all similar; a thin layer of water close to the inside wall flowing upward and a large core of fluid moving downward forming closed streamlines. Fig. 2 is a typical flow pattern determined from a multiple exposure photograph.

The location of the center of the closed streamlines (circulation centers) was expressed by the angle between it and the horizontal axis along with its relative distance from the center, i.e., the distance from the center divided by the radius. The relationship between the angle (in degrees) and Rayleigh number is shown in Fig. 3, and the relative distance from the center is shown in Fig. 4. These figures show that the circulation center moves toward the wall and downward with increasing Rayleigh number between 10^5 and 10^7 .

A natural convection heat transfer flow pattern inside a sphere, for a step change in outside temperature was given by Pustovoit [4]. Fig. 5 shows his solution for $Ra = 2 \times 10^3$ at a dimensionless time of one. The circulation center was located on the horizontal axis with a distance of 0.48 times the radius from the center. Noting that the cross-sectional area for flow is proportional to distance from the center, Pustovoit's results indicate that the outer layer will move slower than the inner core. The present experiments have shown the upward flowing stream close to the wall moves considerably faster than the central core and the circulation center was never found to be less than about 0.7 times the radius from the center. Since the major driving force for convection occurs near the

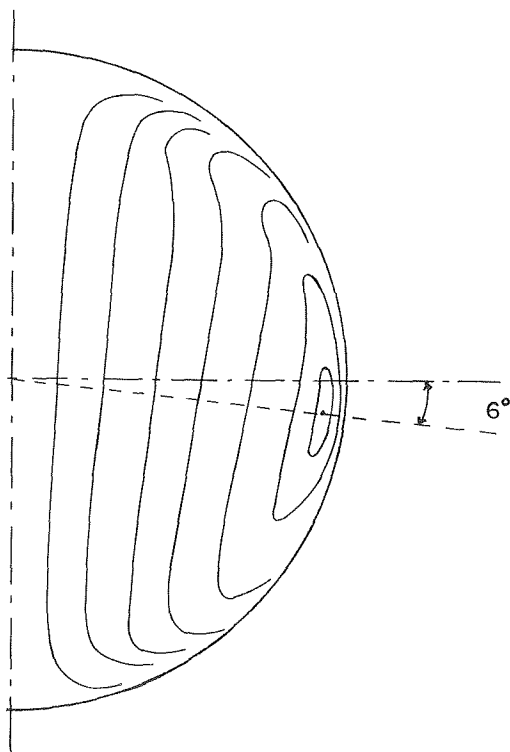


Fig. 2 Natural convection pattern for water during laminar flow in a 500 ml sphere—temperature difference between center and inside wall = 2.5°C, Rayleigh number = 2.8×10^6

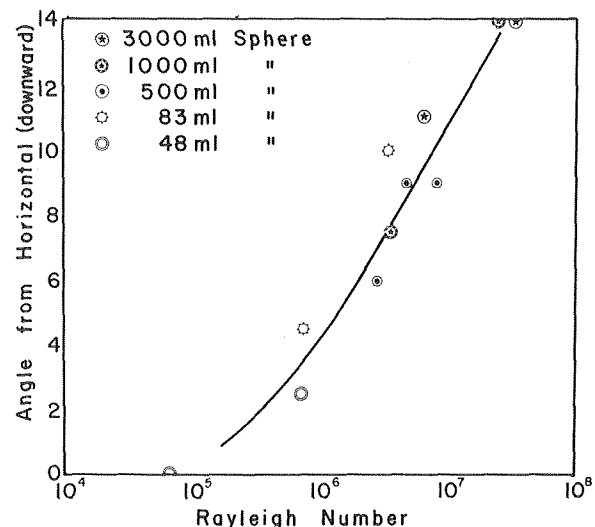


Fig. 3 Effect of Rayleigh number on the location of the circulation center; angle below horizontal

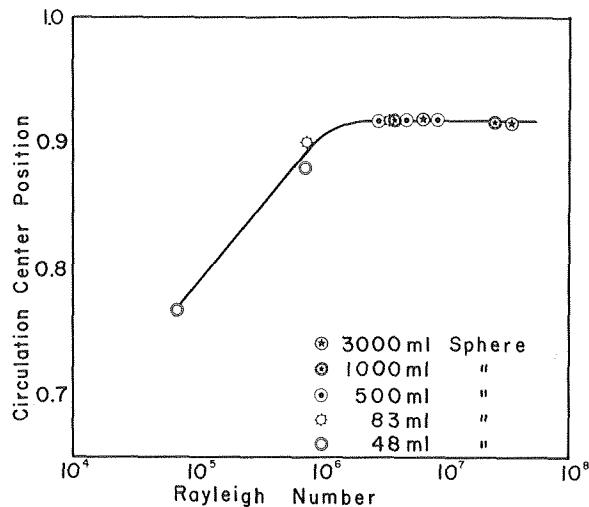


Fig. 4 Effect of Rayleigh number on the location of the circulation center; position = distance from center of sphere/radius

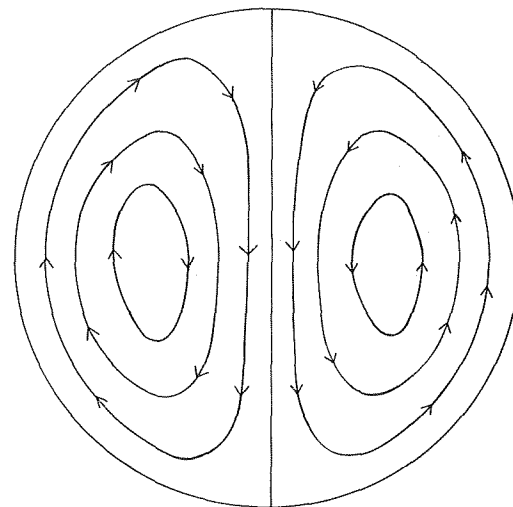


Fig. 5 The theoretical natural convection heat transfer flow pattern at dimensionless time = 1 for $Ra = 2 \times 10^3$ by Pustovoi [4]

wall of the sphere, it would seem reasonable that the upward flowing fluid near the wall would always have an average velocity greater than the downward moving central core. If this logic is valid, then as the Rayleigh number decreases the location of the circulation center should approach a relative position of 0.707 at which point the average upward and downward velocities would be equal.

Recently Whitley and Vachon [6] published numerical solutions of transient laminar free convection in closed spherical containers. They applied implicit central-difference schemes to solve for streamlines and isotherms for air at atmospheric pressure in a 1 ft dia container initially at 32°F subjected to a 10° increase in the wall temperature. The solutions were presented at dimensionless times $\tau = 0.030$, and 0.10 (Figs. 6 and 7). Dimensionless time was defined as

$$\tau = \frac{\alpha t}{R^2};$$

where α was thermal diffusivity, t was time, and R was radius of sphere. This dimensionless time is called the Fourier modulus and has been widely adopted in conduction heat transfer. Their solutions indicated that the thickness of the upward flowing fluid layer decreased as equilibrium was approached. This, in fact, agrees with the results of the present work.

The Fourier moduli at a time equal to three time constants for the spheres in the present experiment were 0.046, 0.062, 0.068, 0.11, and 0.13 for 3000, 1000, 500, 83, and 48 ml spheres, respectively. Furthermore, as was shown in their paper, most of the fluid inside the sphere was within 90 percent of the equilibrium at $\tau = 0.1$. Therefore, their flow pattern at $\tau = 0.1$ can reasonably be compared with that of the present experimental results even though their results were for unsteady-state and this work is for pseudo-steady-state. From their data, the Rayleigh number was estimated to be about 1.7×10^6 at $\tau = 0.1$. The crescent-shaped flow pattern of the circulation rings was in good agreement with the present experimental results; however, the peculiar S-shaped patterns and the recirculation near the bottom of the sphere (Fig. 7) were never observed. They argued that the recirculation pattern at the bottom was a result of the opposing conduction and convection heat transfer trends in this region. In this they assumed that the fluid at the bottom would rise upward upon heating. However, from this work, it seems that the fluid flowing upward along the wall near the bottom causes all the fluid to move along the direction of the wall at these moderate Rayleigh numbers. Thus, no recirculation was observed in the present experimental study except when turbulent flow was approached (Rayleigh numbers above 10^7). Whether or

not this discrepancy would occur in air is not known.

In Whitley and Vachon's numerical solutions, as well as in most other mathematical solutions for natural convection heat transfer, physical properties, with the exception of density, are assumed independent of temperature. For Whitley and Vachon's case of heating air, the viscosity would be larger and the expansion coefficient smaller near the walls of the sphere. Since changes in these properties were not considered, we would expect the actual circulation centers to be somewhat more toward the center of the sphere than shown in Fig. 7. Conversely, for the case of heating water, the

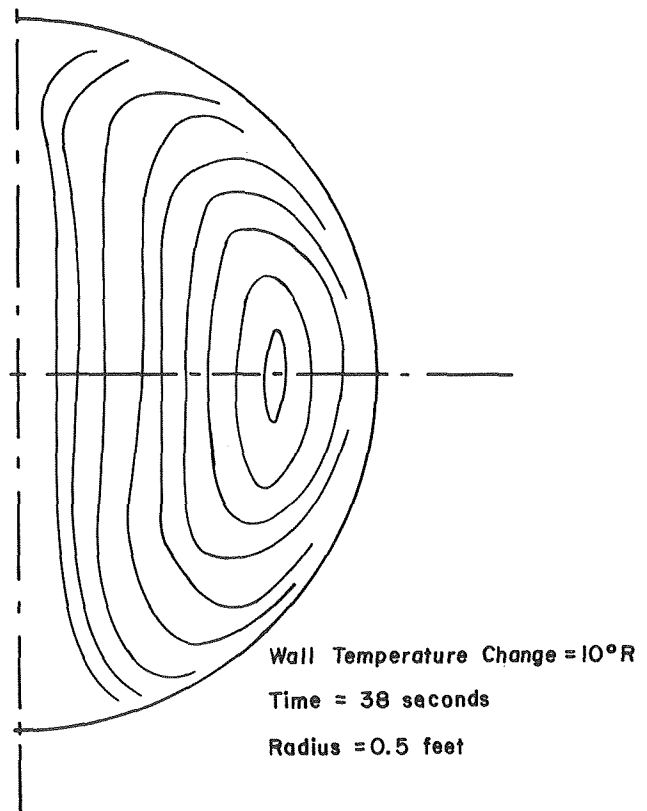


Fig. 6 Dimensionless streamlines at $\tau = 0.030$ in a sphere (Whitley and Vachon [6])

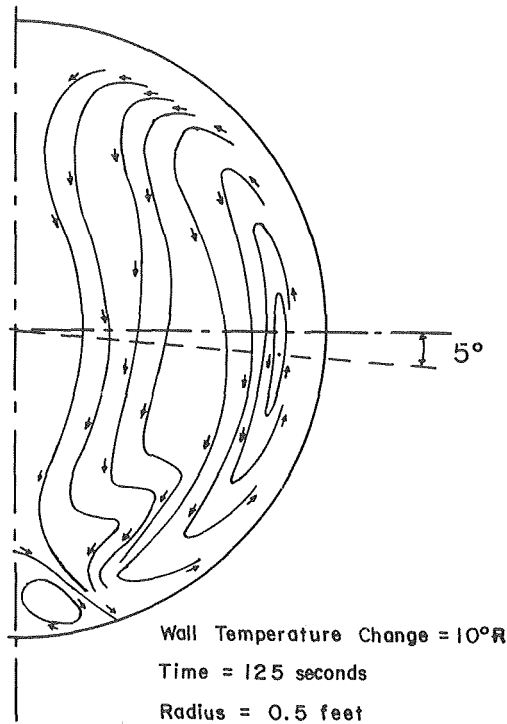


Fig. 7 Dimensionless streamlines at $\tau = 0.10$ in a sphere (Whitley and Vachon [6])

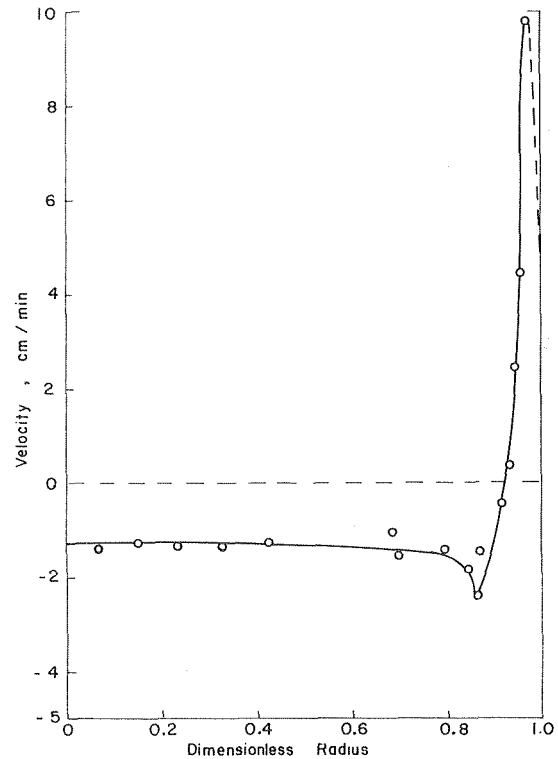


Fig. 8 Velocity profile at horizontal radius in a 3000 ml sphere; $\Delta T = 2.5^\circ\text{C}$, $Ra = 6.5 \times 10^6$

viscosity would be smaller and the expansion coefficient larger near the walls—the combined effect would be that the actual circulation center would be closer to the walls than predicted by Whitley and Vachon. That this was actually the case can be seen by comparing Figs. 2 and 7.

From the present experimental results the position of the circulation center was estimated to be 5.5 deg from the horizontal at a relative radius of 0.91 when $Ra = 1.6 \times 10^6$. Whitley and Vachon's solution for air with constant properties predicts the center to be at 5 deg and at a relative radius of 0.85.

Turbulent flow (or perhaps transitional flow) was found when the Rayleigh number was greater than 10^7 . As the heating started, the fluid close to the inside walls would move up along the walls and down through a central core as was in the case of laminar flow. The circulation center was initially above the horizontal axis, but moved downward after a short period of time. After a time of about one time constant, the fluid at the very bottom would move vertically in a swirl and then spread out somewhere near the center of the sphere. This erratic fluid movement took place every two or three min at first, but increased in frequency with time. After a time of about three time constants the laminar flow pattern was almost destroyed and an irregular flow pattern predominated. A sequence of turbulent flow patterns is given by Chow [7].

2 Velocity Profiles. The local velocity inside the sphere was estimated from the length of the streaks produced by the illuminated particles in the photograph and the time of exposure. Several of the actual photographs are included in reference [7], and they may be obtained from the authors upon request. An example of a pseudosteady-state velocity profile at the horizontal radius is shown in Fig. 8. The general pattern was the same for each of the five spheres and at all Rayleigh numbers studied. There was a thin layer of fluid flowing upward close to the wall with a relatively high velocity of about 10 cm/min (± 1 cm/min); while the larger portion of fluid in the center of the sphere moved downward with a velocity of about 2 cm/min (± 1 cm/min). The maximum downward velocity was found to be about twice the average downward velocity

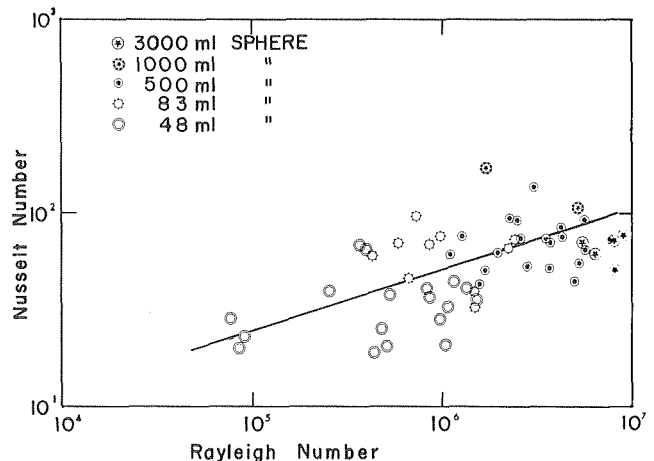


Fig. 9 Heat transfer correlation for natural convection in spheres

and it occurred just inside of the circulation center position. This peculiar phenomenon probably was due to the fact that the temperature was higher and thus the viscosity lower closer to the wall.

The effects of the variation in wall temperature on the flow patterns and velocity profiles are not definitely known. It is felt that these effects were minor since the greatest difference between the actual wall temperature and the calculated average wall temperature would occur at the vertical poles where the heat transfer was essentially by conduction. Since these regions occupied only about 5 percent of the total surface area and since the fluid was stagnant near the poles, the effects on the velocity distribution were probably negligible.

3 Heat Transfer Correlation. It has been shown by dimensional analysis [8] that for natural convection, heat transfer data may be correlated by an equation of the form

$$\text{Nu} = f(\text{Gr}, \text{Pr}).$$

Actually, if inertia forces are assumed to be negligible as compared to buoyancy and viscous forces, similarity considerations predict that the Nusselt number can be expressed as a function of the Rayleigh number alone [9]. That is,

$$\text{Nu} = f(\text{Ra})$$

Experimental studies of natural convection heat transfer correlations by Schmidt [1] and Shaidurov [2] for the case of a sphere; Scanlan, Bishop, and Powe [10] for the case of concentric spheres; and others [11, 12, 13] for the case of horizontal cylinders, all obtained satisfactory correlation by an equation of the form

$$\text{Nu} = c(\text{Ra})^a$$

Therefore, the heat transfer data obtained in this experiment were correlated using Nusselt and Rayleigh numbers only.

The relationship between Nusselt numbers and Rayleigh numbers in the laminar flow region was fitted by a linear least squares correlation. In the range $7.74 \times 10^4 < \text{Ra} < 1.13 \times 10^7$, the best fit of the data was:

$$\text{Nu} = 0.80 \text{Ra}^{0.30} \quad (\sigma = 0.19)$$

The data and correlation are shown in Fig. 9.

E. Schmidt [1], in his investigation of transient heating of a sphere subjected to a step change in uniform wall temperature, obtained an experimental correlation

$$\text{Nu} = 0.098 \text{Ra}^{0.345}$$

Since the characteristic temperature difference used by Schmidt in defining the heat transfer coefficient and that used by the present authors is probably not the same, a direct comparison with his results is impossible. Nevertheless, the slope of the equation should be about the same regardless of how the temperature difference is defined. Hence, the slope of 0.30 obtained in this work seems to agree reasonably well with that of 0.345 by Schmidt.

If we consider the situation as the Rayleigh number decreases toward zero, the heat transfer approaches that for pure conduction. This could be the result of decreasing the heating rate, the sphere size, the gravity field, or the thermal coefficient of expansion; or increasing the viscosity of the fluid. Any of these changes would cause a decrease in the induced convection motion of the fluid, with the ultimate limit of negligible velocity at all points within the fluid—hence, conduction. It has been shown [7] that when the Rayleigh number is less than 10^2 , the heat transfer is essentially by conduction and the Nusselt number should approach 2 as a limit. The heat transfer relationship obtained in this work pre-

dicts a Nusselt number of 3.2 at a Rayleigh number of 10^2 .

The most likely explanations for the large amount of data scatter in Fig. 9 are:

1 Using manual adjustment of the rate of temperature rise in the external bath, it was not possible to maintain the temperature difference better than about $\pm 0.2^\circ\text{C}$ out of a total temperature drop, between bath and sphere center, of 2°C .

2 Most of the data were taken for Rayleigh numbers between 10^6 and 10^7 which was very near the turbulent region. Therefore, transitional effects may have been present though not noticed.

3 The assumption that the Nusselt number can be correlated accurately with the Rayleigh number alone may be in error for this case.

Acknowledgment

The authors wish to express their appreciation to the National Science Foundation and the Kansas State University Engineering Experiment Station for their support of this work.

References

- Schmidt, E., "Versuche zum Wärmeübergang bei Natürlicher Konvektion," *Chemie-Ing.-Techn.*, Vol. 28, Jahrg. Nr. 3.
- Shaidurov, G. F., "On Convective Heat Transfer Across a Spherical Cavity," *Soviet Physics-Technical Physics*, Vol. 3, No. 4, 1958, pp. 799-804.
- Drakhlín, Ye. Kh., "On Heat Convection in a Spherical Cavity," *Zh. Tekhn. Fiz.*, Vol. 22, No. 5, 1952, pp. 829-831.
- Pustovoi, S. P., "Transient Thermal Convection in a Spherical Cavity," *P. M. M.*, Vol. 22, No. 4, 1958, pp. 568-572.
- Zhukhovitsky, Ye. M., "On the Stability of Unevenly Heated Liquid in a Spherical Cavity," *PMM (Journal of Applied Math. and Mechanics)* Vol. 21, No. 5, 1957, pp. 689-693.
- Whitley, H. G., III, and Vachon, R. L., "Transient Laminar Free Convection in Closed Spherical Containers," *JOURNAL OF HEAT TRANSFER*, TRANS. ASME, Series C, Vol. 94, 1972, pp. 360-366.
- Chow, M. Y., "An Experimental Investigation of Natural Convection Heat Transfer Inside a Sphere," PhD dissertation, Kansas State University, 1973.
- Jacob, M., *Heat Transfer*, Vol. 1, Wiley, New York, 1949.
- Grober, H., Erk, S., and Grigull, U., *Fundamentals of Heat Transfer*, Third ed., McGraw-Hill, New York, 1961.
- Scanlan, J. A., Bishop, E. H., and Powe, R. E., "Natural Convection Heat Transfer Between Concentric Spheres," *International Journal of Heat and Mass Transfer*, Vol. 13, 1970, pp. 1857-1872.
- Deaver, F. K., and Eckert, E. R. G., "An Interferometric Investigation of Convective Heat Transfer in a Horizontal Fluid Cylinder With Wall Temperature Increasing at a Uniform Rate," *The Fourth International Heat Transfer Conference, Vol. IV, Session N 1.1*, 1970.
- Hellums, J. D., and Churchill, S. W., "Transient and Steady State, Free and Natural Convection, Numerical Solution," *AIChE Journal*, Vol. 8, No. 5, 1962, pp. 690-695.
- Martini, W. F., and Churchill, S.W., "Natural Convection Inside a Horizontal Cylinder," *AIChE Journal*, Vol. 6, No. 2, 1960, pp. 251-257.

D. W. Pepper¹

Post-doctoral Fellow.

S. C. Lee

Professor.

Department of Mechanical and Aerospace
Engineering and Graduate Center of Cloud
Physics Research,
University of Missouri-Rolla,
Rolla, Mo.

Transport Phenomena in Thermally Stratified Boundary Layers

Studies of heat, mass, and momentum transfer are made to analyze the formation of marine fogs in thermally stratified boundary layers in the atmosphere. The governing partial differential equations of continuity, momentum, temperature, and concentration are used to describe the transport phenomena. An additional equation of turbulence energy is introduced to account for the development of the turbulent motions. Simultaneous solution of this system of equations allows the turbulent exchange coefficients to be treated in the same way as all other dependent parameters. Verification of the theoretical approach is made by comparing the numerical predictions with wind tunnel simulations of neutral, stable, and unstable atmospheres. Application of the theory is extended to the investigation of the formation of advection fog over cold ocean surfaces. In addition to the established criteria obtained from wind tunnel data, the fog model takes into consideration the radiation and sedimentation of fog droplets as well as condensation and evaporation of liquid water.

1 Introduction

Considerable effort has been made in recent years to understand transport phenomena in thermally stratified boundary layers. Adequate knowledge in this area is valuable for predicting the diffusion process of air pollutants in the lower atmosphere as well as for forecasting air-water circulation for weather conditions. Many physical parameters are involved in atmospheric transport processes, such as wind, temperature, and concentration of the diffusing medium as well as the geographical terrain. Studies of atmospheric motions, however, are hindered by the turbulence generated from the interactions of all these related parameters. Moreover, as a result of the random motion of turbulence eddies, field measurements are often insufficient for formulating a reliable mathematical model.

Simulations of atmospheric boundary layers are usually accomplished by wind tunnel modeling and numerical computations. A detailed survey of the literature concerning field measurements, laboratory simulations, and numerical predictions is given by Pepper [1].² Although many questions have been raised as to whether atmospheric turbulence can be realistically simulated in a wind

tunnel, no definite answer is readily available. As a consequence, it appears necessary to develop a realistic model to numerically analyze transport phenomena which not only can be verified by wind tunnel experiments but may also be used for predicting atmospheric motions.

Mathematical analyses of turbulent transport processes are discussed by Hinze [2], Monin and Yaglom [3], and Lumley and Panofsky [4]. Based upon their studies, transport phenomena are normally treated by phenomenological and statistical theories. While physically more realistic than phenomenological models, the use of statistical description requires a large volume of carefully sampled experimental data which are not currently available. Phenomenological theory is based principally upon mixing length theories and turbulence kinetic energy approaches. The mixing length models, based upon the concept developed by Prandtl [5], incorporate rather simple yet successful empirical relations to account for the Reynolds shear stress term in the equations of motion. The use of turbulence kinetic energy to complete the Reynolds equations, first proposed by Kolmogorov [6], is discussed in textbooks by Townsend [7], Hinze [2], Monin and Yaglom [3], Tennekes and Lumley [8], and many others. Following the suggestions of Kolmogorov [6] and Prandtl [5], the turbulent shear stress is related to the turbulence kinetic energy's one-half power. This model is the basis of calculational procedures used by Glushko [9], Patankar and Spalding [10], and Gosman, et al. [11]. A simpler relationship is suggested by Nevzglajdov [12] in which the turbulent shear stress is linearly related to the turbulence kinetic energy. This concept has been successfully used by Bradshaw, et al. [13] and Lee and Harsha [14] in analyzing boundary layer and free tur-

¹ Presently, Savannah River Laboratory, E. I. du Pont de Nemours & Co., Aiken, S. C.

² Numbers in brackets designate References at end of paper.

Contributed by the Heat Transfer Division for publication in the JOURNAL OF HEAT TRANSFER. Manuscript received by the Heat Transfer Division August 5, 1974. Paper No. 75-HT-BB.

bulent flows, respectively.

In lieu of the many different approaches used in closing the differential equations governing turbulent flows, it is necessary to investigate the validity of all available models before conducting an analysis. By using the experimental data of Klebanoff [15] and the neutral wind tunnel data of Schon and Mery [16] as a basis of comparison, it was possible to analyze the three methods of closure that are shown in Fig. 1. The disarray of data points in the Prandtl mixing length model indicates that the mixing length parameter requires modification for each particular problem. The Kolmogorov model, while more adequate than the Prandtl mixing length model, begins to show some scattering in the near wall regions of the boundary layer. The Nevzglajdov model, on the other hand, is simple and gives relatively less scattering for the same data. Similar conclusions are also drawn by Harsha and Lee [17] for free turbulent flows.

The approach adopted in this study attempts to make optimum use of the current advancement in numerical techniques coupled with presently available experimental data for the purpose of realistically predicting atmospheric motions with a minimum of empiricism. Comparison of the numerical results with wind tunnel simulations under various conditions of thermal stratification is to be discussed. Application of the present approach is being made to study the formation and dissipation of marine fog over the ocean.

2 Analysis

The basic equations, which describe the atmospheric boundary layer, consist of continuity, momentum, temperature, and concentration. For two-dimensional, steady-state boundary layer flows, the governing equations may be written as

$$\frac{\partial}{\partial X} \rho U + \frac{\partial}{\partial Z} \rho W = 0 \quad (1)$$

$$\rho U \frac{\partial U}{\partial X} + \rho W \frac{\partial U}{\partial Z} = \frac{\partial}{\partial Z} \left(\mu \frac{\partial U}{\partial Z} - \rho \overline{w'u'} \right) + F_m \quad (2)$$

$$\rho U \frac{\partial T}{\partial X} + \rho W \frac{\partial T}{\partial Z} = \frac{\partial}{\partial Z} \left(\alpha \frac{\partial T}{\partial Z} - \rho \overline{w'T'} \right) + F_h \quad (3)$$

$$\rho U \frac{\partial C^m}{\partial X} + \rho W \frac{\partial C^m}{\partial Z} = \frac{\partial}{\partial Z} \left(D \frac{\partial C^m}{\partial Z} - \rho \overline{w'c'^m} \right) + F_c^m \quad (4)$$

in which U and W are the time-average velocity components in the X and Z directions, respectively; ρ is the density; C^m is the concentration for species m ; T is the mean temperature; the primes denote fluctuating quantities; μ , α , and D are the dynamic viscosity, thermal diffusivity and species diffusivity, respectively;

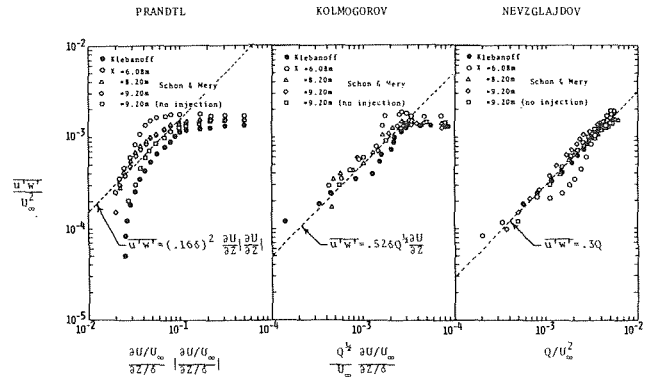


Fig. 1 Data correlation with turbulence models

and F_m , F_h , and F_c^m are the source terms of momentum, energy, and concentration, respectively. Detailed discussion of the source terms is given in the Appendix. Closure of this system of equations is accomplished by using the Boussinesq [18] approximation and the Nevzglajdov [12] model, as modified by Lee and Harsha [14], the apparent turbulence kinetic energy, Q , can be related to the laminar and the turbulent shear stresses as

$$\mu \frac{\partial U}{\partial Z} - \rho \overline{u'w'} = 0.3 \rho Q \left| \frac{\partial U}{\partial Z} \right| \quad (5)$$

It is to be noted that the magnitude of Q is contributed by the shear stresses of the eddy motions in the turbulent layer, the molecular motions in the laminar sublayer, and both laminar and turbulent motions in the transition layer. An additional governing equation for the apparent turbulence kinetic energy is written as

$$\rho U \frac{\partial Q}{\partial X} + \rho W \frac{\partial Q}{\partial Z} = -\frac{\partial}{\partial Z} \left[\rho \overline{w' \left(\frac{P'}{\rho} + Q \right)} \right] + F_q \quad (6)$$

where F_q is the source term for the production and dissipation of turbulence kinetic energy.

Introducing the apparent Prandtl and Schmidt numbers as discussed by Lee, et al. [19], the exchange coefficients of momentum, heat, concentration and turbulence become

$$K_m = \mu - \rho \overline{w'u'} / \frac{\partial U}{\partial Z} = 0.3 \rho Q \left| \frac{\partial U}{\partial Z} \right| \quad (7)$$

$$K_h = \alpha - \rho \overline{w'T'} / \frac{\partial T}{\partial Z} = K_m / \sigma_h \quad (8)$$

Nomenclature

a = empirical constant
 C^m = concentration of species m
 c' = concentration fluctuation
 c_p = specific heat at constant pressure
 \dot{C}_s = rate of formation of liquid water
 D = coefficient of molecular diffusion
 D_q = dissipation of turbulence kinetic energy
 F_c^m = source term for concentration equation
 F_h = source term for temperature equation
 F_m = source term for momentum equation
 F_q = source term for turbulence kinetic energy
 g = gravitational acceleration
 K_c = exchange coefficient of concentration

K_h = exchange coefficient of heat
 K_m = exchange coefficient of momentum
 K_q = exchange coefficient of turbulence kinetic energy
 k_λ = mass absorption coefficient
 L_h = latent heat of vaporization
 P = static pressure
 P' = pressure fluctuation
 P_q = production of turbulence kinetic energy
 Q = kinetic energy of turbulence
 R = radiation energy
 R_a = gas constant of air
 R_i = gradient Richardson number
 R_f = flux Richardson number
 T = mean temperature
 t' = temperature fluctuation
 U = mean velocity in the X -direction
 u' = velocity fluctuation in the X -

direction
 V_d = sedimentation velocity of fog droplets
 W = mean velocity in the Z -direction
 w' = velocity fluctuation in the Z -direction
 X = horizontal distance
 Z = vertical distance
 α = thermal diffusivity
 β = emissivity
 δ = boundary layer thickness
 μ = dynamic viscosity
 ρ = density
 σ = Stefan-Boltzmann constant
 σ_c = turbulent Schmidt number
 σ_h = turbulent Prandtl number
 σ_q = equivalent Prandtl number

$$K_c = D - \overline{\rho w' c'} / \frac{\partial C}{\partial Z} = K_m / \sigma_c \quad (9)$$

and

$$K_q = -\rho w' \left(\frac{P'}{\rho} + Q \right) / \frac{\partial Q}{\partial Z} = K_m / \sigma_q \quad (10)$$

respectively, in which σ_h is the apparent Prandtl number with a numerical value of 0.75, obtained experimentally by Arya [20] for a simulated stable atmosphere, σ_c the apparent Schmidt number, equal to 0.75 as given by Fleagle and Businger [21], and σ_q the equivalent Prandtl number, which is approximately equal to 0.70 as determined by Lee, et al. [22]. Both Prandtl and Schmidt numbers were allowed to vary from 0.4 to 1.0 under various conditions of thermal stability but proved to be insignificant in altering the results to any appreciable degree. For lack of any reliable functional relation to account for the variation in the apparent Prandtl and Schmidt numbers, σ_h and σ_c were assumed to be constant in the study.

Using the concept of exchange coefficients, the governing equations of momentum, heat, mass, and turbulence are parabolic type. The system of equations can be simultaneously solved for the dependent variables of velocity, temperature, concentration, and turbulence using the numerical procedure of Patankar and Spalding [10]. It should be noted that the exchange coefficients are determined locally from the apparent turbulence kinetic energy which is a function of the space coordinates. The detailed numerical scheme and all necessary boundary conditions are given by Pepper [1]. For the purpose of testing the predictability, the developed method is verified with wind tunnel data before being applied to atmospheric problems.

3 Verification With Wind Tunnel Data

Verification of the present model is made by using available experimental data. Comparison with wind tunnel data is made under conditions similar to neutral, stable, and unstable atmospheric boundary layers. While a number of experimental investigations

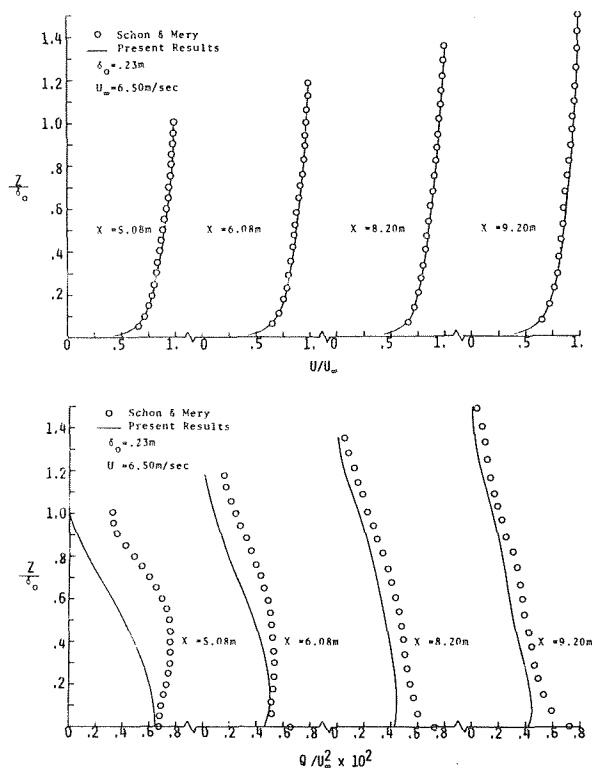


Fig. 2 Comparison of results for a neutral atmosphere

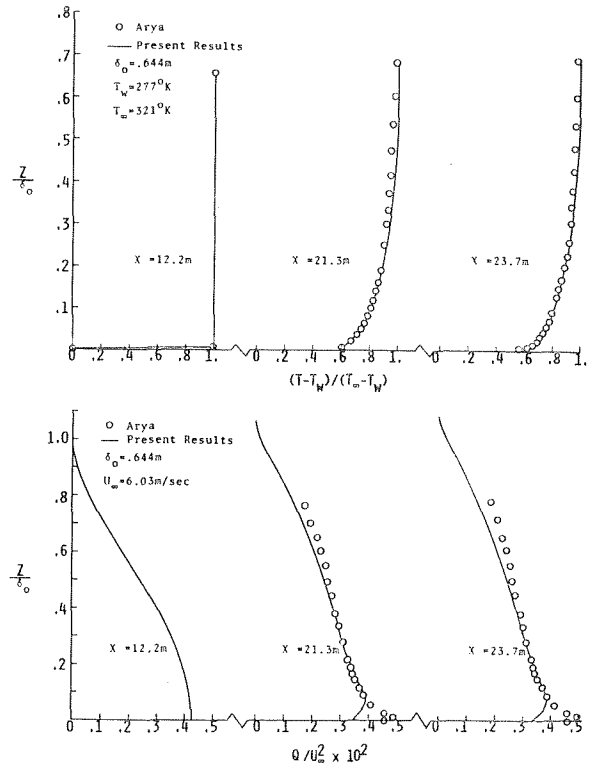


Fig. 3 Comparison of results for a stable atmosphere

have been made under neutral atmospheric conditions in meteorological wind tunnels, only a few cases contain turbulence kinetic energy data which are pertinent to the exchange coefficient model employed here. Similar investigations of experimental work in thermally stratified boundary layers disclose even less available data.

Preliminary investigations are made in a neutral atmosphere by comparing the predicted results with the wind tunnel simulation of Schon and Mery [16] as shown in Fig. 2. The subscript, o, denotes initial conditions. A nondimensional apparent turbulence kinetic energy profile, based upon measurements by Klebanoff [15], is used to generate the initial profile in the numerical scheme. The discrepancy between measured and predicted turbulence kinetic energy is due to the use of the Klebanoff profile which is for fully developed flow, while the initial profile for the Schon and Mery case is still a developing flow. However, the necessity of predicting various atmospheric conditions, without having measured turbulence data as the initial profile, limits our choice to Klebanoff's data for all studied cases. The good agreement in velocity profile comparison indicates that a fully developed turbulent profile for average velocity does not necessarily mean that the turbulence is in equilibrium.

Investigations of stably stratified atmosphere are made by comparing the predicted temperature and turbulence profiles with the wind tunnel simulation data of Arya [20], as shown in Fig. 3. The initial temperature distribution is assumed to be uniform. The Klebanoff turbulence kinetic energy distribution, similar to that for the neutral case, is used for the initial profile. The underprediction of turbulence kinetic energy occurs within 10 percent of the boundary layer near the surface. This discrepancy suggests that the Nevzglajdov model is questionable in the close vicinity of the wall boundary, if the measurements are truly reliable. Once outside this region of the calculated maximum turbulence kinetic energy, the predicted profiles begin to agree with the experimental data. Because the gradient Richardson number, R_i , serves as a quantitative measure of the thermal stratification, the distribution of R_i is plotted as a function of Z/δ_o in Fig. 4. Although a discrep-

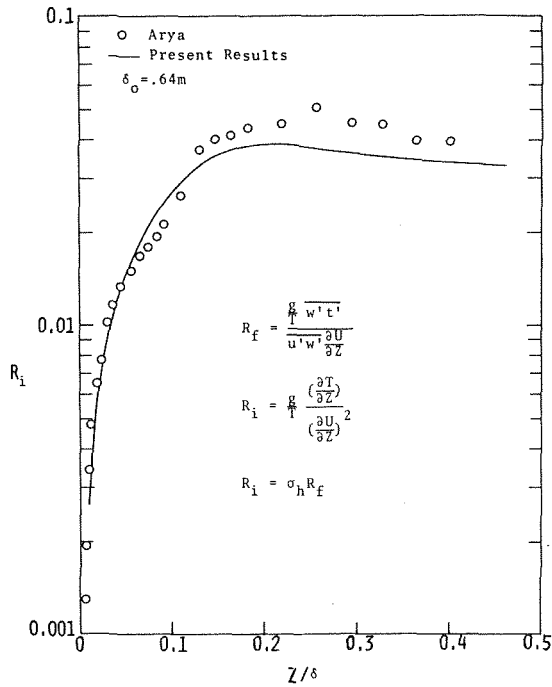


Fig. 4 Richardson number comparison for stable atmosphere

any occurs in the turbulence kinetic energy comparison, the Richardson number predictions agree well with Arya's data even in the lower 10 percent of the boundary layer. The gradient Richardson number, R_i , is related to the flux Richardson number, R_f , by the ratio of the momentum exchange coefficient to the heat exchange coefficient.

Investigations of unstably stratified atmospheres are made by comparing the predicted temperature and concentration profiles

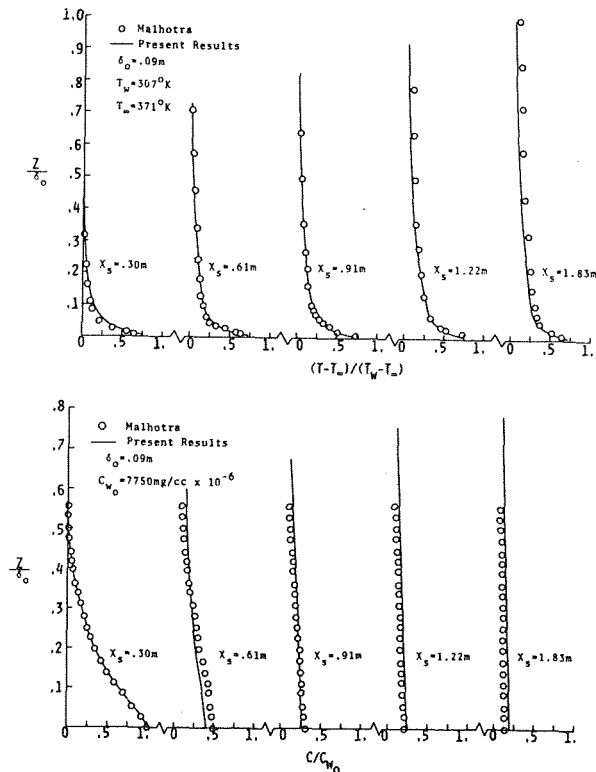


Fig. 5 Comparison of results for an unstable atmosphere

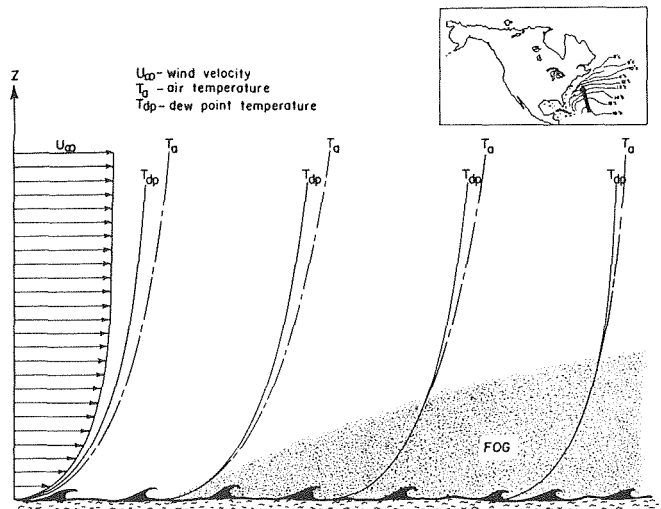


Fig. 6 Schematics of advection fog over the ocean

with the wind tunnel simulation data of Malhotra and Cermak [23] as shown in Fig. 5. Using the measured profiles at a distance of 0.3 m downstream of a simulated source ($X_s = 0.3$ m) as the initial concentration and temperature profiles, the predicted results agree well with the measured data throughout the flow field. No turbulence data are available for comparison even though the standard Klebanoff profile is used as the initial turbulence in the numerical scheme. Predictions, with reasonable accuracy for time-averaged quantities of velocity, temperature, and concentration, appear to be possible using an approximate initial profile for turbulence; if the turbulence energy is being balanced simultaneously with the momentum, heat, and mass, consistently throughout a thermally stratified atmospheric boundary layer. Extension of this method is being made to predict the formation of advection fog occurring over cold sea surfaces.

4 Advection Fog Formation

Because of insufficient information regarding ocean fogs, few studies are available in the literature. However, studies on land fog and coastal fog have been made by Mack, et al. [24], Fisher and Caplan [25], Zdunkowski and Trask [26], and Barker [27]. Consideration of the microphysical processes of condensation, radiation, and sedimentation in developing the advection fog model is based on the current information used for land and coastal fog studies.

Fig. 6 shows schematically the formation of advection fog as warm moist air blows over an aqueous surface with continuously decreasing isotherms. As a result of the transfer of thermal energy between air and ocean, the air temperature near the ocean surface is lowered until the dew point temperature is reached. This process results in the condensation of water vapor into small liquid droplets, if it is assumed that sufficient number of sea salt particles are available as condensation nuclei. A brief outline of the saturation adjustment procedure, developed by McDonald [28] and Asai [29] is given in the Appendix.

Fig. 7 shows the effect of wind velocity on fog development. Wind velocities of 3 and 6 m/s are used for analyzing an atmospheric boundary layer with a thickness of 943 m. Lines of constant temperature, seen to be emitting from the surface, arise from the continuous cooling of the surface, as shown for the wind velocity of 6 m/s case. A similar trend is also found in the wind velocity of 3 m/s case. Defining the fog boundary as the limit where the liquid water content approaches zero, it is noted that an increase in wind velocity results in a decrease of the fog layer height. Moreover, fog only forms in the region where a stable thermal stratification occurs. This result can be qualitatively verified from field ob-

servations. Leipper [30] observed that for a period of two days, fog formed very rapidly when the temperature distribution of a stable atmosphere occurred near the ocean's surface. Liquid water condensed out continuously to form fog particles as long as the stable stratification persisted. Until the temperature distribution near the ocean's surface returned to a neutral atmosphere on the third day, fog began to dissipate. Visibility started to improve on the fourth day as the temperature inversion region lifted up from the ocean surface to the lower atmosphere. Fog became stratus cloud on the fifth day when the lower atmosphere returned to neutral condition.

5 Conclusion

An analytical investigation of turbulent diffusion in thermally stratified boundary layers is made by using a phenomenological theory based upon the apparent turbulence kinetic energy. The exchange coefficient of momentum is determined based on the modified Nevzglajdov model which relates the local shear stress with the local turbulence energy. The exchange coefficient of heat and mass are determined by relating them with the exchange coefficient of momentum through Prandtl and Schmidt numbers. These coefficients can only be evaluated simultaneously with other dependent variables of velocity, temperature, and concentration. Verification of this method is made by using wind tunnel simulations of thermally stratified atmosphere. Predictions for actual conditions can only be quantitatively verified when more completed field data are made available. This study demonstrates that the development of a realistic model for predicting the transport phenomena between atmospheric and aqueous surface layers needs close cooperation among researchers in many disciplinary areas.

Acknowledgments

This research was supported in part by the Office of Naval Research under contract N00014-69-A-0141-0006 with the University of Missouri-Rolla. The computer time was partially supported by the National Center for Atmospheric Research (sponsored by the National Science Foundation), Boulder, Colorado.

References

- 1 Pepper, D. W., "Numerical Simulation of Heat, Mass, and Momentum Transfer in an Atmospheric Boundary Layer," PhD dissertation, Dept. of Mech. and Aero. Engr., Univ. of Mo.-Rolla, Rolla, Mo., 1973, p. 184.
- 2 Hinze, J. O., *Turbulence*, McGraw-Hill, New York-Toronto-London, 1959, p. 586.
- 3 Monin, A. S., and Yaglom, A. M., *Statistical Fluid Mechanics*, Nauka Press, Moscow, English Translation, MIT Press, 1971, p. 769.
- 4 Lumley, J. L., and Panofsky, H. A., *The Structure of Atmospheric Turbulence*, Interscience Publishers, New York-London-Sydney, 1964, p. 239.
- 5 Prandtl, L., "Über Die Ausgebildete Turbulenz," *Z. angew. Math. Mech.*, Vol. 5, 1925, pp. 136-139.

- 6 Kolmogorov, A. M., "Equations of Turbulent Motion of an Incompressible Fluid," *Izv. Akad. Nauk. SSSR Ser. Phys.*, Vol. 6, 1942, pp. 56-58.
- 7 Townsend, A. A., *The Structure of Turbulent Shear Flow*, Cambridge Univ. Press, 1956, p. 315.
- 8 Tennekes, H., and Lumley, J. L., *A First Course in Turbulence*, MIT Press, Cambridge, Mass., 1972, p. 300.
- 9 Glushko, G. S., "Turbulent Boundary Layer on a Flat Plate in an Incompressible Fluid," NASA TT F-10, 080, English translation, *Izv. Akad. Nauk SSSR Ser. Mek.*, No. 4, 1965, pp. 13-23.
- 10 Patankar, S. V., and Spalding, D. B., "A Finite Difference Procedure for Solving the Equations of the Two-Dimensional Boundary Layer," *Intl. J. of Heat and Mass Transfer*, Vol. 10, 1967, pp. 1389-1411.
- 11 Gosman, A. D., Pun, W. M., Runchal, A. K., Spalding, D. B., and Wolfshtein, M., *Heat and Mass Transfer in Recirculation Flows*, Academic Press, London, 1969, p. 338.
- 12 Nevzglajdov, V., "A Phenomenological Theory of Turbulence," *J. of Phys., USSR*, Vol. 9, 1945, pp. 235-243.
- 13 Bradshaw, P., Ferris, D. H., and Attwell, M. P., "Calculation of Boundary Layer Development Using the Turbulent Energy Equation," *J. of Fluid Mech.*, Vol. 28, Part 3, 1967, pp. 593-616.
- 14 Lee, S. C., and Harsha, P. T., "Use of Turbulent Kinetic Energy in Free Turbulent Mixing Studies," *AIAA J.*, Vol. 8, No. 6, 1970, pp. 1026-1032.
- 15 Klebanoff, P. S., "Characteristics of Turbulence in a Boundary Layer With Zero Pressure Gradient," NACA Rept., 1247, 1955, p. 19.
- 16 Schon, J. P., and Mery, P., "A Preliminary Study of the Simulation of Neutral Atmospheric Boundary Layer Using Air Injection in a Wind Tunnel," *Atmos. Environ.*, Vol. 5, 1974, pp. 299-311.
- 17 Harsha, P. T., and Lee, S. C., "Correlation Between Turbulent Shear Stress and Turbulent Kinetic Energy," *AIAA J.*, Vol. 8, No. 8, 1970, pp. 1508-1510.
- 18 Boussinesq, T. V., "Theorie de l'ecoulement Tourbillant," *Mem. Pre. par. div. Sav.*, Vol. 23, 1877, p. 46.
- 19 Lee, S. C., Pepper, D. W., Byrne, W. M., and Tai, R. C., "Heat Mass and Momentum Transfer in Turbulent Boundary Layer Flows," *Proceedings Fifth International Heat Transfer Conference*, Tokyo, Japan, Vol. II, 1974, pp. 104-108.
- 20 Arya, S. P. S., "Structure of Stably Stratified Turbulent Boundary Layer," Tech. Report CER68-69SPSA10, Fluid Dyn. and Diffusion Lab., Colo. State Univ., Fort Collins, Colo., 1968, p. 157.
- 21 Fleagle, R. G., and Businger, J. A., *An Introduction to Atmospheric Physics*, Academic Press, 1963, p. 346.
- 22 Lee, S. C., Harsha, P. T., Auiler, J. E., and Lin, C. L., "Heat Mass and Momentum Transport in Free Turbulent Mixing," *Proc. Heat Transf. Fluid Mech. Inst.*, 1972, pp. 215-230.
- 23 Malhotra, R. C., and Cermak, J. E., "Mass Diffusions in Neutral and Unstably Stratified Boundary Layer Flows," *Intl. J. of Heat and Mass Transfer*, Vol. 7, 1964, pp. 169-186.
- 24 Mack, E. J., Eadie, W. J., Rogers, C. W., Kocmond, W. C., and Pilie, R. J., "A Field Investigation and Numerical Simulation of Coastal Fog," Cornell Aero. Lab., CAL No. CJ-5055-M-1, Project Fog Drops Annual Summary Rep., 1972, p. 136.
- 25 Fisher, E. L., and Caplan, P., "An Experiment in Numerical Prediction of Fog and Stratus," *J. Atmos. Sci.*, Vol. 20, 1963, pp. 425-437.
- 26 Zdunkowski, W. G., and Trask, D. C., "Application of a Radiative-Conductive Model to the Simulation of Nocturnal Temperature Changes Over Different Soil Types," *J. Appl. Meteor.*, Vol. 10, No. 5, 1971, pp. 937-948.
- 27 Barker, E. H., "Oceanic Fog, a Numerical Study," EPRF, Naval Postgraduate School, Tech. Paper 6-73, 1973, p. 65.
- 28 McDonald, J. E., "The Saturation Adjustment in Numerical Modeling of Fog," *J. Atmos. Sci.*, Vol. 20, 1963, pp. 276-478.
- 29 Asai, T., "A Numerical Study of the Air-Mass Transformation Over the Japan Sea in Winter," *J. Meteor. Soc. Japan*, Vol. 43, No. 1, 1965, pp. 1-7.
- 30 Leipper, D. F., "Fog Development at San Diego, California, Sear Sound," *J. Marine Res.*, Vol. 7, 1948, pp. 337-346.
- 31 Murray, F. W., "On the Computation of Saturation Vapor Pressure," *J. Appl. Meteor.*, Vol. 6, 1967, pp. 203-204.
- 32 Plate, E. J., *Aerodynamic Characteristics of Atmospheric Boundary Layers*, U.S.A.E.C. Critical Review Ser., TID-25465, 1971, p. 190.
- 33 Byrne, W. M., and Lee, S. C., "A Differential Method for the Prediction of the Effects of Atmospheric Boundary Layer Turbulence," *Proc. Symp. on Air Pollution Turbulence and Diffusion*, Sandia Lab., Albuquerque, N. Mex., 1972, pp. 231-243.

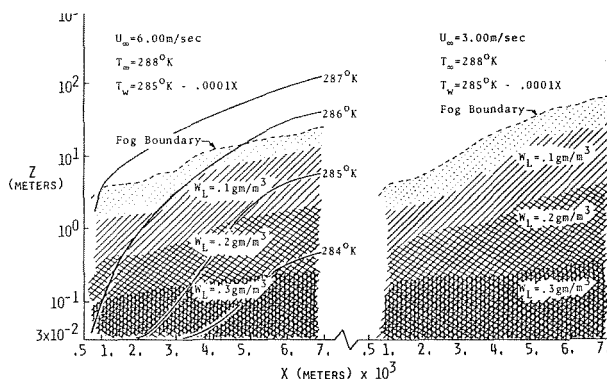


Fig. 7 Fog layer height affected by wind velocity

APPENDIX

The source terms used in the governing equations are derived from information available in the current literature. For the reader's convenience, a brief summary is given in the following.

Momentum Equation. Pressure, gravity, buoyancy, and Coriolis forces may all be involved in the source term; however, in the studied cases, only the pressure force is significant.

$$F_m = -(\partial P / \partial X) \quad (\text{A-1})$$

and

$$P = P_{s_t} \exp(-gZ/R_a T) \quad (\text{A-2})$$

in which P_{s_t} is the atmospheric pressure at sea level, and R_a is the gas constant of air.

Temperature Equation. Latent heat and radiation are considered by the relation

$$F_h = [L_h \dot{C}_s - (\partial R / \partial Z)] / c_p \quad (\text{A-3})$$

in which L_h is the latent heat of evaporation at a given temperature, and \dot{C}_s is the rate of formation of condensed liquid water at a given temperature and its corresponding partial pressure of vapor. In order to calculate \dot{C}_s , the saturation adjustment procedures of McDonald [28] and Asai [29] may be outlined as follows: Assuming air and water vapor can be treated as ideal gases, the amount of condensed liquid water can be expressed as

$$\omega_s = 0.622 \frac{P_v - P_{vg}}{P_a} \approx 0.622 \frac{P_v - P_{vg}}{P} \quad (\text{A-4})$$

for each unit of air mass, in which P_{vg} is the partial pressure of vapor at saturation, P_v is the partial pressure of vapor at each thermodynamic state of the atmosphere, and P_a is the partial pressure of air which is approximately equal to the total pressure of the atmosphere, P . By using the Clausius-Clapeyron equation for liquid-vapor phase change, the change of vapor pressure corresponding to the change of temperature can be written as

$$\frac{P_{vg} - P_g}{T_g - T} = \frac{0.622 P_g L_h}{R_a T^2} \quad (\text{A-5})$$

The saturation vapor pressure, P_g , which is a function of temperature only, is given by Murray [31] as

$$P_g = 6.108 \exp\left\{\frac{17.269(T - 273.16)}{T - 35.86}\right\} \quad (\text{A-6})$$

However, the first law of thermodynamics requires that the pressure and temperature of vapor in an isobaric atmosphere satisfy the following relation

$$\frac{P_v - P_{vg}}{T_g - T} = \frac{c_p p}{0.622 L_h} \quad (\text{A-7})$$

in which c_p is the specific heat of air. By eliminating P_{vg} between equations (A-5) and (A-7), the change of temperature before and after condensation becomes

$$T_g - T = \frac{0.622(p_v - p_g)L_h R_a T^2}{p c_p R_a T^2 + 0.387 L_h^2 p_g} \quad (\text{A-8})$$

By combining equation (A-8), (A-6), and (A-4), the amount of liquid water condensed per unit air mass becomes

$$\omega_s = \frac{c_p}{L_h} (T_g - T) \quad (\text{A-9})$$

The rate of formation of liquid water may then be written as

$$\dot{C}_s = \int_A \rho U \omega_s dZ \quad (\text{A-10})$$

The radiation term occurring in equation (A-3) may be written in the form suggested by Mack, et al. [23]

$$R(Z) = \beta \sigma T_w^4 \exp(-1.6 k_\lambda \int_{Z_b}^{Z_t} \rho \omega^m dZ) \quad (\text{A-11})$$

in which β is the emissivity of a nonblack surface ($\beta = 0.25$), σ is the Stefan-Boltzmann constant, T_w is the surface temperature, k_λ is a single spectrally-averaged mass absorption coefficient ($k_\lambda = 1.5 \times 10 \text{ cm/gm}$), and Z_t and Z_b are the top and bottom of the fog layer, respectively. The gradient of the radiation effect then becomes

$$\frac{\partial R}{\partial Z} = 1.6 \beta \sigma T_w^4 k_\lambda \rho \omega^m \exp(-1.6 k_\lambda \int_{Z_b}^{Z_t} \rho \omega^m dZ) \quad (\text{A-12})$$

in which ω^m is the liquid water content per unit air mass.

Species Equation. Three species are considered in the fog model: air ($m = 1$), water vapor ($m = 2$), and liquid water ($m = 3$). No air can be formed during fog formation and dissipation processes. Consequently,

$$F_c^1 = 0 \quad (\text{A-13})$$

Water vapor can only be formed at the expense of liquid water; thus

$$F_c^2 = -\dot{C}_s \quad (\text{A-14})$$

Liquid water can be formed by condensation of water vapor and also be removed by fallout as water drops. This leads to the expression

$$F_c^3 = \dot{C}_s + \frac{\partial}{\partial Z} (V_d \rho \omega^m) \quad (\text{A-15})$$

where V_d is the falling velocity of water drops

$$V_d = 5.3 \times 10^3 \left(\frac{\omega^m}{N}\right)^{2/3} \quad (\text{A-16})$$

with N representing the number of drops per unit volume. It is noted that equation (A-16) is based on the assumption that all drops are less than $20 \mu\text{m}$ in radius. Assuming a drop concentration of $N = 50 \text{ cm}^{-3}$,

$$V_d = 4 \times 10^2 (\omega^m)^{2/3} \text{ (cm/s)}. \quad (\text{A-17})$$

Turbulence Kinetic Energy. Production, P_q , and dissipation, D_q , of the turbulence kinetic energy are discussed by Lee, et al. [22] and Plate [32]. The production term may be written as

$$P_q = K_m \left(\frac{\partial U}{\partial Z}\right)^2 \left(1 - \frac{R_t}{\sigma_h}\right) \quad (\text{A-18})$$

which consists of turbulence energy generated by the mean shear flow and the thermal stratification. The dissipation term, as discussed by Patankar and Spalding [10] and Glushko [9], may be written as

$$D_q = a \rho Q^{3/2} / \delta \quad (\text{A-19})$$

in which δ is the boundary layer thickness. The coefficient for non-isotropy of the turbulence, a , is given by Byrne and Lee [33] as

$$a = 1.8 \quad \text{for } Z > \frac{\delta}{4} \\ a = 1.8 \left(\frac{\delta}{4Z}\right) \quad \text{for } Z \leq \frac{\delta}{4} \quad (\text{A-20})$$

which agrees with the model used by Bradshaw, et al. [13].

J. P. Quaile
Mechanical Engineer,
Corporate Research and Development,
General Electric Co.,
Schenectady, N. Y.

E. K. Levy
Assoc. Professor,
Department of Mechanical Engineering and Mechanics,
Lehigh University,
Bethlehem, Pa.

Laminar Flow in a Porous Tube With Suction

A theoretical and experimental investigation of the flow in a porous tube with wall suction is described. The flow is steady, laminar, and incompressible with the fluid entering at one end of the circular tube and flowing out through the porous circumferential surface. The study is limited to an inlet velocity profile parabolic in shape and to the case of uniform wall suction.

Introduction

The subject of fluid flow in constant diameter cylindrical tubes with mass transfer at the walls has received much attention recently because of applications to the area of heat pipes. There have been numerous theoretical investigations, almost all dealing with steady, incompressible, laminar flow with either uniform injection or suction, which have attempted to determine the axial pressure variations, wall shear stress, and shapes of the velocity profiles in a porous tube. The resulting theoretical solutions can be broadly classified into two categories.

The similarity or fully developed analyses [1-5]¹ consider only solutions to the equations of motion for which the shapes of the nondimensional velocity profiles do not vary with distance along the tube axis. The results are generally presented in terms of the radial Reynolds number, Re_r . In the case of uniform suction, similarity solutions to the governing equations have been found to exist for $0 < Re_r < 2.3$ and for $Re_r > 9.11$. No similarity solutions have been found for $2.3 < Re_r < 9.11$. In contrast to the suction case, similarity solutions have been found to exist for all values of Re_r for a flow with uniform injection.

The second type of solution, referred to here as the entrance region solution takes into account any changes in the shapes of the nondimensional velocity profiles which might occur downstream of the entrance plane of the tube. Weissberg [6], Busse [7], Bankston and Smith [8, 12], and Hornbeck, et al. [9] have obtained solutions of the entrance region type for both injection and suction for various values of Re_r . Their studies confirm the existence of regions at the entrance of the tubes where the velocity profiles change shape. Obviously in these regions the similarity solutions are not valid, in addition, Weissberg, Bankston and Smith, and Hornbeck all pre-

dicted regions of reverse flow and separation for the case of suction.

Experimentally, very little has been published for laminar porous tube flows. Bundy and Weissberg [10] presented data on overall pressure drop for a circular tube with uniform injection and found good agreement with the fully developed solutions in the range $0 < Re_r < 7.0$. Quaile and Levy [11] published pressure data in the range $2.2 < Re_r < 5$ for a circular tube with uniform suction with a parabolic inlet velocity profile. Their measurements agree well with the available entrance region solutions. No experimental data on velocity profiles have been published for either injection or suction.

In this paper, an analysis of the steady, laminar, incompressible flow in a constant diameter porous tube with uniform mass suction at the wall is developed to obtain independent predictions which can be directly compared with experimental results. Experimental measurements of the axial pressure variations and the velocity profiles are described and compared with the corresponding theoretical solutions. It is shown that reverse flow does occur as predicted, but that the regions of reverse flow are unstable and undergo transition to turbulence at relatively low values of axial flow Reynolds number.

Theory

Consider the steady laminar axisymmetric motion of an incompressible fluid in a right-circular cylindrical cavity (Fig. 1). The tube is closed at the downstream end (at $x = L$) thus requiring that the fluid which enters at $x = 0$ flows out through the porous cylindrical surface. It is assumed that the rate of mass removal is uniform over the length L with the radial velocity at the wall denoted by v_a .

The governing equations based on conservation of mass and momentum can be reduced to simplified, boundary layer type, equations by neglecting transverse pressure variations and longitudinal diffusion of momentum.

$$(ru)_x + (rv)_r = 0 \quad (1)$$

¹ Numbers in brackets designate References at end of paper.

Contributed by the Heat Transfer Division for publication in the JOURNAL OF HEAT TRANSFER. Manuscript received by the Heat Transfer Division March 25, 1974 Paper No. 73-WA/HT-1.

$$\rho[uu_x + vu_r] = -p_x + \mu[u_{rr} + \frac{1}{r}u_r] \quad (2)$$

$$p_r = 0 \quad (3)$$

These assumptions restrict the application of the solution to slender tube configurations, $a/L \ll 1$. Expressed in dimensionless quantities the equations become:

$$(2\eta U)_\xi + (\eta V)_\eta = 0 \quad (4)$$

$$2UU_\xi + VU_\eta = -P_\xi + \frac{1}{\text{Re}_r}[U_{\eta\eta} + \frac{U_\eta}{\eta}] \quad (5)$$

$$P_\eta = 0 \quad (6)$$

Defining the stream function

$$\psi_r = ru \quad \text{and} \quad \psi_x = -rv$$

the dimensionless stream function is written

$$F(\xi, \eta) = \frac{\psi(x, r)}{\psi(x, a)}$$

With the centerline value of ψ equal to zero this becomes

$$F(\xi, 0) = 0; \quad F(\xi, 1) = 1$$

Noting the fact that $\psi(x, a) = u_0 a^2/2 - axv_a$ and $u_0 = (2L/a)v_a$, equation (5) can be transformed to:

$$(1-\xi)[F_\eta F_{\eta\xi} - F_\xi F_{\eta\eta} + \frac{1}{\eta} F_\eta F_\xi] + FF_{\eta\eta} - F^2_\eta - \frac{1}{\eta} FF_\eta - \frac{1}{\text{Re}_r}[\eta F_{\eta\eta\eta} - F_{\eta\eta} + \frac{F_\eta}{\eta}] = -\frac{2\eta^2}{(1-\xi)} P_\xi \quad (7)$$

Using the conditions $u(x, a) = 0$, $v(x, a) = v_a$ and the requirement that the flow be finite and symmetric about the axis of the tube, the four axial boundary conditions on F become

$$F(\xi, 0) = F_\eta(\xi, 0) = F_\eta(\xi, 1) = 0$$

and $F(\xi, 1) = 1$

Expanding the stream function, F , in a power series in η

$$F(\xi, \eta) = \sum_{i=1}^N a_i(\xi)\eta^{2i} \quad (8)$$

with a variable number of terms permits the solution to follow a wide range of velocity profiles, a flexibility not obtainable by solutions with predetermined polynomials such as [6 and 7]. This flexibility is important both in examining effects of input velocity profiles and in solutions for the higher Reynolds numbers where the

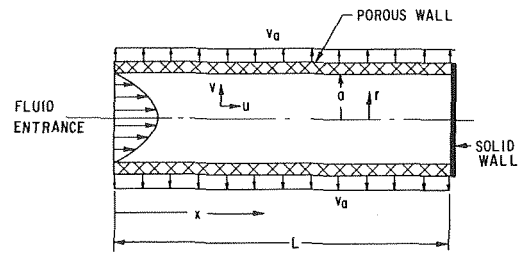


Fig. 1 Porous tube configuration

profiles become more complex displaying areas of reversed flow. Using this expansion in equation (7) then collecting terms with the same powers of η yields

η^2 terms:

$$(1-\xi)4a_1a_{1\xi} - 4a_1^2 - \frac{16}{\text{Re}_r}a_2 = \frac{2P_\xi}{1-\xi} \quad (8a)$$

η^4 terms:

$$(1-\xi)8a_1a_{2\xi} - 8a_1a_2 - \frac{96}{\text{Re}_r}a_3 = 0 \quad (8b)$$

η^6 terms:

$$(1-\xi)[12a_1a_{3\xi} + 8a_2a_{2\xi} - 12a_3a_{1\xi}] - 8a_2^2 - \frac{1}{\text{Re}_r}(288)a_4 = 0 \quad (8c)$$

η^8 terms:

Since equation (6) requires that transverse variations of P be zero, the quantity P_ξ can be determined from equation (7) evaluated at $\eta = 1$. This reduces to

$$\frac{2P_\xi}{(1-\xi)} = -\frac{1}{\text{Re}_r}[2(\text{Re}_r + 1)a_1 + 2\sum_{i=2}^N i(2i-1)(\text{Re}_r - 2i + 3)a_i] \quad (9)$$

The boundary conditions at $\eta = 1$ require that

$$\sum_{i=1}^N a_i = 1; \quad (10)$$

$$\sum_{i=1}^N ia_i = 0 \quad (11)$$

while the boundary conditions at $\eta = 0$ are satisfied automatically by the expansion for F .

Equations (8), (9), (10), and (11) form a complete set of equations for the a_i 's which can be integrated numerically provided suitable boundary conditions at $\xi = 0$ are provided. For the case of a parabolic inlet velocity profile, i.e.,

Nomenclature

a = radius of tube
 a_i = coefficients in the series expansion of F
 F = dimensionless stream function
 L = length of tube
 N = number of terms in expansion of F
 p = static pressure
 P = dimensionless pressure $P = p/(\frac{1}{2}\rho u_0^2)$
 r = radial coordinate
 Re_a = inlet axial flow Reynolds number $\text{Re}_a = 2au_0/\nu$
 Re_r = radial Reynolds number $\text{Re}_r = av_a/\nu$

u = axial component of velocity
 U = nondimensional axial component of velocity $U = u/u_0$
 u_0 = average velocity at inlet ($x = 0$)
 \dot{u}_{av} = local average velocity
 v = radial component of velocity
 v_a = radial component of velocity at the wall
 V = nondimensional radial component of velocity $V = v/v_a$
 x = axial coordinate
 η = dimensionless radial coordinate

$\eta = r/a$
 μ = dynamic viscosity
 ν = kinematic viscosity
 ξ = dimensionless axial coordinate $\xi = x/L$
 τ_w = wall shear stress
 ρ = density
 ψ = stream function

Subscripts

Subscripts x, r, ξ, η indicate differentiation with respect to that variable; double subscripts indicate double differentiation, etc.

$$U = 2(1 - \eta^2)$$

the initial values of a_i become

$$a_1(0) = 2, \quad a_2(0) = -1, \quad \text{and } a_i(0) = 0 \text{ for } i > 2.$$

The required number of equations of Type (8) depend on the number of terms chosen in the stream function expansion. Since the total set of equations is composed of equations (9), (10), and (11) as well as equation (8), Type (8) equations required number $N-2$.

The numerical integration of the equations was accomplished using a Runge-Kutta method. The number of terms used in the power series expansion of the stream function varied with Reynolds number. For each Reynolds number, there existed a definite range in the number of terms for which successful integration could be performed; however, within this range the number of terms did not affect the computed solutions significantly. The number of terms used for the solutions presented here ranged from 4 for $Re_r = 0.1$ to 8 for $Re_r = 4$ to 16 for $Re_r = 30$.

Theoretical Results

The pressure variations along the length of the tube are shown in Fig. 2 for selected values of Re_r . Also included are solutions from references [6, 7, 12]. Unlike other investigators, Bankston and Smith [8, 12] computed both transverse and axial pressure variations. The curves plotted from [12] are the pressure variations along the wall and centerline for $Re_r = 1.0, 2.0,$ and 4.0 with $a/L = 0.04$. The transverse pressure variations are assumed to be zero in the present study. As shown by the computed pressure variations in Fig 2, this simplifying assumption gives good results for the geometry and Reynolds numbers which were tested. It can lead to inaccuracies, however, at the end wall and in regions of reverse flow.

The pressure recovery experienced by the flow at the higher radial Reynolds numbers results in flow separation and reversal at the tube wall for $Re_r > 2.5$, the onset of separation occurring at

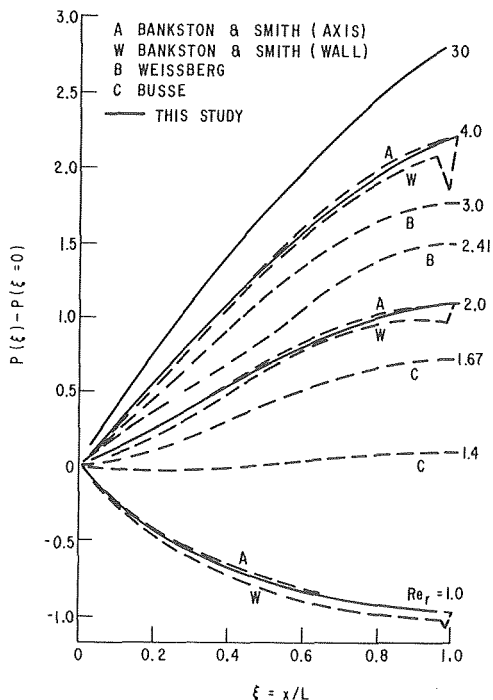


Fig. 2 Axial variations of static pressure

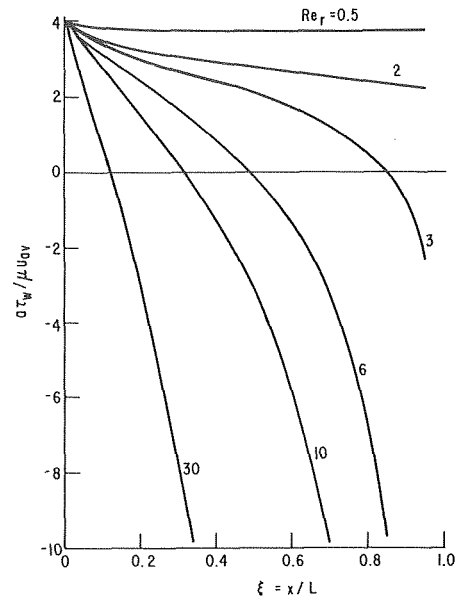


Fig. 3 Axial variations of wall shear stress

the point of zero wall shear stress. Fig. 3 shows the computed axial variations in the nondimensional wall shear stress. Zero shear is predicted to coincide with the end of the tube for a Re_r value between 2.4 and 2.5. This agrees with Weissberg's [6] figure of 2.41.

The computed theoretical velocity profiles are shown in Figs. 7 and 8 for Re_r values of 4.0 and 6.0. These profiles are discussed more fully in the sections which follow.

Experimental Apparatus

An experimental system consisting of two porous tube test sections with a supporting flow loop was used to measure the velocity of the fluid at various locations in the tube and the corresponding axial variations in pressure. The details of the flow loop can be found in [13]. The fluid used was General Electric silicone fluid No. SF-97 with a room temperature viscosity of 50 centistokes. The fluid, a silicone polymer, is a clear, colorless, inert, electrically nonconducting liquid.

The porous tube used for the velocity measurements is shown in its housing in Fig. 4. The tube with a permeability of 1.2×10^{-9} ft² was made by a sintering process out of bronze filter powder by Sintered Metals, Inc. Measurements indicated that the permeability of the tube was low enough to insure uniform suction along the wall over the entire range of Re_r which was studied. The porous tube was preceded by a long solid pipe which developed the desired parabolic inlet velocity profile.

A Disa model 55D01 hot wire anemometer unit with a type 55F32 probe and 55A44 support was used to measure the fluid velocity. The probe was introduced into the flow cavity at the downstream end ($x/L = \xi = 1$) through a pressure fitting. The probe support could be slid up and down through the fitting to achieve the desired axial location of the probe tip. A traversing mechanism was used to move the probe radially in the tube, the probe position being monitored by a linear displacement transducer.

The test section used to measure the axial variations in pressure is similar in design to the velocity test section. This porous tube had a 0.370 in. ID, a 0.875 in. OD, and was 4.9 in. long, with a permeability of 1.5×10^{-9} ft². Here too, the porous tube was preceded by a long impermeable pipe ($L/D = 120$) to develop the parabolic inlet velocity profile. The porous tube was instrumented with 10 equally spaced wall pressure taps for measurement of the axial variations in static pressure; the pressure taps were connected to a Validyne model DP15 variable reluctance pressure transducer through an array of valves. Using the pressure transducer and the system of valves, it was possible to obtain all readings as a differ-

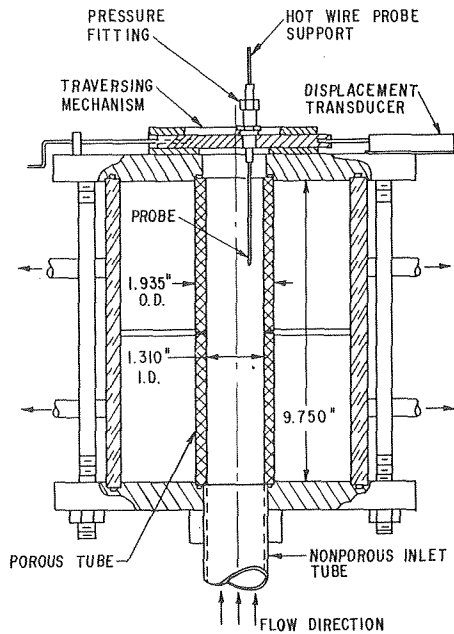


Fig. 4 Experimental test section for velocity measurements

ence in pressure between the pressure tap in question and the tap closest to the tube inlet at ($X/L = 0.05$).

Experimental Results

Pressure Variations. The measured pressure variations are presented in Figs. 5 and 6 as the nondimensional difference in pressure between the points $\xi = 0.95$ and $\xi = 0.05$. These two values represent the locations of the pressure taps closest to the downstream and upstream ends of the porous tube. Also included in the figures are the corresponding theoretical pressure variations obtained from the similarity analyses of [1, 4] and from the inlet region analysis described earlier in this paper.

The similarity pressure variations were computed by integrating the pressure gradients predicted in [1, 4] from $\xi = 0.05$ to $\xi = 0.95$.

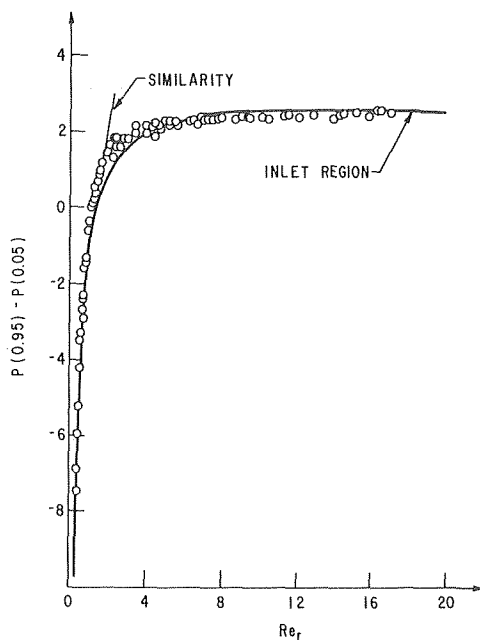


Fig. 5 Experimental pressure variations

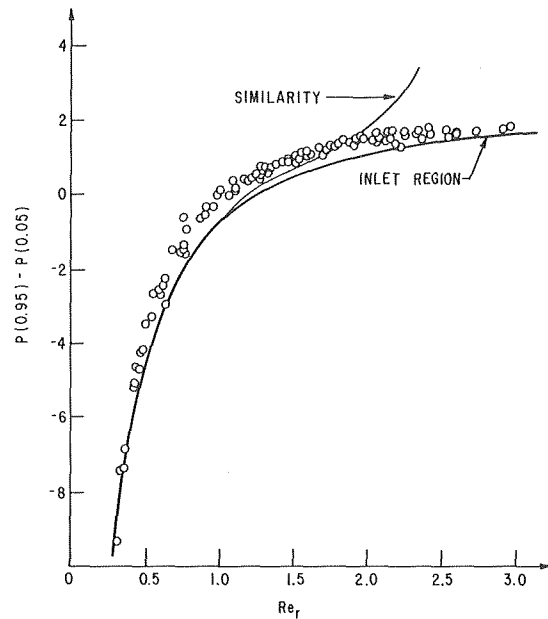


Fig. 6 Experimental pressure variations, low Reynolds number

This method assumes a fully developed flow exists in this entire region, which is of course not valid. In fact the range of validity of the similarity solutions shrinks to a point as $Re_r \rightarrow 2.3$. The curves are included to demonstrate the error introduced if this point is overlooked. As expected the deviation or error in the similarity curve increases as $Re_r \rightarrow 2.3$.

Over the range of Reynolds numbers studied, there is generally good agreement between the experimental data and the inlet region theory. According to the theory, the pressure increases in the direction of flow for $Re_r > 1.25$; adverse pressure gradients were observed experimentally for $Re_r > 1$.

Velocity Profiles. The velocity profiles obtained with the hot wire anemometer probe are presented along with the corresponding theoretical values in Figs. 7 and 8. All the experimental and

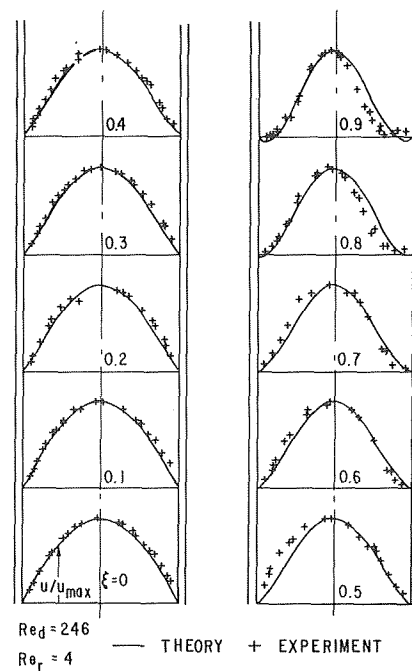


Fig. 7 Velocity profiles, $Re_r = 4$

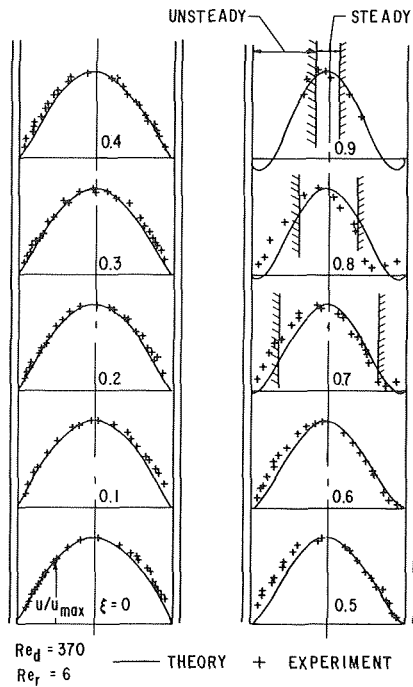


Fig. 8 Velocity profiles, $Re_r = 6$

theoretical velocities are non-dimensionalized with respect to the local centerline values, the height above the axis indicating the relative magnitude of the velocity at that point. For each value of Re_r , velocity profiles are given for values of ξ ranging from 0 to 0.9.

One of the objectives of the experimental part of the study was to determine if the regions of flow reversal predicted by the authors' analysis and by Weissberg [6], Bankston and Smith [8, 12], and Hornbeck [9] actually do exist. Experimental evidence of such separated zones is seen at $\xi = 0.8$ and 0.9 for $Re_r = 4$ (Fig. 7) and at $\xi = 0.7$ and 0.8 for $Re_r = 6$ (Fig. 8). Unfortunately, the anemometer used cannot distinguish between positive and negative velocities and consequently the point of flow reversal appears as a minimum in the data. This minimum may not be indicated exactly at zero since the probe accuracy deteriorates rapidly for extremely low magnitudes of velocity.

Transition to Turbulence. In addition to flow reversals, velocity fluctuations developed in the flow at the higher values of Reynolds number. The fluctuations appeared to originate at the wall near the separation point and spread toward the center line further downstream. The regions of the tube in which fluctuations occurred at $Re_r = 6$ are shown in Fig. 8 by lines enclosing the steady portions of the profiles. Where the magnitude of the veloci-

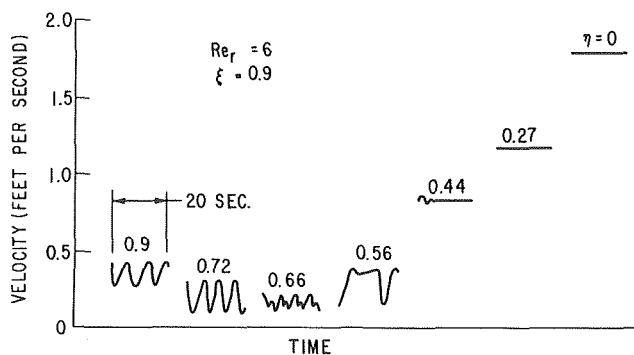


Fig. 9 Radial variations of velocity fluctuations for $Re_r = 6$ and $\xi = 0.9$

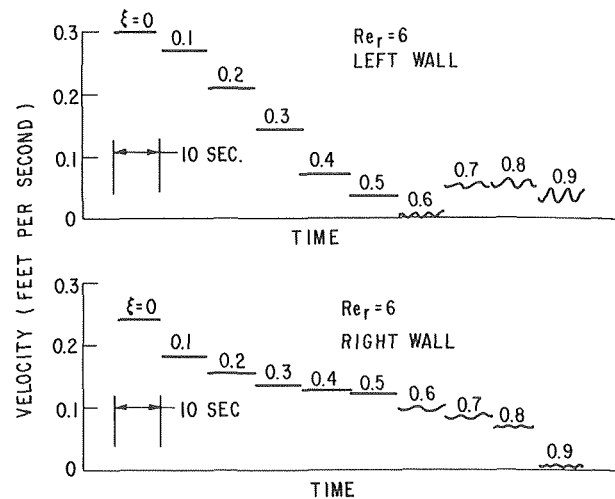


Fig. 10 Axial variations of velocity fluctuations for $Re_r = 6$

ty fluctuations was small, the time average value is included with the velocity profile data. However, in some portions of the tube, the fluctuations were too large to permit measurement of the velocity profiles.

As an indication of the type of fluctuations encountered, velocity is plotted as a function of time in Fig. 9. These measurements were made at various radii for $Re_r = 6$ and $\xi = 0.9$. Note the minimum in the magnitude of velocity at $\eta = 0.66$. Shown in Fig. 10 are the velocity fluctuations for $Re_r = 6$ measured at several axial locations along the tube. These measurements were made at $\eta = 0.901$ at two diametrically opposite locations in the test section. These are denoted in Fig. 10 as the left wall and right wall. A marked asymmetry was evident in those regions of the flow where a reversal and fluctuations were present. This can be seen in Figs. 7, 8, and 10.

No fluctuations were encountered below $Re_r = 6$; the flow reversals observed at $\xi = 0.8$ and 0.9 with $Re_r = 4$ were very steady. Above $Re_r = 6$ the frequency of the disturbances increased with Re_r and were generally beyond the frequency range of the potentiometric recorder used in the study.

As mentioned in the foregoing, the fluctuations appeared to originate at the wall near the separation point. The axial locations of the onset of fluctuations and the positions of apparent flow reversal are plotted in Fig. 11. Flow reversal was observed experimentally only for $Re_r < 6$. Although flow reversal may have occurred at larger values of Re_r , the severity of the velocity fluctuations made it impossible to observe the reversal in this range. Also included in

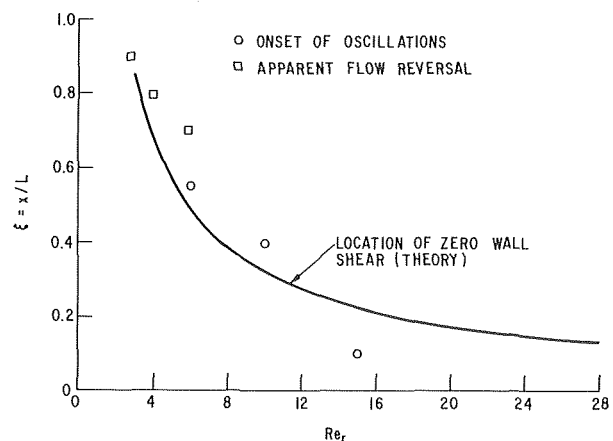


Fig. 11 Locations of points of separation, zero wall shear stress, and onset of fluctuations

the figure is a plot of the points of zero wall shear stress predicted by the theory.

In a tube flow with impermeable walls, the value $Re_d = 2000$ is generally used to denote the lower limit of the region of turbulent flow. The data obtained here show that this criterion is invalid for a tube flow with suction. The inlet axial flow Reynolds number, defined as $Re_d = \rho u_0 2a / \mu$, had the values $Re_d = 370$ for $Re_r = 6$, and $Re_d = 615$ for $Re_r = 10$. The values of the Reynolds number at the actual points of transition (based on the local average axial velocity) were even lower.

While no other studies of the effect of suction on transition in tube flows have been published, investigators have studied the effect of suction and pressure gradients on transition in external boundary layer flows. It has been shown that wall suction and favorable pressure gradients tend to increase the value of the transition Reynolds number, whereas adverse pressure gradients tend to reduce it [14, 15]. In the range of flow rates and Reynolds numbers studied here, the adverse pressure gradient apparently has a stronger influence on transition than suction resulting in the relatively low values of transition Re_d which were observed. More work is needed to determine the transition Reynolds number over a wide range of inlet axial and radial Reynolds numbers and to develop a theoretical model of the effect of suction on transition in tubes.

References

- 1 White, F. M., Jr., "Laminar Flow in a Uniformly Porous Tube," *Journal of Applied Mechanics*, Mar. 1962, p. 201.
- 2 Terrill, R. M., and Thomas, P. W., "On Laminar Flow Through a Uniformly Porous Pipe," *Appl. Sci. Res.*, Vol. 21, Aug. 1969, p. 37.
- 3 Yuan, S. W., and Finkelstein, A. B., "Laminar Flow With Injection and Suction Through a Porous Wall," *Heat Transfer and Fluid Mechanics Institute*, Los Angeles, 1955.
- 4 Kinney, R., "Fully Developed Frictional and Heat Transfer Characteristics of Laminar Flow in Porous Tubes," *International Journal of Heat and Mass Transfer*, Vol. 11, 1968, p. 1393.
- 5 Raithby, G., "Laminar Heat Transfer in the Thermal Entrance Region of Circular Tubes and Two-Dimensional Rectangular Ducts With Wall Suction and Injection," *International Journal of Heat and Mass Transfer*, Vol. 14, 1971, p. 223.
- 6 Weissberg, H., "Laminar Flow in the Entrance Region of a Porous Pipe," *Physics of Fluids*, Vol. 2, No. 5, 1959, p. 510.
- 7 Busse, C., "Pressure Drop in the Vapor Phase of Long Heat Pipes," *Proceedings 1967 Thermionic Conversion Specialist Conference*, Palo Alto, Calif.
- 8 Bankston, C. A., and Smith, H. J., "Incompressible Laminar Flow in Cylindrical Heat Pipes," ASME Paper No. 71-WA/HT-15.
- 9 Hornbeck, R., et al., "Laminar Entry Problem in Porous Tubes," *Physics of Fluids*, Vol. 6, No. 11, 1963, p. 1649.
- 10 Bundy, R., and Weissberg, H., "Experimental Study of Fully Developed Laminar Flow in a Porous Pipe With Wall Injection," *Physics of Fluids*, Vol. 13, No. 10, 1970, p. 2613.
- 11 Quaile, J. P., and Levy, E. K., "Pressure Variations in an Incompressible Laminar Tube Flow With Uniform Suction," AIAA Paper No. 72-257.
- 12 Bankston, C. A., *private communication*.
- 13 Quaile, J. P., "Laminar Flow in a Porous Tube With Wall Suction," PhD thesis, Department of Mechanical Engineering and Mechanics, Lehigh University, Bethlehem, Pa.
- 14 Schlichting, H., *Boundary Layer Theory*, 6th ed., McGraw-Hill, New York, 1968.
- 15 Rosenhead, L., *Laminar Boundary Layers*, Oxford Press, 1963.
- 16 Landau, L. D., and Lifshitz, E. M., *Fluid Mechanics*, Pergamon Press, 1959.

Hiroaki Tanaka

Assoc. Professor,
Department of Mechanical Engineering,
The University of Tokyo,
Bunkyo-Ku, Tokyo 113, Japan

A Theoretical Study of Dropwise Condensation

The so-called steady dropwise condensation consists of the transient dropwise condensation occurring repeatedly from place to place on the tracks of departing drops. By taking statistical and geometrical conditions into account, the author derives fundamental equations describing the process of this transient dropwise condensation. By solving these equations, the existence of a universal drop-size distribution is predicted. Further, by introducing a model for the cycle of drop departure, a general expression for the heat-transfer coefficient under the so-called steady dropwise condensation is obtained.

1 Introduction

A thorough understanding of the mechanism of dropwise condensation requires the knowledge of the heat transfer through a single drop and that of the distribution of drops by sizes. While considerable progress has been made on the former problem [1-3],¹ the latter one is less well understood. Measurements of drop-size distributions are fairly limited [4,5]. A process of coalescence between drops seemed very complex for research workers and prevented their analyzing the drop-size distribution theoretically [6]. In relation to this complexity, considerable effort has recently been directed toward simulating the whole process of dropwise condensation by utilizing digital computers [7-9].

Most of the studies in the past deal with a so-called steady dropwise condensation. In the case of dropwise condensation on a vertical surface, however, a departing drop exposes a bare strip of the surface, on which transient dropwise condensation takes place without delay. In truth, the so-called steady dropwise condensation consists of the transient dropwise condensation occurring repeatedly from place to place on the condenser surface. Thus, there is not much sense in taking an averaged drop-size distribution over the whole condenser surface, but this locally occurring process of transient dropwise condensation onto a bare surface deserves intensive studies. In the following section, the transient dropwise condensation starting simultaneously throughout a considerably large surface will be considered. Then, a mean drop-size distribution over the surface at a certain instant may be defined. Though a drop grows fairly discontinuously by coalescence, a mean growth rate over the surface at a certain instant of drops with a certain size may also be defined. Fundamental equations describing the relation between these two quantities, the dropsize distribution

and the growth rate of drops, will be derived, by taking the statistical and geometrical conditions into account (exclusion between drops is most important). In Section 3, the characteristics of those fundamental equations will be fully analyzed. In Section 4, on the basis of the preceding two sections, the heat transfer under the so-called steady dropwise condensation on an inclined surface is treated, by introducing a simple model for the sweeping cycle of falling drops. In addition, it must be remembered in this paper that the condenser surface is assumed to be at a uniform temperature, by neglecting the effect of conduction in the condenser material.

2 Derivation of the Basic Equations

A bare surface condenses vapor into a large number of initial droplets (having radius R_{\min}). These droplets grow until a critical radius R_{\max} is reached at which time one drop will roll over the surface sweeping it bare again. At time t from the start of this transient process, there may be $N(r,t)dr$ drops per unit area having radii in the interval $[r, r + dr]$. The radii of these drops may grow at a mean rate $\dot{r}_a(r,t)$ both by coalescence and by condensation on themselves (This substantial growth rate is denoted by $\dot{r}_e(r)$). For simplicity, drops are assumed to be hemispherical.

Assuming $r < \rho$, we shall show that the following expression represents the number of small drops per unit area having radii in the interval $[r, r + dr]$ which become extinct within a time interval dt by coalescence with large drops having radii in the interval $[\rho, \rho + d\rho]$.

$$2\pi\rho\{\dot{r}_a(r,t) + \dot{r}_a(\rho,t)\}dt \cdot \psi(r,t;N)N(r,t)dr \cdot N(\rho,t)d\rho, \quad (1)$$

where

$$\psi(r,t;N) = 1/\left\{1 - \int_r^{R_{\max}} \pi p^2 N(p,t)dp\right\} \left\{1 - \frac{r}{r_E(r,t)}\right\}, \quad (2)$$

$$r_E(r,t) = 2\left\{1 - \int_r^{R_{\max}} \pi p^2 N(p,t)dp\right\} / \int_r^{R_{\max}} 2\pi p N(p,t)dp. \quad (3)$$

Fig. 1 (a) illustrates configuration of drops whose radii are larger than r . The hatched region having an area of $\{1 - \int_r^{R_{\max}} \pi p^2 N(p,t)dp\}$ is left for drops whose radii are equal to or smaller

Contributed by the Heat Transfer Division for publication in the JOURNAL OF HEAT TRANSFER. Manuscript received by the Heat Transfer Division June 10, 1974. Paper No. 75-HT-U.

¹ Number in brackets designate References at end of paper.

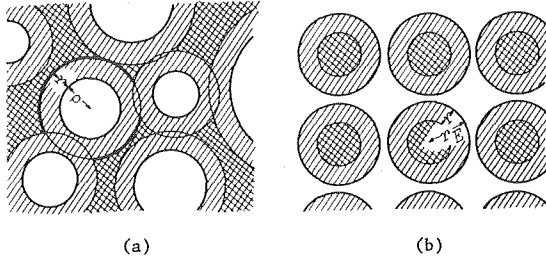


Fig. 1 Configuration of drops

than r . Moreover, the centers of drops with the radius r have to be located within the crosshatched region. Those drops with the radius r whose centers are on the boldly drawn $(\dot{r}_a(r,t) + \dot{r}_a(\rho,t))dt$ wide arcs around the drop with the radius ρ in Fig. 1 (a) become extinct by coalescence. Since the single-hatched annuli around the drops may intersect with one another as seen in Fig. 1 (a), it is very difficult to calculate the required expression strictly for Fig. 1 (a). Then, an idea of the "hydraulic diameter" is introduced in deriving expression (1). Namely, the hatched region in Fig. 1 (a) is replaced by the hatched disks in Fig. 1 (b), in the manner that the ratio of area to perimeter remains unchanged (The radius r_E of the disks is given by equation (3)). Then, the area per unit condenser surface of the crosshatched region in Fig. 1 (a) may be approximated by that of the crosshatched disks in Fig. 1 (b):

$$\pi(r_E - r)^2 \left\{ 1 - \int_r^{R_{\max}} \pi \rho^2 N(\rho, t) d\rho \right\} / \pi r_E^2;$$

and also the total length per unit condenser surface of such arcs as are drawn boldly in Fig. 1 (a) may be approximated by $2\pi\{r_E(r,t) - r\} 2\pi\rho N(\rho, t) d\rho / 2\pi r_E(r,t)$. Thus, the probability of the drops with radii in $[r, r + dr]$ in the crosshatched region where those drops can actually reside is estimated as

$$\frac{N(r, t) dr}{\pi(r_E - r)^2 \left\{ 1 - \int_r^{R_{\max}} \pi \rho^2 N(\rho, t) d\rho \right\} / \pi r_E^2}.$$

By multiplying this by the total area per unit condenser surface of such arcs as are drawn boldly in Fig. 1 (a):

$$2\pi(r_E - r) \frac{2\pi\rho N(\rho, t) d\rho}{2\pi r_E} \cdot \{\dot{r}_a(r, t) + \dot{r}_a(\rho, t)\} dt,$$

we have expression (1).

In the foregoing derivation, we introduced intuitively the idea of the hydraulic diameter to obtain an explicit representation (2) for a factor $\psi(r, t; N)$, which stands for the geometrical condition that drops exclude one another. An alternative representation for ψ

might be obtainable, either by introducing other method of approximation or by calculating exactly the probability of intersections between the single-hatched annuli in Fig. 1 (a). We note that, in either case, the factor ψ should be determined entirely by the drop-size distribution N as a function of r and t (in general, ρ will be also included).

The balance of number of drops having radius r gives

$$\frac{\partial N}{\partial t} = -\frac{\partial N \dot{r}_a}{\partial r} - \int_r^{R_{\max}} 2\pi\rho \{\dot{r}_a(r) + \dot{r}_a(\rho)\} \psi(r; N) N(r) N(\rho) d\rho + \pi R_{\max}^2 N(R_{\max}) \dot{r}_a(R_{\max}) \cdot N(r). \quad (4)$$

Since a quantity $N(r, t) \dot{r}_a(r, t)$ represents the flux per unit condenser area and per unit time of drops whose radii grow exceeding the value r , the first term on the right-hand side of equation (4) denotes the net drop number to be stored at the radius r . The second term on the right-hand side of equation (4), which expresses the number of extinct drops, is obtained by integrating expression (1) with respect to ρ from r to R_{\max} . Thus, the first term minus the second term must equal the left-hand side. Once departure of drops begins, we confine the scope of observation to the upper part of the condenser surface where drops since the start of the process remain never swept by falling drops. The last term on the right-hand side of equation (4) modifies the effect of the reduction due to drop departure of the basic area on which the drop-size distribution should be considered. Namely, the basic area reduces by a factor of $[1 - \pi R_{\max}^2 N(R_{\max}) \dot{r}_a(R_{\max}) dt]$ within a time interval dt .

For the increase in the volume of a drop having radius r due to coalescence, we obtain the left-hand side of equation (5), by computing r and ρ in expression (1), multiplying this expression by the volume $\frac{2}{3}\pi\rho^3$ of a merging drop, and then integrating with respect to ρ from R_{\min} to r . This volume increase must be equal to the difference between the volume change from the apparent growth and that from the substantial growth. Thus we get

$$\int_{R_{\min}}^r \frac{2}{3}\pi\rho^3 \cdot 2\pi\rho \{\dot{r}_a(r) + \dot{r}_a(\rho)\} \psi(\rho; N) N(\rho) d\rho = 2\pi r^2 (\dot{r}_a - \dot{r}_e). \quad (5)$$

The substantial growth rate $\dot{r}_e(r)$ of a hemispherical drop with radius r is virtually determined by heat conduction through itself and is expressed as [1]

$$\dot{r}_e(r) = \frac{8.3}{4} \frac{\lambda}{\rho_l L} \frac{\Delta T}{r}. \quad (6)$$

At extremely low pressures, interfacial mass transfer between the liquid and vapor phases becomes to control the growth rate. Curvature of the liquid-vapor interface also affects the growth rate. At moderate pressures and moderate temperature differences, however, the substantial growth rate is well expressed by equation (6) except very small drops comparable to the initial droplets [9].

Nomenclature

D = mean distance between the nearest neighboring nucleation sites, mm
 h = heat-transfer coefficient, cal/mm²s°C, partly kcal/m²h°C
 L = latent heat of vaporization, cal/g
 l = height of condenser surface, mm
 N = probability density of drop-size distribution, drops/mm²/mm
 n = exponent of r for N in the equilibrium region
 ρ = exponent of r for \dot{r}_a in the equilibrium region

R_{\max} = maximum drop radius, mm
 R_{\min} = minimum drop radius, mm
 r = drop radius, mm
 \dot{r}_a = growth rate of drops, mm/s
 r_E = equivalent radius defined by equation (3), mm
 \dot{r}_e = substantial growth rate of drops, mm/s
 ΔT = difference between saturation temperature and surface temperature, °C
 t = time, s
 \dot{V} = rate of condensation, mm³/mm²s°C

V_c = total volume of drops per unit area, mm³/mm²
 x = distance from top of surface, mm
 α = fraction of area covered by drops
 λ = thermal conductivity of liquid, cal/mm s°C, partly kcal/m h°C
 ν = accumulated number of fallen drops per unit area, drops/mm²
 ψ = defined by equation (2)
 ρ = drop radius, mm
 ρ_l = density of liquid, g/mm³
 τ = period of sweeping cycle, s

It is believed that droplets nucleate at fixed sites which are distributed at random on the condenser surface [2, 10]. As soon as a site is exposed to the vapor phase, it will be occupied by an initial droplet. Hence, the equivalent radius $r_E(R_{min})$ (defined by equation (3)) of the space left for initial droplets may be maintained to be equal to the mean distance D between the nearest neighboring nucleation sites:

$$r_E(R_{min}, t) = D. \quad (7)$$

The fraction $\alpha(t)$ of the area covered by drops, the total volume $V_c(t)$ of drops per unit condenser surface, and the accumulated number $\nu(t)$ of fallen drops per unit area are given by equations (8)–(10), respectively.

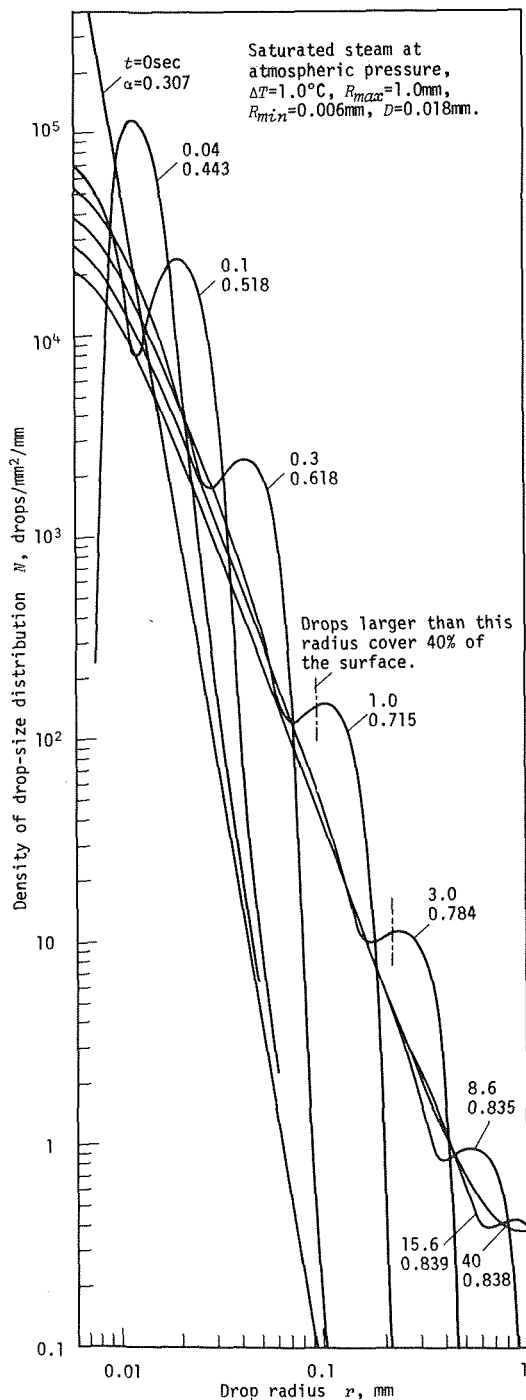


Fig. 2 Variation of drop-size distribution with the passage of time

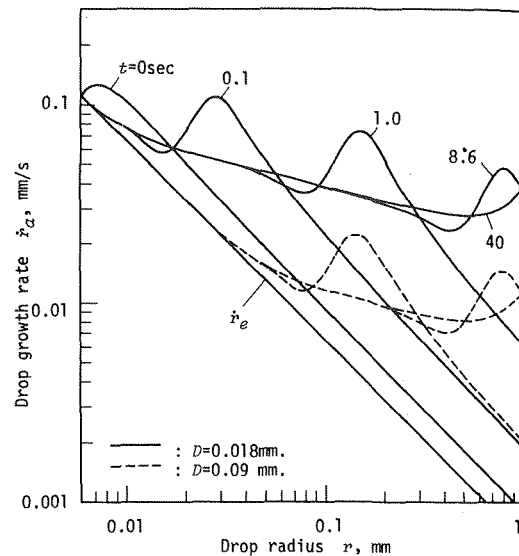


Fig. 3 Variation of drop growth rate with the passage of time

$$\alpha(t) = \int_{R_{min}}^{R_{max}} \pi r^2 N(r, t) dr, \quad (8)$$

$$V_c(t) = \int_{R_{min}}^{R_{max}} \frac{2}{3} \pi r^3 N(r, t) dr, \quad (9)$$

$$\nu(t) = \int_0^t N(R_{max}, t) \dot{r}_a(R_{max}, t) dt. \quad (10)$$

3 Numerical Computation

The simultaneous integro-differential equations (4) and (5) along with the boundary condition (7) fully describe the transient process of drop growth. Those equations are solved numerically by the following method. When $N(r, t_0)$ is given, equation (5) reduces to Volterra's integral equation of the second kind with respect to $\dot{r}_a(r, t, 0)$, and is easily solved by rewriting it to simultaneous linear equations by using trapezoidal rule. Substituting $N(r, t_0)$ and $\dot{r}_a(r, t_0)$ into the right-hand side of equation (4) and using difference analogue and trapezoidal rule yield $\frac{\partial N}{\partial t}(r, t_0)$. By choosing a proper value for a time increment Δt , a new drop-size distribution $N(r, t_0 + \Delta t)$ is obtained (in this place, $N(R_{min}, t_0 + \Delta t)$ is determined from condition (7)). Then the procedure is repeated from the beginning.

Numerical computation was performed for the case where water vapor condenses under the conditions: $\Delta T = 1.0^\circ\text{C}$, $R_{max} = 1.0$ mm, $R_{min} = 0.006$ mm, and $D = 0.018$ mm. For the initial distribution it was assumed that $N \propto r^{-6}$. The computed results for $N(r, t)$ are shown in Fig. 2, and so are those for $\dot{r}_a(r, t)$ and for $r_E(r, t)$ in Figs. 3 and 4, respectively.

Immediately after the start of the process, the distribution curve develops a characteristic profile in the range of comparatively large drops. See the distribution profile in the range of comparatively large drops. From this time on, the drop-size distribution remains similar in the range of comparatively large drops and only the characteristic dimension of the distribution grows with the passage of time. This is well demonstrated by the fact that the distribution curve with its characteristic peak in the large drop range is displaced virtually parallel in the direction of r^{-3} from $t = 0.3$ s to $t = 8.6$ s in Fig. 2. As proved in Appendix A, a completely similar solution exists under the hypothetical condition: $\alpha = \text{const}$. The similar solutions were also computed for $\alpha = 0.7$ and 0.8 , and they proved to coincide with the characteristic profile in Fig. 2 in the range of comparatively large drops. Thus we may refer to this characteristic profile as a *universal distribution for large drop range*. At this juncture, we note that contributions of drops having radii in the interval $[r, r + dr]$ to the covering ratio and to the instantaneous rate of condensation are expressed as

$$d\alpha = \pi r^2 N(r) dr = \pi r^3 N(r) d(\ln r)$$

and as

$$d\dot{V} = 2\pi r^2 (\dot{r}_a / \Delta T) N(r) dr = \frac{8.3}{2} \pi \frac{\lambda}{\rho_1 L} \cdot r^2 N(r) d(\ln r)$$

respectively. Then, as seen in Fig. 2, a little less than a half part of the surface is covered by large drops of an almost uniform size corresponding to the characteristic peak of the universal distribution, while heat is transferred mainly by small drops.

In the range of drops smaller than those dominating ones, the drop-size distribution nearly obeys the straight line: $N \propto r^{-n}$. We refer to this range as an *equilibrium region of small drops*. The distribution curves for $t = 3.0$ s and $t = 8.6$ s in Fig. 2 clearly possess this region. Here the exponent n may be such that, if the lower bound of the equilibrium region of small drops tends to zero (under the conditions: $R_{\min} \rightarrow 0$ and $D \rightarrow 0$), then $\alpha \rightarrow 1.0$. Then, from equation (3) it is easily proved that

$$\frac{r_E(r)}{r} = \text{const} = \frac{n-2}{3-n}$$

in the equilibrium region of small drops. Further, by assuming $\dot{r}_a \propto r^{-p}$ in the equilibrium region of small drops and substituting into equation (5), we find that

$$p = 1 - \left\{ \frac{3}{2} \left(\frac{1}{3-n} - \frac{1}{n-2} \right) - 1 \right\}^{-1}$$

Proofs are given in Appendix B. These relations are well satisfied by $n = 2.68$, $r_E/r = 2.10$ and $p = 0.3$ which values are obtained graphically from Figs. 2-4. As time goes by, the equilibrium region of small drops obviously widens, and the covering ratio increases from $\alpha = 0.618$ at $t = 0.3$ s to $\alpha = 0.835$ at $t = 8.6$ s in Fig. 2.

After the universal distribution for large drop range has developed, microscopic drops whose radii are smaller than the mean distance D between the nearest neighboring nucleation sites begin to follow another characteristic distribution satisfying the condition (7) for drop generation. In Fig. 2 the distribution curves from $t = 0.3$ s to $t = 8.6$ s have the same shape in the region $r < D$ (but they do not coincide because the space left for microscopic drops becomes narrower with the passage of time). And, if we observe the distribution of microscopic drops locally for the space left between large drops, it remains unchanged from $t = 0.3$ s to $t = 8.6$ s. This is demonstrated more clearly by Figs. 3 and 4, in which the curves for $t = 1.0$ s and $t = 8.6$ s coincide with one another in the region $r < D$. (In this respect we should note that, from equation (5), the growth rate $\dot{r}_a(r)$ of a drop with radius r is entirely determined by the local configuration of drops whose radii are smaller than r .) We may refer to this characteristic distribution as a *steady distribution for microscopic drops*. If we assume for R_{\min} a much smaller value than 0.006 mm with $D = 0.018$ mm unchanged, the drop density N of the steady distribution for microscopic drops takes a maximum at about $r = 0.004$ mm and then decreases as r decreases. Thus, drops having radii smaller than $D/3$ are fairly separated with one another as compared with their radii (see Fig. 4). As a result, under the steady distribution for microscopic drops, the drop growth rate \dot{r}_a is equal to the substantial growth rate \dot{r}_e in the region $r < D/3$, and then it describes the characteristic curve departing from \dot{r}_e in the region $D/3 < r < D$. The equilibrium region of small drops begins from about $r = D$. Finally, as time goes by, the characteristic peak of the growth rate curve which corresponds to the universal distribution for large drop range is displaced in the direction of r^{-p} for the equilibrium region of small drops, as is seen in Fig. 3. In the end, whatever value we may assume for R_{\min} satisfying $R_{\min} < D/3$, computed results will be the same as Figs. 2-4 (in the region $r > D/3$) except the time immediately after the start of the process.

When the departure of drops begins at about $t = 10$ s (see Fig. 5), the universal distribution for large drop range in the growing stage breaks down and then a stationary distribution over the whole drop range develops at about $t = 30$ s, as shown for $t = 40$ s in Figs. 2-4.

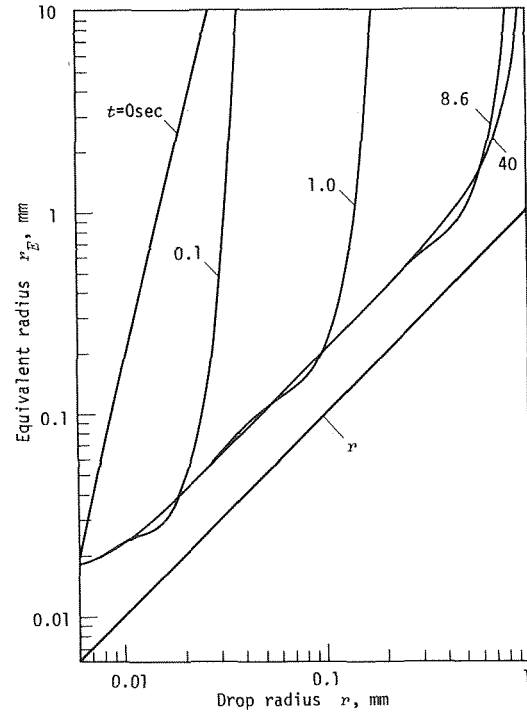


Fig. 4 Variation with the passage of time of equivalent radius of the space left for a drop with radius r

4 Heat-Transfer Coefficient

Computed results for the total volume $V_c(t)$ of drops per unit condenser surface and the accumulated number $\nu(t)$ of fallen drops per unit area defined by equations (9) and (10) are shown in Fig. 5. It can be proved by the method analogous to Appendix A that the characteristic dimension of the universal distribution for large drop range grows in proportion to $t^{1/(p+1)} = t^{0.77}$ (see Appendix C). Then $V_c(t) \propto t^{0.77}$ in the term of drop growth, as is seen in Fig. 5. After the stationary distribution has developed, V_c becomes constant and ν increases at a uniform rate.

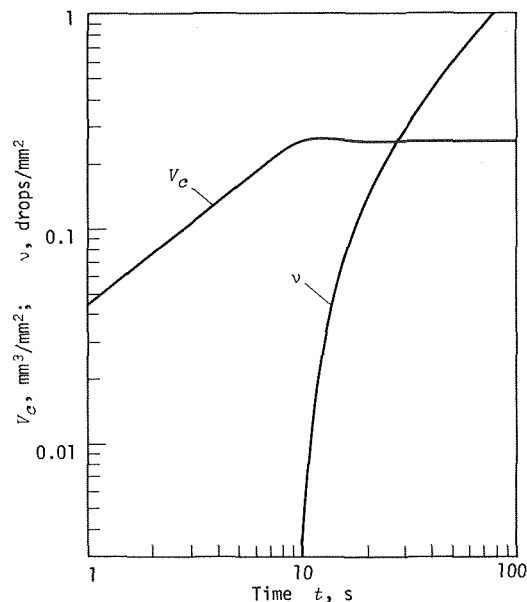


Fig. 5 Variations against time of total volume V_c of drops per unit area and of accumulated number ν of fallen drops per unit area

We can evaluate the heat-transfer coefficient as follows. We direct our attention to a $2R_{\max}$ wide strip in the direction of the steepest descent on the condenser surface, and assume that the length l of the surface in that direction is 50 mm.

(i) At $t_1 = 11.0$ s which satisfies

$$2R_{\max}l\nu(t_1) = 1 \text{ i.e., } \nu(t_1) = 1/2R_{\max}l,$$

the first drop will start from a mean position $x_1 = l/2$ (x denotes the distance from the top of the surface) clearing the strip of condensate of the following volume:

$$V_1 = \frac{2}{3}\pi R_{\max}^3 + 2R_{\max}\frac{l}{2}V_c(t_1) = 15.1(\text{mm}^3).$$

(ii) At $t_2 = 12.6$ s which satisfies

$$2R_{\max}\frac{l}{2}\{\nu(t_2) - \nu(t_1)\} = 1 \text{ i.e., } \nu(t_2) = \frac{1+2}{2R_{\max}l},$$

the second drop will start from a mean position $x_2 = l/2^2$ bringing

$$V_2 = \frac{2}{3}\pi R_{\max}^3 + 2R_{\max}\frac{l}{2^2}V_c(t_2) + 2R_{\max}\cdot(1 - \frac{1}{2})l \cdot V_c(t_2 - t_1) = 11.9(\text{mm}^3).$$

(iii) Similarly, we calculate as

$$\nu(t_i) = (1 + 2 + \dots + 2^{i-1})/2R_{\max}l,$$

and

$$V_i = \frac{2}{3}\pi R_{\max}^3 + 2R_{\max}\frac{l}{2^i}V_c(t_i) + 2R_{\max}\cdot(1 - \frac{1}{2^{i-1}})l \cdot V_c(t_i - t_{i-1}).$$

We thus obtain

$$t_3 = 15.5 \text{ s, } V_3 = 13.0\text{mm}^3; \\ t_4 = 21.0 \text{ s, } V_4 = 18.4\text{mm}^3.$$

(iv) Since $t_5 - t_4 > t_1$, a new drop falls from the lower part swept by the fourth drop, before the fifth drop starts from the top part. Then the above cycle is repeated virtually afresh from the beginning, with a period $\tau = t_4$. Therefore, the mean rate of condensation is

$$\dot{V} = \Sigma V_i / (\tau \cdot 2R_{\max}l \cdot \Delta T) = 2.78 \times 10^{-2}(\text{mm}^3/\text{mm}^2\text{s}^\circ\text{C}). \quad (11)$$

Converting this into a heat-transfer rate, we have $h = 5.16 \times 10^4$ kcal/m²h°C.

Since the basic equation (5) is linear with respect to \dot{r}_a and \dot{r}_e and so is the right-hand side of equation (4), it is clear from equation (6) that the rate of the process is in proportion to $(\lambda/\rho_l L)\Delta T$. Further, it is easy to prove from the basic equations that, if all the geometric dimensions R_{\max} , R_{\min} , D and l concerned with the phenomena are magnified by a factor m , then the phenomena proceed quite similarly, only with the rate of the process at the corresponding stage reduced by a factor $1/m^2$ (see Appendix D). Then, by choosing R_{\max} as a characteristic dimension of the phenomena, the period τ of the foregoing model can be expressed as $\tau \propto R_{\max}^2/(\lambda/\rho_l L)\Delta T$. Thus, the heat-transfer coefficient by dropwise condensation is generally expressed with the aid of equation (11) as

$$h = \rho_l L \cdot \dot{V} = \rho_l L \cdot [R_{\max}^3 / \{ (\lambda/\rho_l L)\Delta T \} \cdot R_{\max}^2 \cdot \Delta T] \cdot \text{Func}(\frac{R_{\min}}{R_{\max}}, \frac{D}{R_{\max}}, \frac{l}{R_{\max}}) = \frac{\lambda}{R_{\max}} \cdot \text{Func}(\frac{R_{\min}}{R_{\max}}, \frac{D}{R_{\max}}, \frac{l}{R_{\max}}). \quad (12)$$

Now the effects of the three factors R_{\min}/R_{\max} , D/R_{\max} and l/R_{\max} will be considered in turn. First, from those mentioned in the

preceding section, it is clear that if $R_{\min} \ll D$ the change of R_{\min} does not affect the process at all. Second, if D is multiplied by 5, the curves of the drop growth rate shift as shown by broken lines in Fig. 3. Thus, as D changes, the rate of the process, accordingly the heat-transfer coefficient, changes in proportion to $D^{p-1} = D^{-0.7}$. Thirdly, if we assume $l = 50 \times 2$ mm and calculate the sweeping cycle as before, then we become aware that, when the first drop has slid down from $x = 50$ mm, the upper half of the strip is left in quite the same situation as the foregoing case of $l = 50$ mm. Hence, in that case, five drops slide down the strip in the same period $\tau = 21.0$ s. In general, if $l = 50 \times 2^n$ mm, $4 + n$ drops slide down the strip in the same τ . Provided a particular point x is swept virtually periodically at intervals of τ_x , the local rate of condensation at that point is expressed as $\dot{V}_x = V_c(\tau_x)/\tau_x \cdot 1/\Delta T$ in place of equation (11). It is clear from the above considerations that even a considerable change of x causes the period τ_x to vary only within a factor of 2 or 3. Then $V_c(\tau_x)/\tau_x$ changes the less since $V_c(t) \propto t^{0.77}$ in the term of drop growth as mentioned before. Thus the local heat-transfer coefficient does not change so much. And the mean heat-transfer coefficient is hardly affected by l . Finally, by determining a numerical constant from the computed result: $h = 5.16 \times 10^4$ kcal/m²h°C for $R_{\max} = 1.0$ mm, $D = 0.018$ mm and $\lambda = 0.586$ kcal/m h°C, equation (12) reduces to

$$\frac{hR_{\max}}{\lambda} = K(\frac{R_{\max}}{D})^{1-p} = 5.3(\frac{R_{\max}}{D})^{0.7}. \quad (13)$$

Substituting $h = 1.7 \times 10^5$ kcal m²h°C and $R_{\max} = 1.0$ mm from recent available data for water vapor at one atmosphere [4, 5, 11, 12], the mean distance D between the nearest neighboring active nucleation sites is estimated to be 0.0033 mm, which value well satisfies the foregoing condition $R_{\min} \ll D$ (R_{\min} is about 2×10^{-5} mm for $\Delta T = 1.0^\circ\text{C}$ at one atmosphere [3]). Then the density of the active sites is about 1×10^5 sites/mm². Under these conditions, the covering ratio α reaches to about 91 percent at the last stage of the process when the stationary distribution develops.

5 Conclusion

In this paper, the transient dropwise condensation onto a bare surface has been fully analyzed. The following remarks can be drawn.

(i) Immediately after the start of the transient condensation, conspicuously large drops of an almost even size cover approximately 40 percent of the surface. Those large drops obey the *universal distribution for large drop range*, and despite the passage of time the drop-size distribution remains similar, only with its characteristic dimension growing with time.

(ii) Drops smaller than those dominating ones form the *equilibrium region of small drops*, and are distributed according to $N \propto r^{-n}$. Here, the exponent $n = 2.68$ satisfies the condition that, if we extend the equilibrium region of small drops to infinitesimally small drops, then the fraction of the area covered by drops tends precisely to unity.

(iii) Microscopic drops having radii smaller than the distance D between the neighboring sites form another characteristic part of the drop-size distribution, the *steady distribution for microscopic drops*.

(vi) When departure of drops begins, the universal distribution for large drop range breaks down and then a stationary distribution develops on the upper part of the surface where drops remain ever since the start of the process.

By introducing a simple model for the sweeping cycle of falling drops, a general expression for the heat-transfer coefficient h under the so-called steady dropwise condensation on an inclined surface has been obtained as equation (13).

References

- 1 Fatica, N., and Katz, D. L., "Dropwise Condensation," *Chem. Engng. Progr.* Vol. 45, 1949, p. 661.
- 2 Umur, A., and Griffith, P., "Mechanism of Dropwise Condensation,"

3 LeFevre, E. J., and Rose, J. W. "A Theory of Heat Transfer by Dropwise Condensation," *Proc. 3rd Int. Heat Transfer Conf.*, Chicago, Vol. 2, 1966, p. 362.

4 Tanasawa, I., and Ochiai, J., "Experimental Study on Dropwise Condensation," *Trans. Japan Soc. Mech. Engrs.* Vol. 38, 1972, p. 3193.

5 Graham, C., and Griffith, P., "Drop Size Distributions and Heat Transfer in Dripwise Condensation," *International Journal of Heat and Mass Transfer*, Vol. 16, 1973, p. 337.

6 Rose, J. W., and Glicksman, L. R., "Dropwise Condensation: The Distribution of Drop Sizes," *International Journal of Heat and Mass Transfer*, Vol. 16, 1973, p. 411.

7 Gose, E. E., Mucciardi, A. N., and Baer, E., "Model for Dropwise Condensation on Randomly Distributed Sites," *International Journal of Heat and Mass Transfer*, Vol. 10, 1967, p. 15.

8 Tanasawa, I., and Tachibana, F., "A Synthesis of the Total Process of Dropwise Condensation Using the Method of Computer Simulation," *Proceedings 4th International Heat Transfer Conference*, Paris, Vol. 16, Csl.3, 1970.

9 Glicksman, L. R., and Hunt, A. R. Jr., "Numerical Simulation of Dropwise Condensation," *International Journal of Heat and Mass Transfer*, Vol. 15, 1972, p. 2251.

10 McCormick, J. L., and Westwater, J. W., "Nucleation Sites for Dropwise Condensation," *Chem. Engng. Sci.* Vol. 20, 1965, p. 1021.

11 Tanner, D. W., Potter, C. J., Pope, D., and West, D., Heat transfer in dropwise condensation, *International Journal of Heat and Mass Transfer* Vol. 8, 1965, p. 419.

12 Citakoglu, E., and Rose, J. W., "Dropwise Condensation: Some Factors Influencing the Validity of Heat-Transfer Measurements," *International Journal of Heat and Mass Transfer*, Vol. 11, 1968, p. 523.

APPENDIX A

We assume a similar solution $N^*(r)$ defined at a time t_0 such that a drop-size distribution at an arbitrary time t can be expressed as

$$N(r, t) = (m(t))^3 N^*(m(t) \cdot r), \quad (14)$$

where $m(t)$ satisfies the condition:

$$m(t_0) = 1. \quad (15)$$

Namely, only the characteristic dimension of the distribution is magnified in proportion to $1/m(t)$, with the relative configuration of drops (accordingly the covering ratio also) unchanged. Similarly, we assume for the growth rate of drops

$$\dot{r}_a(r, t) = m(t) \dot{r}_a^*(m(t) \cdot r), \quad (16)$$

Substituting equations (14) and (16) into the basic equations (4) and (5) by letting $R_{\min} \rightarrow 0, R_{\max} \rightarrow \infty$ and the last term on the right-hand side of equation (4) be omitted yields

$$3m^2 \frac{dm}{dt} N^*(\xi) + m^2 \frac{dm}{dt} \xi \frac{dN^*(\xi)}{d\xi} = -m^5 \frac{dN^*(\xi) \dot{r}_a^*(\xi)}{d\xi} - m^5 \int_{\xi}^{\infty} 2\pi\eta \{ \dot{r}_a^*(\xi) + \dot{r}_a^*(\eta) \} \psi(\xi; N^*) N^*(\xi) N^*(\eta) d\eta, \quad (17)$$

and

$$\int_0^{\xi} \frac{2}{3} \pi \eta^3 \cdot 2\pi \xi \{ \dot{r}_a^*(\xi) + \dot{r}_a^*(\eta) \} \psi(\eta; N^*) N^*(\eta) d\eta = 2\pi \xi^2 \{ \dot{r}_a^*(\xi) - \dot{r}_e^*(\xi) \}, \quad (18)$$

where mr is replaced by ξ and the relation $(1/m)r_e(\xi/m) = \dot{r}_e(\xi)$ is used. In order that equation (17) does not include t but is dependent only on ξ ,

$$m^2 \frac{dm}{dt} = -Cm^5. \quad (19)$$

Integrating this equation by using the condition in equation (15) yields

$$m = \left(\frac{t_0}{t}\right)^{1/2}. \quad (20)$$

In this place the constant C is evaluated from that the process starts at time $t = 0$ as

$$C = \frac{1}{2t_0}. \quad (21)$$

Then equation (17) becomes

$$\frac{1}{2t_0} \{ 3N^*(\xi) + \xi \frac{dN^*}{d\xi} \} = \frac{dN^* \dot{r}_a^*}{d\xi} + \int_{\xi}^{\infty} 2\pi\eta \{ \dot{r}_a^*(\xi) + \dot{r}_a^*(\eta) \} \psi(\xi; N^*) N^*(\xi) N^*(\eta) d\eta. \quad (22)$$

Equations (18) and (22) determine the similar solutions $N^*(\xi)$ and $\dot{r}_a^*(\xi)$.

APPENDIX B

Suppose that $N(r) = Ar^{-n}$ in the equilibrium region of small drops which extends over an interval $[r_1, r_2]$. From the assumption that $\alpha \rightarrow 1$ as $r_1 \rightarrow 0$, we have

$$\int_0^r \pi \rho^2 \cdot A \rho^{-n} d\rho + \int_r^{R_{\max}} \pi \rho^2 N(\rho) d\rho = 1 \quad (23)$$

for $r_1 < r < r_2$. Then equation (3) can be written as

$$r_E(r) = 2 \int_0^r \pi \rho^2 \cdot A \rho^{-n} d\rho / \left[\int_r^{r_2} 2\pi \rho \cdot A \rho^{-n} d\rho + C \right],$$

where $C = \int_{r_2}^{R_{\max}} 2\pi \rho N(\rho) d\rho$. Here we presume that

$$\frac{5}{2} < n < 3. \quad (24)$$

It follows that

$$r_E(r) = \frac{2\pi A}{3-n} r^{3-n} / \left[\frac{2\pi A}{n-2} \{ r^{-(n-2)} - r_2^{-(n-2)} \} + C \right].$$

Further, if $r \ll r_2$, the term $\{ 2\pi A / (n-2) \} r^{-(n-2)}$ dominates in [], and we get

$$\frac{r_E(r)}{r} = \frac{n-2}{3-n}, \quad (25)$$

as asserted. The presumed condition (24) results from the geometrical requirement: $r_E(r) > r$.

Further, we assume that $\dot{r}_a(r) = Br^{-p}$ in the equilibrium region of small drops. Then, equation (5) can be written with the aid of equations (2), (23), and (25) as

$$\int_{r_1}^r \frac{2}{3} \pi \rho^3 \cdot 2\pi r \{ Br^{-p} + B\rho^{-p} \} \cdot \left(1 - \frac{3-n}{n-2} \right) \frac{\pi A}{3-n} \rho^{3-n} d\rho = 1$$

$$A \rho^{-n} d\rho = 2\pi r^2 \cdot Br^{-p}$$

for $r_1 < r < r_2$. Here, the integration from R_{\min} to r_1 has been neglected on the left-hand side of the foregoing equation, and also the term \dot{r}_e has been neglected as compared with \dot{r}_a on the right-hand side. The foregoing equation reduces to

$$\int_{r_1}^r \frac{2}{3} \left\{ \frac{1}{3-n} - \frac{1}{n-2} \right\}^{-1} (r^{-p} + \rho^{-p}) d\rho = r^{1-p}.$$

The integration by assuming $p < 1$ and $r \gg r_1$ yields

$$\frac{2}{3} \left\{ \frac{1}{3-n} - \frac{1}{n-2} \right\}^{-1} \left\{ 1 + \frac{1}{1-p} \right\} r^{1-p} = r^{1-p}.$$

Therefore, we obtain

$$p = 1 - \left\{ \frac{3}{2} \left(\frac{1}{3-n} - \frac{1}{n-2} \right) - 1 \right\}^{-1},$$

as asserted. From this equation, as n goes from $1 + \sqrt{10}/2 = 2.58$ to 3, p increases monotonously from $-\infty$ to 1, becoming 0 for $n = (7 + \sqrt{13})/4 = 2.65$.

APPENDIX C

As proved in Appendix A, the drop growth rate of the completely similar solution which is valid in the whole drop range under the hypothetical condition $\alpha = \text{const.}$ takes the form in equation (16). This form is attributed in its origin to the term \dot{r}_e in the basic

equation (5). However, this term can be neglected except the microscopic drop range. And we know that, under the real condition (7), the translation of the characteristic curve of the growth rate satisfies the form

$$\dot{r}_a(r, t) = \{m(t)\}^{\rho} \dot{r}_a^{**}(m(t) \cdot r) \quad (26)$$

instead of equation (16). Substituting equations (14) and (26) into the basic equation (4), we have the following relation in place of equation (19), in the manner quite similar to Appendix A.

$$m^2 \frac{dm}{dt} = -C' m^{\rho+4}.$$

This equation leads to the conclusion that the characteristic dimension of the universal distribution for large drop range grows in proportion to $1/m \propto t^{1/(\rho+1)}$, as asserted. At this juncture, we should note that an individual drop, or more precisely a mean radius of drops which had the same size at a certain time, does not grow in proportion to $t^{1/(\rho+1)}$, because its growth is described by

$$dr/dt = \dot{r}_a(r, t).$$

APPENDIX D

Suppose that a pair of $N^{**}(r, t)$ and $\dot{r}_a^{**}(r, t)$ is the solution of the basic equations (4) and (5) under the conditions: $(\lambda/\rho L) \Delta T = 1$, $R_{\max} = R_{\max}^{**}$, $R_{\min} = R_{\min}^{**}$ and $D = D^{**}$. Then, it is easy to prove that a pair of

$$N(r, t) = \frac{1}{m^3} N^{**}\left(\frac{r}{m}, \frac{(\lambda/\rho L) \Delta T}{m^2} t\right)$$

and

$$\dot{r}_a(r, t) = \frac{(\lambda/\rho L) \Delta T}{m} \dot{r}_a^{**}\left(\frac{r}{m}, \frac{(\lambda/\rho L) \Delta T}{m^2} t\right)$$

is the solution of the basic equations for an arbitrary condensing substance and an arbitrary ΔT under the conditions: $R_{\max} = mR_{\max}^{**}$, $R_{\min} = mR_{\min}^{**}$ and $D = mD^{**}$.

ERRATA

An errata on G. Ahmadi, "Heat Conduction in Solids With Random Initial Conditions," published in the Nov. 1974 issue of the JOURNAL OF HEAT TRANSFER, pp. 474-477.

Equation (4) should read:

$$\frac{\partial}{\partial t} R_T(\mathbf{x}_1, \mathbf{x}_2, t) = k[(\nabla_1^2 R_T(\mathbf{x}_1, \mathbf{x}_2, t) + \nabla_2^2 R_T(\mathbf{x}_1, \mathbf{x}_2, t))]$$

Equation (6) should read:

$$\frac{\partial R_T}{\partial t}(\mathbf{x}_1, \mathbf{x}_1 + \mathbf{x}, t) = 2k\nabla^2 R_T(\mathbf{x}_1, \mathbf{x}_1 + \mathbf{x}, t)$$

Equation (11) should read:

$$T|_{x=0} = T|_{x=l} = 0$$

Equation (13) should read:

$$T(x, t) = \frac{2}{l} \sum_{n=1}^{\infty} \sin \frac{n\pi x}{l} \exp \{-kn^2\pi^2 t/l^2\}$$

Fig. 1 should read:

The variation of the mean square temperature with x/l and $\theta = kt/l^2$

N. V. Suryanarayana

Michigan Technological University,
Houghton, Mich.

G. L. Malchow¹

University of Illinois,
Urbana, Ill.

Film Condensation on Inclined Plane Surfaces

An experimental investigation of the effect of reduced gravity forces on film condensation heat transfer rates was carried out. Reduced gravity conditions parallel to the condensing surface were obtained by condensing saturated steam at atmospheric pressure on one surface of a copper block whose inclination to the vertical could be varied giving effective body forces from 0.1g to 1g in several discrete steps. Condensation heat transfer data were higher than predicted by Nusselt's correlation. Such increases in heat transfer are shown to be well correlated by an empirical correlation suggested by Kutateladze.

Nusselt [1]² developed an expression for heat transfer coefficient in film condensation on vertical surfaces and horizontal cylinders, assuming laminar flow of the condensate film. Bromley [2] gave a correction to Nusselt's predictions to account for the subcooling. Rohsenow [3] further improved the results by considering the non-linearity of the temperature distribution but retaining the same flow model. Boundary layer type equations were employed by Sparrow and Gregg [4, 5] and Koh, Sparrow and Hartnett [6]; Chen [7, 8] and Koh [9] used the integral form of the boundary layer equations. All of these improvements confirm the validity of Nusselt's correlations for $Pr > 1$ and $C_p \Delta T / h_{fg} \ll 1$, conditions which are usually satisfied when condensing steam. Variable gravity field was considered by Matin [10], Chato [11] and Dhir and Leinhard [12]. All the foregoing analyses assume laminar film condensation without any surface waves on the condensate film. McAdams [13] has compiled a summary of the conclusions of several experimental studies on film condensation heat transfer and many of these show significant deviation from Nusselt's correlation. Rohsenow, Webber, and Ling [14] and Lee [15] considered the effect of turbulence in the condensate film.

Experimental Apparatus and Procedures

The basic scheme for finding the heat transfer rates under reduced gravity conditions was to condense steam on a flat surface whose inclination to the vertical plane could be varied, giving effective nominal gravitational acceleration parallel to the surface from 0.1g to 1g. Fig. 1 is a schematic of the apparatus used in low gravity studies. One surface of a copper block (12 in. long \times 2.5 in.

wide \times 1 in. thick) mounted in a double walled chamber served as the condensing surface. Steam was generated in an electric boiler fed with distilled water and supplied to the chamber through a pressure regulator so that with the steam at 0.5 psig in the condensing chamber, a superheat of up to 2 deg F was always maintained. A small quantity of steam was continuously vented through a valve at the top of the chamber to prevent accumulation of non-condensibles in the chamber.

A 1 in. thick copper block milled out to provide a passage for the cooling water was attached to the bottom surface of the block providing the condensing surface; all surfaces other than the condensing surface were insulated with 2 layers of $\frac{3}{8}$ in. thick Lexan plas-

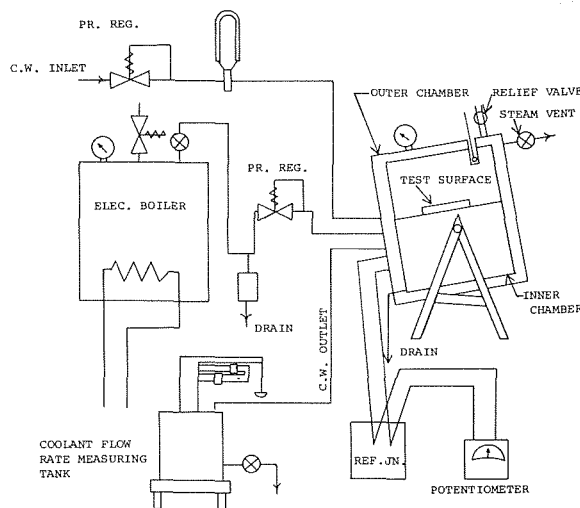


Fig. 1 Schematic of apparatus (low gravity)

¹ The author's affiliation at the time this work was carried out was with Michigan Technological University.

² Numbers in brackets designate References at end of paper.

Contributed by the Heat Transfer Division for publication in the JOURNAL OF HEAT TRANSFER. Manuscript received by the Heat Transfer Division, October 15, 1973. Paper No. 75-HT-DD.

tic. The Lexan insulation was extended $\frac{1}{4}$ in. beyond the condensing surface on all sides except the condensate draining side, ensuring the two-dimensional nature of the condensate flow. Three thermocouple junctions of copper constantan were embedded in the top block, with the junction less than $\frac{1}{16}$ in. below the surface. The cooling water flow rate was computed by measuring the time taken to collect a known quantity of water. The rise in the bulk temperature of the cooling water was measured by thermocouples located at inlet and outlet of the condenser.

The frame on which the condensing surface was mounted could be rotated to obtain reduced gravity conditions parallel to the condensing surface. Six positions of the frame giving nominal gravitational accelerations of 1g, 0.8g, 0.6g, 0.4g, 0.2g, and 0.1g were employed. In any given position of the condenser either cold water at 60 F or warm water, at 130 F was used as the coolant, giving two values of the surface temperature. During the experiments, it was found that care was necessary to ensure that film condensation was the only mode, as, frequently, patches of dropwise condensation or rivulets of the condensate film were observed. Before each series of runs the condensing surface was cleaned with acetone, lightly rubbed with a piece of wet crocus cloth and washed with distilled water. This treatment ensured that the surface was completely wettable and film condensation could be maintained for periods ranging from 1–5 hr. At the end of each series of runs, the surface was visually examined and if there was any evidence of dropwise condensation or rivulets, the entire series was rejected.

At each gravity level 3 sets of data were recorded for two heights of the condensing surface (8 in. and 12 in.) at two temperature levels.

Results and Discussion

The heat transfer rate to the coolant is given by

$$q_e = \dot{m}C_p(T_{co} - T_{ci}) \quad (1)$$

$$T_{co} - T_{ci} = \frac{\Delta E}{(dE/dT)}$$

where

ΔE = the differential thermocouple output between the cooling water inlet and outlet thermocouples

$\frac{dE}{dT}$ = thermocouple output at the average temperature of the coolant/°F

This heat transfer rate is equal to the heat transfer due to con-

densation on the condensing surface plus the heat transfer across the insulation. Heat transfer across the insulation was estimated separately [16] and condensation heat transfer computed.

It is estimated that the uncertainty in ΔT is within 7 percent and that in heat transfer rates is within 6.2 percent. Details of error analysis are given in reference [16]. Three sets of data were taken under each condition; the average deviations in the heat transfer rates from the mean were -1.7 percent, +1.4 percent (with maximum deviations of -4.7 percent, +4.4 percent) and those in ΔT were -1.1 percent, +1.3 percent (with maximum deviations of -2.9 percent, +3.2 percent).

The experimental heat transfer rate was normalized by q_{Nu} , the heat transfer rate given by Nusselt's prediction. The three thermocouples located 4 in. apart in a height of 12 in. indicated different temperatures, the maximum difference being 8 F at low gravity situations. Assuming that the i th thermocouple indicates the average temperature of the surface from a height of Z_{i-} to Z_{i+} from the top of the surface, following Nusselt's development, we have

$$\frac{d\delta^4}{dZ} = \frac{4K\mu\Delta T_i}{a\rho(\rho - \rho_v)h_{fg}'} = C \quad (2)$$

Here δ = thickness of the condensate film. Integrate from Z_{i-} to $Z(Z_{i-} \leq Z \leq Z_{i+})$ and obtain

$$\delta = [C(Z - Z_{i-}) + \delta_{i-}^4]^{1/4} \quad (3)$$

$$q_i = \frac{4}{3} \frac{Kb\Delta T_i}{C} ([C(Z_{i+} - Z_{i-}) + \delta_{i-}^4]^{3/4} - \delta_{i-}^3) \quad (4)$$

$$q_{Nu} = \sum_{i=1}^N q_i \quad (5)$$

$$q_{Nu-1g} = \frac{q_{Nu}}{(a/g)^{1/4}}$$

where N represents the number of thermocouples in the condensing surface. An allowance for the subcooling of the condensate was made by using the modified enthalpy of vaporization given by [3]

$$h_{fg}' = h_{fg} + 0.68C_p\Delta T \quad (6)$$

Fig. 2 is a plot of α versus a/g . Each plotted point represents the average value of α for 12 runs (3 runs under each conditions, 2 surface heights and 2 levels of surface temperature). The vertical line through a plotted point represents the range of values obtained for these 12 runs. From this plot it is seen that experimental values are 50–60 percent higher than predicted by equation (5). Results of

Nomenclature

a = acceleration parallel to the condensing surface, ft/hr²
 $\left(\frac{a}{g} = \sin \theta\right)$
 b = width, ft.
 C_p = specific heat capacity at constant pressure, Btu/lbm °F
 g = standard gravitational acceleration, ft/hr² (4.169×10^8 ft/hr²)
 h_{fg} = enthalpy of vaporization, Btu/lbm
 h_{fg}' = modified enthalpy of vaporization, Btu/lbm
 k = thermal conductivity, Btu/hr ft °F
 \dot{m} = rate of cooling water flow, lbm/hr
 Pr = Prandtl number, dimension-

less
 q_e = heat transfer rate, experimental, Btu/hr
 q_{Nu-1g} = heat transfer rate, Nusselt's correlation, at standard gravity, Btu/hr
 $q_{Nu} = q_{Nu-1g} \left(\frac{a}{g}\right)^{1/4}$
 Re = condensate Reynolds number, $\frac{\Gamma}{\mu}$
 T_s = saturation temperature, °F
 T_w = condensing surface temperature, °F
 T_{ci} = cooling water temperature at inlet, °F
 T_{co} = cooling water temperature at outlet, °F
 $\Delta T = (T_s - T_w)$, °F
 $\Delta T_c = (T_{co} - T_{ci})$, °F

$\alpha = \frac{q_e}{q_{Nu}}$, dimensionless
 $\beta = \frac{q_e}{q_{Nu} 0.8 Re^{0.11}}$, dimensionless
 Γ = condensate mass flow rate per unit width of condensing surface, lbm/hr ft
 $\gamma = \frac{q_e}{q_{Nu-1g} 0.8 Re^{0.11}}$, dimensionless
 δ = condensate film thickness, ft
 θ = angle of inclination of condensing surface with the horizontal plane
 ρ = density, lbm/ft³
 μ = viscosity, lbm/hr ft

Note: All quantities without the subscript v refer to condensate; those that have a subscript v , refer to vapor

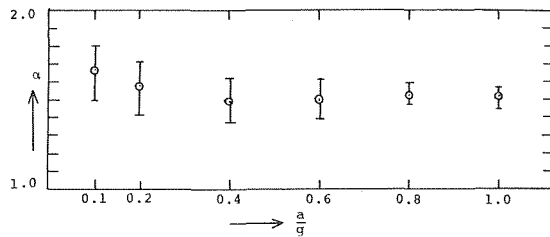


Fig. 2 Condensation heat transfer rate versus a/g

other workers with vertical plates and cylindrical tubes show deviations of 0–70 percent from Nusselt's predictions. In general, those with low condensate Reynolds numbers of up to 50 [17, 22–25] correlate well with Nusselt's equation, experimental heat transfer coefficients being 0–20 percent higher than predicted. Condensation heat transfer data at higher condensate Reynolds numbers are scarce. The data of Burov (as quoted by Fujii and Uehara, reference [26]) show a deviation of up to 20 percent. Compilation of experimental data by McAdams [13] show experimental values up to 70 percent higher than predicted. The data of Raben et al [27] with steam condensing on the outside of a 38 in. high, 1 in. dia tube, for condensate Reynolds number in the range of 100–200, show experimental heat transfer coefficients up to 22 percent higher than predicted, the deviation increasing with increasing Reynolds number. The more recent experimental work by Spencer, et al. [28] on the effect of ripples shows that condensation heat transfer coefficients for Freon 12 are 40–60 percent higher than predicted for Re in the range of 50–100 for 8 in. long, 4 in. dia vertical cylinder. Present data (with Re in the range of 50–135) show good correlation with the results of Spencer [28], but are higher than those of Raben, et al. [27].

Nusselt's predictions were obtained under the assumption of absence of turbulence in the condensate film and a smooth condensate surface without any surface waves. Rohsenow, et al. [14] in their solution for heat transfer rates with a turbulent condensate film, suggest a critical Reynolds number of 450. Much lower values of Re_{cr} , as low as 60, have been used but it is reported by Kutateladze [18] that changing the critical Reynolds number in the range 60–400 has only a slight effect on the average heat transfer rates. In the present study, the maximum value of Re attained was 135 and based on the above discussion, it can be concluded that the probable onset of turbulence alone is not sufficient to explain the much higher heat transfer rates that have been observed.

It is known that for a film flowing down a plane, surface waves occur for some value of Re. In a recent study by Marschall and Lee [19], it has been concluded that for condensation of steam, such waves can be expected at a distance of around 0.01 in. below the top of the surface; this confirms that in most applications such waves are to be expected. Hypothesizing that the effect of such waves is to increase heat transfer rates, an effort has been made to relate such increases to the amplitude of oscillation of these waves [20]. However, as there is no known way of determining the amplitude of these surface waves, empirical relations based on experi-

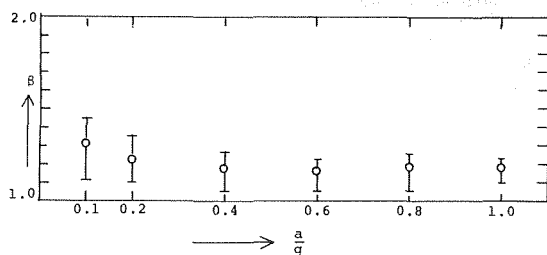


Fig. 3 Condensation heat transfer rate versus a/g

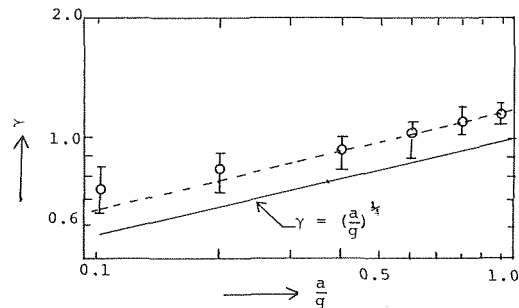


Fig. 4 Effect of a/g on heat transfer rate

mental data have been developed [18, 20]. For film condensation of steam, Kutateladze [18] suggests the following empirical relation:

$$\frac{q_e}{q_{Nu}} = 0.8 Re^{0.11} \quad (7)$$

in the range of Re from 10 to 500. Based on this relation, Fig. 3 is a plot of β versus a/g . This plot shows that experimental data are better correlated by equation (7), the average deviation from the correlation being approximately 19 percent higher but as much as 30 percent higher at $a/g = 0.1$.

Analytical results of interfacial instability [19, 29] show the incipience of surface waves at a relatively low Reynolds number of about 8 even at $\sin\theta = 0.1$, so that the effect of ripples can be expected to be significant for all values of $\sin\theta$ used in the present work. These analyses also show that condensation should have a stabilizing effect with decreasing values of θ . However, the present data show greater departure from predictions by Nusselt's equation at low values of $\sin\theta$. At this stage, no explanations can be given for this apparent contradiction between analysis and experimental data.

To show the effect of gravitational force, Fig. 4 is a plot γ versus a/g . From this plot it can be concluded that condensation heat transfer rates vary with $1/4$ power of the gravitational force.

From Figs. 2, 3, and 4, it is seen that the deviation of experimental values from Nusselt's prediction tends to be higher at small angles of inclination of the condensing surface (corresponding to $a/g = 0.1$) than at larger angles of inclination. At very small angles of inclination, the effect of hydrostatic head should become more significant; in the limiting case of a horizontal plate, it is only the hydrostatic head that maintains the flow of the condensate. The ratio of the effect of hydrostatic head to that due to body force parallel to the condensing surface is given by $[\rho g \cos\theta (d\delta/dZ)]/\rho g \sin\theta$ and an estimate of this ratio (with $d\delta/dZ$ calculated from Nusselt's analysis) indicates that the effect of hydrostatic head is confined to a very small distance near the leading edge and is not significant down to values of $a/g = 0.1$.

An estimate of condensation heat transfer rates on horizontal surfaces was also made using the analysis of Leppert and Nimmo [21] and the upper limits of such heat transfer rates are only 18 percent to 20 percent of those obtained at $a/g = 0.1$ at the same average condensing surface temperatures. It, therefore, appears reasonable to conclude that the effect of hydrostatic head is small and that Nusselt type analysis is a reasonable approximation in the present experiments.

Fig. 5 is a plot of surface temperature versus a/g , the average ΔT being the arithmetic average of the ΔT indicated by the surface thermocouples. As can be expected, because of higher heat transfer coefficients with increasing a/g , ΔT decreases with an increase in a/g , leading to a higher surface temperature. For a given coolant temperature and flow rate in a condenser of this type, such an increase in surface temperature should lead to a higher heat transfer rate. This is confirmed in Fig. 6, showing a plot of q_e versus a/g .

The support of the National Science Foundation under Grant GK-27818 for this work, is gratefully acknowledged. The authors

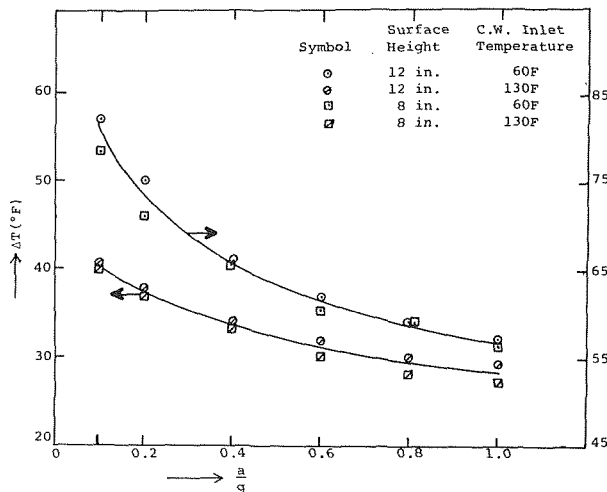


Fig. 5 Condensing surface temperature versus a/g

also wish to thank Messrs. Jim Bowes and Gary Dawson, Graduate Students, and Ernest Gasperich and Alfred Hendrickson, Machinists, for their assistance in various phases of this study.

References

- 1 Kreith, F., "Principles of Heat Transfer," *International Text Book*, 1973.
- 2 Bromley, L. A., "Effect of Heat Capacity of Condensate," *Ind. Eng. Chem.*, Vol. 44, 1952, pp. 2966-2968.
- 3 Rohsenow, W. M., "Heat Transfer and Temperature Distribution in Laminar Film Condensation," *TRANS. ASME* Vol. 78, 1956, pp. 1645-1648.
- 4 Sparrow, E. M., and Gregg, J. L., "A Boundary Layer Treatment of Laminar Film Condensation," *JOURNAL OF HEAT TRANSFER*, *TRANS. ASME*, Series C, Vol. 81, 1959, pp. 13-18.
- 5 Sparrow, E. M., and Gregg, J. L., "Laminar Condensation Heat Transfer on a Horizontal Cylinder," *JOURNAL OF HEAT TRANSFER*, *TRANS. ASME*, Series C, Vol. 81, 1959, pp. 291-296.
- 6 Chen, Michael Ming, "An Analytical Study of Laminar Film Condensation: Part 1—Flat Plates," *JOURNAL OF HEAT TRANSFER*, *TRANS. ASME*, Series C, Vol. 83, 1961, pp. 48-54.
- 7 Chen, Michael Ming, "An Analytical Study of Laminar Film Condensation: Part 2—Single and Multiple Horizontal Tubes," *JOURNAL OF HEAT TRANSFER*, *TRANS. ASME*, Series C, Vol. 83, 1961, pp. 55-60.
- 8 Koh, J. C. Y., "An Integral Treatment of Two-Phase Boundary Layer in Film Condensation," *JOURNAL OF HEAT TRANSFER*, *TRANS. ASME*, Series C, Vol. 83, 1961, pp. 359-362.
- 9 Koh, J. C. Y., Sparrow, E. M., and Hartnett, J. P., "The Two Phase Boundary Layer in Laminar Film Condensation," *International Journal of Heat and Mass Transfer*, Vol. 2, 1961, pp. 69-82.
- 10 Matin, Shaik A., "A Similarity Solution for the Condensate Film on a Vertical Flat Plate in Presence of Variable Gravity Field," *ASME Paper No. 65-AV-42*.
- 11 Chato, J. C., "Condensation in a Variable Acceleration Field and the Condensing Thermosyphon," *Journal of Engineering for Power*, *TRANS. ASME*, Series A, Vol. 87, 1965, pp. 355-360.
- 12 Dhir, Vijay and Lienhard, John, "Laminar Film Condensation on Plane and Axisymmetric Bodies in Non-Uniform Gravity," *JOURNAL OF HEAT TRANSFER*, *TRANS. ASME*, Series C, Vol. 93, 1971, pp. 97-100.
- 13 McAdams, W. H., *Heat Transmission*, McGraw Hill, New York, 3rd ed.
- 14 Rohsenow, W. M., Webber, J. H., and Ling, A. T., "Effect of Vapor Velocity on Laminar and Turbulent Film Condensation," *TRANS. ASME* Vol. 78 1956, pp. 1637-1643.
- 15 Lee, John, "Turbulent Film Condensation," *A.I.Ch.E. Journal*, Vol. 10, 1964, pp. 540-544.
- 16 Suryanarayana, N. V., "Condensation Heat Transfer Under Low and High Gravity Conditions," Report to NSF, Contract No. GK-27818, Michigan Technological University, Houghton, Mich.
- 17 Mills, A. F., and Seban, R. A., "The Condensation Coefficient of Water," *International Journal of Heat and Mass Transfer*, Vol. 10, 1967, pp. 1815-1827.

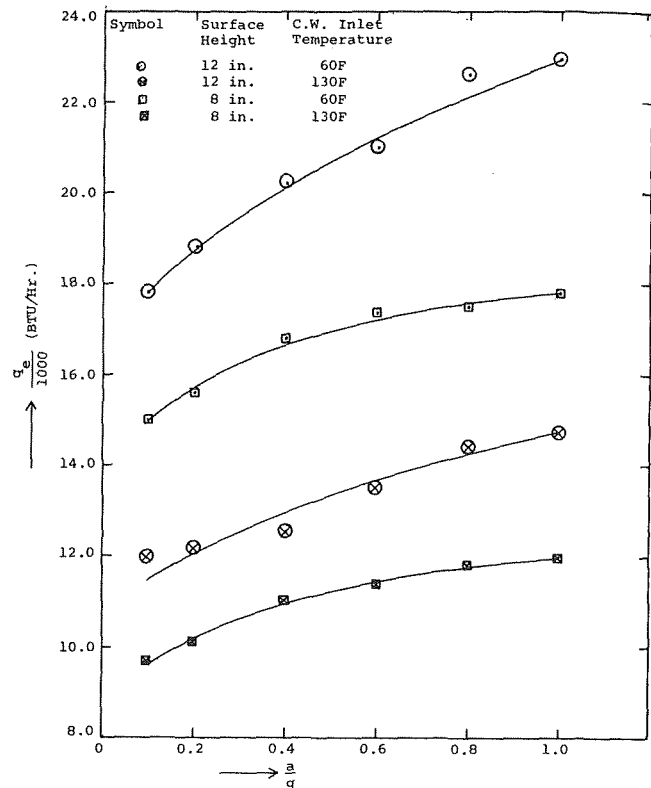


Fig. 6 Heat transfer rate versus a/g

- 18 Kutateladze, S. S., *Fundamentals of Heat Transfer*, Academic Press Inc., 1963.
- 19 Marschall, E., and Lee, C. Y., "Stability Characteristics of Condensate Films," *Wärme-und Stoffübertragung*, Vol. 1, 1973, pp. 32-37.
- 20 Suryanarayana, N. V., and Merte (Jr.), H., "Film Boiling on Vertical Surfaces," *JOURNAL OF HEAT TRANSFER*, *TRANS. ASME*, Series C, Vol. 94, 1972, pp. 377-384.
- 21 Leppert, G., and Nimmo, B., "Laminar Film Condensation on Surfaces Normal to Body or Inertial Forces," *JOURNAL OF HEAT TRANSFER*, *TRANS. ASME*, Series C, Vol. 90, 1968, pp. 178-179.
- 22 Tanner, D. W., Pope, D., Potter, C. J., and West, D., "Heat Transfer in Dropwise Condensation at Low Steam Pressures in the Absence and Presence of Non-Condensable Gases," *International Journal of Heat and Mass Transfer*, Vol. 11, 1968, pp. 181-190.
- 23 Slegers, L., and Seban, R. A., "Laminar Film Condensation of Steam Containing Small Concentrations of Air," *International Journal of Heat and Mass Transfer*, Vol. 13, 1970, pp. 1941-1947.
- 24 Al-Diwani, H. K., and Rose, J. W., "Free Convection Film Condensation of Steam in the Presence of Non-Condensing Gases," *International Journal of Heat and Mass Transfer*, Vol. 16, 1973, pp. 1359-1369.
- 25 Hampson, as quoted in reference [23].
- 26 Tetsu Fujii and Haruo Uehara, "Laminar Filmwise Condensation on a Vertical Surface," *International Journal of Heat and Mass Transfer*, Vol. 15, 1972, pp. 217-233.
- 27 Raban, I. A., Commerford, George, and Dietert, Robert, "An Investigation of the Use of Acoustic Vibrations to Improve Heat Transfer Rates and Reduce Scaling in Distillation Units Used for Saline Water Conversion," Research and Development Report No. 49, Office of Saline Water, U.S. Department of the Interior, Mar. 1961.
- 28 Spencer, Donald L., Chang, Ki Il, and Moy, Han Chuan, "Experimental Investigation of Stability Effects in Laminar Film Condensation on a Vertical Cylinder," *Proceedings Fourth International Heat Transfer Conference*, Paris, Vol. VI, CS 2.3, 1970.
- 29 Bankoff, George S., "Stability of Liquid Flow Down a Heated Inclined Plate," *International Journal of Heat and Mass Transfer*, Vol. 14, 1971, pp. 377-385.

U. Narusawa
Research Associate.

G. S. Springer
Professor.

Department of Mechanical Engineering,
The University of Michigan,
Ann Arbor, Mich.

Measurement of the Condensation Coefficient of Mercury by a Molecular Beam Method

The condensation coefficient of mercury was determined by measuring the number flux of a mercury vapor beam incident on, and reflected from, a liquid mercury surface. For a clean surface the condensation coefficient was found to be between 0.65 and 1.

1 Introduction

In recent years, many experiments have been performed to determine the condensation and evaporation coefficients (σ) of liquid metal vapors. The available data, however, are scattered over a wide range. The reported values of these coefficients vary from as low as 0.01 to as high as ~ 1.0 . Although such scatter in the data may have been caused by several effects, it is generally recognized that the experimental results were most likely affected by one or more of the following factors: insufficient knowledge of the surface temperature, presence of noncondensable gases in the system, and impurities on the liquid surface. A slight inaccuracy in the liquid surface temperature may introduce a several hundred percent error in σ [1, 2].¹ One or two percent noncondensable gas in the vapor may change the value of σ by an order of magnitude [3, 4]. Impurities on the surface may result in a five to ten-fold decrease in σ [5].

The aim of this investigation was to measure the condensation coefficient of mercury in a manner which requires neither an accurate knowledge of the liquid surface temperature nor the elimination of all noncondensable gases. A molecular beam apparatus was employed in the experiments in which the number of mercury vapor molecules impinging upon, and reflected from, a liquid mercury surface was measured. From a knowledge of these molecular fluxes condensation coefficients could be determined.

2 Experimental Apparatus

The vacuum chamber (110 cm high and 90 cm dia, Fig. 1) was constructed of stainless steel, and was equipped with appropriate valves, sight windows, and feedthroughs. The chamber was con-

nected to two diffusion and to two mechanical pumps. Cold traps, cooled by liquid nitrogen, were installed between the vacuum chamber and the diffusion pumps to collect harmful mercury vapors. A liquid nitrogen trap (30 cm dia and 40 cm high) was also attached to the top of the vacuum chamber to provide an additional pumping surface. The pressure inside the chamber was measured either by a McLeod gauge or by an ionization gauge.

The molecular-beam source had two parts, an oven and a molec-

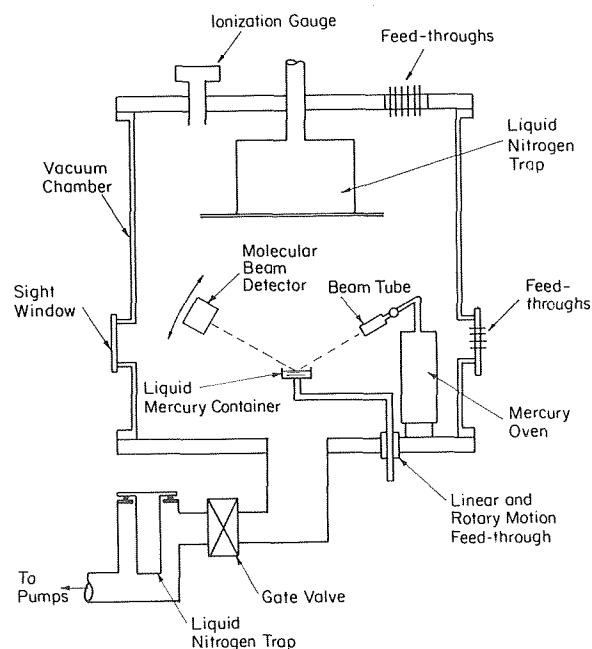


Fig. 1 Schematic of the vacuum chamber

¹ Numbers in brackets designate References at end of paper.

Contributed by the Heat Transfer Division for publication in the JOURNAL OF HEAT TRANSFER. Manuscript received by the Heat Transfer Division June 14, 1974. Paper No. 75-HT-Q.

ular beam tube (Fig. 2). The oven was an 8 cm dia and 17 cm long stainless steel cylindrical container surrounded by heating elements. The heating elements were controlled by a Variac located outside the vacuum chamber. The temperature of the oven was measured by thermocouples embedded into the oven. In order for the mercury vapor to form a molecular beam, the exit from the oven was made of a 0.2 cm ID and 7 cm long stainless steel tube. A valve, controlled from the outside of the vacuum chamber, was installed between the oven and the tube. The temperature of the tube and the valve was also controlled by heating wires and was monitored by thermocouples. The tube was placed concentrically inside a 2.5 cm dia and 8 cm long cylinder which had a 0.3 cm dia hole at its end. This hole was aligned with the tube exit so that only the center "core" of the molecules coming out of the tube entered the vacuum system directly. The molecules retained inside the cylinder were removed by a separate pumping system connected to the cylinder. The molecular beam streaming out of the cylinder was interrupted by a chopper operating at a frequency of 800 cps.

The molecular beam detector consisted of an ionizing box, an electron gun, an ion pullout lens, and an electron multiplier (Figs. 3 and 4). The ionizing box was covered on two opposite sides with fine mesh grids (2 cm \times 2 cm) which transmitted the molecular beam. An electron gun [6], comprised of a tungsten filament and electron accelerating plates, was mounted on a third vertical side. A "sheet" of electrons, generated by the tungsten filament and accelerated by the plates, passed through the molecular beam. Collisions between the electrons and the molecules in the beam produced ions. These ions were "focused" by an ion pullout lens located on the top of the box. The ion pullout lens was made of three closely spaced metal sheets with holes in their centers [6]. Different voltages were applied on each sheet, with the highest voltage on the bottom plate and the lowest on the top plate. The focused ions were then fed into an electron multiplier placed at the lens exit. Bombardment of the ions on the dinode surface of the electron multiplier caused emission of electrons. The numbers of electrons emitted by the electron multiplier was proportional to the number of molecules in the molecular beam.

In addition to the number density of the beam, the output signal from the electron multiplier depended also on the following factors: (a) the intensity of the electrons coming out of the electron gun, (b) the effectiveness of the ion-pullout lens, and (c) the gain of the electron multiplier. The intensity of the electrons was controlled by the filament temperature and by the voltages of the electron accelerating plates. The effectiveness of the ion pullout lens was regulated by changing the voltages applied to the lens

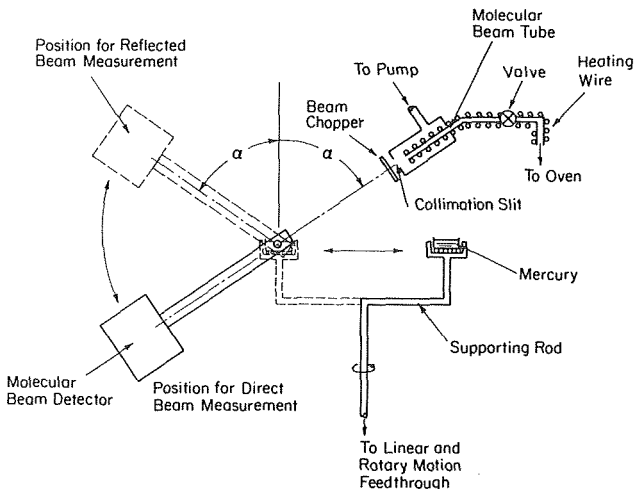


Fig. 2 Schematic of the molecular beam apparatus

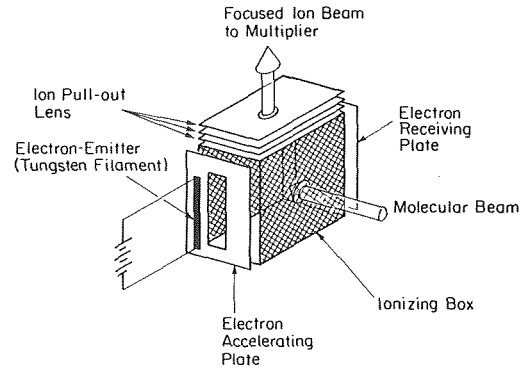


Fig. 3 Schematic of the molecular beam detector

plates. The electron multiplier gain was varied by changing the potential difference between the inlet and outlet of the dinode surfaces.

The signal from the electron multiplier was fed into a signal tuned amplifier. The output signal of this amplifier provided a measure of the number density in the molecular beam.

The entire molecular beam detector was mounted on a frame connected to a linear-rotary motion feedthrough. The molecular beam detector could be rotated with its center of rotation corresponding to the middle of the liquid mercury target (Figs. 2 and 5). The distance between the beam tube and the collimation slit was $\frac{1}{2}$ cm, between the collimation slit and the chopper was $1\frac{1}{2}$ cm, from the chopper to the ionizing box 13 cm, from the chopper to the liquid mercury surface 8 cm, and from the liquid mercury surface to the ionizing 10 cm. The angles θ between the vertical direction and both the beam tube and the molecular beam detector were 55 deg (Fig. 5).

The liquid mercury target was made of stainless steel (3.0 cm long, 1.5 cm wide, and $\frac{1}{2}$ cm deep) with heating elements and a thermocouple attached to its bottom (Figs. 1 and 2). Note that the thermocouple measured the temperature at the bottom of the container and not the surface temperature of the liquid. As will be shown in Section 4, an accurate knowledge of the surface temperature was not needed in the experiments. Linear and rotary motion feedthroughs connected to the container made it possible to move the container in or out of the path of the molecular beam.

3 Experimental Procedure

The vacuum chamber was evacuated to about 2×10^{-6} mmHg,

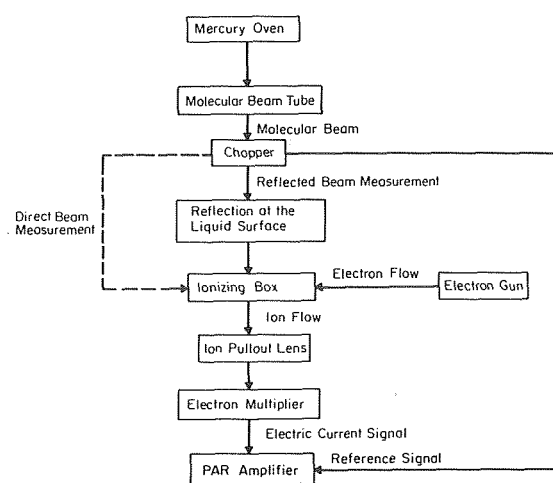


Fig. 4 The molecular beam detection system

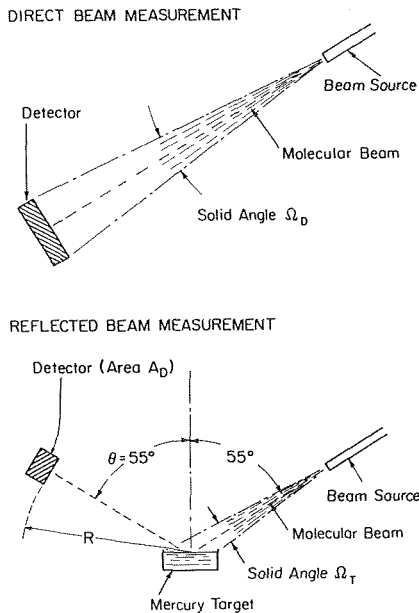


Fig. 5 Position of the molecular beam detector during "direct beam" and "reflected beam" measurements

the liquid mercury oven was heated, and mercury vapor was generated. When the desired temperature inside the oven was attained the chopper was set to operation, the molecular beam detector was energized, the valve between the oven and the beam tube was opened, and the molecular beam was directed toward the ionizing box of the beam detector. The Variacs controlling the heaters, and the voltage power supplies controlling the molecular beam detector were then adjusted until the best output signal (in terms of signal magnitude and noise level) was attained on the meter of the signal tuned amplifier. After this optimization, the beam detector was aligned with the beam and the output signal from the amplifier was recorded in the absence of the liquid container ("direct measurement," Fig. 5). Then, the mercury container was moved into its proper position (i.e., where the mercury surface intercepted the molecular beam), and the molecular beam detector was rotated so that a fraction of the molecules reflected from the liquid mercury impinged on the ionizing box ("reflected beam measurement," Figs. 2 and 5). The output signal from the signal tuned amplifier was then again recorded.

Triple distilled mercury was used in the experiments. The condition of the mercury in the container was checked by application of a light beam on the surface. Throughout the tests the surface remained mirror-like and (at least to the extent of this criterion) "uncontaminated."

4 Results and Discussions

The condensation coefficient is defined as

$$\sigma_c \equiv \frac{N_i - N_R}{N_i} \quad (1)$$

where N_i is the number of molecules impinging upon the liquid surface and N_R is the number of molecules reflected from the surface (per unit time). In terms of the signal output of the signal tuned amplifier, equation (1) may be written as (see Appendix)

$$\sigma_c \equiv 1 - \beta \frac{S_r}{S_D} \quad (2)$$

Where S_D is the signal during "direct" measurements (Fig. 5) and S_r is the signal when the molecular beam is reflected from the liquid surface. β is a constant. If all the molecules are reflected specu-

larly β is unity, if the reflection from the surface is completely diffuse β is 52.7 (see Appendix, Equations (A.6), (A.8)).

The intensity of the molecular beam issuing from the source (i.e., the signal during direct measurement, S_D) depends on the temperature of the mercury oven. The measured S_D values as a function of this temperature are shown in Fig. 6. The intensity of the beam reflected from the mercury surface (i.e., the signal during reflected beam measurements S_r) may depend on the oven temperature, on the temperature of the liquid mercury and on the condition of the surface.

When the surface was clean, reflected beam measurements were performed at an oven temperature of 120°C. At lower oven temperatures the signals, produced by the reflected molecules, were too weak to detect. The liquid mercury temperature was varied between 20–40°C. In this range the target temperature did not appear to have a measurable effect on the output signal and, consequently, on the condensation coefficient.

During these measurements the output signal fluctuated by about ± 0.01 mV, which was the smallest unit on the meter. These fluctuations were due to (a) unavoidable noise in the signal, and (b) fluctuation of the angle of the reflected beam caused by slight vibration of the liquid surface. Nevertheless, the output signal S_r never exceeded 0.03 mV. The highest value of S_r yields the lowest value of σ_c . Therefore, 0.03 mV was used in calculating σ_c . Accordingly, from equation (2), the condensation coefficient is 0.65 for diffuse reflection and ~ 1.0 for specular reflection. Since diffuse and specular reflections give the lower and upper limits of σ_c , the condensation coefficient is in the range 0.65–1.0. The value of σ_c cannot be determined more accurately because of the fluctuations in the output signal and lack of knowledge of the precise angular distribution of the reflected molecules.

A summary of the available condensation coefficient values is given in Table 2. As can be seen, the condensation coefficient obtained in this investigation generally agrees with the σ values reported in the literature. The lower σ values reported by Sukhatme and Rohsenow [7], and by Misra and Bonilla [8] may have been due to surface contamination. This conclusion is supported by the data of Adt, Hatsopoulos, and Bornhorst [5], which indicate that surface contamination reduces the value of σ significantly.

It is worth noting that the magnitude of the condensation coefficient resulting from the molecular beam experiment is of the same order as obtained in more "conventional" condensation and evapo-

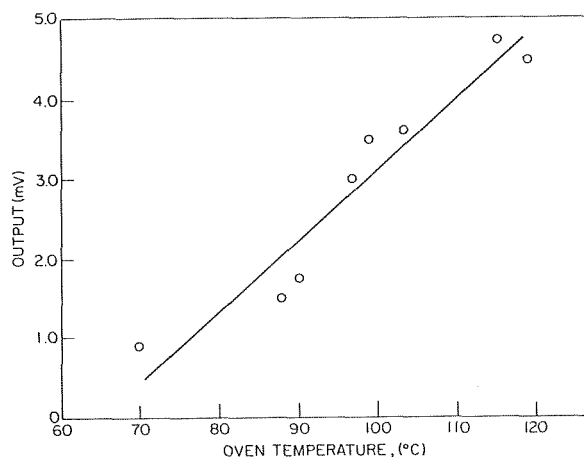


Fig. 6 Results of the direct-beam measurements—output signal versus oven temperature

Table 1 The results of reflected beam measurements

Surface Condition	Oven Temperature (°C)	Target Temperature (°C)	Output Signal (mV)		$(\sigma_c)_{\text{diff}}$	$(\sigma_c)_{\text{spec}}$
			Reflected Beam S_r	Direct Beam S_D		
Clean	120	20	< 0.03	4.50	> 0.65	~1.0
		30	< 0.03	4.50	> 0.65	~1.0
		40	< 0.03	4.50	> 0.65	~1.0

ration experiments. On this basis, it appears that the collimated nature of the beam (as opposed to the "random" impact of the vapor molecules in condensation experiments) does not affect the value of σ .

Acknowledgments

This work was supported by the National Science Foundation under grant number GK 33197.

References

- 1 Wilcox, S. J., and Rohsenow, W. M., "Film Condensation of Potassium Using Copper Condensing Block for Precise Wall Temperature Measurement," JOURNAL OF HEAT TRANSFER, TRANS. ASME, Series C, Vol. 92, 1970, pp. 359-371.
- 2 Meyrial, P. M., Morin, N. M., Wilcox, S. J., and Rohsenow, W. M., "Effect of Precision of Measurement on Reported Condensation Coefficients for Liquid Metals—Including Condensation Data on a Horizontal Surface," Proceedings of the 4th International Heat Transfer Conference, Vol. VI, Paper CS1.1, 1970.
- 3 Turner, R. H., Mills, A. F., and Denny, V. E., "The Effect of Noncondensable Gas on Laminar Film Condensation of Liquid Metals," ASME Paper No. 72-WA/HT-9.
- 4 Minkowycz, W. J., and Sparrow, E. M., "Condensation Heat Transfer in the Presence of Noncondensables, Interfacial Resistance, Superheating, Variable Properties and Diffusion," International Journal of Heat and Mass Transfer, Vol. 9, 1966, pp. 1125-1144.
- 5 Adt, R. R. Jr., Hatsopoulos, G. N., and Bornhorst, W. J., "A Study of the Liquid-Vapor Phase Change of Mercury Based on Irreversible Thermodynamics," JOURNAL OF HEAT TRANSFER, TRANS. ASME, Series C, Vol. 94, 1972, pp. 257-261.
- 6 Pierce, J. R., Theory and Design of Electron Beams, Van Nostrand, Princeton, 1949.

- 7 Sukhatme, S. P., and Rohsenow, W. M., "Heat Transfer During Film Condensation of a Liquid Metal Vapor," JOURNAL OF HEAT TRANSFER, TRANS. ASME, Series C, Vol. 88, 1966, pp. 19-29.
- 8 Misra, B., and Bonilla, C. F., "Heat Transfer in the Condensation of Metal Vapors, Mercury and Sodium up to Atmospheric Pressure," Chem. Engr. Prog. Sym., No. 18, Vol. 52, 1956, pp. 7-21.
- 9 Ivanovskii, M. N., Sorokin, V. P., and Tchulkov, B. A., "Heat and Mass Transfer at Condensation of Metal Vapors in Tubes," Proceedings of the 4th International Heat Transfer Conference, Vol. VI, Paper CS1.5, 1970.
- 10 Wylie, K. F., and Brodkey, R. S., "Transport Phenomena at the Liquid-Vapor Interface of Mercury Using a Radioactive Tracer," International Symposium on Two-Phase Systems, Israel, Paper 1.1, 1971.
- 11 Scott, P. B., "Molecular Beam Velocity Distribution Measurements," M. I. T. Fluid Dynamics Research Laboratory Report No. 65-1, 1965.
- 12 Loeb, L. B., The Kinetic Theory of Gases, Dover, 1961.
- 13 Gebhardt, B., Heat Transfer, McGraw-Hill, New York, 1971.

APPENDIX

Derivation of Equation (2). The condensation coefficient is defined as

$$\sigma_c \equiv \frac{N_i - N_R}{N_i} \tag{A.1}$$

where N_i and N_R are the total number of molecules impinging upon and reflected from the liquid surface per unit time. We assume that the molecules leaving the beam tube follow the cosine distribution law. Then, the number of molecules incident on the target per unit time is

$$N_i = N_D \frac{\Omega_T}{\Omega_D} \tag{A.2}$$

where N_D is the number of molecules arriving per unit time at the detector during "direct beam measurements," $\Omega_D (=0.01)$ is the solid angle subtended by the detector (Fig. 5) and $\Omega_T (=0.026)$ is the solid angle subtended by the target (Fig. 5).

If all molecules were specularly reflected from the target then the number of molecules intercepted per unit time by the detector during reflected beam measurements would be

$$N_r = N_R \frac{\Omega_D}{\Omega_T} \tag{A.3}$$

Equations (A.2) and (A.3) and (A.1) yield

$$(\sigma_c)_{\text{spec}} = 1 - \frac{N_r}{N_D} \tag{A.4}$$

The signal output of the molecular beam detector, S , depends on the density of the molecular beam N , on the efficiencies of the ionizing box, η_i , the ion pullout lens, η_L , and the electron multiplier, η_e , and on the electron multiplier gain G [11, 12]. Assuming that η_i , η_L , and η_e are independent of N and keeping G constant, S is directly proportional to N [11, 12], i.e.,

$$\frac{S_r}{S_D} = \frac{N_r}{N_D} \tag{A.5}$$

Equations (A.4) and (A.5) give

$$(\sigma_c)_{\text{spec}} = 1 - \frac{S_r}{S_D} \tag{A.6}$$

Table 2 Summary of reported values of the condensation coefficient of mercury

Investigators	Surface Condition	Experiment	
Present investigation	0.65 ~ 1.0	clean	horizontal surface (molecular-beam method)
Adt, Hatsopoulos & Bornhorst (1972)	0.9 0.4	clean contaminated	evaporation from a horizontal surface (mass and heat transfer measurements)
Wylie & Brodkey (1971)	0.61	clean	condensation on a horizontal flowing liquid (radioactive tracer method)
Misra & Bonilla (1956)	0.02 ~ 0.61	unspecified*	condensation on a vertical cylinder (heat transfer measurement)
Sukhatme & Rohsenow (1966)	0.365 ~ 0.605	unspecified*	condensation on a vertical cylinder (heat transfer measurement)
Ivanovskii, Sorokin, & Tchulkov (1970)	0.71 ~ 1.0	unspecified	condensation on a horizontal surface (heat transfer measurement)

* surface is likely to be clean because it is continuously replenished.

If all molecules were reflected diffusely then the number of molecules intercepted per unit time by the detector located at $\theta = 55^\circ$ would be [13]

$$N_r = N_R \frac{A_D \cos \theta}{\pi R^2} \quad (\text{A.7})$$

where $A_D (=4 \text{ cm}^2)$ is the area of the detector and $R (=10 \text{ cm})$ is the

distance from the detector to the target (Fig. 5). Substituting equations (A.2) and (A.7) into equation (A.1) and using the relationship given by equation (A.5) we obtain

$$(\sigma_c)_{\text{diff}} = 1 - \frac{\pi R^2}{A_D \cos \theta} \frac{\Omega_D}{\Omega_T} \frac{S_r}{S_D} = 1 - 52.7 \frac{S_r}{S_D} \quad (\text{A.8})$$

C. M. Voutsinos
Senior Mechanical Engineer,
Canatom Limited, Montreal, Canada

R. L. Judd
Assoc. Professor,
McMaster University,
Hamilton, Canada

Laser Interferometric Investigation of the Microlayer Evaporation Phenomenon

An experimental investigation is presented in which the growth and evaporation of the microlayer underlying a bubble forming on a glass heater surface has been studied using laser interferometry and high speed photography. The results presented for a single bubble indicate that the microlayer thickness is of the order of 5 μm . Subsequent analysis of these results confirms that the microlayer evaporation phenomenon is a significant heat transfer mechanism, representing approximately 25 percent of the total nucleate boiling heat transfer rate for the conditions investigated.

Introduction

The role of the microlayer evaporation phenomenon, in which energy is transferred from a nucleate boiling heat transfer surface by the evaporation of a thin layer of liquid at the base of the bubbles has been the subject of considerable investigation for some years. Moore and Mesler [1]¹ were the first to obtain indirect evidence substantiating the existence of the microlayer when they interpreted rapid fluctuations in the temperature of a surface on which nucleate boiling was occurring as indication of the evaporation of a thin liquid layer underlying the bubbles. Confirmation of this interpretation was provided by Hendricks and Sharp [2] who conducted a combined photographic/thermometric investigation in which it was shown that decreasing surface temperature correlated with vapor bubble growth while increasing surface temperature occurred after vapor bubble departure. In this way, it was demonstrated that the temperature fluctuations observed by Moore and Mesler were inconsistent with convective cooling resulting from flow currents induced by the growth and departure or collapse of the bubbles.

Direct evidence of the existence of the microlayer was provided by Sharp [3] and Hospeti and Mesler [4]. Using interferometric techniques, the former investigator was able to observe the evaporation and dryout of a thin film of liquid underlying each bubble while the latter investigators were able to conclude that a microlayer had formed by investigating the deposition of material suspended in solution in the vicinity of each nucleation site as a result of evaporation and dryout of the liquid film. Cooper and Lloyd [5] performed a thermometric investigation in which a bubble was ini-

tiated at a predetermined location and caused to grow over an array of surface mounted resistance thermometers which enabled the temporal variation in temperature at the interface between surface and microlayer to be determined. From an analysis of the local enthalpy extraction at the location of each of the resistance thermometers, Cooper and Lloyd were able to deduce that the initial microlayer thickness $\delta_0(r)$, the thickness prior to evaporation, was the order of 10 μm for toluene and isopropyl alcohol boiling on a glass surface. Jawurek [6] performed a photographic investigation in which the interference patterns formed by the destructive cancellation of the light reflected from the interface between the microlayer and the vapor within the bubble with the light reflected from the interface between the glass surface and the microlayer beneath the bubble, were analyzed. In this way, Jawurek determined that instantaneous microlayer thickness $\delta(r,t)$ for methanol boiling on a glass surface was less than 1 μm . Foltz and Mesler [7] studied the formation of bubbles in water at naturally occurring nucleation sites on a Pyrex glass heater surface. Using the transient temperature response of a single surface mounted resistance thermometer in conjunction with the assumption of uniform microlayer thickness, these authors deduced that the microlayer thickness ranged from 3.3 μm to 9.4 μm , but were unable to correlate the thickness with either of the system parameters saturation pressure or initial surface temperature.

In a recent paper, Judd [8] reviewed the experimental microlayer thickness investigations of Cooper and Lloyd [5] and Jawurek [6] and compared the results with his own. The latter results had been obtained from an interferometric investigation of dichloromethane boiling on a glass surface, very similar to that undertaken by Jawurek, and appeared to be in better agreement with the results reported by Jawurek than with the results reported by Cooper and Lloyd. It is now known that these results were not correct and that the microlayer is considerably thicker than previously thought; failure of the optical filter to properly isolate the spectral lines in the range from 0.5770 μm to 0.5791 μm from the re-

¹ Numbers in brackets designate References at end of paper.

Contributed by the Heat Transfer Division for publication in the JOURNAL OF HEAT TRANSFER. Manuscript received by the Heat Transfer Division May 30, 1974. Paper No. 75-HT-T.

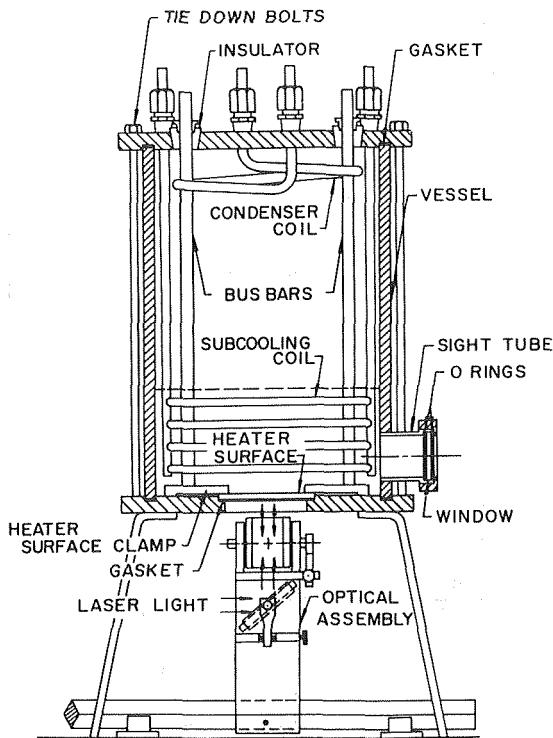


Fig. 1 Test assembly

remainder of the spectrum led to the formation of indistinct fringes which resulted in erroneous determination of the fringe orders. As the result of an improvement in spectral purity of the source of illumination used in the interferometer, many more fringes were observed in the microlayer underlying the bubbles than had been observed previously for the same fluid/surface combination under similar test conditions. The purpose of this paper is to describe the modified experimental investigation and to present some results concerning the contribution of microlayer evaporation heat transfer to the nucleate boiling heat transfer process.

Experimental Investigation

Similar to the previous investigation, dichloromethane (methylene chloride) was boiled on a borosilicate glass heater surface coated with a half wavelength thickness of stannic oxide which conducted electric current and generated heat causing the liquid to boil. The glass heater surface, the test vessel, and associated equipment are depicted in Fig. 1. The interferometer used in the previous investigation was modified to accept a SPECTRA PHYSICS Model 125A 50 mW Helium Neon laser ($\lambda = 0.6328 \mu\text{m}$) as the

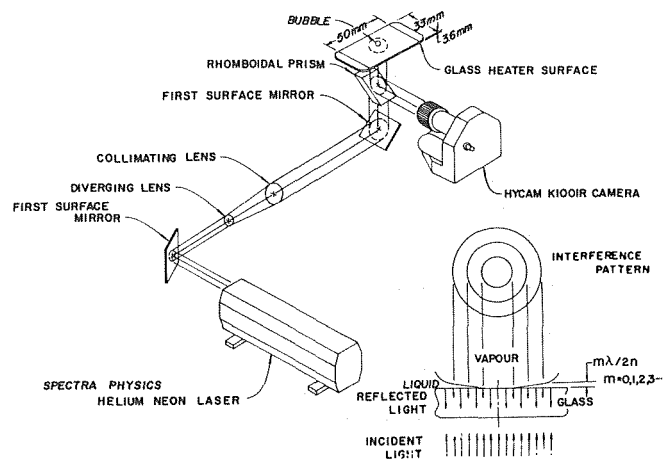


Fig. 2 Schematic representation of Interferometer

source of illumination as depicted in Fig. 2. The light emitted by the laser was reflected by a first surface mirror through a diverging lens and a collimating lens which together enlarged the beam diameter tenfold. The collimated coherent monochromatic beam of light was then directed upward through a rhomboidal prism by means of a first surface mirror located beneath the test vessel to illuminate the boiling phenomenon occurring at the upper side of the glass heater surface. The image produced whenever a bubble occurred was deflected into the objective lens of a 16 mm Hycam K1001R high-speed camera by the rhomboidal prism.

The test procedure used was identical to that used previously; boiling taking place at the randomly located naturally occurring nucleation sites in the stannic oxide coating was observed in a region near the center of the glass heater surface. During each experiment comprised of a number of tests at different levels of heat flux under saturated and subcooled boiling conditions, the pressure in the test vessel was maintained constant at approximately one half atmosphere in order to decrease the number of active nucleation sites and to increase the size of the vapor bubbles, thereby simplifying the photographic analysis. Surface temperature measurements and liquid temperature measurements made with appropriately located thermocouples were obtained after test conditions had been established and maintained for approximately five minutes, at which time a length of Kodak 4X film was exposed.

Analysis

Representative bubble photographs are shown in Fig. 3 in which pictorial descriptions of the bubble profiles accompany each photograph. It must be emphasized that the profile of the bubble cap is entirely conjectural since the depth of field of the optical system

Nomenclature

A = undetermined coefficient	r = radius	
c_l = specific heat of liquid	$R(t)$ = bubble radius	
C = bubble growth constant	S = similarity parameter, $r/2\sqrt{\alpha_l t}$	$\delta_0(r)$ = initial microlayer thickness
f = frequency of bubble emission	t = time	$\delta(r, t)$ = instantaneous microlayer thickness
h_{fg} = latent heat	$(T_w - T_{sat})$ = superheat	ϵ = parameter, $1 - \rho_v/\rho_l$
k_l = thermal conductivity of liquid	$(T_{sat} - T_\infty)$ = subcooling	θ = temperature difference, $T(r, t) - T_\infty$
m = fringe order	u = velocity of liquid	λ = wavelength of laser light
n = refractive index	V_B = bubble volume	ν_l = kinematic viscosity of liquid
N/A = active site density	V_E = volume of microlayer evaporated	ρ_l = density of liquid
P_{sat} = saturation pressure	x = dummy variable	ρ_v = density of vapor
q/A = heat flux	α_l = thermal diffusivity of liquid	τ = departure time

was such that only detail within the microlayer region would be visible. The particular sequence of photographs presented was filmed at 2500 frames/s. The heat flux q/A was 60.9 kW/m^2 ($19,200 \text{ Btu/hr ft}^2$), the superheat ($T_w - T_{\text{sat}}$) was 20.5°C (36.9°F), the subcooling ($T_{\text{sat}} - T_\infty$) was 5.6°C (10.2°F) and the saturation pressure P_{sat} was 48.0 kN/m^2 ($14.2'' \text{ Hg}$). Examination of the photographs reveals that the bubble grows rapidly. The particular bubble depicted grew to departure size and detached in approximately 6 ms. The initial growth rate was extremely rapid as evidenced by the blurred image in the first photograph. Careful examination of the particular frame enlarged 100 times revealed eight interference fringes within a circle 0.37 mm radius real size. In the second photograph, the rate of bubble growth had slowed to the point where twenty-two concentric circular fringes can be seen. Asymmetry has commenced in the third photograph so that the fringes are no longer concentric within the outline of the bubble. The broadening of the fringes seen in the fourth figure is indicative of a decrease in the slope of the liquid vapor interface as depicted, perhaps as a result of liquid inflow at the base of the bubble. It is apparent that the dry spot beneath the bubble grows continually.

Fig. 4 depicts the development of the periphery of the microlayer and dry spot as a function of time. Assuming the bubble to be hemispherical during the initial growth period, then in agreement with the observations of Sernas and Hooper [8], the bubble would appear to grow in proportion to the square root of time in accordance with the relationship

$$R(t) = 2C\sqrt{\alpha_1 t} \quad (1)$$

The assumption of the hemispherical bubble cannot be verified by the experimental measurements, but since the conditions governing the formation of hemispherical bubbles described by Sernas and Hooper [9] and Johnson, de la Pena, and Mesler [10] were ob-

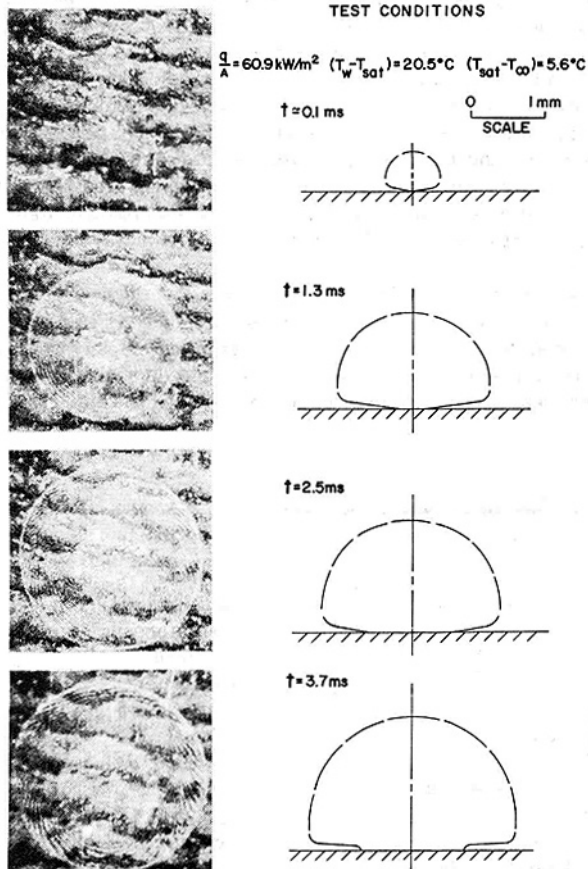


Fig. 3 Representative bubble photographs

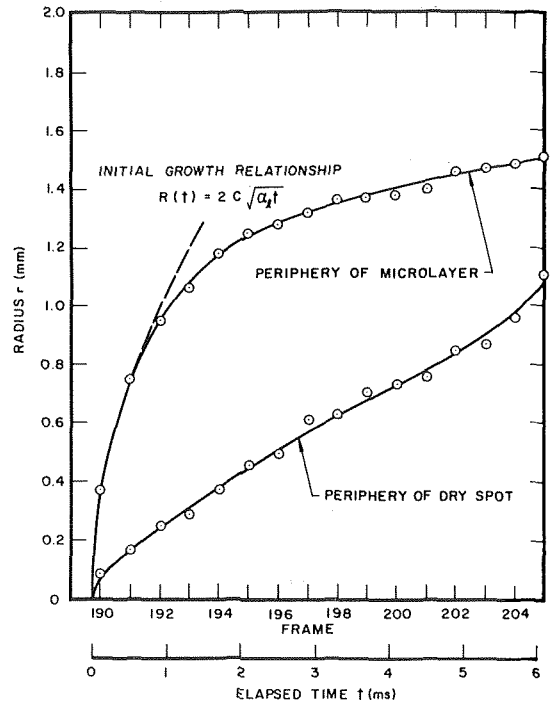


Fig. 4 Microlayer history

served in the present investigation as well, the assumption is felt to be justified.

Fig. 5 illustrates the variation of the circumferentially averaged instantaneous microlayer thickness $\delta(r,t)$ with elapsed time and depicts the initial microlayer thickness $\delta_0(r)$ obtained by plotting the locus of points at which the gradient $\partial\delta(r,t)/\partial r$ approaches infinity. The validity of the profile obtained in this manner is argued below from an energy consideration within a hemispherical bubble growing into a slightly subcooled liquid, which represents the present situation. Although the presence of a temperature gradient in the liquid is acknowledged, this feature leads to considerable complication in the formulation of the mathematical model. Accordingly, a uniformly subcooled liquid was postulated with the realization that the initial microlayer thickness computed will be somewhat greater than that which exists in reality, since the liquid evaporated will be the only source of the vapor contained within the bubble and the energy conducted away by the liquid upon the condensation of the vapor.

The conduction equation in spherical coordinates as it applies to the liquid outside the bubble is given by

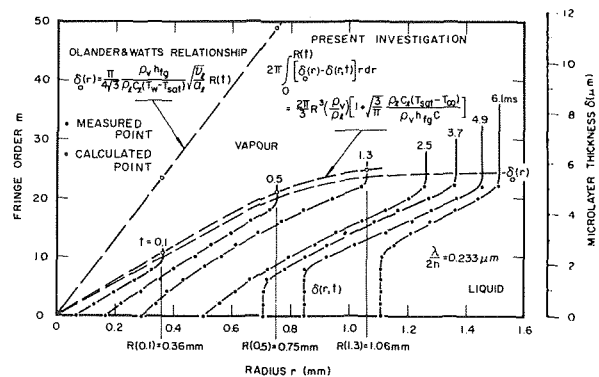


Fig. 5 Microlayer profiles

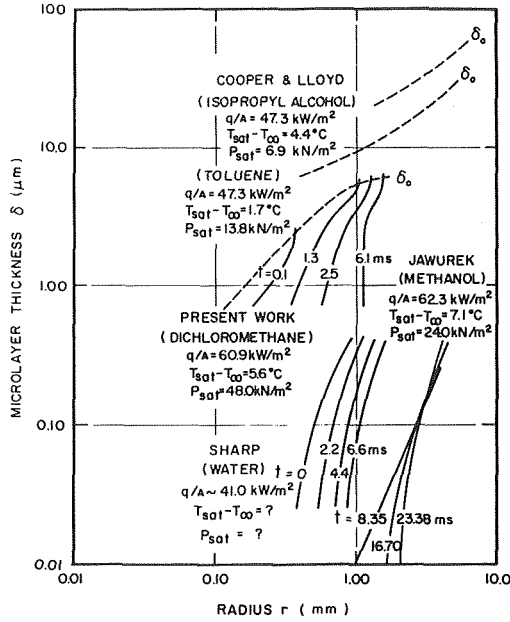


Fig. 6 Microlayer thickness results

$$\frac{\partial \theta}{\partial t} + u \frac{\partial \theta}{\partial r} = \alpha_l \left[\frac{\partial^2 \theta}{\partial y^2} + \frac{2}{r} \frac{\partial \theta}{\partial r} \right] \quad (2)$$

where $\theta(r, t) = T(r, t) - T_\infty$, $u = \epsilon(R/r)^2 dR/dt$, $\epsilon = 1 - \rho_v/\rho_l$ and $R(t) = 2C\sqrt{\alpha_l t}$. The appropriate boundary conditions are $\theta(R, t) = T_{\text{sat}} - T_\infty$ and $\theta(\infty, t) = 0$ while the initial condition which applies is $\theta(r, 0) = 0$. Since the continuity equation is violated only in close proximity to the heater surface, a solution similar to that derived by Scriven [10] may be assumed to apply throughout the conduction domain. In the present situation, heat flows away from the bubble which could not grow if it were not supplied with energy from the microlayer in the form of vapor in excess of that condensed at the liquid vapor interface.

A heat balance at the interface yields the relationship

$$\begin{aligned} -k_l \frac{\partial \theta(R, t)}{\partial r} &= \frac{\rho_v h_{fg}}{2\pi R^2} \left[\frac{\rho_l}{\rho_v} \frac{dV_E}{dt} - \frac{dV_B}{dt} \right] \\ &= \rho_v h_{fg} \left[\frac{1}{2\pi R^2} \left(\frac{\rho_l}{\rho_v} \right) \frac{dV_E}{dt} - \frac{dR}{dt} \right] \quad (3) \end{aligned}$$

where

$$V_E = 2\pi \int_0^{R(t)} [\delta_0(r) - \delta(r, t)] r dr.$$

Using this equation to evaluate the undetermined coefficient in Scriven's relationship

$$\frac{d\theta(S)}{dS} = \frac{A}{S^2} \exp \left(-S^2 + \frac{2\epsilon C^3}{S} \right) \quad (4)$$

where $S = r/2\sqrt{\alpha_l t} = C$ at $r = R$, then one obtains

$$A = -2 \frac{\rho_v h_{fg}}{\rho_l c_l} \left[\left(\frac{\rho_l}{\rho_v} \right) \frac{\sqrt{t/\alpha_l}}{2\pi R^2} \frac{dV_E}{dt} - C \right] C^2 \exp(C^2 + 2\epsilon C^2) \quad (5)$$

Integrating equation (4) and noting that $\theta(\infty) = 0$, gives

$$\begin{aligned} \theta(S) &= +2 \frac{\rho_v h_{fg}}{\rho_l c_l} \left[\left(\frac{\rho_l}{\rho_v} \right) \frac{\sqrt{t/\alpha_l}}{2\pi R^2} \frac{dV_E}{dt} - C \right] C^2 \exp(C^2 + 2\epsilon C^2) \\ &\quad \int_S^\infty \frac{1}{x^2} \exp \left(-x^2 + \frac{2\epsilon C^3}{x} \right) dx \quad (6) \end{aligned}$$

Finally, setting $\theta(C) = T_{\text{sat}} - T_\infty$ and manipulating mathematically

$$\frac{dV_E}{dt} = 2\pi \left(\frac{\rho_v}{\rho_l} \right) R^2 \sqrt{\frac{\alpha_l}{t}} C$$

$$\left[1 + \frac{\rho_l c_l (T_{\text{sat}} - T_\infty) / \rho_v h_{fg}}{2C^3 \exp(C^2 + 2\epsilon C^2) \int_C^\infty \frac{1}{x^2} \exp \left(-x^2 + \frac{2\epsilon C^3}{x} \right) dx} \right] \quad (7)$$

According to Scriven

$$2C^3 \exp(C^2 + 2\epsilon C^2) \int_C^\infty \frac{1}{x^2} \exp \left(-x^2 + \frac{2\epsilon C^3}{x} \right) dx = \sqrt{\frac{\pi}{3}} C \quad (8)$$

when the ratio ρ_v/ρ_l approaches zero as it does in the present case. Consequently, the volume of liquid evaporated from the microlayer in the time interval 0 to t is given by

$$\begin{aligned} 2\pi \int_0^{R(t)} [\delta_0(r) - \delta(r, t)] r dr \\ = \frac{2\pi}{3} R^3 \left(\frac{\rho_v}{\rho_l} \right) \left[1 + \sqrt{\frac{3}{\pi}} \frac{\rho_l c_l (T_{\text{sat}} - T_\infty)}{\rho_v h_{fg} C} \right] \quad (9) \end{aligned}$$

where $C = 60.0$ is obtained by fitting equation (1) to the experimental data; the term $\sqrt{3/\pi} \rho_l c_l (T_{\text{sat}} - T_\infty) / \rho_v h_{fg} C$ which is equivalent to 0.265 in the present investigation represents the fraction of the bubble volume condensed at the vapor liquid interface.

One microlayer thickness profile satisfying equation (9) at $R = 0.36, 0.75$ and 1.06 mm has been presented in Fig. 5. Although this profile is not unique, it is a very probable solution for the case of a hemispherical bubble growing into a uniformly subcooled liquid. It is not unreasonable that the microlayer thickness predicted is somewhat greater than that obtained by plotting the locus of inflection points, since the theoretical solution ignores the energy flowing into the bubble from the superheated liquid in the vicinity of the heater surface.

The theoretical relationship derived by Olander and Watts [11] to predict initial microlayer thickness

$$\delta_0(r) = \frac{\pi}{4\sqrt{3}} \frac{\rho_v h_{fg}}{\rho_l c_l (T_w - T_{\text{sat}})} \sqrt{\frac{v_l}{\alpha_l}} R(t) \quad (10)$$

has been plotted in Fig. 5 for the sake of comparison. It can be seen that the initial microlayer profile predicted is approximately twice as great as the experimentally determined initial microlayer profile, although the reason for the discrepancy is not readily apparent. The premise upon which the theoretical relationship was founded is that the initial microlayer thickness is analogous to the displacement thickness in fluid mechanics, and consequently the theoretical relationship is based upon a solution of the boundary layer equations governing flow in a semi-infinite medium into which a hemispherical bubble is growing. Although simplifying assumptions were involved in order to solve the boundary layer equations, inclusion of the terms omitted by the original authors only served to increase the thickness of the predicted initial microlayer profile.

The contribution of microlayer evaporation heat transfer to the nucleate boiling heat transfer process can be assessed once the validity of the initial microlayer profile has been established since the heat transferred can be computed by

$$(q/A)_{\text{Microlayer}} = 2\pi \rho_l h_{fg} \frac{N}{A} \int_0^{R(t)} [\delta_0(r) - \delta(r, \tau)] r dr \quad (11)$$

where $\delta(r, \tau)$ represents the instantaneous microlayer profile at the instant of departure $t = \tau$. For the bubble under consideration, equation (11) yields $(q/A)_{\text{Microlayer}} = 16.4$ kW/m² which is approximately 25 percent of the total rate of heat transfer $(q/A)_{\text{Total}} = 60.9$ kW/m².

Fig. 6 shows the profiles presented in Fig. 5 replotted on logarithmic coordinates in order to accommodate the results of Sharp, Cooper and Lloyd, and Jawurek. The microlayer thickness results of the present investigation are consistent with those of Moore and Mesler (2.3 μm) and Foltz and Mesler (3.3 μm to 9.4 μm) and in better agreement with the results reported by Cooper and Lloyd than with those reported by Sharp and by Jawurek. The fact that the instantaneous microlayer thickness results of Sharp and Ja-

wurek are more than one order of magnitude smaller than the initial microlayer thickness results of Moore and Mesler, Foltz and Mesler, and Cooper and Lloyd may not be significant since the test conditions are obviously different so that differences in microlayer thickness should be expected. However, the possibility exists that Sharp's and Jawurek's results are in error for a reason similar to that which invalidated Judd's earlier work as discussed in the introduction, since all of these investigations involved the use of interferometry.

Concluding Remarks

The results of the present investigation confirm that the microlayer evaporation phenomenon is a significant heat transfer mechanism. It now remains to determine the relative significance of this mechanism to the nucleate boiling heat transfer process at various levels of heat flux, subcooling, and system pressure.

References

- 1 Moore, F. D., and Mesler, R. B., "The Measurement of Rapid Surface Temperature Fluctuations During Nucleate Boiling of Water," *AIChE Journal*, Vol. 7, 1961.
- 2 Hendricks, R. C., and Sharp, R. R., "Initiation of Cooling due to Bub-

ble Growth on a Heating Surface," NASA TN D-2990, 1964.

- 3 Sharp, R. R., "The Nature of Liquid Film Evaporation During Nucleate Boiling," NASA TN D-1997, 1964.

- 4 Hospeti, N. B., and Mesler, R. B., "Deposits Formed Beneath Bubbles During Nucleate Boiling of Radioactive Calcium Sulfate Solutions," *AIChE Journal*, Vol. 11, 1965.

- 5 Cooper, M. G., and Lloyd, A. J. L., "The Microlayer in Nucleate Pool Boiling," *International Journal of Heat and Mass Transfer*, Vol. 12, 1969.

- 6 Jawurek, H. H., "Simultaneous Determination of Microlayer Geometry and Bubble Growth in Nucleate Boiling," *International Journal of Heat and Mass Transfer*, Vol. 12, 1969.

- 7 Foltz, G. E., and Mesler, R. B., "The Measurement of Surface Temperatures With Platinum Films During Nucleate Boiling of Water," *AIChE Journal*, Vol. 11, 1970.

- 8 Judd, R. L., "Comparison of Experimental Microlayer Thickness Results," *CSME Transactions*, Vol. 1, 1972.

- 9 Sernas, V., and Hooper, F. C., "The Initial Vapour Bubble Growth on a Heated Wall During Nucleate Boiling," *International Journal of Heat and Mass Transfer*, Vol. 12, 1969.

- 10 Johnson, M. A., de la Pena, J., and Mesler, R. B., "Bubble Shapes in Nucleate Boiling," *Chem. Engng. Prog. Symp. Series*, Vol. 62, 1966.

- 11 Scriven, L. E., "On the Dynamics of Phase Growth," *Chem. Engng. Sci.*, Vol. 10, 1959.

- 12 Olander, R. R., and Watts, R. G., "An Analytical Expression of Microlayer Thickness in Nucleate Boiling," *JOURNAL OF HEAT TRANSFER, TRANS. ASME, Series C*, Vol. 91, 1969.

M. Shoukri,
Graduate Student.

R. L. Judd
Assoc. Professor.

Mechanical Engineering Department,
McMaster University,
Ontario, Canada

Nucleation Site Activation in Saturated Boiling

An experimental investigation is presented for the boiling of distilled degassed water at atmospheric pressure on a single copper surface with different surface finishes, in which the activation of nucleation cavities under the influence of different levels of heat flux was investigated. The measured active cavity radii showed good agreement with the active cavity radii predicted by the Hsu model. As a result of this investigation, it would appear that smaller cavities are better able to entrap vapor residue and be activated by their neighbors when boiling is initiated on the surface than larger cavities and that the reason for the relatively high levels of superheat at incipience commonly encountered is the nonexistence of sufficiently large cavities with the prerequisite residue of vapor. The correlation suggested by Brown relating the active site density $(N/A)_{r_c}$ as a function of cavity radius r_c in the form $(N/A)_{r_c} \propto (1/r_c)^m$ was confirmed. On the basis of this work Griffith and Wallis' recommendation that the parameter group $[2\sigma T_s / \rho_v h_{fg} (T_w - T_s)]$ be used to characterize a boiling surface was substantiated.

Introduction

In the process of nucleate pool boiling, casual observation shows bubble streams originating from specific locations on the surface; microscopic observation of these locations reveals a cavity or a scratch where a bubble formed. Corty and Foust [1],¹ Bankoff [2-4], and others advanced the postulate that bubbles originate at a heating surface from cavities in which a gas or a vapor phase pre-exist, which has since been confirmed by many experimental investigations. Under certain conditions, the nucleus formed in a cavity becomes unstable and a bubble grows and departs after which liquid closes in over the cavity trapping a residue of vapor, which becomes the nucleus for the next bubble.

Therefore, the problem of nucleation can be resolved into three parts: (1), the conditions necessary to initially entrap vapor or gas in surface cavities; (2), the stability of a cavity containing entrapped gas or vapor; (3), the conditions that govern the formation of a bubble from an active cavity with trapped vapor. The first part was investigated by Bankoff [3], who presented a quantitative explanation which is widely accepted for determining whether or not a surface cavity of known shape and size in contact with a given liquid would entrap gas or vapor. A discussion of the part (2) can be found in references [1, 2, 4] in which it was generally con-

cluded that cavities having large depth to width ratio are more stable. With respect to part (3), all investigators are in agreement about the criterion for bubble growth which is that the thermal layer surrounding the nucleus must be at a mean temperature equal to, or greater than, the temperature of the vapor in the nucleus. This condition allows an inward flow of heat from the superheated thermal layer to the nucleus through the vapour-liquid interface.

In studying the thermostatic equilibrium of a nucleus surrounded by a superheated liquid, Griffith and Wallis [5] and Rohsenow [6] determined the superheat required for equilibrium of a nucleus of radius r to be

$$T_v = T_s + \frac{2\sigma T_s}{r\rho_v h_{fg}} \quad (1)$$

Nuclei of radius greater than r predicted by equation (1) should become bubbles and grow; those of smaller radius should collapse. This relationship has been confirmed experimentally by Tucker and Ward [7].

In an attempt to incorporate the temperature distribution in the superheated thermal layer adjacent to the surface into an expression for predicting nucleation conditions, models were proposed by Hsu [8] and by Han and Griffith [9], respectively. Both models assumed that the principal mechanism of heat transfer by which the nucleation cavities were activated was transient conduction to and subsequent replacement of the superheated thermal layer around the nucleation cavities. Hsu assumed the existence of a limiting thermal layer of constant thickness and derived the following mathematical expression capable of predicting the maximum and minimum sizes of nucleation cavities as a function of the surface

¹ Numbers in brackets designate References at end of paper.

Contributed by the Heat Transfer Division for publication in the JOURNAL OF HEAT TRANSFER. Manuscript received by the Heat Transfer Division June 24, 1974. Paper No. 75-HT-X.

temperature, fluid properties, and the thermal layer thickness

$$r_{c \text{ min}}^{\text{max}} = \frac{\delta}{2C_1} \left\{ 1 - \frac{\theta_s}{\theta_w} \pm \left[\left(1 - \frac{\theta_s}{\theta_w} \right)^2 - \frac{4AC_3}{\delta\theta_w} \right]^{1/2} \right\} \quad (2)$$

where $C_1 = (1 + \cos\beta)/\sin\beta$ and $C_3 = 1 + \cos\beta$.

Han and Griffith [9] were also able to develop an equation of the same nature which permitted the thermal layer thickness to vary with time, capable of predicting the maximum and minimum sizes of nucleation cavities according to

$$r_{c \text{ min}}^{\text{max}} = \frac{\delta(T_w - T_s)}{3(T_w - T_\infty)} \left\{ 1 \pm \left[1 - \frac{12(T_w - T_\infty)T_s\sigma}{(T_w - T_s)^2\delta\rho_v h_{fg}} \right]^{1/2} \right\} \quad (3)$$

Both of the proposed models for nucleation require knowledge of the superheated layer thickness which was lacking at the time they were formulated. Recently, Weibe and Judd [10] performed an experimental investigation of temperature profiles in boiling water adjacent to a copper surface for heat fluxes of 63,000, 158,000, and 315,000 W/m² at various levels of subcooling ranging from 0°C to 58°C. These profiles, based upon new data for saturated and subcooled boiling enabled the extrapolated superheat layer thickness to be determined under actual boiling conditions.

Although it has been indicated qualitatively by Corty and Foust [1], Jakob [11], Kurihara and Myers [12], and Hatton and Hall [13] that for a given superheat, the rate of heat transfer increased as the macroscopic roughness increased, none of the many models for predicting rates of nucleate boiling heat transfer have been able to incorporate this effect since the nucleation characteristics of a surface are relatively insensitive to the surface macroroughness as measured by a profilometer. Another approach which customarily has been used is to describe the surface nucleation characteristics by correlating the total number of active sites at certain boiling conditions. Kurihara and Myers [12] derived an equation relating the temperature difference and the surface conditions with the active site density. The equation could not predict the active site density at a particular set of conditions but could predict the difference in site density between two different conditions.

Gaertner [14] developed an expression to predict the nucleation site density in the form of

$$(N/A) = N_0 \exp(-k/T_w^3) \quad (4)$$

where k is a function of the fluid properties and surface conditions. Later, Anderson, Judd, and Merte [15] showed that for a particular surface, k is independent of the fluid properties.

Griffith and Wallis [5] carried out extensive controlled experiments in which they investigated the nucleation properties of single artificial cavities formed in a copper surface and obtained boiling data for water, methanol, and ethanol on different copper surfaces finished with emery paper. The authors confirmed that nucleation occurs from pre-existing gas-filled cavities on the surface. Furthermore, a single parameter $r_c = [2\sigma T_s / \rho_v h_{fg} (T_w - T_s)]$ was found to be sufficient to characterize such an active cavity since

the surface superheat at which a cavity would become active was found to be fixed by the fluid properties through this relationship. For a particular surface, a single plot of active site density N/A versus the parameter grouping $[2\sigma T_s / \rho_v h_{fg} (T_w - T_s)]$ was obtained. Consequently, it was concluded that the nucleation characteristics of a surface would be known if the size distribution of active sites on the surface were known. Similarly, Anderson, Judd, and Merte [15] were able to draw their data together for boiling of five different fluids on a glass surface into a single curve of active site density N/A against the parameter group $[2\sigma T_s / \rho_v h_{fg} (T_w - T_s)]$.

Brown [16] investigated bubble nucleation from different surfaces with various surface finishes. One distinguishing feature of Brown's work was the fact that the number of active sites per unit area $(N/A)_{r_c}$ with radii larger than r_c was correlated by the power law

$$(N/A)_{r_c} \propto (1/r_c)^m \quad (5)$$

In the present investigation, the activation of nucleation sites on a copper surface with different surface finishes was investigated and an attempt was made to characterize these different boiling surfaces according to this relationship.

Experimental Apparatus

A sectional view of the test assembly is shown in Fig. 1. The test assembly was comprised of a plexiglass vessel surrounding a cylindrical copper test specimen on the upper surface of which boiling took place. The copper test specimen was 25 mm dia at the boiling surface. A 400 W cartridge heater was inserted inside the test specimen in a cylindrical hole machined to fit the heater. A stainless steel sleeve 150 mm long, 25 mm outer dia reduced to 1.25 mm wall thickness at the upper end was epoxied to the test specimen thereby creating a 2.5 mm thick air gap between the specimen and the sleeve which served as an insulating layer.

The test assembly was mounted on an X-Y stage provided with two micrometers capable of reading to ± 0.0025 mm which provided a controlled and accurate travel of the whole test assembly in two normal directions. A microscope with a focussing telescopic eyepiece was mounted on the center line of the test assembly in its central position. Various interchangeable lenses were used in the investigation to obtain the most favorable view of the boiling phenomenon occurring at the upper surface of the copper test specimen. The microscope together with the X-Y stage was used to locate the active sites by moving the apparent nucleation sites to the center of the microscope field of view and reading the corresponding values of X and Y.

A Polaroid camera was mounted on the microscope to enable photography of the test specimen surface. During the photographing, the objective lens of the microscope was replaced by a Watson 16 mm interference objective, a microscopic objective lens with a built-in interferometer for the examination of surfaces by reflected light. This interference objective provided the possibility of obtaining both interferograms and microphotographs of the test

Nomenclature

A = parameter $A = 2\sigma T_s / \rho_v h_{fg}$, m²K
 C_1 = constant $C_1 = (1 + \cos \sin \beta)$
 C_2 = constant $C_2 = 1/\sin \beta$
 C_3 = constant $C_3 = 1 + \cos \beta$
 $f(N/A)$ = frequency of occurrence of nucleation site density
 h_{fg} = latent heat of vaporization, Ws/kg
 N_0 = constant in equation (4),

m^{-2}
 N/A = total nucleation site density, m⁻²
 $(N/A)_{r_c}$ = nucleation site density for cavities of radius equal to or greater than r_c , m⁻²
 q/A = heat flux, W/m²
 r = radius, m
 r_c = cavity radius, m
 T = temperature, °C
 δ = extrapolated thermal layer thickness, m

θ = temperature difference $\theta = (T - T_\infty)$, °C
 β = contact angle
 ρ = density, kg/m³
 σ = surface tension, Nm

Subscripts

l = liquid
 v = vapor
 w = surface
 ∞ = bulk
 s = saturation

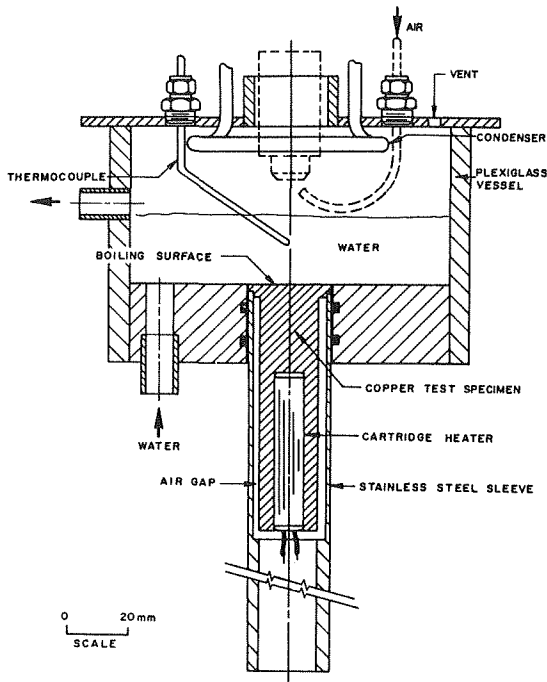


Fig. 1 Sectional view of test assembly

specimen surface by a simple adjustment.

Test Conditions

The investigation was carried out at standard atmospheric pressure upon a single high purity copper test specimen with three different surface finishes:

1. A standard machine shop finished surface having a $0.400 \mu\text{m}$ center line average finish as indicated by a Talysurface profile. Before this surface was tested it had been subjected to various boiling processes over a period of three months during the preliminary preparation of this experimental study, during which time a hard coating had been deposited on the surface.
2. A fine machined surface having $0.125 \mu\text{m}$ center-line average finish. This surface was prepared by machining on a lathe with a sharpened oil stoned tool using extra fine feed to produce the smoothest mechanically finished surface obtainable.
3. A mirror polished surface which was produced using six micron and one micron diamond pastes in kerosene lubricant as the polishing medium resulting in a $0.100 \mu\text{m}$ center-line average finish.

For each of the three surface finishes, tests were carried out under saturated boiling conditions using distilled degassed water. Heat flux was incrementally decreased from a heat flux level of about $500,000 \text{ W/m}^2$, the maximum obtainable with the test apparatus, in order to guarantee full activation of the nucleation sites. Although the heat flux and the surface superheat were measured up to this limit, the observation of the individual nucleation active sites was possible only up to $200,000 \text{ W/m}^2$. An investigation to obtain the size and distribution of the nucleation sites was carried out at three levels of heat flux for each surface, selected to cover the range of heat flux from $60,000$ to $200,000 \text{ W/m}^2$.

Test Procedures

When thermal equilibrium was attained as indicated by invariant measurements of the thermocouples at the specimen center line and the temperature of the bulk water, observation of the boiling phenomenon using the microscope with $15\times$ overall magnification was commenced. The microscope field of view was 2.5 mm dia at this level of magnification. The number of nucleation sites in the microscope field of view at four or five different locations cho-

sen arbitrarily were counted, their locations were determined using the readings of the X-Y stage and the average nucleation site density at this particular condition of heat flux and surface superheat was determined.

After recording the locations of the nucleation sites, the experiment was interrupted, the surface was dried, and the plexiglass vessel was moved out of the way. The objective lens was replaced by the Watson interference objective having an overall magnification of $120\times$. By resetting the X-Y stage to the previously determined coordinates, it was possible to relocate the nucleation sites. Photomicrographs of the nucleation sites were taken and examined using a travelling microscope in order to measure the average radius of the nucleation cavities. Most of the observed cavities had approximately circular mouths; the very few scratches observed were excluded.

For each level of heat flux, the minimum and maximum radii of the observed nucleation sites were determined and the distribution of active site radius was analyzed statistically. A histogram of the relative frequencies of occurrence was constructed to obtain the active site distribution as a function of the radius.

Discussion of the Results

The results of the present investigation are presented in reference [17]. As anticipated, the boiling characteristic curves which are shown in Fig. 2 indicate that decreasing surface macroroughness shifts the boiling curve to higher superheat for the same heat flux. However, it was noted earlier that boiling is governed by surface microroughness, so that it is not possible to deduce anything concerning the nature of the surfaces from such characteristic curves.

In studying the nucleation phenomenon both Hsu and Han and

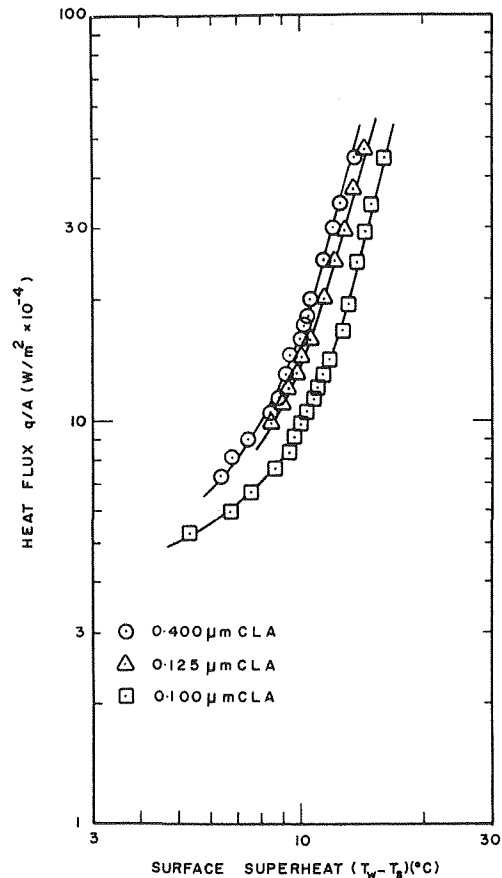


Fig. 2 Boiling characteristic curves

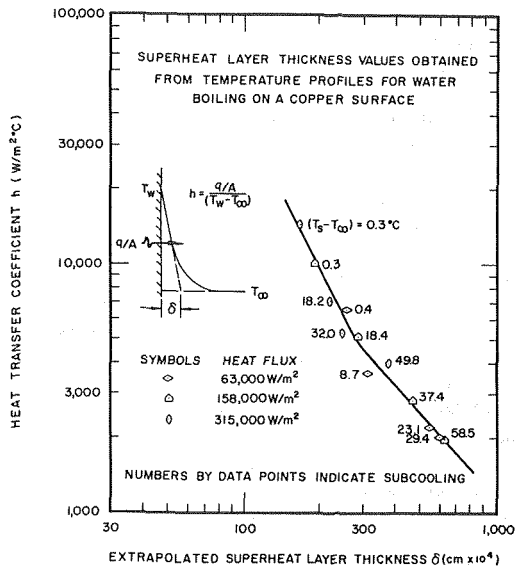


Fig. 3 Superheat layer thickness correlation

Griffith models were considered. Inasmuch as the comparison between experiment and theory were quite similar for both models, only the Hsu model has been treated in this paper. Equation (2), the mathematical relationship derived by Hsu, predicts the range of potentially active cavities which could be activated at various levels of surface superheat. Hsu assumed the thermal layer thickness δ to be constant for a particular heat flux and system pressure due to the lack of information about the thermal layer thickness, but as explained earlier, Wiebe and Judd have shown that the thermal layer thickness varies with the heat transfer coefficient. Consequently, in evaluating equation (2), the thermal layer thickness δ was assumed to vary with heat transfer coefficient h in the manner depicted in Fig. 3 which has been reproduced from reference [10]. This procedure was justified by arguing that during boiling the thermal layer thickness is established by the level of turbulence which is relatively insensitive to differences in surface finish but proportional to the boiling heat transfer coefficient. The contact angle β was taken to be 70 deg in accordance with the measurements of Rao [18] who reported values of contact angle from 66 deg to 72 deg for water boiling on a copper surface.

By plotting the cavity radius r_c predicted by equation (2) for three surfaces tested against surface superheat θ_w , Fig. 4 was obtained. The minimum and maximum radii of the active cavities observed experimentally at three levels of surface superheat for each surface have been superimposed for the sake of comparison, and it may be seen that the experimental results tend to fall along the lower branch of the curve. This observation can be explained qualitatively; in spite of the wide range of nucleation cavities which could be activated according to the Hsu model, cavities of larger radii were not active on the surfaces tested, presumably because the smaller cavities exist in greater numbers than the larger cavities and are apparently better able to hold a residue of vapour and be activated by their neighbours when boiling is initiated on the surface. No cavities having radii in the vicinity of the upper branch of the curve were observed to be active despite the fact that such cavities did exist on the surfaces tested.

It is a matter of some importance to consider the incipience phenomenon. Incipient boiling is the condition at which the first cavity nucleates and may be considered to occur when the steady-state temperature profile in the thermal layer adjacent to the surface is just tangent to the contour represented by equation (2). Provided that cavities of the particular radius corresponding to the point of tangency exist having a residue of vapor trapped within them, the first bubble will appear. However, in many of the references, it would seem that the experimental observation of incipience did

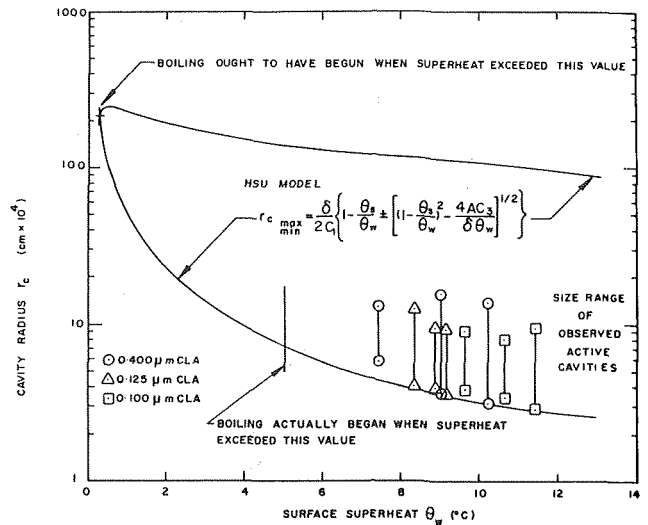


Fig. 4 Presentation of experimental results

not occur until higher incipience superheats than those predicted by the proposed model were attained. In the present work, the surface superheat calculated by substituting the incipient thermal layer thickness obtained from reference [10] in equation (2) is about 0.25°C while no significant boiling was observed until surface superheat exceeded 5.0°C. This lack of agreement is most likely explained by the nonexistence of sufficiently large cavities with the prerequisite residue of vapor. For example, in the present work the radius of the nucleation cavity that could be activated at 0.25°C superheat is of the order of 0.022 cm while the largest cavity observed to be active had a 0.002 cm radius. Murphy and Bergles [19] have presented a comprehensive analysis of the conditions which must be satisfied in order for nucleation to occur which considers the effects of dissolved gas upon the incipience phenomenon.

Brown [16] suggested that the site density $(N/A)_{rc}$ for nucleation cavities of radius greater than, or equal to r_c could be correlated according to equation (5), which will yield the total active site density (N/A) when the minimum cavity radius $r_{c\min}$ is substituted. This relationship was tested in the present investigation. The range of nucleation cavity radius determined in the manner explained before was divided into constant logarithmic intervals, and for each interval, the corresponding number of nucleation cavities per unit area equal to or larger than the radius at this interval was

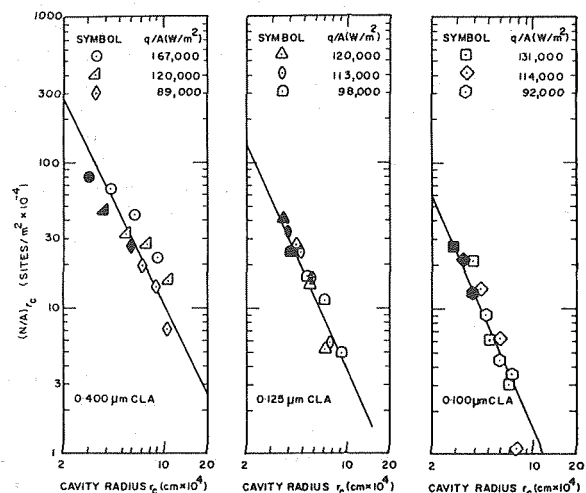


Fig. 5 Cavity size distribution

plotted in the manner suggested by equation (5) for each of the surfaces tested at each of the three levels of heat flux. The correlations shown in Fig. 5 represent the characteristics of the surfaces tested when boiling water only. It is observed that a single correlation was obtained independent of the heat flux and that the only effect of increasing heat flux was to extend the range of active nucleation sites to smaller cavity sizes. The darkened symbols in Fig. 5 indicate the total active site density corresponding to the minimum observed cavity radius at the particular level of heat flux. It is presumed that a correlation based upon these darkened symbols only should yield the same relationship. This treatment of the data is conceptually the same idea proposed by Griffith and Wallis [5]; their correlation of the total nucleation site density (N/A) with cavity radius r_c as predicted by $[2\sigma T_s/\rho_v h_{fg} (T_w - T_s)]$ represents the relationship which would be obtained by correlating the darkened symbols in Fig. 5 since $r_c = [2\sigma T_s/\rho_v h_{fg} (T_w - T_s)]$ is the minimum active cavity radius at a particular level of heat flux. One can conclude that the smoother the surface, the more the correlation of $(N/A)_{r_c}$ versus r_c shifts to the left on the graph, indicating a decrease in the number of nucleation cavities of the same cavity radius. In addition, the exponent m of the correlated relationship appears to vary slightly, having a tendency to increase with the smoothness of the surface.

The ability of the parameter group $[2\sigma T_s/\rho_v h_{fg} (T_w - T_s)]$ to represent the minimum nucleation cavity radius is confirmed by Fig. 6. The data points on the graph are the darkened symbols on Fig. 5. Except for a single data point which is most likely in disagreement because no smaller cavity was observed in the randomly chosen fields of view of the microscope, good agreement was observed suggesting the use of such a group to predict the minimum active cavity radius in opposition to determining it experimentally. In this way, surface nucleation characteristics could be derived by correlating (N/A) versus $[2\sigma T_s/\rho_v h_{fg} (T_w - T_s)]$ rather than by correlating $(N/A)_{r_c}$ versus r_c as was done in the present investigation, with considerable saving of effort.

In investigating the statistical distribution of cavity radius as a random variable, no known statistical distribution was capable of fitting the data. For each surface, the only consistent features of these distributions were that for an increase of heat flux or surface superheat, the mean of the distribution moved to lower values of cavity radius indicating that smaller cavities had been activated. The area under the distribution curve was observed to increase with an increase of heat flux or surface superheat, indicating the increase of the total number of active nucleation sites.

It was possible to generate three-dimensional plots of surface su-

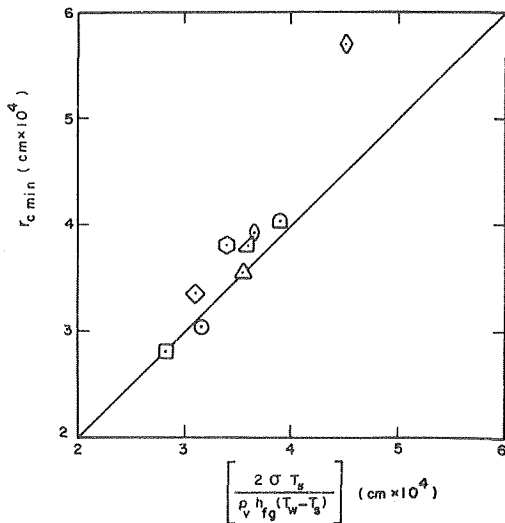


Fig. 6 Comparison of observed and predicted minimum cavity size

perheat θ_w , nucleation cavity radius r_c and frequency of occurrence of nucleation site density $f(N/A)$ for each surface. The resulting three-dimensional surface generated characterizes the nucleation behavior of a boiling surface. Fig. 7 represents one such plot for the surface having $0.400 \mu\text{m}$ CLA finish. In the horizontal plane, a plot of the Hsu model predictions has been superimposed for comparison.

Conclusions

The investigation presents a set of measurements for saturated nucleate boiling water on a copper surface with three different surface finishes. The cavity activation model proposed by Hsu was compared with the measured nucleation cavity radii data which had a tendency to fall in the lower portion of the predicted range of cavity radii. The model for predicting the activation of nucleation cavities represents a necessary but nonsufficient condition for cavities to nucleate since some cavities that satisfy the model were observed to be inactive under test conditions. Apparently, small cavities are better able to entrap vapor residue and be activated by their neighbours when boiling is initiated on the surface since few of the large cavities were observed to nucleate. Incipience was observed to occur at higher superheat than that predicted by the model examined, presumably because of the nonexistence of sufficiently large cavities with the prerequisite residue of vapor.

The relationship recommended by Brown to correlate the active site density as a function of cavity radius was found to fit the data. The parameter group $[2\sigma T_s/\rho_v h_{fg} (T_w - T_s)]$ is recommended for predicting the minimum nucleation cavity radius and, therefore, the usage of this parameter group with Brown's correlation is recommended as a sufficient method for describing the nucleation characteristics of a boiling surface.

References

- 1 Corty, C., and Foust, A. S., "Surface Variables in Nucleate Boiling," *Chem. Eng. Progress Symp. Series*, Vol. 51, No. 17, 1955, p. 1.

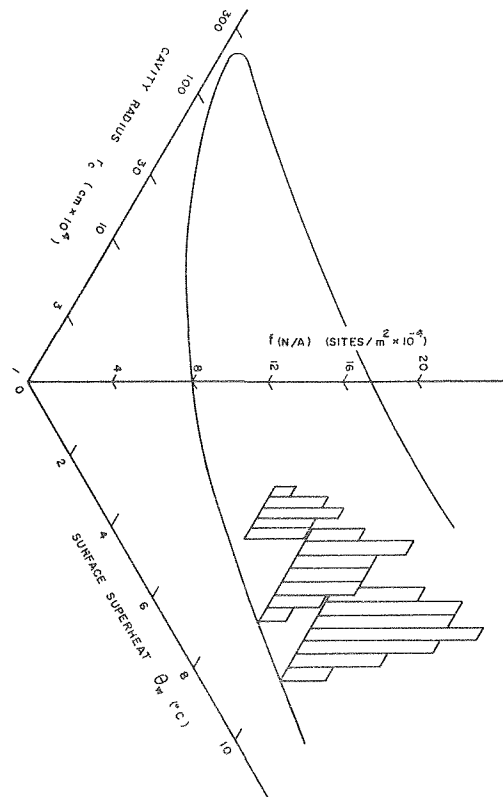


Fig. 7 Nucleation characteristics of the $0.400 \mu\text{m}$ CLA surface

- 2 Bankoff, S. G., "On the Mechanism of Subcooled Nucleate Boiling," *Chem. Eng. Progress Symp. Series*, Vol. 57, 1961.
- 3 Bankoff, S. G., "Entrapment of Gas in the Spreading of Liquid Over a Rough Surface," *AIChE Journal*, Vol. 4, 1958, p. 24.
- 4 Bankoff, S. G., "Ebullition From Solid Surface in the Absence of Pre-Existing Gaseous Phase," *TRANS. ASME*, Vol. 79, 1957, p. 375.
- 5 Griffith, P., and Wallis, J. D., "The Role of Surface Conditions in Nucleate Boiling," *Chem. Eng. Progress Symp. Series*, Vol. 56, 1960, p. 49.
- 6 Rohsenow, W. M., "Nucleation With Boiling Heat Transfer," *Proceedings ASME Joint Fluids Engineering and Heat Transfer Division Symposium on the Role of Nucleation in Boiling and Cavitation*, Detroit, 1970.
- 7 Tucker, A. S., and Ward, C. A., "An Examination of the Predicted Critical Size of Bubbles in Liquid-Gas Solutions," *Proceedings of the Fourth Canadian Congress of Applied Mechanics*, Montreal, May 28-June 1, 1973.
- 8 Hsu, Y. Y., "On the Size Range of Active Nucleation Cavities on a Heating Surface," *JOURNAL OF HEAT TRANSFER, TRANS. ASME, Series C*, Vol. 94, 1962, p. 207.
- 9 Han, C., and Griffith, P., "The Mechanism of Heat Transfer in Nucleate, Pool Boiling," *International Journal of Heat and Mass Transfer* Vol. 8, 1965, p. 887.
- 10 Weibe, J. R., and Judd, R. L., "Superheat Layer Thickness Measurements in Saturated and Subcooled Nucleate Boiling," *JOURNAL OF HEAT TRANSFER, TRANS. ASME, Series C*, Vol. 93, 1971, p. 445.
- 11 Jakob, M., *Heat Transfer*, Vol. 1, Wiley, New York, 1949, p. 631.
- 12 Kurihara, H. M., and Myers, J. E., "The Effect of Superheat and Surface Roughness on Boiling Coefficients," *AIChE Journal*, Vol. 6, 1960, p. 83.
- 13 Hatton, A. P., and Hall, I. S., "Photographic Study of Boiling on Prepared Surfaces," *Proceedings of the Third International Heat Transfer Conference*, Chicago, 1966.
- 14 Gaertner, R. F., "Distribution of Active Sites in Nucleate Boiling of Liquids," *Chem. Eng. Progress Symp. Series*, Vol. 59, 1963.
- 15 Anderson, D., Judd, R. L., and Merte, H., "Site Activation Phenomenon in Saturated Nucleate Boiling," *Proceedings ASME Joint Fluids Engineering and Heat Transfer Symposium on the Role of Nucleation in Boiling and Cavitation*, Detroit, 1970.
- 16 Brown, W. T., "Study of Flow Surface Boiling," PhD thesis, Mech. Eng. Dept., M.I.T., 1967.
- 17 Shoukri, M. S. M., "Nucleation Site Activation in Saturated Boiling," M. Eng. thesis, McMaster University, Hamilton, Ontario, Canada, 1974.
- 18 Rao, S. N., "Effect of Surface Active Agents in Boiling Heat Transfer," M. Eng. thesis, McMaster University, Hamilton, Ontario, 1967.
- 19 Murphy, R. W., and Bergles, A. E., "Subcooled Flow Boiling of Fluorocarbons—Hysteresis and Dissolved Gas Effects on Heat Transfer," *Proceedings of the Heat Transfer and Fluid Mechanics Institute*, Stanford University, 1972.

W. Leidenfrost

School of Mechanical Engineering, Purdue
University, West Lafayette, Ind.

New Method to Determine Latent Heat of Liquids by Means of Dielectric Data

A new method to determine heat of vaporization by means of dielectric data is described which allows one to obtain specific volumes introduced into Clausius-Clapeyron's equation. Isochoric observations are not needed in most cases. An instrument is described for the observation of dielectric data, vapor pressure curve, p - T relationships in superheated state and also molecular weight and polarizability. The measurements to be performed are listed. The validity of the method is checked by using data observed in a similar instrument. The latent heat obtained by the new method is in excellent agreement with literature data. The new method, therefore, can be used advantageously to determine, in not too elaborate test equipment, latent heat, and other properties easily, quickly, and reliably.

Introduction

The evaluation of any thermodynamic process involving a phase change requires the knowledge of latent heat. The proper design of any device operating by a thermodynamic vapor cycle is possible only when both the latent heat of vaporization and condensation are known at the respective state conditions. In many instances these conditions must be varied for one or the other reason and multiple informations of the thermodynamic properties must be provided.

The latent heat data not only determine the amounts of heat added to or withdrawn from a thermodynamic cycle per unit mass, but also provide information of the rate of heat because the latent heat is an important parameter of condensing heat transfer coefficient or the heat flux under nucleate or film boiling.

For common fluids already used in cyclic devices latent heat data and other thermodynamic properties are normally provided in form of steam-type tables or Mollier charts.

For newly developed fluids or common fluids newly proposed for thermodynamic cycles, data are not available and must be established. Data can be obtained approximately from Trouton's rule stating that the ratio of molar latent heat and absolute saturation temperatures is a constant, or more precisely by measurements. The latent heat of vaporization can be determined calorimetrically by either observing the heat of condensation of saturated vapor or by measuring the steady-state boiling rate under constant electri-

cal heat input. Both measurements, like in any other calorimeter-type investigation, are influenced by heat leakages and also by possible deviation from isothermal and isobaric conditions. Precise measurements are time consuming, require elaborate equipment and test cells, and need painstaking attention to details.

The generation of steam-type tables requires data of vapor pressure, specific volumes of both saturated liquid and vapor and p - T relationships in superheated states of liquid and vapor. From the vapor pressure curve and the saturation densities the latent heat can be determined at any temperature from the Clausius-Clapeyron equation.

The determination of saturation densities requires isochoric measurements which normally are quite involved for reasons that the container enclosing the test sample must be kept uniform in temperature and its volume must be known precisely for the p and T conditions of the measurements and the mass enclosed in the container must also be known as precisely as for the calorimeter measurements. There are other methods known to determine the latent heat of vaporization. Liley [1],¹ for example, relates the latent heat to the difference of saturated liquid and vapor thermal conductivities. This method provides good results especially in the neighborhood (50–100°C) of the critical point. The measurements of thermal conductivity, however, are very difficult to perform especially when high accuracy is required. Very close to critical state conditions the observation of thermal conductivity is practically impossible because free convective heat transfer cannot be prevented.

The new method to be described avoids most of the difficulties

Contributed by the Heat Transfer Division for publication in the JOURNAL OF HEAT TRANSFER. Manuscript received by the Heat Transfer Division May 2, 1974. Paper No. 75-HT-R.

¹ Numbers in brackets designate References at end of paper.

inherent to other latent heat measurement techniques.

The method applies the Clausius-Clapeyron equation and determines the saturation densities from dielectric data and the Clausius-Mossotti relationship.

Constant volume measurements are either eliminated completely or have to be carried out only for one of the state conditions and only when molecular weight or polarizability (and its temperature dependence) of the test fluid are not known. Capacitance values can be obtained with extreme accuracy and rather easily, therefore the new method provides a simple means to determine latent heat of vaporization and specific densities.

Theory of the Measurements

The Clausius-Mossotti relationship is given as:

$$\frac{\epsilon - 1}{\epsilon + 2} \frac{1}{\rho} = \frac{4}{3} \pi \frac{N}{M} \alpha \quad (1)$$

where

- N = Avogadro number
- M = molecular weight
- α = molecular polarizability
- ϵ = dielectric constant
- ρ = density

The polarizability α is virtually independent of state of phase and for nonpolar substances also independent of temperature.² For polar substances α must be replaced by

$$\alpha = (a + \alpha_T) \quad (2)$$

where a is the temperature independent polarizability and α_T the temperature dependent one, α_T decreases with increasing temperature.²

For a pure substance the molecular weight in liquid and vapor state is identical (excluding special cases such as the immediate vicinity of critical point) and generally the following equation must hold true

$$\frac{\epsilon_v - 1}{\epsilon_v + 2} \frac{V_v}{(a + \alpha_T)_v} = \frac{\epsilon_l - 1}{\epsilon_l + 2} \frac{V_l}{(a + \alpha_T)_l} \quad (3)$$

where V_v and V_l are the specific volumes of vapor and liquid, respectively. If an instrument is considered which enhouses a capacitor arrangement and being filled once with saturated vapor (indicated by subscripts) and once with saturated liquid at identical thermal equilibrium (same p and T , identical geometry of capacitor and α_T), equation (3) becomes

$$\left[\frac{\epsilon_v - 1}{\epsilon_v + 2} V_v \right]_s = \left[\frac{\epsilon_l - 1}{\epsilon_l + 2} V_l \right]_s \quad (4)$$

or

$$\left[\frac{C_v - C}{C_v + 2C} V_v \right]_s = \left[\frac{C_l - C}{C_l + 2C} V_l \right]_s$$

where C_v and C_l are the capacitance measured when the capacitor was charged with saturated vapor or liquid. The subscript s on the brackets indicates saturation condition. $C = B \cdot \epsilon_0 \cdot 1$ with B the geometric constant (area/thickness), ϵ_0 = permittivity of free space. C is the capacitance of the arrangement at the respective state condition and filled with a fluid of dielectric constant equal unity. The B or C values must be known as a function of p and T which can be easily determined by measuring with a fluid of well-known pressure and temperature dependence of its dielectric constant. Each side of equation (4) is equal to the right side of equation (1) and $(V_v - V_l)_s$

$$(V_v - V_l)_s = \frac{4}{3} \pi \frac{N}{M} (a + \alpha_T) \left[\frac{\epsilon_v + 2}{\epsilon_v - 1} - \frac{\epsilon_l + 2}{\epsilon_l - 1} \right]$$

or

$$(V_v - V_l)_s = \frac{4}{3} \pi \frac{N}{M} (a + \alpha_T) \left[\frac{C_v + 2C}{C_v - C} - \frac{C_l + 2C}{C_l - C} \right] \quad (5)$$

The C 's can be determined easily with 0.01 percent absolute and 0.001 percent relative accuracy. Whenever the molecular weight and polarizability of the test fluid are known, equation (5) can be introduced into the Clausius-Clapeyron equation to determine precisely the latent heat L providing the vapor pressure curve has been established.

$$L = T \frac{dp}{dT} (V_v - V_l) \quad (6)$$

Isochoric measurements are not needed.

If the dependence of vapor pressure on temperature, molecular weight M , and α_T are not known, the vapor pressure curve must be established and at least two observations under constant volume condition become necessary. The first isochoric measurement is conducted at low pressure (small mass) and high temperature and the molecular weight is obtained from ideal gas relationship. The second constant volume determination preferably in vapor state measures the dielectric constant or capacitance as a function of temperature. (An instrument obviously can be provided to measure the foregoing quantities simultaneously.)

For nonpolar substances the specific susceptibility is independent of temperature³ and the measurement will yield a constant K

$$K = \frac{\epsilon_R - 1}{\epsilon_R + 2} \left[\frac{V_{p,T}}{M} \right] = \frac{4}{3} \pi \frac{N}{M} \alpha \quad (7)$$

³ See footnote No. 2.

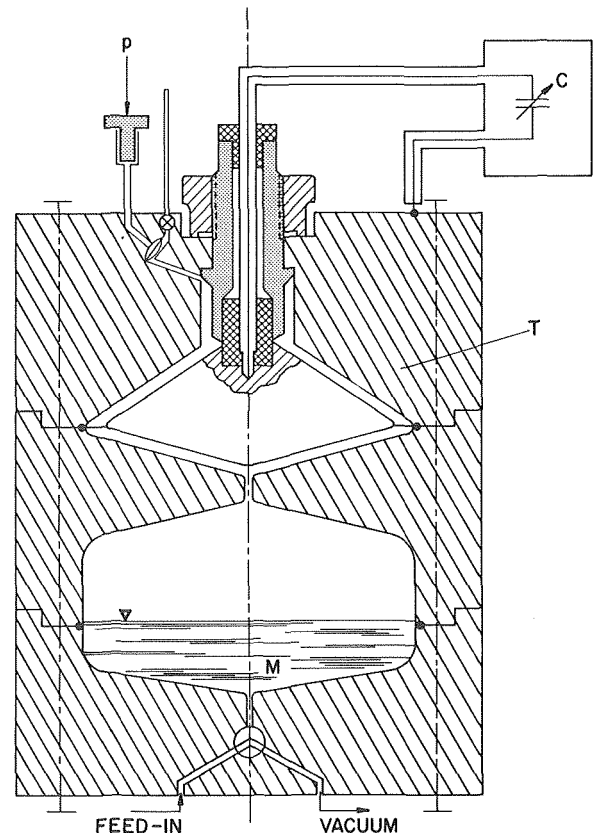


Fig. 1 Instrument to measure p - V - T and dielectric data and molecular weight of fluids

² See standard textbook on physics such as *Elektrizitätslehre*, Pohl Vol. II, or *Optik und Atomphysik*, Springer Verlag, Vol. III 1964.

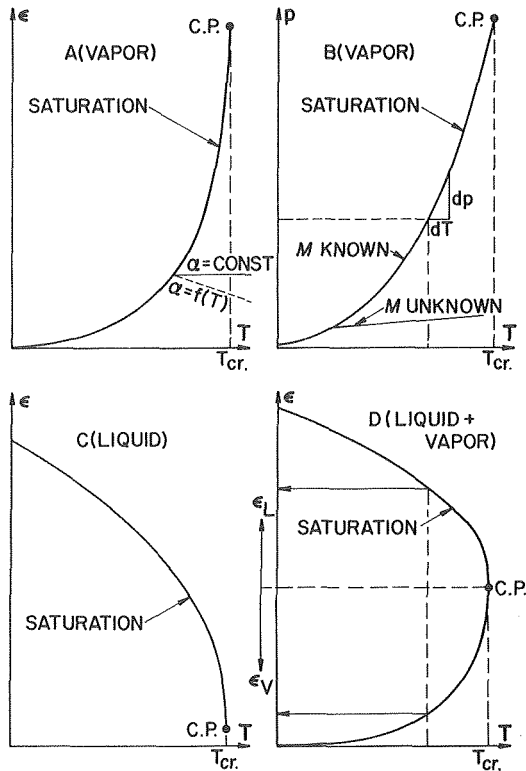


Fig. 2 Results of various measurement (schematic)

from which α can be determined. ϵ_R is the dielectric constant observed at reference condition when the instrument of volume $V_{p,T}$ was charged with mass M of the sample ($M =$ molecular weight).

For polar substances, ϵ will decrease with T as indicated by a broken line in Fig. 2(a) and from the measured curve ($a + \alpha T$) can be determined

$$K_T = \frac{\epsilon_R - 1}{\epsilon_R + 2} \left[\frac{V_{p,T}}{M} \right]_R = \frac{4}{3} \pi \frac{N}{M} (a + \alpha T) \quad (7a)$$

Introducing equation (7) or (7a) into the Clausius-Clapeyron relationship yields

$$L = T \frac{dp}{dT} K_{T_s} \left[\frac{\epsilon_v + 2}{\epsilon_v - 1} - \frac{\epsilon_l + 2}{\epsilon_l - 1} \right] \quad (8)$$

where K_{T_s} is the proper value of K or K_T at the respective saturation condition.

All the measurements mentioned or discussed so far can be performed in a rather simple instrument.

An Instrument to Measure Vapor Pressure Molecular Weight Polarizability and Saturation Densities for the Determination of Latent Heat of Vaporization.

Fig. 1 shows schematically an axial cross section of the instrument which is composed of three parts of an outside body fitted and held together securely by bolts. This body can be maintained at any desired temperature. There are two cavities, the lower one contains the test fluid (liquid and vapor). The upper cavity is filled almost completely by a solid body of the same shape and centered such as to provide a uniform gap width (filled with vapor). The inner body is made out of the same material as the outside body and is supported by a rod built as a double electrically shielded lead. The arrangement represents a capacitor whose geometry must be determined by measurements discussed in the foregoing. The completely surrounded electrode is connected to one side of a

capacitance bridge. The other side of the bridge is connected to the outside body. The three-lead technique allows capacitance values to be observed without influences of the lead-ins. The volume of the capacitor occupied by the test fluid is small compared with the total volume of the two cavities. The test fluid is in contact with one side of a differential pressure transducer built into the upper part of the outside body. The other side of the transducer is connected by an inert gas line to a pressure balance.

The following measurements must be performed with the instrument:

Case (a) Molecular Weight and Polarizability of the Test Fluid Are Known. Under these conditions basically only a few observations are needed for the determination of latent heat.

The evacuated instrument is charged with a mass M close to a critical mass and sealed hermetically and varied stepwise in temperature from close to freezing to critical conditions.

Whenever thermal equilibrium has been established pressure and capacitance are recorded. The $p-T$ observation yield the vapor pressure curve and the $\epsilon-T$ data represent dielectric saturation values of the vapor because the capacitor has been filled during the heating only with vapor in equilibrium with the liquid.

The instrument is now completely filled with the test fluid in liquid state (this also could be accomplished by just placing the instrument upside down or by providing a capacitor arrangement also in the liquid filled region), and capacitance values are measured over the same range of temperature than above. The pressure is regulated for each temperature condition to be slightly higher than the respective vapor pressure in order to avoid boiling. These measurements establish the liquid saturation dielectric constant. The vapor pressure curve allows to determine dp/dT at any temperature. Together with the respective ϵ_v and ϵ_l data the latent heat can be computed from equation (6).

Case (b) Molecular Weight and Polarizability of the Test

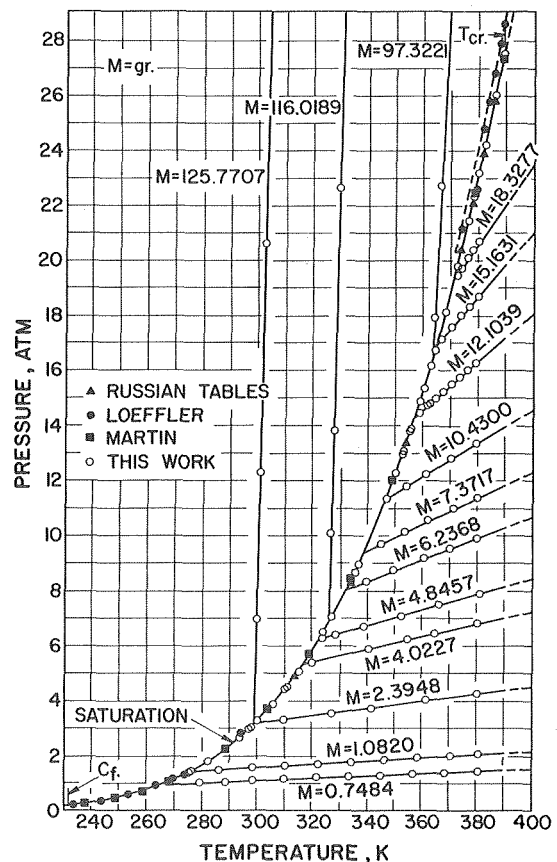


Fig. 3 $p-T$ Diagram of Octafluorocyclobutane, C_4F_8 , measured with different masses M in M.P.I.

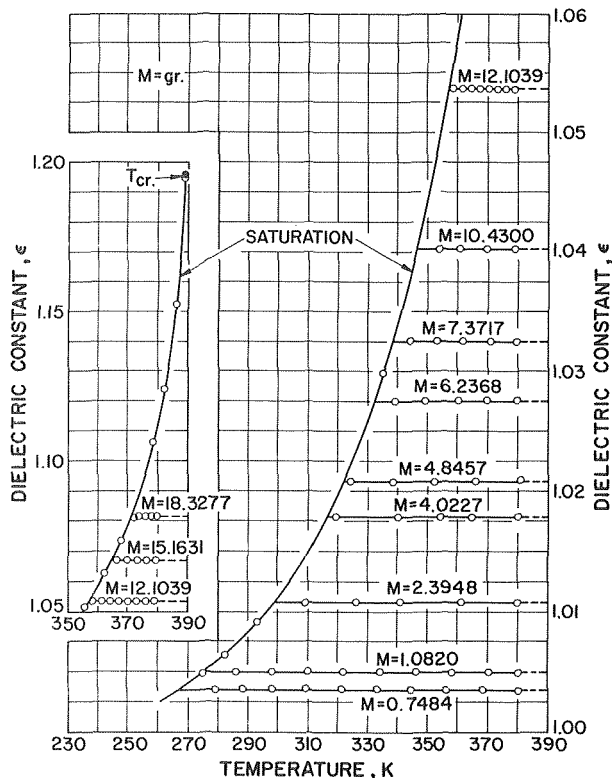


Fig. 4 Dielectric constant $\epsilon = f(T)$ of C_4F_8 vapor measured with different masses M in M.P.I.

Fluid Are Not Known. In this case the two unknown properties must be provided by additional measurements with the instrument before latent heat can be obtained from dielectric data. The determination of M and α or α_T require isochoric measurements and the total volume of the instrument accommodating the test fluid must be known.

The test procedures are as follows:

1 The same measurements described under Case (a), in the foregoing are repeated.

2 The instrument is charged with a well defined amount of mass of the test fluid. Heating of the sample will initially cause a pressure change in accordance with the vapor pressure curve until all the liquid has been evaporated. Further temperature increase will cause superheated condition. Whenever the mass has been chosen small enough the observed pressure in the superheated state will be low and at high temperature the ideal gas relationship can be applied to obtain the molecular weight. The capacitance values observed in the superheated region will either show no temperature dependence or will decrease with temperature assuming constant density condition. In the first case the fluid is nonpolar, i.e., its polarizability is constant. The capacitance decrease with temperature indicates a polar fluid and a temperature dependent polarizability. Whatever the case might be, the measurements yield the polarizability and the constant K can be computed. Introducing the data observed under (b) 2., and (b) 1., into equation (8) yields the latent heat of vaporization. It is obvious that the instrument can be used to determine p - T relationships for various masses of test fluid both in superheated liquid and vapor state.

The results of the measurement just described are plotted schematically as a function of T in Fig. 2. Fig. 2 (A) represents the saturation vapor ϵ -dependence; Fig. 2(B) shows the vapor pressure curve; Fig. 2(C) gives the saturated liquid dielectric constant and Fig. 2(D) combines Figs. 2(A) and 2(C).

For any saturation temperature p and dp/dT and ϵ_v and ϵ_l can be obtained from the curves as shown by a dotted line. The data introduced into equation (6) yield the latent heat at the respective

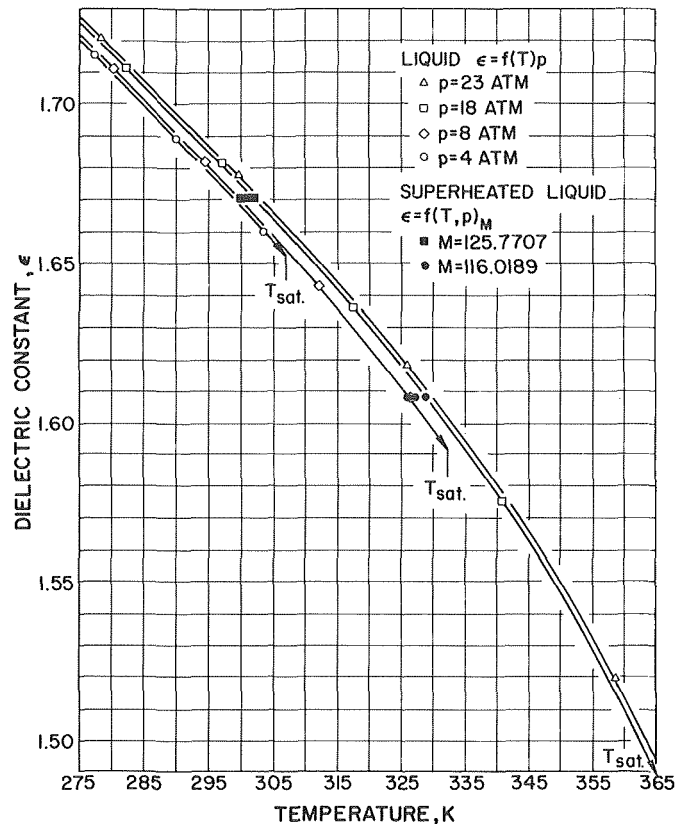


Fig. 5 Dielectric constant $\epsilon = f(T)p$ of C_4F_8 liquid and $\epsilon = f(T,p)_M$ in superheated liquid state

temperature.

The dielectric constants from Fig. 2(d) give

$$V_v = K_{T_s} \frac{\epsilon_v + 2}{\epsilon_v - 1}$$

and

$$V_l = K_{T_s} \frac{\epsilon_l + 2}{\epsilon_l - 1}$$

(9)

Equation (9) demonstrates that the ϵ - T plot of Fig. 2(D) represents V - T and Figs. 2(B) and 2(D) therefore represent the total p - V - T relationship at saturated state conditions. Fig. 2(D) indicates $\epsilon_v = \epsilon_l$ and $d\epsilon/dT = \infty$ at critical point condition and if anomalies are neglected in the critical region.

Experimental Proof of the Applicability of the New Method

A multiproperty instrument MPI had been developed by the author for the simultaneous measurements of many properties of fluids [2]. This instrument allows also the data discussed in the previous cases (a) and (b) to be observed.

Tests were conducted on Octafluorocyclobutane (C_4F_8) and the results of interest to this article are presented in the following figures. Fig. 3 represents the vapor pressure curve and p - T data in superheated state of liquid and vapor. Fig. 4 brings the dielectric constant of the saturated region. Fig. 5 shows the dielectric constant of the liquid observed as a function of temperature at various pressures. From this figure data of saturated condition can be obtained by extrapolation. Fig. 6 represents ϵ - T of both saturated liquid and vapor.

⁴The volume of MPI at reference condition $T_r = 298.15^\circ K$, $p_r = 1$ atm, is $V_r = 84.79904$ cm³. $V_{p,T} = V_r(1 + \alpha_T \Delta T + \alpha_p \Delta p)$ with $\alpha_T = 2.871922 \times 10^{-5}$ (K)⁻¹, $\alpha_p = 1.74399 \times 10^{-6}$ (atm)⁻¹.

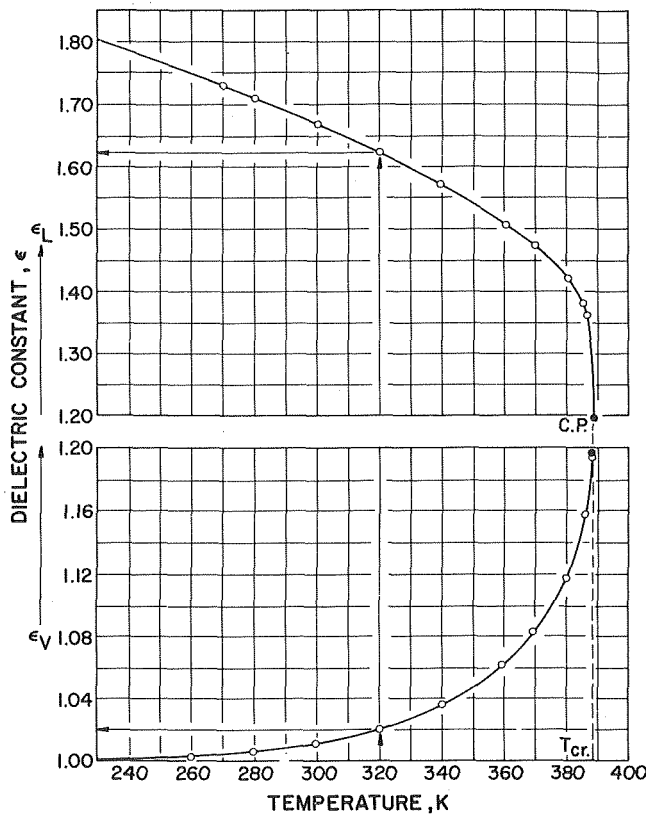


Fig. 6 Dielectric constant ϵ_1 and ϵ_v of C_4F_8 at saturated liquid and vapor condition

The data of Fig. 4 corrected for change of volume⁴ of the instrument with pressure and temperature will demonstrate constant specific susceptibility and constant polarizability. Any ϵ value of this figure at saturated or superheated condition with respective mass M and the volume of the instrument at the proper pressure and temperature will yield the constant K defined by equation (7) in the foregoing. It was evaluated to be

$$K = 0.123985 \text{ cm}^3/\text{gr}$$

Selecting $T_s = 320 \text{ K}$ yields from Fig. 3 saturation pressure and the slope of the vapor pressure curve

$$\frac{dp}{dT} = 0.16128 \text{ atm/K}$$

and Fig. 6 provides

$$\epsilon_v = 1.01960$$

$$\epsilon_l = 1.62101$$

Introducing these values into equation (8) results

$$L = 22.052 \text{ kcal/kg}$$

The comparison with references [3] (22.391), [4] (22.170), and [5] (22.084) data is excellent and demonstrates the validity of the new method.

Limitation of the Method and Alternatives

Unfortunately, there are some instances where the new method cannot be used for the determination of latent heat.

It was stated in the foregoing that the capacitance values can be measured by a capacitance bridge with utmost accuracy. This, however, does not mean identical accuracy in the application in the Clausius-Mossotti equation and the other relationships derived in the foregoing for the following reason. The dielectric constants of all gases and vapors approach unity at low pressures. Due to this fact the $\epsilon - 1$ term might become uncertain by a large percentage despite the fact that the capacitance value was measured with an accuracy of 0.01 or 0.001 percent. Therefore, at low pressures and at low dielectric values the new method is limited in its application. On the other hand, at these conditions it might be possible to compute the specific vapor volume from the ideal gas relationship.

The capacitance bridge in addition loses sensitivity and accuracy whenever the fluid in the capacitor is an electrical conductor. In this case the method still could be applied by determining the index of refraction instead of the dielectric constant. The ϵ must then be replaced by n^2 in the foregoing equations. Optical observations, however, necessitate windows which normally interfere with the measurements and furthermore the windows make it difficult or even impossible to provide isothermal conditions of the instrument.

In many instances the specific volume of the liquid is small compared with the specific volume of the vapor and an erroneous estimation of the liquid density will not introduce too large uncertainties of the latent heat computed from equation.

Acknowledgments

The research with the multipurpose instrument was sponsored by National Science Foundation under a grant, GK-34078, to Purdue University. The support is gratefully acknowledged. The new method described in this article was a by-product of the work performed.

References

- 1 Liley, P. E., "Correlations for Thermal Conductivity and Latent Heat of Saturated Fluids Near the Critical Point," *Proceedings of the 5th Symposium on Thermophysical Properties*, ASME, New York, 1970, pp. 197-199.
- 2 Leidenfrost, W., "Theory, Design, and Use of the Multi-Purpose Instrument for Determining Many Properties and a New Unsteady Temperature-Free Measurement of Heat Transfer and Thermal Properties," *Int. T. Heat and Mass Transfer, Progress in Heat and Mass Transfer*, Vol. 4, Pergamon Press, London, 1971 pp. 333-407.
- 3 Löffler, H. T., and Matthias, H., "Thermodynamische Eigenschaften von Octofluorocyclobutan C_4F_8 ," *Kältetechnik*, Vol. 18/6, 1966, pp. 240-241; see also, Matthias, H., PhD thesis, Berlin, 1965.
- 4 Martin, T. T., "Thermodynamic Properties of Freon—C315 Refrigerant," E. I. duPont deNemours Technical Bulletin T-C318, 1964.
- 5 Vargaftik, B., *Handbook of Thermophysical Properties of Gases and Liquids*, Nauka Press, Moscow, 1972.

R. T. Bailey¹

Research Assist.

J. W. Mitchell

Professor.

W. A. Beckman

Professor.

Department of Mechanical Engineering,
University of Wisconsin,
Madison, Wisc.

Convective Heat Transfer From a Desert Surface

The convective heat transfer relations for atmospheric flow over sparsely vegetated areas are reviewed and compared to existing relations for flow in rough ducts. Experimental convection coefficients obtained at four desert sites are compared to the analytical relations.

The experimental equipment for measuring the heat transfer convection coefficient between air and ground in a desert environment consists of two electrically heated plates positioned flush with the ground. Measurements of power dissipation and surface temperatures allow direct calculation of the convection coefficient.

The experimental heat transfer results are correlated with micrometeorological models from which a soil roughness height is calculated. This roughness parameter is shown to characterize air flow near the soil surface, and may be significantly different from the roughness parameter ordinarily determined from velocity profiles. A simplified heat transfer correlation is presented for desert surfaces.

Introduction

Due to the recent interest in ecological simulation, heat and mass transfer relations which accurately model the outdoor environment are currently being developed [1].² One of the variables important in these simulations is the soil surface temperature. This, in turn, depends on accurate expressions for convective heat flux in terms of the temperature difference between the soil surface and the air. The meteorological theories and relations developed to date are generally written in terms of the air temperatures and velocities with surface temperature as a parameter. Thus, while these expressions are of value in experimentally evaluating convective heat fluxes, they cannot be used for the prediction purposes.

In this paper, convective heat flux expressions based on the temperature difference between the soil surface and the air are developed and evaluated. The experimental technique used to obtain data for comparison with the model predictions and the results of the experiments are described.

Atmospheric air flow is similar to the fully developed turbulent flow in ducts in many respects. Both flows are highly turbulent in nature and the surfaces are aerodynamically rough. The atmospheric boundary layer is fully developed and the velocity profile does not change in the flow direction. However, in atmospheric flows there is neither a reference velocity nor a physical length pa-

rameter to characterize the flow as there is for internal flows. Thus the conventional Nusselt-Reynolds relations developed for fully developed internal flows are not directly applicable, and new relations must be developed. In order to provide a base for the relations developed in this paper, some of the expressions for velocity profiles and heat flux for both internal and atmospheric flows will be briefly reviewed.

For fully developed turbulent flow in smooth tubes, three regimes exist near the wall: the laminar sublayer, buffer layer, and turbulent core. The overall temperature difference reflects the contribution of the resistance of each layer. The temperature profile above the top of the buffer layer is given by [2]

$$T_0 - T = (q_0 / \rho c_p u_*') [5Pr + 5\ln(5Pr + 1) + 2.5\ln(\frac{u_*' z}{30\nu})] \quad (1)$$

Equation (1) can be rewritten in terms of a Stanton number based on the shear velocity to allow comparison with the atmospheric relations.

$$St = q_0 / [\rho c_p u_*' (T_0 - T)] \\ = 1 / [5Pr + 5\ln(5Pr + 1) + 2.5\ln(\frac{u_*' z}{30\nu})] \quad (2)$$

Equation (2) will be used as a base to compare to the rough tube and atmospheric relations developed later.

The velocity profile for adiabatic atmospheric flow over a rough surface is based on the Rossby modification of the Prandtl mixing length theory and is given by [e.g., 3, 4].

$$(u/u_*') = (1/K)\ln(z/z_0 + 1) \quad (3)$$

¹ Presently at Babcock and Wilcox, Alliance, Ohio.

² Numbers in brackets designate References at end of paper.

Contributed by the Heat Transfer Division for publication in the JOURNAL OF HEAT TRANSFER. Manuscript received by the Heat Transfer Division, April 15, 1974. Paper No. 75-HT-AA.

where z_0 , the roughness height, is a constant of integration and depends on the local surface roughness. The development of equation (3) is based on the assumption that the shear stress is constant with height and equal to the value at the surface. From experiments using pipes roughened with sand grains, z_0 has been found to be related to the size of the roughness elements, ϵ , and is approximately equal to $\epsilon/30$, [3]. Equation (3) is valid when the air temperature is greater than or equal to that at the surface (inversion and adiabatic conditions).

Under conditions of heat transfer from the surface to the air, the velocity profile is distorted due to free convection forces. A measure of the influence of the thermal instability caused by surface heating is the Monin-Obukhov length, defined as

$$L = -\rho c_p u_*^3 T / (K g q_0) \quad (4)$$

where q_0 is positive in the upward direction. For adiabatic ($L = \infty$) and inversion conditions ($L > 0$), the flow is stable and the profile is given by equation (3). Relations describing the resulting profile for lapse conditions ($L < 0$) are discussed in references [4–6].

The differential equations describing the turbulent exchange of momentum and energy can be used to develop a convection heat transfer relation for atmospheric flows. The turbulent transport equations in terms of eddy diffusivities are used to relate heat flux and shear stress

$$q = c_p \tau (\epsilon_h / \epsilon_m) (\partial T / \partial z) / (\partial u / \partial z) \quad (5)$$

Equation (5) is used extensively by meteorologists to compute the convective heat flux. In the atmospheric boundary layers the flow is like Couette flow and both the heat flux and shear stress are constant with height and equal to their values at the surface [3, 4, 7, 8]. In order to evaluate q from equation (5), the partial derivatives are replaced by finite differences. This procedure, while allowing computation of surface heat flux, does not provide a predictive relation for given atmospheric conditions.

In order to provide a predictive relation, equation (5) can be integrated from the surface ($z = 0$) to a reference height ($z = z_r$). In performing the integration, it is assumed that the eddy diffusivity for heat is 1.6 times that for momentum [3, 4] and that the velocity profile is that for adiabatic flows (equation (3)). The result, termed the adiabatic Stanton number, is

$$St_{\text{adiabatic}} = 1.6K / \ln(z_r / z_0 + 1) \quad (6)$$

The extension to nonadiabatic flows has also been carried out by a number of authors (equations (3) and (4)).

The effect of wall roughness on heat transfer in fully developed

turbulent pipe flow has been studied by Dipprey and Sabersky [9] and Owen and Thompson [10]. The theoretical models are based on a detailed picture of assumed flow behavior in the vicinity of the roughness elements. In both of these studies, an expression for a sublayer Stanton number St_s is developed, which is defined in terms of the temperature difference across the sublayer. As shown by Garratt and Hicks [11], the relation developed by Owen and Thompson is adequate for atmospheric flows, and can be written as

$$St_s = 1.61(u_* z_0 / \nu)^{0.45} \quad (7)$$

The sublayer Stanton number is, basically, the reciprocal of the sublayer thermal resistance, and is added in series to the smooth flow thermal resistance to get the overall thermal resistance. The overall Stanton number St_0 is then defined as

$$St_0 = (1/St + 1/St_s)^{-1} = St(1 + St/St_s)^{-1} \quad (8)$$

where St is evaluated from equation (2) or (6) as appropriate. The relative effect of the sublayer resistance will be discussed later.

In order to use these relations for predictive purposes, it is necessary to know the soil surface roughness length z_0 for the particular location. This is usually obtained by fitting velocity profile measurements at several heights to the velocity profile expression. In the experimental work described herein it is demonstrated that for vegetated surfaces the z_0 obtained in this manner does not accurately reflect the convection heat transfer at the ground surface. Thus, z_0 must be obtained from direct measurements of the convective heat flux.

In previous studies, the convective heat flux has been experimentally determined using several methods. Overall energy balances have been used, and, alternatively, equation (5) has been combined with measured temperature and velocity differences. In this paper, a third method of experimentally determining the convective heat flux is presented. The power dissipation from two electrically heated plates positioned flush with the ground is measured and combined with measurements of plate temperature to directly evaluate the surface convection coefficient. The convective heat flux is then computed using this convection coefficient and the measured temperature difference between the soil surface and the air. As discussed later, this procedure provides a direct measurement of the convection heat transfer, and may be more accurate than that obtained from the other techniques.

Experimental Equipment

A cross-sectional view of the experimental equipment is shown

Nomenclature

c_p = specific heat	q_{conv} = convection heat flow	
g = acceleration due to gravity	q_{cond} = conduction heat flow	
h = convection heat transfer coefficient	$q_{\text{l.w.,net}}$ = net longwave radiation heat flow	z_r = reference height
\bar{h} = average experimental convection coefficient	q_{sol} = solar energy absorbed by convection plate	z_0 = soil surface roughness height
h_{mean} = mean experimental convection coefficient	q_{stor} = heat stored in convection plate	Δx = conduction flow path
K = Karman constant (0.4)	St = Stanton number, $\bar{h} / (\rho c_p u_*)$	Δ = thermal boundary layer thickness
k = thermal conductivity	t = time	Δ_2 = enthalpy thickness
L = Monin-Obukhov length, equation (4)	T = air temperature at any height z	ϵ = average height of roughness elements; also long wavelength emissivity of convection plate
m = mass of convection plate	T_r = air temperature at height z_r	ϵ_h = eddy diffusivity for heat
P = electric power dissipation per unit area	T_b = temperature at bottom of convection box	ϵ_m = eddy diffusivity for momentum
Pr = Prandtl number	T_0 = surface temperature	ν = air kinematic viscosity
q = heat flux	u = air velocity at any height z	ρ = density of air
q_0 = soil surface convection heat flow	u_* = shear velocity, $\sqrt{\tau_0 / \rho}$	σ = Stephan-Boltzmann constant
	X = plate length	τ_0 = surface shear stress
	z = height above the ground surface	τ = shear stress at any height z

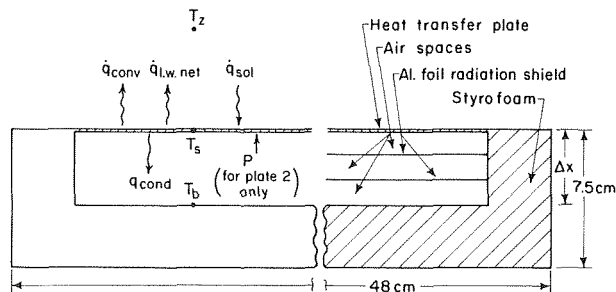


Fig. 1 Schematic of convection box and heat flows

on the right-hand side of Fig. 1. Each of the two convection boxes consists of three essential parts: the heat transfer plate, Styrofoam insulation and radiation shields. The heat transfer plate is 30 cm square and is housed in a Styrofoam container 48 cm square by 7.5 cm deep. Each heat transfer plate consists of an electric heater, copper-constantan thermocouples and a heat transfer surface. The electric heater is made from aluminum foil cut in the form of a continuous strip and is bonded with epoxy to the aluminum foil heat transfer surface. Four thermocouples are embedded in the epoxy between the surface and the heater at different locations in order to determine the average plate temperature. The aluminum foil radiation shields minimize the radiant and convective heat transfer between the back of the heat transfer surface and the styrofoam insulation.

The left side of Fig. 1 is a schematic of the heat flows for the two convection boxes. Plate 2 is heated electrically with a constant power P , while Plate 1 is unheated. The energy balance for Plate 1 is

$$q_{sol,1} - q_{l.w.,net,1} - q_{cond,1} - q_{conv,1} = q_{stor,1} \quad (9)$$

where heat flow to the plate is positive. The energy balance for Plate 2 is

$$P + q_{sol,2} - q_{l.w.,net,2} - q_{cond,2} - q_{conv,2} = q_{stor,2} \quad (10)$$

Both plates are constructed of the same material and the thermal and radiative properties of the two convection boxes are assumed to be the same. It is also assumed that equal amounts of solar radiation are incident on each plate, that conduction between the plate and the Styrofoam is one-dimensional and that the convection coefficients and heat capacities of the two plates are the same. Equation (9) is subtracted from equation (10) and expressions for the various heat fluxes in terms of temperatures and thermal properties are substituted. The resultant equation is solved for the convection coefficient

$$h = \frac{P}{(T_{02} - T_{01})} - \frac{k_{air}}{\Delta x} \left(1 - \frac{T_{b2} - T_{b1}}{T_{02} - T_{01}}\right) - \epsilon \sigma \frac{(T_{02}^4 - T_{01}^4)}{(T_{02} - T_{01})} - \frac{(mc_p)_{plate}}{(T_{02} - T_{01})} \frac{d(T_{02} - T_{01})}{dt} \quad (11)$$

Equation (11) can be simplified for small temperature differences, $T_{02} - T_{01}$, by linearizing the radiation term. The convection coefficient is then given by

$$h = \frac{P}{\Delta T_0} - \frac{k_{air}}{\Delta x} \left(1 - \frac{\Delta T_b}{\Delta T_0}\right) - 4\epsilon \sigma T_{01}^3 - \frac{(mc_p)_{plate}}{\Delta T_0} \frac{d(\Delta T_0)}{dt} \quad (12)$$

where $\Delta T = (T_{02} - T_{01})$ and $\Delta T_b = (T_{b2} - T_{b1})$.

Experiments and calculations have shown that over a five min time period (the minimum test time) the energy storage term in equation (12) is less than 2 percent of the value of $P/\Delta T_0$ and can be neglected. Experiments under normal operating conditions have shown that the other loss terms vary from 1.0 to 1.4W/m²C

with an average value of 1.2W/m²C. The error introduced by using the average value is dependent on the magnitude of $P/\Delta T_0$, but is usually less than 2 percent. Equation (12) then reduces to

$$h = P/\Delta T_0 - 1.2W/m^2C \quad (13)$$

If it is assumed that the measurement errors in P and ΔT_0 are 5 percent and 2 percent, respectively, then, based on the above information, the uncertainty in h for nominal conditions is ± 10 percent.

Experimental Procedure

In field tests the convection boxes are buried so that the plate surface is flush with the surrounding ground. Also, the convection boxes are placed near each other and aligned such that a line drawn between the centers of the boxes is perpendicular to the estimated mean direction of the air flow. Placement of the boxes in this manner increases the probability that the assumption of equal convection coefficients is valid. If the boxes were aligned parallel to the air flow, changes in wind speed would always be "seen" by one plate before the other.

Electric power is supplied to one of the plates using a 6 V d-c battery and is calculated from the heating element resistance and the measure voltage difference. The eight thermocouples in the two plates are connected to form a thermopile which allows an accurate measurement of the average plate temperature difference, ΔT_0 . The thermopile output is measured continuously by using a millivolt recorder. A cup anemometer mounted at a reference height is used to determine the average wind velocity over the time of the test period. The reference height is unspecified and could be any reasonable height. However, over short time periods the wind velocity at heights of 2 m or greater can be essentially uncoupled from the air flow near the ground and the convection heat flow at the ground surface. For this reason a reference height of 0.4 m or less was chosen for all experiments.

Two convection coefficients can be calculated from the data. An average convection coefficient, \bar{h} , is based on the average temperature difference, ΔT_0 , over any time period. The mean convection coefficient, h_{mean} , is calculated by averaging the instantaneous value of the convection coefficient over the same time period. Both methods have been employed using a time period of five min and the differences between \bar{h} and h_{mean} were less than 2 percent. The average convection coefficient is presented in the section on experimental results.

Results and Discussion

Experiments using the convection boxes were performed on desert sites at Kelso, California; Rock Valley, Nevada; Tucson, Arizona; and Spring Green, Wisconsin. The vegetation at Kelso and Rock Valley was sparse and ranged in height to 2 m and 0.6 m respectively, while the vegetation at Tucson was dense and ranged in height to 4 m. The Spring Green site consisted of a barren sandy area with essentially no vegetation situated in a prairie. In addition to the convection box measurements described previously, hourly measurements of incident solar radiation, and temperatures down to 0.6 m in the soil and up to 2 m in the air were recorded. Velocity profiles were determined using seven cup anemometers mounted at heights from 0.2 to 2 m [12].

In addition to the data obtained in these convection experiments, the extensive data of Sellers and Dryden [13] were used to provide an independent check on the accuracy of the convection box results. The test site used by Sellers and Dryden was located in the desert near Tucson and the data were recorded during climatic conditions similar to the present tests. The data include one-half hr averaged measurements of convective heat flux, surface temperature, and air velocity and temperature at a height of 0.67 m.

The value of the roughness height z_0 was determined using equation (6) together with the experimental values of reference

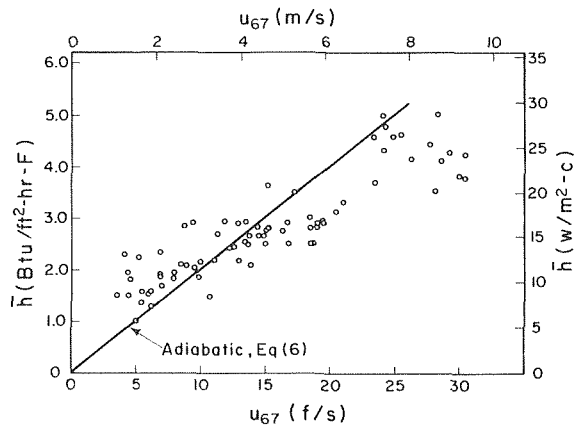


Fig. 2 Heat transfer coefficient as a function of the velocity at 67 cm for data of Sellers and Dryden [13]

height, air temperature, air velocity, and soil surface temperature. For each site, the experimental and calculated convection coefficients were compared for each set of measurements to determine z_0 . An average z_0 for the particular site was then obtained.

In Figs. 2 and 3 the convection coefficients for the data of Sellers and Dryden [13] and for Tucson, respectively, are plotted as a function of the air velocity measured at the reference height. Also shown is the theoretical relation for neutral conditions. As can be seen from comparing Figs. 2 and 3, the data from the two different types of experiments are very similar in magnitude, in velocity dependence and in scatter about the theoretical relation. Thus, the present technique produces experimental results similar in character to those obtained from the direct (energy balance) measurements of Sellers and Dryden.

The values of z_0 obtained from the foregoing method of analysis are 0.02 cm for Tucson and Kelso, and 0.01 cm for Spring Green, Rock Valley, and the site of Sellers and Dryden. Sellers and Dryden report a value for z_0 at their site of 0.0134 cm, which was determined by fitting experimental velocities measured during neutral conditions with the profile given by equation (3). The lack of vegetation at their site means that the z_0 determined from the velocity profiles is representative of the surface roughness. This agreement between the two determinations of z_0 for the data of Sellers and Dryden, and the general agreement between the values of z_0 for the different sites further substantiates the validity of the convection box technique.

The two plate temperatures differ slightly (less than 2°C) from that of the surrounding desert surface due to differences in solar

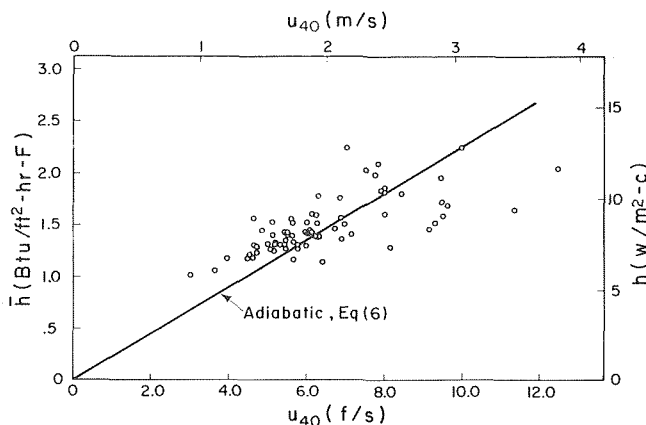


Fig. 3 Heat transfer coefficient as a function of the velocity at 40 cm for Tucson

properties and the electrical heating. There is, then a thermal starting length effect in which the experimentally determined heat transfer coefficient is different from that for the surrounding surface. In order to estimate the magnitude of this effect, an integral analysis was performed to determine the variation of Stanton number with flow length.

The integral energy equation for a hydrodynamically fully established flow with constant fluid properties is [2].

$$St_x = q_0 / [\rho c_p u_* (T_0 - T_\Delta)] = d\Delta_2 / dx \quad (14)$$

where St_x is the local Stanton number. The enthalpy thickness Δ_2 is given by

$$\Delta_2 = \int_0^\Delta (u/u_*) [1 - (T_0 - T)/(T_0 - T_\Delta)] dz \quad (15)$$

In the analysis, it is assumed that the velocity profile near the surface is adequately represented by the adiabatic profile, equation (3). The analogy between heat and momentum transfer is assumed to hold so that the temperature profile may be represented by

$$(T_0 - T)/(T_0 - T_\Delta) = \frac{\ln(z/z_0 + 1)}{\ln(\Delta/z_0 + 1)} \quad (16)$$

Equation (14) was solved for Δ as a function of distance using equations (3), (15), and (16). The local Stanton number St_x was then determined, and the average Stanton number \bar{St} over the length of the plate X determined by the integration

$$\bar{St} = \int_0^1 St_x d(x/X) \quad (17)$$

The average Stanton number is plotted as a function of distance in Fig. 4 for $z_0 = 0.01$ cm and $z_r = 40$ cm. This result demonstrates that the starting length is short (less than about 0.05 m), and that the starting length effect on the heat transfer coefficient is on the order of 10 percent for the 0.3 m plate. This effect is within the accuracy of the tests.

There are several reasons why the analysis can only indicate the magnitude of the starting length effect. The basic formulation of the problem assumes that the thermal boundary layer develops in a conventional manner, and thus the integral analysis Stanton number continually decreases with flow length. Accepted meteorological theory shows that the flow is fully established, like tube flow, and that the transport mechanism across the boundary layer is conduction. The Stanton number is then, in reality, constant with length. Thus, unless the entire flow field is modeled, the integral analysis can indicate only a relative influence of the starting length effect.

A second point of concern is the possibility that the velocity profile may change shape due to the change in surface roughness. There is probably a simultaneous hydrodynamic and thermal development over the aluminum plate. The problem of a developing

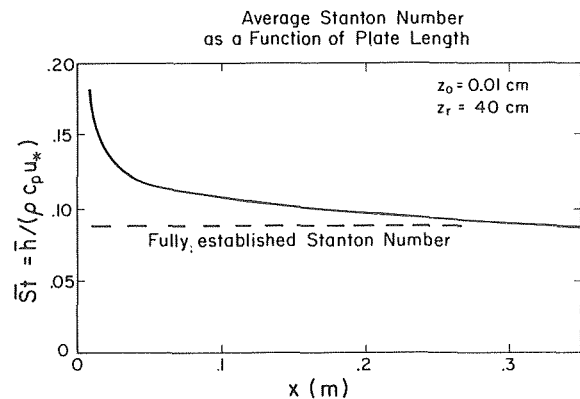


Fig. 4 Average Stanton number as a function of flow length based on an integral analysis

velocity profile is currently receiving some attention in the meteorological field, but the results are inconclusive at present.

The integral analysis demonstrates that the starting length and change in surface roughness effects are probably small. Further confirmation that the effect of a change in surface roughness is small was obtained during testing at Kelso. A uniform layer of sand was sprinkled over both convection plate surfaces. The heat transfer data for these tests are indistinguishable within the scatter of the data from experiments with the aluminum surfaces clear of sand. These results help substantiate that the convection box technique is valid for determining heat transfer coefficients.

The velocity profile measurements recorded at each site were also used to evaluate z_0 . However in the presence of both large (vegetation) and small (sand) roughness elements, the local shear stress and thus the calculated value of z_0 is a function of height [14]. For the Tucson and Rock Valley sites, the least-squares estimates of z_0 made using the anemometer measurements are 0.46 cm and 3.3. cm, respectively [12]. The corresponding values from the heat transfer experiments are 0.02 cm and 0.01 cm, respectively. These differences in z_0 between the heat transfer experiments and the velocity measurements reflect the distortion of the velocity profile by the vegetation. This demonstrates that the roughness length obtained using velocity profile measurements may not be useful in the calculation of heat transfer.

The effect of thermal stability on heat transfer can also be determined by representing the data in nondimensional form. In Figs. 5 and 6 the Stanton number is presented as a function of z_r/L for the sites with a z_0 of 0.01 cm and 0.02 cm, respectively. It is seen that the data are correlated within a scatter of about ± 20 percent on this basis, and that the data for different sites but with the same z_0 are also correlated. The data from the present tests represent a minimum test time of five min while the data of Sellers and Dryden represent one half hr test periods. The scatter of the present data is comparable to that found in the literature [e.g., 3] and is reduced if the data are averaged over a longer time period.

It is also apparent that the Stanton number is a weak function of instability, (z_r/L), and can be approximated by a linear relationship. A satisfactory fit to the data in Figs. 5 and 6 is

$$St = (1 + 0.1z_r/L)St_{\text{adiabatic}} \quad (18)$$

Equation (18) also indicates the relative importance of the physical parameters z_0 , z_r , and L . The heat transfer coefficient is primarily governed by the soil roughness height, while the degree of instability (the magnitude of z_r/L) primarily affects the coupling between the events at the surface and at the reference height.

The effect of surface roughness on the heat transfer is shown in Fig. 7, where the heat transfer coefficient is plotted as a function of shear velocity using the smooth tube relation equation (2), the micrometeorological flow relation equation (6), and micrometeorological flow including the roughness effect, equation (9) where appropriate, it is assumed that the reference height is 0.4 m, the eddy diffusivity ratio is 1.6 z_0 is 0.01 cm, and the adiabatic profile, equation (3), is valid. The smooth tube relation gives lower results than the wholly rough relations but by only about 25 percent. The data are skewed about these two analytical results with a spread on the order of ± 15 percent. The inclusion of the sublayer roughness effect increases the accuracy of the correlation.

The development of the theoretical relations has assumed that the flow is fully rough: i.e., $z_0 u_* / \nu$ is greater than 2.5 [3]. For a roughness height of 0.01 cm, the air flow is fully rough if the value of u_* is greater than about 0.43 m/s, corresponding to a velocity at 0.4 m of greater than about 8.5 m/s. Conversely, for smooth flow to exist, u_* must be less than about 0.03 m/s with a corresponding velocity at 0.4 m of less than about 0.6 m/s. Thus, most of the data presented here as well as that of Sellers and Dryden [13] lies in the transition range between smooth and wholly rough flow. This may possibly help explain the lack of agreement between the data and the theoretical relations.

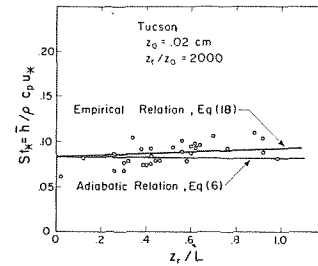


Fig. 5 Stanton number as a function of nondimensional height for Tucson

Conclusions

Based on the results of this study, the following conclusions can be drawn.

1 Relationships for convection heat transfer coefficients from sparsely vegetated surfaces can be developed in terms of the temperature difference between the soil surface and the air at some height. The parameter required for this calculation is the surface roughness height z_0 . The variables required are the air velocity and temperature at a reference height and the soil surface temperature.

2 The formulation for a convection heat transfer coefficient that appears to best represent the data combines the thermal resistance due to roughness elements with the thermal resistance due to the atmospheric flow. The overall Stanton number can be calculated from equation (8), with the sublayer Stanton number calculated from equation (7). The atmospheric flow Stanton number for both adiabatic and lapse conditions can best be represented by equation (18).

3 For surfaces with large roughness elements (e.g., sparse vegetation on a desert), the roughness height z_0 as determined by velocity profile measurements does not characterize the heat transfer from the bare surface.

Acknowledgment

The authors would like to acknowledge the financial support of the University of Wisconsin Department of Mechanical Engineering, the Engineering Experiment Station and the Wisconsin Alumni Research Foundation. The assistance of the Desert Biome Group of the International Biological Program (IBP) is appreciated. Portions of this research were also supported by NSF Grant GB-31043.

References

- Beckman, W. A., Mitchell, J. W., and Porter, W. P., "Thermal Model for Prediction of a Desert Iguana's Daily and Seasonal Procedure," JOURNAL OF HEAT TRANSFER, TRANS. ASME, Series C, Vol. 95, No. 2, May 1973, pp. 257-262.
- Kays, W. M., *Convective Heat and Mass Transfer*, McGraw-Hill,

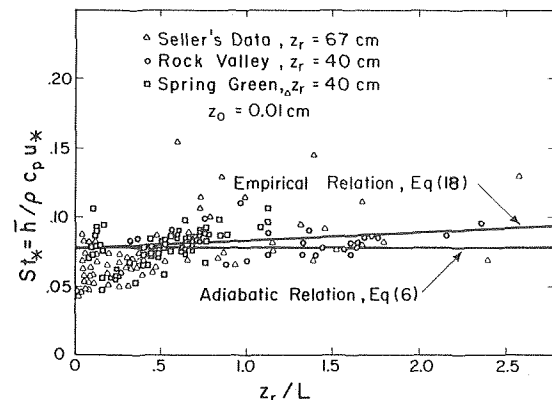


Fig. 6 Stanton number as a function of nondimensional height for Rock Valley, Spring Green, and data of Sellers and Dryden [13]

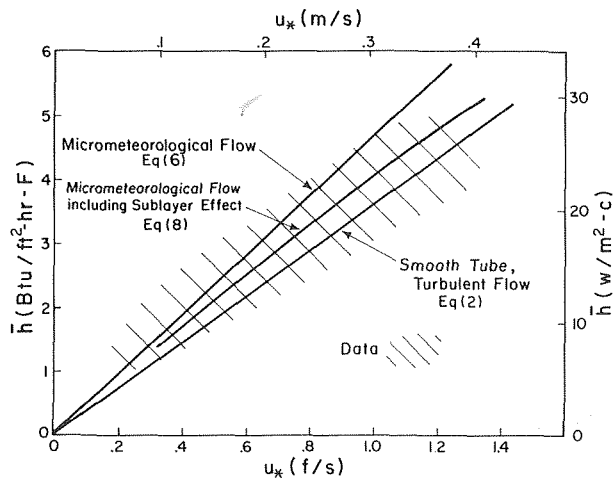


Fig. 7 Analytical expressions for heat transfer coefficient as a function of shear velocity in comparison with data

New York, 1966.

3 Sutton, O. G., *Micrometeorology*, McGraw Hill, New York, 1953, pp.

77-83.

4 Webb, E. K., "Aerial Microclimate," *Meteorological Monographs*, Vol. 6 No. 28 Chapter 2, 1965, pp. 27-58.

5 Lumley, J. L., and Panofsky, H. A., *The Structure of Atmospheric Turbulence*, Wiley, New York, 1964, pp. 102-107.

6 Fleagle, R. G. and Businger, J. A., *An Introduction to Atmospheric Physics*, New York, 1963, pp. 187-205.

7 *Exploring the Atmosphere's First Mile*, Pergamon Press, New York, Lettau, H. H. and Davidson, B., eds., Vol. 1, 1957, p. 307.

8 Sellers, W. D., *Physical Climatology*, The University of Chicago Press, 1965, p. 152-154.

9 Dipprey, D. F. and Sabersky, R. H., "Heat and Momentum Transfer in Smooth and Rough Tubes at Various Prandtl Numbers," *International Journal of Heat and Mass Transfer*, Vol. 6, May 1963, pp. 329-353.

10 Owen, P. R., and Thomson, W. R., "Heat Transfer Across Rough Surfaces," *Journal of Fluid Mechanics*, Vol. 15, Mar. 1963, pp. 321-334.

11 Garratt, J. R., and Hicks, B. B., "Momentum, Heat and Water Vapour Transfer to and From Natural and Artificial Surfaces," *Q. J. Royal Meteor. Soc.* Vol. 99, 1973, pp. 680-687.

12 Mitchell, J. W., Beckman, W. A., Bailey, R. T., and Porter, W. P., "Microclimate Modeling of the Desert," Presented at the International Seminar on Heat and Mass Transfer in the Environment of Vegetation, Dubrovnik, Yugoslavia, Aug. 1974.

13 Sellers, W. D., and Dryden, P. S., "An Investigation of Heat Transfer From Bare Soil," Final Rept. DA-AMC-28-043-66-627, University of Arizona, Inst. of Atmospheric Physics, Dec. 1965.

14 Marshall, J. K., "Drag Measurements in Roughness Arrays of Varying Density and Distribution," *Agric. Met.*, Vol. 8, 1971, pp. 269-292.

E. G. Plett
A. C. Alkidas
R. E. Shrader
M. Summerfield

Guggenheim Aerospace Propulsion
Laboratories,
Aerospace and Mechanical Sciences Department,
Princeton University,
Princeton, N. J.

Erosion of Metals by High Pressure Combustion Gases: Inert and Reactive Erosion

An experimental and theoretical investigation of the erosion of various metals by high temperature, high pressure flows of combustion gases is described. The erosion process was categorized as either inert or a combination of inert and reactive erosion. Experimental results indicated the existence of two thresholds, the first represents the onset of erosion and the second the transition from purely inert to inert plus reactive erosion. Inert erosion was modeled by means of the melt and wipe-off theory. Experimental results are presented to demonstrate various erosion regimes and to identify the conditions for inert and reactive erosion.

1 Introduction

The thermal erosion process of metals can be classified into two categories with respect to the magnitude of reactivity of the metal with the oxidizing atmosphere; namely, inert and reactive erosion. In the first category, the erosion is purely a melting process, whereas in the second category, which represents a much more complex process, the metal is chemically attacked by the hot gases. This chemical attack may occur prior to melting in the form of surface reactions, or in the form of gaseous reactions after inert melting and evaporation of the melt. Metals in general have large heats of reaction, a property that has been used advantageously in the propulsion field, (aluminized propellants). Consequently, if the conditions in the erosion process are such as to promote combustion of the metal with the neighboring gas, then the reactive erosion can become catastrophic, since a large amount of the heat generated by the combustion process returns to the gas-solid interface, severely augmenting the amount of erosion.

This paper presents an experimental and analytical study of the thermal erosion of various metals by high temperature, high pressure combustion gases. In the experimental investigation, solid propellant combustion products were used as the high temperature source. The theoretical analysis is confined to the case of inert erosion which was modeled as a melt and wipe-off process, i.e., when

the temperature at the gas-solid interface reaches the melting (solidus) temperature of the metal, and melting of the metal occurs, the melt is removed by the shearing forces of the convective flow of the gas over the surface.

In addition to inert and reactive erosion, there exists a third possible process that may cause erosion of metals in a high temperature environment. This erosion process which can be included within the sphere of influence of heat transfer will be termed thermo-mechanical erosion. In this case, the erosion of the metal surface is attributed to the decrease of the yield strength of the material as a result of the increase of the temperature of the metal due to heating by the gas. The frictional aerodynamic forces acting on the surface of the metal succeed in removing the weakened parts of the metal, which are then carried away by the gaseous stream. Although the removal of mass due to thermo-mechanical erosion may be important in very high-speed flows where the aerodynamic forces are of considerable magnitude, in the experiments undertaken in the present investigation, it proved to be unimportant. The proof lies mainly in the successful prediction of the onset of erosion by the melt and wipe-off theory (MWO) presented later in the paper, and in the appearance of spherical metal particles on a plate placed in front of the eroding orifice (the particles appeared to have been molten and resolidified on the plate), as well as the spectroscopic evidence of metal combustion in the case of reactive erosion.

2 Related Literature

The erosion of metals for such applications as rocket nozzles, gas turbine blades, or gun tubes has been the subject of various investigations. A review of representative literature of this type is given in reference [1].² None of the previous studies investigated the ero-

¹ Based on work performed under contract DAAG46-72-C-0078 issued by the U. S. Army Materials and Mechanics Research Center, Watertown, Mass., and under contract DAAA-25-71-C0109, issued by the U. S. Army, Frankford Arsenal, Philadelphia, Pa.

Contributed by the Heat Transfer Division for publication in the JOURNAL OF HEAT TRANSFER. Manuscript received by the Heat Transfer Division May 2, 1974. Paper No. 75-HT-M.

² Numbers in brackets designate References at end of paper.

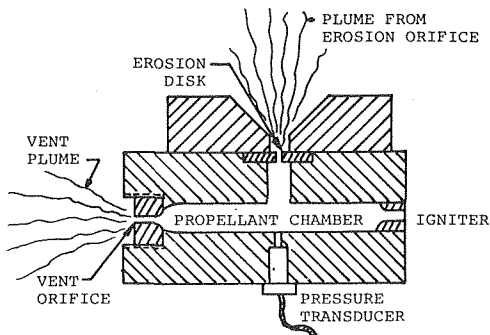


Fig. 1 Schematic of the combustion chamber used for erosion experiments

sive nature of aluminum, as was done in the study being reported herein.

Vieille [2] measured the erosion of pure metals and alloys in the form of vent plugs fitted to a closed chamber. Gunpowder was used to provide the high temperature erosion gases. His conclusion was that erosion is a function of the melting point of the material; the higher the melting point the smaller the erosion. This simple conclusion is not necessarily true. In the case of brass, although its melting temperature is about 800°K less than that of titanium, brass exhibits a much greater resistance to erosion. The magnitude of the inert erosion is controlled not only by the melting temperature but by other thermal properties such as the thermal conductivity, specific heat, and density. At the same time, we must keep in mind that erosion may occur by heterogeneous reactions prior to melting. A simple criterion for erosion resistance is given in the Results and Discussion Section of this paper.

Several analytical investigations have been reported on the ablation problem which are related to our melt and wipe-off model. In the case of a semi-infinite slab, solutions were obtained numerically by Landau [3], and by means of an integral approach by Goodman [4]. Citron [5] devised a successive-approximation method to solve the finite thickness slab case. An implicit numerical technique was used by Dewey, et al. [6] to solve the moving boundary problem in cylindrical coordinates. Explicit numerical techniques for moving boundary problems have been developed by Crank [7] and Murray and Landis [8].

3 Experimental Apparatus

A schematic representation of the vented-combustor erosion test apparatus is shown in Fig. 1. It consists of a small combustion chamber into which a pre-weighed amount of propellant is placed, a steel vent orifice, a pre-drilled test disk serving as the test orifice, a pressure transducer, and an ignition mechanism. The rapid burning of the propellant powder in the combustor generates a supply of hot, high pressure propellant gas. For a given propellant loading, the pressure-time curve is controlled by the flow through the vent orifice whose initial area is about 20 times the area of the

test orifice. When extremely large erosion rates are experienced, the test orifice may become as large as the vent orifice during the experiment. Thus, the erosion process produces secondary effects in the combustor.

The propellant used for this study was IMR-4198 which has an isochoric flame temperature of about 3000°K. The composition of the propellant and products of combustion are as follows:

Propellant composition (average)

93 percent Nitrocellulose (13.37 percent N)
6 percent Dinitrotoluene
0.7 percent Diphenylamine
0.3 percent Graphite
0.1-1 percent Potassium Sulphate
0.1 percent Dust and Foreign matter

Product composition (at 3000°K)

45.6 percent CO
10.2 percent CO ₂
12.4 percent H ₂
19.6 percent H ₂ O
11.4 percent N ₂

The combustor chamber conditions are pulse-like transients as indicated by a typical experimental pressure-time trace shown in Fig. 2(a). Due to the transient nature of the flow, the combustor peak pressure has been used as the parameter representing the gaseous condition. This is a logical choice, because the temperature of the combustion products in the chamber is approximately equal to the isochoric flame temperature of the powder propellant, independent of pressure until the burning is completed, then decreases slightly with the mass efflux from the chamber, Fig 2(b). The pressure histories of the various firings are roughly similar. In addition, the total mass flow through the orifice, and hence the density averaged over the flow time (heat transfer rate is density dependent through the Reynolds number scaling), is proportional to the total mass in the chamber which is proportional to the peak pressure and temperature attained. Since the temperature and pressure histories are approximately the same for each firing, peak pressure is the only independent variable.

Repeatability of the pressure peak is better than 95 percent. That is, successive firings with identical initial conditions produce less than 5 percent deviation in the peak pressure, for pressures above 200 MN/M². Below this, the loading density of the chamber is too low to ensure as good repeatability. In each case, however, the measured peak pressure was used to correlate data. An approximate relationship between mass of propellant and peak pressure can be obtained by comparing the upper and lower horizontal scales of Fig. 6.

Enlargement of the orifice and/or mass loss of the test disk indicates erosion of the test sample by the hot gas. In addition to the mass loss and change of diameter of the test orifice, which were carefully noted for each test, the nature of the erosion was noted, as to whether the leading edge of the orifice was most severely eroded as expected on the basis of boundary layer inert heating, or whether the trailing edge region was enlarged over that further upstream, suggesting possible additional heat input from chemical

Nomenclature

h = convective heat transfer coefficient	face	ΔM_m = mass melted during time interval Δt
h_{te} = effective convective coefficient	r_o = initial radius of orifice	Δr_s = increase in orifice radius due to metal removal
k = thermal conductivity	Re = Reynolds number	ρ_s = density of solid phase
l = thickness of the test disk	t = time	
m = mass	T = temperature	
Nu = Nusselt number	T_m = melting or solidus temperature	Subscripts
Pr = Prandtl number	α = thermal diffusivity	s = test disk conditions (solid phase)
q_w = test orifice surface heat flux	β = defined in text following equation (4)	t = test orifice conditions (gaseous phase)
r = radial coordinate		0 = initial conditions
r_s = radial position of gas-solid inter-	ΔH_m = heat of melting	

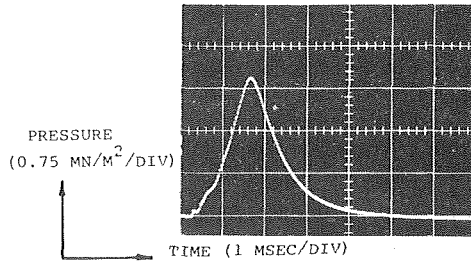


Fig. 2(a) Oscilloscope trace showing the measured pressure variation with time during an erosion firing

reactions in the boundary layer.

4 Analysis

To evaluate the experimental results obtained from the erosion tests described in the previous section, theoretical predictions of the following physical processes must be obtained: (a) The combustion of the propellant in the combustor that results in the production of high pressure, high temperature gas, coupled with the gas outflow through the vent and test orifices, (b) The heating and subsequent erosion of the test orifice by the stream of hot gases flowing through it. Although these processes are interrelated, they were treated separately for the purpose of focusing on the physics governing the individual processes.

Since the main theme of this paper relates to the erosion of metals by the hot propellant gases, the analysis which was used to calculate the conditions in the combustor will not be dealt with. Suffice it to say that the pressure-time history was calculated using a simple model for the burning process. The agreement between predicted and measured pressure-time histories was found to be very good when the calculated erosion agreed with the observed erosion, but deviations were found to be significant if the actual erosion, which enlarges the passage for the escaping gases, was much larger than the predicted erosion; in such cases, the measured pressure declined more rapidly than the predicted pressure. Included in this calculation scheme was a prediction of the gas temperature history which, together with the pressure, is needed for the convective heat transfer calculations.

Heat Transfer Calculations. In the present formulation, only the inert thermal erosion process will be considered. The time duration can be divided into two periods: heating period and melting period. The heating period starts at the beginning of the flow and ends when the surface temperature of the solid reaches its melting (solidus) temperature. During this period, heat is convected to the solid solely to raise its temperature. During the melting period, which continues as long as the rate of heat input from the gas is greater than the rate of conduction into the solid, the difference between the heat transfer to the solid surface and the heat transfer to the interior of the solid is used to melt a portion of the solid.

The principal assumption used in the mathematical formulation is that the melt is completely removed (wiped-off) by the aerodynamic forces of the high speed flow as soon as it forms. Consequently, the receding surface remains at the melting temperature of the substance under consideration. The convective heat flux to the solid surface was calculated using the empirical correlation of a turbulent boundary layer flow over a flat plate. The effect of cur-

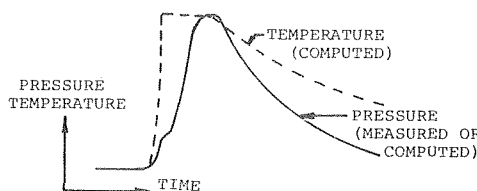


Fig. 2(b) Sketch of approximate relationship between pressure and temperature as they vary with time during an experiment

vature on the boundary layer heat transfer was neglected because the calculated maximum boundary layer displacement thickness was much smaller than the radius of curvature of the orifice. For radial one-dimensional calculations, the average convective coefficient along the length of the orifice was utilized. The effects of mass transfer and radiation were neglected. The thermal properties of the solid material were assumed to be independent of temperature. In the heat transfer calculations, the properties of the gas were evaluated at the film temperature. Finally, the Prandtl number was assumed constant, whereas the coefficient of viscosity was scaled according to the Sutherland formula.

The Fourier equation of heat conduction in cylindrical coordinates was used to compute temperatures in the solid [9]

$$\frac{\partial T_s}{\partial t} = \alpha_s \left[\frac{\partial^2 T_s}{\partial r^2} + \frac{1}{r} \frac{\partial T_s}{\partial r} \right] \quad (1)$$

The initial condition was:

$$T_s(0, r) = T_0 = \text{constant} \quad (2)$$

If t_m denotes the time required for the surface of the metal to reach its melting temperature, during the heating period ($0 \leq t < t_m$) the boundary conditions are:

$$\left. \begin{aligned} -k_s \frac{\partial T_s}{\partial r}(t, r_0) &= q_w = h_{te}(T_t - T_{aw}) \\ T_s(t, \infty) &= T_0 \end{aligned} \right\} \quad (3)$$

and

For high speed flows, the adiabatic wall temperature was substituted [9] for the wall temperature in the convective heat transfer relation, as indicated here.

The convective heat transfer coefficient, h_t , was obtained from the following empirical nondimensional heat transfer relation for turbulent flow over a flat plate [9]

$$\text{Nu} = 0.037 (\text{Pr})^{1/3} (\text{Re})^{0.8} \quad (4)$$

where

$$h_{te} = \beta h_t = \beta \text{Nu} \cdot k/l$$

Although the boundary layer is thin compared to the hole diameter for most cases, the surfaces of the erosion holes are not expected to be as smooth as required to allow the strict application of equation (4), especially after erosion begins; the factor β was introduced to correct for such nonideal flat plate behavior. An appropriate value for β was arrived at by adjusting its value until predicted results agreed with experiment for a metal such as brass which will not burn. This same value of β was then used to determine the regime of inert vs reactive erosion of aluminum, as will be discussed later. A typical value of $\beta = 1.25$ was found to correlate results. During the melting period ($t \geq t_m$), the boundary conditions are:

$$\left. \begin{aligned} T_s(t, r_s) &= T_m \\ T_s(t, \infty) &= T_0 \end{aligned} \right\} \quad (5)$$

where r_s denotes the instantaneous position of the gas-solid interface. The rate of surface regression dr_s/dt , is obtained from an energy balance of the moving boundary, i.e.,

$$q_w = \rho_s \Delta H_m \frac{dr_s}{dt} - k_s \frac{\partial T_s}{\partial r}(t, r_s) \quad (6)$$

The boundary conditions given by equation (3) again apply after the pressure and temperature of the hot gas have dropped below the values needed to sustain the surface at its solidus temperature.

Numerical Solution. The equations were solved numerically using a forward difference in time technique. The numerical solutions of the heat conduction equation under various boundary conditions have been well studied [10]. In this investigation, an explicit numerical scheme was used. Due to the regressing surface, the nodes were shifted between succeeding time steps, by an amount corresponding to the change of radius of the gas-solid interface.

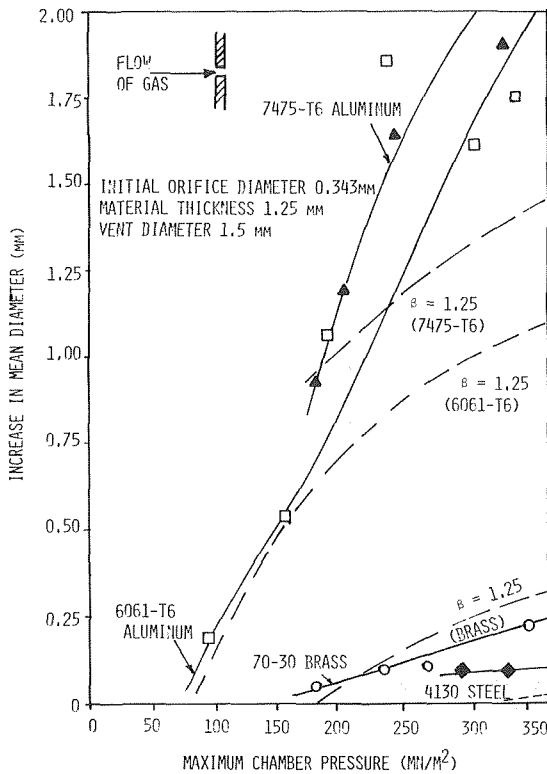


Fig. 3 Comparison of measured erosion with predicted amount, based on melt and wipe-off model, for 7475-T6 and 6061-T6 aluminum, 70-30 brass and 4130 steel.

The change of radius of the interface is

$$\Delta r_s = \Delta M_m / 2\pi\rho_s r_s \quad (7)$$

where ΔM_m is the amount melted during the time interval Δt , r_s is the radius of the orifice during this time interval and ρ_s is the density of the solid material. To allow for the temperature gradient in the solid, the temperature at each node must be changed as it is shifted in space, to correspond to its new location. For a general point being moved outward by Δr_s , using linear interpolation, the corrected temperature $T_{r+\Delta r_s}$ becomes

$$T_{r+\Delta r_s} = T_r + (T_{r+\Delta r} - T_{r-\Delta r}) \frac{\Delta r_s}{2\Delta r}$$

This shifting procedure is applicable only for an infinite system, as in the present case. Similar schemes could be used for a slab of finite thickness.

5 Results and Discussion

Comparison of Numerical and Experimental Results. Erosion data obtained for various metals are shown in Figs. 3 and 4 along with the theoretical MWO curves. For aluminum alloys, data fall within the MWO range at lower pressures (inert erosion) but exceed the theoretical prediction for peak pressures above 160. MN/m² (reactive erosion). The mechanical strength of the metal is not a dominant factor in the erosion process as shown from a comparison of the two aluminum alloys 7475-T6 and 6061-T6. The 7000 series aluminum alloy is of superior strength. The measured erosion of steel and brass fall close to the numerical results indicating inert erosion. (It was on the basis of this agreement that $\beta = 1.25$ was adopted.)

Fig. 4 shows data for the erosion of two titanium alloys. With Ti-6-4, the erosion apparently begins when predicted by the MWO theory, but immediately exceeds the amount predicted. Similarly with Ti-65A, below about 150. MN/m² firing pressure, no appreciable erosion is predicted or observed. Abruptly at slightly higher peak pressures, the observed erosion exceeds by far the predicted erosion, based on melting only. It seems, therefore, that the excess

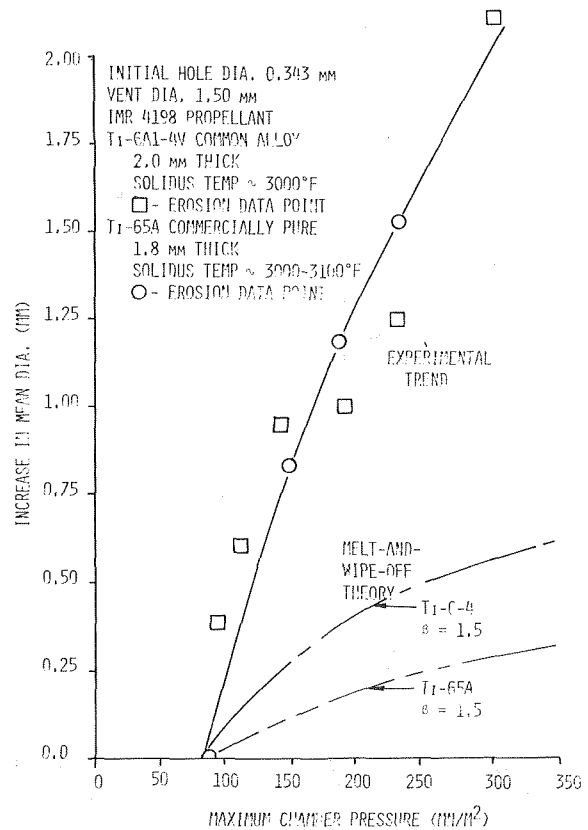


Fig. 4 Comparison of measured erosion with predicted amount, based on melt and wipe-off model, for two types of titanium

erosion begins immediately at the onset of melting erosion and that it is due to a reactive mechanism since the amount cannot be explained on the basis of melting only.

In the case of aluminum and titanium alloys, the aluminum and titanium oxides formed on the parent metal surface by room-temperature oxidation offer reactive erosion protection. But unlike aluminum oxide, titanium oxide is soluble in the metal [11]. The solubility of the oxide reduces its protective effect as shown by a comparison of the initiation of reactive erosion of aluminum and titanium alloys.

Further evidence to support the melt and wipe-off theory as the correct interpretation of the first stage of the erosion process for aluminum is given in Fig. 5, where a photograph of the downstream face of the test disk is shown. The accumulation of alumi-

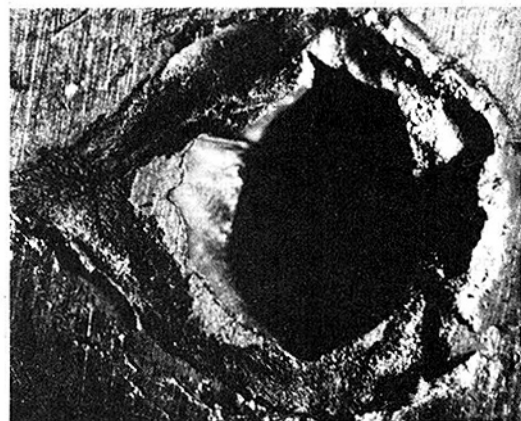


Fig. 5 Photograph of downstream face of test disk after firing, showing what appears to be metal which had flowed out of the orifice while molten and then solidified

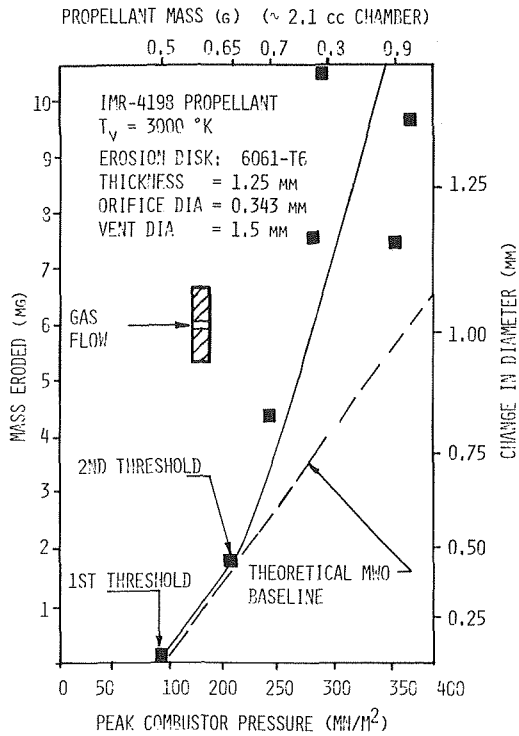


Fig. 6 Mass erosion data of 6061-T6 aluminum compared with melt and wipe-off prediction, illustrating the two thresholds

num around the lip of the orifice is clearly visible, some of which appears to have been molten.

First and Second Thresholds of Erosion. Results of erosion experiments with 6061-T6 aluminum alloy of 1.25 mm thickness

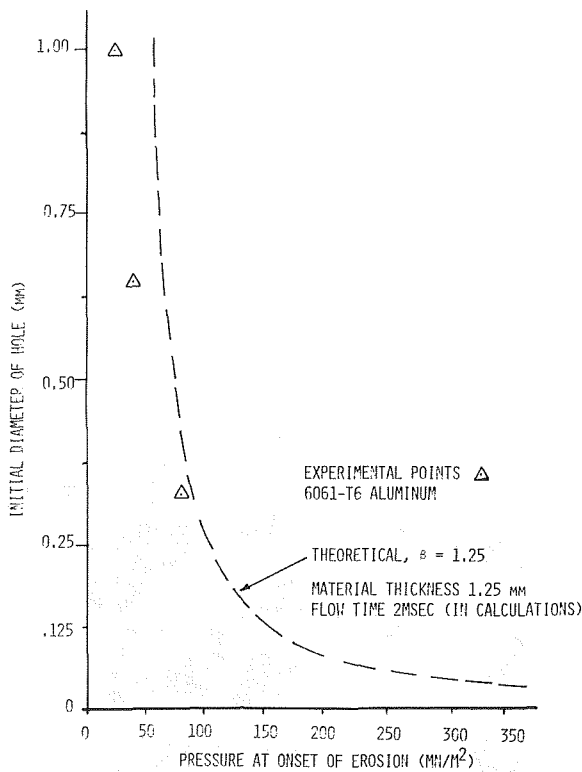


Fig. 7 Effect of initial hole diameter on pressure of the first threshold. The effects in the boundary layer of the cylindrical geometry would become noticeable at very small hole sizes, but in that case, the onset would be delayed even further

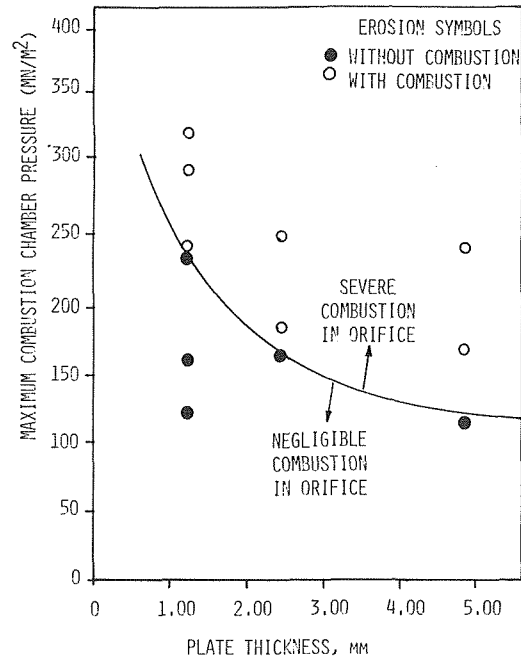


Fig. 8 Effect of disk thickness on the pressure of onset of the second threshold

are shown in Fig. 6. The experimental line indicates the existence of two thresholds. The first threshold represents the onset of erosion, i.e., the condition at which the degree of erosion becomes significant. The second threshold represents the condition where the transition from inert erosion to reactive erosion occurs. Above the second threshold the erosion greatly exceeds the amount predicted by the melt and wipe-off theory.

As stated in the Introduction, the first threshold or onset of erosion depends on various parameters such as the thermal properties of the substance and the geometry of the flow. For a semi-infinite slab exposed to a triangular heat transfer cycle, Dorrance [12] concluded that for a desirable nonmelting heat sink, the parameter $(c\rho k)^{1/2} (T_m - T_o)$ should be as high as possible. For a given heat flux, the time required for the surface of the substance to reach its melting temperature is proportional to this parameter, (see also ref [3]). In units of $\text{cal/cm}^2\text{s}^{1/2}$, pure Al has a value of about 360, 6061-T6 Al a value of 280, 7475-T6 Al a value of 200, 4130 steel a value of 420, pure titanium a value of 260 and 70-30 brass a value of 375 for this parameter. This correlation agrees with the experimental results presented in Figs. 3 and 4 which indicate that the first

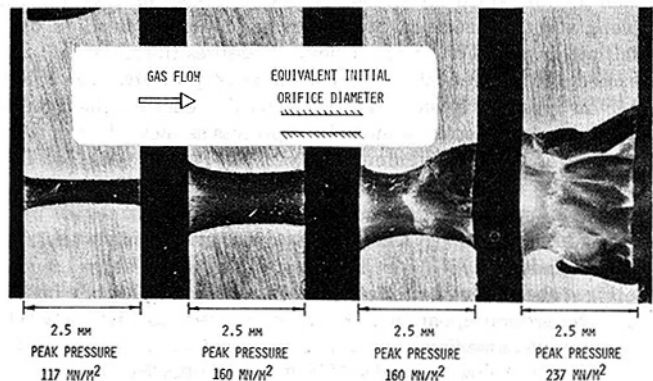


Fig. 9 Series of eroded orifices sectioned to reveal the inner contours, and the change of shape of these contours with progression from the first to the second threshold

threshold for steel and brass erosion occurs at higher pressures than that of aluminum and titanium alloys.

The initial onset of inert (MWO) erosion depends also on the orifice size as shown in Fig. 7. The greater the orifice diameter, the smaller is the proportion of heat dissipated to the interior of the substance, hence, the greater is the susceptibility to erosion. In the limit of an infinite radius, i.e., a one-dimensional slab, the heat dissipated is minimum. Thus, a cylindrical geometry is more erosion resistant than a plane slab in so far as the inert, melt and wipe-off mode of erosion is concerned.

A parameter affecting the transition from inert to reactive erosion is the time of residence of the oxidizing gaseous species in contact with the solid phase or with the eroding metal gases. For given conditions of the gaseous phase, the time of residence will depend solely on the thickness of the test disk (the time for the gaseous oxidizer to pass over it). The longer the test orifice the longer the time available for reaction. The effect of disk thickness on the second threshold is shown in Fig. 8. The solid line separates the regions of inert and reactive erosion. The minimum pressure above which chemical reaction occurs decreases with the increase of thickness of the disk. Ignition and subsequent combustion of the metal in the orifice may occur when the chemical time, t_{ch} , of the reaction is shorter than the residence time, t_r , of the gaseous particles in the orifice. All other parameters being the same, the chemical time is inversely proportional to pressure, p , whereas the residence time is proportional to the length of the orifice, l . Therefore, the condition for reaction to occur in the orifice (excess erosion) is when the ratio of $(t_r/t_{ch}) \propto (l \cdot p)$ exceeds some critical value, i.e.,

$$l \cdot p > (l \cdot p)_{crit}$$

where $(l \cdot p)_{crit}$ is the condition at which the ratio of the residence time (directly proportional to l) to the reaction time (inversely proportional to p) is large enough to allow burning within the orifice.

The catastrophic effect of reactive erosion is demonstrated in Fig. 9. The photograph shows a series of eroded orifices sectioned to reveal their inner contours. The first one (117. MN/M² peak pressure) showing very little erosion, was just above the first threshold. The last one (237. MN/m²) was well above the second threshold. It exhibits severe downstream divergence (coning) due to the onset of an aluminum vapor flame in the boundary layer. The two inner photographs represent the transition region, i.e., near the second threshold.

6 Conclusions

Results of erosion experiments of various metals in contact with a high temperature gaseous stream indicate the existence of two thresholds. The first threshold represents the onset of erosion, whereas, the second threshold represents the transition from inert to inert plus reactive erosion.

For given free stream conditions the onset of erosion depends on the geometry of the flow and the thermal properties of the sub-

stance under investigation. The inert erosion resistance of materials can be evaluated by the magnitude of the parameter $(c \rho k)^{1/2} (T_m - T_o)$. The possibility of surface reactions prior to melting is excluded from this evaluation.

The mechanism of inert erosion consists of: (a) melting of a solid as a result of the heat transfer to the gas-solid interface, and (b) removal of the melt by the shearing forces of the gaseous stream. This mechanism has been modeled in the analytical study of this investigation.

Reactive erosion results when chemical reactions occur between the high temperature gaseous oxidizing stream and the metal. Reactive erosion is characterized by an appreciable augmentation in the eroded mass of the metal and by the presence of combustion products of the gas-metal reaction in the flowing stream. The latter statement refers to the spectroscopic investigation of the erosion of aluminum and the presence of AlO in the gaseous stream.

In the temperature and pressure range of the present experimental investigation, the erosion of brass and steel fall within the inert classification, while results obtained in the case of aluminum alloys show clearly the presence of the second threshold. The pressure necessary to experience the second threshold varies inversely with the test disk thickness. As the thickness increases, the pressure of onset of the second threshold approaches the pressure of onset of the first threshold (minimum p_{max} for onset of erosion). For titanium alloys, reactive erosion occurs concurrent with the onset of erosion. In this case, the first and second thresholds coincide.

References

- 1 Plett, E. G., and Summerfield, M., "Erosive Effects of Combustion Gases on Metallic Combustion Chambers," AD 890 865 Aug. 1971.
- 2 Vieille, P., "Etude Sur les Phenomenes d'erosion produits par les explosifs," Mem. poudres sal petres 11, 1901, pp. 157-219.
- 3 Landau, H. H., "Heat Conduction in Melting Solid," *Quart. of Applied Math.*, Vol. 8, 1950, pp. 81-94.
- 4 Goodman, T. R., "Application of Integral Methods to Transient Non-linear Heat Transfer," *Advances in Heat Transfer*, Vol. 1, 1964, pp. 51-122.
- 5 Citron, S. J., "Heat Conduction in a Melting Slab," *J. Aero/Space Sc.*, Vol. 27, 1960, p. 219.
- 6 Dewey, C. F., Schlesinger, S. I., and Sashkin, L., "Temperature Profiles in a Finite Solid With Moving Boundary," *J. Aero/Space Sc.*, Vol. 26, 1959, pp. 59-64.
- 7 Crank, J., "Two Methods for the Numerical Solution of Moving Boundary Problems in Diffusion and Heat Flow," *Quart. J. of Mech. and Applied Math.*, Vol. 10, 1957, pp. 220-231.
- 8 Murray, W. D., and Landis, F., "Numerical and Machine Solutions of Transient Heat-Conduction Problems Involving Melting or Freezing. Part I. Method of Analysis and Sample Solution," *JOURNAL OF HEAT TRANSFER, TRANS. ASME, Series C*, Vol. 81, 1959, pp. 106-112.
- 9 Rohsenow, W. H., and Choi, H., *Heat, Mass, and Momentum Transfer*, Prentice-Hall, Inc., N.J., 1961, p. 269.
- 10 Richtmyer, R. D., and Morton, K. W., *Difference Methods for Initial-Value Problems*, Interscience Publishers, N.Y., 1957, p. 185.
- 11 Brzustowski, T.A., and Glassman, I., "Spectroscopic Investigation of Metal Combustion," *Heterogeneous Combustion*, H. AG., Wolfhard, et al., eds., 1964, pp. 41-73.
- 12 Dorrance, W. H., *Viscous Hypersonic Flow*, McGraw-Hill, New York, 1962, pp. 62-67.

K. A. Bunting
G. Cornfield

The Electricity Council Research Centre,
Capenhurst, Chester,
Ch1 6ES, England

Toward a General Theory of Cutting: A Relationship Between the Incident Power Density and the Cut Speed

A relationship between the power density incident on a material and the resulting cut speed is developed in terms of the thermal properties of the material. The expression obtained is general and is shown to be in good agreement with experimental results. It is shown that the efficiency of energy utilization is influenced by the incident power density and the jet diameter. The theory indicates that to maximize cut speed and energy utilization the jet diameter should be as small as possible consistent with an attainable power density.

1 Introduction

There is a wide range of thermal cutting techniques available for the shaping of materials. For example, lasers, electron beams, plasma jets and oxy-fuel cutting are widely used for metal cutting, and more recently lasers and plasma jets have been used to cut a wide range of nonmetallic materials [1-12].¹ A feature common to the vast majority of these cutting operations is that they occur as a result of melting and/or vaporizing the material by a cylindrical beam which transfers its energy to the material through a moving circular spot. When the cut speed is low, a cylindrical region, with a diameter equal to that of the circular spot, and bounded by the melting point isotherm results and the cut is produced by movement of this region through the metal in the direction of cutting. However, in general the region bounded by the melting point isotherm has a lune shaped cross section (see Fig. 1); its shape being determined by the thermal properties of the material, the cut speed and the incident power density. A typical cutting situation for no appreciable temperature gradient perpendicular to the top surface of the material is shown schematically in Fig. 1. The energy to melt or vaporize the material is considered to be supplied through a circular spot of radius R and the cut speed is such that the material is just cut with a clean edge.

A number of theories have been developed from which the cut speed, in terms of the thermal properties of the material, can be calculated. Moss and Sheward [13] took the simplest approach and

calculated the cut speed from the energy required to remove the material from the cut region neglecting heat losses. Christensen, et al. [14] has compared the theoretical and experimental recrystallization and zone widths, and peak temperatures using a point source of heat for welding. Rosenthal [14] considered a line source of heat, which is closer to the practical situation, and neglected latent heat. Wells [16] simplified the expression given by Rosenthal. Apps and Milner [17] improved the agreement between the expression given by Wells and experiment by allowing for the latent heat of fusion even though the correction as applied was incorrect. Swift-Hook and Gick [18] have compared a theoretical relationship based on a line source of heat and involving various parameters with experiment. Arata and Miyamoto [19] derived the temperature distribution for a rectangular source moving in a direction perpendicular to the surface of a semi-infinitely thick block. The latent heat of fusion was neglected. While the expression derived was not directly relevant to the cutting situation an expression based on it for a moving band source of heat is. The cut speeds in copper, iron, mild steel, and aluminium determined experimentally and presented in this paper are compared with values calculated using the equations developed by Moss and Sheward, Rosenthal, Wells, and Arata and Miyamoto. The cut speed in a number of different materials is calculated using the present theory and compared with values obtained experimentally using a laser both with and without gas assistance. In addition, a few results comparing the welding speed in stainless steel (taking the weld edges to be defined by the melting point isotherms) using a laser are compared with the calculated values. The agreement between theory and experiment is generally substantially improved by considering a circular spot rather than a line source. The relationship between the incident power density on the material and the cut speed is derived using certain simplifying assumptions discussed next.

¹ Numbers in brackets designate References at end of paper.

Contributed by the Heat Transfer Division for publication in the JOURNAL OF HEAT TRANSFER. Manuscript received by the Heat Transfer Division January 3, 1974. Paper No. 75-HT-W.

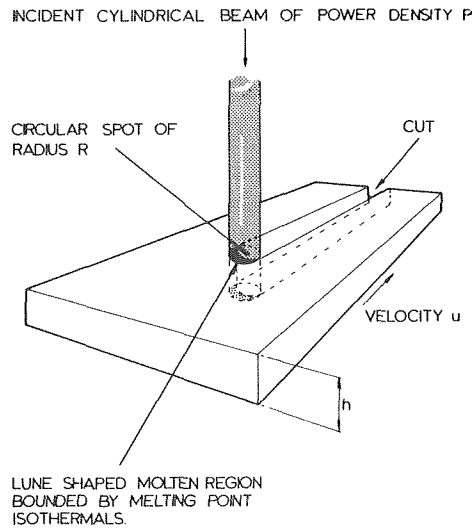


Fig. 1 Typical cutting situation

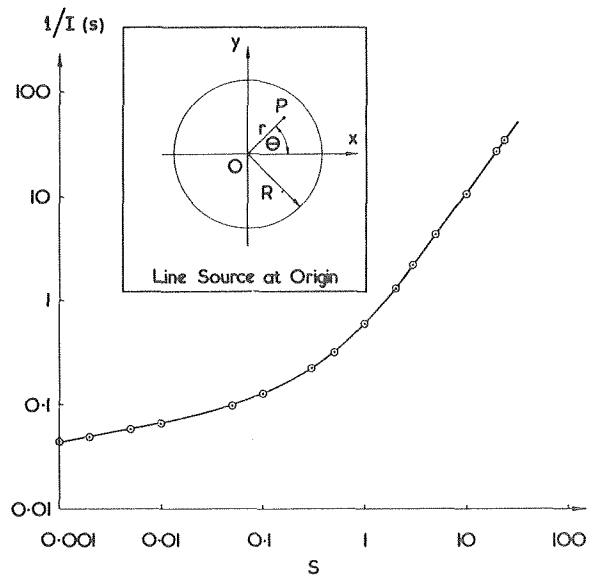


Fig. 2 Integral $1/I(s)$

2 Theory

(a) **Derivation of the Relation Between the Cut Speed and the Incident Power Density.** For the purposes of the theory, which is restricted to cutting by thermal as opposed to thermal/chemical means, it is assumed (1) that no appreciable temperature gradient exists in the material perpendicular to the surface, (2) that the heat lost by radiation is negligible, (3) the effect of the latent heat of fusion is negligible, (4) that the effects of gravity and surface tension are negligible (this is probably justified when a stream of gas is used in the cutting process, especially with both subsonic and supersonic plasma jets) and (5) the power density in the incident beam is uniform. With assumption (1) the temperature distribution for a point source of strength q (i.e. the energy released per second is q) moving across an infinite two-dimensional sheet is the same as that of a line source perpendicular to the surface strength q/h moving through an infinite medium, where "h" is the thickness of the sheet. Thus the three-dimensional problem can be reduced to a two-dimensional problem.

Consider a line source of strength q/h at the origin O with the medium moving at velocity u in the x -direction relative to the source (Fig. 2) and take the initial temperature of the medium as T_0 . The temperature at point (x, y) is then given by [16].

$$T(x, y) - T_0 = \frac{q}{2\pi hk} \exp(ux/2\alpha) [K_0 u(x^2 + y^2)^{1/2}/2\alpha] \quad (1)$$

where α is the thermal diffusivity of the medium, k is the thermal conductivity of the medium and K_0 is a zeroth order, modified Bessel function of the second kind.

Although equation (1) has been used with great effect by several authors, in particular Rosenthal [15] and Wells [16], its use in pre-

dicting the cut speed obtained with high power density devices, such as plasma jets, is limited. The characteristic length for a moving line source is given as $2\alpha/u$ [20]. Equation (1) will give inaccurate results if used to predict temperatures around the circumference of the cutting beam when the characteristic length is of the same order as, or less than, the cut width. The resulting error will increase as the power density and hence the cut speed is increased. Thus equation (1) will be generalized to predict the temperature distribution obtained with a moving diffuse heat source.

The temperature at (x, y) due to a line source at $P(r \cos \theta, r \sin \theta)$ is given by

$$T(x, y) - T_0 = \frac{q}{2\pi hk} [\exp u(x - r \cos \theta)/2\alpha] \times [K_0 u((x - r \cos \theta)^2 + (y - r \sin \theta)^2)^{1/2}/2\alpha] \quad (2)$$

Now the temperature distribution resulting from a diffuse source of heat of radius R with a power density of q' per unit area is the linear sum of the temperature distributions resulting from the infinitesimal line sources of which it is composed. Thus, since the line source at $r \cos \theta, r \sin \theta$ ($r \leq R$) has strength $q' r dr d\theta$, the net temperature distribution is given by:

$$T(x, y) - T_0 = \frac{q'}{2\pi hk} \int_0^R r dr \int_0^{2\pi} [\exp u(x - r \cos \theta)/2\alpha] \times [K_0 u((x - r \cos \theta)^2 + (y - r \sin \theta)^2)^{1/2}/2\alpha] d\theta \quad (3)$$

By equation (1) $T(0, R) - T_0 =$

$$\frac{q'}{2\pi hk} \int_0^R r dr \int_0^{2\pi} [\exp -ur \cos \theta/2\alpha] \times [K_0 u(R^2 - 2rR \sin \theta + r^2)^{1/2}/2\alpha] d\theta \quad (4)$$

Nomenclature

h = thickness of material
 k = thermal conductivity
 k_1 = fraction of incident energy transmitted to the material
 K_0 = zeroth order, modified Bessel function of the second kind
 P = power density in incident energy source

q = strength of line heat source
 q' = strength of diffuse heat source
 r = cylindrical coordinate
 R = radius of diffuse heat source i.e., half cut width
 $T(x, y)$ = temperature at (x, y)
 T_0 = initial temperature of material
 $T_{m.p.}$ = temperature at the melting point

u = speed of movement of diffuse heat source i.e., cut speed
 W_s = specific energy
 x, y } = Cartesian coordinates
 α = thermal diffusivity
 ρ = density of material
 θ = polar coordinate

Table 1 Comparison of the various theoretical cut speeds with the experimental cut speed, copper

Thickness cm	Cut width cm	Characteristic length/cut width	Cut speed cm/s					
			Moss & Sheward	Rosenthal	Wells	Arata & Miyamoto	Present work	Experimental
*0.0067	0.041	4.93	52.6	15.0	18.6	17.8	15.1	8.8
0.0071	0.038	2.30	49.9	12.2	15.4	14.7	12.5	20.3
0.0071	0.024	13.5	103	32.6	40.7	33.4	5.51	5.49
0.124	0.57	0.359	25.9	8.1	16.4	6.40	10.9	8.69
0.124	0.33	0.461	41.6	13.5	26.3	10.8	17.7	11.7
**0.2	0.16	13.3	11.2	2.67	3.21	3.08	2.62	0.833
***1.91	0.64	3.28	5.34	2.01	2.53	2.27	2.07	0.847
3.18	0.64	3.28	5.45	2.08	2.61	2.33	2.12	0.847

* Measurements by Bunting some of which are reported in the literature (25)

** Electrical efficiency of plasma torch taken as 0.65 (34)

*** Electrical efficiency of plasma torch taken as 0.65 (35)

Dimensionalize by writing $r' = r/R$ giving

$$T(0, R) - T_0 = \frac{q'R^2}{2\pi hk} \int_0^1 r' dr' \int_0^{2\pi} [\exp - sr' \cos \theta] K_0 s (r'^2 - 2r' \sin \theta + 1)^{1/2} d\theta$$

where

$$s = uR/2\alpha \quad (5)$$

It is convenient to write

$$T(0, R) - T_0 = \frac{q'R^2}{2\pi hk} I(s) \quad (6)$$

where

$$I(s) = \int_0^1 r' dr' \int_0^{2\pi} [\exp - sr' \cos \theta] K_0 s (r'^2 - 2r' \sin \theta + 1)^{1/2} d\theta \quad (7)$$

$1/I(s)$, plotted logarithmically for convenience, is shown in Fig. 2.

It is shown in the literature [20, 21] that the cut edges are coincident with the melting point isothermals. Thus, to cut a material the melting point isothermal is at $(0, R)$. If the incident power density is written as P we have

$$q' = k_1 P \quad (8)$$

where k_1 is the fraction of the incident energy transmitted to the material. For cutting by equation (6)

$$q'/h = \frac{2k(T_{m,p} - T_0)}{R^2} \cdot \frac{1}{I(s)} \quad (9)$$

Equation (9) holds for uniform heat transfer within the cut, par-

allel to the surface. Uniform heat transfer occurs when the characteristic length for heat penetration across the thickness of the material is much greater than the thickness of the material i.e.,

$$\left(\frac{2R\alpha}{u}\right)^{1/2} \gg h \quad (10)$$

For any process which increases the uniformity of heat transfer within the cut parallel to the surface, for example axial movement of the anode root when cutting with a transferred plasma torch [22], this restriction does not apply.

From equation (8) q'/h , R or u can be obtained knowing the other two variables. In Tables 1 and 2 experimental values of cut speed are compared with those calculated from equations (8) and (9) with k_1 taken as unity and those calculated using expressions developed by Moss and Sheward, Rosenthal, Wells, and Arata and Miyamoto. The parameter q'/h is shown as a function of u for various cut widths for copper and iron in Figs. 3 and 4, respectively. A graph of cut speed as a function of cut width for various values of power density per unit thickness is shown in Fig. 5. Experimental values of q'/h for plasma cutting derived from equation (8) with k_1 taken as unity are compared with theoretical values of q'/h derived from equation (9) in Tables 3 and 4. Experimental values of q'/h for laser cutting of various materials both with [12] and without gas assistance [26], are compared with q'/h obtained from equation (9) in Tables 5 and 6. Some results for laser welding of stainless steel are also given in Table 5. The value of $T_{m,p}$ and the average thermal diffusivity and thermal conductivity were ob-

Table 2 Comparison of the various theoretical cut speeds with the experimental cut speed, iron/mild steel

Thickness cm	Cut width cm	Characteristic length/cut width	Cut speed cm/s					
			Moss & Sheward	Rosenthal	Wells	Arata & Miyamoto	Present work	Experimental
*0.0025h	0.050	<0.258	85.3	20.7	57.6	15.6	32.3	>21.7
0.0127	0.069	0.739	30.8	10.2	20.0	10.3	4.90	5.49
**0.1	0.12	2.06	15.0	5.32	9.59	5.71	6.73	1.13
0.2	0.075	2.36	7.48	2.99	3.75	5.59	3.08	1.58
***0.335	0.476	0.116	13.7	2.52	6.41	1.69	4.76	5.08
1.27	0.516	0.183	6.34	1.73	4.23	1.47	2.37	2.95
2.54	0.516	0.321	3.17	1.16	2.01	1.30	1.44	1.69
5.08	0.952	0.347	1.34	0.528	0.826	0.657	0.626	0.847

* Unpublished measurements (Bunting)

** Electrical efficiency of plasma torch taken as 0.65 (34)

*** Electrical efficiency of plasma torch taken as 0.65 (35)

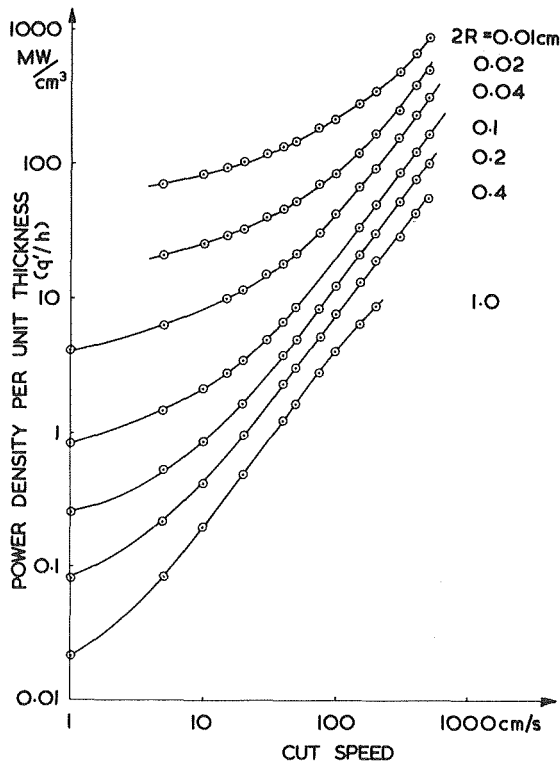


Fig. 3 Power density per unit thickness as a function of cut speed, copper

tained from data given in the literature [27-31]. The temperature at which wood is sufficiently pyrolyzed for the carbon to disintegrate [32, 33] was used to evaluate equation (9) for wood.

(b) **An Expression for the Specific Energy.** The specific energy for a given material [23-25] is defined as the energy required at the material surface to remove unit mass of material from the cut region. It is a measure of the efficiency of energy utilization in the cut region. The specific energy, W_s , can be written (5) as

$$W_s = \frac{\pi R P}{2u h \rho} \quad (11)$$

where ρ is the density of the material.

By equations (8) and (9)

$$W_s = \frac{\pi^2 k (T_{m,p} - T_0)}{u \rho R k_1} \cdot \frac{1}{I(s)} \quad (12)$$

W_s as a function of u is shown for copper, iron and aluminum in Fig. 6. W_s is evaluated for $R = 0.01$ cm and 0.5 cm, these values encompassing typical experimental cut widths.

3 Discussion

When cutting with a plasma jet some spreading of the jet occurs on contact with the material to be cut. Without knowledge of the relationship between the plasma jet diameter and the cut width, prediction of the cut speed from the power density and the beam diameter is necessarily imprecise. Cut widths greater than the jet width by factors in the range 1-2 were measured by Bunting [23,25]. In this connection information relating the beam diameter to the cut width is required for lasers and electron beams, if this approach is to be employed.

Comparison of the results shown in Tables 1-6 is complicated by possible experimental error. However, the results presented in Tables 1 and 2 indicate, in agreement with common sense, that the simple approach adopted by Moss and Sheward becomes more accurate as the thickness and cut width increase i.e., as the effect of losses decreases. The mean difference between experiment and

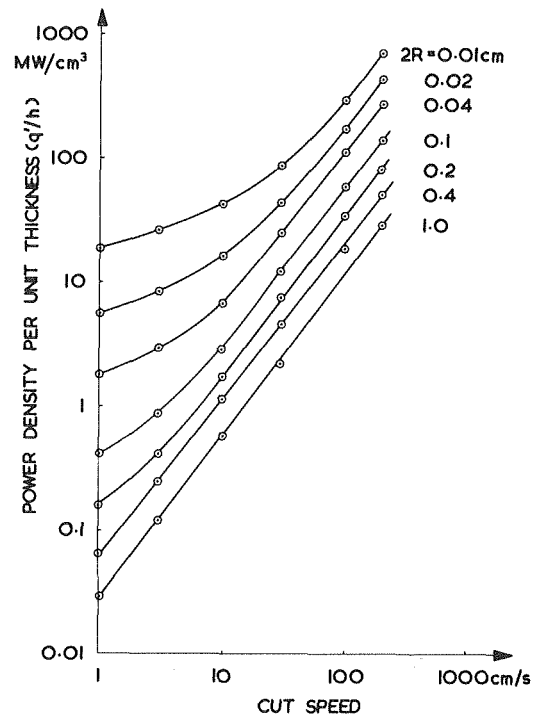


Fig. 4 Power density per unit thickness as a function of cut speed, iron

theory for copper and iron, respectively, are 643 percent and 349 percent (Moss and Sheward), 142 percent and 104 percent (Rosenthal), 210 percent and 186 percent (Wells), 172 percent and 134 percent (Arata and Miyamoto), and 82 percent and 96 percent (present work). It is indicated that the simplification made by Wells is considerably less accurate than the original expression developed by Rosenthal while the expression developed in the present work is, on average, in substantially better agreement with the experimental results than the theory due to Rosenthal. As predicted the difference between the predictions of Rosenthal's theory and those of the present theory and experiment increases as the ratio of the characteristic length to the cut width decreases. For example, the mean error for a ratio < 1 is 41 percent (Rosenthal) and 21 percent (present work) with 86 percent of the results within 80 percent of the experimental value, 57 percent within 40 percent, 29 percent within 20 percent, and 14 percent within 10 percent for Rosenthal and 100 percent within 80 percent, 86 percent within 40 percent, 71 percent within 20 percent, and 14 percent within 10 percent for the present work.

Table 3 Comparison of theoretical and experimental values of power density per unit thickness, cutting copper using a plasma jet

Thickness cm	Cut width cm	Cut speed cm/s	1/I(s)	Power density per unit thickness	
				Theoretical MW/cm ²	Experimental MW/cm ²
* 0.0067	0.041	8.80	0.131	7.68	9.77
0.0071	0.038	20.3	0.189	12.9	10.0
0.0071	0.024	5.49	0.0930	15.8	15.5
0.124	0.57	8.69	0.839	0.265	0.345
0.124	0.33	11.7	0.667	0.599	0.961
** 0.2	0.16	0.833	0.0932	0.356	0.533
*** 1.91	0.64	0.847	0.156	0.0375	0.0645
3.18	0.64	0.847	0.156	0.0375	0.0648

* Measurements by Bunting some of which are reported in the literature (25)

** Electrical efficiency of plasma torch taken as 0.65 (34)

*** Electrical efficiency of plasma torch taken as 0.65 (35)

Table 4 Comparison of theoretical and experimental values of power density per unit thickness, cutting iron and mild steel using a plasma jet

Thickness cm	Cut Width cm	Cut Speed cm/s	1/t(s)	Power density per unit thickness	
				Theoretical MW/cm ²	Experimental MW/cm ²
* 0.00254	0.050	21.7	1.29	13.1	22.0
0.0127	0.069	5.49	0.416	2.21	2.01
** 0.1	0.16	0.83	0.198	0.355	1.61
0.2	0.13	1.50	0.252	0.640	1.29
*** 0.635	0.476	5.08	3.54	0.398	0.372
1.27	0.516	2.96	1.96	0.190	0.146
2.54	0.516	1.69	1.00	0.0951	0.0791
5.08	0.952	0.847	0.909	0.0253	0.0182

- * Unpublished measurements (Bunting)
- ** Electrical efficiency of plasma torch taken as 0.65 (34)
- *** Electrical efficiency of plasma torch taken as 0.65 (35)

Calculation of the characteristic length for heat penetration across the thickness of the material shows that it is greater than the thickness of the metal for most of the experimental results in Tables 3 and 4. However, the theoretical and experimental power densities per unit thickness for aluminum (not shown) are in good agreement even though the characteristic length for heat penetration across the thickness of the material was generally less than the thickness of the material. For plasma cutting using transferred or nontransferred arcs, agreement between theoretical and experimental values of q'/h is not dependent upon whether the characteristic length is greater than or less than the thickness of the material. This is a reflection on the processes taking place in the cut region, heat transferred to the walls of the cut by turbulent transfer from the plasma being one possible contributor, and implies that, at least for plasma jets, the use of equation (9) is not restricted to cutting situations where the characteristic length is greater than the material thickness.

Curves of q'/h as a function of u can be used to closely predict the average energy density in the cut region (Tables 3 and 4) the agreement for aluminum not being as good as for copper and iron. Values of k_1 (the fraction of the energy incident on the material surface transmitted to the material) can be deduced from results given in the literature [21]. Values in the range 0.69–0.77 are obtained assuming 65 percent [10,13, 23, 34, 35] of the power input to the torch emerges in the plasma jet. Correction of the results in Tables 3 and 4 to account for k_1 would generally improve agreement between experiment and theory. The percentage difference between the theoretical and experimental cut speeds is substantially greater than that for the corresponding values of q'/h . Thus the mean difference between the theoretical and experimental

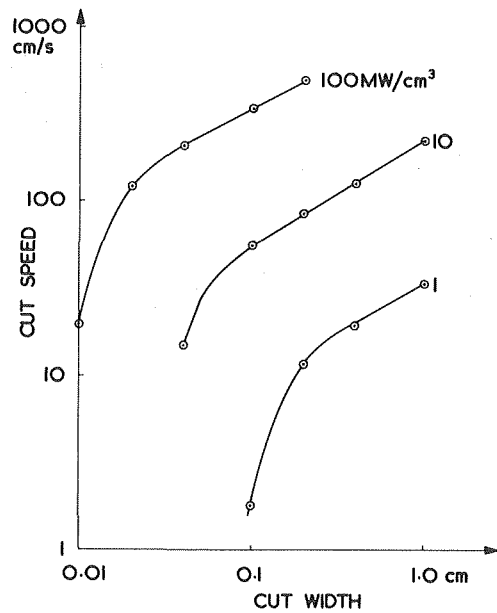


Fig. 5 Cut speed as a function of cut width for various constant values of power density per unit thickness, copper

values of q'/h is <34 percent including the results shown for aluminum.

The curves showing power density per unit thickness as a function of cut speed become linear for high cut speeds. The wider the jet width (cut width) the lower the value of cut speed at which the curve becomes linear. Comparison of Figs. 3 and 4 shows that, in agreement with experiment, the power density to cut copper is greater than that to cut iron at the same speed. However, at higher cut speeds than those employed for these measurements the corresponding curves for copper and iron cross and the required power density for a given cut speed, is then less for copper. The explanation is as follows. In order to cut there has to be sufficient energy conducted to the edge of the spot to cause melting. At low speeds materials with a low thermal conductivity will lose less heat to the bulk of the material outside the cut region. This will increase the cutting efficiency, as more heat will be available to melt the material within the cut region. However, at high speeds when heat losses outside the cut region becomes negligible, a high thermal conductivity will become advantageous in allowing more heat to be conducted from the center of the spot to the edge. Clearly for a larger jet diameter the linear part of the curve is reached at lower cut speeds because the heat from the center of the spot has further to travel. Thus, the power density per unit thickness to cut iron, which has a lower diffusivity than copper, will be greater than that

Table 5 Comparison of theoretical and experimental values of power density per unit thickness for various materials, laser cutting and welding

Material	Application	Thickness cm	Cut speed cm/s	Cut width cm	Power density per unit thickness MW/cm ²	
					Experimental	Present work
Aluminium	cutting	1.27	3.81	0.102	1.46	0.412
Carbon steel	cutting	0.635	3.81	0.102	2.91	1.04
304 stainless steel	cutting	0.475	2.12	0.203	1.30	0.260
Plywood	cutting	2.54	2.54	0.152	0.173	0.110
Glass	cutting	0.953	2.54	0.102	2.59	0.523
Concrete	cutting	3.81	0.0847	0.635	0.00663	0.00224
304 stainless steel	welding	2.03	2.12	0.330	0.115	0.164
304 stainless steel	welding	1.27	4.24	0.229	0.384	0.530
304 stainless steel	welding	0.889	1.27	0.229	0.219	0.147

Table 6 Comparison of theoretical and experimental values of power density per unit thickness for various steel plates, gas assisted laser cutting

Material	Thickness cm	Cut speed cm/s	Cut width cm	Power density per unit thickness M/cm^2	
				Experimental	Present work
Steel St37	0.1	5.00	0.01	29.5	42.3
Steel St37	0.3	1.00	0.02	2.44	5.83
Galvanised steel plate	0.075	5.83	0.01	39.0	33.7
Austenitic steel (18 Cr, 8 Ni)	0.1	2.50	0.01	29.3	24.0

for copper in the high cut speed region. The minimum in the curves showing the specific energy as a function of cut speed (Fig. 6) which implies a maximum in the efficiency of energy utilization, can be similarly explained. It is shown that the minimum occurs for increasing values of cut speed as the jet diameter decreases. Estimates of the energy required to cut a given length of cut show that this decreases substantially as the jet diameter decreases. For example, the energy required to cut copper 1 cm thick at 2 cm/s is 2.9 kJ/cm for a cut width of 0.02 cm and 14.1 kJ/cm for a cut width of 1.0 cm. The corresponding figures for iron are 1.1 kJ/cm and 28 kJ/cm, respectively. The energy required also decreases with increasing power density up to some limiting value.

The theoretical values of q'/h shown in Tables 5 and 6 are approximate because of lack of knowledge of the precise nature of some of the materials and the difficulty in obtaining data. The agreement between experiment and theory is fair. However, the experimental values of q'/h for cutting (Table 5) are significantly higher than the theoretical values. It is expected that this is due, on the one hand, to taking k_1 as unity when in fact substantial reflection of laser energy by vaporized material occurs, and, on the other hand, to the requirement for a temperature greater than the melting point in the cut region because there is no gas stream to expel the molten material from the cut region. Agreement between the theoretical and experimental values of q'/h for welding is reasonably good; the experimental value being lower for weld depths of 1.27 and 2.03 cm and higher for a weld depth of 0.889 cm. The experimental and theoretical values of q'/h for gas assisted laser cutting are in good agreement.

4 Conclusions

A relationship between the incident power density per unit thickness and the cut speed in terms of the thermal properties of the material has been established. The theory is generally in substantially better agreement with experiment than previous theories which either neglect losses or are limited to situations where the characteristic length ($2\alpha/u$) is large compared to the cut width. It is indicated that by means of the relationship developed the cut speed in any material can be predicted knowing the incident power density and the thermal properties of the material. There is an optimum power density and cut speed for a given jet diameter which maximizes the efficiency of the cutting process. Comparison of the power density per unit thickness for the same cut speed and cut width for copper and iron (Fig. 4 and 5) shows that the energy required per unit length of cut decreases for decreasing cut width (jet diameter). For example, the energy required to cut copper 1 cm thick at 2 cm/s is 2.9 kJ/cm for a cut width of 0.02 and 14.1 kJ/cm for a cut width of 1.0 cm. The corresponding figures for iron are 1.1 kJ/cm and 28 kJ/cm, respectively. The energy required also decreases with increasing incident power density up to some limiting value (see Fig. 6). Thus there is a strong incentive to develop small diameter, high power density sources for cutting.

References

1. Adams, C. M., and Hardway, A. G., "Fundamentals of Laser Beam Machining and Drilling," *I.E.E.E. Trans. on Indust. and Gen. Applications*,

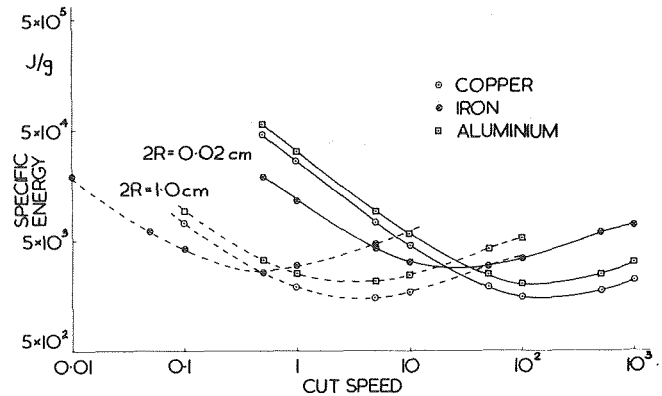


Fig. 6 Specific energy as a function of cut speed for copper, iron and aluminum

- 1965 pp. 90-96.
2. Lunau, F. W., and Paine, E. W., "CO₂ Laser Cutting," *Welding and Metal Fabrication*, Vol. 37, No. 1, Jan. 1969, pp. 9-14.
 3. Hawn, J. R., et al., "The Application of Lasers to Industry," *I.E.E.E. Trans. on Indust. & Gen. Applications*, Vol. 4, No. 4, July/Aug. 1968, pp. 379-389.
 4. Fletcher, M. J., "Welding Metal Fabric," Vol. 41, No. 9, 1973, pp. 308-311.
 5. Schumacker, B. W., "Electron Beams as Tools," *Umshau Wiss and Tech.*, Vol. 71 No. 25, Dec. 1971, pp. 929-9.
 6. Rice, R. W., "Arc, Laser and Electron Beam Machining of Ceramics," Naval Res. Lab., Washington D. C., U.S.A., May 1972.
 7. "Plasma Cutting—a Progress Report," *Weld. Eng.*, Vol. 58, No. 3, p. 973.
 8. Farwer, A., and Antoniette, A., "Plasma Cutting Aluminium and Its Alloys," *Aluminio*, Vol. 41, No. 9, Sept. 1972, pp. 472-477.
 9. Merkhher, A. M., et al., "Equipment for Plasma Cutting of Stainless Steel in Mass Production," *Weld. Prod.* Vol. 18, No. 9, 1971.
 10. Bunting, K. A., "Cloth Cutting by Plasma Jet," *Journal of the Textile Inst.*, Vol. 62, No. 9, Sept. 1971, pp. 482-494.
 11. Humphreys, J. F., "The Application of a Non-Transferred Plasma Torch to the Cutting of a Range of Non-Metallic Material," Electricity Council Research Centre Report R465, Jan. 1972.
 12. Born, K., et al., "Plasma-, Laser-, Electron Beam; Three Beam Welding and Cutting Processes Compared," *Blech*, Vol. 20, No. 9, Sept. 1973, pp. 363-376.
 13. Moss, A. R., and Sheward, J. A., "The Arc Plasma Cutting of Non-Metallic Materials," *I.E.E. Conf. on Electrical Methods of Machining, Forming and Coating*, Mar. 1970, pp.41-47.
 14. Christensen, N. Davies, V., de L., and Gjermundsen, K., "Distribution of Temperature in Arc Welding," *Brit. Weld. J.* Feb. 1965, pp. 54-75.
 15. Rosenthal, D., *Trans. Inst. Min. Mech. Eng.*, Vol. 68, 1946, pp. 849-865.
 16. Wells, A. A., *Welding J.*, Vol. 31, 1952, pp. 263s-266s.
 17. Apps, R. L., and Milner, D. R., "Heat Flow in Argon-Arc Welding," *Brit. Weld. J.*, Oct. 1955, pp. 475-485.
 18. Swift-Hook, D. T., and Gick, A. E. F., *The Weld. J. Res. Supplement*, 1973, pp. 492-493.
 19. Arata, Y., and Miyamoto, I., "Theoretical Analysis of Weld Penetration Due to High Energy Density Beam," *Trans. of J.W.R.I.*, Vol. 1, No. 1, 1972.
 20. Carslaw, H. S., and Jaeger, J. C., "Conduction of Heat in Solids," Clarendon Press, Oxford 1959, p. 267.
 21. Browning, J. A. and Hazard, C., *British Welding Journal*, Sept. 1963, pp.462-469.
 22. Kudinov, V. V., Taran, V. D., and Brochenin, V. I., *Weld. Prod. R.*, Vol. 17, 1970, pp. 3-5.
 23. Humphreys, J. F., and Lawton, J., "Arcs With Free Anode Roots in the Presence of Gas Flow and Magnetic Fields," *B. J. App. Phys. D.*, Vol. 5, 1971, pp. 701-709.
 24. Bunting K. A., and Cornfield G., "Supersonic Plasma Jets," Electricity Council Research Centre Report M.395, July 1971.
 25. Bunting K. A., "Metal Foil Cutting by Plasma," *Metal Construction and Brit. Welding Journal*, Vol. 4, No. 3, Mar. 1972.
 26. Bunting K. A., "Foil Cutting by Plasma," Electricity Council Research Centre Report R377, June 1971.
 27. Locke, E. V., et al., "Deep Penetration Welding With High Power CO₂ Lasers," *I.E.E.E. J. Quantum Electronics*, Vol. QE8, No. 2, Feb. 1972.
 28. Snithells C. J., *Metals Reference Book, Volume 1*, Butterworths, London, 1967.
 29. *Handbook of Chemistry and Physics*, 51st ed., The Chemical Rubber

Co., Cleveland, Ohio, 1970-1971.

- 30 *Metall Zeitschrift Für Technik*, Industrie und Handel, July 1968.
- 31 *Thermophysical Prop. Matter, TPRC Data Series*, IFI/Plenum, New York-Washington, 1970.
- 32 *Smithsonian Physical Tables*, Smithsonian Institute, 1964.
- 33 Schaffer, E. L., "Rev. Inform. Related to the Charring Rate of Wood." U.S.D.A. Forrest Service Research Note FPL-1045, 1966.
- 34 Kollmann, F., "Wood and Fire," *J. Wood*, Vol. 31, No. 5, 1966.
- 35 Phillips, K., "Production and Application of Plasma Jets," *A.E.I. Engineering*, Jan/Feb. 1965.
- 36 Sheward, J. A., "The Design and Testing of a Plasma Jet," National Physical Laboratory Report, I.M.U. Ex 1, Sept. 1966.
- 37 Shapiro, I. S., Beider, B. D., and Persits, L. M., "Welding Prod., Vol. 16, No. 2, Feb. 1969.
- 38 Levin, M. L., 2nd Commonwealth Welding Conference, 1965 pp. 8.1-8.4.

A. F. Emery
P. Kramar
A. W. Guy
J. C. Lin

University of Washington,
Seattle, Wash.

Microwave Induced Temperature Rises in Rabbit Eyes in Cataract Research

Microwave power deposition patterns and temperature distributions were measured for rabbit eyes exposed to localized near zone 2450 MHz radiation and good agreement was obtained between the measured and predicted transient temperature fields. The lenses were biomicroscopically examined to determine the minimum exposure times necessary to produce posterior lens opacity (cataracts) and these times are correlated with the temperature calculations to suggest that a threshold temperature level exists.

Introduction

The results of previous microwave cataractogenesis research on test animals have not provided sufficient quantitative data to describe the relationship between various physical parameters and the biological changes in the eye. Until these relationships can be accurately delineated, animal research will not be useful in establishing safety criteria for human exposure to microwaves whether from antennas or from ovens. The research reported here has been formulated to relate exposure field strengths, absorbed power patterns, and induced temperature distributions. Based upon the observations reported by Lerman [1],¹ Duke-Elder [2], and Mehta and Maisel [3] in which heat was shown to cause partial or total structural rearrangement of the peptide chains in the eye, with beta and gamma crystallins showing changes at temperatures as low as 50°C, and upon the microwave work of Daily [4], Richardson [5], Osborne [6], Carpenter [7], and Williams [8] and upon our previous work, one of our conjectures about the origin of cataract is: "Upon exposure to a source of radiation which produces local temperature elevations in the eye, if any portion of the lens achieves a sufficiently high temperature a cataract will form." The proof of this hypothesis then relies upon the ability to either predict or to measure the temperature of the lens for various exposure conditions. Inasmuch as temperatures cannot be measured in human subjects, the research was organized to determine if we could predict the temperature rises in test animals, and then use these methods to predict the temperatures effects in humans who may be inadvertently exposed to microwave radiation. In Section 2

we describe the method of measuring the absorbed power distributions and in Section 3 the model used for predicting the temperature elevations is discussed. In Section 4, experimental techniques are described and in Section 5 the theoretical and experimental values are compared. Section 6 details some of the recent hypothermia experiments.

2 Microwave Power Absorption Patterns (Dosimetry)

To determine the microwave energy which is absorbed by the eye, eight month old New Zealand albino rabbits were anesthetized and exposed to a 2450 MHz diathermy "C" director at 5 cm from the cross-over point to the corneal surface. A 1mm hole was made in the cornea and a hollow glass micropipette (1.4mmOD), closed at one end, was inserted into the hole. Fig. 1 describes the eye and the pipette location. Following the procedure of [9] an iron constantan thermocouple was inserted into the micropipette and the temperature measured. The thermocouple was then removed and a short exposure (20 s or less) of high power microwave radiation (540 mW/cm²)² imposed. Immediately after cessation of the radiation the thermocouple was reintroduced and the temperature measured as a function of time. Numerical computations and a series of experiments showed that the temperature decayed slowly and that the temperature recorded when the thermocouple was stable was within 0.5 percent of the value at the cessation of irradiation. Since the exposure time was very short, and the conduction was minimal, the power absorbed could be related to the temperature rise by,

$$\dot{q}\Delta t = \rho c \Delta T \quad (1)$$

¹ Numbers in brackets designate references at end of paper.

Contributed by the Heat Transfer Division for publication in the JOURNAL OF HEAT TRANSFER. Manuscript received by the Heat Transfer Division February 20, 1974. Paper No. 75-HT-0.

² The incident power is expressed in terms of the microwave power which would pass through an area 1 cm² normal to and immediately in front of the cornea, but in the absence of the eye.

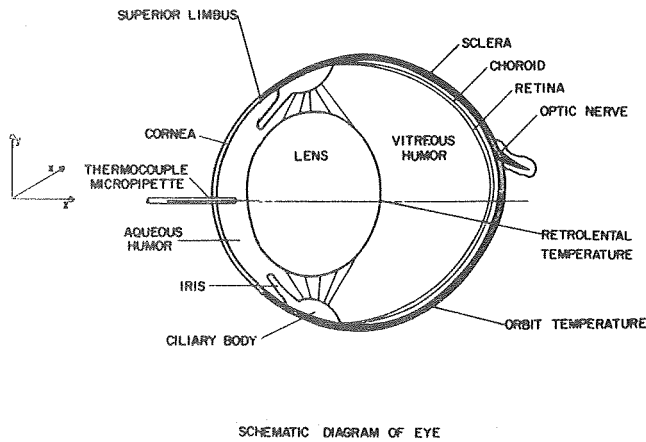


Fig. 1 Vertical section of a rabbit eye

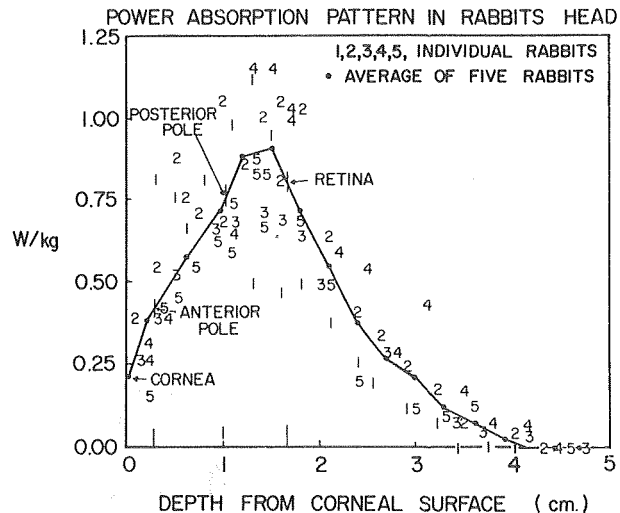


Fig. 2 Power absorption pattern in the eye and head of rabbits exposed to 2450 MHz "C" director. The dipole was horizontally polarized and is 5 cm from the corneal surface. Values are for 1 mW/cm² incident

The probe was then introduced further into the eye and the process repeated. This survey was continued until the probe reached the bony orbit. The animals were then sacrificed and the power measurements continued into the remainder of the head.

After the measurements were completed, the fellow eye was enucleated and frozen. After complete solidification, the eye was bisected sagittally and anterior-posterior measurements were made of the corneal thickness, anterior chamber depth, lens thickness, and the distance between the posterior capsule and the retina. These dimensions were used as a guide in gauging the location of the probe in the other eye, because passage of the probe into the lens prevented direct visualization of its tip.

Prior to the animals' sacrifice, the rectal temperature and pulse rate were continuously monitored to assure normal physiological behavior during the test. In general, the rabbits showed an average increase of 1°C in rectal temperature and a 30 percent increase in pulse rate for a 20 s exposure—suggesting that the thermoregulatory system of the anesthetized rabbit responds rapidly to the energy absorbed by the head.

Fig. 2 illustrates that power deposition pattern for five test animals and the mean distribution. The absorbed power peaks mid-way between the lens and the retinal surface with maximum absorption of 0.92 W/Kg per 1 mW/cm² incident power. To ensure that the micropipette did not affect the deposition, tests were also made by inserting a micropipette vertically 3.5mm behind the superior limbus and on the anterior-posterior axis and agreement was found between the two techniques to within 2 percent.

3 The Theoretical Thermal Model

Having determined the power deposition pattern, it was then necessary to postulate a thermal model which could be used to predict the temperature distribution in the eye. Fig. 3 depicts the assumed thermal model and identifies the major heat pathways.

A Internal Conduction. The three major thermal parts of the eye are: the vitreous humor; the lens; the aqueous humor. The vitreous humor is a gelatinous-like material whose thermal conductivity in beef eyes is 0.59 W/m-°C [10]. No precise values are as

yet available for rabbit eyes (reference [11] suggests 0.45 W/m-°C) although electron microscopy suggests that the vitreous humor is similar in both species. The value for beef eyes was thus adopted for the rabbit eye.

Based upon the electrical conductivities of the vitreous humor and the lens of beef eyes [10] the rabbit lens was estimated to have a conductivity of 0.21 W/m-°C. Because of this low conductivity and the very large lens size in the rabbit, the lens creates a significant thermal barrier. The aqueous humor is a saline-like solution whose pressure maintains the external shape of the cornea and in beef eyes has a conductivity of 0.58 W/m-°C. Although this fluid is continually replenished from the body at a rate of 0.002 cm³/min [12], it is not felt that the velocities associated with this replenishment will augment the heat transfer. In addition to the thermal conductance of the fluid, the free convection cell set up by the temperature difference between the cornea and the lens creates a slowly moving circulation [13]. The increase in the conductance of the aqueous humor was estimated to be less than 5 percent by using reported correlations for the free convection of fluids in narrow rectangular vertical enclosures [14].

B Arterial Heat Transfer. In the normal eye, the temperature distribution is established primarily by the temperature of the arterial blood supplied to the choroid, the retina and the sclera (hereafter this group is termed the choroid). Blood is also supplied to the ciliary body and to the iris. In view of the geometric positions of the latter structures, they are considered as separate major arterial supplies. The normal rabbit's arterial blood enters the vascular bed of the choroid at a temperature near 37°C and exits at a slightly lower temperature, due to the heat transfer to the vitreous humor. The precise mechanism by which heat is transferred from the blood to the humors in the vascular beds is unknown although it is common to treat such vascular beds in the body as counterflow heat exchangers [15, 16]. At present, the most useful thermal point of view is to regard these vascular beds as heat exchangers in which the blood enters at a fixed arterial temperature and exits at the

Nomenclature

A = area (m²)
 c = specific heat capacity (joules/Kg-°C)
 h = convective heat transfer coefficient (W/m²-°C)
 k = thermal conductivity (W/m-°C)

\dot{m} = flow rate (cm³/s)
 q = heat transfer (W/m²)
 \dot{q} = rate of energy deposition (W/Kg)
 t = time (s)
 T = temperature (°C)
 ρ = density (Kg/m³)

Subscripts
 ti = tissue
 bl = blood
 c = convection
 r = radiation
 e = evaporation

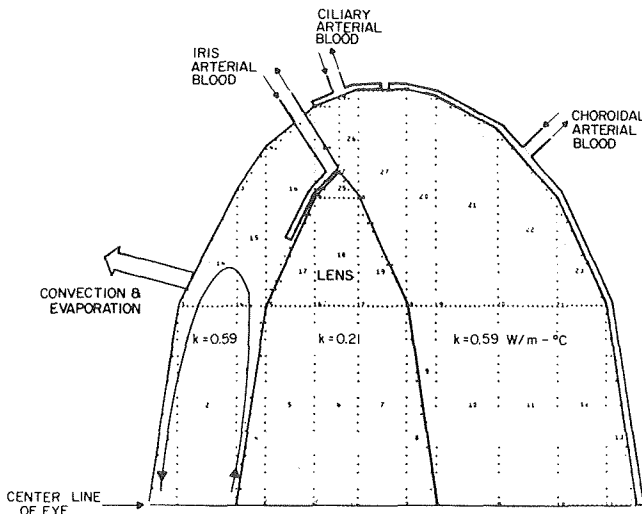


Fig. 3 Finite element model of an eye

equilibrium tissue temperature [16].

For this model of the vascular beds, heat transfer can be expressed as,

$$q = (\dot{m}C)_{bt}(T_{bt} - T_{ti}) \quad (2)$$

or the arterial blood can be regarded as a convective heat transfer boundary condition with an equivalent heat transfer coefficient of

$$hA = (\dot{m}C)_{bt} \quad (3)$$

where A is the surface area of the choroid, sclera, and retina.

In the unheated eye most of the heat transferred to the ambient air comes from the blood near the ciliary body and the heat conducted through the vitreous humor is sufficiently small enough that the temperature distribution in the vitreous humor is governed more by the blood temperature than by the effective heat transfer coefficient. By contrast, the irradiated eye must transfer the considerable amount of energy absorbed in the vitreous humor and the temperature levels in the vitreous humor are determined equally as much by the arterial blood flow rate as by the arterial blood temperature. The primary difficulty then lies in determination of the blood flow rate, \dot{m} . Because of the size of the eye and the multitudinous pathways of blood, the blood flow rates are very difficult to determine. O'Day, et al. [17] have suspended microspheres in the arterial system and optically determined their density in the blood supply of the eye. Their values for the ocular blood flow rates in rabbits are,

choroid	64 percent of total ocular supply
ciliary and iris	27 percent
sclera	2 percent
retina	6 percent

Alm and Bill [18] report for cats,

iris	6 percent
ciliary	25 percent
choroid	69 percent

Unfortunately, separate blood flow rates for the ciliary and the iris are not available for rabbits.

Taking the same ratio for iris and ciliary in rabbits, as reported for cats (since the overall percentages for the choroid group are not significantly different, i.e., 72 percent and 69 percent) we have,

iris	5 percent
ciliary	22 percent
choroid, sclera and retina	72 percent

Calculations for the separate ciliary and iris blood flows and for combined blood flows have not shown any significant differences in the temperature distributions.

We leave the question of the total blood flow rate for Section 4.

C Evaporation. The cornea is the only surface at which heat escapes from the normal eye. Because of the geometric situation of the cornea, it is exposed to either forced or natural convection and this heat transfer is augmented by evaporation from the corneal surface. Unfortunately, the rate of evaporation is never uniquely specified. Blinking or the presence of tears (tearing), or any other form of copious irrigation of the eye, can cause an order of magnitude increase in the evaporative heat transfer.

Since all the test animals' eyelids were sutured to prevent blinking and since no abnormal tearing was noted during all but the last portion of the experiment, the evaporation was presumed to take place in a laminar flow atmosphere. Heat transfer estimates based upon laminar flow over a vertical flat plate [19, 20] gave the values,

$$\begin{aligned} h_c &= 10 \text{ W/m}^2 - ^\circ\text{C} \quad (\text{convection}) \\ h_r &= 6 \text{ W/m}^2 - ^\circ\text{C} \quad (\text{radiation}) \\ L_e &= 12 \text{ W/m}^2 - \text{mmHg} \quad (\text{evaporation}) \end{aligned}$$

D Numerical Results. Using the above data, the eyeball was modelled by a finite element nodal point network of rectangles and triangles as indicated in Fig. 3. The temperatures were then computed using the University of Washington Finite Element Thermal Analyzer. Assuming a retinal temperature of 37.1°C (thus eliminating the need for a knowledge of the blood flow), and ambient conditions of 25°C and 35 percent relative humidity, the center-line temperatures shown on Fig. 4 were obtained. Data from Schwartz and Feller [21] for the same retinal temperature gave the circled points. The agreement between the two indicates that the

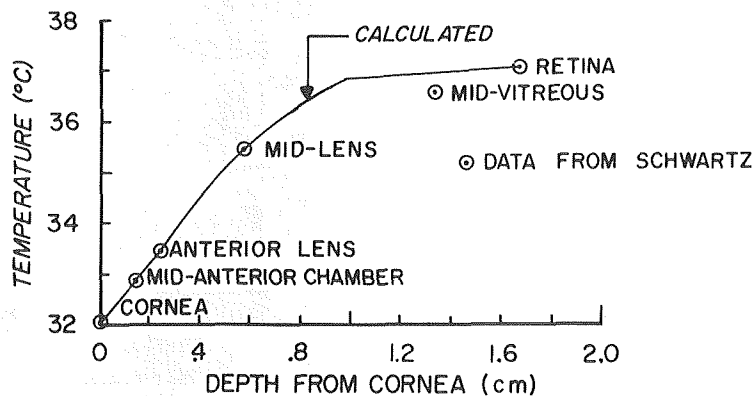


Fig. 4 Comparison of steady-state temperature patterns

conductivity values were reasonably accurate. It is of interest to note that the three-dimensional heat transfer effects tend to smooth out the temperature distribution and to eliminate some of the discontinuity in slope that one expects from a one-dimensional model.

4 Experimental Temperature Measurements

In contrast to the dosimetry surveys (Section 2), the temperatures in rabbit eyes exposed under the same conditions as the cataract studies were measured only at two points in the eye: (1) directly behind the lens with a micropipette inserted from above (retrolental temperature); (2) in the orbit, between the globe and the bone (orbit temperature). These temperatures were recorded approximately every 5 min. The procedure was to expose the test animal to a continuous source of radiation. At 5 min the radiation was stopped and the iron-constantan thermocouple inserted into the micropipette, read and then withdrawn. The radiation was then restarted. This process was repeated until a desired response time had been reached and the radiation was terminated. The thermocouple was then placed in the micropipette and continuously monitored throughout the cooldown period. Fig. 5 illustrates a typical temperature trace for an irradiation level of 200 mW/cm². Steady-state is reached at about 15 min, but there is a further slow rise due to the gradual rectal temperature rise. This latter effect is most noticeable at long times where the elevation of all temperatures is clearly seen. In general since the microwave radiation power absorption is not restricted to the eye, but exists throughout the head and part of the body of the animal, there is a general elevation of the blood temperature. After the radiation has been terminated, a period of several hours is required before the animal's physiological state returns to normal.

Fig. 6 illustrates the retrolental temperature changes at three different radiation power levels.

5 Comparison of Theory and Experiment

Although the test results shown in Fig. 4 suggest that the conductivities of the eye are realistic, the major question of the arterial blood supply remains unanswered. The blood perfusing the choroid not only acts as the major source of heat for the normal eye, but also acts as the primary source of cooling for the heated eye. Data from Alm and Bill [18], O'Day [17], and Trokel [22] suggest a total blood flow of 1-2 cm³/min in each rabbit eye. The use of equation (3) leads to values of h of 150 to 300 W/m²·°C. These low values of the convective heat transfer coefficient (corresponding to 25 to 50 Btu/hr-ft²·°F) coupled with the presence of the thermal barrier effect of the lens imply that realistic calculations will be sensitive to the blood supply rate. A series of tests were performed with various assumed blood rates for an eye subjected to a 22 min exposure of 100 mW/cm² incident radiation. The numerical results were compared to an experimental test result. Although no numerical result was in total agreement with the measured data, the calculation based upon a blood flow rate of 1.7 cm³/min (or $h = 250$ W/m²·°C) gave results which were acceptable as shown in the following

	Measured	Calculated
Arterial blood temperature	39.0	39.0
Orbit	40.1	40.27
Vitreous	41.0	41.2
Vitreous (no irradiation)	38.0	38.1

Using this value of ocular blood flow, computations were performed for different radiation levels. Except for the hypothermia case (Section 6) the computations always overestimated the peak vitreous temperature. A series of computations were then performed with varying blood flow rates in order to match the steady-state values of the vitreous and orbit temperature. Fig. 5 illustrates the comparison between the measured and predicted temperatures (based on $\dot{m}_{bl} = 2.7$ cm³/min) for the heating and cool down phase.

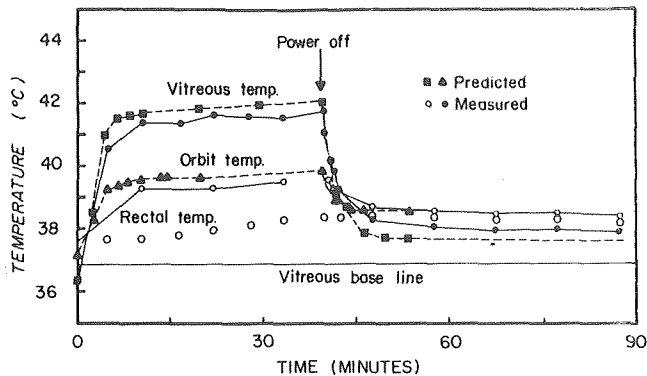


Fig. 5 Intraocular temperatures in rabbit during acute exposure to near field 2450 MHz radiation

Fig. 6 illustrates the transient calculations and the respective blood flow rates. The increased estimated blood flow rates are linearly related to the retrolental temperature. Blood perfusion experiments on human forearm skin [23] have shown that skin blood flow is constant for normal and slightly subcooled temperatures and approximately linearly related to the rise above normal of the local skin temperature with the increase being facilitated by a dilation of the blood vessels rather than by any change in blood pressure. Biomicroscopical (slit-lamp) examination of the iris at zero, 100 mW/cm² radiation of normothermic animals or 300 mW/cm² radiation of hypothermic animals showed only the normally visible peripheral arcade, but the 200 and 300 mW/cm² radiation levels revealed previously narrowed or invisible vessels to be dilated. We are not suggesting that the choroidal blood vessels respond to temperature precisely as the arm does, but they are part of the uvea tract, as is the iris, and a dilation in response to temperature is not unreasonable. For the 200, 300, and 540 mW/cm² exposure tests, panting, and increased respiration rates, increased pulse rates occurred in all the rabbits in conjunction with the dilated iris vessels. The nature of the calculated blood flow rate dependence upon temperature and the good agreement of the calculated transient temperature suggest that the thermal model is reasonable and can be used to compute both the transient response and the arterial blood supply rate. In all cases the measured values are lower than

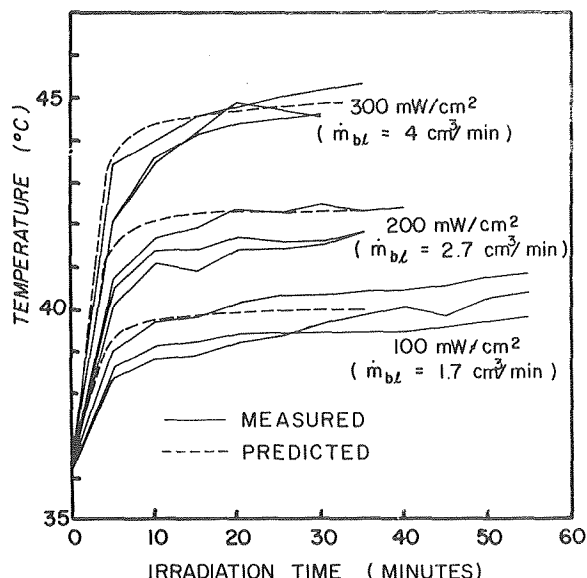


Fig. 6 Measured and predicted changes in retrolental temperature during acute exposure of rabbit to near zone 2450 MHz radiation (three rabbits tested per exposure level)

MICROWAVE CATARACTOGENESIS

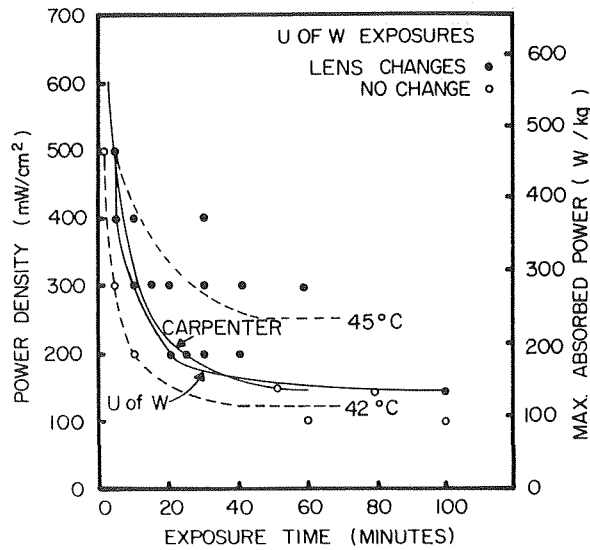


Fig. 7 Computed and measured time and power density thresholds for near field 2450 MHz induced lens opacities in rabbits and computed retrolental temperature time-power relationship

the predicted until a reasonably steady state is reached. Much of the disparity is due to the time lag between the termination at the microwave and the insertion and reading of the thermocouple. It must be emphasized that the agreement can never be more than approximate. Each rabbit was subjected to different ambient conditions, had a different nonirradiated temperature profile in the eye, had an apparently different blood flow, responded differently to anesthesia and differently to the radiation. Furthermore, the basic heat loss mechanism of the rabbit (panting and convection from the ears) is quite variable and difficult to numerically prescribe. The data presented represent approximately 80 percent of the rabbits tested. The remaining 20 percent exhibited noticeable irregularities in physiological response during or after the tests. Fig. 7 shows the approximate power-time relationships for 42 and 45°C temperatures at the posterior surface of the lens.

Simultaneously with the thermal tests, a series of exposures were made without temperature measurements to detect the genesis of cataracts. The animal eyes were examined with a slit-lamp ophthalmoscope before and after the tests in which only one eye was exposed to the radiation. Cataracts were judged to exist when the slit-lamp examination revealed either areas of opacity at the rear of the lens or a significant number of vacuoles formed along

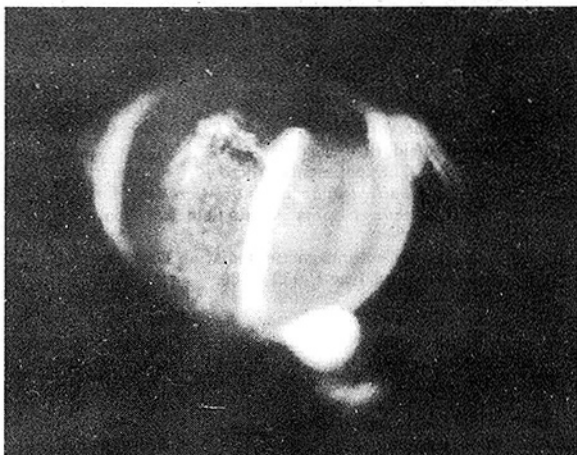


Fig. 8 Slit lamp photograph of lens opacities produced by microwave heating

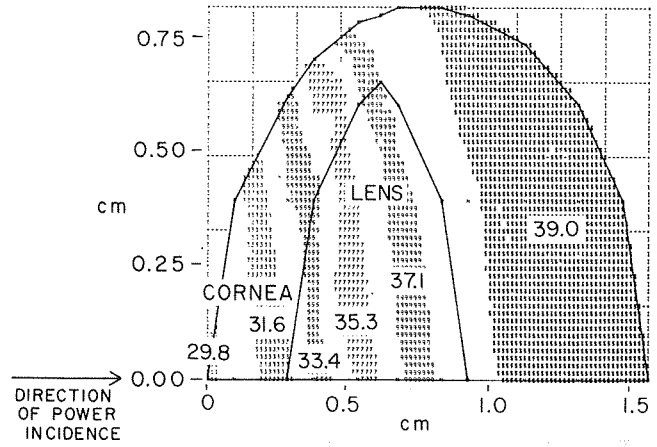


Fig. 9 Isotherm patterns in the rabbit eye with fully dilated iris

the posterior suture line. Fig. 8 is a slit lamp photograph of an eye with the opacity of the posterior surface of the lens revealed as the fibrous looking area. The bright band of light is simply the reflection of the slit lamp from the anterior surface of the lens. A normal eye would show only the slit band. Some of the cataracts did not form for several days, while others eventually disappeared at periods as long as 12 months after exposure, but all were classified as cataracts. Thus our cataract formation exposure times represent a lowest threshold. Fig. 7 is a plot of the minimum exposure time necessary to produce an opacity at any given microwave radiation power level. The dark circles represent cataract forming exposure levels and the light represent undamaged eye exposure times. For power levels below 150 mW/cm², the required exposure time is greater than 100 min. Carpenter's [24] data for rabbits are also shown. The dashed lines represent the numerically determined approximate power-exposure times relationships to achieve 42°C and 45°C at the rear of the lens. A comparison of the cataract data with the computed curves suggest that a critical temperature for cataracts may be of the order of 43°C.

It is normal for most animals to dilate or constrict the pupil to accommodate changes in incident light levels. There did appear to be some constriction of the iris due to the energy absorption. Fig. 9 shows the calculated isotherm patterns in the eye for the fully dilated iris. There was no easily discernible change in the patterns

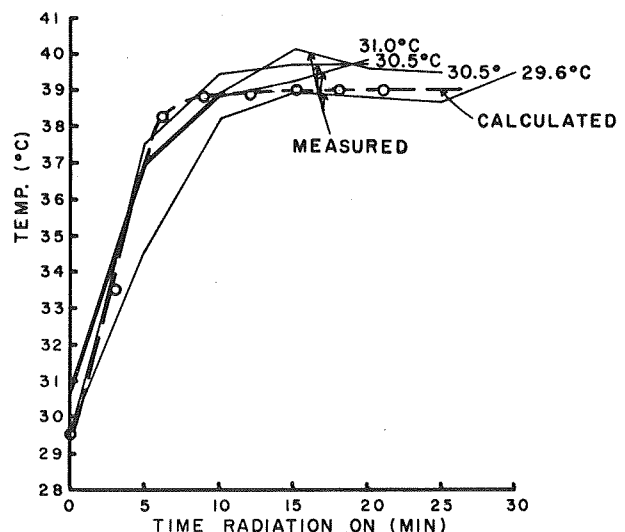


Fig. 10 Measured and predicted retrolental temperature in hypothermic rabbits exposed to microwave radiation

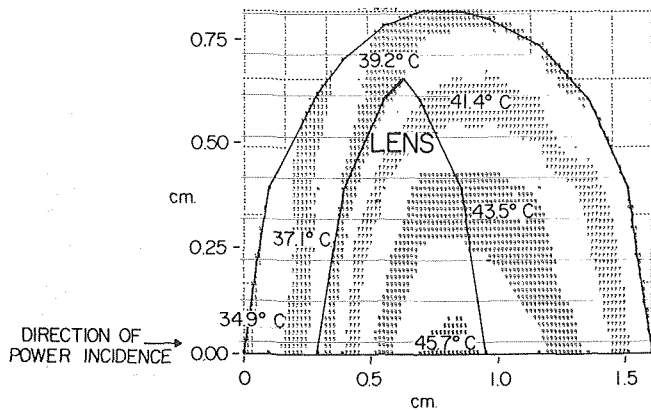


Fig. 11 Isotherm patterns in the eye of rabbits exposed to 10 mW/cm² of 2450 MHz radiation

for the fully constricted iris although the full constriction lowered the peak temperature by 0.5°C.

6 Hypothermia

A series of rabbits were subjected to artificially induced general hypothermia with the body temperature maintained at a temperature estimated to be low enough to ensure that the maximum eye temperature never reached 40°C, 3°C below our estimated threshold. Fig. 10 compares the measured and the predicted temperatures based upon the 1.7 cm³/min ocular blood flow. The agreement is good and the maximum temperature did not reach the threshold value. Examination did not reveal any cataracts in any of the rabbits exposed during hypothermia.

7 Low-Level Irradiation—10mW/cm²

For comparison, and to establish a sense of proportions, a numerical test was made for the present safety standard of 10 mW/cm² [25]. The isotherm patterns are illustrated in Fig. 11. Two effects are most noticeable: (1) the maximum temperature did not exceed the orbital blood supply temperature; (2) the isotherm pattern showed no localized heating near the posterior surface of the lens (compare with Fig. 9). At this low level of irradiation, the only effect of heating is a minor elevation of temperature throughout the entire lens. The maximum temperature was well below the suspected cataractogenic temperature, therefore, cataract production through the absorption of microwave radiation is unlikely. However, long term low level irradiation may produce cataracts, although present tests do not indicate this.

8 Conclusions

A finite element thermal model of the rabbit eye when coupled with an estimated arterial blood flow has been shown to be capable of simulating the transient thermal response of an irradiated eye. Calculations based on this model, and experimental observations of the genesis of cataracts, appear to lend support to the hypothesis of microwave radiation induced cataractogenesis being related to temperature elevation. Further work needs to be done to establish more precise values of the thermal properties, blood flow and the effects of short but repeated exposures to sub-threshold radiation levels.

Acknowledgment

This work was supported in part by the Office of Naval Research under Contract No. N00014-67-A-0103-0025, in part by a grant from the Association of Home Appliance Manufacturers, and in part by the Social and Rehabilitation Service Grant No. 16-P-5681810-12.

References

- Lerman, S., *Cataracts, Chemistry, Mechanisms, and Therapy*, C. T. Thomas, Springfield, Ill., 1964, p.127.
- Duke-Elder, S., *System of Ophthalmology, Diseases of Lens and Vitreous; Glaucoma and Hypotony*, published by Henry Kimpton, London, 1969, p. 81.
- Mehta, P. P., and Maisel, H., "Effect of Heat on Bovine Lens Protein," *Experientia*, Vol. 22, 1967, p. 818.
- Dally, L., Wakin, K. G., Herrick, J. F., and Parkhill, E. M., "Effects of Microwave Diathermy on the Eye," *Amer. J. Physiol.*, Vol. 155, 1948, p. 432.
- Richardson, A. W., Duane, T. D., and Hines, H. M., "Experimental Lenticular Opacities Produced by Microwave Irradiations," *Arch. Phys. Med.*, Vol. 29, 1948 pp. 765-769.
- Osborne, S. L., and Frederick, J. N., "Microwave Radiation: Heating of Human and Animal Tissues by Means of High Frequency Current With Wavelength of Twelve Centimeters," *J. Amer. Med. Assoc.*, Vol. 137, 1948, pp. 1030-1040.
- Carpenter, R. L., and Van Ummerson, C. A., "The Action of Microwave Power on the Eye," *J. Microwave Power*, Vol. 3, 1968, pp. 3-19, and private communication.
- Williams, D. B., Monahan, J. P., Nicholson, W. J. and Aldrich, J. J., "Biological Effects Studies on Microwave Radiation: Time and Power Thresholds for the Production of Lens Opacities by 12.3 cm Microwaves," *USAF School of Aviation Medicine*, Dept. 55-94, 1955.
- Johnson, C. C., and Guy, A. W., "Nonionizing Electromagnetic Wave Effects in Biological Materials and Systems," *Proc. IEEE*, 1972, pp. 672-718.
- Pauly, H., and Schwan, H. P., "The Dielectric Properties of the Bovine Eye Lens," *IEEE Trans. Bio-Med. Eng.*, July 1964, pp. 103-109.
- White, T. J., et al., "Chorioretinal Thermal Behavior," *Bull. Math. Biophys.*, Vol. 5, 1970, p.315.
- Adler's Physiology of the Eye*, Moses, R. A., ed., Fifth ed., C. V. Mosby, St. Louis, 1970, p. 272.
- Ibid.*, p. 253.
- Emery, A. F., and MacGregor, R. K., "Free Convection Through Vertical Plane Layers of Moderate and High Prandtl Number Fluids," *J. OF HEAT TRANSFER*, Series C, Vol. 91, 1969, pp. 391-404.
- Keller, K. H., and Seiler, L. Jr., "An Analysis of Peripheral Heat Transfer in Man," *ibid. Appl. Phys.*, Vol. 30, May 1971, pp. 779-786.
- Nevens, R. G., and Darwish, M. A., "Heat Transfer Through Subcutaneous Tissue as Heat Generating Porous Material," Chapter 21, *Physiological and Behavioral Temperature Regulation*, C. C. Thomas, Publisher, Springfield, Ill., 1970.
- O'Day, D. M., Fish, M. B., Aronson, S. B., Pollycove, M., and Coon, A., "Ocular Blood Flow Measurements by Nuclide Labelled Microspheres," *Arch. Ophthalmol.*, Vol. 86, 1971, pp. 205-209.
- Alm, A., and Bill, A., "Ocular and Optic Nerve Blood Flow at Normal and Increased Intraocular Pressures in Monkeys," *Exp. Eye Res.* Vol. 15, 1973, pp. 15-29.
- Jakob, M., *Heat Transfer*, Wiley, New York, 1949.
- Bird, R. B., Stewart, M., and Lightfoot, E., *Transport Phenomena*, Wiley, New York, 1960.
- Schwartz, B., and Feller, M. R., "Temperature Gradients in the Rabbit Eye," *Invest. Ophthalmol.*, Vol. 1, 1962, pp. 513-521.
- Trokel, S., "Quantitative Studies of Choroidal Blood Flow by Reflective Densitometry," *Invest. Ophthalmol.*, Vol. 4, 1971, pp. 1129-1140.
- Benzinger, T. H., "Peripheral Cold Reception and Central Warm Reception, Sensory Mechanisms of Behavioral and Autonomic Thermostasis," *Physiological and Behavioral Temperature Regulation*, Charles C. Thomas, Publisher, Springfield, Ill., 1970.
- Carpenter, R. L., "Experimental Microwave Cataract: A Review," *Biological Effects and Health Implications of Microwave Radiation*, Symp. Proc. Public Health Service, Bureau of Radiological Health Dept. BRH/DBE 70-2, 1970.
- "Safety Level of Electromagnetic Radiation With Respect to Personnel," *Amer. National Stand. Inst. C-95.1*, 1966.

This section consists of contributions of 1500 words or less (about 5 double-spaced typewritten pages, including figures). Technical briefs will be reviewed and approved by the specific division's reviewing committee prior to publication. After approval such contributions will be published as soon as possible, normally in the next issue of the journal.

Free Convection From a Horizontal Cylinder With Isothermal and Constant Heat Flux Surface Conditions

C. B. Kim,¹ T. J. Pontikes,² and D. E. Wollersheim³

Approximate solutions for free convection heat transfer from a horizontal cylinder have been developed by several authors. Levy [1]⁴ provided an approximate integral solution for the isothermal cylinder to Newtonian fluids. For non-Newtonian fluids, an approximate integral solution has been presented by Gentry and Wollersheim [2] for the isothermal case and by Kim [3] for the constant flux case. These solutions are obtained by assuming a high Prandtl number so that the inertial terms in the momentum equation can be neglected. Since a Newtonian fluid is a special case of the non-Newtonian model, the solutions for Newtonian fluids can be obtained from reference [2, 3]. For the isothermal case, Gentry's expression for local Nusselt number reduces to that of Levy for the Newtonian case. For the constant flux case, the solution of Kim can be used for both the Newtonian and non-Newtonian cases.

The present study is an attempt to verify experimentally these integral solutions for Newtonian fluids by comparing them with data for local free convection from a horizontal cylinder to mineral oil for both the isothermal and constant flux surface conditions. Mineral oil has been used because of its high Prandtl number (>1000).

From reference [1, 2] the local Nusselt number expression for convection from an isothermal horizontal cylinder to a Newtonian fluid can be expressed as

$$N_{Nu_i} = \frac{h_c R}{k} = 0.513 (N_{Gr_i} N_{Pr})^{1/4} \frac{(\sin\phi)^{1/3}}{(\int_{\phi=0}^{\phi} (\sin\phi)^{1/3} d\phi)^{1/4}} \quad (1)$$

where

¹ Graduate Student, Department of Mechanical and Aerospace Engineering, University of Missouri-Columbia, Columbia, Mo.

² Mechanical Engineer, Fluor-Pioneer Inc., Chicago, Ill.

³ Assoc. Professor, Department of Mechanical and Aerospace Engineering, University of Missouri-Columbia, Columbia, Mo.

⁴ Numbers in brackets designate References at end of technical brief.

Contributed by the Heat Transfer Division of THE AMERICAN SOCIETY OF MECHANICAL ENGINEERS. Manuscript received by the Heat Transfer Division October 4, 1974.

$$N_{Gr_i} = \frac{\rho^2 R^3 \beta g (T_w - T_\infty)}{\mu^2} \quad (2)$$

$$N_{Pr} = \frac{\mu C_p}{k} \quad (3)$$

R is the radius of the cylinder and ϕ is the angle measured from the lower stagnation point.

For a constant heat flux horizontal cylinder, reference [3] gives the local Nusselt number for Newtonian fluids as follows:

$$N_{Nu_c} = 0.594 (N_{Gr_c} N_{Pr})^{1/5} \frac{(\sin\phi)^{1/4}}{(\int_{\phi=0}^{\phi} (\sin\phi)^{1/4} d\phi)^{1/5}} \quad (4)$$

where

$$N_{Gr_c} = \frac{\rho^2 R^4 \beta g q_0}{\mu^2 k} \quad (5)$$

and q_0 is the constant heat flux supplied to the surface of the cylinder.

Experimental Results

In order to achieve the isothermal and constant heat flux surface, an aluminum cylindrical test section was constructed of twenty independently heated segments. Each segment is electrically heated and copper-constantan thermocouples are installed within the aluminum segment. Surface temperatures were then determined from these measured values using Fourier's conduction equation. The ten channel power supply and controller unit consisted of a triac trigger unit, sensistor bridge circuit, and voltage measurement circuit.

Experimental free convection data for mineral oil were obtained for both isothermal and constant heat flux cases. All local free convection data were expressed in terms of dimensionless groups and compared with integral solutions shown in equations (1) and (4). The temperature differences for the isothermal case ranged from 20°F to 46°F and the maximum surface temperature was 122.5°F while the constant heat flux values ranged from 219.5 Btu/hr-ft² to 333.6 Btu/hr-ft² with maximum temperature differences of 30.4°F and 40.7°F, respectively. All physical properties appearing in the dimensionless groups were evaluated at the local film temperature which is taken to be the mean of the surface and bulk fluid temperatures. Graphical presentations of local free convection results and comparisons with integral solutions are shown in Figs. 1 and 2. In addition the results for heat transfer to air from an isothermal cylinder as determined by Eckert [4] are presented for comparison in Fig. 1. The poor correlation is undoubtedly due to our high Prandtl number assumption. Similar results for water [2] are also presented.

The experimental results for mineral oil as shown in Figs. 1 and

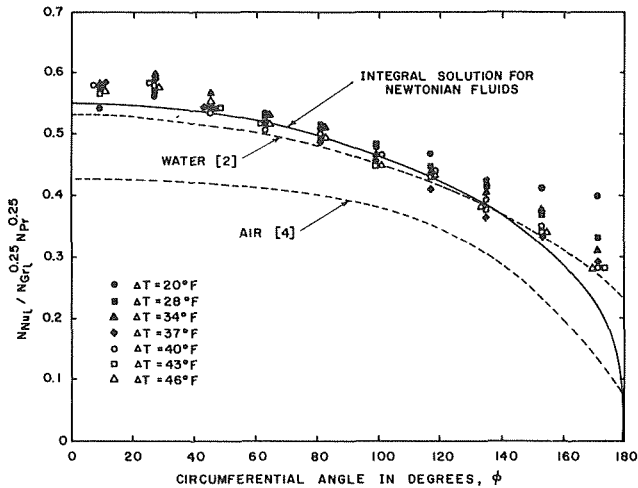


Fig. 1 Isothermal heat transfer results for mineral oil

2 agree quite well with integral solutions for angles smaller than about 150 deg. However, at angles higher than 150 deg, experimental values for the local free convection coefficients are higher than the integral solutions in both cases. This phenomenon is primarily attributable to boundary layer interaction in the upper stagnation region which is not accounted for in the integral solution. As a result the integral solution is not valid as the upper stagnation region is approached.

Average free convection results were obtained by integrating local Nusselt, Prandtl, and Grashof numbers over the test section surface area, and the average Nusselt numbers for all experimental data were obtained from a least square fit to be

$$(N_{Nu_i})_{avg} = 0.89 (N_{Gr_i} N_{Pr})^{0.19} \quad (6)$$

$$(N_{Nu_c})_{avg} = 0.57 (N_{Gr_c} N_{Pr})^{0.20} \quad (7)$$

The average expression for the isothermal case agrees quite well with McAdams' [5] correlation. Further details regarding the present work may be found in reference [6, 7].

References

- 1 Levy, S., "Integral Methods in Natural Convection Flow," *Journal of Applied Mechanics*, 1955, pp. 512-522.
- 2 Gentry, C. C., and Wollersheim, D. E., "Local Free Convection to Non-Newtonian Fluids From a Horizontal, isothermal Cylinder," *JOURNAL OF*

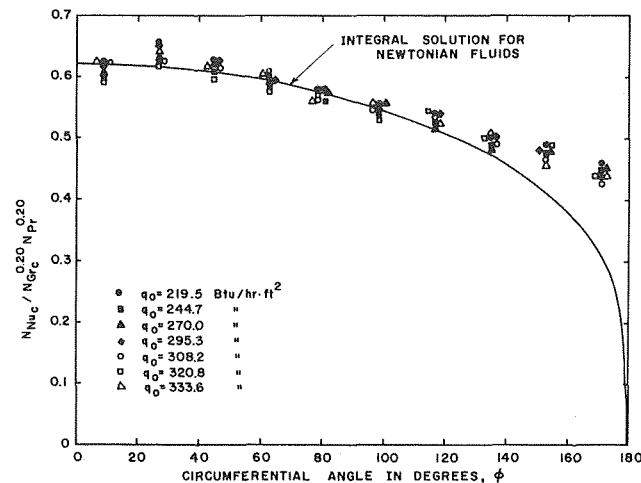


Fig. 2 Constant heat flux heat transfer results for mineral oil

HEAT TRANSFER, TRANS. ASME, Series C, Vol. 96, No. 1, Feb. 1974, pp. 3-8.

3 Kim, C. B., "Free Convection Heat Transfer From a Horizontal Cylinder to Dilatant Fluids," PhD thesis, University of Missouri-Columbia, Columbia, Mo., 1975.

4 Eckert, E. R. G., and Soehngen, E. E., "Studies on Heat Transfer in Laminar Free Convection with the Zehnder-Mach Interferometer," USAF Air Material Command. Tech. Report No. 5747, Dayton, Ohio, 1948.

5 McAdams, W. H., *Heat Transmission*, Third ed., McGraw-Hill, New York, 1954, pp. 175-177.

6 Kim, C. B., "Free Convection Heat Transfer From an Isothermal Horizontal Cylinder to Mineral Oil," MS thesis, University of Missouri-Columbia, Columbia, Mo., 1973.

7 Pontikes, T. J., "Free Convection Heat Transfer to Mineral Oil From a Horizontal Cylinder Under Constant Surface Heat Flux," MS thesis, University of Missouri-Columbia, Columbia, Mo., 1974.

Lower Bounds to the Critical Rayleigh Number for Completely Confined Fluids Inside Arbitrary Configurations

D. Pnueli¹

Introduction

A quiescent, quasi-incompressible (Boussinesq [1])² fluid is completely confined inside an arbitrarily shaped container with good heat conducting rigid walls. An external temperature distribution is imposed on the container walls such that a constant temperature gradient is set in the fluid and on the inside of the container walls. This temperature gradient is parallel and opposite to gravity, i.e., the fluid is "heated from below" and heavier fluid layers are supported by lighter ones. A small disturbance in the original rest state may cause the onset of a convective motion in the fluid (in which case the situation is defined *thermally unstable*), or it may decay in time (*thermally stable* case). The problem of thermal stability is to determine whether a given situation is stable or unstable.

A fairly extensive survey of published investigations in this field is available in various sources, e.g., Chandrasekhar [2]. A more limited survey which is directly connected with this work, is presented by Sherman and Ostrach [3].

At present there is no available method of solution for a general three-dimensional configuration. Because instability is associated with a marked increase in heat transfer rates, the numerical value of the *critical Rayleigh number*, which is the instability criterion, is of extreme interest in the design and evaluation of porous insulating materials or convection inhibitors.

A method to obtain lower bounds for the most general geometry, and a modification of this method for some particular regions, were presented by Sherman and Ostrach [3].

The contribution of this paper is that:

- (a) It modifies the method to obtain better (2.5 times higher than in [3]) lower bounds for the most general configuration.
- (b) It further improves the lower bound for cylindrical configurations of arbitrary cross section.
- (c) It improves the method for the particular configurations considered in [3].

¹ Faculty of Mechanical Engineering, Technion-Israel Institute of Technology, Haifa, Israel

Contributed by the Heat Transfer Division of THE AMERICAN SOCIETY OF MECHANICAL ENGINEERS. Manuscript received by the Heat Transfer Division May 31, 1974.

² Numbers in brackets designate References at end of technical brief.

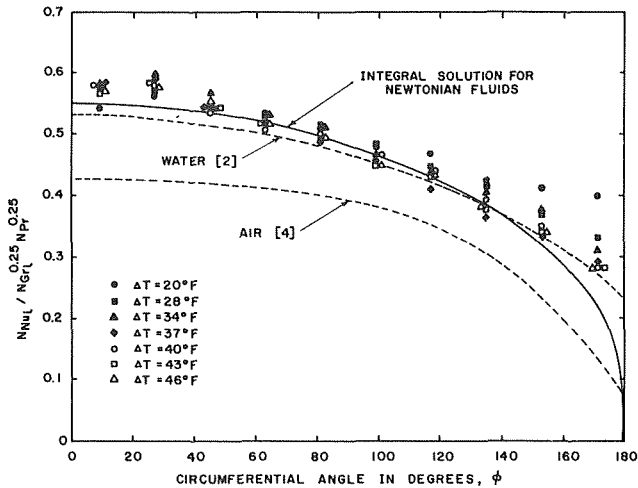


Fig. 1 Isothermal heat transfer results for mineral oil

2 agree quite well with integral solutions for angles smaller than about 150 deg. However, at angles higher than 150 deg, experimental values for the local free convection coefficients are higher than the integral solutions in both cases. This phenomenon is primarily attributable to boundary layer interaction in the upper stagnation region which is not accounted for in the integral solution. As a result the integral solution is not valid as the upper stagnation region is approached.

Average free convection results were obtained by integrating local Nusselt, Prandtl, and Grashof numbers over the test section surface area, and the average Nusselt numbers for all experimental data were obtained from a least square fit to be

$$(N_{Nu_i})_{avg} = 0.89 (N_{Gr_i} N_{Pr})^{0.19} \quad (6)$$

$$(N_{Nu_c})_{avg} = 0.57 (N_{Gr_c} N_{Pr})^{0.20} \quad (7)$$

The average expression for the isothermal case agrees quite well with McAdams' [5] correlation. Further details regarding the present work may be found in reference [6, 7].

References

- 1 Levy, S., "Integral Methods in Natural Convection Flow," *Journal of Applied Mechanics*, 1955, pp. 512-522.
- 2 Gentry, C. C., and Wollersheim, D. E., "Local Free Convection to Non-Newtonian Fluids From a Horizontal, isothermal Cylinder," *JOURNAL OF*

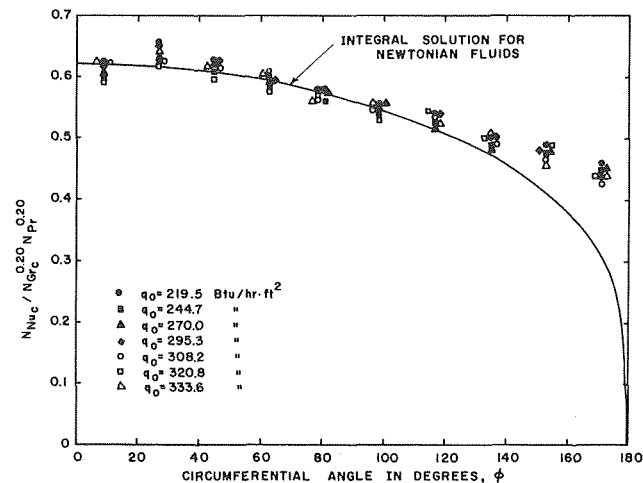


Fig. 2 Constant heat flux heat transfer results for mineral oil

HEAT TRANSFER, TRANS. ASME, Series C, Vol. 96, No. 1, Feb. 1974, pp. 3-8.

3 Kim, C. B., "Free Convection Heat Transfer From a Horizontal Cylinder to Dilatant Fluids," PhD thesis, University of Missouri-Columbia, Columbia, Mo., 1975.

4 Eckert, E. R. G., and Soehngen, E. E., "Studies on Heat Transfer in Laminar Free Convection with the Zehnder-Mach Interferometer," USAF Air Material Command. Tech. Report No. 5747, Dayton, Ohio, 1948.

5 McAdams, W. H., *Heat Transmission*, Third ed., McGraw-Hill, New York, 1954, pp. 175-177.

6 Kim, C. B., "Free Convection Heat Transfer From an Isothermal Horizontal Cylinder to Mineral Oil," MS thesis, University of Missouri-Columbia, Columbia, Mo., 1973.

7 Pontikes, T. J., "Free Convection Heat Transfer to Mineral Oil From a Horizontal Cylinder Under Constant Surface Heat Flux," MS thesis, University of Missouri-Columbia, Columbia, Mo., 1974.

Lower Bounds to the Critical Rayleigh Number for Completely Confined Fluids Inside Arbitrary Configurations

D. Pnueli¹

Introduction

A quiescent, quasi-incompressible (Boussinesq [1])² fluid is completely confined inside an arbitrarily shaped container with good heat conducting rigid walls. An external temperature distribution is imposed on the container walls such that a constant temperature gradient is set in the fluid and on the inside of the container walls. This temperature gradient is parallel and opposite to gravity, i.e., the fluid is "heated from below" and heavier fluid layers are supported by lighter ones. A small disturbance in the original rest state may cause the onset of a convective motion in the fluid (in which case the situation is defined *thermally unstable*), or it may decay in time (*thermally stable* case). The problem of thermal stability is to determine whether a given situation is stable or unstable.

A fairly extensive survey of published investigations in this field is available in various sources, e.g., Chandrasekhar [2]. A more limited survey which is directly connected with this work, is presented by Sherman and Ostrach [3].

At present there is no available method of solution for a general three-dimensional configuration. Because instability is associated with a marked increase in heat transfer rates, the numerical value of the *critical Rayleigh number*, which is the instability criterion, is of extreme interest in the design and evaluation of porous insulating materials or convection inhibitors.

A method to obtain lower bounds for the most general geometry, and a modification of this method for some particular regions, were presented by Sherman and Ostrach [3].

The contribution of this paper is that:

- (a) It modifies the method to obtain better (2.5 times higher than in [3]) lower bounds for the most general configuration.
- (b) It further improves the lower bound for cylindrical configurations of arbitrary cross section.
- (c) It improves the method for the particular configurations considered in [3].

¹ Faculty of Mechanical Engineering, Technion-Israel Institute of Technology, Haifa, Israel

Contributed by the Heat Transfer Division of THE AMERICAN SOCIETY OF MECHANICAL ENGINEERS. Manuscript received by the Heat Transfer Division May 31, 1974.

² Numbers in brackets designate References at end of technical brief.

Analysis

(a) **General Geometry.** The nondimensional linearized equations for marginal stability are borrowed from Sherman and Ostrach [3]:

$$\frac{\partial u}{\partial x} + \frac{\partial v}{\partial y} + \frac{\partial w}{\partial z} = 0 \quad (1)$$

$$\nabla^2 u - \frac{\partial P}{\partial x} = 0 \quad (2)$$

$$\nabla^2 v - \frac{\partial P}{\partial y} = 0 \quad (3)$$

$$\nabla^2 w - \frac{\partial P}{\partial z} - R_{ac}\theta = 0 \quad (4)$$

$$\nabla^2 \theta - w = 0 \quad (5)$$

$$u = v = w = \theta = 0 \text{ on } B \quad (6)$$

with the variational formulation

$$R_{ac} = \min \frac{\int_c [(\nabla u)^2 + (\nabla v)^2 + (\nabla w)^2] dV}{\int_c (\nabla \theta)^2 dV} \quad (7)$$

i.e., of all u, v, w, θ that satisfy equations (1), (5), and (6), those which make R_{ac} in equation (7) a minimum are the solution.

Sherman and Ostrach [3] suggest a lower bound in the form

$$R_{ac} > \min \frac{\int_c [(\nabla u)^2 + (\nabla v)^2 + (\nabla w)^2] dV}{\int_c [u^2 + v^2 + w^2] dV} \times \min \frac{\int_c (\nabla^2 \theta)^2 dV}{\int_c (\nabla \theta)^2 dV} \quad (8)$$

They also proved a theorem stating, that among all regions of a given volume, the sphere has the smallest value of the first eigenvalue of the Helmholtz equation.³ Formally:

$$\left. \begin{aligned} \nabla^2 f + K^2 f &= 0 \text{ in } C \\ f &= 0 \text{ on } B \end{aligned} \right\} \quad (9)$$

which has the equivalent variational formulation

$$K^2 = \min \frac{\int_c (\nabla f)^2 dV}{\int_c f^2 dV} \quad (10)$$

yields the smallest K^2 value for the sphere; thus K is the first root of $J_{1/2}(Kr) = 0$, i.e.,

$$K^2 = \frac{\pi^2}{r^2} = 4\pi^2 \quad (11)$$

They then proceed to show that both terms on the right-hand side of equation (8) are bounded from below by K^2 , and obtain the lower bound $(4\pi^2)^2$. This result, which does not use equation (1) at all, is too low.

Consider w in equation (5). Because of equation (1)

$$\int_{S_z} w dx dy = 0 \text{ (Ostrach and Pnueli [5])} \quad (12)$$

Equation (12) does not imply that equation (1) is satisfied. However, it rules out the first eigenfunction of the Helmholtz equation, which does not change sign, and with it the first eigenvalue. The lower bound is thus obtained by the second eigenvalue, which unfortunately is not known in general. Still, a lower bound to the second eigenvalue can be obtained as a particular case of a theorem proved by Pnueli [6]. This lower bound comes out to be:

$$\int_c (\nabla w)^2 dV / \int_c w^2 dV > \pi^2 / s^2 \quad (13)$$

³ Their proof holds for arbitrary regions with piecewise smooth boundaries, including multiply connected regions. Note the similarity between this theorem and that for two-dimensional regions with the circle yielding the smallest eigenvalue, as proved by Polya and Szego [4], which also holds for multiply connected regions.

where $4/3\pi s^3 = V/2$, V the total volume of the region. The same argument can now be repeated⁴ for u and v , to yield

$$\frac{\int_c (\nabla u)^2 dV}{\int_c u^2 dV} > \pi^2 / s^2 \quad (14)$$

$$\frac{\int_c (\nabla v)^2 dV}{\int_c v^2 dV} > \pi^2 / s^2 \quad (15)$$

Equations (13), (14), and (15) together yield:

$$\frac{\int_c [(\nabla u)^2 + (\nabla v)^2 + (\Delta w)^2] dV}{\int_c [u^2 + v^2 + w^2] dV} > \pi^2 / s^2 \quad (16)$$

Consider now the second variational problem in the right-hand side of equation (7). Equation (5) yield $\nabla^2 \theta = 0$ on B . Together with $\theta = 0$ on B , the Euler-Lagrange equation of this variational problem is:

$$\left. \begin{aligned} \nabla^2(\nabla^2 \theta) + N^2(\nabla^2 \theta) &= 0 \text{ in } C \\ (\nabla^2 \theta) &= 0 \text{ on } B \end{aligned} \right\} \quad (17)$$

Furthermore, equation (5) yields

$$\int_{S_z} (\nabla^2 \theta) dx dy = \int_{S_z} w dx dy = 0 \quad (18)$$

Denote $(\nabla^2 \theta)$ by W and repeat the considerations as for w , hence

$$\frac{\int_c (\nabla^2 \theta)^2 dV}{\int_c (\nabla \theta)^2 dV} > \pi^2 / s^2 \quad (19)$$

Substitution of equations (16) and (19) in equation (8) yield

$$R_{ac} > \pi^4 / s^4 \quad (20)$$

s is the radius of a sphere of half the volume of the original region.

Denote the radius of a sphere having the same volume as the original volume by R ; then $R = s \times 2^{1/3}$ and equation (20) has the form

$$R_{acD} > \pi^4 \times 2^{4/3} / R^4 = 1559 \times 2^{4/3} / D^4 = 3927 / D^4 \quad (21)$$

or, expressed in terms of h :

$$R_{ach} > 3927(h/D)^4$$

A lower bound, which is $2^{4/3} = 2.5194$ times higher than that of Sherman and Ostrach [3], has been obtained. For a region of volume V (nondimensional with respect to its height h), equation (21) becomes:

$$R_{ach} > 1657.2(h/V^{1/3})^4 = 1657.2/V^{4/3} \quad (22)$$

Equation (22) can be directly applied in cases where most details of the geometry are not known, i.e., except for estimates of h and V , which is typical for porous insulating materials.

(b) **Vertical Cylinders of Arbitrary Cross Section.** Let the cylinder height be h and its cross-sectional area A (all lengths are made nondimensional with respect to A).

Inspection of equation (7) yields:

$$R_{ac} > \min \frac{\int_c (\nabla w)^2 dV}{\int_c w^2 dV} \times \min \frac{\int_c (\nabla^2 \theta)^2 dV}{\int_c (\nabla \theta)^2 dV} \quad (23)$$

Denoting first w by W and then $\nabla^2 \theta$ by W , the same considerations which led to the previous results for the general configuration now yield

$$R_{ac} > K^4 \quad (24)$$

⁴ $s_x \int u dy dz = s_y \int v dx dz = 0$ for the same reason as equation (12).

Table 1 Some numerical values for R_{ac}

Configuration	Lower Bounds					Published Values
	This Investigation			From Ref. [3]		
	Sec. a.	Sec. b.	Sec. c.	General	Particular	
Rectangular Cylinder of Sides						Ref. [8]
2, 2	262	359	495	105		2950
1, 1	1657	2127	3510	660	3510	6500
1, 1/2	4160	6795	7890	1660		16500
1/2, 1/2	10500	23984	42958	4900		45000
Circular Cylinder of Radius						Ref. [9]
2	57	155	184	28		1886
1	361	410	600	144		2545
1/2	912	2630	4730	364	4290	11725
Elliptical Cylinder of Half Axes						
2, 1	143.5	245		57		
2, 1/2	362	452		144		
Ellipsoid of Half Axes						
2, 1				98		
2, 1/2	246			248		
Tetrahedron						
	12700			5060		

where K^2 is the eigenvalue in

$$\left. \begin{aligned} \nabla^2 W + K^2 W &= 0 \text{ in } C \\ W &= 0 \text{ on } B \\ \int_A W dx dy &= 0 \end{aligned} \right\} \quad (25)$$

For a vertical cylinder equation (25) admits separation of the z variable, i.e.,

$$W = \alpha(x, y)\xi(z); \quad \xi = \sin \frac{z\pi}{h} = \sin z\pi \quad (26)$$

hence

$$\left. \begin{aligned} \frac{\partial^2 \alpha}{\partial x^2} + \frac{\partial^2 \alpha}{\partial y^2} + L^2 \alpha &= 0 \\ \alpha &= 0 \text{ on } B \\ \int_A \alpha dx dy &= 0 \end{aligned} \right\} \quad (27)$$

where

$$K^2 = L^2 + \pi^2 \quad (28)$$

Since the smallest K^2 is required, equation (27) is considered for the smallest L^2 . For the general case no exact solution of equation (27) will be available, and lower bounds to L^2 must be sought.

A lower bound for L^2 is obtained by the solution of the Helmholtz equation for α over a circular region of half the area⁵ A ,

⁵ Note the similarity to the general case, where a spherical region of half the volume has been used.

(nondimensional with respect to its height h) as shown by Pnueli [7]:

$$\left. \begin{aligned} L^2 &> 2.4048^2 \times 2\pi/A \quad (J_0(2.4048) = 0) \\ \text{and} \\ K^2 = L^2 + \pi^2 &> 2.4048^2 \times 2\pi/A + \pi^2 \end{aligned} \right\} \quad (29)$$

Equation (24) now yields:

$$R_{ach} > [36.35/A + 9.87]^2 \quad (30)$$

To apply equation (30) only the height and the area of the cross section of the cylinder need be known. Because K^2 for a sphere is lower bound for K^2 for a circular cylinder, equation (22) would always yield lower values than equation (30). Thus, when applicable, equation (30) yields better lower bounds.

(c) **Particular Configurations.** Particular configurations are defined as those for which the exact solution of the Helmholtz equation:

$$\left. \begin{aligned} \nabla^2 W + K^2 W &= 0 \text{ in } C \\ W &= 0 \text{ on } B \\ \int_S W dx dy &= 0 \end{aligned} \right\} \quad (31)$$

is known. The considerations of equation (23) and (24) apply here too, and once K^2 is exactly known, equation (24) still yield a lower bound to R_{ac} .

Because both equation (22) and equation (30) yield lower bounds to K^4 (as obtained by equation (31)), this last method, when applicable, supplies lower bounds better than the other two.

Sherman and Ostrach [3] have applied the same considerations as in this section. However, they applied it to equation (8) and not to equation (23) as done here. Therefore, they had to use the lowest (i.e., worst) value obtained for either u , v , or w . The results obtained here are therefore better (see numerical example).

(d) **Numerical Examples.** The calculation of the lower bounds is simple and direct. Some typical numerical values are presented in Table 1 as a demonstration and also for comparison with other known values. In all examples critical Rayleigh number refers to the height of the configuration, and all dimensions are scaled with respect to the height.

References

- 1 Boussinesq, J., *Theorie Analytique de la Chaleur*, Vol. 2, Gauthier-Villars, Paris, 1903, p. 172.
- 2 Chandrasekhar, S., *Hydrodynamic and Hydromagnetic Stability*. Oxford Press, 1961.
- 3 Sherman, M., and Ostrach, S., "Lower Bounds to the Critical Rayleigh Number in Completely Confined Regions," *Journal of Applied Mechanics*, TRANS. ASME, Series E, Vol. 34, 1967, pp. 308-312.
- 4 Polya, G., and Szego, G., *Isoperimetric Inequalities in Mathematical Physics*, Princeton University Press, Princeton, N. J., 1951, p. 168.
- 5 Ostrach, S., and Pnueli, D., "The Thermal Instability of Completely Confined Fluids," *JOURNAL OF HEAT TRANSFER*, Trans. ASME, Series C, Vol. 85, 1963, pp. 1346-1354.
- 6 Pnueli, D., "Lower Bounds to the N'th Eigenvalue of the Helmholtz Equations Over Three-Dimensional Regions of Arbitrary Shape," *Journal of Applied Mechanics*, Trans ASME, Series E.
- 7 Pnueli, D., "Lower bounds to the N'th eigenvalue of the Helmholtz equation," *Journal of Applied Mechanics*, TRANS. ASME, Series E, Vol. 36, No. 3, 1969, p. 630.
- 8 Davis, S. H., "Convection in a Box: Linear Theory," *Journal of Fluid Mechanics*, 30, 1967, pp. 465-478.
- 9 Charlson, G. S., and Sani, R. L., "Thermoconvective Instability in a Bounded Cylindrical Fluid Layer," *International Journal of Heat and Mass Transfer*, Vol. 13, 1970, pp. 1479-1496.

The Effect on Laminar Free Convection Heat Transfer of the Temperature Dependence of the Coefficient of Volumetric Expansion

A. Brown¹

The momentum and energy boundary-layer equations are solved by the approximate integral technique for laminar free convection with the coefficient of volumetric expansion being temperature dependent. It is found that for common fluids, allowance cannot be made for the temperature dependence of the coefficient of volumetric expansion on heat transfer by using constant properties evaluated at film temperature.

Introduction

Most fluids have properties which are dependent on temperature and ignoring these dependencies can introduce serious errors in the evaluation of heat transfer. Sparrow and Gregg [5],² showed that in order to account for the temperature dependence of properties, common to gases other than the coefficient of volumetric expansion, the properties should be evaluated at the reference temperature T_r in the case of laminar free convection from an isothermal vertical plate, where

$$T_r = T_w - 0.38(T_w - T_\infty)$$

and where, T_w is the wall temperature and T_∞ the bulk fluid temperature. The coefficient of volumetric expansion β should be taken as $1/T_\infty$, which is strictly correct for perfect gases only. This procedure has been shown to be adequate over the range

$$0.5 < \frac{T_w}{T_\infty} < 3.0$$

Mercury was found to be a minor exception, in so far as all properties should be evaluated at the reference temperature. Minkowycz and Sparrow [3] found from their computer results for steam that the reference temperature rule applied provided the coefficient of value 0.38 was replaced by a coefficient of value 0.46 and β was evaluated at the bulk steam temperature. If β is evaluated as $1/T_\infty$ significant errors can arise under some conditions particularly for temperatures close to the saturation temperature. For low and moderate steam pressures the reference temperature rule gave agreement with the variable property heat transfer to within one percent. Similar accuracy was obtained at high pressures by the use of a multiplier incorporating a linear relationship in pressure.

A number of other studies have been carried out on free convection in fluids close to their critical points where fluid properties change rapidly. It is to be expected that in these regions the simple approximation will be inadequate but the present work is more interested in fluids far removed from their critical points and hence much more stable.

The coefficient of volumetric expansion β has a major bearing on free convection heat transfer via a buoyancy term $(\rho_\infty - \rho)g$ in the momentum equation, where ρ is density and g the acceleration due to gravity. It is conventional to assume that β is constant, as mentioned in the foregoing, and from its definition the buoyancy term in the momentum equation is approximated to $\beta_\infty \rho_\infty \theta_w g$, where $\theta_w = T_w - T_\infty$. However, for many fluids β can vary appreciably with

temperature and any such interdependence infers a corresponding relationship between density and temperature via the definition of β .

Barrow and Sitharamarao [1] investigated the effect of the temperature dependence of β on laminar free convection heat transfer from a constant temperature vertical flat plate. However they ignored the temperature dependence of density due to that of β . This article is a continuation of their work and as in other situations the particular case considered has implications in all free convection situations.

Solution of the Momentum and Energy Equations

The coefficient of volumetric expansion of a fluid is defined by

$$\beta = -\frac{1}{\rho} \left(\frac{\partial \rho}{\partial T} \right)_p \quad (1)$$

For many fluids the coefficient of volumetric expansion is temperature dependent, Barrow and Sitharamarao [1], and the commonest interrelationship between β and T is linear, that is,

$$\beta = \beta_\infty (1 + c(T - T_\infty)) = \beta_\infty (1 + c\theta). \quad (2)$$

The dependence of the coefficient of volumetric expansion on temperature infers a corresponding dependence between the density and temperature, and for a linear dependence of β on T it follows that

$$\rho = \rho_\infty \exp(-\beta_\infty \theta (1 + \frac{c}{2} \theta)). \quad (3)$$

The integral form of the momentum and energy equations for free convection laminar heat transfer are readily available in the literature, Eckert and Drake [2], and if it is assumed that the thermal and boundary layers are identical, they respectively become

$$\frac{d}{dx} \int_0^\delta u^2 \exp(-\beta_\infty \theta (1 + \frac{c}{2} \theta)) dy = g \int_0^\delta (1 - \exp(-\beta_\infty \theta (1 + \frac{c}{2} \theta))) dy - \nu \left(\frac{du}{dy} \right)_w \quad (4)$$

and

$$\frac{d}{dx} \int_0^\delta \theta u \exp(-\beta_\infty \theta (1 + \frac{c}{2} \theta)) dy = -\alpha \left(\frac{d\theta}{dy} \right)_w \quad (5)$$

where the symbols have their normal meaning. The interrelationship between ρ and T should have only secondary effects on the velocity and temperature profiles and, therefore, it is reasonable to assume the conventional free convection profiles, Eckert and Drake [2], that is,

$$u = u_1 \frac{y}{\delta} (1 - \frac{y}{\delta})^2 = u_1 z^2 (1 - z) \quad (6)$$

and

$$\theta = \theta_w (1 - \frac{y}{\delta})^2 = \theta_w z^2 \quad (7)$$

and that

$$u_1 = a_1 x^m \text{ and } \delta = a_2 x^n$$

giving

$$m = \frac{1}{2} \text{ and } n = \frac{1}{4}$$

It follows, therefore, that in the presence of temperature dependent β and ρ that comparing the heat transfer in laminar free convection for the case when account is taken of variable β and ρ with the case of constant β and ρ gives

$$\frac{\text{Nu}(\text{variable } \beta \text{ and } \rho)}{\text{Nu}(\text{constant } \beta \text{ and } \rho)} = \left[\frac{\text{Pr} + \frac{20}{21} \left(\frac{1 + \beta_\infty \theta_w \left(\frac{7}{12} + \frac{13c\theta_w}{33} \right)}{1 + \beta_\infty \theta_w \left(\frac{13}{28} + \frac{c\theta_w}{3} \right)} \right)}{(\text{Pr} + \frac{20}{21}) \left(1 + \frac{3c\theta_w}{10} \right) (1 - \beta_\infty \theta_w \left(\frac{15}{28} + \frac{c\theta_w}{6} \right))} \right]^{-1/4} \quad (8)$$

¹ Senior Lecturer, Department of Mechanical Engineering and Engineering Production, University of Wales Institute of Science and Technology, Cardiff, CF1 3NU, U.K.

² Numbers in brackets designate References at end of paper.

Contributed by the Heat Transfer Division of THE AMERICAN SOCIETY OF MECHANICAL ENGINEERS. Manuscript received by the Heat Transfer Division May 6, 1974.

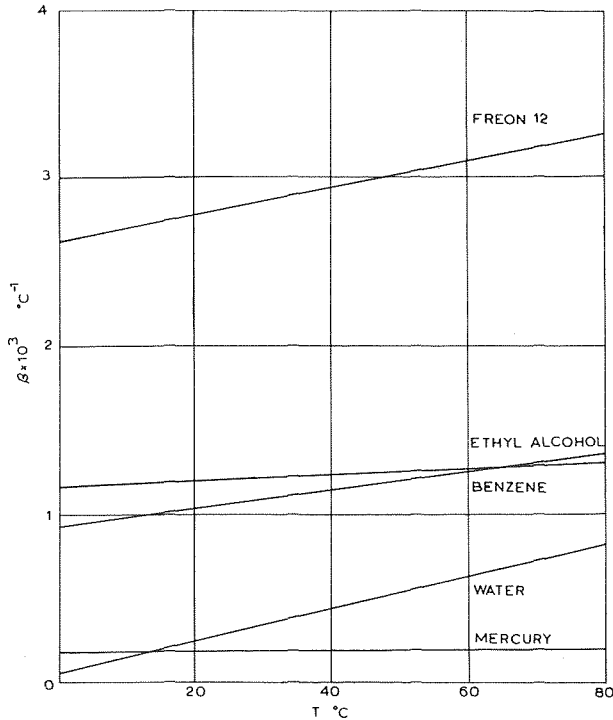


Fig. 1 Variation of β with temperature for some common fluids

Barrow and Sitharamarao [1], considered the effect of the temperature dependence of the coefficient of volumetric expansion on the heat transfer in laminar free convection but ignored the inferred temperature dependence of density. That is, they used equation (2) but assumed that the density of the fluid was constant and from these two conditions derived the following relationship

$$\frac{Nu(\text{variable } \beta \text{ and constant } \rho)}{Nu(\text{constant } \beta \text{ and } \rho)} = \left(1 + \frac{3c\theta_w}{5}\right)^{1/4} \quad (9)$$

The Numerical Effect on Heat Transfer of Variable β

The variation of the coefficient of volumetric expansion with temperature for a number of common fluids, as listed in the Smithsonian Physical tables, Fowle [4], is illustrated in Fig. 1 and values of β_∞ and c are listed in Table 1.

Consider the case of water with $\theta_w = 60^\circ\text{C}$ and $T_\infty = 20^\circ\text{C}$. From Table 1 it follows that $\beta_\infty\theta_w = 1.532 \times 10^{-2}$ and $c\theta_w = 2.130$ and, therefore, equation (8) gives

$$\frac{Nu(\text{variable } \beta \text{ and } \rho)}{Nu(\text{constant } \beta \text{ and } \rho)} = \left(\frac{Pr + 0.955}{1.618(Pr + 0.952)}\right)^{-1/4} \quad (10)$$

whereas, equation (9) gives

$$\frac{Nu(\text{variable } \beta \text{ and constant } \rho)}{Nu(\text{constant } \beta \text{ and } \rho)} = (2.278)^{1/4} = 1.228 \quad (11)$$

For water at 20°C the Prandtl number is 6.85 and therefore, for Pr based on bulk fluid temperature gives from equation (10)

$$\left(\frac{Nu(\text{variable } \beta \text{ and } \rho)}{Nu(\text{constant } \beta \text{ and } \rho)}\right) (Pr \text{ at } T_\infty) = (1.617)^{1/4} = 1.128$$

whereas, from equation (11)

$$\frac{Nu(\text{variable } \beta \text{ and constant } \rho)}{Nu(\text{constant } \beta \text{ and } \rho)} = (2.278)^{1/4} = 1.228$$

Ignoring the variation of β and ρ with temperature introduced an error in heat transfer of +12.8 percent, whereas, if the effect of variation of ρ is omitted the suggested error is overestimated at +22.8 percent. If in obtaining numerical values for the Nusselt number ratios of equations (8) and (9), the coefficient of volumetric expansion in the Nusselt number corresponding to constant β and ρ is based on film and wall temperatures instead of bulk fluid temperatures, the errors are -5.8 percent and -15.1 percent, and +2.4 percent and -7.7 percent, respectively. The corresponding errors for ethyl-alcohol, Freon 12, benzene and mercury have been calculated and are tabulated in Table 2 along with those of water, where the film temperature $T_f = (T_w + T_\infty)/2$.

Discussion

For some fluids the errors which are introduced into heat transfer by assuming that the coefficient of volumetric expansion is independent of temperature can be significant, see the first row of Table 2. Ignoring the fact that a variation with temperature of the coefficient of volumetric expansion of a fluid implies a particular relationship between its density and temperature, Barrow and Sitharamarao [1], tends to overestimate these errors. Also, from Barrow and Sitharamarao's work it appears that if the value of the coefficient of volumetric expansion used is that based on film temperature the errors are minimized, +2.4 percent for water, +0.7 percent for ethyl alcohol, +0.4 percent for Freon 12, +0.1 percent for benzene and 0.0 percent for mercury. However, the more correct approach which takes account of variable density as well as variable coefficient of volumetric expansion disagrees with their findings. Only in the case of water would the use of film temperature in determining a value for the coefficient of volumetric expansion give least error. The real conclusion to be drawn is that the effect of the temperature dependence of the coefficient of volumetric expansion on heat transfer is more complex than the effects of other temperature dependent properties. In order to ascertain values of this effect equation (8) should be evaluated for every case considered.

Table 1 Property values of some fluids

	Water	Ethyl Alcohol	Saturated Freon 12	Benzene	Mercury
$\beta_{20^\circ\text{C}}$	0.255×10^{-3}	1.037×10^{-3}	2.787×10^{-3}	1.205×10^{-3}	0.182×10^{-3}
c	35.50×10^{-3}	5.207×10^{-3}	2.867×10^{-3}	1.395×10^{-3}	0.043×10^{-3}

Table 2 Heat transfer errors due to ignoring variable β

	Water		Ethyl alcohol		Saturated Freon 12		Benzene		Mercury	
	equation (8)	equation (9)	equation (8)	equation (9)	equation (8)	equation (9)	equation (8)	equation (9)	equation (8)	equation (9)
β at $T_\infty = 20^\circ\text{C}$	1.128	1.228	1.012	1.044	0.985	1.025	0.996	1.012	0.998	1.000
β at $T_f = 50^\circ\text{C}$	0.942	1.024	0.976	1.007	0.963	1.004	0.985	1.001	0.998	1.000
β at $T_w = 80^\circ\text{C}$	0.849	0.923	0.946	0.975	0.841	0.986	0.972	0.987	0.998	1.000

In cases where the Prandtl number is large and $\beta_{\infty}\theta_w$ is relatively small equation (8) can be simplified to become

$$\frac{Nu_{(\text{variable } \beta \text{ and } \rho)}}{Nu_{(\text{constant } \beta \text{ and } \rho)}} = \left(\left(1 + \frac{3c\theta_w}{10} \right) (1 - \beta_{\infty}\theta_w(0.536 + \frac{c\theta_w}{6})) \right)^{1/4} \quad (12)$$

If the variation of the coefficient of volumetric expansion with temperature is excessive, equation (8) cannot be used. In this case the integrals used in obtaining equation (8) are so complicated that they would have to be determined numerically.

It is of interest to note that if β is defined by

$$\beta = - \frac{1}{\rho_{\infty}} \left(\frac{\partial \rho}{\partial T} \right)_p$$

and

$$\beta = \beta_{\infty}(1 + c\theta)$$

it can be shown to a first order approximation that

$$\frac{Nu_{(\text{variable } \beta \text{ and } \rho)}}{Nu_{(\text{constant } \beta \text{ and } \rho)}} = \left(\left(1 + \frac{3c\theta_w}{10} \right) (1 - \beta_{\infty}\theta_w(0.536 + \frac{c\theta_w}{6})) \right)^{1/4} \quad (13)$$

which is identical with equation (12). Using this last equation instead of equation (8) gives the following values to the ratio of Nusselt numbers for β_{∞} determined at 20°C, 1.128 for water, 1.013 for ethyl alcohol, 0.988 for Freon 12, 0.996 for benzene and 0.99 for mercury.

References

- 1 Barrow, H. and Sitharamarao, T. L., "The Effect of Variable β on Free Convection," *British Chemical Engineering*, Vol. 16, No. 8, 1971, p. 704.
- 2 Eckert, E. R., and Drake, R. M., *Analysis of Heat and Mass Transfer*, McGraw Hill, New York, 1972.
- 3 Minkowycz, W. J., and Sparrow, E. M., "Free Convection Heat Transfer to Steam Under Variable Property Conditions," *International Journal of Heat and Mass Transfer*, Vol. 9, 1966, p. 145.
- 4 Fowle, F. E., "Smithsonian Physical Tables," Smithsonian Institution, Washington, 1934.
- 5 Sparrow, E. M., and Gregg, J. L., "The Variable Fluid-Property Problem in Free Convection," *Recent Advances in Heat and Mass Transfer*, McGraw Hill, New York, 1961.

Combined Free and Forced Convection Laminar Heat Transfer in a Vertical Annulus

D. Maitra¹ and K. Subba Raju²

Nomenclature

- C_p = specific heat, Kcal/kg°C
 de = equivalent diameter, m
 g = acceleration due to gravity, m/hr²
 g_c = conversion factor, Kgm/Kgf hr²
 h = heat transfer coefficient, Kcal/hr m² °C
 K = thermal conductivity, Kcal/hr m °C
 Nu = Nusselt number = $h de/K$, dimensionless
 p = pressure, Kgf/m²

¹ Research Scholar, Department of Chemical Engineering, Indian Institute of Technology, Madras, India. (Presently with R&D Unit, Bharat Heavy Electricals Ltd., Hyderabad, India)

² Assist. Professor, Department of Chemical Engineering, Indian Institute of Technology, Madras, India.

Contributed by the Heat Transfer Division of THE AMERICAN SOCIETY OF MECHANICAL ENGINEERS. Manuscript received by the Heat Transfer Division April 11, 1974.

- P = pressure drop parameter = $\frac{de^3}{\alpha\nu} \left[\frac{g_c}{\rho_{in}} \left(\frac{\partial p}{\partial z} \right) + g \right]$, dimensionless
 Pe = Peclet number = $de u_b \rho C_p / K$, dimensionless
 q = heat flux, Kcal/hr m²
 r = radial distance from the centre of the annulus, m
 R = dimensionless radial distance = r/de
 Ra = Rayleigh number = $de^3 g \beta \tau / \alpha \nu$, dimensionless
 Re = Reynolds number = $de u_b / \nu$, dimensionless
 t = temperature, °C
 u = velocity, m/hr
 U = dimensionless velocity = $u Pe / u_b P$
 z = axial distance from the heated inlet, m
 α = thermal diffusivity, m²/hr
 β = coefficient of thermal expansion, 1/°C
 θ = dimensionless temperature = $(t_w - t) / P\tau$
 μ = viscosity, Kg/m hr
 ν = kinematic viscosity, m²/hr
 ρ = density, Kg/m³
 τ = temperature gradient along the heated wall = $de \frac{dt_w}{dz}$, °C

Subscripts

- 1 = refers to inner wall
 2 = refers to outer wall
 b = refers to bulk average condition
 w = refers to heated wall condition

Introduction

In recent years several attempts have been made to study theoretically and experimentally the effect of free convection on laminar forced convection in vertical channels. Hallman [1, 2]³ Hanratty, Rosen, and Kabel [3], and Morton [4] presented exact solutions for the effect of free convection on fully developed laminar flow in circular tubes. A few investigators [1, 5-7] obtained experimental data in vertical tubes for mixed convection heat transfer.

Sherwin [8] presented a theoretical analysis of mixed convection heat transfer for fully developed flow in vertical annulus, and criteria for flow reversal, velocity and temperature profiles, and Nusselt number for radius ratio of 3 were also reported. Sherwin and Wallis [9, 10] provided solutions for developing flow in annulus. Rokerya and Iqbal [11] investigated theoretically the effect of viscous dissipation on combined free and forced convection through vertical annulus. Very limited experimental data on combined free and forced convection heat transfer in annulus are available in literature [8, 10, 12].

The previous experimental and theoretical investigations are restricted to low Raleigh number range ($Ra < 10^4$), while in actual practice the Raleigh number can be higher for fluids having larger coefficients of thermal expansion. The present investigations were initiated to study theoretically and experimentally the effect of free convection on laminar flow heat transfer in vertical annulus. The exact solution for Nusselt number is presented for higher range of Raleigh number not presently available in literature, extending the work of Sherwin [8]. Experimental heat transfer data obtained using direct current heating at the inner wall are compared with the exact solution deduced.

Theory

Consider fully developed laminar flow of a fluid through a vertical annulus in upward direction under pressure gradient. Constant heat flux is maintained at inner wall; the outer wall being adiabatic. Viscous dissipation, pressure work, and axial conduction term in the energy equation are assumed to be negligible. All fluid properties are assumed to be constant, except the variation of the den-

³ Numbers in brackets designate Reference at the end of technical brief.

In cases where the Prandtl number is large and $\beta_{\infty}\theta_w$ is relatively small equation (8) can be simplified to become

$$\frac{Nu_{(\text{variable } \beta \text{ and } \rho)}}{Nu_{(\text{constant } \beta \text{ and } \rho)}} = \left(\left(1 + \frac{3c\theta_w}{10} \right) (1 - \beta_{\infty}\theta_w(0.536 + \frac{c\theta_w}{6})) \right)^{1/4} \quad (12)$$

If the variation of the coefficient of volumetric expansion with temperature is excessive, equation (8) cannot be used. In this case the integrals used in obtaining equation (8) are so complicated that they would have to be determined numerically.

It is of interest to note that if β is defined by

$$\beta = - \frac{1}{\rho_{\infty}} \left(\frac{\partial \rho}{\partial T} \right)_p$$

and

$$\beta = \beta_{\infty}(1 + c\theta)$$

it can be shown to a first order approximation that

$$\frac{Nu_{(\text{variable } \beta \text{ and } \rho)}}{Nu_{(\text{constant } \beta \text{ and } \rho)}} = \left(\left(1 + \frac{3c\theta_w}{10} \right) (1 - \beta_{\infty}\theta_w(0.536 + \frac{c\theta_w}{6})) \right)^{1/4} \quad (13)$$

which is identical with equation (12). Using this last equation instead of equation (8) gives the following values to the ratio of Nusselt numbers for β_{∞} determined at 20°C, 1.128 for water, 1.013 for ethyl alcohol, 0.988 for Freon 12, 0.996 for benzene and 0.99 for mercury.

References

- 1 Barrow, H. and Sitharamarao, T. L., "The Effect of Variable β on Free Convection," *British Chemical Engineering*, Vol. 16, No. 8, 1971, p. 704.
- 2 Eckert, E. R., and Drake, R. M., *Analysis of Heat and Mass Transfer*, McGraw Hill, New York, 1972.
- 3 Minkowycz, W. J., and Sparrow, E. M., "Free Convection Heat Transfer to Steam Under Variable Property Conditions," *International Journal of Heat and Mass Transfer*, Vol. 9, 1966, p. 145.
- 4 Fowle, F. E., "Smithsonian Physical Tables," Smithsonian Institution, Washington, 1934.
- 5 Sparrow, E. M., and Gregg, J. L., "The Variable Fluid-Property Problem in Free Convection," *Recent Advances in Heat and Mass Transfer*, McGraw Hill, New York, 1961.

Combined Free and Forced Convection Laminar Heat Transfer in a Vertical Annulus

D. Maitra¹ and K. Subba Raju²

Nomenclature

- C_p = specific heat, Kcal/kg°C
 de = equivalent diameter, m
 g = acceleration due to gravity, m/hr²
 g_c = conversion factor, Kgm/Kgf hr²
 h = heat transfer coefficient, Kcal/hr m² °C
 K = thermal conductivity, Kcal/hr m °C
 Nu = Nusselt number = $h de/K$, dimensionless
 p = pressure, Kgf/m²

¹ Research Scholar, Department of Chemical Engineering, Indian Institute of Technology, Madras, India. (Presently with R&D Unit, Bharat Heavy Electricals Ltd., Hyderabad, India)

² Assist. Professor, Department of Chemical Engineering, Indian Institute of Technology, Madras, India.

Contributed by the Heat Transfer Division of THE AMERICAN SOCIETY OF MECHANICAL ENGINEERS. Manuscript received by the Heat Transfer Division April 11, 1974.

P = pressure drop parameter = $\frac{de^3}{\alpha\nu} \left[\frac{g_c}{\rho_{in}} \left(\frac{\partial p}{\partial z} \right) + g \right]$, dimensionless

Pe = Peclet number = $de u_b \rho C_p / K$, dimensionless

q = heat flux, Kcal/hr m²

r = radial distance from the centre of the annulus, m

R = dimensionless radial distance = r/de

Ra = Rayleigh number = $de^3 g \beta \tau / \alpha \nu$, dimensionless

Re = Reynolds number = $de u_b / \nu$, dimensionless

t = temperature, °C

u = velocity, m/hr

U = dimensionless velocity = $u Pe / u_b P$

z = axial distance from the heated inlet, m

α = thermal diffusivity, m²/hr

β = coefficient of thermal expansion, 1/°C

θ = dimensionless temperature = $(t_w - t) / P \tau$

μ = viscosity, Kg/m hr

ν = kinematic viscosity, m²/hr

ρ = density, Kg/m³

τ = temperature gradient along the heated wall = $de \frac{dt_w}{dz}$, °C

Subscripts

1 = refers to inner wall

2 = refers to outer wall

b = refers to bulk average condition

w = refers to heated wall condition

Introduction

In recent years several attempts have been made to study theoretically and experimentally the effect of free convection on laminar forced convection in vertical channels. Hallman [1, 2]³ Hanratty, Rosen, and Kabel [3], and Morton [4] presented exact solutions for the effect of free convection on fully developed laminar flow in circular tubes. A few investigators [1, 5-7] obtained experimental data in vertical tubes for mixed convection heat transfer.

Sherwin [8] presented a theoretical analysis of mixed convection heat transfer for fully developed flow in vertical annulus, and criteria for flow reversal, velocity and temperature profiles, and Nusselt number for radius ratio of 3 were also reported. Sherwin and Wallis [9, 10] provided solutions for developing flow in annulus. Rokerya and Iqbal [11] investigated theoretically the effect of viscous dissipation on combined free and forced convection through vertical annulus. Very limited experimental data on combined free and forced convection heat transfer in annulus are available in literature [8, 10, 12].

The previous experimental and theoretical investigations are restricted to low Raleigh number range ($Ra < 10^4$), while in actual practice the Raleigh number can be higher for fluids having larger coefficients of thermal expansion. The present investigations were initiated to study theoretically and experimentally the effect of free convection on laminar flow heat transfer in vertical annulus. The exact solution for Nusselt number is presented for higher range of Rayleigh number not presently available in literature, extending the work of Sherwin [8]. Experimental heat transfer data obtained using direct current heating at the inner wall are compared with the exact solution deduced.

Theory

Consider fully developed laminar flow of a fluid through a vertical annulus in upward direction under pressure gradient. Constant heat flux is maintained at inner wall; the outer wall being adiabatic. Viscous dissipation, pressure work, and axial conduction term in the energy equation are assumed to be negligible. All fluid properties are assumed to be constant, except the variation of the den-

³ Numbers in brackets designate Reference at the end of technical brief.

sity in the buoyancy term of the equation of motion. There exists a linear temperature gradient along the heated wall far from the entrance. Under these conditions and also with usual assumptions, the momentum and energy equations can be written in the dimensionless form as

$$\frac{d^2 U}{dR^2} + \frac{1}{R} \frac{dU}{dR} = -1 + Ra\theta \quad (1)$$

$$\frac{d^2 \theta}{dR^2} + \frac{1}{R} \frac{d\theta}{dR} = -U \quad (2)$$

The boundary conditions are

$$U = 0 \text{ and } \theta = 0 \text{ at } R = R_1 \quad (3)$$

$$U = 0 \text{ and } \frac{d\theta}{dR} = 0 \text{ at } R = R_2 \quad (4)$$

Combining equations (1) and (2), the following fourth-order differential equation results

$$\left[\frac{d^2}{dR^2} + \frac{1}{R} \frac{d}{dR} \right]^2 U = -RaU \quad (5)$$

The general solution of the equation (5) can be written in terms of Kelvin functions as:

$$U = C_1 \text{ber} [Ra^{1/4} \cdot R] + C_2 \text{bei} [Ra^{1/4} \cdot R] + C_3 \text{ker} [Ra^{1/4} \cdot R] + C_4 \text{kei} [Ra^{1/4} \cdot R] \quad (6)$$

The constants $C_1, C_2, C_3,$ and C_4 are determined from boundary conditions of equations (3) and (4). Using polynomial expressions for Kelvin functions [13], the velocity and temperature profiles are computed on IBM 360 computer.

Having obtained velocity and temperature profiles, Nusselt number can be evaluated using the following equation:

$$Nu = \frac{\int_{R_1}^{R_2} RU dR}{\int_{R_1}^{R_2} RU\theta dR} \left(\frac{\partial \theta}{\partial R} \right)_{R=R_1} \quad (7)$$

The theoretical Nusselt numbers are presented and compared with those obtained experimentally.

Results and Discussion

Theoretical Results. The computed velocity and temperature profiles and pressure drop parameters for various radius ratios and at various Raleigh numbers up to $Ra = 10^8$ were presented in detail in a thesis by one of the authors [14].

The Nusselt number variation with Raleigh number for various radius ratios is shown in Fig. 1. Free convection effects are less predominant when $Ra < 10^3$. Beyond this value, a steep increase in

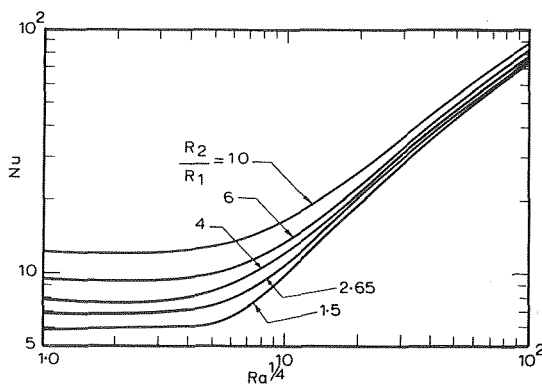


Fig. 1 Variation of Nusselt number with $Ra^{1/4}$

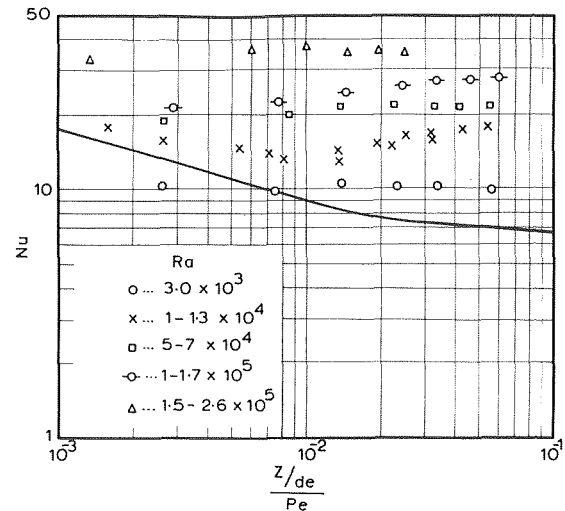


Fig. 2 Comparison of typical experimental Nusselt numbers with the theoretical prediction in the entrance region of the annulus

Nusselt number occurs for all radius ratios and the variation of Nusselt number can approximately be represented as $Nu \propto Ra^{1/4}$. At $Ra = 1$ the Nusselt number approaches that of forced convection solution of Lundberg, et al. [15].

Experimental Results. Experimental data for Reynolds number from 1200 down to 200 and for Raleigh number up to 2.5×10^5 were obtained for water flowing in an annulus with constant heat flux at the inner wall. The annular heat transfer section (2165 mm long) was formed by an inner brass tube 15.85 mm OD and an outer glass tube 42 mm ID. The local Nusselt number at eight axial locations were computed using the following equation

$$Nu = \frac{h de}{K} = \frac{de}{K} \frac{q}{t_w - t_b} \quad (8)$$

The local Nusselt numbers are plotted according to the usual coordinates in Fig. 2; in comparison with theoretical curve for $r_2/r_1 = 2.5$ based on constant property analysis of Lundberg, et al. [15]. The effect of natural convection is obvious as it is apparent that an increase in Rayleigh number causes higher Nusselt number. Fully developed flow appears to be established at about $(z/d)/Pe = 1.5 \times 10^{-3}$, beyond which the Nusselt numbers are approximately constant. In the case of combined free and forced convection, the fully developed condition is attained at much shorter distance than that for pure forced convection. This observation suggests that most of the data lie in the fully developed region. However thermal entrance length depends on Rayleigh number. The exact criteria for the transition between thermal entrance and fully developed flow regions is to be established.

The local Nusselt numbers measured beyond $z/de = 10$ are compared with the present theoretical analysis as shown in Fig. 3. The theoretical line for $r_2/r_1 = 2.5$ based on constant property analysis of Lundberg, et al. [15] is also shown in the same figure. The experimental Nusselt numbers follow the same trend as the present theoretical analysis but are, on the average, 45 percent higher. The results do not indicate clearly the dependence of Nusselt number on Reynolds number, whereas the heat transfer data of Sherwin and Wallis [10] in annulus and of Sheele and Hanratty [7] in circular tube exhibited such dependence clearly.

The discrepancy between the theoretical and experimental results may be attributed to the fact that at high Raleigh number the distortion of velocity profile gives rise to instability and therefore unsteady flow which in turn causes higher heat transfer performance. However, the present theoretical analysis with the consideration of variable density accounts for the experimental data more closer than those predicted by constant property analysis.

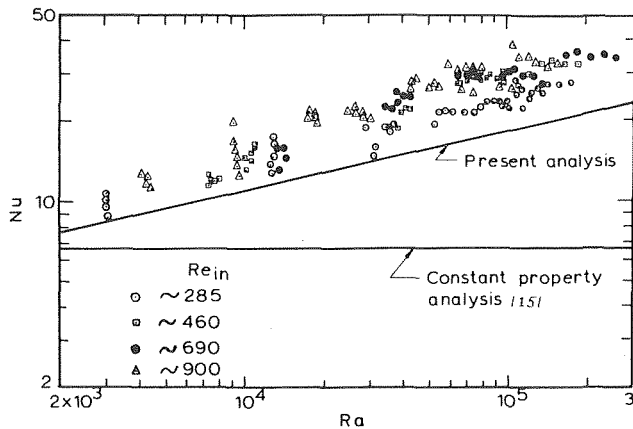


Fig. 3 Comparison of experimental Nusselt numbers with theoretical analyses

References

- Hallman, T. M., "Combined Forced and Free Convection in a Circular Tube," PhD thesis, Purdue University, 1958.
- Hallman, T. M., "Combined Forced and Free Laminar Heat Transfer in Vertical Tubes With Uniform Internal Heat Generation," *TRANS. ASME*, Vol. 78, 1956, pp. 1831-1841.
- Hanratty, T. J., Rosen, E. M., and Kabel, R. L., "Effect of Heat Transfer on Flow Fields at Low Reynolds Number in Vertical Tubes," *Industrial Engineering Chemistry*, Vol. 50, 1958, pp. 815-820.
- Morton, B. R., "Laminar Convection in Uniformly Heated Vertical Pipes," *Journal of Fluid Mechanics*, Vol. 8, 1960, pp. 227-240.

- Jackson, T. W., Harrison, W. B., and Boelter, W. C., "Combined Free and Forced Convection in a Vertical Tube," *TRANS. ASME*, Vol. 80, 1958, pp. 739-745.
- Kemeny, G. A., and Somers, E. V., "Combined Free and Forced-Convective Flow in a Vertical Circular Tubes—Experiments With Water and Oil," *JOURNAL OF HEAT TRANSFER*, *TRANS. ASME*, Series C, Vol. 84, 1962, pp. 339-346.
- Scheele, G. F., and Hanratty, T. J., "Effect of Natural Convection Instabilities on Rates of Heat Transfer at Low Reynolds Numbers," *AICHE Journal*, Vol. 9, 1963, pp. 183-185.
- Sherwin, K., "Laminar Convection in Uniformly Heated Vertical Concentric Annuli," *British Chemical Engineering*, Vol. 13, 1968, pp. 569-574.
- Sherwin, K., and Wallis, J. D., "A Theoretical Study of Combined Natural and Forced Laminar Convection for Developing Flow Down Vertical Annuli," Fourth International Heat Transfer Conference, Paris, Vol. IV, Paper No. NC 3.9, 1970.
- Sherwin, K., and Wallis, J. D., "Combined Natural and Forced Laminar Convection for Upflow Through Heated Annuli," Heat and Mass Transfer by Combined Forced and Natural Convection; Thermodynamics and Fluid Mechanics Conference; Inst. Mechanical Engineers, 1972, pp. 1-5.
- Rokerya, M. S., and Iqbal, M., "Effects of Viscous Dissipation on Combined Free and Forced Convection Through Vertical Concentric Annuli," *International Journal of Heat and Mass Transfer*, Vol. 14, 1971, pp. 491-495.
- Beck, F., "Wärmeübergang und Druckverlust in Senkrechten Konzentrischen und Exzentrischen Ringspalten bei erzwungener Strömung and freier Konvektion," *Chemie-Ing.-Techn.*, Vol. 35, 1963, pp. 837-844.
- Abramowitz, M., and Stegun, I. A., *Handbook of Mathematical Functions*, Dever Publications, Inc., New York, 1965, p. 384.
- Maitra, D., "Laminar Flow Heat Transfer and Void Fraction in Subcooled Boiling in a Vertical Annulus," PhD thesis, Indian Institute of Technology, Madras, 1973.
- Lundberg, R. E., McCuen, P. A., and Reynolds, W. C., "Heat Transfer in Annular Passages—Hydrodynamically Developed Laminar Flow With Arbitrary Prescribed Wall Temperature or Heat Fluxes," *International Journal of Heat and Mass Transfer*, Vol. 6, 1963, pp. 495-529.

On the Determination of Temperature Distribution in Laminar Pipe Flow With a Step Change in Wall Heat Flux

C. E. Smith,¹ M. Faghri,² and J. R. Welty³

Nomenclature

- $$A = \frac{D^2 Q}{16k}$$
- $$B = \frac{\mu v^2}{k}$$
- D = inside pipe diameter
 k = thermal conductivity
 $Pe = \frac{Dv}{\alpha}$, the Peclet number
 Q = volumetric rate of heat generation
 q = dimensionless wall heat flux (see equation (2))
 R = eigenfunctions (see equations (6), (7), and (12))
 r, ϕ, z = cylindrical coordinates (r and z are ratios of distance to pipe radius)
 t = temperature
 v = mean fluid velocity
 α = thermal diffusivity
 λ = eigenvalues (see equations (6), (7), and (12))
 μ = viscosity coefficient
 I, II = superscripts indicating regions $z < 0$, $z > 0$, respectively

¹ Professor, Oregon State University, Corvallis, Ore. Mem. ASME.

² Assist. Professor, Aria-Mehr University, Tehran, Iran.

³ Professor and Head, Department of Mechanical Engineering, Oregon State University, Corvallis, Ore. Mem. ASME.

Contributed by the Heat Transfer Division of THE AMERICAN SOCIETY OF MECHANICAL ENGINEERS. Manuscript received by the Heat Transfer Division June 14, 1974.

Predictions of temperature distribution in a fluid-carrying pipe, in the region near an axial discontinuity in wall heat flux, have previously involved fairly lengthy computations. A solution, in the form of a series of product solutions to the differential equation, provides a procedure which is far simpler than any previously published. The simplification results from the use, not previously made for this problem, of orthogonality relationships among solution components. These relationships are demonstrated here, and their use in constructing solutions for temperature distribution shown.

Background

A number of studies have been directed toward the prediction of the temperature distribution in the thermal entry region of a pipe containing laminar forced flow, in which a step change in wall heat flux occurs in the axial direction. Even with the idealizations of constant fluid properties and steady fluid and heat flow, these predictions have required rather extensive numerical computation. This is to be expected with a finite-difference approach to the governing equations, such as those constructed by Petukhov and Tsvetkov [1],⁴ and Hennecke [2].

Hsu [3, 4] has approached the calculation by constructing a series of product solutions, which leads to the determination of a set of eigenfunctions expressing the radial variation of temperature. This approach is potentially much superior to numerical integration, from the standpoint of the insight it can provide as well as reduced computation. Unfortunately, little of its simplicity has been realized, due to an apparent lack of understanding of the orthogonality relationships among the eigenfunctions. Without proper use of these relationships, the computations become significantly more involved, and insight into the system correspondingly more difficult to realize.

⁴ Numbers in brackets designate References at end of technical brief.

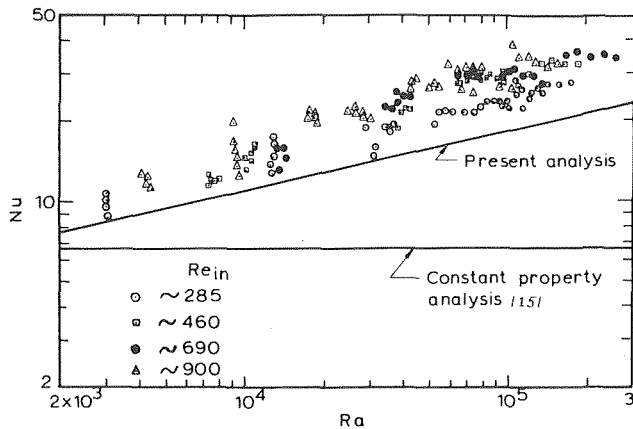


Fig. 3 Comparison of experimental Nusselt numbers with theoretical analyses

References

- Hallman, T. M., "Combined Forced and Free Convection in a Circular Tube," PhD thesis, Purdue University, 1958.
- Hallman, T. M., "Combined Forced and Free Laminar Heat Transfer in Vertical Tubes With Uniform Internal Heat Generation," *TRANS. ASME*, Vol. 78, 1956, pp. 1831-1841.
- Hanratty, T. J., Rosen, E. M., and Kabel, R. L., "Effect of Heat Transfer on Flow Fields at Low Reynolds Number in Vertical Tubes," *Industrial Engineering Chemistry*, Vol. 50, 1958, pp. 815-820.
- Morton, B. R., "Laminar Convection in Uniformly Heated Vertical Pipes," *Journal of Fluid Mechanics*, Vol. 8, 1960, pp. 227-240.
- Jackson, T. W., Harrison, W. B., and Boelter, W. C., "Combined Free and Forced Convection in a Vertical Tube," *TRANS. ASME*, Vol. 80, 1958, pp. 739-745.
- Kemeny, G. A., and Somers, E. V., "Combined Free and Forced-Convective Flow in a Vertical Circular Tubes—Experiments With Water and Oil," *JOURNAL OF HEAT TRANSFER*, *TRANS. ASME*, Series C, Vol. 84, 1962, pp. 339-346.
- Scheele, G. F., and Hanratty, T. J., "Effect of Natural Convection Instabilities on Rates of Heat Transfer at Low Reynolds Numbers," *AICHE Journal*, Vol. 9, 1963, pp. 183-185.
- Sherwin, K., "Laminar Convection in Uniformly Heated Vertical Concentric Annuli," *British Chemical Engineering*, Vol. 13, 1968, pp. 569-574.
- Sherwin, K., and Wallis, J. D., "A Theoretical Study of Combined Natural and Forced Laminar Convection for Developing Flow Down Vertical Annuli," Fourth International Heat Transfer Conference, Paris, Vol. IV, Paper No. NC 3.9, 1970.
- Sherwin, K., and Wallis, J. D., "Combined Natural and Forced Laminar Convection for Upflow Through Heated Annuli," Heat and Mass Transfer by Combined Forced and Natural Convection; Thermodynamics and Fluid Mechanics Conference; Inst. Mechanical Engineers, 1972, pp. 1-5.
- Rokerya, M. S., and Iqbal, M., "Effects of Viscous Dissipation on Combined Free and Forced Convection Through Vertical Concentric Annuli," *International Journal of Heat and Mass Transfer*, Vol. 14, 1971, pp. 491-495.
- Beck, F., "Wärmeübergang und Druckverlust in Senkrechten Konzentrischen und Exzentrischen Ringspalten bei erzwungener Strömung und freier Konvektion," *Chemie-Ing.-Techn.*, Vol. 35, 1963, pp. 837-844.
- Abramowitz, M., and Stegun, I. A., *Handbook of Mathematical Functions*, Dever Publications, Inc., New York, 1965, p. 384.
- Maitra, D., "Laminar Flow Heat Transfer and Void Fraction in Subcooled Boiling in a Vertical Annulus," PhD thesis, Indian Institute of Technology, Madras, 1973.
- Lundberg, R. E., McCuen, P. A., and Reynolds, W. C., "Heat Transfer in Annular Passages—Hydrodynamically Developed Laminar Flow With Arbitrary Prescribed Wall Temperature or Heat Fluxes," *International Journal of Heat and Mass Transfer*, Vol. 6, 1963, pp. 495-529.

On the Determination of Temperature Distribution in Laminar Pipe Flow With a Step Change in Wall Heat Flux

C. E. Smith,¹ M. Faghri,² and J. R. Welty³

Nomenclature

- $$A = \frac{D^2 Q}{16k}$$
- $$B = \frac{\mu v^2}{k}$$
- D = inside pipe diameter
 k = thermal conductivity
 $Pe = \frac{Dv}{\alpha}$, the Peclet number
 Q = volumetric rate of heat generation
 q = dimensionless wall heat flux (see equation (2))
 R = eigenfunctions (see equations (6), (7), and (12))
 r, ϕ, z = cylindrical coordinates (r and z are ratios of distance to pipe radius)
 t = temperature
 v = mean fluid velocity
 α = thermal diffusivity
 λ = eigenvalues (see equations (6), (7), and (12))
 μ = viscosity coefficient
 I, II = superscripts indicating regions $z < 0$, $z > 0$, respectively

¹ Professor, Oregon State University, Corvallis, Ore. Mem. ASME.

² Assist. Professor, Aria-Mehr University, Tehran, Iran.

³ Professor and Head, Department of Mechanical Engineering, Oregon State University, Corvallis, Ore. Mem. ASME.

Contributed by the Heat Transfer Division of THE AMERICAN SOCIETY OF MECHANICAL ENGINEERS. Manuscript received by the Heat Transfer Division June 14, 1974.

Predictions of temperature distribution in a fluid-carrying pipe, in the region near an axial discontinuity in wall heat flux, have previously involved fairly lengthy computations. A solution, in the form of a series of product solutions to the differential equation, provides a procedure which is far simpler than any previously published. The simplification results from the use, not previously made for this problem, of orthogonality relationships among solution components. These relationships are demonstrated here, and their use in constructing solutions for temperature distribution shown.

Background

A number of studies have been directed toward the prediction of the temperature distribution in the thermal entry region of a pipe containing laminar forced flow, in which a step change in wall heat flux occurs in the axial direction. Even with the idealizations of constant fluid properties and steady fluid and heat flow, these predictions have required rather extensive numerical computation. This is to be expected with a finite-difference approach to the governing equations, such as those constructed by Petukhov and Tsvetkov [1],⁴ and Hennecke [2].

Hsu [3, 4] has approached the calculation by constructing a series of product solutions, which leads to the determination of a set of eigenfunctions expressing the radial variation of temperature. This approach is potentially much superior to numerical integration, from the standpoint of the insight it can provide as well as reduced computation. Unfortunately, little of its simplicity has been realized, due to an apparent lack of understanding of the orthogonality relationships among the eigenfunctions. Without proper use of these relationships, the computations become significantly more involved, and insight into the system correspondingly more difficult to realize.

⁴ Numbers in brackets designate References at end of technical brief.

In this note, the orthogonality relationships among these eigenfunctions are demonstrated, and the use of these to compute the thermal entry region temperature shown. The system considered by Hsu [4] is a special case of that presented here, in which internal energy sources and circumferential variation in temperature are absent.

Model for Thermal Entry Region

The following differential equation models the steady-state transfer of heat in a circular pipe, carrying fluid in a fully-developed laminar flow, in which heat generation and fluid properties are constant:

$$\frac{1}{r}(rt_r)_r + \frac{1}{r^2}t_{\phi\phi} + t_{zz} - \text{Pe}(1-r^2)t_z = -4A - 16\text{Br}^2 \quad (1)$$

The first three terms on the left-hand side of (1) represent conduction effects, and the remaining term the effect of convection; thus the parameter Pe is a measure of the importance of convection compared with conduction. The terms on the right-hand side represent local sources of heat generation, the second arising from dissipation of mechanical energy through viscosity.

Consider now an infinitely long pipe, in which a wall flux is imposed, varying arbitrarily around the circumference, and constant in the axial direction except for a single step change. That is,

$$t_r(1, \phi, z) = \begin{cases} q^{\text{I}}(\phi) & z < 0 \\ q^{\text{II}}(\phi) & z > 0 \end{cases} \quad (2)$$

If the right-hand members of (1) and (2) represent the only heat inputs to the fluid, we may expect that at points well-removed from the discontinuity the temperature will approach a "fully-developed" distribution, in which the axial gradient is constant. That is,

$$t_z \rightarrow b^{\text{I}} \text{ as } z \rightarrow -\infty; \quad t_z \rightarrow b^{\text{II}} \text{ as } z \rightarrow \infty \quad (3)$$

Balance of energy at the surface $\phi = \text{constant}$ requires that

$$t(r, \phi, z) = t(r, \phi + 2\pi, z); \quad t_\phi(r, \phi, z) = t_\phi(r, \phi + 2\pi, z) \quad (4)$$

and a similar balance at $z = 0$ leads to the matching condition

$$t(r, \phi, 0-) = t(r, \phi, 0+); \quad t_z(r, \phi, 0-) = t_z(r, \phi, 0+) \quad (5)$$

Equations (1) through (4) can be satisfied by a solution to equation (1) of the form

$$t = -(A + \text{Br}^2)r^2 + a^i + b^i \left[z + \frac{\text{Pe}r^2}{4} \left(1 - \frac{r^2}{4} \right) \right] + \sum_{n=1}^{\infty} r^n (a_n^i \cos n\phi + b_n^i \sin n\phi) + \sum_{m=1}^{\infty} \sum_{n=0}^{\infty} R_{mn}^i(r) (a_{mn}^i \cos n\phi + b_{mn}^i \sin n\phi) e^{-\lambda_{mn}^i z} \quad (6)$$

where the superscripts $i = \text{I}, \text{II}$ refer to the regions $z < 0$ and $z > 0$, respectively. The λ_{mn} and R_{mn} are eigenvalues and eigenfunctions satisfying

$$\left[\frac{d}{dr} \left(r \frac{d}{dr} \right) - \frac{n^2}{r} \right] R + \lambda \text{Pe} r (1 - r^2) R + \lambda^2 r R = 0 \quad (7a)$$

$$R(0) \text{ Finite}; \quad R'(1) = 0 \quad (7b)$$

In order that (6) satisfy (3), the λ_{mn}^{I} must be the negative eigenvalues and the λ_{mn}^{II} the positive eigenvalues. A number of the eigenvalues and eigenfunctions for $n = 0$ have been computed by Hsu [4], who used a numerical integration, and for $n = 0, 1, 2$ by Faghri [5], who developed power series for the R_{mn} . The important orthogonality relationships among the eigenfunctions are given in the next section.

The constants $(a^{\text{II}} - a^{\text{I}})$, b^{I} , and b^{II} may be determined from the boundary conditions (3), after integrating (1) through the region $(z^{\text{I}}, z^{\text{II}})$ and using equation (6). This energy balance can be brought to the form

$$\frac{\text{Pe}}{4}(a^{\text{II}} - a^{\text{I}}) - \frac{1}{4} \left(2 - \frac{7\text{Pe}^2}{96} \right) (b^{\text{II}} - b^{\text{I}}) + \frac{\text{Pe} b^{\text{II}}}{4} z^{\text{II}}$$

$$- \frac{\text{Pe} b^{\text{I}}}{4} z^{\text{I}} = [2(A + 2B) + \frac{1}{2\pi} \int_0^{2\pi} q^{\text{II}} d\phi] z^{\text{II}} - [2(A + 2B) + \frac{1}{2\pi} \int_0^{2\pi} q^{\text{I}} d\phi] z^{\text{I}}$$

It follows from the fact that this must hold for arbitrary z^{I} and z^{II} that

$$a^{\text{II}} - a^{\text{I}} = \frac{2}{\pi} \left(\frac{2}{\text{Pe}^2} - \frac{7}{96} \right) \int_0^{2\pi} (q^{\text{II}} - q^{\text{I}}) d\phi \quad (8a)$$

$$b^{\text{I}} = \frac{8(A + 2B)}{p} + \frac{2}{\pi \text{Pe}} \int_0^{2\pi} q^{\text{I}}(\phi) d\phi \quad i = \text{I}, \text{II} \quad (8b)$$

The constants a_n^i and b_n^i may be determined from the boundary conditions (2), with the usual Fourier analysis:

$$\begin{cases} a_n^i \\ b_n^i \end{cases} = \frac{1}{n\pi} \int_0^{2\pi} q^i(\phi) \begin{cases} \cos n\phi \\ \sin n\phi \end{cases} d\phi \quad i = \text{I}, \text{II} \quad (9)$$

The matching conditions (5), together with Fourier analysis with respect to ϕ , lead to

$$\sum_{m=1}^{\infty} a_{m0}^{\text{II}} \begin{Bmatrix} R_{m0}^{\text{II}} \\ \lambda_{m0}^{\text{II}} R_{m0}^{\text{II}} \end{Bmatrix} - \sum_{m=1}^{\infty} a_{m0}^{\text{I}} \begin{Bmatrix} R_{m0}^{\text{I}} \\ \lambda_{m0}^{\text{I}} R_{m0}^{\text{I}} \end{Bmatrix} = \begin{cases} a^{\text{II}} - a^{\text{I}} + (b^{\text{II}} - b^{\text{I}}) \frac{\text{Pe}r^2}{4} \left(1 - \frac{r^2}{4} \right) \\ b^{\text{II}} - b^{\text{I}} \end{cases} \quad (10a)$$

$$\sum_{m=1}^{\infty} C_{mn}^{\text{II}} \begin{Bmatrix} R_{mn}^{\text{II}} \\ \lambda_{mn}^{\text{II}} R_{mn}^{\text{II}} \end{Bmatrix} - \sum_{m=1}^{\infty} C_{mn}^{\text{I}} \begin{Bmatrix} R_{mn}^{\text{I}} \\ \lambda_{mn}^{\text{I}} R_{mn}^{\text{I}} \end{Bmatrix} = \begin{cases} (C_n^{\text{II}} - C_n^{\text{I}}) r^n \\ 0 \end{cases} \quad C = a, b; \quad n = 1, 2, 3, \dots \quad (10b)$$

These equations are of the form (14) given in the next section. The orthogonality relationships presented there permit calculation of the coefficients as follows:

$$a_{m0}^i = \frac{\int_0^1 R_{m0}^i \{ [\text{Pe}(1-r^2) + \lambda_{m0}^i] [a^i - a^j + (b^i - b^j)] \times \frac{\text{Pe}r^2}{2} (1 - \frac{r^2}{4}) + b^i - b^j \} r dr}{\int_0^1 (R_{m0}^i)^2 [\text{Pe}(1-r^2) + 2\lambda_{m0}^i] r dr} \quad (11a)$$

$$C_{mn}^i = \frac{\int_0^1 R_{mn}^i [\text{Pe}(1-r^2) + \lambda_{mn}^i] (C_n^i - C_n^j) r^{n+1} dr}{\int_0^1 (R_{mn}^i)^2 [\text{Pe}(1-r^2) + 2\lambda_{mn}^i] r dr} \quad (11b)$$

$$(i, j) = (\text{I}, \text{II}), (\text{II}, \text{I}); \quad C = a, b; \quad n = 1, 2, 3, \dots$$

Orthogonality

Consider the eigenvalues $\lambda_{m\nu}$ and corresponding eigenfunctions $R_{m\nu}(r)$ satisfying

$$(rR')' + \left[-\frac{\nu^2}{r} + \lambda p r (1 - r^2) + \lambda^2 r \right] R = 0 \quad r_1 < r < r_2 \quad (12a)$$

(p and ν^2 positive real numbers) along with an appropriate set of boundary conditions which satisfy

$$rR R' \Big|_{r=r_1}^{r=r_2} = 0 \quad (12b)$$

The equations arising in the foregoing heat transfer problem are the special case in which ν is an integer, p is the Peclet number, $r_1 = 0$ and $r_2 = 1$.

The orthogonality relationships are most readily determined after the above is written in the form

$$[A] \{S\} + \lambda [B] \{S\} = \{0\} \quad (12c)$$

in which

$$\{S\} = \begin{Bmatrix} R \\ \lambda R \end{Bmatrix}; \quad [A] = \begin{bmatrix} L & 0 \\ 0 & -r \end{bmatrix}$$

$$[B] = \left[\frac{br(1-r^2)}{r} \frac{r_1}{0} \right]; \quad L = \frac{d}{dr} \left(r \frac{d}{dr} \right) - \frac{\nu^2}{r}$$

The i th and j th eigenvalues and eigenfunctions satisfy

$$[A]\{S\}_i + \lambda_i[B]\{S\}_i = \{0\} \quad (i)$$

$$[A]\{S\}_j + \lambda_j[B]\{S\}_j = \{0\} \quad (j)$$

Premultiplication of equation (i) by $\{S\}_j^T$, premultiplication of equation (j) by $\{S\}_i^T$, integration over the interval (r_1, r_2) , account of the self-adjoint property of L with (12b),

$$\int_{r_1}^{r_2} u L v dr = - \int_{r_1}^{r_2} \left(\frac{\nu^2}{r} u v + r u' v' \right) dr = \int_{r_1}^{r_2} v L u dr,$$

and subtraction, yield

$$(\lambda_i - \lambda_j) \int_{r_1}^{r_2} \{S\}_i^T [B] \{S\}_j dr = 0$$

Therefore, when $\lambda_i \neq \lambda_j$, we have the following orthogonality relationships:

$$\int_{r_1}^{r_2} \{S\}_i^T [B] \{S\}_j dr = \int_{r_1}^{r_2} [p(1-r^2) + (\lambda_i + \lambda_j)] r R_i R_j dr = 0 \quad (13a)$$

$$- \int_{r_1}^{r_2} \{S\}_i^T [A] \{S\}_j dr = \int_{r_1}^{r_2} \left[\left(\frac{\nu^2}{r^2} + \lambda_i \lambda_j \right) R_i R_j + R_i' R_j' \right] r dr = 0 \quad (13b)$$

Given the two equations

$$\begin{Bmatrix} F(r) \\ G(r) \end{Bmatrix} = \sum_k c_k \begin{Bmatrix} R_k \\ \lambda_k R_k \end{Bmatrix} \quad (14a)$$

the orthogonality relationship (13a) may be used to evaluate the coefficients, as

$$c_k = \frac{\int_{r_1}^{r_2} R_k [p(1-r^2) + \lambda_k] F + G] r dr}{\int_{r_1}^{r_2} R_k^2 [p(1-r^2) + 2\lambda_k] r dr} \quad (14b)$$

Completeness

The validity of the solution (6) depends upon whether the expansions in (10) actually converge to the functions in the right-hand members of (10). This raises the basic question with regard to (12) and (14):

Do the R_k and $\lambda_k R_k$ form a "doubly complete" set of functions, such that some class of pairs of functions can be expanded in the manner indicated by (14)?

The fact that pairs of piecewise differentiable functions can be so expanded in the special case $p = 0$ (in which the R_k become Bessel functions) would lead one to suspect that this is also the case for $p \neq 0$. Also, computations by Hsu (even though made without the help of the orthogonality relationships, and for the special case $a_n^i = b_n^i = 0$) were stated to agree well with a numerical solution.

Although neither of these observations provides the answer to the completeness question, we believe that a rigorous investigation will show the validity of the expansion upon which this solution is based.

References

- Petukhov, B. S., and Tsvetkov, F. F., *Inz.-Fiz. Zh.*, Vol. 4, 1961, pp. 10-17; *Transl. No. FTD TT-61-321* Jan. 29, 1962.
- Hennecke, D. K., "Heat Transfer by Hagen-Poiseuille Flow in the Thermal Development Region With Axial Conduction," *Wärme-Stoffübertragung Bd.*, Vol. 1, 1968, pp. 177-184.
- Hsu, Chia-Jung, "Theoretical Solutions for Low-Peclet-Number Ther-

mal-Entry-Region Heat Transfer in Laminar Flow Through Concentric Annuli," *International Journal of Heat and Mass Transfer*, Vol. 13, 1970, pp. 1907-1924.

4 Hsu, Chia-Jung, "An Exact Analysis of Low-Peclet-Number Thermal-Entry-Region Heat Transfer in Transversely Nonuniform Velocity Fields," *AIChE Journal*, Vol. 17, No. 3, May, 1971, pp. 732-740.

5 Faghri, M., PhD dissertation, Department of Mechanical Engineering, Oregon State University, Corvallis, Ore. 1974.

Laminar Film Condensation on a Vertical Plate—Effect of Magnetic Field

K. N. Murty,¹ C. K. Sarma² and P. K. Sarma²

Introduction

A detailed review of the condensation heat transfer investigations for several geometries of the surface and for various combinations of the boundary conditions is presented in reference [1].³ In this brief, the authors propose to investigate theoretically the effect of weak magnetic field on condensation heat transfer. The results, which are basically derived for the case of a variable magnetic field of the form $B_y^2 x^{1/2} = \text{constant}$, can as well be extended to the case of a magnetic field of finite intensity.

Analysis

A vertical plate is maintained at a uniform temperature T_w , on which vapors of liquid metals condense under a thermal potential $\Delta T = T_s - T_w$. A weak magnetic field of flux density " B_y " is introduced normal to the plate as shown in Fig. 1. Assuming the interface to remain at the saturation temperature T_s and neglecting the effects of interfacial shear and of the magnetic field on the vapors, the equations of continuity, conservation of momentum, and energy can be expressed, respectively, as

$$\frac{\partial u}{\partial x} + \frac{\partial v}{\partial y} = 0 \quad (1)$$

$$\rho \left[u \frac{\partial u}{\partial x} + v \frac{\partial u}{\partial y} \right] = \mu \frac{\partial^2 u}{\partial y^2} + g(\rho - \rho_v) - \sigma B_y^2 u \quad (2)$$

and

$$u \frac{\partial T}{\partial x} + v \frac{\partial T}{\partial y} = \alpha \frac{\partial^2 T}{\partial y^2} + \frac{\sigma B_y^2 u^2}{\rho C_p} \quad (3)$$

The boundary conditions are

$$\text{at } y = 0, \quad u = 0, \quad v = 0, \quad T = T_w \quad (4)$$

and

$$\text{at } y = \delta, \quad \frac{\partial u}{\partial y} = 0 \text{ (assumed)}, \quad T = T_s \quad (5)$$

For the problem stated, a similarity solution is not feasible. As such, the influence of a weak magnetic field on the condensation phenomena is obtained by the perturbation technique.

Let the stream function ψ be defined as

$$\psi = 4\nu c x^{3/4} F(\eta, \beta) \quad (6)$$

where

$$\eta = cy/x^{1/4}, \quad \beta = \left[\frac{\nu c^2 \sigma B_y^2 x^{1/2}}{g(\rho - \rho_v)} \right]$$

¹ Research Scholar, U.G.C., Government of India, College of Engineering, Andhra University, Waltair, India.

² College of Engineering, Andhra University, Waltair, India.

³ Numbers in brackets designate References at end of technical brief.

$$[B] = \left[\frac{br(1-r^2)}{r} \frac{r_1}{0} \right]; \quad L = \frac{d}{dr} \left(r \frac{d}{dr} \right) - \frac{\nu^2}{r}$$

The i th and j th eigenvalues and eigenfunctions satisfy

$$[A]\{S\}_i + \lambda_i[B]\{S\}_i = \{0\} \quad (i)$$

$$[A]\{S\}_j + \lambda_j[B]\{S\}_j = \{0\} \quad (j)$$

Premultiplication of equation (i) by $\{S\}_j^T$, premultiplication of equation (j) by $\{S\}_i^T$, integration over the interval (r_1, r_2) , account of the self-adjoint property of L with (12b),

$$\int_{r_1}^{r_2} u L v dr = - \int_{r_1}^{r_2} \left(\frac{\nu^2}{r} u v + r u' v' \right) dr = \int_{r_1}^{r_2} v L u dr,$$

and subtraction, yield

$$(\lambda_i - \lambda_j) \int_{r_1}^{r_2} \{S\}_i^T [B] \{S\}_j dr = 0$$

Therefore, when $\lambda_i \neq \lambda_j$, we have the following orthogonality relationships:

$$\int_{r_1}^{r_2} \{S\}_i^T [B] \{S\}_j dr = \int_{r_1}^{r_2} [p(1-r^2) + (\lambda_i + \lambda_j)] r R_i R_j dr = 0 \quad (13a)$$

$$- \int_{r_1}^{r_2} \{S\}_i^T [A] \{S\}_j dr = \int_{r_1}^{r_2} \left[\left(\frac{\nu^2}{r^2} + \lambda_i \lambda_j \right) R_i R_j + R_i' R_j' \right] r dr = 0 \quad (13b)$$

Given the two equations

$$\begin{Bmatrix} F(r) \\ G(r) \end{Bmatrix} = \sum_k c_k \begin{Bmatrix} R_k \\ \lambda_k R_k \end{Bmatrix} \quad (14a)$$

the orthogonality relationship (13a) may be used to evaluate the coefficients, as

$$c_k = \frac{\int_{r_1}^{r_2} R_k [p(1-r^2) + \lambda_k] F + G] r dr}{\int_{r_1}^{r_2} R_k^2 [p(1-r^2) + 2\lambda_k] r dr} \quad (14b)$$

Completeness

The validity of the solution (6) depends upon whether the expansions in (10) actually converge to the functions in the right-hand members of (10). This raises the basic question with regard to (12) and (14):

Do the R_k and $\lambda_k R_k$ form a "doubly complete" set of functions, such that some class of pairs of functions can be expanded in the manner indicated by (14)?

The fact that pairs of piecewise differentiable functions can be so expanded in the special case $p = 0$ (in which the R_k become Bessel functions) would lead one to suspect that this is also the case for $p \neq 0$. Also, computations by Hsu (even though made without the help of the orthogonality relationships, and for the special case $a_n^i = b_n^i = 0$) were stated to agree well with a numerical solution.

Although neither of these observations provides the answer to the completeness question, we believe that a rigorous investigation will show the validity of the expansion upon which this solution is based.

References

- 1 Petukhov, B. S., and Tsvetkov, F. F., *Inz.-Fiz. Zh.*, Vol. 4, 1961, pp. 10-17; *Transl. No. FTD TT-61-321* Jan. 29, 1962.
- 2 Hennecke, D. K., "Heat Transfer by Hagen-Poiseuille Flow in the Thermal Development Region With Axial Conduction," *Wärme-Stoffübertragung Bd.*, Vol. 1, 1968, pp. 177-184.
- 3 Hsu, Chia-Jung, "Theoretical Solutions for Low-Peclet-Number Ther-

mal-Entry-Region Heat Transfer in Laminar Flow Through Concentric Annuli," *International Journal of Heat and Mass Transfer*, Vol. 13, 1970, pp. 1907-1924.

4 Hsu, Chia-Jung, "An Exact Analysis of Low-Peclet-Number Thermal-Entry-Region Heat Transfer in Transversely Nonuniform Velocity Fields," *AIChE Journal*, Vol. 17, No. 3, May, 1971, pp. 732-740.

5 Faghri, M., PhD dissertation, Department of Mechanical Engineering, Oregon State University, Corvallis, Ore. 1974.

Laminar Film Condensation on a Vertical Plate—Effect of Magnetic Field

K. N. Murty,¹ C. K. Sarma² and P. K. Sarma²

Introduction

A detailed review of the condensation heat transfer investigations for several geometries of the surface and for various combinations of the boundary conditions is presented in reference [1].³ In this brief, the authors propose to investigate theoretically the effect of weak magnetic field on condensation heat transfer. The results, which are basically derived for the case of a variable magnetic field of the form $B_y^2 x^{1/2} = \text{constant}$, can as well be extended to the case of a magnetic field of finite intensity.

Analysis

A vertical plate is maintained at a uniform temperature T_w , on which vapors of liquid metals condense under a thermal potential $\Delta T = T_s - T_w$. A weak magnetic field of flux density " B_y " is introduced normal to the plate as shown in Fig. 1. Assuming the interface to remain at the saturation temperature T_s and neglecting the effects of interfacial shear and of the magnetic field on the vapors, the equations of continuity, conservation of momentum, and energy can be expressed, respectively, as

$$\frac{\partial u}{\partial x} + \frac{\partial v}{\partial y} = 0 \quad (1)$$

$$\rho \left[u \frac{\partial u}{\partial x} + v \frac{\partial u}{\partial y} \right] = \mu \frac{\partial^2 u}{\partial y^2} + g(\rho - \rho_v) - \sigma B_y^2 u \quad (2)$$

and

$$u \frac{\partial T}{\partial x} + v \frac{\partial T}{\partial y} = \alpha \frac{\partial^2 T}{\partial y^2} + \frac{\sigma B_y^2 u^2}{\rho C_p} \quad (3)$$

The boundary conditions are

$$\text{at } y = 0, \quad u = 0, \quad v = 0, \quad T = T_w \quad (4)$$

and

$$\text{at } y = \delta, \quad \frac{\partial u}{\partial y} = 0 \text{ (assumed)}, \quad T = T_s \quad (5)$$

For the problem stated, a similarity solution is not feasible. As such, the influence of a weak magnetic field on the condensation phenomena is obtained by the perturbation technique.

Let the stream function ψ be defined as

$$\psi = 4\nu c x^{3/4} F(\eta, \beta) \quad (6)$$

where

$$\eta = cy/x^{1/4}, \quad \beta = \left[\frac{\nu c^2 \sigma B_y^2 x^{1/2}}{g(\rho - \rho_v)} \right]$$

¹ Research Scholar, U.G.C., Government of India, College of Engineering, Andhra University, Waltair, India.

² College of Engineering, Andhra University, Waltair, India.

³ Numbers in brackets designate References at end of technical brief.

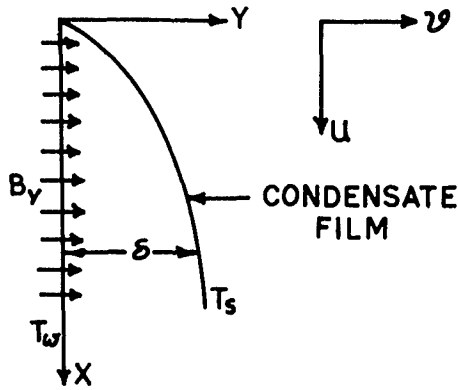


Fig. 1 Physical model and coordinates

and

$$c = \left[\frac{g(\rho - \rho_v)}{4\nu^2\rho} \right]^{1/4}$$

Also

$$\theta = \theta(\eta, \beta) = \frac{T_s - T}{T_s - T_w} \quad (7)$$

Then, the conservation equations reduce to

$$\frac{\partial^3 F}{\partial \eta^3} + 3F \frac{\partial^2 F}{\partial \eta^2} - 2 \left(\frac{\partial F}{\partial \eta} \right)^2 + 1 - 2\beta \left[\frac{\partial F}{\partial \eta} \frac{\partial^2 F}{\partial \eta \partial \beta} - \frac{\partial F}{\partial \beta} \frac{\partial^2 F}{\partial \eta^2} + 2 \frac{\partial F}{\partial \eta} \right] = 0 \quad (8)$$

$$\frac{\partial^2 \theta}{\partial \eta^2} + \text{Pr} (3F + 2\beta \frac{\partial F}{\partial \beta}) \frac{\partial \theta}{\partial \eta} - 2\beta \text{Pr} \left(\frac{\partial \theta}{\partial \beta} + 32\beta^2 E_{cm} \frac{\partial F}{\partial \eta} \right) \frac{\partial F}{\partial \eta} = 0 \quad (9)$$

where $E_{cm} = [g(\rho - \rho_v)/\sigma B_y^2]^2 / C_p \Delta T$. The boundary conditions (4) and (5) are transformed to

at

$$\eta = 0, \quad \frac{\partial F}{\partial \eta} = 0, \quad \theta = 1 \quad (10)$$

and

$$3F + 2\beta \frac{\partial F}{\partial \beta} = 0$$

at

$$\eta = \eta_6, \quad \frac{\partial^2 F}{\partial \eta^2} = 0 \quad \text{and} \quad \theta = 0 \quad (11)$$

To the foregoing set of equations, we add the interface balance that renders the analytical results meaningful with regard to the phenomena under consideration, viz.,

$$h_{fg} \frac{d}{dx} \int_0^{\delta} \rho_L u dy = -K_L \frac{\partial T}{\partial y} \Big|_{y=\delta} \quad (12)$$

Equation (12) on transformation yields

$$\frac{C_p \Delta T}{h_{fg} \text{Pr}} = \frac{3F(\eta_6)}{\theta'(\eta_6)} \quad (13)$$

We assume the solutions in the form of series as follows:

$$F(\eta, \beta) = F_0(\eta) + \beta F_1(\eta) + \beta^2 F_2(\eta) + \dots \quad (14)$$

$$\theta(\eta, \beta) = \theta_0(\eta) + \beta \theta_1(\eta) + \beta^2 \theta_2(\eta) + \dots \quad (15)$$

where $\beta \ll 1$ and positive. When β assumes zero, the problem corresponds to the one already solved by Sparrow, et al. [2]. The proposition of " β " assuming a negative value, though mathematically feasible, has not got any practical significance. Substituting equations (14) and (15) in equations (8) and (9) and collecting like powers of β gives ordinary differential equations for the F_i and θ_i , which are omitted here to conserve space. Furthermore, equation (13) takes the form

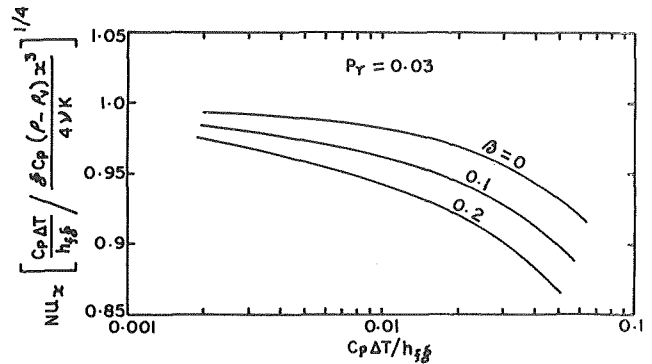


Fig. 2 Local heat transfer results

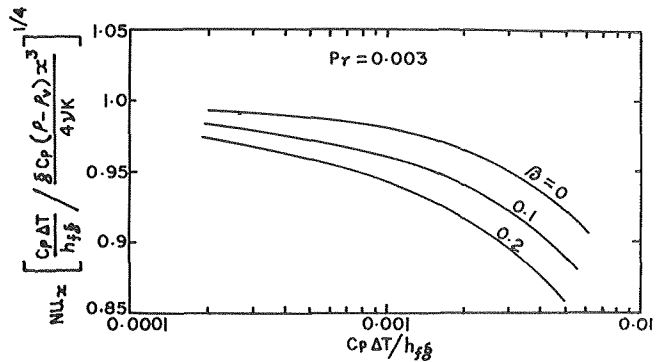


Fig. 3 Local heat transfer result.

$$\frac{C_p \Delta T}{h_{fg} \text{Pr}} = \frac{3[F_0(\eta_6) + \beta F_1(\eta_6) + \beta^2 F_2(\eta_6) + \beta^3 F_3(\eta_6) + \dots]}{[\theta_0'(\eta_6) + \beta \theta_1'(\eta_6) + \beta^2 \theta_2'(\eta_6) + \beta^3 \theta_3'(\eta_6) + \dots]} \quad (16)$$

The first three functions in the equations (14) and (15) were solved on an IBM 1130 employing Runge-Kutta's numerical method.

Results

Heat Transfer Coefficient. The heat transfer coefficient at any location x from the leading point can be obtained as

$$h_x \Delta T = -K_L \frac{\partial T}{\partial y} \Big|_{y=0} \quad (17)$$

or, in terms of transformed variables

$$\text{Nu}_x \left[\frac{C_p \Delta T}{h_{fg}} \frac{g(\rho - \rho_v) x^3}{4\nu K_L} \right]^{1/4} = \left[\frac{C_p \Delta T}{h_{fg} \text{Pr}} \right]^{1/4} [\theta_0'(0) + \beta \theta_1'(0) + \beta^2 \theta_2'(0) + \dots] \quad (18)$$

Figs. 2 and 3 reveal the variation of the local Nusselt number Nu_x , for $\text{Pr} = 0.003$ and 0.03 , with $C_p \Delta T / h_{fg}$ for different values of β . As the value of β increases, the condensation heat transfer rates decrease. Thus, the application of magnetic field may serve as a potential method to inhibit and suppress the process of condensation in instances where it is desired. In conclusion, the ponderomotive force developed due to the application of magnetic field retards the flow of the condensate and thus makes the condensate film thicker relative to the zero magnetic field case. Hence, the condensation heat transfer decreases.

Acknowledgments

The authors thank the Board of Research Studies, Andhra University, Waltair, India, for having given free computer time. One of the authors (Mr. K. N. Murty) is thankful to the U.G.C., Govt. of India for the financial assistance. The authors sincerely thank Prof. E. M. Sparrow for his constructive remarks.

References

- 1 Merte, Herman, Jr., "Advances in Heat Transfer" Vol. 9, Thomas F. Irvine and J. P. Hartnett, eds., 1973, pp. 181-272.
- 2 Sparrow, E. M., and Gregg, J. L., "A Boundary Layer Treatment of Laminar Film Condensation," JOURNAL OF HEAT TRANSFER, TRANS. ASME Series C, Vol. 81, 1959, pp. 13-18.

Laminar Film Condensation With Heat Generation¹

M. Epstein² and D. H. Cho²

Nomenclature

- c = specific heat of liquid film
 g = acceleration due to gravity
 h_{fg} = latent heat of condensation
 k = thermal conductivity of liquid film
 q = local wall heat flux
 \bar{q} = average wall heat flux
 \bar{q}_{Nu} = average wall heat flux based on Nusselt theory
 Q = volumetric heat generation rate in liquid film
 R = radius of tube or duct
 T = local temperature within liquid film
 T_w = wall temperature
 T_{sat} = saturation temperature
 u = local velocity of falling liquid film in x -direction
 \bar{u} = average velocity of falling liquid film in x -direction
 x = coordinate measuring distance along wall from leading edge
 X = dimensionless distance along wall; equation (8)
 y = coordinate measuring distance normal to wall
 δ = thickness of condensate layer
 δ_t = terminal thickness of condensate layer
 $\Delta T = (T_{sat} - T_w)$
 ν = kinematic viscosity of liquid film
 ξ = dimensionless thickness of condensate layer; equation (7)
 ρ = density of liquid film
 ρ_v = density of vapor
 $\phi = c\Delta T/h_{fg}$

This note investigates the steady-state vapor condensation of a heat-generating fluid on a vertical surface. This phenomenon is of interest in analyzing certain hypothetical accident situations of liquid-metal-cooled fast-breeder reactors ("LMFBRs"). For example, a loss of coolant flow may result in the disruption of the reactor core that involves fuel melting. In the absence of reactor shutdown, the molten fuel would continuously be heated and a boiling pool of fuel would be formed in a subassembly duct. In regions within and above such a boiling pool, characterized by volumetric heat generation rates that can exceed $100 \text{ cal cm}^{-3} \text{ s}^{-1}$ and void fractions larger than 50 percent, film condensation of heat-generating fuel vapor is probably the most significant mode of heat loss to the sides of the pool. Using Nusselt's method [1],³ we obtain a simple closed-form solution for the problem.

When inertia terms are neglected, as is usual in simple conden-

sation theory, we obtain the parabolic velocity profile within the condensed film falling under gravity:

$$u = \frac{g\delta^2}{\nu} \left[\frac{y}{\delta} - \frac{1}{2} \left(\frac{y}{\delta} \right)^2 \right] \quad (1)$$

The foregoing expression obeys the boundary conditions $u = 0$ at $y = 0$ and $\partial u/\partial y = 0$ (zero shear stress) at $y = \delta$. The energy equation for the heat-generating film, neglecting convection, is given by the conduction equation

$$k \frac{d^2 T}{dy^2} = -Q \quad (2)$$

where Q is the volumetric heat generation rate. Assuming the liquid temperature at $y = \delta$ to be the vapor saturation temperature at the system pressure, T_{sat} , the solution of equation (2) is given by

$$T = T_w - \frac{Q\delta^2}{2k} \left[\left(\frac{y}{\delta} \right)^2 - \frac{y}{\delta} \right] + \Delta T \frac{y}{\delta} \quad (3)$$

where ΔT is the temperature drop across the film ($\Delta T = T_{sat} - T_w$). Equating the heat liberation by condensation with the heat conduction into the film leads to

$$h_{fg} \frac{d}{dx} (\rho \delta \bar{u}) = k \left(\frac{\partial T}{\partial y} \right)_{y=\delta} \quad (4)$$

where \bar{u} is the average velocity within the film and is given by (see equation (1))

$$\bar{u} = \frac{1}{\delta} \int_0^\delta u \, dy = \frac{1}{3} \frac{g\delta^2}{\nu} \quad (5)$$

Combining equations (3), (4), and (5) yields the following differential equation for the condensate film thickness, δ , as a function of the distance along the vertical wall, x :

$$\frac{d\xi^2}{dX} = \frac{1 - \xi^2}{\xi^2} \quad (6)$$

where we introduced the dimensionless variables

$$\xi \equiv \left(\frac{Q}{2k\Delta T} \right)^{1/2} \delta \quad (7)$$

and

$$X \equiv \frac{\nu Q^2 x}{2g\rho h_{fg} k \Delta T} \quad (8)$$

Integration of equation (6) with the boundary condition $\delta(0) = \xi(0) = 0$ gives

$$X = -\ln(1 - \xi^2) - \xi^2 \quad (9)$$

The local heat transfer at the surface of the vertical wall, q , follows from differentiating equation (3) and is

$$\frac{q}{(2Qk\Delta T)^{1/2}} = \frac{1}{2} (\xi^{-1} + \xi) \quad (10)$$

It can readily be shown that the average heat flux, \bar{q} , is

$$\frac{\bar{q}}{(2Qk\Delta T)^{1/2}} = \frac{\ln(1 + \xi) - \ln(1 - \xi) - (1/3)\xi^3 - 2\xi}{-\ln(1 - \xi^2) - \xi^2} \quad (11)$$

For the no-heat generation limit this becomes the Nusselt expression (in terms of the dimensionless distance X)

$$\frac{\bar{q}_{Nu}}{(2Qk\Delta T)^{1/2}} = \frac{2}{3} \frac{1}{(2X)^{1/4}} \quad (12)$$

Equation (12) is obtained by noting that for small ξ , $X = \xi^4/2$ from equation (9) and $\bar{q}/(2Qk\Delta T)^{1/2} = 2/(3\xi)$ from equation (11). Both ξ and \bar{q} (normalized by \bar{q}_{Nu}) are plotted in Fig. 1.

We see that with a volume heat source present the heat flux to the wall is higher than its value with no heat source present. Fig. 1 shows that for $X > 10^{-2}$, the effect of heat generation on the wall heat flux is significant. In addition, heat generation results in a reduced film thickness and will cause the film to approach the terminal thickness $\delta_t = (2k\Delta T/Q)^{1/2}$ for $X > 3$. The above observations are easily explained. The volume heat source raises the temperature of the liquid at every point $0 < y < \delta$ in the film at a given location x . This results in a larger temperature gradient at the wall ($y = 0$) compared with the temperature gradient $\Delta T/\delta$ for the no-

¹ Work performed under the auspices of the U. S. Atomic Energy Commission.

² Reactor Analysis and Safety Division, Argonne National Laboratory, Argonne, Ill.

³ Numbers in brackets designate references at end of technical brief.

Contributed by the Heat Transfer Division of THE AMERICAN SOCIETY OF MECHANICAL ENGINEERS. Manuscript received by the Heat Transfer Division July 22, 1974.

References

- 1 Merte, Herman, Jr., "Advances in Heat Transfer" Vol. 9, Thomas F. Irvine and J. P. Hartnett, eds., 1973, pp. 181-272.
- 2 Sparrow, E. M., and Gregg, J. L., "A Boundary Layer Treatment of Laminar Film Condensation," JOURNAL OF HEAT TRANSFER, TRANS. ASME Series C, Vol. 81, 1959, pp. 13-18.

Laminar Film Condensation With Heat Generation¹

M. Epstein² and D. H. Cho²

Nomenclature

- c = specific heat of liquid film
 g = acceleration due to gravity
 h_{fg} = latent heat of condensation
 k = thermal conductivity of liquid film
 q = local wall heat flux
 \bar{q} = average wall heat flux
 \bar{q}_{Nu} = average wall heat flux based on Nusselt theory
 Q = volumetric heat generation rate in liquid film
 R = radius of tube or duct
 T = local temperature within liquid film
 T_w = wall temperature
 T_{sat} = saturation temperature
 u = local velocity of falling liquid film in x -direction
 \bar{u} = average velocity of falling liquid film in x -direction
 x = coordinate measuring distance along wall from leading edge
 X = dimensionless distance along wall; equation (8)
 y = coordinate measuring distance normal to wall
 δ = thickness of condensate layer
 δ_t = terminal thickness of condensate layer
 $\Delta T = (T_{sat} - T_w)$
 ν = kinematic viscosity of liquid film
 ξ = dimensionless thickness of condensate layer; equation (7)
 ρ = density of liquid film
 ρ_v = density of vapor
 $\phi = c\Delta T/h_{fg}$

This note investigates the steady-state vapor condensation of a heat-generating fluid on a vertical surface. This phenomenon is of interest in analyzing certain hypothetical accident situations of liquid-metal-cooled fast-breeder reactors ("LMFBRs"). For example, a loss of coolant flow may result in the disruption of the reactor core that involves fuel melting. In the absence of reactor shutdown, the molten fuel would continuously be heated and a boiling pool of fuel would be formed in a subassembly duct. In regions within and above such a boiling pool, characterized by volumetric heat generation rates that can exceed $100 \text{ cal cm}^{-3} \text{ s}^{-1}$ and void fractions larger than 50 percent, film condensation of heat-generating fuel vapor is probably the most significant mode of heat loss to the sides of the pool. Using Nusselt's method [1],³ we obtain a simple closed-form solution for the problem.

When inertia terms are neglected, as is usual in simple conden-

sation theory, we obtain the parabolic velocity profile within the condensed film falling under gravity:

$$u = \frac{g\delta^2}{\nu} \left[\frac{y}{\delta} - \frac{1}{2} \left(\frac{y}{\delta} \right)^2 \right] \quad (1)$$

The foregoing expression obeys the boundary conditions $u = 0$ at $y = 0$ and $\partial u / \partial y = 0$ (zero shear stress) at $y = \delta$. The energy equation for the heat-generating film, neglecting convection, is given by the conduction equation

$$k \frac{d^2 T}{dy^2} = -Q \quad (2)$$

where Q is the volumetric heat generation rate. Assuming the liquid temperature at $y = \delta$ to be the vapor saturation temperature at the system pressure, T_{sat} , the solution of equation (2) is given by

$$T = T_w - \frac{Q\delta^2}{2k} \left[\left(\frac{y}{\delta} \right)^2 - \frac{y}{\delta} \right] + \Delta T \frac{y}{\delta} \quad (3)$$

where ΔT is the temperature drop across the film ($\Delta T = T_{sat} - T_w$). Equating the heat liberation by condensation with the heat conduction into the film leads to

$$h_{fg} \frac{d}{dx} (\rho \delta \bar{u}) = k \left(\frac{\partial T}{\partial y} \right)_{y=\delta} \quad (4)$$

where \bar{u} is the average velocity within the film and is given by (see equation (1))

$$\bar{u} = \frac{1}{\delta} \int_0^\delta u \, dy = \frac{1}{3} \frac{g\delta^2}{\nu} \quad (5)$$

Combining equations (3), (4), and (5) yields the following differential equation for the condensate film thickness, δ , as a function of the distance along the vertical wall, x :

$$\frac{d\xi^2}{dX} = \frac{1 - \xi^2}{\xi^2} \quad (6)$$

where we introduced the dimensionless variables

$$\xi \equiv \left(\frac{Q}{2k\Delta T} \right)^{1/2} \delta \quad (7)$$

and

$$X \equiv \frac{\nu Q^2 x}{2g\rho h_{fg} k \Delta T} \quad (8)$$

Integration of equation (6) with the boundary condition $\delta(0) = \xi(0) = 0$ gives

$$X = -\ln(1 - \xi^2) - \xi^2 \quad (9)$$

The local heat transfer at the surface of the vertical wall, q , follows from differentiating equation (3) and is

$$\frac{q}{(2Qk\Delta T)^{1/2}} = \frac{1}{2} (\xi^{-1} + \xi) \quad (10)$$

It can readily be shown that the average heat flux, \bar{q} , is

$$\frac{\bar{q}}{(2Qk\Delta T)^{1/2}} = \frac{\ln(1 + \xi) - \ln(1 - \xi) - (1/3)\xi^3 - 2\xi}{-\ln(1 - \xi^2) - \xi^2} \quad (11)$$

For the no-heat generation limit this becomes the Nusselt expression (in terms of the dimensionless distance X)

$$\frac{\bar{q}_{Nu}}{(2Qk\Delta T)^{1/2}} = \frac{2}{3} \frac{1}{(2X)^{1/4}} \quad (12)$$

Equation (12) is obtained by noting that for small ξ , $X = \xi^4/2$ from equation (9) and $\bar{q}/(2Qk\Delta T)^{1/2} = 2/(3\xi)$ from equation (11). Both ξ and \bar{q} (normalized by \bar{q}_{Nu}) are plotted in Fig. 1.

We see that with a volume heat source present the heat flux to the wall is higher than its value with no heat source present. Fig. 1 shows that for $X > 10^{-2}$, the effect of heat generation on the wall heat flux is significant. In addition, heat generation results in a reduced film thickness and will cause the film to approach the terminal thickness $\delta_t = (2k\Delta T/Q)^{1/2}$ for $X > 3$. The above observations are easily explained. The volume heat source raises the temperature of the liquid at every point $0 < y < \delta$ in the film at a given location x . This results in a larger temperature gradient at the wall ($y = 0$) compared with the temperature gradient $\Delta T/\delta$ for the no-

¹ Work performed under the auspices of the U. S. Atomic Energy Commission.

² Reactor Analysis and Safety Division, Argonne National Laboratory, Argonne, Ill.

³ Numbers in brackets designate references at end of technical brief.

Contributed by the Heat Transfer Division of THE AMERICAN SOCIETY OF MECHANICAL ENGINEERS. Manuscript received by the Heat Transfer Division July 22, 1974.

heat generation case. On the other hand, the value of the temperature gradient at the liquid film-vapor interface ($y = \delta$) is smaller than $\Delta T/\delta$. Consequently, there will be a smaller mass flow of condensate. The temperature gradient at $y = \delta$ is negligible for $X > 3$ causing vapor condensation to cease and, consequently, the film thickness to reach a terminal value. In this region of constant film thickness, the heat conducted to the wall equals the heat generated in the liquid film. It is interesting to point out that the film behavior illustrated in Fig. 1 is superficially similar to that of laminar film condensation with a uniform suction velocity at the wall [2-4]. In film condensation with suction, however, the reduced film thickness is caused by the removal of liquid material from the condensate film via suction at the wall. The terminal film thickness is attained when the vapor condensation rate and the liquid suction rate are locally in balance. In this case, the heat of condensation is always removed at the wall.

In LMFBR safety applications, heat generation occurs in both the vapor and condensed liquid, so that a temperature gradient will also be generated in the vapor causing it to be superheated. Therefore, boundary condition (4) is not strictly applicable and its use constitutes an approximation to the true picture. For nuclear fuel vapor condensation in a vertical tube or duct of radius R , it can be shown that the temperature gradient in the vapor is negligible providing that

$$(\rho_v R)/(\rho \delta_t) \ll 1 \quad (13)$$

where ρ_v is the vapor density.

The effect of liquid convection on the heat-transfer rate can be estimated in a manner similar to that of reference [5], viz., the velocity and temperature distributions given by equations (1) and (3) are introduced into the integral form of the energy equation which includes the convection terms. This equation can be integrated in an elementary fashion, and the result yields the following corrected form for the dimensionless film thickness:

$$X = \left(1 + \frac{3}{8} \phi - \frac{7}{24} \phi\right) [-\ln(1 - \xi^2) - \xi^2] + \frac{7}{48} \phi \xi^4 \quad (14)$$

where

$$\phi \equiv \frac{c \Delta T}{h_{fg}} \quad (15)$$

In the no-heat generation limit, equation (14) becomes

$$X = \left(1 + \frac{3}{8} \phi\right) \frac{\xi^4}{2} \quad (16)$$

which corresponds to Rohsenow's first-order correction given in reference [5]. For no-heat generation, the convection effect is equivalent to correcting the latent heat, h_{fg} , by a constant factor. Equation (14) indicates that such a simple correction does not exist when heat generation effects are important. It appears, how-

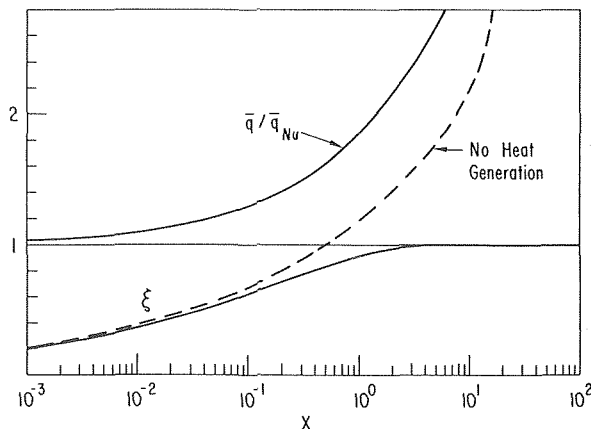


Fig. 1 Normalized heat flux and dimensionless film thickness versus dimensionless distance

ever, that the correction for convective effect is smaller for heat generation than for no heat generation.

References

- 1 Nusselt, W., "Die Oberflächenkondensation des Wasserdampfes," *Z. Ver. Deutsch. Ing.*, Vol. 60, 1916, pp. 541-546, 569-575.
- 2 Jain, K. C., and Bankoff, S. G., "Laminar Film Condensation on a Porous Vertical Wall With Uniform Suction Velocity," *JOURNAL OF HEAT TRANSFER*, TRANS. ASME, Series C, Vol. 86, No. 4, Nov. 1964, pp. 481-489.
- 3 Yang, J. W., "Effect of Uniform Suction on Laminar Film Condensation on a Porous Vertical Wall," *JOURNAL OF HEAT TRANSFER*, TRANS. ASME, Series C, Vol. 92, No. 2, May 1970, pp. 252-256.
- 4 Lienhard, J., and Dhir, V., "A Simple Analysis of Laminar Film Condensation With Suction," *JOURNAL OF HEAT TRANSFER*, TRANS. ASME, Series C, Vol. 94, No. 3, Aug. 1972, pp. 334-336.
- 5 Rohsenow, W. M., "Heat Transfer and Temperature Distribution in Laminar-Film Condensation," *TRANS. ASME*, Vol. 78, 1956, pp. 1645-1648.

Nonstationary Homogeneous Nucleation¹

K. G. Harstad²

Nomenclature

- A_c = characteristic molecular area in the liquid phase
- C = proportionality constant for the quasi-equilibrium drop distribution
- F = free energy parameter
- g = number of molecules in a condensation drop
- g^* = number of molecules in a drop of critical size
- I = net flux function for drop growth
- I^* = nucleation rate flux function
- k = Boltzmann's constant
- m = molecular mass
- N_g = number density of drops composed of g molecules
- p = vapor pressure
- $p_s(T)$ = saturation vapor pressure for a flat surface
- T = vapor temperature
- t = time
- α_c = condensation accommodation coefficient
- β = free molecular flow particle flux
- $\Delta \xi$ = difference interval for variable ξ
- $\Delta \phi_g$ = free energy of formation of a drop of g molecules
- $\Delta \phi^*$ = maximum free energy (which defines the critical drop size)
- θ = nondimensional time variable
- θ_R = nondimensional relaxation time
- ξ = drop area variable
- ρ_l = liquid mass density
- $\sigma(T)$ = surface tension of the liquid
- ω = surface tension parameter

¹ This work presents the results of one phase of research carried out in the Jet Propulsion Laboratory, California Institute of Technology, under Contract NAS7-100, sponsored by the National Aeronautics and Space Administration.

² Member of Technical Staff, Propulsion Research and Advanced Concepts Section, Jet Propulsion Laboratory, Pasadena, Calif.

Contributed by the Heat Transfer Division of THE AMERICAN SOCIETY OF MECHANICAL ENGINEERS. Manuscript received by the Heat Transfer Division July 3, 1974.

heat generation case. On the other hand, the value of the temperature gradient at the liquid film-vapor interface ($y = \delta$) is smaller than $\Delta T/\delta$. Consequently, there will be a smaller mass flow of condensate. The temperature gradient at $y = \delta$ is negligible for $X > 3$ causing vapor condensation to cease and, consequently, the film thickness to reach a terminal value. In this region of constant film thickness, the heat conducted to the wall equals the heat generated in the liquid film. It is interesting to point out that the film behavior illustrated in Fig. 1 is superficially similar to that of laminar film condensation with a uniform suction velocity at the wall [2-4]. In film condensation with suction, however, the reduced film thickness is caused by the removal of liquid material from the condensate film via suction at the wall. The terminal film thickness is attained when the vapor condensation rate and the liquid suction rate are locally in balance. In this case, the heat of condensation is always removed at the wall.

In LMFBR safety applications, heat generation occurs in both the vapor and condensed liquid, so that a temperature gradient will also be generated in the vapor causing it to be superheated. Therefore, boundary condition (4) is not strictly applicable and its use constitutes an approximation to the true picture. For nuclear fuel vapor condensation in a vertical tube or duct of radius R , it can be shown that the temperature gradient in the vapor is negligible providing that

$$(\rho_v R)/(\rho \delta_t) \ll 1 \quad (13)$$

where ρ_v is the vapor density.

The effect of liquid convection on the heat-transfer rate can be estimated in a manner similar to that of reference [5], viz., the velocity and temperature distributions given by equations (1) and (3) are introduced into the integral form of the energy equation which includes the convection terms. This equation can be integrated in an elementary fashion, and the result yields the following corrected form for the dimensionless film thickness:

$$X = (1 + \frac{3}{8} \phi - \frac{7}{24} \phi^2) [-\ln(1 - \xi^2) - \xi^2] + \frac{7}{48} \phi \xi^4 \quad (14)$$

where

$$\phi \equiv \frac{c \Delta T}{h_{fg}} \quad (15)$$

In the no-heat generation limit, equation (14) becomes

$$X = (1 + \frac{3}{8} \phi) \frac{\xi^4}{2} \quad (16)$$

which corresponds to Rohsenow's first-order correction given in reference [5]. For no-heat generation, the convection effect is equivalent to correcting the latent heat, h_{fg} , by a constant factor. Equation (14) indicates that such a simple correction does not exist when heat generation effects are important. It appears, how-

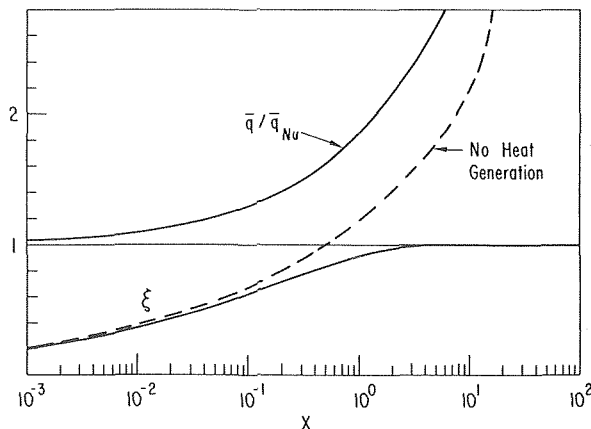


Fig. 1 Normalized heat flux and dimensionless film thickness versus dimensionless distance

ever, that the correction for convective effect is smaller for heat generation than for no heat generation.

References

- 1 Nusselt, W., "Die Oberflächenkondensation des Wasserdampfes," *Z. Ver. Deutsch. Ing.*, Vol. 60, 1916, pp. 541-546, 569-575.
- 2 Jain, K. C., and Bankoff, S. G., "Laminar Film Condensation on a Porous Vertical Wall With Uniform Suction Velocity," *JOURNAL OF HEAT TRANSFER*, TRANS. ASME, Series C, Vol. 86, No. 4, Nov. 1964, pp. 481-489.
- 3 Yang, J. W., "Effect of Uniform Suction on Laminar Film Condensation on a Porous Vertical Wall," *JOURNAL OF HEAT TRANSFER*, TRANS. ASME, Series C, Vol. 92, No. 2, May 1970, pp. 252-256.
- 4 Lienhard, J., and Dhir, V., "A Simple Analysis of Laminar Film Condensation With Suction," *JOURNAL OF HEAT TRANSFER*, TRANS. ASME, Series C, Vol. 94, No. 3, Aug. 1972, pp. 334-336.
- 5 Rohsenow, W. M., "Heat Transfer and Temperature Distribution in Laminar-Film Condensation," TRANS. ASME, Vol. 78, 1956, pp. 1645-1648.

Nonstationary Homogeneous Nucleation¹

K. G. Harstad²

Nomenclature

- A_c = characteristic molecular area in the liquid phase
- C = proportionality constant for the quasi-equilibrium drop distribution
- F = free energy parameter
- g = number of molecules in a condensation drop
- g^* = number of molecules in a drop of critical size
- I = net flux function for drop growth
- I^* = nucleation rate flux function
- k = Boltzmann's constant
- m = molecular mass
- N_g = number density of drops composed of g molecules
- p = vapor pressure
- $p_s(T)$ = saturation vapor pressure for a flat surface
- T = vapor temperature
- t = time
- α_c = condensation accommodation coefficient
- β = free molecular flow particle flux
- $\Delta \xi$ = difference interval for variable ξ
- $\Delta \phi_g$ = free energy of formation of a drop of g molecules
- $\Delta \phi^{\ddagger}$ = maximum free energy (which defines the critical drop size)
- θ = nondimensional time variable
- θ_R = nondimensional relaxation time
- ξ = drop area variable
- ρ_l = liquid mass density
- $\sigma(T)$ = surface tension of the liquid
- ω = surface tension parameter

¹ This work presents the results of one phase of research carried out in the Jet Propulsion Laboratory, California Institute of Technology, under Contract NAS7-100, sponsored by the National Aeronautics and Space Administration.

² Member of Technical Staff, Propulsion Research and Advanced Concepts Section, Jet Propulsion Laboratory, Pasadena, Calif.

Contributed by the Heat Transfer Division of THE AMERICAN SOCIETY OF MECHANICAL ENGINEERS. Manuscript received by the Heat Transfer Division July 3, 1974.

A commonly used mathematical model for the homogenous nucleation and condensation of a supersaturated vapor to the liquid phase is based on classical liquid drop thermodynamics [1-6].³ The theory is reviewed and discussed in [1, 2, 3, 6]. Although this theory is subject to controversy (particularly with respect to the distribution constant C defined in the following), it is felt that the basic physics of nucleation is properly described [3, 6]. The results of computer calculation of the relaxation time to steady-state nucleation using the theory are presented in this brief.

Assuming a finite probability for a vapor molecule sticking to another molecule or molecular cluster upon collision, thermal fluctuations in a vapor will lead to drop formation. If the vapor is undersaturated with respect to a drop of size g , classical statistical mechanics gives a quasi-equilibrium distribution of drops $N_g = C \cdot \exp(-\Delta\phi_g/kT)$ for an appropriate constant C . From thermodynamics, the free energy is $\Delta\phi_g = gkT \ln(p_s/p) + g^{2/3}A_c\sigma$ where $A_c \equiv (4\pi)^{1/3}(3m/\rho_l)^{2/3}$. The Boltzmann-like distribution represents a balance between the effect of thermal collisions and the tendency for drops to vaporize. The drop formation or nucleation equations are formed assuming that only binary collisions between a drop and a vapor molecule (monomer) are important, i.e., the drop size changes by addition or subtraction of a single molecule at a time. This means that the vapor must be sufficiently tenuous and that the concentration of dimers and higher order polymers must be much smaller than the monomer concentration. The sticking ability of a molecule upon collision is characterized by the condensation accommodation coefficient α_c . The free molecular flow particle flux $\beta \equiv p/(2\pi mkT)^{1/2}$ and the drop area is $g^{2/3}A_c$, giving a growth collision frequency of $g^{2/3}\alpha_c A_c \beta$. The evaporation rate is given by the principle of detailed balancing using the quasi-equilibrium distribution: $(g-1)^{2/3}\alpha_c A_c \beta \exp((\Delta\phi_g - \Delta\phi_{g-1})/kT)$. Let variable θ be a dimensionless time variable: $d\theta = \alpha_c A_c \beta(t) dt$. The binary collision equation is

$$\frac{dN_g}{d\theta} = I_{g-1} - I_g \text{ where } I_g = g^{2/3}(N_g - N_{g+1} \exp((\Delta\phi_{g+1} - \Delta\phi_g)/kT))$$

or⁴

$$\frac{\partial N_g}{\partial \theta} = -\frac{\partial I}{\partial g} \text{ and } I = -g^{2/3} \left(\frac{\partial N_g}{\partial g} + \frac{N_g}{kT} \frac{\partial \Delta\phi_g}{\partial g} \right)$$

The net flux of drops making the transition $g \rightarrow g+1$ is given by $\alpha_c A_c \beta I$. The nucleation rate is given by the flux function I at the critical drop size⁵ $g^* = (2\omega/3 \ln(p/p_s))^3$ where the surface tension parameter $\omega \equiv \sigma A_c/kT$ and $p > p_s$. (The vapor is undersaturated for drops with $g < g^*$.) The steady state nucleation limit is given by $\partial N_g/\partial \theta \rightarrow 0$ or

$$I = (C/3)(\omega/\pi)^{1/2} \exp(-\Delta\phi^*/kT)$$

and

$$N_g = C/2 \exp(-\Delta\phi_g/kT) \operatorname{erfc} \left(3(g^{2/3} - g^{*2/3}) \times \ln(p/p_s)/4\omega^{1/2} \right)$$

if $\ln(p/p_s) \ll \omega^{3/2}$. Here $\Delta\phi^* \equiv \Delta\phi_g|_{g=g^*}$ and it is assumed that the quasi-equilibrium distribution is approached for $g \rightarrow 0$. The steady state distribution is only qualitatively correct if $g \gg g^*$.

A drop area variable $\xi \equiv 3g^{2/3}/2$. Let $\Psi \equiv \ln(g^{1/3}N_g)$ and $F \equiv \Delta\phi_g/kT - \ln(g/3)$. The formation equation is put in the form

$$\frac{\partial \Psi}{\partial \theta} = \frac{\partial^2}{\partial \xi^2} (\Psi + F) + \frac{\partial \Psi}{\partial \xi} \frac{\partial}{\partial \xi} (\Psi + F)$$

³ Numbers in brackets designate References at the end of the technical brief.

⁴ The first order differences in discrete variable g resulting from the binary collision rate equations are replaced by differentials. Then g is considered continuous.

⁵ Conversely, this formula can be considered to give the saturation pressure p of a drop of size g^* . Note that $p \rightarrow p_s$ as $g^* \rightarrow \infty$.

The logarithmic distribution function Ψ is used since N_g is expected to depend strongly (in an exponential manner) on the variables p , T , and g . Such a behavior is awkward from the standpoint of numerical integration. The above equation is converted to a set of forty total differential equations in the variable θ by the use of finite differences in the variable ξ . (This mimics the differences in variable g in the original binary collision rate equations.) The difference interval is restricted to $0.4 \leq \Delta\xi \leq 1.1$ (this is sufficiently small for good numerical accuracy [6] and corresponds to $\Delta g \leq 5$). For the calculations of relaxation times, conditions (p, T) are taken constant, the quasi-equilibrium distribution is assumed on the lower boundary ($\xi \equiv 4, g \simeq 4$), and null drop number densities are assumed initially and on the upper boundary ($\xi = 4 + 41 \Delta\xi$). The first order differential equations were solved on a UNIVAC 1108 utilizing a JPL Subroutine Library integrator SVDQ.

In terms of the maximum critical flux I_{\max}^* , a relaxation time θ_R is defined as that (first) time when $I^* = 0.9 I_{\max}^*$. I_{\max}^* was found to be approximately the same as the steady state flux given above and $I^* = I_{\max}^*$ at a time roughly twice θ_R . The results are given in Fig. 1. No computations were performed for $\theta > 200$. Further relaxation beyond the (near) steady-state condition toward the quasi-equilibrium distribution (that is, condensation) with a decrease in I^* was apparent for the extremes in g^* shown in the figure. A very slow further relaxation also seemed to occur with the surface tension parameter $\omega = 5$. Of course, the nucleation equation given in the foregoing is too simple to accurately portray any such condensation process where energy considerations are important. Thus there is limited significance to these results with $\theta \gg \theta_R$. Further details on the numerical procedures and results are given in [6].

Comparisons with the numerical results of Courtney [4] are given in [6]. Drop number densities versus time for water vapor nucleation are given in [4]; fluxes are not presented. Agreement of results for undersaturated drops is good [6]. Abraham [5] gives numerical calculations for three conditions: $\omega = 9.9$ and $g^* = 72$ giving $\theta_R \simeq 26$, $\omega = 12.1$ and $g^* = 48$ giving $\theta_R \simeq 14$ and $\omega = 14.0$ and

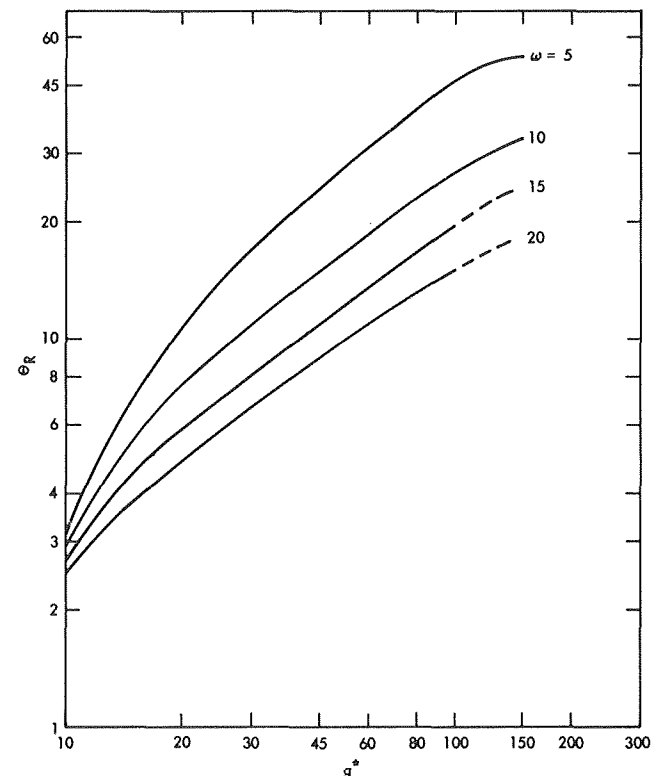


Fig. 1 Nondimensional nucleation relaxation time θ_R versus critical drop size g^* for various values of the surface tension parameter ω (see text)

$g^* = 35$ giving $\theta_R \approx 8$ (notation of present work). These three points are located in the intermediate region of Fig. 1 and are approximately consistent with present results. Theoretical estimates by several authors of the relaxation time based on diverse approximations to the nucleation equation [3] yield the result $\theta_R \sim \omega^{-1}g^{*2/3}$. This agrees only qualitatively with the curves shown in Fig. 1; a curve fit based on this form results in a RMS error of about 23 percent and a maximum deviation by a factor of 3 (small ω and g^*).

The use of the logarithmic distribution and nonlinear equation enables fast computation of the relaxation for a given condition, the computer time being on the order of 20 s to 1 min. This is much faster than previous calculations [4, 5].

It should be pointed out that the calculation of the nucleation relaxation time is independent of the value of C . Also, it does not depend on identifying the surface tension parameter ω to the bulk liquid properties but only requires that the form of the free energy dependence on g be the same as that of classical drop thermodynamics.

The curves in Fig. 1 provide a means of rough estimation of the

limit to the validity of steady-state nucleation theory. Physical times can be easily calculated from the parameters ω , g^* , α_c and β .

Acknowledgment

The author wishes to thank the referees for pointing out some references [3, 5] unknown to him.

References

- Hill, P. G., Witting, H., and Demetri, E. P., "Condensation of Metal Vapors during Rapid Expansion," JOURNAL OF HEAT TRANSFER Series C, Vol. 85, Nov. 1963, pp. 303-317.
- Hidy, G. M., and Brock, J. R., *The Dynamics of Aerocolloidal Systems*, Pergamon Press, Oxford, 1970.
- Abraham, F. F., *Homogeneous Nucleation Theory*, Academic Press, N. Y. (1974).
- Courtney, W. G., "Non-Steady-State Nucleation," *J. Chem. Phys.*, Vol. 36, Apr. 1962, pp. 2009-2017.
- Abraham, F. F., "Multistate Kinetics in Nonsteady-State Nucleation: A Numerical Solution," *J. Chem. Phys.*, Vol. 51, Aug. 1969, pp. 1632-1638.
- Harstad, K. G., "Nonstationary Homogeneous Nucleation," JPL Tech. Mem. 33-666, Jet Propulsion Laboratory, Pasadena, Calif., Jan. 1974.

Application of the Reynolds Flux Model of Critical Heat Flux for Direct Heat Flux Scaling in Nonuniform Rod Bundles

J. C. Purcupile,¹ F. E. Motley,² and F. F. Cadek³

Nomenclature

- c_1 = critical heat flux constant
 c_2 = liquid vapor exchange proportionality factor
 D = inside diameter, ft
 G = mass velocity, lb_m/hr-ft²
 h_{fg} = latent heat of vaporization, Btu/lb_m
 H = enthalpy, Btu/lb_m
 K = basic heat flux scaling constant
 X = flowing equilibrium quality—defined in subcooled region as $\frac{H_b - H_s}{h_{fg}}$
 q = critical heat flux, Btu/hr-ft²
 α = void fraction
 μ = viscosity, lb_m/hr-ft
 ρ = density, lb_m/ft³

Subscripts

- b = bulk or average fluid condition
 l = liquid
 R = refrigerant
 s = saturation condition associated with exit pressure
 v = vapor
 w = water

- exit = exit condition
 local = local condition
 m = maximum

Introduction

The idea of using a Reynolds flux model to predict CHF was developed in [6]⁴ and this model was used to scale CHF in tubes in [7]. This paper extends this method of scaling, based on the Reynolds flux model, to rod bundles with nonuniform heat flux.

All the data reported by Motley, et al. [2] for R-11 and Rosal, et al. [5] for water was analyzed with Cobra III [8] computer code. The R-11 transport properties replaced the water transport properties in the appropriate subroutines. The computer code includes the Levy [4] void model as modified by Rowe [8]. The boiling mixing was assumed to be the same as subcooled mixing and a modified Armand [9] bulk void correlation was used. Also a modified Martinielli-Nelson friction multiplier was included in the code. Only data where the local bulk fluid temperature in the hot channel at the measured CHF elevation was subcooled is used in this study.

Direct Heat Flux Scaling

At the same equivalent pressure⁵ and local equilibrium qualities at CHF, it was shown in [7] for uniform axial heat flux:

$$\left[\frac{q}{h_{fg}G} \right]_w = K \left[\frac{1 - \alpha_R}{1 - \alpha_w} \right]^{0.4} \left[\frac{\mu_w}{\mu_R} \right]^{0.6} \left[\frac{q}{h_{fg}G} \right]_R$$

where:

$$K = \frac{c_{1w}}{c_{1R}}$$

This expression was modified for non-uniform axial heat-flux by replacing (X_{exit}) in the correlation presented in [6] with the local equilibrium quality where CHF occurs (X_{local}). This correlation then can be used to calculate K . This is done by calculating c_1 for each data point and then averaging the c_1 's at each pressure for both water and refrigerants.

For each test section, the value of the CHF scaling constant (K) was then calculated from the average values of c_1 in water and R-11 at the same equivalent pressure. The values of scaling constant

¹ Assoc. Professor, Department of Mechanical Engineering, Carnegie-Mellon University, Pittsburgh, Pa. Mem. ASME.

² Nuclear Fuel Division, Westinghouse Electric Corporation, Pittsburgh, Pa. Mem. ASME.

³ Nuclear Fuel Division, Westinghouse Electric Corporation, Pittsburgh, Pa. Mem. ASME.

Contributed by the Heat Transfer Division of THE AMERICAN SOCIETY OF MECHANICAL ENGINEERS. Manuscript received by the Heat Transfer Division June 27, 1974.

⁴ Numbers in brackets designate References at end of technical briefs.

⁵ Equivalent pressure is defined as the pressure where the liquid-to-vapor density ratio is the same for both refrigerant and water.

$g^* = 35$ giving $\theta_R \approx 8$ (notation of present work). These three points are located in the intermediate region of Fig. 1 and are approximately consistent with present results. Theoretical estimates by several authors of the relaxation time based on diverse approximations to the nucleation equation [3] yield the result $\theta_R \sim \omega^{-1}g^{*2/3}$. This agrees only qualitatively with the curves shown in Fig. 1; a curve fit based on this form results in a RMS error of about 23 percent and a maximum deviation by a factor of 3 (small ω and g^*).

The use of the logarithmic distribution and nonlinear equation enables fast computation of the relaxation for a given condition, the computer time being on the order of 20 s to 1 min. This is much faster than previous calculations [4, 5].

It should be pointed out that the calculation of the nucleation relaxation time is independent of the value of C . Also, it does not depend on identifying the surface tension parameter ω to the bulk liquid properties but only requires that the form of the free energy dependence on g be the same as that of classical drop thermodynamics.

The curves in Fig. 1 provide a means of rough estimation of the

limit to the validity of steady-state nucleation theory. Physical times can be easily calculated from the parameters ω , g^* , α_c and β .

Acknowledgment

The author wishes to thank the referees for pointing out some references [3, 5] unknown to him.

References

- Hill, P. G., Witting, H., and Demetri, E. P., "Condensation of Metal Vapors during Rapid Expansion," JOURNAL OF HEAT TRANSFER Series C, Vol. 85, Nov. 1963, pp. 303-317.
- Hidy, G. M., and Brock, J. R., *The Dynamics of Aerocolloidal Systems*, Pergamon Press, Oxford, 1970.
- Abraham, F. F., *Homogeneous Nucleation Theory*, Academic Press, N. Y. (1974).
- Courtney, W. G., "Non-Steady-State Nucleation," *J. Chem. Phys.*, Vol. 36, Apr. 1962, pp. 2009-2017.
- Abraham, F. F., "Multistate Kinetics in Nonsteady-State Nucleation: A Numerical Solution," *J. Chem. Phys.*, Vol. 51, Aug. 1969, pp. 1632-1638.
- Harstad, K. G., "Nonstationary Homogeneous Nucleation," JPL Tech. Mem. 33-666, Jet Propulsion Laboratory, Pasadena, Calif., Jan. 1974.

Application of the Reynolds Flux Model of Critical Heat Flux for Direct Heat Flux Scaling in Nonuniform Rod Bundles

J. C. Purcupile,¹ F. E. Motley,² and F. F. Cadek³

Nomenclature

- c_1 = critical heat flux constant
 c_2 = liquid vapor exchange proportionality factor
 D = inside diameter, ft
 G = mass velocity, lb_m/hr-ft²
 h_{fg} = latent heat of vaporization, Btu/lb_m
 H = enthalpy, Btu/lb_m
 K = basic heat flux scaling constant
 X = flowing equilibrium quality—defined in subcooled region as $\frac{H_b - H_s}{h_{fg}}$
 q = critical heat flux, Btu/hr-ft²
 α = void fraction
 μ = viscosity, lb_m/hr-ft
 ρ = density, lb_m/ft³

Subscripts

- b = bulk or average fluid condition
 l = liquid
 R = refrigerant
 s = saturation condition associated with exit pressure
 v = vapor
 w = water

- exit = exit condition
 local = local condition
 m = maximum

Introduction

The idea of using a Reynolds flux model to predict CHF was developed in [6]⁴ and this model was used to scale CHF in tubes in [7]. This paper extends this method of scaling, based on the Reynolds flux model, to rod bundles with nonuniform heat flux.

All the data reported by Motley, et al. [2] for R-11 and Rosal, et al. [5] for water was analyzed with Cobra III [8] computer code. The R-11 transport properties replaced the water transport properties in the appropriate subroutines. The computer code includes the Levy [4] void model as modified by Rowe [8]. The boiling mixing was assumed to be the same as subcooled mixing and a modified Armand [9] bulk void correlation was used. Also a modified Martinielli-Nelson friction multiplier was included in the code. Only data where the local bulk fluid temperature in the hot channel at the measured CHF elevation was subcooled is used in this study.

Direct Heat Flux Scaling

At the same equivalent pressure⁵ and local equilibrium qualities at CHF, it was shown in [7] for uniform axial heat flux:

$$\left[\frac{q}{h_{fg}G} \right]_w = K \left[\frac{1 - \alpha_R}{1 - \alpha_w} \right]^{0.4} \left[\frac{\mu_w}{\mu_R} \right]^{0.6} \left[\frac{q}{h_{fg}G} \right]_R$$

where:

$$K = \frac{c_{1w}}{c_{1R}}$$

This expression was modified for non-uniform axial heat-flux by replacing (X_{exit}) in the correlation presented in [6] with the local equilibrium quality where CHF occurs (X_{local}). This correlation then can be used to calculate K . This is done by calculating c_1 for each data point and then averaging the c_1 's at each pressure for both water and refrigerants.

For each test section, the value of the CHF scaling constant (K) was then calculated from the average values of c_1 in water and R-11 at the same equivalent pressure. The values of scaling constant

¹ Assoc. Professor, Department of Mechanical Engineering, Carnegie-Mellon University, Pittsburgh, Pa. Mem. ASME.

² Nuclear Fuel Division, Westinghouse Electric Corporation, Pittsburgh, Pa. Mem. ASME.

³ Nuclear Fuel Division, Westinghouse Electric Corporation, Pittsburgh, Pa. Mem. ASME.

Contributed by the Heat Transfer Division of THE AMERICAN SOCIETY OF MECHANICAL ENGINEERS. Manuscript received by the Heat Transfer Division June 27, 1974.

⁴ Numbers in brackets designate References at end of technical briefs.

⁵ Equivalent pressure is defined as the pressure where the liquid-to-vapor density ratio is the same for both refrigerant and water.

Table 1

Test description flux shape—spacer grid type	CHF scaling constant K
$u \sin u$ —simple support grid	1.52
$u \sin u$ —mixing grid A	1.52
$\cos u$ —mixing grid B	1.66

K were found to be independent of pressure. The calculated values of the CHF scaling constant are presented in Table 1.

The measured CHF in water was then compared with the predicted CHF based on the values of c_1 from R-11 and the scaling constant from Table 1. These comparisons are presented in Figs. 1 and 2.

Discussion

Since K (Table 1) was not a unique constant—1.52 for the $u \sin u$ test section and 1.66 for the $\cos u$ test section—it is recognized that we still do not have a generalized model for different axial flux shapes in the subcooled boiling regime. While we still need both water and refrigerant data, there are a number of reasons why refrigerant tests are valuable. First, in some instances due to power limitations, only low inlet subcooling CHF data can be taken. In this case, the refrigerant data is used to predict CHF with highly subcooled inlet conditions. Second, refrigerant tests are considerably cheaper due to power savings and reduced test section maintenance costs.

The refrigerant tests can also be used to predict changes in CHF as a result of changes in grids. For example, referring to Fig. 1, refrigerant tests scaled the water results using the same scaling constant (K) for simple support grids and mixing grids. This indicates that changing grid types has the same effect in Freon as in water and that a designer may be able to optimize the rod bundle thermal hydraulics with refrigerant tests and then verify the end result with water.

References

- 1 Coeffield, R. D., Jr., Rohrer, W. M., Jr., and Tong, L. S., "A Subcooled DNB Investigation of Freon-113 and Its Similarity to Subcooled Water DNB Data," Nuclear Engineering and Design, May 19, 1969, pp. C-1-C-11.
- 2 Motley, F. E., Cadek, F. F., Cermak, J. O., Tong, L. S., Gouse, S. W., Paul, F., and Purcupile, J. C., "CHF Data From Freon-11 Flow for Scaling CHF in Water," International Symposium on Two-Phase Systems, Haifa, Israel, 1971.
- 3 Stevens, G. F., and Kirby, G. J., "A Quantitative Comparison Between

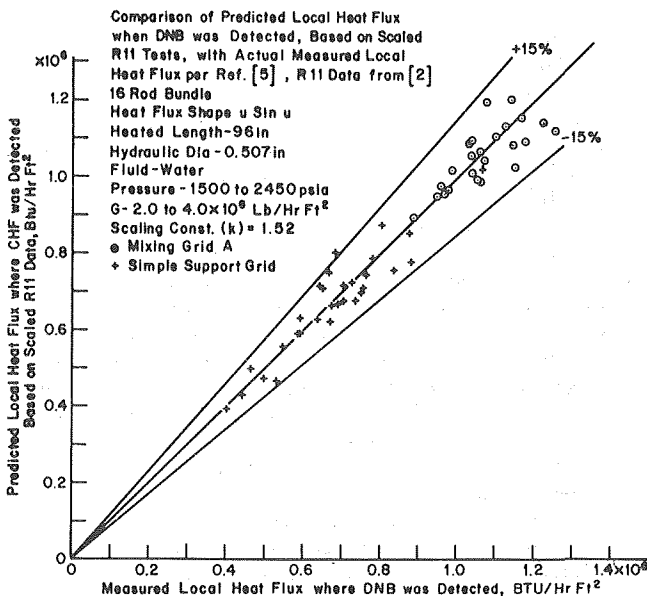


Fig. 1

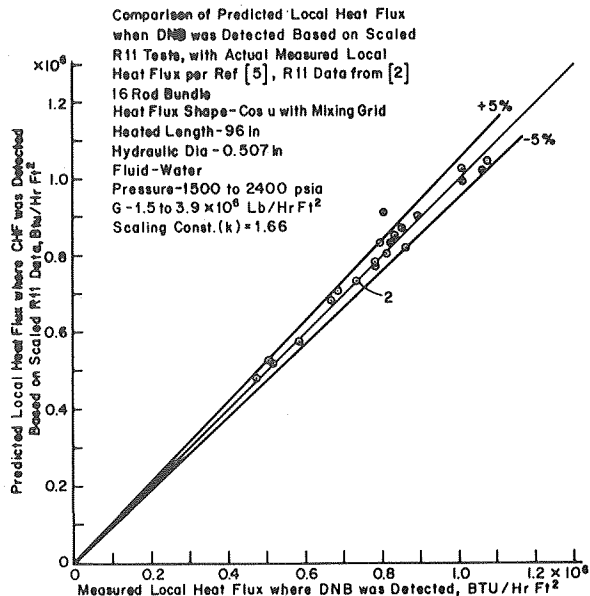


Fig. 2

Burnout Data for Water at 1000 psia and Freon-12 at 155 psia. Uniformly Heated Round Tubes, Vertical Upflow," AEEW-R327, 1964.

4 Levy, S., "Forced Convection Subcooled Boiling—Prediction of Vapor Volumetric Fraction," International Journal of Heat and Mass Transfer, Vol. 10, Pergamon Press, Great Britain, 1967, pp 951-965.

5 Rosal, E. R., Cermak, J. O., Tong, L. S., Casterline, J. E., and Matzner, B., "Rod Bundle Axial Non-Uniform Heat Flux DNB Tests and Data (under preparation)."

6 Purcupile, J. C., and Gouse, S. W., Jr., "Reynolds Flux Model of Critical Heat Flux in Subcooled Forced Convection Boiling," ASME Paper No. 72-HT-4.

7 Purcupile, J. C., Tong, L. S. and Gouse, S. W., Jr., "Refrigerant—Water Scaling of Critical Heat Flux in Round Tubes—Subcooled Forced Convection Boiling," JOURNAL OF HEAT TRANSFER, TRANS. ASME, Series C, Vol. 55, May 1973.

8 Rowe, D. S., "Cobra III: A Digital Computer Program for Steady State and Transient Thermal-Hydraulic Analysis of Rod Bundle Nuclear Fuel Elements," BNWL-B-82.

9 Armand, A. A., "The Resistance During the Movement of a Two-Phase System in Horizontal Pipes," AERE Trans 828 Izvestiya Vsesojuznogo Teplotekhnicheskogo Instituta 1946.

Thermal Stresses in a Sphere Due to Local Heating Followed by Complete Cooling

T. S. Chen,¹ K. Thirumalai,² and J. B. Cheung³

Introduction

The present study was carried out to examine the response of rocks and related brittle solids to high energy surface heating fol-

¹ Department of Mechanical Engineering, University of Missouri-Rolla, Rolla, Mo. Mem. ASME

² Twin Cities Mining Research Center, U. S. Bureau of Mines, Twin Cities, Minn.

³ Twin Cities Mining Research Center, U. S. Bureau of Mines, Twin Cities, Minn. Mem. ASME

Contributed by the Heat Transfer Division of The American Society of Mechanical Engineers. Manuscript received by the Heat Transfer Division November 28, 1973.

Table 1

Test description flux shape—spacer grid type	CHF scaling constant K
$u \sin u$ —simple support grid	1.52
$u \sin u$ —mixing grid A	1.52
$\cos u$ —mixing grid B	1.66

K were found to be independent of pressure. The calculated values of the CHF scaling constant are presented in Table 1.

The measured CHF in water was then compared with the predicted CHF based on the values of c_1 from R-11 and the scaling constant from Table 1. These comparisons are presented in Figs. 1 and 2.

Discussion

Since K (Table 1) was not a unique constant—1.52 for the $u \sin u$ test section and 1.66 for the $\cos u$ test section—it is recognized that we still do not have a generalized model for different axial flux shapes in the subcooled boiling regime. While we still need both water and refrigerant data, there are a number of reasons why refrigerant tests are valuable. First, in some instances due to power limitations, only low inlet subcooling CHF data can be taken. In this case, the refrigerant data is used to predict CHF with highly subcooled inlet conditions. Second, refrigerant tests are considerably cheaper due to power savings and reduced test section maintenance costs.

The refrigerant tests can also be used to predict changes in CHF as a result of changes in grids. For example, referring to Fig. 1, refrigerant tests scaled the water results using the same scaling constant (K) for simple support grids and mixing grids. This indicates that changing grid types has the same effect in Freon as in water and that a designer may be able to optimize the rod bundle thermal hydraulics with refrigerant tests and then verify the end result with water.

References

- 1 Coeffield, R. D., Jr., Rohrer, W. M., Jr., and Tong, L. S., "A Subcooled DNB Investigation of Freon-113 and Its Similarity to Subcooled Water DNB Data," Nuclear Engineering and Design, May 19, 1969, pp. C-1-C-11.
- 2 Motley, F. E., Cadek, F. F., Cermak, J. O., Tong, L. S., Gouse, S. W., Paul, F., and Purcupile, J. C., "CHF Data From Freon-11 Flow for Scaling CHF in Water," International Symposium on Two-Phase Systems, Haifa, Israel, 1971.
- 3 Stevens, G. F., and Kirby, G. J., "A Quantitative Comparison Between

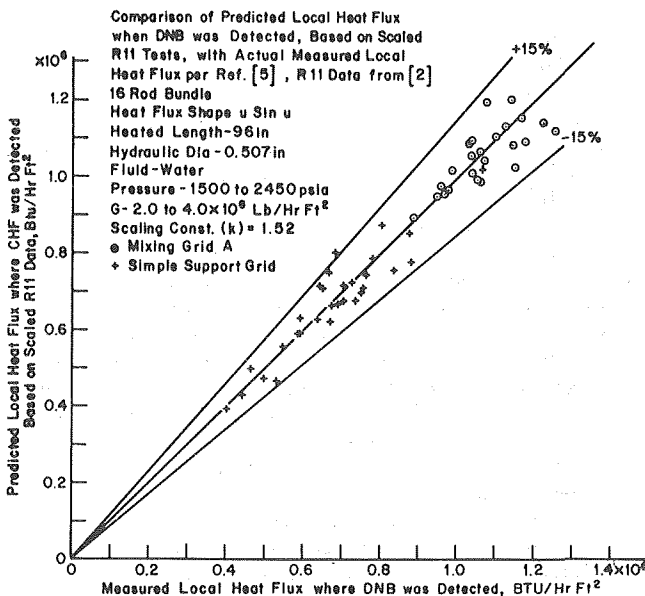


Fig. 1

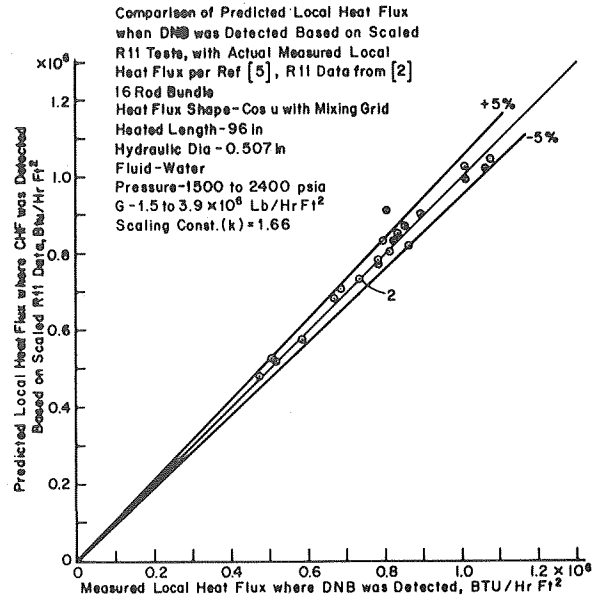


Fig. 2

Burnout Data for Water at 1000 psia and Freon-12 at 155 psia. Uniformly Heated Round Tubes, Vertical Upflow," AEEW-R327, 1964.

4 Levy, S., "Forced Convection Subcooled Boiling—Prediction of Vapor Volumetric Fraction," International Journal of Heat and Mass Transfer, Vol. 10, Pergamon Press, Great Britain, 1967, pp 951-965.

5 Rosal, E. R., Cermak, J. O., Tong, L. S., Casterline, J. E., and Matzner, B., "Rod Bundle Axial Non-Uniform Heat Flux DNB Tests and Data (under preparation)."

6 Purcupile, J. C., and Gouse, S. W., Jr., "Reynolds Flux Model of Critical Heat Flux in Subcooled Forced Convection Boiling," ASME Paper No. 72-HT-4.

7 Purcupile, J. C., Tong, L. S. and Gouse, S. W., Jr., "Refrigerant—Water Scaling of Critical Heat Flux in Round Tubes—Subcooled Forced Convection Boiling," JOURNAL OF HEAT TRANSFER, TRANS. ASME, Series C, Vol. 55, May 1973.

8 Rowe, D. S., "Cobra III: A Digital Computer Program for Steady State and Transient Thermal-Hydraulic Analysis of Rod Bundle Nuclear Fuel Elements," BNWL-B-82.

9 Armand, A. A., "The Resistance During the Movement of a Two-Phase System in Horizontal Pipes," AERE Trans 828 Izvestiya Vsesojuznogo Teplotekhnicheskogo Instituta 1946.

Thermal Stresses in a Sphere Due to Local Heating Followed by Complete Cooling

T. S. Chen,¹ K. Thirumalai,² and J. B. Cheung³

Introduction

The present study was carried out to examine the response of rocks and related brittle solids to high energy surface heating fol-

¹ Department of Mechanical Engineering, University of Missouri-Rolla, Rolla, Mo. Mem. ASME

² Twin Cities Mining Research Center, U. S. Bureau of Mines, Twin Cities, Minn.

³ Twin Cities Mining Research Center, U. S. Bureau of Mines, Twin Cities, Minn. Mem. ASME

Contributed by the Heat Transfer Division of The American Society of Mechanical Engineers. Manuscript received by the Heat Transfer Division November 28, 1973.

lowed by cooling and to evaluate the feasibility of its application to crushing hard rocks. This concept of weakening and breaking of rocks is known [1, 2],⁴ but the supporting theoretical or experimental studies are not available in the literature.

Recent advances in high temperature technology provide high energy heaters such as the oxygen-fuel oil supersonic burners, high energy carbon arc and induction-type plasma heaters, lasers, and electron beam guns for industrial heating applications. These high energy heating tools are also suitable for localized rapid heating of rocks. Cooling can generally be achieved by quenching heated rocks.

The specific objectives of this brief are to extend the analysis of [3] to a cooling period that follows an initial heating period and to determine and interpret certain experimental results.

Analysis

Consider a homogeneous, isotropic, and elastic sphere of radius r_0 , which is initially ($t \leq 0$) at zero reference temperature. During the time period $0 \leq t \leq t_H$, part of its spherical surface is subjected to axisymmetric heating with a prescribed surface heat flux $F(\theta)$, where the angle θ is measured from the axis of thermal symmetry. The unheated surface of the sphere is assumed to be insulated. For time $t \geq t_H$, the entire surface of the sphere is cooled in a fluid environment having heat transfer coefficient h and temperature T_∞ . The temperature solution at time $t = t_H$ is derived in [3] and is denoted by $T(r, \mu, t_H)$, where $\mu = \cos\theta$ and r is the radial coordinate.

The temperature solution for the cooling period can be carried out in a manner similar to that for the heating period described in [3]. This gives

$$T(r, \mu, t^*) - T_\infty = \sum_{n=0}^{\infty} \sum_{m=1}^{\infty} \frac{(2n+1)\gamma_{nm}^2}{[\gamma_{nm}^2 - n(n+1) + B_i(B_i - 1)]J_{n+1/2}(\gamma_{nm})} \cdot \left\{ \int_{-1}^1 \int_0^1 [T(r, \mu, t_H) - T_\infty] \frac{J_{n+1/2}(\frac{\gamma_{nm}r}{r_0})}{\gamma_{nm}^2 \gamma_{nm}^{1/2}} P_n(\mu) r^2 dr d\mu \right\} (1)$$

$$\cdot \frac{J_{n+1/2}(\frac{\gamma_{nm}r}{r_0})}{\gamma_{nm}^{1/2}} P_n(\mu) e^{-\kappa \gamma_{nm}^2 t^* / r_0^2}$$

where $t^* = t - t_H$, κ is thermal diffusivity, P_n is Legendre polynomial of degree n of the first kind, J_ν is Bessel function of the first kind of fractional order ν , γ_{nm} are the positive roots of

$$\gamma_{nm} J_{n-1/2}(\gamma_{nm}) = [(n+1) - B_i] J_{n+1/2}(\gamma_{nm}) \quad (2)$$

and

$$B_i = \frac{hr_0}{K} \quad (3)$$

is the Biot number.

The linear thermoelastic equilibrium equations and the stress displacement equations can be solved in conjunction with the traction-free condition $\sigma_{rr} = \sigma_{r\theta} = 0$ at $r = r_0$. The details of the solution method and the results for the case of heating are given in [3] and are, therefore, omitted here.

The expressions for the dimensionless radial stress $\bar{\sigma}_{RR}$ and tangential stress $\bar{\sigma}_{\theta\theta}$ during the subsequent cooling process are found to be

$$\bar{\sigma}_{RR} = 2 \sum_{n=0}^{\infty} \sum_{m=1}^{\infty} D_{nm} \left[\frac{2}{\gamma_{nm} R} \frac{J_{n-1/2}(\gamma_{nm} R)}{R^{1/2}} - \frac{(n+1)(n+2) J_{n+1/2}(\gamma_{nm} R)}{\gamma_{nm}^2 R^2} \right] P_n(\mu) e^{-\gamma_{nm}^2 \tau^*}$$

$$+ \sum_{n=2}^{\infty} n(n-1) a_n R^{n-2} P_n(\mu) + \sum_{n=1}^{\infty} (n+1)[(n+1)(n+2) - 2\nu] b_n R^n P_n(\mu) \quad (4)$$

$$\bar{\sigma}_{\theta\theta} = -2 \sum_{n=0}^{\infty} \sum_{m=1}^{\infty} D_{nm} \left\{ \frac{J_{n-1/2}(\gamma_{nm} R)}{\gamma_{nm} R^{3/2}} P_n(\mu) + \left[\left(1 - \frac{n+1}{\gamma_{nm}^2 R^2}\right) P_n(\mu) - \frac{\mu}{\gamma_{nm}^2 R^2} P_n'(\mu) + \frac{1-\mu^2}{\gamma_{nm}^2 R^2} P_n''(\mu) \right] \times \frac{J_{n+1/2}(\gamma_{nm} R)}{R^{1/2}} \right\} e^{-\gamma_{nm}^2 \tau^*} + \sum_{n=2}^{\infty} a_n R^{n-2} [\mu P_n'(\mu) - n^2 P_n(\mu)] + \sum_{n=1}^{\infty} b_n R^n \{ (n+5-4\nu)\mu P_n'(\mu) - (n+1)[(n+1)^2 + 2(n+1) - 1 + 2\nu] P_n(\mu) \} \quad (5)$$

where $\bar{\sigma}_{ij} = \sigma_{ij}/[G(1+\nu)q_0 r_0 \alpha / K(1-\nu)]$ with G , ν , α , and K denoting, respectively, shear modulus, Poisson's ratio, coefficient of thermal expansion, and thermal conductivity, $R = r/r_0$, $\tau^* = \kappa t^* / r_0^2$, $P_n' = dP_n/d\mu$, $P_n'' = d^2P_n/d\mu^2$,

$$D_{nm} = \frac{(2n+1)\gamma_{nm}^2}{[\gamma_{nm}^2 - n(n+1) + B_i(B_i - 1)]J_{n+1/2}(\gamma_{nm})} \times \left[\int_{-1}^1 \int_0^1 \frac{T(r, \mu, t_H) - T_\infty}{q_0 r_0 / K} \frac{J_{n+1/2}(\frac{\gamma_{nm}r}{r_0})}{R^{1/2}} P_n(\mu) R^2 dR d\mu \right] \quad (6)$$

and

$$a_n = \frac{\eta_n [3n+2+2\nu-n^3+2\nu n] + \xi_n [2-(n+1)^2-2\nu]}{2(n-1)[n^2+n+1+\nu(2n+1)]}, \quad n=2, 3, \dots \quad (7)$$

$$b_n = \frac{\xi_n + n\eta_n}{2[n^2+n+1+\nu(2n+1)]}, \quad n=0, 1, 2, \dots \quad (8)$$

with

$$\xi_n(\tau^*) = -2 \sum_{m=1}^{\infty} D_{nm} [n(n+1) + B_i] \frac{J_{n+1/2}(\gamma_{nm})}{\gamma_{nm}^2} e^{-\gamma_{nm}^2 \tau^*} \quad (9)$$

$$\eta_n(\tau^*) = -2 \sum_{m=1}^{\infty} D_{nm} (1 + B_i) \frac{J_{n+1/2}(\gamma_{nm})}{\gamma_{nm}^2} e^{-\gamma_{nm}^2 \tau^*} \quad (10)$$

Results

To illustrate the results, Fig. 1 shows the computed tangential stress distributions $\sigma_{\theta\theta}$ for a 10 cm dia Sioux quartzite sphere heated under $q_0 = 0.95$ cal/cm²s over its hemispherical surface ($\theta_0 = 90$ deg) for 30 s and then cooled over its entire surface for 30 s. The properties of the Sioux quartzite used in the calculations are $G = 8.79 \times 10^5$ N/cm², $K = 1.3 \times 10^{-2}$ cal/cm-s-°C, $\alpha = 1.25 \times 10^{-5}$ °C⁻¹, $\kappa = 2.5 \times 10^{-2}$ cm²/s, and $\nu = 0.24$. An inspection of the figure reveals that tensile and compressive tangential stresses are induced, respectively, in the inner and outer region of the sphere during heating. The maximum tensile tangential stress is seen to have a magnitude of about 3000 N/cm² and to occur within about 2.7 cm from the spherical surface. The tensile strength of Sioux quartzite is about 2000 N/cm². The prescribed heating conditions will, therefore, provide the stress potential for fragmenting the rock specimen. In the subsequent cooling period, a stress reversal takes place in the outer layer of the sphere, giving tensile tangential stresses that are maximum at the surface and that progressively decrease in the interior of the sphere.

In the experiments, rock spheres of Sioux quartzite and Dresser basalt that are 10 cm in dia were insulated over the hemispherical surface and inserted in a radiative heat system controlled to transfer uniform heat flux into the spherical surface. The specimens

⁴ Numbers in brackets designate References at end of paper.

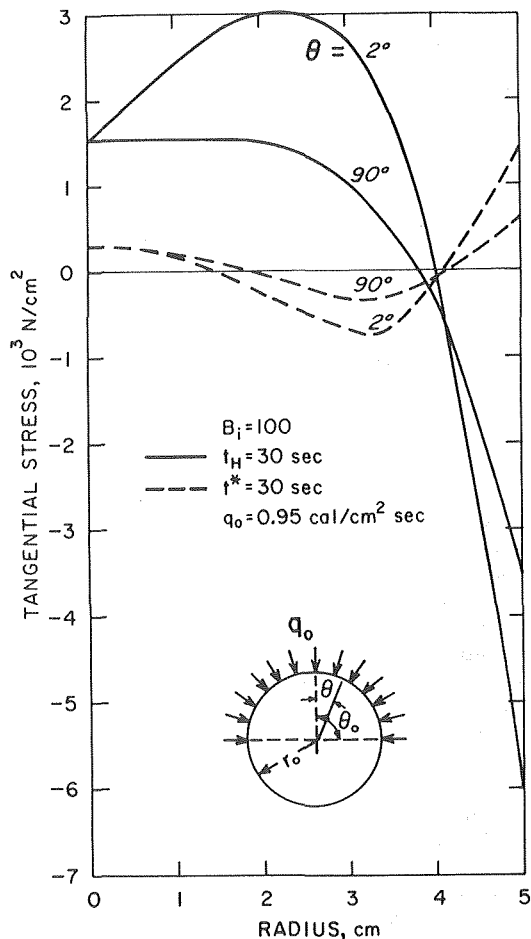


Fig. 1 Distribution of tangential stresses during partial heating and cooling of sioux quartzite

were heated over the exposed hemispherical surface at various constant fluxes until cracks were observed on the surfaces; the time periods for the crack occurrence were recorded. From these time periods, the corresponding maximum tensile tangential stresses were calculated. The results are presented in Fig. 2 with circles, and the analytically predicted maximum tensile tangential stresses versus time are illustrated with lines. It can be seen from the figure that the predicted tangential stresses in all cases exceed the tensile strength of the rock specimens and that the agreement between analysis and theory is very good. The locations of maximum tensile tangential stresses are the locations for crack initiation through the application of the tensile stress fracture criterion. The experimentally observed and analytically predicted locations of fracture initiation are shown in Fig. 3. The thickness of the broken pieces of rocks was found to be within 2–2.5 cm.

To examine the effect of cooling on fragmentation, spherical rock specimens that were insulated over the hemispherical surface were heated for short periods of time over the exposed surface such that complete fragmentation of the spheres did not take place during heating, and then were quenched with water. The results showed that cooling propagated fractures that were induced during heating in the interior of the sphere, but did not create new fractures at the specimen surface.

Concluding Remarks

The present analysis indicates that tensile stresses are induced in the interior of a sphere during heating and that subsequent cooling generates tensile tangential stresses at and close to the spherical surface. The internal tensile stress concentrations induced during heating create a potential for initiating fracture and

fragmentation. From the experiments, it was found that fracture and fragmentation are confined to the surface area exposed to heating.

Rocks are weak in tension. Fragmentation of rocks by tensile stresses represents an efficient approach to breaking rocks. It is concluded from the present study that tensile stresses exceeding the strength of rocks can be induced in the interior of rocks by localized surface heating that produces fracture and fragmentation. Cooling of heated rocks augments fracture propagation and fragmentation but does not significantly vary the fragmentation characteristics induced by heating. The tensile stress concentrations in

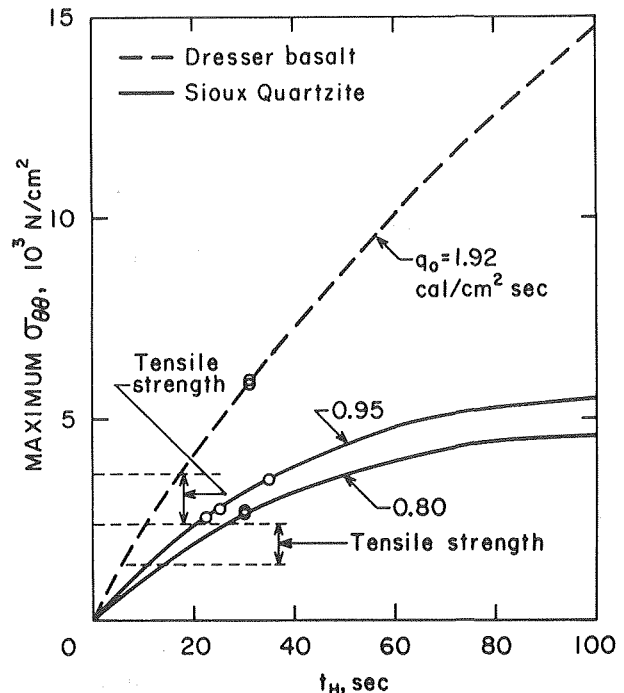


Fig. 2 Variation of maximum tensile tangential stress with heating time at $\theta = 2^\circ$

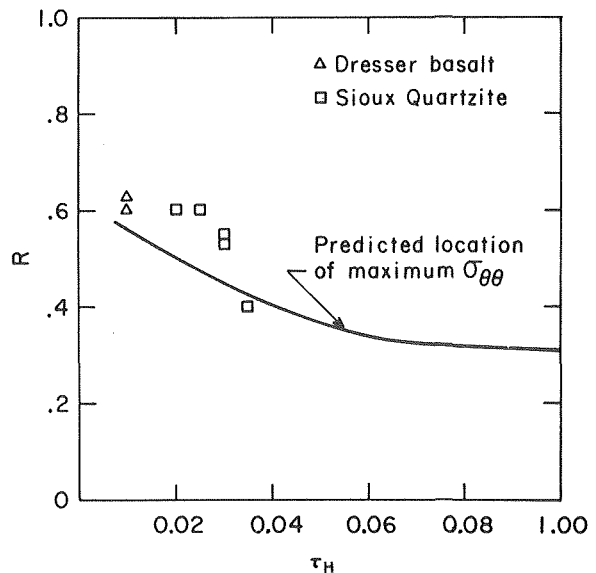


Fig. 3 Variation of location of maximum tensile tangential stress with heating time at $\theta = 2^\circ$

rock material flaws and microstructural cracks will play a dominant role in inducing fracture and fragmentation by heating and cooling.

Acknowledgments

This study was carried out by the Bureau of Mines in cooperation with the U. S. Army Mobility Equipment Research and Development Center (MERDC).

References

- 1 Thirumalai, K., "Potential of Internal Heating Method for Rock Fragmentation," *Proceedings of Twelfth Symposium on Rock Mechanics*, 1970, pp. 697-719.
- 2 Thirumalai, K., and Cheung, J. B., "A Study on a New Concept of Thermal Hard Rock Crushing," *Proceedings of Fourteenth Symposium on Rock Mechanics*, ASCE, 1972, pp. 527-554.
- 3 Cheung, J. B., Chen, T. S., and Thirumalai, K., "Transient Thermal Stresses in a Sphere by Local Heating," *Journal of Applied Mechanics*, TRANS. ASME (in press); see also ASME Paper No. 74-WA/APM-9.

Heating Time and Heating Temperature Dependence of Thermal Conductivity of As-Received Aluminum Alloy 2024-T351

S. Al-Araji¹ and J. V. Beck²

1 Introduction

When as-received aluminum alloy 2024-T351 is heated to 350°F (450°K), changes in the microstructure take place. These changes are further enhanced by heating to higher temperatures and/or for longer times. This heating results in increases in the room-temperature values of the thermal conductivity (k) of the alloy. These changes are functions of the heating temperature and also of the heating time because the microstructure changes with time. No data are known to be extant showing heating time as well as heating temperature variations of k for aluminum alloy 2024-T351. However, there are data in the literature concerning time at temperature effects on the properties of some materials [1, 2].³

This work is important for several reasons. First, the data for this particular alloy are needed for such applications as nuclear reactors, where this material, if used, might be exposed to a sudden heating condition. Next, the experimental procedure and the demonstration of a successful application of it is significant. Finally, there are many other materials which change during heating. These include biological products which dry and otherwise change during slow heating. The techniques mentioned in this study might also be applicable to such cases.

A simplified method proposed by Beck and Al-Araji [3] was used to determine the transient values of k .

2 Experiment

The specimen is made of aluminum alloy 2024-T351, which is composed of aluminum, 3.8-4.9 percent copper, 0.50 percent silicon, 0.50 percent iron, 0.3-0.9 percent manganese, 1.2-1.8 percent magnesium, 0.10 percent chromium, 0.25 percent zinc, and 0.15 percent others. It is solution heat-treated and stress-relieved.

¹Instructor (now with the Consumers Power Co.; Jackson, Mich.) Department of Mechanical Engineering, Michigan State University, E. Lansing, Mich.

²Professor, Department of Mechanical Engineering and Division of Engineering Research, Michigan State University, E. Lansing, Mich.

³Numbers in brackets designate References at end of technical brief.

Contributed by the Heat Transfer Division of THE AMERICAN SOCIETY OF MECHANICAL ENGINEERS. Manuscript received by the Heat Transfer Division June 28, 1974.

Because of the particular structure of the alloy, the experimental strategy was developed [4] to be as follows: (1) testing the specimen at room temperature, (2) heating the specimen to and holding it at the desired temperature, then performing the tests, and (3) cooling the specimen down to room temperature and testing it at that temperature. That is, the specimen is tested first at room temperature conditions to determine its thermal conductivity in the as-received state, then heated to the desired temperature and held at that temperature until it is over-aged. During this period the thermal conductivity of the specimen is determined at different intervals of time. The time intervals between tests are determined by the temperature level at which the specimen is held. The higher the temperature at which the specimen is maintained, the more rapidly the specimen reaches its over-aged condition.

3 Experimental Results

Twelve specimens were tested in the temperature range 375-425°F (464-491°K) to find the k values in that temperature range.

The thermal conductivity values obtained using this method of testing are compared with those compiled by the Thermophysical Properties Research Center (TPRC) [5] in Fig. 1.

It should be noted that the values given by TPRC are for aluminum alloy 2024-T4, the same alloy but with a different initial heat treatment designated by "T4," which indicates that the alloy had been solution heat-treated and naturally aged to a substantially stable condition. This difference in initial heat treatments might account for the difference between the TPRC values and the present results.

The lower dashed line in Fig. 1 depicts the initial values (zero-time) of k in the present study; zero-time values are given from room temperature (about 540°R or 300°K) to about 885°R or 491°K. The final values of k (over-aged values) found in the present study are depicted by the upper dashed line for the same temperature range. Note that Fig. 1 shows that the k value at room temperature for the over-aged condition is much higher than that in the as-received condition, while that for the temperature at 491°K is not.

Details of the time variation of the thermal conductivity k suggested by Fig. 1 are interesting. Just below 350°F (450°K) it takes several days for changes in the properties to occur. Below 300°F (422°K) it may take weeks or months; we did not investigate this range. The average k values for all specimens tested in the temperature range 375-425°F (464-491°K) are shown in Fig. 2. These values seem to exhibit a certain pattern. This pattern begins with the k value of the specimen when it is first brought to its nominal temperature; then k increases to some maximum value while the specimen is maintained at the nominal temperature. The rate of increase of the thermal conductivity depends on the temperature level, with the higher temperatures causing more rapid changes in

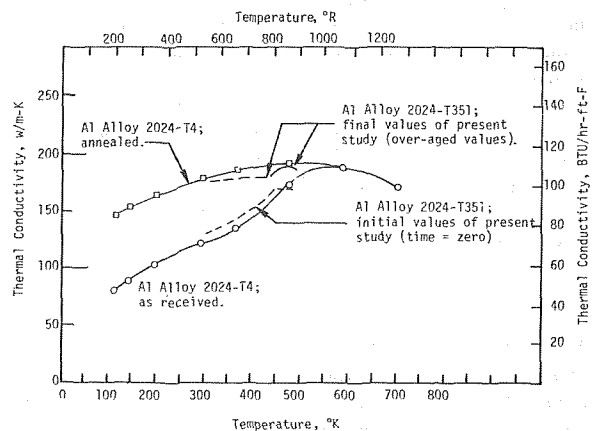


Fig. 1 Thermal conductivity of aluminum alloy 2024-T4 given by TPRC [5] and of aluminum alloy 2024-T351 of present study

rock material flaws and microstructural cracks will play a dominant role in inducing fracture and fragmentation by heating and cooling.

Acknowledgments

This study was carried out by the Bureau of Mines in cooperation with the U. S. Army Mobility Equipment Research and Development Center (MERDC).

References

- 1 Thirumalai, K., "Potential of Internal Heating Method for Rock Fragmentation," *Proceedings of Twelfth Symposium on Rock Mechanics*, 1970, pp. 697-719.
- 2 Thirumalai, K., and Cheung, J. B., "A Study on a New Concept of Thermal Hard Rock Crushing," *Proceedings of Fourteenth Symposium on Rock Mechanics*, ASCE, 1972, pp. 527-554.
- 3 Cheung, J. B., Chen, T. S., and Thirumalai, K., "Transient Thermal Stresses in a Sphere by Local Heating," *Journal of Applied Mechanics*, TRANS. ASME (in press); see also ASME Paper No. 74-WA/APM-9.

Heating Time and Heating Temperature Dependence of Thermal Conductivity of As-Received Aluminum Alloy 2024-T351

S. Al-Araji¹ and J. V. Beck²

1 Introduction

When as-received aluminum alloy 2024-T351 is heated to 350°F (450°K), changes in the microstructure take place. These changes are further enhanced by heating to higher temperatures and/or for longer times. This heating results in increases in the room-temperature values of the thermal conductivity (k) of the alloy. These changes are functions of the heating temperature and also of the heating time because the microstructure changes with time. No data are known to be extant showing heating time as well as heating temperature variations of k for aluminum alloy 2024-T351. However, there are data in the literature concerning time at temperature effects on the properties of some materials [1, 2].³

This work is important for several reasons. First, the data for this particular alloy are needed for such applications as nuclear reactors, where this material, if used, might be exposed to a sudden heating condition. Next, the experimental procedure and the demonstration of a successful application of it is significant. Finally, there are many other materials which change during heating. These include biological products which dry and otherwise change during slow heating. The techniques mentioned in this study might also be applicable to such cases.

A simplified method proposed by Beck and Al-Araji [3] was used to determine the transient values of k .

2 Experiment

The specimen is made of aluminum alloy 2024-T351, which is composed of aluminum, 3.8-4.9 percent copper, 0.50 percent silicon, 0.50 percent iron, 0.3-0.9 percent manganese, 1.2-1.8 percent magnesium, 0.10 percent chromium, 0.25 percent zinc, and 0.15 percent others. It is solution heat-treated and stress-relieved.

¹Instructor (now with the Consumers Power Co.; Jackson, Mich.) Department of Mechanical Engineering, Michigan State University, E. Lansing, Mich.

²Professor, Department of Mechanical Engineering and Division of Engineering Research, Michigan State University, E. Lansing, Mich.

³Numbers in brackets designate References at end of technical brief.

Contributed by the Heat Transfer Division of THE AMERICAN SOCIETY OF MECHANICAL ENGINEERS. Manuscript received by the Heat Transfer Division June 28, 1974.

Because of the particular structure of the alloy, the experimental strategy was developed [4] to be as follows: (1) testing the specimen at room temperature, (2) heating the specimen to and holding it at the desired temperature, then performing the tests, and (3) cooling the specimen down to room temperature and testing it at that temperature. That is, the specimen is tested first at room temperature conditions to determine its thermal conductivity in the as-received state, then heated to the desired temperature and held at that temperature until it is over-aged. During this period the thermal conductivity of the specimen is determined at different intervals of time. The time intervals between tests are determined by the temperature level at which the specimen is held. The higher the temperature at which the specimen is maintained, the more rapidly the specimen reaches its over-aged condition.

3 Experimental Results

Twelve specimens were tested in the temperature range 375-425°F (464-491°K) to find the k values in that temperature range.

The thermal conductivity values obtained using this method of testing are compared with those compiled by the Thermophysical Properties Research Center (TPRC) [5] in Fig. 1.

It should be noted that the values given by TPRC are for aluminum alloy 2024-T4, the same alloy but with a different initial heat treatment designated by "T4," which indicates that the alloy had been solution heat-treated and naturally aged to a substantially stable condition. This difference in initial heat treatments might account for the difference between the TPRC values and the present results.

The lower dashed line in Fig. 1 depicts the initial values (zero-time) of k in the present study; zero-time values are given from room temperature (about 540°R or 300°K) to about 885°R or 491°K. The final values of k (over-aged values) found in the present study are depicted by the upper dashed line for the same temperature range. Note that Fig. 1 shows that the k value at room temperature for the over-aged condition is much higher than that in the as-received condition, while that for the temperature at 491°K is not.

Details of the time variation of the thermal conductivity k suggested by Fig. 1 are interesting. Just below 350°F (450°K) it takes several days for changes in the properties to occur. Below 300°F (422°K) it may take weeks or months; we did not investigate this range. The average k values for all specimens tested in the temperature range 375-425°F (464-491°K) are shown in Fig. 2. These values seem to exhibit a certain pattern. This pattern begins with the k value of the specimen when it is first brought to its nominal temperature; then k increases to some maximum value while the specimen is maintained at the nominal temperature. The rate of increase of the thermal conductivity depends on the temperature level, with the higher temperatures causing more rapid changes in

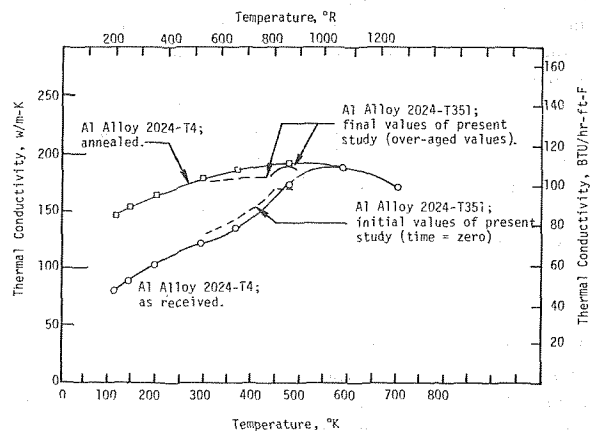


Fig. 1 Thermal conductivity of aluminum alloy 2024-T4 given by TPRC [5] and of aluminum alloy 2024-T351 of present study

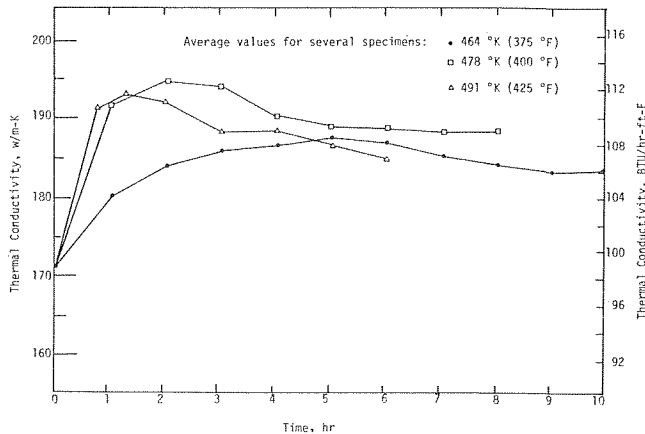


Fig. 2 Thermal conductivity as a function of heating time at 464, 478, and 491°K for aluminum alloy 2024-T351

k. The thermal conductivity dwells at its maximum value for a short time, after which it starts to drop until it reaches a constant value which is greater than the value when first brought to the nominal temperature. By this stage the specimen has become over-aged.

It was found that the over-aged value of thermal conductivity for aluminum alloy 2024-T351 at room temperature, as well as at

the high temperatures 375–425°F (464–491°K), is close to that obtained by the regular annealing process which tends to yield slightly higher values [4].

4 Conclusions

The changes of the thermal conductivity of aluminum alloy 2024-T351 due to heating of the specimen have been determined for the temperature range from 375° to 425°F (464–491°K). Such results have not previously been reported. In the alloy, precipitation is enhanced above 350°F (450°K) which causes changes in the properties with heating time.

Acknowledgment

This research was partially supported by the National Science Foundation under Grant No. GK-16526. The detailed comments of two referees are greatly appreciated.

References

- 1 Mizushima, S., "Rate of Graphitization of Carbon," *Proceedings of the Fifth Conference on Carbon*, Vol. 2, MacMillan, New York, 1963.
- 2 Strauss, H. E., "Thermal Conductivity of Carbon at High Temperature," *Ibid.*
- 3 Beck, J. V., and Al-Araji, S., "Investigation of a New Simple Transient Method of Thermal Property Measurement," *JOURNAL OF HEAT TRANSFER*, TRANS. ASME, Series C, Vol. 96, 1974, pp. 59–64.
- 4 Al-Araji, S. R., "Experimental Investigation of Transient Thermal Property Changes of Aluminum 2024-T351," PhD dissertation, Michigan State University, 1973.
- 5 Touloukian, Y. S., *Thermophysical Properties of High Temperature Solid Materials*, MacMillan, New York, 1967.

Discontinuities in Radiative Transfer Analysis Using Quadrature Formulas

K. C. Weston¹ and D. W. Drago²

Introduction

Errors incurred in the use of Gaussian Quadrature in solutions of the equation of radiative transfer for plane-parallel layers involving Fresnel reflection and transmission have been considered by several authors [1, 2].³ Reference [2] indicates that it is necessary to increase the order of quadrature to maintain a given accuracy when the index of refraction increases. A significant source of error in problems of this type involves the presence of a discontinuity in the intensity field at the critical angle for total internal reflection. A simple model of the discontinuity error is developed here. This model shows that the error for a given quadrature order is not necessarily a monotonic function of the index of refraction as the references imply. It is, in fact, possible to reduce errors under certain conditions by decreasing rather than by increasing quadrature order. It is thus shown that the discontinuity error can sometimes be greatly reduced by careful selection of the quadrature order. This can be significant to those with limited computer storage capacity.

Also considered is the proposal [1, 2, 3] that quadrature formulae should be applied separately in forward and backward hemi-

spheres because of the discontinuity in intensity at nonreflecting, bounding surfaces. The computational findings of reference [1], indicating that such errors were not observed, are clarified analytically here using the discontinuity model.

Fresnel Boundary Transmission Error

First, consider the calculation of the transmission of a uniformly diffuse, incident flux through a plane, Fresnel-reflecting surface bounding a transparent medium with a perfectly absorbing rear boundary. For a medium index of refraction $n_2 > 1.0$, rays transmitted across the boundary are compressed within the critical cone defined by the half angle $\theta_c = \arcsin(1/n_2)$. In this case no radiation is present in directions outside the critical cone. The integrated transmission of the Fresnel boundary is:

$$T = \frac{2}{I_{IN}} \int_0^1 \mu I(\mu) d\mu \quad (1)$$

where $\mu = \cos \theta$, I_{IN} is the directionally independent incident intensity and $I(\mu)$ is the intensity inside medium 2. Utilizing Gaussian Quadrature of order k , the transmission may be approximated by:

$$T' = \frac{2}{I_{IN}} \sum_{i=1}^k a_i \mu_i I_i \quad (2)$$

where the a_i are Gaussian weights.

The error, E , associated with the quadrature approximation may be defined as:

$$E = \frac{T - T'}{T} \quad (3)$$

The open symbols in Fig. 1 show the error in the Fresnel transmission as a function of the medium index of refraction for $k = 10$ and $k = 16$. Here the exact transmission T was determined as $1 - R$ from the integrated Fresnel reflectance values given in reference [4]. It is clear that the error for a given quadrature order vanishes for certain refractive indices but becomes quite large for other in-

¹ Assoc. Professor, University of Tulsa, Tulsa Okla. Mem. ASME.

² Research Assistant, University of Tulsa, Tulsa, Okla.

³ Numbers in brackets designate References at end of technical brief.

Contributed by the Heat Transfer Division of THE AMERICAN SOCIETY OF MECHANICAL ENGINEERS. Manuscript received by the Heat Transfer Division May 6, 1974.

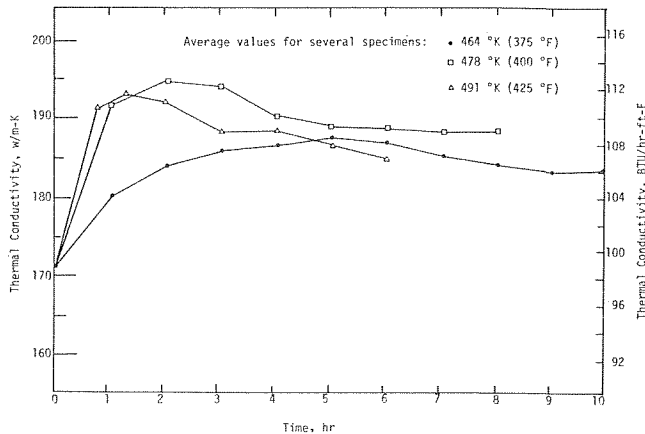


Fig. 2 Thermal conductivity as a function of heating time at 464, 478, and 491°K for aluminum alloy 2024-T351

k. The thermal conductivity dwells at its maximum value for a short time, after which it starts to drop until it reaches a constant value which is greater than the value when first brought to the nominal temperature. By this stage the specimen has become over-aged.

It was found that the over-aged value of thermal conductivity for aluminum alloy 2024-T351 at room temperature, as well as at

the high temperatures 375–425°F (464–491°K), is close to that obtained by the regular annealing process which tends to yield slightly higher values [4].

4 Conclusions

The changes of the thermal conductivity of aluminum alloy 2024-T351 due to heating of the specimen have been determined for the temperature range from 375° to 425°F (464–491°K). Such results have not previously been reported. In the alloy, precipitation is enhanced above 350°F (450°K) which causes changes in the properties with heating time.

Acknowledgment

This research was partially supported by the National Science Foundation under Grant No. GK-16526. The detailed comments of two referees are greatly appreciated.

References

- 1 Mizushima, S., "Rate of Graphitization of Carbon," *Proceedings of the Fifth Conference on Carbon*, Vol. 2, MacMillan, New York, 1963.
- 2 Strauss, H. E., "Thermal Conductivity of Carbon at High Temperature," *Ibid.*
- 3 Beck, J. V., and Al-Araji, S., "Investigation of a New Simple Transient Method of Thermal Property Measurement," *JOURNAL OF HEAT TRANSFER*, TRANS. ASME, Series C, Vol. 96, 1974, pp. 59–64.
- 4 Al-Araji, S. R., "Experimental Investigation of Transient Thermal Property Changes of Aluminum 2024-T351," PhD dissertation, Michigan State University, 1973.
- 5 Touloukian, Y. S., *Thermophysical Properties of High Temperature Solid Materials*, MacMillan, New York, 1967.

Discontinuities in Radiative Transfer Analysis Using Quadrature Formulas

K. C. Weston¹ and D. W. Drago²

Introduction

Errors incurred in the use of Gaussian Quadrature in solutions of the equation of radiative transfer for plane-parallel layers involving Fresnel reflection and transmission have been considered by several authors [1, 2].³ Reference [2] indicates that it is necessary to increase the order of quadrature to maintain a given accuracy when the index of refraction increases. A significant source of error in problems of this type involves the presence of a discontinuity in the intensity field at the critical angle for total internal reflection. A simple model of the discontinuity error is developed here. This model shows that the error for a given quadrature order is not necessarily a monotonic function of the index of refraction as the references imply. It is, in fact, possible to reduce errors under certain conditions by decreasing rather than by increasing quadrature order. It is thus shown that the discontinuity error can sometimes be greatly reduced by careful selection of the quadrature order. This can be significant to those with limited computer storage capacity.

Also considered is the proposal [1, 2, 3] that quadrature formulae should be applied separately in forward and backward hemi-

spheres because of the discontinuity in intensity at nonreflecting, bounding surfaces. The computational findings of reference [1], indicating that such errors were not observed, are clarified analytically here using the discontinuity model.

Fresnel Boundary Transmission Error

First, consider the calculation of the transmission of a uniformly diffuse, incident flux through a plane, Fresnel-reflecting surface bounding a transparent medium with a perfectly absorbing rear boundary. For a medium index of refraction $n_2 > 1.0$, rays transmitted across the boundary are compressed within the critical cone defined by the half angle $\theta_c = \arcsin(1/n_2)$. In this case no radiation is present in directions outside the critical cone. The integrated transmission of the Fresnel boundary is:

$$T = \frac{2}{I_{IN}} \int_0^1 \mu I(\mu) d\mu \quad (1)$$

where $\mu = \cos \theta$, I_{IN} is the directionally independent incident intensity and $I(\mu)$ is the intensity inside medium 2. Utilizing Gaussian Quadrature of order k , the transmission may be approximated by:

$$T' = \frac{2}{I_{IN}} \sum_{i=1}^k a_i \mu_i I_i \quad (2)$$

where the a_i are Gaussian weights.

The error, E , associated with the quadrature approximation may be defined as:

$$E = \frac{T - T'}{T} \quad (3)$$

The open symbols in Fig. 1 show the error in the Fresnel transmission as a function of the medium index of refraction for $k = 10$ and $k = 16$. Here the exact transmission T was determined as $1 - R$ from the integrated Fresnel reflectance values given in reference [4]. It is clear that the error for a given quadrature order vanishes for certain refractive indices but becomes quite large for other in-

¹ Assoc. Professor, University of Tulsa, Tulsa Okla. Mem. ASME.

² Research Assistant, University of Tulsa, Tulsa, Okla.

³ Numbers in brackets designate References at end of technical brief.

Contributed by the Heat Transfer Division of THE AMERICAN SOCIETY OF MECHANICAL ENGINEERS. Manuscript received by the Heat Transfer Division May 6, 1974.

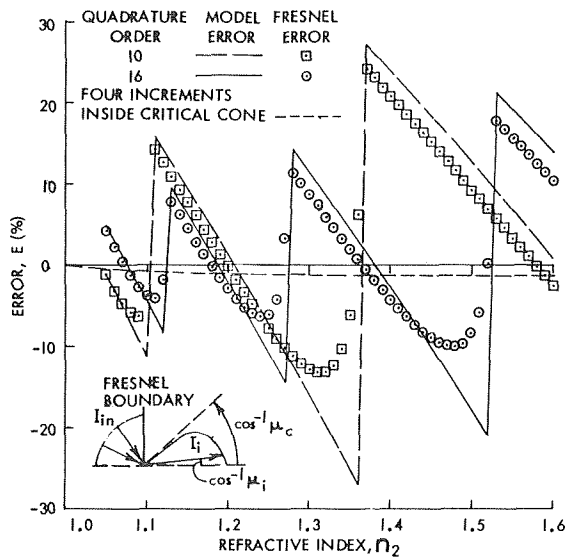


Fig. 1 Error in transmission of a plane, fresnel surface bounding a transparent medium—no rear surface reflection or emission

intermediate values. The greatest part of this error may be shown to be due to the location of the quadrature points relative to the location of the discontinuity at the critical angle by considering the following simple analytical model.

Consider the error in T associated with the discontinuity model given by:

$$I(\mu) = \begin{cases} I_t & \mu_c < \mu \leq 1.0 \\ I_0 & 0 \leq \mu < \mu_c \end{cases} \quad (4)$$

where I_t and I_0 are constants and $\mu_c = \cos \theta_c$. Applying equations (1)–(3) to the model (4) yields the error equation:

$$E = 1 - 2 \frac{\sum_{i=1}^{k_t} a_i \mu_i + \frac{T_0}{I_t} \sum_{i=k_t+1}^{k/2} a_i \mu_i}{1 - (\mu_c)^2 (1 - \frac{I_0}{I_t})} \quad (5)$$

where k_t corresponds to the last Gaussian direction within the critical cone. The approximate error function given by equation (5) for $I_0/I_t = 0$ is compared in Fig. 1 with the exact Fresnel transmission error discussed in the foregoing. It is seen that the simple discontinuity model provides a good indication of the regions in which the error in the Fresnel transmission is large and shows that the total error is dominated by the discontinuity error.

Scattering Integral Error

We now consider the application of a similar discontinuity model to the estimation of the error in the Gaussian approximation of the isotropic scattering integral in the equation of radiative transfer:

$$\mu \frac{dI}{d\tau} = -I + \frac{\omega}{2} \int_{-1}^1 Id\mu \quad (6)$$

where ω is the albedo and τ is the optical depth.

The error in the approximation $\sum_{i=1}^{k_t} a_i I_i$ of the scattering integral in equation (6) may be estimated by using a discontinuity model, analogous to equation (4), given by:

$$I(\mu) = \begin{cases} I_t & \mu_c < \mu \leq 1.0 \\ I_0 & -1 \leq \mu < \mu_c \end{cases} \quad (7)$$

The model is expected to yield a good approximation for media of small and moderate optical thickness and for a nonreflecting rear boundary. The resulting error estimate E_s for the scattering integral is given by:

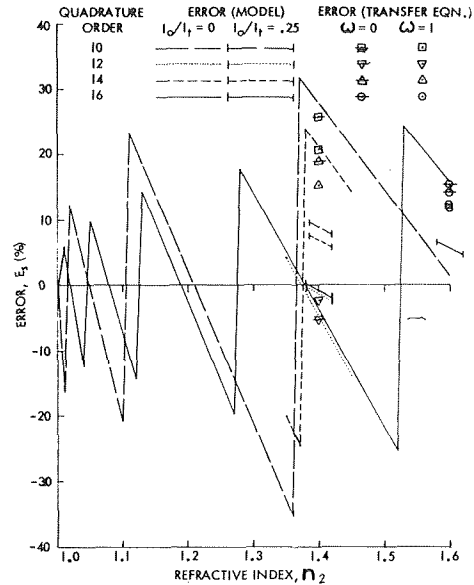


Fig. 2 Error in isotropic scattering integral—no rear surface reflection or emission

$$E_s = 1 - \frac{\sum_{i=1}^{k_t} a_i I_i}{\int_{-1}^1 Id\mu} = 1 - \frac{\sum_{i=1}^{k_t} a_i + \frac{I_0}{I_t} [2 - \sum_{i=1}^{k_t} a_i]}{1 - \mu_c + \frac{I_0}{I_t} (1 + \mu_c)} \quad (8)$$

It is evident that the error given by equation (8) vanishes for a uniform intensity field given by $I_0/I_t = 1.0$. The error in the scattering integral, as predicted by equation (8) for $I_0/I_t = 0$, is shown in Fig. 2 for refractive indices up to 1.6 for $k = 10$ and $k = 16$. It is seen that for $n_2 = 1.4$ an error of over 25 percent is anticipated in the scattering integral for tenth order quadrature, while about 3 percent error is expected using sixteenth order quadrature. For $n_2 = 1.6$, however, the situation is reversed—a significantly smaller error is expected for tenth order quadrature than for sixteenth.

Errors determined from iterative solutions of the transfer equation utilizing Gaussian Quadrature for an absorbing, nonscattering medium of unit optical thickness are compared in Fig. 2 with the model estimates from equation (8) for a refractive index of 1.4 and a location immediately inside the Fresnel boundary. Here the transfer equation errors for $k = 10, 12,$ and 14 are referenced to a value of the integral determined by applying the small discontinuity model error estimate for sixteenth order quadrature from Fig. 2 to the sixteenth order transfer equation solution quadrature as follows:

$$\int_{-1}^1 Id\mu = \frac{1}{1 - (E_s)_{16}} \sum_{i=1}^{16} a_i I_i \quad (9)$$

It is seen that equation (8) well approximates the transfer equation errors for a nonscattering medium with $n_2 = 1.4$. Similar results for $n_2 = 1.6$, where the tenth order transfer equation solution quadrature (corrected using the tenth order estimate as discussed in the foregoing) was taken as reference, are also shown in Fig. 2. Two symbols are employed to show the range of the error between front and rear surfaces. Again a good approximation is evident. The differences between the transfer equation and model errors, of course, may be attributed to the nonuniformity of the radiation in the critical cone due to the Fresnel transmission of the boundary and the small errors in the corrections.

It is of greater interest to examine the influence of the discontinuity error in a case in which scattering is important. Fig. 8 of reference [5], for instance, presents an intensity distribution for an isotropically scattering medium for $n_2 = 1.4$ and unit optical thickness using tenth order quadrature. This computation is compared in Fig. 3 with similar computations for $k = 10, 12, 14,$ and 16

performed by the authors. Agreement of both results for $k = 10$ indicates that the black paint boundary condition of reference [5] is well approximated using a uniform specular reflectance of 0.03. Significant differences are apparent however in the intensity distributions for the several quadrature orders. These differences clearly correlate with the discontinuity model calculations for $I_0/I_t = 0$ presented in Fig. 2. For the more reasonable value of $I_0/I_t = 0.25$, the relative positions are also as expected but the estimated errors are substantially reduced.

The errors in the intensity integral for $k = 10, 12$ and 14 for the front surface distributions of Fig. 3 are also shown in Fig. 2. Again the sixteenth order value corrected by the discontinuity error estimate was used to provide a reference value as in the nonscattering case discussed in the foregoing. Fig. 2 shows that the discontinuity model for $I_0/I_t = 0.25$ significantly underestimates the errors in the transfer equation solution quadratures. Recognizing that the areas under the intensity distributions of Fig. 3 represent the values of the integrals in question, the differences between the curves for $-1 \leq \mu \leq \mu_c$ indicates errors which are distinct from the discontinuity errors approximated by equation (8). These differences arise primarily from feedback of the discontinuity error through the iteration of the transfer equation. The initial discontinuity error in the scattering integral approximation introduces errors in the intensities through the transfer equation (6) which upon application of the quadrature formula produces further error in the scattering integral. This error accumulation evidently is a convergent process which produces a significantly greater total error than the discontinuity error alone. This is exemplified by the differences between the discontinuity model calculations for $I_0/I_t = 0.25$ and the transfer equation values with scattering shown in Fig. 2. For the nonscattering case the feedback loop is obviously absent, thus accounting for the successful estimation of that error using the idealized model.

Error For Discontinuity at $\mu = 0$

It has been demonstrated that the presence of a discontinuity in a radiation field at the critical angle can introduce significant error in quadrature calculations. Let us now consider the proposal [1, 2, 3] that special treatment may be desirable in dealing with discontinuities in the field in directions parallel to the boundaries ($\mu = 0$). The discontinuity model (7) may be applied to this case if $\mu_c = 0$, I_t and I_0 are interpreted as arbitrary directionally-independent intensities in the forward and rearward hemispheres, respectively, and k_t is taken as $k/2$. Since $\sum_{i=1}^{k/2} a_i = 1.0$, equation (8) shows that the error for such a discontinuity is identically zero regardless of the values of I_t and I_0 . Because the discontinuity at $\mu = 0$ gen-

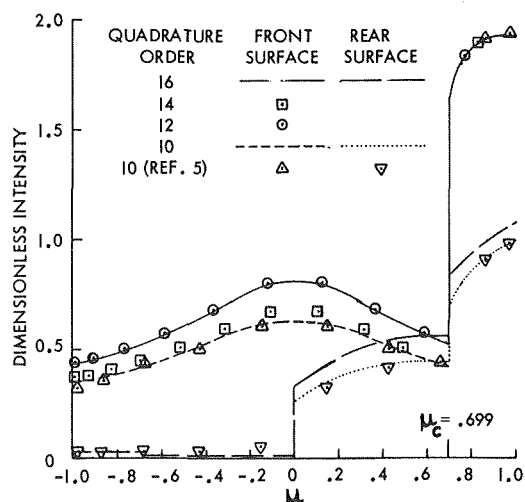


Fig. 3 Intensity distribution for diffuse incident flux— $\tau_0 = 1.0$, $\omega = 1.0$, $n_2 = 1.4$, no emission

erates no error, any improvement achieved through the use of separate quadratures in the half-intervals (as discussed in [1, 2]) accrues from an improved approximation of the integrals of the separate continuous distributions. Intensity functions which vary rapidly near $\mu = 0$, in some cases, may be better represented by utilizing separate quadratures due to the placement of quadrature points closer to $\mu = 0$. For sufficiently high quadrature order or for sufficiently slow intensity variation near $\mu = 0$ no improvement in accuracy using separate quadratures is to be expected. This evidently was the case for the calculations of references [1, 2].

Discontinuity Error Avoidance

While separate Gaussian quadratures may not be needed to cope with intensity variations near $\mu = 0$, it does seem constructive to suggest the use of separate quadratures on either side of the critical angle for total internal reflection. An example of the error reduction obtainable with only a crude approximation is shown in Fig. 1. There the small error (less than 1.4 percent for $n_2 \leq 1.6$) in the transmission of the Fresnel boundary computed by approximating the integral in equation (1) using four equal increments in μ within the critical angle shows clearly the advantage of discontinuity error avoidance. More sophisticated quadrature formulae and higher quadrature orders may of course be used to reduce the error further.

Acknowledgments

The authors wish to acknowledge helpful discussions with Dr. Albert C. Reynolds, Jr., of the Department of Mathematics of the University of Tulsa. Support of this work under NASA Grant NGR 37-008-003 is also gratefully acknowledged.

References

- Hottel, H. C., Sarofim, A. F., Evans, L. B., and Vasalos, I. A. "Radiative Transfer in Anisotropically Scattering Media: Allowance for Fresnel Reflection at the Boundaries," JOURNAL OF HEAT TRANSFER, TRANS. ASME, Series C, Vol. 96, Feb. 1968, pp. 56-62.
- Roux, J. A., and Smith, A. M. "Comparison of Three Techniques for Solving the Radiative Transport Equation," AIAA Paper No. 73-751, July 1973.
- Sykes, J. B. "Approximate Integration of Equation of Transfer," Monthly Notes, Royal Astronomical Society, Vol. III, 1951.
- Judd, Deane B. "Fresnel Reflection of Diffusely Incident Light," Journal of Research, National Bureau of Standards, Vol. 29, Nov. 1942, pp. 329-332.
- Roux, J. A., Smith, A. M., and Shahrokhi, F., "Effect of Boundary Conditions On the Radiative Reflectance of Dielectric Coatings," AIAA Paper No. 73-148, Jan. 1973.

Effect of Radiative Cooling on the Temperature Distribution in MHD Channel Flows

D. R. Wilson¹ and A. Haji-Sheikh²

Nomenclature

- a = channel half-width
 B_z = magnetic field intensity

¹ Aerospace Engineering Department, The University of Texas at Arlington, Arlington, Texas.

² Mechanical Engineering Department, The University of Texas at Arlington, Arlington, Texas.

Contributed by the Heat Transfer Division of THE AMERICAN SOCIETY OF MECHANICAL ENGINEERS. Manuscript received by the Heat Transfer Division March 1, 1974.

performed by the authors. Agreement of both results for $k = 10$ indicates that the black paint boundary condition of reference [5] is well approximated using a uniform specular reflectance of 0.03. Significant differences are apparent however in the intensity distributions for the several quadrature orders. These differences clearly correlate with the discontinuity model calculations for $I_0/I_t = 0$ presented in Fig. 2. For the more reasonable value of $I_0/I_t = 0.25$, the relative positions are also as expected but the estimated errors are substantially reduced.

The errors in the intensity integral for $k = 10, 12$ and 14 for the front surface distributions of Fig. 3 are also shown in Fig. 2. Again the sixteenth order value corrected by the discontinuity error estimate was used to provide a reference value as in the nonscattering case discussed in the foregoing. Fig. 2 shows that the discontinuity model for $I_0/I_t = 0.25$ significantly underestimates the errors in the transfer equation solution quadratures. Recognizing that the areas under the intensity distributions of Fig. 3 represent the values of the integrals in question, the differences between the curves for $-1 \leq \mu \leq \mu_c$ indicates errors which are distinct from the discontinuity errors approximated by equation (8). These differences arise primarily from feedback of the discontinuity error through the iteration of the transfer equation. The initial discontinuity error in the scattering integral approximation introduces errors in the intensities through the transfer equation (6) which upon application of the quadrature formula produces further error in the scattering integral. This error accumulation evidently is a convergent process which produces a significantly greater total error than the discontinuity error alone. This is exemplified by the differences between the discontinuity model calculations for $I_0/I_t = 0.25$ and the transfer equation values with scattering shown in Fig. 2. For the nonscattering case the feedback loop is obviously absent, thus accounting for the successful estimation of that error using the idealized model.

Error For Discontinuity at $\mu = 0$

It has been demonstrated that the presence of a discontinuity in a radiation field at the critical angle can introduce significant error in quadrature calculations. Let us now consider the proposal [1, 2, 3] that special treatment may be desirable in dealing with discontinuities in the field in directions parallel to the boundaries ($\mu = 0$). The discontinuity model (7) may be applied to this case if $\mu_c = 0$, I_t and I_0 are interpreted as arbitrary directionally-independent intensities in the forward and rearward hemispheres, respectively, and k_t is taken as $k/2$. Since $\sum_{i=1}^{k/2} a_i = 1.0$, equation (8) shows that the error for such a discontinuity is identically zero regardless of the values of I_t and I_0 . Because the discontinuity at $\mu = 0$ gen-

erates no error, any improvement achieved through the use of separate quadratures in the half-intervals (as discussed in [1, 2]) accrues from an improved approximation of the integrals of the separate continuous distributions. Intensity functions which vary rapidly near $\mu = 0$, in some cases, may be better represented by utilizing separate quadratures due to the placement of quadrature points closer to $\mu = 0$. For sufficiently high quadrature order or for sufficiently slow intensity variation near $\mu = 0$ no improvement in accuracy using separate quadratures is to be expected. This evidently was the case for the calculations of references [1, 2].

Discontinuity Error Avoidance

While separate Gaussian quadratures may not be needed to cope with intensity variations near $\mu = 0$, it does seem constructive to suggest the use of separate quadratures on either side of the critical angle for total internal reflection. An example of the error reduction obtainable with only a crude approximation is shown in Fig. 1. There the small error (less than 1.4 percent for $n_2 \leq 1.6$) in the transmission of the Fresnel boundary computed by approximating the integral in equation (1) using four equal increments in μ within the critical angle shows clearly the advantage of discontinuity error avoidance. More sophisticated quadrature formulae and higher quadrature orders may of course be used to reduce the error further.

Acknowledgments

The authors wish to acknowledge helpful discussions with Dr. Albert C. Reynolds, Jr., of the Department of Mathematics of the University of Tulsa. Support of this work under NASA Grant NGR 37-008-003 is also gratefully acknowledged.

References

- Hottel, H. C., Sarofim, A. F., Evans, L. B., and Vasalos, I. A. "Radiative Transfer in Anisotropically Scattering Media: Allowance for Fresnel Reflection at the Boundaries," JOURNAL OF HEAT TRANSFER, TRANS. ASME, Series C, Vol. 96, Feb. 1968, pp. 56-62.
- Roux, J. A., and Smith, A. M. "Comparison of Three Techniques for Solving the Radiative Transport Equation," AIAA Paper No. 73-751, July 1973.
- Sykes, J. B. "Approximate Integration of Equation of Transfer," Monthly Notes, Royal Astronomical Society, Vol. III, 1951.
- Judd, Deane B. "Fresnel Reflection of Diffusely Incident Light," Journal of Research, National Bureau of Standards, Vol. 29, Nov. 1942, pp. 329-332.
- Roux, J. A., Smith, A. M., and Shahrokhi, F., "Effect of Boundary Conditions On the Radiative Reflectance of Dielectric Coatings," AIAA Paper No. 73-148, Jan. 1973.

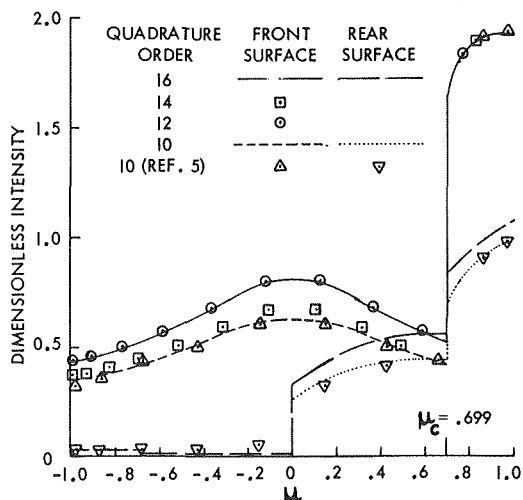


Fig. 3 Intensity distribution for diffuse incident flux— $\tau_0 = 1.0$, $\omega = 1.0$, $n_2 = 1.4$, no emission

Effect of Radiative Cooling on the Temperature Distribution in MHD Channel Flows

D. R. Wilson¹ and A. Haji-Sheikh²

Nomenclature

- a = channel half-width
 B_z = magnetic field intensity

¹ Aerospace Engineering Department, The University of Texas at Arlington, Arlington, Texas.

² Mechanical Engineering Department, The University of Texas at Arlington, Arlington, Texas.

Contributed by the Heat Transfer Division of THE AMERICAN SOCIETY OF MECHANICAL ENGINEERS. Manuscript received by the Heat Transfer Division March 1, 1974.

E_y = electric field intensity
 Ec = Eckert number, $\bar{u}^2/C_v T_w$
 Ha = Hartmann number, $aB_z\sqrt{\sigma/\mu}$
 J_y = dimensionless current density, $j_y/\bar{\sigma}\bar{u}\bar{B}_z$
 K = load factor, $E_y/\bar{u}\bar{B}_z$
 k = thermal conductivity
 N_R = radiation parameter, $a^2\alpha\sigma_R T_w^4/\mu\bar{u}$
 Pr = Prandtl number, $\mu C_v/k$
 \dot{q}_R = radiation heat transfer rate per unit area
 Re = Reynolds number, $\rho\bar{u}a/\mu$
 T = temperature
 u = velocity
 Z = dimensionless z -coordinate, z/a
 α = absorption coefficient
 θ = dimensionless temperature parameter, $(T - T_w)/(\bar{u}^2/C_v)$
 μ = viscosity coefficient
 σ = electrical conductivity
 σ_R = Stefan-Boltzmann constant
 τ = optical coordinate
 ϕ = temperature ratio, T/T_w

Introduction

In the analysis of the flow through MHD generators and accelerators, the effect of radiative cooling on the temperature distribution has generally been neglected. The recent trend toward the development of MHD channels operating at higher temperature levels, and involving the use of seeded plasmas with significant radiative characteristics, could possibly lead to a situation in which radiative cooling might exert a significant effect on the temperature profile. In view of the sensitive temperature dependence of the electrical conductivity of seeded gases, variations in the temperature profile produced by radiative cooling could lead to substantial variations in the electrical conductivity, with an attendant effect on the electrical performance of the MHD channel.

In order to provide a preliminary estimate of the possible magnitude of the effect of radiative cooling on the performance of MHD channels, the following simplified analysis is presented.

Analytical Model

In order to simplify the analysis, the channel flow was considered to be a fully-developed, laminar, incompressible flow between infinite parallel plates (see Fig. 1). The magnetic Reynolds number was assumed to be small, thereby neglecting the flow-induced perturbations on the applied magnetic field, Hall effects were neglected, and the electrical conductivity was assumed constant. Furthermore, a constant wall temperature was assumed, and the axial convection term, $\rho u C_v \partial T/\partial x$, was neglected in comparison to the conduction, radiation, viscous dissipation, and MHD terms in the energy equation. With these assumptions, the momentum and energy equations for MHD channel flow reduce to (reference [1])¹

$$-\frac{dp}{dx} + \mu \frac{d^2 u}{dz^2} + j_y B_z = 0 \quad (1)$$

and

$$\mu \left(\frac{du}{dz} \right) + k \frac{\partial^2 T}{\partial z^2} - \frac{\partial \dot{q}_R}{\partial z} + \frac{j_y^2}{\sigma} = 0 \quad (2)$$

For a nonradiating fluid ($\partial \dot{q}_R/\partial z = 0$), these equations can be integrated directly to obtain the classical Hartmann flow velocity and temperature profiles for MHD channel flow (reference [1]).

Several of these assumptions are somewhat unrealistic for practical application to MHD channel flows. For example, many practical MHD devices operate in the entrance region where the axial convection term is likely to be important. The convection term was neglected in this case, however, to provide a direct assessment of the effect of radiative cooling on the temperature distribution.

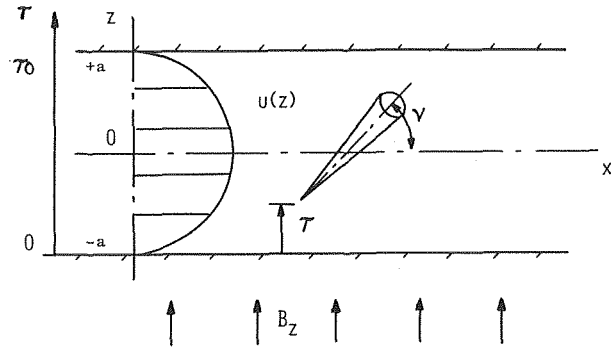


Fig. 1 Geometry employed for radiation cooling analysis

This was most conveniently accomplished by extending the classical Hartmann solution of reference [1], which was also based on a neglect of the convection term, to include the radiative transport term. Perhaps more critical is the assumption of an incompressible flow with constant electrical conductivity, since this removes the coupling between the energy and momentum equations that is likely to be of major importance for radiating MHD channel flows. It was felt, however, that before attempting the difficult solution of the coupled flow problem, a solution to the simpler uncoupled flow problem would be useful in determining whether the effect of radiative cooling was likely to be significant or not.

In order to simplify the estimate of the effect of radiation cooling on the temperature distribution, the fluid was assumed to be a nonscattering, grey fluid and the walls were assumed to be black surfaces. For these assumptions, the radiation term in equation (2) can be written as (reference [2])

$$\frac{\partial \dot{q}_R}{\partial z} = \alpha a \left[-2\sigma_R T_w^4 E_2(\tau) - 2\sigma_R T_w^4 E_2(\tau_0 - \tau) - 2\sigma_R \int_0^{\tau_0} T^4(t) E_1(|\tau - t|) dt + 4\sigma_R T^4(\tau) \right] \quad (3)$$

where

$$E_n(t) = \int_0^1 (\cos \nu)^{n-2} e^{-t/\cos \nu} d(\cos \nu) \quad (4)$$

are the exponential integral functions, and

$$\tau = \int_0^z \alpha dz \quad (5)$$

is the optical thickness. By substituting equation (3) into (2) and introducing the temperature ratio ϕ

$$\phi = \frac{T}{T_w} = \frac{\bar{u}^2}{C_v T_w} \theta + 1 = Ec_w \theta + 1 \quad (6)$$

together with appropriate dimensionless variables, one can obtain

$$\frac{d^2 \phi}{dz^2} = -PrEc_w \left[\left(\frac{dU}{dz} \right)^2 + Ha^2 J_y^2 \right] - 2PrN_R Ec_w \left[E_2(\tau) + E_2(\tau_0 - \tau) + \int_0^{\tau_0} \phi^4(t) E_1(|\tau - t|) dt - 2\phi^4(\tau) \right] \quad (7)$$

Equation (7) is a second-order, nonlinear, integro-differential equation whose solution gives the temperature distribution in the channel.

The solution of equation (7) was achieved by making a finite difference approximation for the second derivative term on the left-hand side, and replacing the exponential integral functions by the exponential kernel functions (reference [2]). This allows equation (7) to be replaced by a set of nonlinear integral equations that were solved by an iterative process employing the Hartmann solution of reference [1] for the initial estimate of the temperature profile. The procedure is described in detail in reference [3].

Typical Results

The results of some calculations are presented in Figs. 2 and 3. The conditions represent a MHD accelerator ($K = 2$) with a center

¹ Numbers in brackets designate References at end of technical brief.

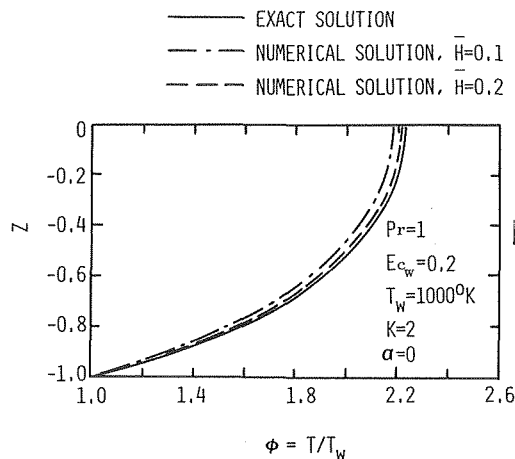


Fig. 2 Nonradiating solution, comparison of numerical solution for $\bar{H} = 0.1$ and 0.2 with exact solution

line-to-wall temperature ratio slightly greater than 2. The results presented in Fig. 2 are for a nonradiating solution ($\alpha = 0$) and are presented to indicate the accuracy of the finite-difference method for two different step sizes. Although it is recognized that the accuracy of the finite difference solution for the linear nonradiating solution does not guarantee a similar accuracy for the nonlinear radiating solution, the results of solutions based on different step sizes and different initial temperature profiles indicate that the convergence of the iterative procedure for the nonlinear solution is similar to that shown in Fig. 2.

The results of calculations for different values of the mean absorption coefficient α are presented in Fig. 3. These results indicate that a significant cooling effect is possible, as indicated by the reduction of the temperature near the center of the channel, for large values of α . This is in apparent contradiction to the results of Viscanta presented in reference [2], where the effect of radiation on the temperature profile is shown to be small for $\tau_0 \ll 1$. There are several important differences between Viscanta's results and the results of Fig. 3 however. Viscanta included the axial convection term, with the result that the radiative term is balanced by convective transport as well as conduction and viscous dissipation. In our model, the convective transport term is omitted, and as a consequence, the radiative transport of heat must be balanced against the conduction, viscous dissipation, and the MHD dissipation terms. Moreover, Viscanta's results are based on a constant value of T_w/T_c , which means that the profiles shown are not at the same axial position in the channel. Our results, without convec-

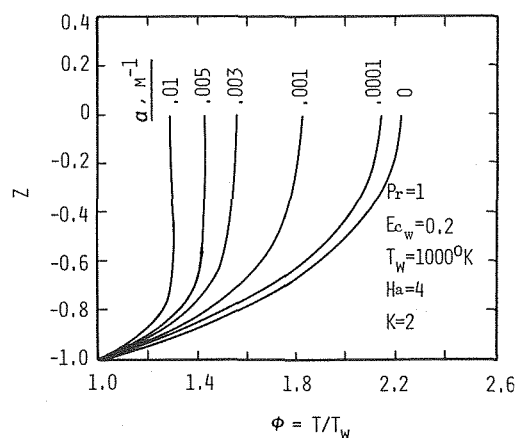


Fig. 3 Effect of mean absorption coefficient on temperature distribution in an MHD channel flow

tion, are presented at a fixed axial location, and consequently the effect of radiative cooling is more pronounced.

Concluding Remarks

The lower values of α ($\alpha \sim 0.0001/\text{m}$) are thought to be representative of conditions typically encountered in MHD channels employing seeded noble gases. For these devices, the effect of radiative cooling does not appear to be of major significance. However, MHD channels employing certain seeded combustion gas mixtures are likely to encounter higher values of the effective absorption coefficient. For these devices, the results of Fig. 3 indicate that the effect of radiative cooling could be significant, particularly when the coupling between the energy and momentum equation resulting from a consideration of the temperature dependency of the electrical conductivity is considered.

As a result, an extension of the present study to include the effects of axial convection, compressibility, and the temperature dependence of the electrical conductivity appears to be well-justified.

References

- 1 Sutton, G. W., and Sherman, A., *Engineering Magnetohydrodynamics*, McGraw-Hill, New York, 1965.
- 2 Sparrow, E. M., and Cess, R. D., *Radiation Heat Transfer*, Brooks/Cole Publishing Co., Belmont, Calif., 1966.
- 3 Wilson, Donald R., "Analysis of MHD Channel Flows by a Coupled Core Flow-Boundary Layer Model," PhD dissertation, The University of Texas at Arlington, Dec. 1973.

Flame Spread Over Thin Solid Fuels¹

P. J. Pagni²

Introduction

The problem of flame spread is of both fundamental and applied interest. Fundamentally one would like to determine the precise mechanisms governing the flame propagation rate. From an applied standpoint, flame spread modeling is one of the simpler technical tasks within the literally terribly significant problem of fire safety [1].³

Flames spreading over solid fuels may be segregated according to the following criteria: (1) unsteady or steady propagation rates, (2) porous or solid fuels, (3) thermally thin or thick fuels, (4) natural or forced ambient flow, (5) ambient flow in the direction of propagation or opposed to it, and (6) laminar or turbulent flames. This study is restricted to steady propagation of turbulent flames over thin, low porosity fuels under forced ambient flows in the direction of flame propagation. The results apply to flame spread through fabrics and similar urban materials and through some types of forest floor litter. The analogous high porosity case has been examined [2]. Good agreement with experiment was obtained. The alternative problem of steady, laminar, opposed flow over solid fuels has also been examined [3, 4].

Experimental comparisons are not presented primarily because quantitative values of the required thermophysical properties are not yet available. Some useful experiments, aimed at providing this information, are underway [5].

¹ This work was supported by NSF Grant GK-43. The assistance of J. Han, R. Toossi and M. Sahota is appreciated.

² Assist. Professor, University of California, Berkeley, Calif.

³ Numbers in brackets designate References at end of technical brief.

Contributed by the Heat Transfer Division of THE AMERICAN SOCIETY OF MECHANICAL ENGINEERS. Manuscript received by the Heat Transfer Division September 4, 1974.

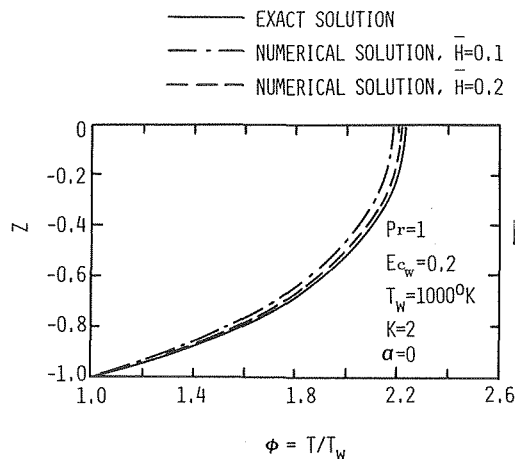


Fig. 2 Nonradiating solution, comparison of numerical solution for $\bar{H} = 0.1$ and 0.2 with exact solution

line-to-wall temperature ratio slightly greater than 2. The results presented in Fig. 2 are for a nonradiating solution ($\alpha = 0$) and are presented to indicate the accuracy of the finite-difference method for two different step sizes. Although it is recognized that the accuracy of the finite difference solution for the linear nonradiating solution does not guarantee a similar accuracy for the nonlinear radiating solution, the results of solutions based on different step sizes and different initial temperature profiles indicate that the convergence of the iterative procedure for the nonlinear solution is similar to that shown in Fig. 2.

The results of calculations for different values of the mean absorption coefficient α are presented in Fig. 3. These results indicate that a significant cooling effect is possible, as indicated by the reduction of the temperature near the center of the channel, for large values of α . This is in apparent contradiction to the results of Viscanta presented in reference [2], where the effect of radiation on the temperature profile is shown to be small for $\tau_0 \ll 1$. There are several important differences between Viscanta's results and the results of Fig. 3 however. Viscanta included the axial convection term, with the result that the radiative term is balanced by convective transport as well as conduction and viscous dissipation. In our model, the convective transport term is omitted, and as a consequence, the radiative transport of heat must be balanced against the conduction, viscous dissipation, and the MHD dissipation terms. Moreover, Viscanta's results are based on a constant value of T_w/T_c , which means that the profiles shown are not at the same axial position in the channel. Our results, without convec-

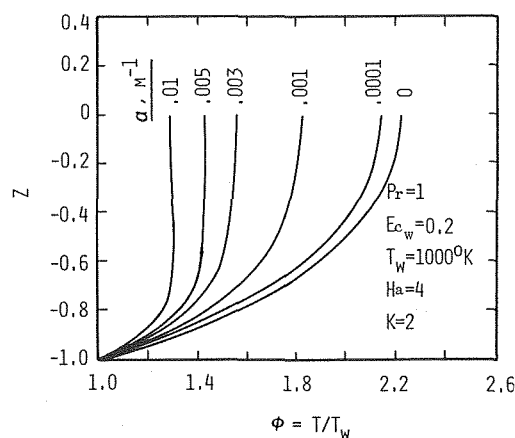


Fig. 3 Effect of mean absorption coefficient on temperature distribution in an MHD channel flow

tion, are presented at a fixed axial location, and consequently the effect of radiative cooling is more pronounced.

Concluding Remarks

The lower values of α ($\alpha \sim 0.0001/\text{m}$) are thought to be representative of conditions typically encountered in MHD channels employing seeded noble gases. For these devices, the effect of radiative cooling does not appear to be of major significance. However, MHD channels employing certain seeded combustion gas mixtures are likely to encounter higher values of the effective absorption coefficient. For these devices, the results of Fig. 3 indicate that the effect of radiative cooling could be significant, particularly when the coupling between the energy and momentum equation resulting from a consideration of the temperature dependency of the electrical conductivity is considered.

As a result, an extension of the present study to include the effects of axial convection, compressibility, and the temperature dependence of the electrical conductivity appears to be well-justified.

References

- 1 Sutton, G. W., and Sherman, A., *Engineering Magnetohydrodynamics*, McGraw-Hill, New York, 1965.
- 2 Sparrow, E. M., and Cess, R. D., *Radiation Heat Transfer*, Brooks/Cole Publishing Co., Belmont, Calif., 1966.
- 3 Wilson, Donald R., "Analysis of MHD Channel Flows by a Coupled Core Flow-Boundary Layer Model," PhD dissertation, The University of Texas at Arlington, Dec. 1973.

Flame Spread Over Thin Solid Fuels¹

P. J. Pagni²

Introduction

The problem of flame spread is of both fundamental and applied interest. Fundamentally one would like to determine the precise mechanisms governing the flame propagation rate. From an applied standpoint, flame spread modeling is one of the simpler technical tasks within the literally terribly significant problem of fire safety [1].³

Flames spreading over solid fuels may be segregated according to the following criteria: (1) unsteady or steady propagation rates, (2) porous or solid fuels, (3) thermally thin or thick fuels, (4) natural or forced ambient flow, (5) ambient flow in the direction of propagation or opposed to it, and (6) laminar or turbulent flames. This study is restricted to steady propagation of turbulent flames over thin, low porosity fuels under forced ambient flows in the direction of flame propagation. The results apply to flame spread through fabrics and similar urban materials and through some types of forest floor litter. The analogous high porosity case has been examined [2]. Good agreement with experiment was obtained. The alternative problem of steady, laminar, opposed flow over solid fuels has also been examined [3, 4].

Experimental comparisons are not presented primarily because quantitative values of the required thermophysical properties are not yet available. Some useful experiments, aimed at providing this information, are underway [5].

¹ This work was supported by NSF Grant GK-43. The assistance of J. Han, R. Toossi and M. Sahota is appreciated.

² Assist. Professor, University of California, Berkeley, Calif.

³ Numbers in brackets designate References at end of technical brief.

Contributed by the Heat Transfer Division of THE AMERICAN SOCIETY OF MECHANICAL ENGINEERS. Manuscript received by the Heat Transfer Division September 4, 1974.

Model

Most flame propagation over solid surfaces may be viewed qualitatively following manner. Energy released in the flame heats the fuel ahead of the flame raising its temperature. The flame front moves to that point over the solid where sufficient pyrolysis has occurred to exceed the lean flammability limit in the gas phase. Mass transport from the solid to the flame and subsequent combustion there completes the cycle. Steady propagation results when the rate of energy transport ahead of the flame is just sufficient to sustain the flame. The following approximations are appropriate: (1) energy transfer is rate controlling; (2) flame properties are assumed known. This assumption conveniently decouples the flame spread problem into a flame structure problem and an energy transport problem; (3) steady propagation exists; (4) the fuel temperature at the flame front is the ignition temperature. In general, the temperature at which significant pyrolysis occurs depends on the thermal history of the fuel, the rate of heating and the surrounding geometry. However, for many fuels the pyrolysis activation energy is so large that very small temperature variations ameliorate these unmanageable dependencies, especially over the limited range of oxidizer states consistent with urban fire safety problems; and (5) the energy absorbed by pyrolysis and water evaporation ahead of the flame is negligible.

In general, the fuel bed surface at the flame is not orthogonal to the propagation direction and numerical solutions are required. However, in the limiting case, when the time to burn through the thin slab of fuel is short compared to the flame propagation time, the flame configuration is given by Fig. 1. Note that the temperature field remains two-dimensional. The origin is placed on the flame of the length L . The fuel moves into the flame with the flame spread velocity. The fuel bed thickness is l . The imposed flow velocity is U_∞ ; Ω_s is the angle between the fuel bed normal and the gravity vector. The angle between the fuel bed normal and the flame is $\theta = \Omega_s + \Omega_w$, where $\Omega_w = \tan^{-1}(1.4 \text{ Re}/G^{0.5})$, with $\text{Re} = U_\infty L/\nu$ and $G = gL^3/\nu^2$, is an empirically determined [6] flame tilt angle.

Boundary Conditions

The fuel temperature at the flame is the ignition temperature $T'(0, y') = T_{ig}$. Far ahead of the flame, the fuel is at the ambient temperature $T'(\infty, y') = T_\infty$. Primes indicate dimensional quantities. The heat flux across the plane $y' = 0$ dominates the problem. The radiation contribution is

$$q_r(x') = a\epsilon \sigma T_{f1}^4 \{0.5 \exp[\tan \theta - x'/(L \cos \theta)]\} \quad (1)$$

where a is fuel absorptivity, ϵ is flame emissivity [7], T_{f1} is flame temperature and the shape factor is approximated by an exponential. Radiative cooling along the surface $y' = 0$, $x' > 0$ is neglected.

Convective heating by hot flame gases is approximated [2] as

$$q_c(x') = 0.37 \text{ Re}^{0.8} \text{ Pr}^{0.33} (k/L) \times (T_{f1} - T_f) \exp(-0.19 \text{ Pr}^{-0.67} x'/L) \quad (2)$$

Here $\text{Pr} = \nu/\alpha$, $T_f = 0.5(T_{ig} + T_\infty)$, and an averaged turbulent heat transfer coefficient for a flat plate, an averaged fuel surface temperature, and an approximate gas phase temperature distribution are used. The assumption of forced convection in equation (2), the exponential approximation in equation (1) and the empirical expression for Ω_w limit this analysis to $\theta \leq 45^\circ$. Once the general nature of the solution is known, a more accurate temperature field can be found from the coupled set of gas and solid phase momentum and energy equations. The boundary condition at the surface is now $\partial T'(0, x')/\partial y' = -(q_r + q_c)/k_f$. Similar transfer at the lower surface, $y' = l$, may be included as required. Introducing the non-dimensional quantities $T = (T' - T_\infty)/\Delta T$, $\Delta T = T_{ig} - T_\infty$, $x = x'/l$ and $y = y'/l$, the boundary conditions become

$$T(0, y) = 1 \quad T(\infty, y) = 0$$

$$\frac{\partial T}{\partial y}(x, 0) = -c_1 e^{-b_1 x} - c_2 e^{-b_2 x}, \quad \frac{\partial T}{\partial y}(x, 1) = c e^{-bx}$$

where

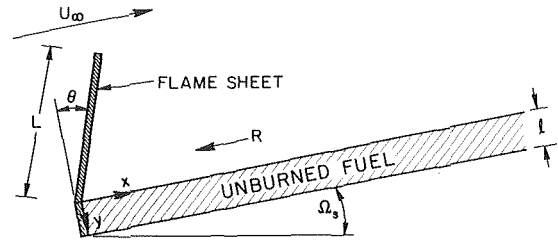


Fig. 1 Schematic of flame and fuel structure model

$$b_1 = l/(L \cos \theta), \quad c_1 = 0.5 \text{ St} \exp(\tan \theta) l/L, \\ b_2 = 0.19 \text{ Pr}^{-0.67} l/L, \quad c_2 = 0.37 \text{ Re}^{0.8} \text{ Pr}^{0.33} \eta_f l/L, \quad (3) \\ \eta_f = k(T_{f1} - T_f)/k_f \Delta T, \quad \text{and} \quad \text{St} = aL \epsilon \sigma T_{f1}^4/k_f \Delta T$$

is a Stefan number. The lower surface gradient is arbitrarily chosen as cooling with the same functional form.

Temperature Field

The governing equation is

$$\frac{\partial^2 T}{\partial x^2} + P \frac{\partial T}{\partial x} + \frac{\partial^2 T}{\partial y^2} = 0 \quad (4)$$

Where $P = Rl/\alpha_f$ is the Peclet number. The solution is obtained by superposition of four solutions to equation (4), T_i , each with one nonhomogeneous boundary condition. Finite cosine transforms in y reduce the Neumann conditioned problems to

$$\frac{d^2 \theta_i}{dx^2} + \frac{Pd\theta_i}{dx} - s^2 \pi^2 \theta_i = -c_i e^{-b_i x} \quad i = 1, 2, 3 \quad (5)$$

subject to

$$\theta_i(0) = 0 \quad \text{and} \quad \theta_i(\infty) = 0$$

where

$$c_3 = (-1)^{s+1} c, \quad b_3 = b$$

and

$$\theta_i(x, s) = \int_0^1 T_i(x, y) \cos(s\pi y) dy \quad s = 0, 1, 2, \dots$$

The solution to equation (5) is

$$\theta_i(x, s) = c_i [\exp(-b_i x) - \exp(-0.5P + \lambda)x]/(z_i^2 + s^2 \pi^2) \quad (6)$$

where

$$z_i^2 = b_i(P - b_i) \quad \text{and} \quad \lambda = 0.5P(1 + 4s^2 \pi^2/P^2)^{0.5}$$

Inverting equation (6) gives the solution,

$$T(x, y) = \sum_{i=1}^4 T_i(x, y) = \sum_{i=1}^3 \{\theta_i(x, 0) + 2 \sum_{s=1}^{\infty} \theta_i(x, s) \cos(s\pi y)\} + \exp(-Px) \quad (7)$$

This clearly satisfies the x conditions. Assume for brevity that the lower surface is adiabatic, $c = 0$. Introducing the Fourier expansion

$$\frac{\cosh(z(1-y))}{z \sinh z} = \frac{1}{z^2} + 2 \sum_{s=1}^{\infty} \frac{\cos(s\pi y)}{(z^2 + s^2 \pi^2)} \quad (8)$$

clarifies that the y conditions are satisfied.

$$T(x, y) = \sum_{i=1}^2 \{c_i \exp(-b_i x) \frac{\cosh(z_i(1-y))}{z_i \sinh z_i} - \frac{c_i \exp(-Px)}{z_i^2} - 2c_i \sum_{s=1}^{\infty} \frac{\exp(-(0.5P + \lambda)x)}{(z_i^2 + s^2 \pi^2)} \cos(s\pi y)\} + \exp(-Px) \quad (9)$$

In the limit $P \rightarrow \infty$, the isotherms move parallel to the surface and the thin fuel model is not valid. In the limit $P \rightarrow 0$, there is no en-

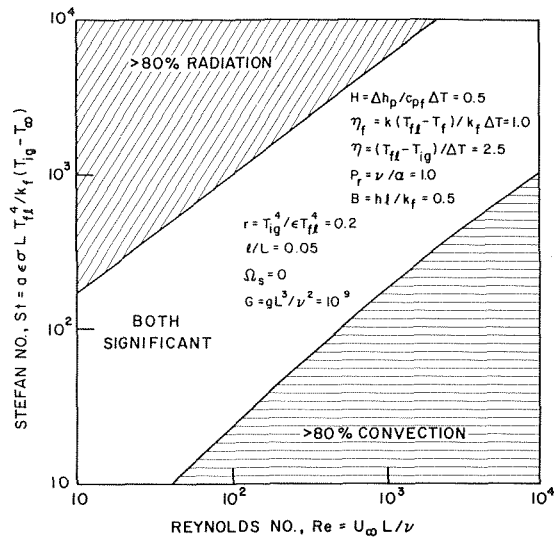


Fig. 2 Regions in parameter space (\sim flame height versus \sim imposed flow velocity) where convective or radiative preheating dominates, i.e., contributes more than 80 percent of the flame spread rate as given by equation (13). (values listed for the fixed parameters correspond approximately to cellulosic fuels)

ergy sink and a steady solution cannot exist. The thin fuel configuration, Fig. 1, is thus appropriate only for moderate Peclet number.

Flame Spread

Continuity requires that

$$\dot{m} = -Rl\rho_f \quad (10)$$

where \dot{m} is the mass loss rate per unit length of the line fire. An energy balance on the surface at $x' = 0$, $0 \leq y' \leq l$, similarly requires

$$q' = -\dot{m}\Delta h_p - k_f \int_0^l \frac{\partial T'}{\partial x'}(0, y') dy' \quad (11)$$

where Δh_p is the fuel enthalpy of pyrolysis and q' is the energy transport from the flame to the surface, $x' = 0$. The radiative and convective components to this end heating are, respectively, $a\sigma l(\epsilon T_{f1}^4 - T_{ig}^4)$ and $hl(T_{f1} - T_{ig})$ where h is an average heat transfer coefficient.

Introducing equations (9) and (10) into equation (11) yields the nondimensional flame spread rate,

$$P = (q + c_1/b_1 + c_2b_2)/(1 + H), \quad (12)$$

where

$$q = [a\sigma(\epsilon T_{f1}^4 - T_{ig}^4) + h(T_{f1} - T_{ig})] l/k_f \Delta T$$

and

$$H = \Delta h_p/c_{pf} \Delta T.$$

Rearranging equation (12) using equation (3) gives

$$P = \{St[0.5 \cos \theta \exp(\tan \theta) + l/L(1 - r)] + B\eta + 2Re^{0.3}Pr\eta_f\}/(1 + H) \quad (13)$$

where $r = T_{ig}^4/\epsilon T_{f1}^4$, $B = hl/k_f$ and $\eta = (T_{f1} - T_{ig})/\Delta T$. The first and last terms are due to the radiative and convective heating of the upper surface. The second and third terms describe the inputs along $x = 0$, which are small compared to the upper surface fluxes. As shown in Fig. 2, radiation dominates when L is large and $U_\infty \rightarrow 0$. Convection dominates small flames with strong imposed flow. For most conditions both terms are significant.

In summary, analytic expressions for the fuel temperature field and flame spread rate have been obtained for thin nonporous fuels. The import of radiative and convective effects has been approximately quantified.

References

- 1 "America Burning," National Commission on Fire Prevention and Control, U.S. Gov. Printing Office, Washington, D.C., 1973.
- 2 Pagni, P. J., and Peterson, T. G., "Flame Spread Through Porous Fuels," Fourteenth Symp. (Int'l) on Combustion, The Combustion Institute, Pittsburgh Pa., 1973, pp. 1099-1107.
- 3 de Ris, J. N., "Spread of a Laminar Diffusion Flame," Twelfth Symp. (Int'l) on Combustion, The Combustion Institute, Pittsburgh Pa., 1971, pp. 241-252.
- 4 Magee, R. S., and McAlevy, R. F., "The Mechanism of Flame Spread," Journal of Fire and Flammability, Vol. 2, 1971, pp. 271-297.
- 5 Wulff, W., et al., "Study of Hazards From Burning Apparel and the Relation of Hazards to Test Methods," Final Reports, Mechanical Engineering, Georgia Institute of Technology, Atlanta, Ga., 1971, 1972.
- 6 Putnam, A. A., "A Model Study of Wind-Blown Free-Burning Fires," Tenth Symposium (Int'l) on Combustion, The Combustion Institute, Pittsburgh Pa., 1965, pp. 1039-1046.
- 7 Felske, J. D., and Tien, C. L., "Calculation of the Emissivity of Luminous Flames," Combustion Science and Technology, Vol. 7, 1973, pp. 25-31.

Numerical Prediction of High Altitude Zero-Pressure Balloon Vertical Motion

J. F. Kreider¹ and F. Kreith²

Nomenclature

- A = area
- C_D = drag coefficient
- C_M = virtual displacement coefficient
- c_v = specific heat at constant volume
- d = thickness
- \dot{E} = exhaust rate of balloon gas through expulsion duct and valve
- L_F = free lift, see [1]³
- M = molecular weight
- m = mass
- P = pressure
- q_1 = rate of heat transfer by convection from the skin to the lift gas
- q_2 = rate of adsorption of solar radiation
- q_3 = rate of adsorption of infrared radiation
- q_4 = rate of heat transfer by convection from the atmosphere to the skin
- q_5 = rate of radiant heat transfer from the skin
- R = universal gas constant
- S = surface area
- T = temperature
- t = time
- U = velocity
- V = volume
- z = altitude of geometric height
- ρ = mass density
- $Re = \frac{UV^{1/3} \times 1.24}{\nu}$ (Reynolds number based on diameter of equivalent sphere)

¹ President, Environmental Consulting Services, Boulder, Colo., and Consultant to National Scientific Balloon Facility.

² Professor, University of Colorado, and Consultant to National Scientific Balloon Facility, Environmental Consulting Services, Inc., Boulder, Colo.

Contributed by the Heat Transfer Division of THE AMERICAN SOCIETY OF MECHANICAL ENGINEERS. Manuscript received by the Heat Transfer Division March 4, 1974.

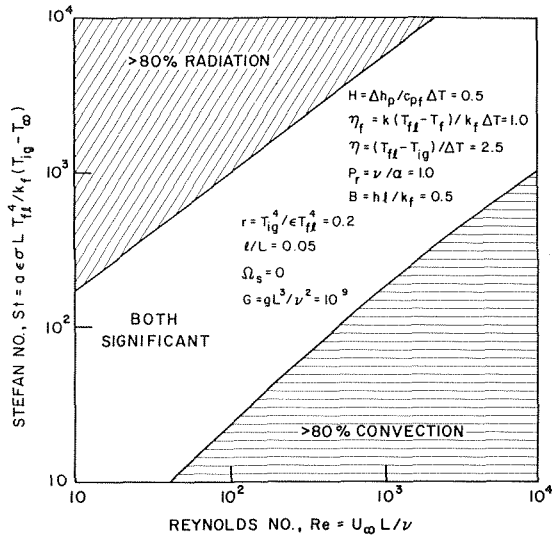


Fig. 2 Regions in parameter space (\sim flame height versus \sim imposed flow velocity) where convective or radiative preheating dominates, i.e., contributes more than 80 percent of the flame spread rate as given by equation (13). (values listed for the fixed parameters correspond approximately to cellulosic fuels)

ergy sink and a steady solution cannot exist. The thin fuel configuration, Fig. 1, is thus appropriate only for moderate Peclet number.

Flame Spread

Continuity requires that

$$\dot{m} = -Rl\rho_f \quad (10)$$

where \dot{m} is the mass loss rate per unit length of the line fire. An energy balance on the surface at $x' = 0$, $0 \leq y' \leq l$, similarly requires

$$q' = -\dot{m}\Delta h_p - k_f \int_0^l \frac{\partial T'}{\partial x'}(0, y') dy' \quad (11)$$

where Δh_p is the fuel enthalpy of pyrolysis and q' is the energy transport from the flame to the surface, $x' = 0$. The radiative and convective components to this end heating are, respectively, $a\sigma l(\epsilon T_{ff}^4 - T_{ig}^4)$ and $hl(T_{ff} - T_{ig})$ where h is an average heat transfer coefficient.

Introducing equations (9) and (10) into equation (11) yields the nondimensional flame spread rate,

$$P = (q + c_1/b_1 + c_2b_2)/(1 + H), \quad (12)$$

where

$$q = [a\sigma(\epsilon T_{ff}^4 - T_{ig}^4) + h(T_{ff} - T_{ig})]l/k_f\Delta T$$

and

$$H = \Delta h_p/c_{pf}\Delta T.$$

Rearranging equation (12) using equation (3) gives

$$P = \{St[0.5 \cos \theta \exp(\tan \theta) + l/L(1 - r)] + B\eta + 2Re^{0.3}Pr\eta_f\}/(1 + H) \quad (13)$$

where $r = T_{ig}^4/\epsilon T_{ff}^4$, $B = hl/k_f$ and $\eta = (T_{ff} - T_{ig})/\Delta T$. The first and last terms are due to the radiative and convective heating of the upper surface. The second and third terms describe the inputs along $x = 0$, which are small compared to the upper surface fluxes. As shown in Fig. 2, radiation dominates when L is large and $U_{\infty} \rightarrow 0$. Convection dominates small flames with strong imposed flow. For most conditions both terms are significant.

In summary, analytic expressions for the fuel temperature field and flame spread rate have been obtained for thin nonporous fuels. The import of radiative and convective effects has been approximately quantified.

References

- 1 "America Burning," National Commission on Fire Prevention and Control, U.S. Gov. Printing Office, Washington, D.C., 1973.
- 2 Pagni, P. J., and Peterson, T. G., "Flame Spread Through Porous Fuels," Fourteenth Symp. (Int'l) on Combustion, The Combustion Institute, Pittsburgh Pa., 1973, pp. 1099-1107.
- 3 de Ris, J. N., "Spread of a Laminar Diffusion Flame," Twelfth Symp. (Int'l) on Combustion, The Combustion Institute, Pittsburgh Pa., 1971, pp. 241-252.
- 4 Magee, R. S., and McAlevy, R. F., "The Mechanism of Flame Spread," Journal of Fire and Flammability, Vol. 2, 1971, pp. 271-297.
- 5 Wulff, W., et al., "Study of Hazards From Burning Apparel and the Relation of Hazards to Test Methods," Final Reports, Mechanical Engineering, Georgia Institute of Technology, Atlanta, Ga., 1971, 1972.
- 6 Putnam, A. A., "A Model Study of Wind-Blown Free-Burning Fires," Tenth Symposium (Int'l) on Combustion, The Combustion Institute, Pittsburgh Pa., 1965, pp. 1039-1046.
- 7 Felske, J. D., and Tien, C. L., "Calculation of the Emissivity of Luminous Flames," Combustion Science and Technology, Vol. 7, 1973, pp. 25-31.

Numerical Prediction of High Altitude Zero-Pressure Balloon Vertical Motion

J. F. Kreider¹ and F. Kreith²

Nomenclature

- A = area
- C_D = drag coefficient
- C_M = virtual displacement coefficient
- c_v = specific heat at constant volume
- d = thickness
- \dot{E} = exhaust rate of balloon gas through expulsion duct and valve
- L_F = free lift, see [1]³
- M = molecular weight
- m = mass
- P = pressure
- q_1 = rate of heat transfer by convection from the skin to the lift gas
- q_2 = rate of adsorption of solar radiation
- q_3 = rate of adsorption of infrared radiation
- q_4 = rate of heat transfer by convection from the atmosphere to the skin
- q_5 = rate of radiant heat transfer from the skin
- R = universal gas constant
- S = surface area
- T = temperature
- t = time
- U = velocity
- V = volume
- z = altitude of geometric height
- ρ = mass density
- $Re = \frac{UV^{1/3} \times 1.24}{\nu}$ (Reynolds number based on diameter of equivalent sphere)

¹ President, Environmental Consulting Services, Boulder, Colo., and Consultant to National Scientific Balloon Facility.

² Professor, University of Colorado, and Consultant to National Scientific Balloon Facility, Environmental Consulting Services, Inc., Boulder, Colo.

Contributed by the Heat Transfer Division of THE AMERICAN SOCIETY OF MECHANICAL ENGINEERS. Manuscript received by the Heat Transfer Division March 4, 1974.

Subscripts

- a = atmospheric air
- B = ballast
- b = balloon system
- d = ducting
- f = balloon skin fabric
- g = balloon gas
- p = payload
- v = valve

Introduction

A detailed analysis of the dynamics and heat transfer characteristics of zero-pressure, high altitude, plastic-film balloons is presented in reference [1]. This analysis shows that the vertical motion of such balloons can be modeled mathematically by six simultaneous, nonlinear, ordinary differential equations, but evaluates the nonconstant coefficients in these equations from conventional heat transfer and drag coefficient correlations for spheres. However, zero-pressure balloons are shaped more like onions and the values of the coefficients obtained from correlations for spheres can be improved to yield better agreement between the predicted and the observed vertical motion of zero-pressure balloons by using data from carefully monitored flights. This note presents the empirical flight correlation method used to obtain improved values for the convection heat transfer coefficients to the interior and from the exterior surfaces of such balloons.

The asymmetric, time dependent geometric configuration of zero-pressure, high altitude balloons presents significant difficulty in computing inner and outer convective heat transfer coefficients numerically; therefore, the empirical method described herein has been used to quantify the several convective regimes which occur during a balloon flight.

If the equations of motion, conservation of mass, and the first law of thermodynamics for a balloon system are formulated with the averaging assumptions outlined in [1], the vertical balloon trajectory is described by the following set of simultaneous differential equations:

$$L_F - 1/2 C_D \rho_a \left| \frac{dz}{dt} \right| \frac{dz}{dt} A_b = [m_g + m_f + m_B + m_p + C_M \rho_a V_g] \frac{d^2 z}{dt^2} \quad (1)$$

$$\frac{dV_g}{dt} = \frac{R}{M_g P_a} (m_g \frac{dT_g}{dt} + T_g \frac{dm_g}{dt} + \frac{g m_g \bar{T}_g M_a}{RT_a} \frac{dz}{dt}) \quad (2)$$

$$\frac{dm_g}{dt} = \rho_{ga} \dot{E}_a + \rho_{gv} \dot{E}_v \quad (3)$$

$$\frac{d}{dt} (c_v m \bar{T})_g = q_1 + \frac{RT_g}{M_g} \frac{dm_g}{dt} - P_a \frac{dV_g}{dt} + (c_v \bar{T})_g \frac{dm_g}{dt} \quad (4)$$

$$\frac{d}{dt} \int \int_{S_f} c_f \rho_f d_f T_f dS_f = c_f m_f \frac{dT_f}{dt} = q_2 + q_3 + q_4 - q_5 - q_1 \quad (5)$$

$$U = dz/dt \quad (6)$$

The dependent variables in these equations are the balloon lift-gas temperature, the balloon fabric temperature, the balloon volume, the balloon lift-gas mass, the vertical velocity of the balloon, and the balloon altitude.

In order to obtain a unique solution to these six equations it is necessary to specify a number of additional parameters as well as the initial conditions. The most important of these parameters are the transport properties, the molecular weight, and the specific heat of the balloon lift-gas; the balloon fabric solar and infrared radiation absorptance; the balloon system weight and its volume; the

"black ball" radiometer profile which describes the IR radiation field seen by the balloon and the atmospheric temperature profile. In addition, the following initial conditions must be specified: time of launch (GMT) and date, latitude and longitude of launch site, the initial "free lift," and the initial temperatures of the balloon fabric and lift-gas. In all, a total of 33 parameters and initial conditions are necessary for a solution to the set of equations. Since the equations are nonlinear with nonconstant coefficients, a computerized numerical method is required for their solution.

Computer Model and Sensitivity Analysis

The FORTRAN program developed for this study and detailed instructions for its use are presented in reference [2]. All but five of the 33 parameters and initial conditions required for a solution of the equation set may be readily specified to good accuracy by reference to handbooks, *The American Ephemeris and Nautical Almanac*, radiosonde data, and measurements normally made at a balloon launch site.

The parameters more difficult to evaluate are:

- 1 internal convection coefficient;
- 2 external convection coefficient;
- 3 fabric, multiple-pass solar absorptance;
- 4 fabric, multiple-pass infrared absorptance;
- 5 black ball profile.

The last of these parameters, the black ball profile can, however, be specified by a simple rule of thumb which has previously been found to be approximately correct for many balloon flights [2]. According to this rule the black ball temperature decreases linearly from its surface value to 75 percent of that value at the tropopause and remains uniform above the tropopause. Once the balloon has ascended to the tropopause nearly all infrared radiation sources lie below it. Since a parameter sensitivity analysis showed that, of the five parameters which were not known precisely, the fabric infrared absorptance and black ball profile have the smallest effect on balloon ascent-phase behavior, this simplified treatment of the black ball profile was considered adequate. However, during the float phase after sunset, the infrared radiation environment and fabric absorptance are more important in determining the balloon energy balance and float altitude. Fabric infrared absorptance values for both polyester (polyethylene terephthalate) and polyethylene balloon films as given in reference [3] were used. The asymptotic (tropopause) value of black ball temperature described the infrared environment at float adequately for the model calibration.

The multiple-pass solar radiation absorptance, to which balloon performance was found to be more sensitive, was evaluated by a method described in reference [3], where solar absorptance data for more than 50 samples of balloon fabrics are given. However, the convection coefficients for the interior surface, which the sensitivity analysis showed to be the most important of the five parameters, and for the exterior surface of the balloon were the most difficult to evaluate since heretofore no heat transfer measurements or theoretical analyses have been made on objects having the shape and the size of balloons (a fully inflated balloon can be as large as a football field). These two parameters were considered to be adjustable in the model-calibration computer runs. The parameterizations of the convection coefficients (equations (18), (20), and (29) in [1]), which assumed the balloon to be a sphere, were used as the first approximations for q_1 and q_4 in the model calibration described in the following.

Model Validation and Evaluation of Convection Coefficients

In order to develop a fundamentally accurate model with a minimum of adjustable coefficients, all parameters except the two convection coefficients were evaluated independently from information in the literature or measurements taken at the balloon launch site. The two adjustable coefficients in the computer model were

¹ Numbers in brackets designate References at end of technical brief.

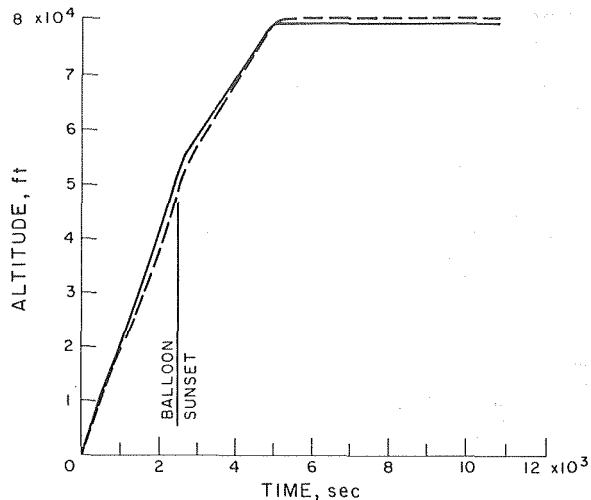


Fig. 1 Vertical trajectory of stratoscope S4-2 Flight. July, 1965, 5.5 million ft³ Mylar balloon, He lift-gas. Solid line-model prediction; dashed line-flight data.

calibrated using data provided by the National Scientific Balloon Facility from four recent, accurately monitored, zero-pressure balloon flights. These flights spanned a twenty-fold range of balloon volume, daytime and nighttime launches, both hydrogen and helium lift gases, and polyester and polyethylene balloon materials. The measured time-altitude trajectories of two of the calibration flights are shown in Figs. 1 and 2 along with the model predictions, using the best fit values for the internal and external convection coefficients. The agreement is seen to be excellent during both the ascent and float phases. Based upon the results of the present model calibration it is suggested that for zero-pressure balloons, the rate of convection heat transfer q_4 from the atmosphere to the balloon fabric be increased by 50 percent over the value calculated from equations (18) and (20) in [1] and that q_1 , the heat transfer between the fabric and the lift gas, be increased by a factor of three over the value computed from equation (29) in [1]. These suggested values of convective coefficients have been determined for large plastic balloons. Their use for other, similar enclosures should be undertaken only with care. It should be noted that in a survey of free convection in enclosures Ostrach [4] concluded that published free convection Nusselt number correlations contain variations of the same order of magnitude as those found in this study. In the absence of any extant theoretical analyses of convection in a balloon-like enclosure, only the present empirical result can be cited for the proposed three-fold magnitude change which lies within the accuracy band of prior enclosed-convection measurements.

As described in reference [2], an asymptotic value of the fully turbulent drag coefficient $C_D = 0.5$ was found appropriate for a zero-pressure balloon for $Re > 3 \times 10^5$. This value is 67 percent greater than the analogous asymptotic value for a sphere. Reynolds' analogy, as extended by Von Karman, would then predict a heat transfer coefficient, for the exterior of a balloon, 67 percent greater than that for a sphere. The best-fit convection coefficient value of 50 percent greater heat transfer for a balloon in fully turbulent flow would then seem to be justified by the Reynolds analogy for forced convection.

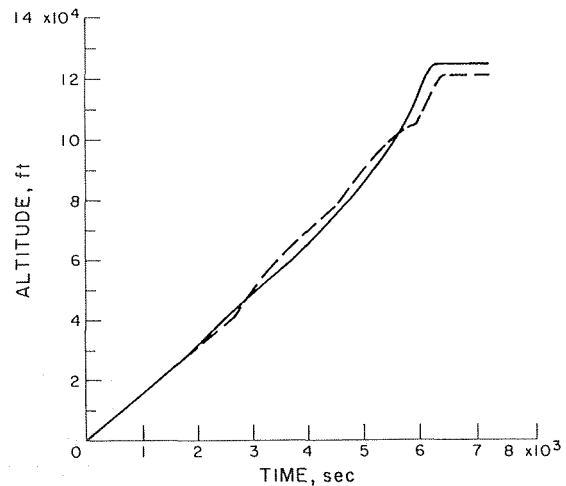


Fig. 2 Vertical trajectory of hydrogen flight. July, 1970, 1.5 million ft³ polyethylene balloon, H₂ lift-gas. Solid line-model prediction; dashed line-flight data.

Figs. 1 and 2 show a model float altitude prediction 1 percent higher than measured and 2 percent lower than measured, respectively. All four model calibration flights [2] showed measured float levels differing from predicted float levels by 2 percent at most. This accuracy is considered to be good, although some improvement might be possible by using a more detailed analysis of the infrared environment at float. Such refinement is not judged to be warranted, however, since a 1 percent rms prediction of float altitude is entirely acceptable in the scientific ballooning community.

In addition to trajectory correlations, it is possible to validate a computer model by correlating measured and computed balloon fabric and gas temperatures during a flight. However, in order to determine flight values of the average temperatures, \bar{T}_f and \bar{T}_g , upon which model computations are based, an unmanageably large grid of thermocouples or thermistors would be needed inside the balloon and on its surface. However, field measurements of local fabric and gas temperatures show the same trends as the model computations of average temperature, although numerical equivalence is not achieved because the small sample of gas and fabric temperatures measured does not permit an accurate calculation of space-averaged values of T_f and T_g .

Acknowledgment

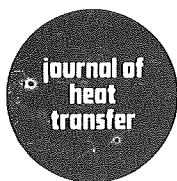
Acknowledgment is made to the National Center for Atmospheric Research, sponsored by the National Science Foundation, for computer time used in this research. The work was conducted under contract No. 36563-72 with the National Scientific Balloon Facility.

1 Kreith, F., "Thermal Design of High-Altitude Balloons and Instrument Packages," *JOURNAL OF HEAT TRANSFER*, TRANS. ASME, Series C, Vol. 92, Aug. 1970, pp. 307-332.

2 Kreith, F., and Kreider, J. F., *Numerical Prediction of the Performance of High Altitude Balloons*, TN/STR-65, National Center for Atmospheric Research, Boulder, Colo., 1974, 132 pp.

3 Dingwell, I. W., *Thermal Radiation Properties of Some Polymer Balloon Fabrics*, A. D. Little, Inc., Cambridge, Mass., 1967, 43 pp.

4 Ostrach, S., "Natural Convection in Enclosures," *Advances in Heat Transfer*, Vol. 8, Academic Press, Inc., New York, 1972, pp. 161-226.



Development and Evaluation of a Remote Sensing Technique for Determining the Temperature Distribution in Semitransparent Solids¹

J. V. Beck.² The authors are to be complimented for an excellent paper on recovering internal temperatures in semitransparent solids utilizing measurements of the emerging spectral emission. The method developed is correctly termed a remote sensing technique, but it is important to realize that it is just one of many inverse problems. Determination of constants in mathematical models utilizing measurements includes many inverse problems and is a discipline that is now called parameter estimation. Recognition that a problem involves parameter estimation opens up the results of the past decade's considerable research on related inverse problems. For example, many insights, numerical procedures, and computer programs have been developed [1-3].³

Since measurements invariably contain errors, parameter estimation is firmly based on probability and statistics. The authors are well aware that measurements are not errorless; consequently, they have investigated the effects of errors. Apparently the errors investigated in the paper are additive; are independent; and have a zero mean, constant variance, and a Gaussian distribution. These conditions are distinct and individually important, but are not all explicitly stated. Some readers might think that the work "random" implies independence, but it does not. When many measurements are taken for one "specimen," the errors may be random, but they are not necessarily independent. In contrast to independent errors, correlated errors appear to be related. An example of this is when the measurements are consistently high for many consecutive time steps. An inspection of a number of figures in the same issue of the JOURNAL OF HEAT TRANSFER suggests that correlated errors are quite common. Some examples are Fig. 4 of [4], Fig. 2 of [5], and Fig. 4 of [6]. (Incidentally, each of these examples involves estimating parameters.) If the errors are indeed correlated rather than independent, one might desire to use some other method instead of least squares [7] or to investigate certain types of correlated errors in feasibility studies.

The paper mentions two optimization problems. The first—the major one considered—involves minimizing the sum of squares function. The second one involves the optimum experiment design, but no basic criterion is utilized. Contributions of parameter estimation include a basic criterion for optimum experiments and methods for employing it. See, for example, reference [2, p. 266], where the Δ criterion involving sensitivity coefficients is discussed. Also see reference [1, p. 264]

¹ By R. E. Chupp and R. Viskanta, published in the Aug. 1974 issue of the JOURNAL OF HEAT TRANSFER, TRANS. ASME, Series C, Vol. 96, pp. 391-397.

² Professor, Department of Mechanical Engineering, Michigan State University, East Lansing, Mich.

³ Numbers in brackets designate Additional References at end of discussion.

Additional References

- 1 Bard, Y., *Nonlinear Parameter Estimation*, Academic Press, New York, 1974.
- 2 Himmelblau, D. M., *Process Analysis by Statistical Methods*, Wiley New York, 1970.
- 3 Beck, J. V., and Arnold, K. J., *Parameter Estimation in Engineering and Science*, Bound notes, Michigan State University, 1974.
- 4 Copley, J. A., and Thomas, W. C., "Two-Dimensional Transient Temperature Distribution in Cylindrical Bodies With Pulsating Time and Space Dependent Boundary Conditions," JOURNAL OF HEAT TRANSFER, TRANS. ASME, Series C, Vol. 96, 1974, pp. 300-306.
- 5 Clift, R., Grace, J. R., and Sallazzo, V., "Continuous Slug Flow in Vertical Tubes," JOURNAL OF HEAT TRANSFER, TRANS. ASME, Series C, Vol. 96, 1974, pp. 371-376.
- 6 Chiesa, F. M., and Guthrie, R. I. L., "Natural Convective Heat Transfer Rates During the Solidification and Melting of Metals and Alloy Systems," JOURNAL OF HEAT TRANSFER, TRANS. ASME, Series C, Vol. 96, 1974, pp. 377-384.
- 7 Beck, J. V., "Parameter Estimation With Cumulative Errors," *Technometrics*, Vol. 16, No. 1, 1974, pp. 85-92.

Authors' Closure

The authors wish to thank Professor Beck for his relevant comments. The information on recent literature is particularly valuable, and the discussion of the types of errors involved in the inversion problem is especially appreciated. The optimization procedure employed in the inversion technique was chosen because it had been applied successfully to many nonlinear problems and was readily available. The experiment was designed to be as simple as possible while still yielding the desired spectral emission data. The results presented in the paper demonstrate the feasibility and potential of the approach. We realize that the optimization technique, error criterion, and experiment could be improved. However, recovery of the temperature distribution from remotely sensed spectral emission data is somewhat unique among the numerous inverse problems. We would therefore welcome parameter estimation studies using procedures developed in references [1, 2, 3 and 7] cited by Professor Beck to improve the technique. Experimental spectral emission data presented in references [5, 25, and 26] of the paper might be useful in these studies.

Transient Heat Transfer Analysis of Alloy Solidification

Y. K. Chuang² The authors have demonstrated successfully the use of heat-balance integral technique in solving moving boundary problems in a binary system. One special feature of this work is the treatment of various types of solidification progressions with convective boundary condition at the surface, which corresponds to many practical situations frequently encountered in engineering.

For a multicomponent system, special attention has to be paid to the solute rejection and diffusion in connection with the solidification. Owing to the lower solubility in the solid, the concentration is being continuously enriched in the liquid phase by the solute rejected from the interface. This would increase the interface concentration from time to time, which causes certain concentration differences inside the solid known as the microsegregation.

¹ By J. C. Muehlbauer, J. D. Hatcher, D. W. Lyons, and J. E. Sunderland, published in the Aug. 1973 issue of JOURNAL OF HEAT TRANSFER, TRANS. ASME, Series C, Vol. 95, No. 3, pp. 324, 331.

² Max-Planck-Institut für Eisenforschung GMBH, Düsseldorf, West Germany.

Obviously, the resulting solidification would depend on the extent of solute diffusion and on the partition coefficient between the solid and the liquid.

While complete treatment of the coupled problem is rather complicated, limiting cases do exist in the circumstances when the diffusion is either too slow or too fast. A particular example is the solidification of a plain carbon steel, which has negligible carbon microsegregation under the usual casting condition [1]. Therefore, the solidification can be readily predicted by solving numerically or approximately [2, 3] the conduction equation, with local solidification extent determined by thermodynamic equilibrium.

In general, the heat generation rate in the mushy zone can be written as $\lambda \partial f_s / \partial t$, where f_s represents the solid fraction at certain position. As an approximation in this paper, the f_s is assumed to be a linear function of the temperature, which leads to $-\lambda \Delta T$ as presented in the form of pseudospecific heat \tilde{C}_p . Since the actual solidus temperature is always below the equilibrium value as a result of the segregation, certain error would be introduced in case that normal ΔT is assumed.

The solidification of a Pb-Sn alloy (50-50 or 80-20) involves fairly small diffusion rate of Sn in the solid, and thus a substantial deviation from the equilibrium solidification is to be expected. Furthermore, the two phase region would terminate at the point where temperature is 183 deg C because of the eutectic solidification and thus an extra heat source term must be added to equations (6d) and (14c).

Finally, the accuracy of the calculation must be further judged from the agreement with experimental results in predicting the positions at various solid fractions. This is thought to be one of the most important pieces of information required for determining the final material structure.

Additional References

- 1 Chuang, Y. K., Wepner, W., and Schwerdtfeger, K., "Berechnung der interdendritischen Anreicherung von Kohlenstoff und Sauerstoff bei der Erstarrung von Stahl," *Arch. Eisenhüttenwes.*, Vol. 44, 1973, p. 243.
- 2 Chuang, Y. K., and Schwerdtfeger, K., "Experimentelle und theoretische Untersuchung der Erstarrung einer Eisen-Kohlenstoff-Legierung mit 0.6%C," *Arch. Eisenhüttenwes.*, Vol. 44, 1973, p. 341.
- 3 Schwerdtfeger, K., "Anwendung der Methode des Warmebilanz-integrals zur Berechnung der Erstarrungsgeschwindigkeit von Eisen-Kohlenstoff-Legierungen," *Arch. Eisenhüttenwes.*, Vol. 44, 1973, p. 411.

Laminar Film Condensation on Nonisothermal and Arbitrary-Heat-Flux Surfaces and on Fins¹

M. Ünsal² and W. C. Thomas,³ The authors have analyzed various nonisothermal wall condensation problems. Their similarity solution results, however, are different from the results in [12]⁴ where the same problem was solved by perturbation methods. It is shown in [12] that the solution of equations (1) and (3) subject to conditions (2) and (4) reduces to the solution from a Nusselt-type

¹ By J. H. Lienhard and V. K. Dhir, published in the May 1974 issue of the JOURNAL OF HEAT TRANSFER, TRANS. ASME, Series C, Vol. 96, No. 2, pp. 197-203.

² Research Assistant, Mechanical Engineering Department, Virginia Polytechnic Institute and State University, Va.

³ Assoc. Professor, Mechanical Engineering Department, Virginia Polytechnic Institute and State University, Va.

⁴ Numbers in brackets designate Additional References at end of discussion.

analysis as $\eta_0 \rightarrow 0$. We note, that introducing the expressions corresponding to the Nusselt analysis

$$F = -\frac{\eta^3}{6} + \eta_0 \frac{\eta^2}{2}, \quad \theta = 1 - \frac{\eta}{\eta_0} \quad (42)$$

and taking

$$\frac{1}{\eta_0^4} > > 1 \quad (43)$$

in equations (14) and (17), the result is $B = (\frac{1}{3}m + 1)^{1/4}$ which agrees with Fig. 5. The results in [12], however, give $B = (m + 1)^{1/4}$ which corresponds precisely to a Nusselt-type solution. It appears that the authors have neglected an inconsistency in their analysis. They transform equation (13) into (14) assuming that $\theta'(0)$ is constant (independent of x). Subsequently, they find in equation (17) that $\theta'(0)$ varies with x —a consequence which is not strictly consistent with a similarity hypothesis [13].

In order to be consistent, it would be necessary to transform (13) into (14) taking into account the variation of $\theta'(0)$ with x , i.e., introducing (5) into (13), and integrating the left side of (13) by parts to obtain

$$\frac{c_p \Delta T}{h_{fg}} = - (4m + 3) F(\eta_0) [\theta'(0) + (4m + 3) \int_0^{\eta_0} \theta F' d\eta - \frac{1}{x^{m+3/4}} \int_0^x x^{m+3/4} \frac{d\theta'(0)}{dx} dx]^{-1} \quad (44)$$

If (17), (42), (43), and (44) are used to evaluate B , the result is $B = (m + 1)^{1/4}$. With the latter value of B , the solution of the full boundary layer equations approaches the results from a Nusselt-type analysis as $\eta_0 \rightarrow 0$. We would be interested in the authors comments as to whether their calculations establish the validity of (42) and (43) in the limit as $c_p \Delta T / h_{fg} \rightarrow 0$. If their numerical solutions approach equation (42) and justify (43) in this limit then the difference in the values of B may be only a result of the inconsistency in the transformation. This could account for the differences, which are quite significant for $m < 0$, in the heat transfer solutions from the two theories.

Additional References

- 12 Ünsal Mazhar, and Thomas, W. C., "Perturbation Solutions for Laminar Film Condensation on a Vertical Non-Isothermal Wall," to be published.
- 13 Hansen, A. G., *Similarity Analyses of Boundary Value Problems in Engineering*, Prentice-Hall, Inc., Englewood Cliffs, N. J., 1964, pp. 9-11.

Author's Closure

The authors would like to thank Mr. Ünsal and Professor Thomas for the interest they have shown in our paper. In the first part of the paper we carried out local similar solutions of the boundary layer equations for film condensation on a nonisothermal wall. Our aim in this part of the paper was to show that for practical applications, Nusselt-Rohsenow theory gave results which were reasonably accurate. However, while making an overall energy balance over a certain length of the film, we should have made a correction for the x -dependency of $\theta'(0)$. The discussers have rightly pointed it out. As $c_p \Delta T / h_{fg} \rightarrow 0$, the ratio of local Nusselt numbers for local similar solutions and Nusselt-Rohsenow theory would then approach unity for all values of m greater than -1 .

For very small values of $c_p \Delta T / h_{fg}$, the inertia contribution becomes negligible and it is quite justified to assume the velocity and temperature profiles given by equation (42). The computer solutions do verify this. The velocity profiles for negative values of m have a point of inflexion at a distance of about $0.6 \eta_0$ from the wall.